Issues 1-4

2018 | Volume 14

The Journal on Advanced Studies in Theoretical and Experimental Physics, including Related Themes from Mathematics

PROGRESS IN PHYSICS

“All scientists shall have the right to present their scientific research results, in whole or in part, at relevant scientific conferences, and to publish the same in printed scientific journals, electronic archives, and any other media.” — Declaration of Academic Freedom, Article 8

ISSN 1555-5534

The Journal on Advanced Studies in Theoretical and Experimental Physics, including Related Themes from Mathematics

PROGRESS IN PHYSICS

A quarterly issue scientific journal, registered with the Library of Congress (DC, USA). This journal is peer reviewed and included in the abstracting and indexing coverage of: Mathematical Reviews and MathSciNet (AMS, USA), DOAJ of Lund University (Sweden), Scientific Commons of the University of St. Gallen (Switzerland), Open-J-Gate (India), Referativnyi Zhurnal VINITI (Russia), etc.

Electronic version of this journal:
http://www.ptep-online.com

Postal Address

Department of Mathematics and Science,
University of New Mexico,
705 Gurley Ave., Gallup, NM 87301, USA

ISSN: 1555-5534 (print)
ISSN: 1555-5615 (online)

Standard Address Number: 297-5092
Printed in the United States of America

January 2018 **Vol. 14, Issue 1**

CONTENTS

Information for Authors

Progress in Physics has been created for rapid publications on advanced studies in theoretical and experimental physics, including related themes from mathematics and astronomy. All submitted papers should be professional, in good English, containing a brief review of a problem and obtained results.

All submissions should be designed in LaTeX format using *Progress in Physics* template. This template can be downloaded from *Progress in Physics* home page http://www.ptep-online.com

Preliminary, authors may submit papers in PDF format. If the paper is accepted, authors can manage LaTeXtyping. Do not send MS Word documents, please: we do not use this software, so unable to read this file format. Incorrectly formatted papers (i.e. not LaTeXwith the template) will not be accepted for publication. Those authors who are unable to prepare their submissions in LaTeXformat can apply to a third-party payable service for LaTeX typing. Our personnel work voluntarily. Authors must assist by conforming to this policy, to make the publication process as easy and fast as possible.

Abstract and the necessary information about author(s) should be included into the papers. To submit a paper, mail the file(s) to the Editor-in-Chief.

All submitted papers should be as brief as possible. Short articles are preferable. Large papers can also be considered. Letters related to the publications in the journal or to the events among the science community can be applied to the section *Letters to Progress in Physics*.

All that has been accepted for the online issue of *Progress in Physics* is printed in the paper version of the journal. To order printed issues, contact the Editors.

Authors retain their rights to use their papers published in *Progress in Physics* as a whole or any part of it in any other publications and in any way they see fit. This copyright agreement shall remain valid even if the authors transfer copyright of their published papers to another party.

Electronic copies of all papers published in *Progress in Physics* are available for free download, copying, and re-distribution, according to the copyright agreement printed on the titlepage of each issue of the journal. This copyright agreement follows the *Budapest Open Initiative* and the *Creative Commons Attribution-Noncommercial-No Derivative Works 2.5 License* declaring that electronic copies of such books and journals should always be accessed for reading, download, and copying for any person, and free of charge.

Consideration and review process does not require any payment from the side of the submitters. Nevertheless the authors of accepted papers are requested to pay the page charges. *Progress in Physics* is a non-profit/academic journal: money collected from the authors cover the cost of printing and distribution of the annual volumes of the journal along the major academic/university libraries of the world. (Look for the current author fee in the online version of *Progress in Physics*.)

Astrobiological Aspects of Global Scaling

Hartmut Müller

E-mail: hm@interscalar.com

In this paper we apply chain systems of harmonic quantum oscillators as a fractal model of matter to the analysis of astrophysical and biological metric data. Astrobiological aspects of global scaling are discussed.

Introduction

Already in [1] we have shown that scale invariance is a fundamental characteristic of chain systems of harmonic oscillators. In [2] we applied this model on chain systems of harmonic quantum oscillators and could show that particle rest masses coincide with the eigenstates of the system. This is valid not only for hadrons, but for mesons and leptons as well. On this background we proposed scaling as model of mass emergency [3] and introduced our fractal model of matter as a chain system of oscillating protons and electrons. Andreas Ries [4] demonstrated that this model allows for the prediction of the most abundant isotope of a given chemical element.

Our fractal model of matter as a chain system of oscillating protons and electrons provides also a good description of the mass distribution of large celestial bodies in the Solar System [5]. Physical properties of celestial bodies such as mass, size, rotation and orbital period can be understood as macroscopic quantized eigenstates in chain systems of oscillating protons and electrons [6]. This allows to see a connection between the stability of the Solar system and the stability of electron and proton and consider scale invariance as a forming factor of the Solar system.

In [7] we have calculated the model masses of unknown planets in the Solar system which correspond well with the hypothesis of Batygin and Brown [8] about a new gas giant called "planet 9" and with the hypothesis of Volk and Malhotra [9] about an unknown Mars-to-Earth mass "planet 10" beyond Pluto.

In [6] we have proposed a new interpretation of the cosmic microwave background as a stable eigenstate in a chain system of oscillating protons. Therefore, our model may be of cosmological significance as well.

In [10] we applied our model to the domain of biophysics and have demonstrated that the frequency ranges of electrical brain activity and of other cyclical biological processes correspond with eigenstates in chain systems of oscillating protons and electrons. This would indicate that biological cycles may have a subatomic origin.

Scale invariance as a property of the metric characteristics of biological organisms is well studied [11, 12] and it is not an exclusive characteristic of adult physiology. Furthermore, many metric characteristics of human physiology, for example, the frequency ranges of electrical brain activity [13, 14], are common to most mammalian species.

In this paper we demonstrate how the scale invariance of our fractal model of matter as a chain system of oscillating protons and electrons allows us to see a connection between the metric characteristics of biological organisms and those of the celestial bodies. This connection could be of astrobiological significance.

Methods

In [1] we have shown that the set of natural frequencies of a chain system of similar harmonic oscillators coincides with a set of finite continued fractions $\mathcal{F}$, which are natural logarithms:

$$\ln(\omega_{jk}/\omega_{00}) = n_{j0} + \cfrac{z}{n_{j1} + \cfrac{z}{n_{j2} + \ddots + \cfrac{z}{n_{jk}}}} = \tag{1}$$

$$= [z, n_{j0}; n_{j1}, n_{j2}, \ldots, n_{jk}] = \mathcal{F},$$

where ω_{jk} is the set of angular frequencies and ω_{00} is the fundamental frequency of the set. The denominators are integer: $n_{j0}, n_{j1}, n_{j2}, \ldots, n_{jk} \in \mathbb{Z}$, the cardinality $j \in \mathbb{N}$ of the set and the number $k \in \mathbb{N}$ of layers are finite. In the canonical form, the numerator z equals 1.

For finite continued fractions $\mathcal{F}$ (1), ranges of high distribution density (nodes) arise near reciprocal integers 1, 1/2, 1/3, 1/4, ... which are the attractor points of the distribution.

Any finite continued fraction represents a rational number [15]. Therefore, all natural frequencies ω_{jk} in (1) are irrational, because for rational exponents the natural exponential function is transcendental [16]. It is probable that this circumstance provides for high stability of an oscillating chain system because it prevents resonance interaction between the elements of the system [17]. Already in 1987 we have applied continued fractions of the type $\mathcal{F}$ (1) as criterion of stability in engineering [18, 19].

In the case of harmonic quantum oscillators, the continued fractions $\mathcal{F}$ (1) not only define fractal sets of natural angular frequencies ω_{jk} , oscillation periods $\tau_{jk} = 1/\omega_{jk}$ and wavelengths $\lambda_{jk} = c/\omega_{jk}$ of the chain system, but also fractal sets of energies $E_{jk} = \hbar \cdot \omega_{jk}$ and masses $m_{jk} = E_{jk}/c^2$ which correspond with the eigenstates of the system. For this reason, we call the continued fraction $\mathcal{F}$ (1) the "fundamental

Fig. 1: The canonical projection of $\mathcal{F}$ (natural logarithmic representation).

fractal" of eigenstates in chain systems of harmonic quantum oscillators.

Normal matter is formed by nucleons and electrons because they are exceptionally stable. Furthermore, protons and neutrons have similar rest masses (the difference being only 0.14 percent). This allows us to interpret the proton and the neutron as similar quantum oscillators with regard to their rest masses. Therefore, in [3, 6] we have introduced a fractal model of matter as a chain system of oscillating protons and electrons.

Table 1 shows the basic set of electron and proton units that can be considered as a fundamental metrology (c is the speed of light in vacuum, $\hbar$ is the reduced Planck constant).

We hypothesize that scale invariance based on the fundamental fractal $\mathcal{F}$ (1), calibrated on the metric properties of the proton and electron, is a universal characteristic of organized matter. This hypothesis we have called 'global scaling' [6].

Results

Let's start with the metric characteristics large celestial bodies. The current amount of the Solar mass supports our hypothesis of global scaling, because it corresponds to a main attractor node of the $\mathcal{F}$ (1) calibrated on the electron. In fact, the natural logarithm of the Sun-to-electron mass ratio is close to an integer number:

$$\ln\left(\frac{\mathrm{M_{Sun}}}{\mathrm{m_{electron}}}\right) = \ln\left(\frac{1.9884 \cdot 10^{30}\ \mathrm{kg}}{9.10938356 \cdot 10^{-31}\ \mathrm{kg}}\right) = 138.936$$

The electron rest mass is $\mathrm{m}_e = 9.10938356 \cdot 10^{-31}$ kg [20].

In the canonical form of the fundamental fractal $\mathcal{F}$ (1), shorter continued fractions correspond with more stable eigenstates of a chain system of harmonic oscillators. Therefore, integer logarithms represent the most stable eigenstates (main attractor nodes).

Table 1: The basic set of physical properties of the electron and proton. Data taken from Particle Data Group [20]. Frequencies, oscillation periods and the proton wavelength are calculated.

property	electron	proton
rest mass m	$9.10938356(11) \cdot 10^{-31}$ kg	$1.672621898(21) \cdot 10^{-27}$ kg
energy $\mathrm{E} = \mathrm{m}c^2$	0.5109989461(31) MeV	938.2720813(58) MeV
angular frequency $\omega = \mathrm{E}/\hbar$	$7.76344071 \cdot 10^{20}$ Hz	$1.42548624 \cdot 10^{24}$ Hz
oscillation period $\tau = 1/\omega$	$1.28808867 \cdot 10^{-21}$s	$7.01515 \cdot 10^{-25}$ s
wavelength $\lambda = c/\omega$	$3.8615926764(18) \cdot 10^{-13}$ m	$2.1030891 \cdot 10^{-16}$ m

In the framework of our model of matter, the correspondence of the Sun-to-electron mass ratio with a main attractor node of the fundamental fractal $\mathcal{F}$ (1) is a criterion of high stability of the chain system of quantum oscillators that appears as the star we call 'Sun'. Therefore, the current body mass of the Sun is not casual, but an essential aspect of its stability.

Also the correspondence of the current radius of the Sun with a main attractor node (integer logarithm) now we can understand as criterion of its stability:

$$\ln\left(\frac{\mathrm{R_{Sun}}}{\lambda_{\mathrm{electron}}}\right) = \ln\left(\frac{6.96407 \cdot 10^{8}\ \mathrm{m}}{3.8615926764 \cdot 10^{-13}\ \mathrm{m}}\right) = 48.945$$

The angular Compton wavelength of the electron is $\lambda_e = 3.8615926764 \cdot 10^{-13}$ m [20].

The natural logarithm of the proton-to-electron mass ratio is approximately 7.5 and consequently, the fundamental fractal $\mathcal{F}$ calibrated on the proton will be shifted by 7.5 logarithmic units relative to the $\mathcal{F}$ calibrated on the electron:

$$\ln\left(\frac{1.672621898 \cdot 10^{-27}\ \mathrm{kg}}{9.10938356 \cdot 10^{-31}\ \mathrm{kg}}\right) \approx 7.5$$

Consequently, integer logarithms of the proton $\mathcal{F}$ correspond to half logarithms of the electron $\mathcal{F}$ and vice versa. Therefore, all the most stable eigenstates are connected through division of the integer logarithms by 2.

As we have seen above, the Solar mass coincides with the main attractor and stability node $[139; \infty]$ of the $\mathcal{F}$ calibrated on the electron. Dividing the logarithm $139/2 = 69.5$ we receive the logarithm of the node $[69; 2]$ that is the main node $[62; \infty]$ of the $\mathcal{F}$ calibrated on the proton, because $69.5 - 7.5 = 62$.

This main node corresponds to the mass: $\mathrm{m}_p \cdot \exp(62) = 1.4$ Kg, where $\mathrm{m}_p = 1.672621 \cdot 10^{-27}$ kg is the proton rest mass [20]. Probably, the mass range around 1.4 kg isn't noticeable in astrophysics, but in biophysics it is. This mass range is typical for the adult human brain [21] represented by 7 billion samples (current terrestrial population of homo sapiens).

At the same time, the Solar mass is near the node $[131; 2]$ of the $\mathcal{F}$ calibrated on the proton, because $139 - 7.5 = 131.5$. Dividing the logarithm $131.5/2 = 65.75$ we receive a logarithm that corresponds to the significant subnode $[66; -4]$ in the range of the world statistical average adult human body mass: $\mathrm{m}_p \cdot \exp(65.75) = 60$ kg [20].

Jupiter's body mass coincides with the main attractor node [132; ∞] of the electron-calibrated $\mathcal{F}$ (1):

$$\ln\left(\frac{\mathrm{M_{Jupiter}}}{\mathrm{m_{electron}}}\right) = \ln\left(\frac{1.8986 \cdot 10^{27}\ \mathrm{kg}}{9.10938356 \cdot 10^{-31}\ \mathrm{kg}}\right) = 131.98$$

Dividing the logarithm $132/2 = 66$ we receive the logarithm of the main node [66; ∞] that corresponds to the mass: $\mathrm{m}_e \cdot \exp(66) = 42$ g. This mass range coincides with the average mass of the human spinal cord [23].

At the same time, Jupiter's body mass is near the node [124; 5] of the proton-calibrated $\mathcal{F}$ (1):

$$\ln\left(\frac{\mathrm{M_{Jupiter}}}{\mathrm{m_{proton}}}\right) = \ln\left(\frac{1.8986 \cdot 10^{27}\ \mathrm{kg}}{1.672621 \cdot 10^{-27}\ \mathrm{kg}}\right) = 124.47$$

The half value of this logarithm $124.47/2 = 62.24$ corresponds to the mass: $\mathrm{m}_p \cdot \exp(62.24) = 1.78$ kg that is the range of the adult human liver [21]. It is remarkable that the most massive planet of the Solar System corresponds with the most massive organ of the human organism – the liver.

Saturn's body mass is near the subnode [123; 4] of the proton-calibrated $\mathcal{F}$ (1):

$$\ln\left(\frac{\mathrm{M_{Saturn}}}{\mathrm{m_{proton}}}\right) = \ln\left(\frac{5.6836 \cdot 10^{23}\ \mathrm{kg}}{1.672621 \cdot 10^{-27}\ \mathrm{kg}}\right) = 123.26$$

The half value of this logarithm $123.26/2 = 61.63$ corresponds to the mass: $\mathrm{m}_p \cdot \exp(61.63) = 0.975$ kg that is the range of the adult human lungs [21]. It is remarkable that the second massive planet of the Solar System corresponds with the second massive organ of the human organism – the lungs.

The radius of Saturn is near the main node [54; ∞] of the $\mathcal{F}$ calibrated on the proton:

$$\ln\left(\frac{\mathrm{R_{Saturn}}}{\lambda_{\mathrm{proton}}}\right) = \ln\left(\frac{6.0268 \cdot 10^{7}\ \mathrm{m}}{2.1030891 \cdot 10^{-16}\ \mathrm{m}}\right) = 54.01$$

Dividing the logarithm $54/2 = 27$ we receive the logarithm of the main node [27; ∞] that corresponds to the wavelength $\lambda_p \cdot \exp(27) = 0.11$ mm that coincides with the size of the human fertile oocyte (zygote) [24].

As shown above, the Solar radius coincides with the main node [49; ∞] of the $\mathcal{F}$ calibrated on the electron. Dividing the logarithm $49/2 = 24.5$ we receive the logarithm of the node [24; 2] that is the main node [32; ∞] of the $\mathcal{F}$ calibrated on the proton, because $24.5 + 7.5 = 32$. This logarithm corresponds to the wavelength $\lambda_e \cdot \exp(24.5) = 16.6$ mm that coincides with the object focal length of the human eye [25] that is also the length of the newborn eyeball.

At the same time, the Solar radius is near the node [56; 2] of the $\mathcal{F}$ calibrated on the proton:

$$\ln\left(\frac{\mathrm{R_{Sun}}}{\lambda_{\mathrm{proton}}}\right) = \ln\left(\frac{6.96407 \cdot 10^{8}\ \mathrm{m}}{2.103089 \cdot 10^{-16}\ \mathrm{m}}\right) = 56.46$$

The angular Compton wavelength of the proton is $\lambda_p = 2.103089 \cdot 10^{-16}$ m [20].

Dividing the logarithm $56.5/2 = 28.25$ we receive the logarithm of the significant subnode [28; 4] that corresponds to the wavelength $\lambda_p \cdot \exp(28.25) = 0.39$ mm that coincides with the second focal length [26] behind the retina of the human eye.

Already in 1981 Leonid Chislenko [27] did demonstrate that ranges of body masses and sizes preferred by the most quantity of biological species show an equidistant distribution on a logarithmic scale with a scaling factor close to 3. Probably, this is a consequence of global scaling, if we consider that the scaling factor $e = 2.718\ldots$ connects the main attractor nodes of stability in the fundamental fractal $\mathcal{F}$.

Conclusion

Applying our fractal model of matter as chain system of oscillating protons and electrons to the analysis of astrophysical and biophysical metric data we can assume that the metric characteristics of biological organisms and those of the Solar system have a common subatomic origin. However, there is a huge field of research where various discoveries are still to be expected.

Acknowledgements

The author is grateful to Viktor Panchelyuga and Leili Khosravi for valuable discussions.

Submitted on November 5, 2017

References

1. Müller H. Fractal Scaling Models of Resonant Oscillations in Chain Systems of Harmonic Oscillators. *Progress in Physics*, 2009, v. 5, no. 2, 72–76.
2. Müller H. Fractal Scaling Models of Natural Oscillations in Chain Systems and the Mass Distribution of Particles. *Progress in Physics*, 2010, v. 6, no. 3, 61–66.
3. Müller H. Emergence of Particle Masses in Fractal Scaling Models of Matter. *Progress in Physics*, 2012, v. 8, no. 4, 44–47.
4. Ries A. Qualitative Prediction of Isotope Abundances with the Bipolar Model of Oscillations in a Chain System. *Progress in Physics*, 2015, v. 11, 183–186.
5. Müller H. Fractal scaling models of natural oscillations in chain systems and the mass distribution of the celestial bodies in the Solar System. *Progress in Physics*, 2010, v. 6, no. 3, 61–66.
6. Müller H. Scale-Invariant Models of Natural Oscillations in Chain Systems and their Cosmological Significance. *Progress in Physics*, 2017, v. 13, 187–197.
7. Müller H. Global Scaling as Heuristic Model for Search of Additional Planets in the Solar System. *Progress in Physics*, 2017, v. 13, 204–206.
8. Batygin K., Brown M.E. Evidence for a distant giant planet in the Solar System. *The Astronomical Journal,* 2016, v. 151.
9. Volk K., Malhotra R. The curiously warped mean plane of the Kuiper belt. arXiv:1704.02444v2 [astro-ph.EP], 19 June 2017.
10. Müller H. Chain Systems of Harmonic Quantum Oscillators as a Fractal Model of Matter and Global Scaling in Biophysics. *Progress in Physics*, 2017, v. 13, no. 4, 231–233.

11. Barenblatt G.I. Scaling. Cambridge University Press, 2003.
12. Schmidt-Nielsen K., Scaling. Why is the animal size so important? Cambridge University Press, 1984.
13. Sainsbury R.S., Heynen A., Montoya C.P. Behavioral correlates of hippocampal type 2 theta in the rat. *Physiol. Behavior*, 1987, v. 39 (4), 513–519.
14. Stewart M., Fox S.E., Hippocampal theta activity in monkeys. *Brain Research*, 1991, v. 538 (1), 59–63.
15. Khintchine A.Ya. Continued fractions. University of Chicago Press, Chicago 1964.
16. Hilbert D. Über die Transcendenz der Zahlen e und π. *Mathematische Annalen*, 1893, 43, 216–219.
17. Panchelyuga V.A., Panchelyuga M.S. Resonance and Fractals on the Real Numbers Set. *Progress in Physics*, 2012, v. 8, no. 4, 48–53.
18. Müller H. The general theory of stability and objective evolutionary trends of technology. Applications of developmental and construction laws of technology in CAD. Volgograd, VPI, 1987 (in Russian).
19. Müller H. Superstability as a developmental law of technology. Technology laws and their Applications. Volgograd-Sofia, 1989 (in Russian).
20. Olive K.A. et al. (Particle Data Group), *Chin. Phys. C*, 2016, v. 38, 090001. Patrignani C. et al. (Particle Data Group), *Chin. Phys. C*, 2016, v. 40, 100001.
21. Singh D. et al. Weights of human organs at autopsy in Chandigarh zone of north-west India. *JIAFM*, 2004, v. 26 (3), 97-99.
22. Walpole S.C. et al. The weight of nations: an estimation of adult human biomass. *BMC Public Health*, 2012, v. 12 (1), 439.
23. Watson C., Paxinos G., Kayalioglu G. The Spinal Cord. Amsterdam: Elsevier, 2009.
24. Zamboni L., Mishell D.R., Bell J.H., Baca M. Fine structure of the human ovum in the pronuclear stage. *Journal of Cell Biology* 1966, 30(3), 579–600.
25. Hunt et al. Light, Color and Vision. Chapman and Hall, Ltd, London, 1968.
26. Ebenholtz S.M. Oculomotor Systems and Perception. Cambridge Univ. Press, 2001.
27. Chislenko L.L. The structure of fauna and flora in connection with the sizes of the organisms. Moscow, 1981 (in Russian).

Modified Standard Einstein's Field Equations and the Cosmological Constant

Faisal A. Y. Abdelmohssin
IMAM, University of Gezira, P.O. BOX: 526, Wad-Medani, Gezira State, Sudan
Sudan Institute for Natural Sciences, P.O. BOX: 3045, Khartoum, Sudan
E-mail: f.a.y.abdelmohssin@gmail.com

The standard Einstein's field equations have been modified by introducing a general function that depends on Ricci's scalar without a prior assumption of the mathematical form of the function. By demanding that the covariant derivative of the energy-momentum tensor should vanish and with application of Bianchi's identity a first order ordinary differential equation in the Ricci scalar has emerged. A constant resulting from integrating the differential equation is interpreted as the cosmological constant introduced by Einstein. The form of the function on Ricci's scalar and the cosmological constant corresponds to the form of Einstein-Hilbert's Lagrangian appearing in the gravitational action. On the other hand, when energy-momentum is not conserved, a new modified field equations emerged, one type of these field equations are Rastall's gravity equations.

1 Introduction

In the early development of the general theory of relativity, Einstein proposed a tensor equation to mathematically describe the mutual interaction between matter-energy and spacetime as [13]

$$R_{ab} = \kappa T_{ab} \tag{1.1}$$

where κ is the Einstein constant, T_{ab} is the energy-momentum, and R_{ab} is the Ricci curvature tensor which represents geometry of the spacetime in presence of energy-momentum.

Einstein demanded that conservation of energy-momentum should be valid in the general theory of relativity since energy-momentum is a tensor quantity. This was represented as

$$T_{ab;b} = 0 \tag{1.2}$$

where semicolon (;) represents covariant derivatives. But equation (1.2) requires

$$R_{ab;b} = 0 \tag{1.3}$$

too which is not always true.

Finally, Einstein presented his standard field equations (EFEs) describing gravity in the tensor equations form, namely, [2–5, 8–12]

$$G_{ab} = \kappa T_{ab} \tag{1.4}$$

where G_{ab} is the Einstein tensor given by

$$G_{ab} = R_{ab} - \frac{1}{2}\, g_{ab} R \tag{1.5}$$

where, R, is the Ricci scalar curvature, and g_{ab} is the fundamental metric tensor.

In his search for analytical solution to his field equations he turned to cosmology and proposed a model of static and homogenous universe filled with matter. Because he believed of the static model for the Universe, he introduced a constant term in his standard field equations to represent a kind of "anti gravity" to balance the effect of gravitational attractions of matter in it.

Einstein modified his standard equations by introducing a term to his standard field equations including a constant which is called the cosmological constant Λ, [7] to become

$$R_{ab} - \frac{1}{2}\, g_{ab} R + g_{ab}\Lambda = \kappa T_{ab} \tag{1.6}$$

where Λ is the cosmological constant (assumed to have a very small value). Equation (1.6) may be written as

$$R_{ab} - \frac{1}{2}\,(R - 2\Lambda)\, g_{ab} = \kappa T_{ab} \tag{1.7}$$

Einstein rejected the cosmological constant for two reasons:

- The universe described by this theory was unstable.
- Observations by Edwin Hubble confirmed that the universe is expanding.

Recently, it has been believed that this cosmological constant might be one of the causes of the accelerated expansion of the Universe [15].

Einstein has never justified mathematically introduction of his cosmological constant in his field equations.

Based on that fact I have mathematically done that using simple mathematics.

2 Modified standard Einstein's field equations

I modified the (EFEs) by introducing a general function $L(R)$ of Ricci's scalar into the standard (EFEs). I do not assume a concrete form of the function. The modified (EFEs), then becomes

$$R_{ab} - g_{ab} L(R) = \kappa T_{ab} \tag{2.1}$$

Taking covariant derivative denoted by semicolon (;) of both sides of equation (2.1) yields

$$R_{ab;b} - [g_{ab}L(R)]_{;b} = \kappa T_{ab;b} \tag{2.2}$$

Since covariant divergence of the metric tensor vanishes, equation (2.2) may be written as

$$R_{ab;b} - g_{ab}\left(\frac{\mathrm{d}L}{\mathrm{d}R}\right)R_{;b} = \kappa T_{ab;b} \tag{2.3}$$

Substituting the Bianchi identity

$$R_{;c} = 2g^{ab}R_{ac;b} \tag{2.4}$$

in equation (2.3) and requiring the covariant divergence of the energy-momentum tensor to vanish (i.e. energy-momentum is conserved), namely, equation (1.2), we arrive at

$$R_{ab;b} - g_{ab}\left(\frac{\mathrm{d}L}{\mathrm{d}R}\right)(2g^{ac}R_{ab;c}) = 0 \tag{2.5}$$

Rearranging equation (2.5) we get

$$R_{ab;b} - 2\left(\frac{\mathrm{d}L}{\mathrm{d}R}\right)(g_{ab}g^{ac})R_{ab;c} = 0 \tag{2.6}$$

Substituting the following identity equation

$$g_{ab}g^{ac} = \delta^c_b \tag{2.7}$$

in equation (2.6), we get

$$R_{ab;b} - 2\left(\frac{\mathrm{d}L}{\mathrm{d}R}\right)\left(\delta^c_b\right)R_{ab;c} = 0 \tag{2.8}$$

By changing the dummy indices, we arrive at

$$R_{ab;b}\left(1 - 2\frac{\mathrm{d}L}{\mathrm{d}R}\right) = 0 \tag{2.9}$$

We have either,

$$R_{ab;b} = 0, \tag{2.10}$$

or

$$1 - 2\left(\frac{\mathrm{d}L}{\mathrm{d}R}\right) = 0 \tag{2.11}$$

Equation (2.10) is not always satisfied as mentioned before. Whilst, equation (2.11) yields

$$\frac{\mathrm{d}L}{\mathrm{d}R} = \frac{1}{2} \tag{2.12}$$

This has a solution

$$L(R) = \frac{1}{2}R - C \tag{2.13}$$

where C is a constant.

Interpreting the constant of integration C, as the cosmological constant Λ, the functional dependence of $L(R)$ on Ricci scalar may be written as

$$L(R) = \frac{1}{2}(R - 2\Lambda) \tag{2.14}$$

Equation (2.14) is the well known Lagrangian functional of the Einstein-Hilbert action with the cosmological constant.

3 The Modified Equations and the Einstein Spaces

In absence of energy-momentum i.e. in a region of spacetime where is there no energy, a state which is different from vacuum state everywhere in spacetime, equation (2.1) becomes

$$R_{ab} - g_{ab}L(R) = 0 \tag{3.1}$$

Contacting equation (3.1) with g^{ab}, we get

$$R - NL(R) = 0 \tag{3.2}$$

where N is the dimension of the spacetime. Equation (3.2) yields

$$L(R) = \frac{1}{N}R \tag{3.3}$$

Substituting equation (3.3) in equation (3.1), we get

$$R_{ab} = \frac{1}{N}g_{ab}R \tag{3.4}$$

Equation (3.4) is the Einstein equation for Einstein spaces in differential geometry [1, 2];

$$R_{ab} = I\,g_{ab} \tag{3.5}$$

where I is an invariant. This implies that the function I proposed, $L(R)$, is exactly the same as the invariant I in Einstein spaces equation when contacted with g^{ab}.

A 2D sections of the 4D spacetime of Einstein spaces are geometrically one of the geometries of spacetime which satisfies the standard Einstein's field equations in absence of energy-momentum.

A naive substitution of $N = 4$ into equation (3.4) would lead to an identity from which Ricci scalar could not be calculated, because it becomes a non-useful equation, it gives $R = R$.

4 The modified equations and gravity equations with non-conserved energy-momentum

Because in general relativity spactime itself is changing, the energy is not conserved, because it can give energy to the particles and absorb it from them [2].

In cosmology the notion of dark energy – represented by term introduced by Einstein – and dark matter is a sort of sources of energy of unknown origin.

It is possible to incorporate the possibility of non-conserved energy-momentum tensor in the modified equations. In this case equation (2.9) should become

$$R_{ab;b}\left(1 - 2\frac{\mathrm{d}L}{\mathrm{d}R}\right) = \kappa T_{ab;b} \tag{4.1}$$

where $T_{ab;b} \neq 0$. Since $R_{ab;b}$ is not always equals to zero, this implies that the bracket in the LHS of equation (4.1) is not zero in any case.

Let us assume it is equal to D , where D is a dimensionless constant, i.e.

$$1 - 2\frac{dL}{dR} = D \tag{4.2}$$

Then, equation (4.2) becomes

$$\frac{dL}{dR} = \frac{1}{2}(1 - D) \tag{4.3}$$

Now, integrating equation (4.3) yields

$$L(R, D) = \frac{1}{2}(1 - D)R - E \tag{4.4}$$

where E is a constant. When $D = 0$, equation (4.4) should reduce to equation (2.13), the equation in case of conserved energy-momentum, for which $E = \Lambda$. So, equation (4.4) becomes

$$L(R, D) = \frac{1}{2}(1 - D)R - \Lambda \tag{4.5}$$

Finally, the modified equations (equation (2.1)) in case of non-conserved energy-momentum become

$$R_{ab} - \frac{1}{2}(1 - D)\, g_{ab}R + \Lambda g_{ab} = \kappa T_{ab} \tag{4.6}$$

5 The modified equations and the Rastall gravity equations

Rastall [14] introduced a modification to the Einstein field equations, in which the covariant conservation condition $R_{ab;b} = 0$ is no longer valid.

In his theory he introduced a modification to the Einstein field equations without the cosmological constant which read

$$R_{ab} - \frac{1}{2}(1 - 2\lambda\kappa)\, g_{ab}R = \kappa T_{ab} \tag{5.1}$$

where λ is a free parameter. When $\lambda = 0$, we recover the standard Einstein's field equations. Comparing Rastall's equations in equation (5.1) with equation (4.6) without the cosmological constant, we deduce

$$D = 2\lambda\kappa \tag{5.2}$$

Acknowledgements

I gratefully acknowledge IMAM, University of Gezira, P.O. BOX: 526, Wad-Medani, Gezira State, Sudan, for full financial support of this work.

Submitted on November 5, 2017

References

1. Besse A.L. Einstein Manifolds. Classics in Mathematics. Berlin, Springer, 1987.
2. Misner C.W., Thorne K.S., Wheeler J.A. Gravitation, San Francisco: W. H. Freeman, 1973.
3. Landau L.D., Lifshitz E.M. The Classical Theory of Fields. 4th edition, Butterworth-Heinemann, 1975.
4. Hartle J.B. Gravity: An Introduction to Einstein's General Relativity, Addison-Wesley, 2003.
5. Carroll S. Spacetime and Geometry: An Introduction to General Relativity, Addison-Wesley, 2003.
6. Sharan P. Spacetime, Geometry and Gravitation, Springer, 2009.
7. D'Inverno R. Introducing Einstein's Relativity, Clarendon Press, 1992.
8. Hobson M.P., Efstathiou G.P, Lasenby A.N. General Relativity: An Introduction for Physicists, Cambridge University Press, 2006.
9. Schutz B.A. First Course in General Relativity. Cambridge University Press, 1985.
10. Foster J., Nightingale J.D. A Short Course in General Relativity. 3rd edition, Springer, 1995.
11. Wald R.M. General Relativity, Chicago University Press, 1984.
12. Hawking S.W., Israel W. Three Hundred Years of Gravitation, Cambridge University Press, 1987.
13. Mehra J. Einstein, Hilbert, and The Theory of Gravitation, Historical Origins of General Relativity Theory, Springer, 1974.
14. Rastall P. Phys. Rev. D6, 3357 1972.
15. Riess A., et al. Observational Evidence from Supernovae for an Accelerating Universe and a Cosmological Constant. *The Astronomical Journal*, 1998, v. 116(3), 1009–1038.

Bosons and Fermions as Dislocations and Disclinations in the Spacetime Continuum

Pierre A. Millette

PierreAMillette@alumni.uottawa.ca, Ottawa, Canada

We investigate the case for dislocations (translational displacements) and disclinations (rotational displacements) in the Spacetime Continuum corresponding to bosons and fermions respectively. The massless, spin-1 screw dislocation is identified with the photon, while edge dislocations correspond to bosons of spin-0, spin-1 and spin-2. Wedge disclinations are identified with quarks. We find that the twist disclination depends both on the space volume ℓ^3 of the disclination and on the length ℓ of the disclination. We identify the ℓ^3 twist disclination terms with the leptons, while the ℓ twist disclination which does not have a longitudinal (massive) component, is identified with the massless neutrino. We perform numerical calculations that show that the dominance of the ℓ and ℓ^3 twist disclination terms depend on the extent ℓ of the disclination: at low values of ℓ, the "weak interaction" term ℓ predominates up to about 10^{-18} m, which is the generally accepted range of the weak force, while at larger values of ℓ, the "electromagnetic interaction" term ℓ^3 predominates. The value of ℓ at which the two interactions in the total strain energy are equal is given by $\ell = 2.0 \times 10^{-18}$ m.

1 Introduction

Elementary quantum particles are classified into bosons and fermions based on integral and half-integral multiples of $\hbar$ respectively, where $\hbar$ is Planck's reduced constant. Bosons obey Bose-Einstein statistics while fermions obey Fermi-Dirac statistics and the Pauli Exclusion Principle. These determine the number of non-interacting indistinguishable particles that can occupy a given quantum state: there can only be one fermion per quantum state while there is no such restriction on bosons.

This is explained in quantum mechanics using the combined wavefunction of two indistinguishable particles when they are interchanged:

$$\begin{aligned} \text{Bosons}: \quad & \Psi(1,2) = \Psi(2,1) \\ \text{Fermions}: \quad & \Psi(1,2) = -\Psi(2,1)\,. \end{aligned} \tag{1}$$

Bosons commute and as seen from (1) above, only the symmetric part contributes, while fermions anticommute and only the antisymmetric part contributes. There have been attempts at a formal explanation of this phenomemon, the spin-statistics theorem, with Pauli's being one of the first [1]. Jabs [2] provides an overview of these and also offers his own attempt at an explanation.

However, as Feynman comments candidly [3, see p. 4-3],

> We apologize for the fact that we cannot give you an elementary explanation. An explanation has been worked out by Pauli from complicated arguments of quantum field theory and relativity. He has shown that the two must necessarily go together, but we have not been able to find a way of reproducing his arguments on an elementary level. It appears to be one of the few places in physics where there is a rule which can be stated very simply, but for which no one has found a simple and easy explanation. The explanation is deep down in relativistic quantum mechanics. This probably means that we do not have a complete understanding of the fundamental principle involved. For the moment, you will just have to take it as one of the rules of the world.

The question of a simple and easy explanation is still outstanding. Eq. (1) is still the easily understood explanation, even though it is based on the exchange properties of particles, rather than on how the statistics of the particles are related to their spin properties. At this point in time, it is an empirical description of the phenomenon.

2 Quantum particles from STC defects

Ideally, the simple and easy explanation should be a *physical* explanation to provide a complete understanding of the fundamental principles involved. The Elastodynamics of the Spacetime Continuum (*STCED*) [6,7] provides such an explanation, based on dislocations and disclinations in the spacetime continuum. Part of the current problem is that there is no understandable physical picture of the quantum level. *STCED* provides such a picture.

The first point to note is that based on their properties, bosons obey the superposition principle in a quantum state. In *STCED*, the location of quantum particles is given by their deformation displacement u^μ. Dislocations [7, see chapter 9] are translational displacements that commute, satisfy the superposition principle and behave as bosons. As shown in section §3-6 of [7], particles with spin-0, 1 and 2 are described by

$$u^{\mu;\nu} = \varepsilon^{\mu\nu}_{(0)} + \varepsilon^{\mu\nu}_{(2)} + \omega^{\mu\nu}_{(1)}\,, \tag{2}$$

i.e. a combination of spin-0 $\varepsilon^{\mu\nu}_{(0)}$ (mass as deformation particle aspect), spin-1 $\omega^{\mu\nu}_{(1)}$ (electromagnetism) and spin-2 $\varepsilon^{\mu\nu}_{(2)}$

(deformation wave aspect), where

$$\varepsilon^{\mu\nu} = \frac{1}{2}\,(u^{\mu;\nu} + u^{\nu;\mu}) = u^{(\mu;\nu)} \tag{3}$$

and

$$\omega^{\mu\nu} = \frac{1}{2}\,(u^{\mu;\nu} - u^{\nu;\mu}) = u^{[\mu;\nu]} \tag{4}$$

which are solutions of wave equations in terms of derivatives of the displacements $u^{\mu;\nu}$ as given in chapter 3 of [7].

Disclinations [7, see chapter 10], on the other hand, are rotational displacements that do not commute and that do not obey the superposition principle. You cannot have two rotational displacements in a given quantum state. Hence their number is restricted to one per quantum state. They behave as fermions.

Spinors represent spin one-half fermions. Dirac spinor fields represent electrons. Weyl spinors, derived from Dirac's four complex components spinor fields, are a pair of fields that have two complex components. Interestingly enough, "[u]sing just one element of the pair, one gets a theory of massless spin-one-half particles that is asymmetric under mirror reflection and ... found ... to describe the neutrino and its weak interactions" [4, p. 63].

"From the point of view of representation theory, Weyl spinors are the fundamental representations that occur when one studies the representations of rotations in four-dimensional space-time... spin-one-half particles are representation of the group SU(2) of transformations on two complex variables." [4, p. 63]. To clarify this statement, each rotation in three dimensions (an element of SO(3)) corresponds to two distinct elements of SU(2). Consequently, the SU(2) transformation properties of a particle are known as the particle's spin.

Hence, the unavoidable conclusion is that bosons are dislocations in the spacetime continuum, while fermions are disclinations in the spacetime continuum. Dislocations are translational displacements that commute, satisfy the superposition principle and behave as bosons. Disclinations, on the other hand, are rotational displacements that do not commute, do not obey the superposition principle and behave as fermions.

The equations in the following sections of this paper are derived in Millette [7]. The constants $\bar{\lambda}_0$ and $\bar{\mu}_0$ are the Lamé elastic constants of the spacetime continuum, where $\bar{\mu}_0$ is the shear modulus (the resistance of the continuum to *distortions*) and $\bar{\lambda}_0$ is expressed in terms of $\bar{\kappa}_0$, the bulk modulus (the resistance of the continuum to *dilatations*) according to

$$\bar{\lambda}_0 = \bar{\kappa}_0 - \bar{\mu}_0/2 \tag{5}$$

in a four-dimensional continuum.

3 Dislocations (bosons)

Two types of dislocations are considered in this paper: screw dislocations (see Fig. 1) and edge dislocations (see Fig. 2).

Fig. 1: A stationary screw dislocation in cartesian (x, y, z) and cylindrical polar (r, θ, z) coordinates.

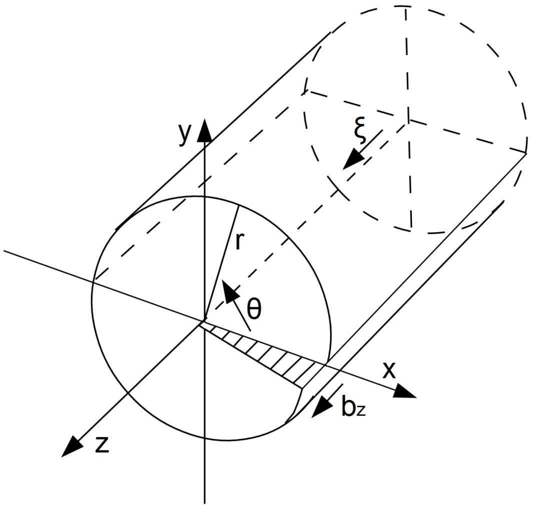

Fig. 2: A stationary edge dislocation in cartesian (x, y, z) and cylindrical polar (r, θ, z) coordinates.

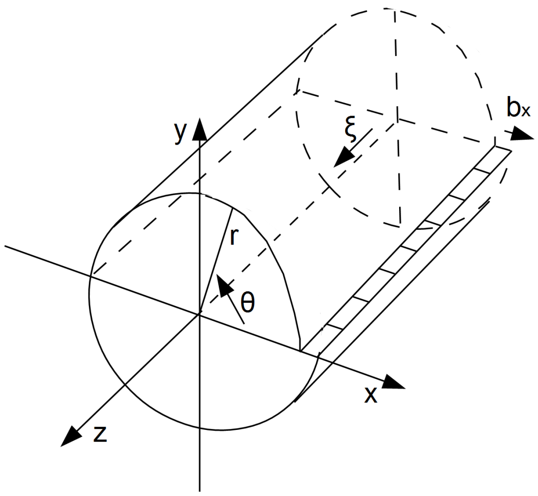

Dislocations, due to their translational nature, are defects that are easier to analyze than disclinations.

3.1 Screw dislocation

The screw dislocation is analyzed in sections §9-2 and §15-1 of [7]. It is the first defect that we identified with the photon due to its being massless and of spin-1. Consequently, its longitudinal strain energy is zero

$$W^S_\parallel = 0. \tag{6}$$

Its transverse strain energy is given by [7, eq. (16.5)]

$$W^S_\perp = \frac{\bar{\mu}_0}{4\pi}\, b^2\, \ell\, \ln\frac{\Lambda}{b_c}\,, \tag{7}$$

where b is the spacetime Burgers dislocation vector [9], ℓ is the length of the dislocation, b_c is the size of the core of the dislocation, of order b_0, the smallest spacetime Burgers dislocation vector [10], and Λ is a cut-off parameter corresponding to the radial extent of the dislocation, limited by the average distance to its nearest neighbours.

3.2 Edge dislocation

The edge dislocation is analyzed in sections §9-3, §9-5 and §15-2 of [7]. The longitudinal strain energy of the edge dislocation is given by [7, eq. (16.29)]

$$W^E_\parallel = \frac{\bar{\kappa}_0}{2\pi}\, \bar{\alpha}_0^2 \left(b_x^2 + b_y^2\right) \ell\, \ln\frac{\Lambda}{b_c} \tag{8}$$

where

$$\bar{\alpha}_0 = \frac{\bar{\mu}_0}{2\bar{\mu}_0 + \bar{\lambda}_0}\,, \tag{9}$$

ℓ is the length of the dislocation and as before, Λ is a cut-off parameter corresponding to the radial extent of the dislocation, limited by the average distance to its nearest neighbours. The edge dislocations are along the z-axis with Burgers vector b_x for the edge dislocation proper represented in Fig. 2, and a different edge dislocation with Burgers vector b_y which we call the gap dislocation. The transverse strain energy is given by [7, eq. (16.54)]

$$W^E_\perp = \frac{\bar{\mu}_0}{4\pi} \left(\bar{\alpha}_0^2 + 2\bar{\beta}_0^2\right)\left(b_x^2 + b_y^2\right) \ell\, \ln\frac{\Lambda}{b_c} \tag{10}$$

where

$$\bar{\beta}_0 = \frac{\bar{\mu}_0 + \bar{\lambda}_0}{2\bar{\mu}_0 + \bar{\lambda}_0}\,. \tag{11}$$

The total longitudinal (massive) dislocation strain energy $W^D_\parallel$ is given by (8)

$$W^D_\parallel = W^S_\parallel + W^E_\parallel = W^E_\parallel\,, \tag{12}$$

given that the screw dislocation longitudinal strain energy is zero, while the total transverse (massless) dislocation strain energy is given by the sum of the screw (along the z axis) and edge (in the $x-y$ plane) dislocation transverse strain energies

$$W^D_\perp = W^S_\perp + W^E_\perp \tag{13}$$

to give

$$W^D_\perp = \frac{\bar{\mu}_0}{4\pi} \left[b_z^2 + \left(\bar{\alpha}_0^2 + 2\bar{\beta}_0^2\right)\left(b_x^2 + b_y^2\right)\right] \ell\, \ln\frac{\Lambda}{b_c}\,. \tag{14}$$

It should be noted that as expected, the total longitudinal (massive) dislocation strain energy $W^D_\parallel$ involves the spacetime bulk modulus $\bar{\kappa}_0$, while the total transverse (massless) dislocation strain energy $W^D_\perp$ involves the spacetime shear modulus $\bar{\mu}_0$.

Fig. 3: Three types of disclinations: wedge (top), splay (middle), twist (bottom) [5, 7].

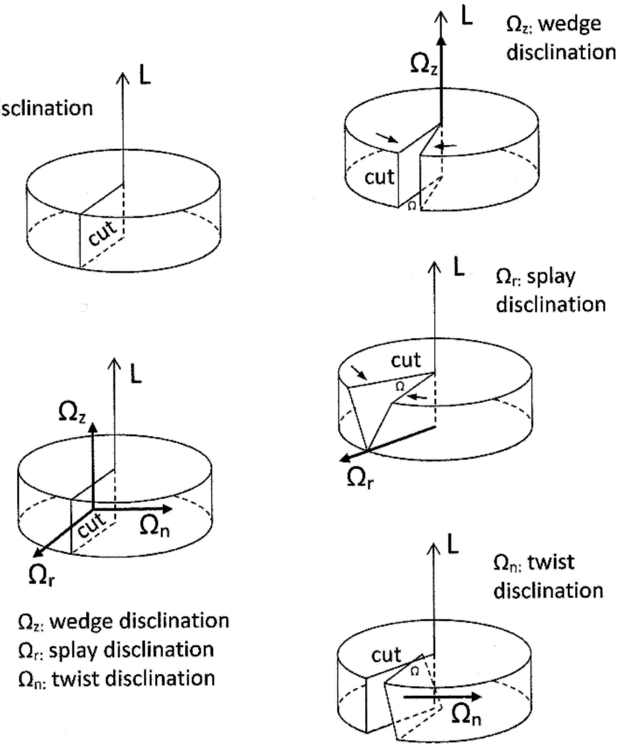

The total strain energy of dislocations

$$W^D = W^D_\parallel + W^D_\perp \tag{15}$$

provides the total energy of massive and massless bosons, with $W^D_\parallel$ corresponding to the longitudinal particle aspect of the bosons and $W^D_\perp$ corresponding to the wave aspect of the bosons. As seen in [11], the latter is associated with the wavefunction of the boson. The spin characteristics of these was considered previously in section 2, where they were seen to correspond to spin-0, spin-1 and spin-2 solutions.

4 Disclinations (fermions)

The different types of disclinations considered in this paper are given in Fig. 3. Disclinations are defects that are more difficult to analyze than dislocations, due to their rotational nature. This mirrors the case of fermions, which are more difficult to analyze than bosons.

4.1 Wedge disclination

The wedge disclination is analyzed in sections §10-6 and §15-3 of [7]. The longitudinal strain energy of the wedge disclination is given by [7, eq. (16.62)]

$$\begin{aligned} W_{\parallel}^{W} = \frac{\bar{\kappa}_0}{4\pi}\,\Omega_z^2\,\ell\Big[&\bar{\alpha}_0^2\left(2\Lambda^2\ln^2\Lambda - 2b_c^2\ln^2 b_c\right) + \\ &+\bar{\alpha}_0\bar{\gamma}_0\left(2\Lambda^2\ln\Lambda - 2b_c^2\ln b_c\right) + \\ &+\tfrac{1}{2}(\bar{\alpha}_0^2+\bar{\gamma}_0^2)\left(\Lambda^2 - b_c^2\right)\Big] \end{aligned} \tag{16}$$

where Ω^μ is the spacetime Frank vector,

$$\bar{\gamma}_0 = \frac{\bar{\lambda}_0}{2\bar{\mu}_0 + \bar{\lambda}_0} \tag{17}$$

and the other constants are as defined previously. In most cases $\Lambda \gg b_c$, and (16) reduces to

$$W_{\parallel}^{W} \simeq \frac{\bar{\kappa}_0}{2\pi}\,\Omega_z^2\,\ell\,\Lambda^2\Big[\bar{\alpha}_0^2\,\ln^2\Lambda + \bar{\alpha}_0\bar{\gamma}_0\ln\Lambda + \tfrac{1}{4}(\bar{\alpha}_0^2+\bar{\gamma}_0^2)\Big] \tag{18}$$

which is rearranged as

$$W_{\parallel}^{W} \simeq \frac{\bar{\kappa}_0}{2\pi}\,\bar{\alpha}_0^2\,\Omega_z^2\,\ell\,\Lambda^2\left[\ln^2\Lambda + \frac{\bar{\gamma}_0}{\bar{\alpha}_0}\,\ln\Lambda + \frac{1}{4}\left(1+\frac{\bar{\gamma}_0^2}{\bar{\alpha}_0^2}\right)\right]. \tag{19}$$

The transverse strain energy of the wedge disclination is given by [7, eq. (16.70)]

$$\begin{aligned} W_{\perp}^{W} = \frac{\bar{\mu}_0}{4\pi}\,\Omega_z^2\,\ell\Big[&\bar{\alpha}_0^2\left(\Lambda^2\ln^2\Lambda - b_c^2\ln^2 b_c\right) - \\ &-\left(\bar{\alpha}_0^2 - 3\bar{\alpha}_0\bar{\beta}_0\right)\left(\Lambda^2\ln\Lambda - b_c^2\ln b_c\right) + \\ &+\frac{1}{2}\left(\bar{\alpha}_0^2 - 3\bar{\alpha}_0\bar{\beta}_0 + \frac{3}{2}\bar{\beta}_0^2\right)\left(\Lambda^2 - b_c^2\right)\Big]. \end{aligned} \tag{20}$$

In most cases $\Lambda \gg b_c$, and (20) reduces to

$$\begin{aligned} W_{\perp}^{W} \simeq \frac{\bar{\mu}_0}{4\pi}\,\Omega_z^2\,\ell\Big[&\bar{\alpha}_0^2\,\Lambda^2\ln^2\Lambda - \\ &-\left(\bar{\alpha}_0^2 - 3\bar{\alpha}_0\bar{\beta}_0\right)\Lambda^2\ln\Lambda + \\ &+\frac{1}{2}\left(\bar{\alpha}_0^2 - 3\bar{\alpha}_0\bar{\beta}_0 + \frac{3}{2}\bar{\beta}_0^2\right)\Lambda^2\Big] \end{aligned} \tag{21}$$

which is rearranged as

$$\begin{aligned} W_{\perp}^{W} \simeq \frac{\bar{\mu}_0}{4\pi}\,\bar{\alpha}_0^2\,\Omega_z^2\,\ell\,\Lambda^2\Big[&\ln^2\Lambda - \left(1 - 3\,\frac{\bar{\beta}_0}{\bar{\alpha}_0}\right)\ln\Lambda + \\ &+\frac{1}{2}\left(1 - 3\,\frac{\bar{\beta}_0}{\bar{\alpha}_0} + \frac{3}{2}\,\frac{\bar{\beta}_0^2}{\bar{\alpha}_0^2}\right)\Big]. \end{aligned} \tag{22}$$

We first note that both the longitudinal strain energy $W_{\parallel}^{W}$ and the transverse strain energy $W_{\perp}^{W}$ are proportional to Λ^2 in the limit $\Lambda \gg b_c$. The parameter Λ is equivalent to the extent of the wedge disclination, and we find that as it becomes more extended, its strain energy is increasing parabolically. This behaviour is similar to that of quarks (confinement) which are fermions. In addition, as $\Lambda \to b_c$, the strain energy decreases and tends to 0, again in agreement with the behaviour of quarks (asymptotic freedom).

We thus identify wedge disclinations with quarks. The total strain energy of wedge disclinations

$$W^{W} = W_{\parallel}^{W} + W_{\perp}^{W} \tag{23}$$

provides the total energy of the quarks, with $W_{\parallel}^{W}$ corresponding to the longitudinal particle aspect of the quarks and $W_{\perp}^{W}$ corresponding to the wave aspect of the quarks. We note that the current classification of quarks include both ground and excited states – the current analysis needs to be extended to excited higher energy states.

We note also that the rest-mass energy density $\rho^W c^2$ of the wedge disclination (see [7, eq. (10.102)]) is proportional to $\ln r$ which also increases with increasing r, while the rest-mass energy density $\rho^E c^2$ of the edge dislocation and $\rho^T c^2$ of the twist disclination (see [7, eqs. (9.134) and (10.123)] respectively) are both proportional to $1/r^2$ which decreases with increasing r as expected of bosons and leptons.

4.2 Twist disclination

The twist disclination is analyzed in sections §10-7 and §15-4 of [7]. Note that as mentioned in that section, we do not differentiate between twist and splay disclinations in this subsection as twist disclination expressions include both splay disclinations and twist disclinations proper. Note also that the Frank vector $(\Omega_x, \Omega_y, \Omega_z)$ corresponds to the three axes (Ω_r, Ω_n, Ω_z) used in Fig. 3 for the splay, twist and wedge disclinations respectively.

The longitudinal strain energy of the twist disclination is given by [7, eq. (16.80)]

$$W_{\parallel}^{T} = \frac{\bar{\kappa}_0}{6\pi}\,\bar{\alpha}_0^2\,\left(\Omega_x^2 + \Omega_y^2\right)\ell^3\ln\frac{\Lambda}{b_c}\,. \tag{24}$$

One interesting aspect of this equation is that the twist disclination longitudinal strain energy $W_{\parallel}^{T}$ is proportional to the cube of the length of the disclination (ℓ^3), and we can't dispose of it by considering the strain energy per unit length of the disclination as done previously. We can say that the twist disclination longitudinal strain energy $W_{\parallel}^{T}$ is thus proportional to the space volume of the disclination, which is reasonable considering that disclinations are rotational deformations. It is also interesting to note that $W_{\parallel}^{T}$ has the familiar dependence $\ln\Lambda/b_c$ of dislocations, different from the functional dependence obtained for wedge disclinations in section 4.1. The form of this equation is similar to that of the longitudinal strain energy for the stationary edge dislocation (see [7, eq. (16.15)]) except for the factor $\ell^3/3$.

The transverse strain energy of the twist disclination is given by [8]

$$\begin{aligned} W_\perp^T = \frac{\bar{\mu}_0}{2\pi}\,\frac{\ell^3}{3}\Big[&\left(\Omega_x^2+\Omega_y^2\right)\left(\bar{\alpha}_0^2+\tfrac{1}{2}\,\bar{\beta}_0^2\right)+\\ &+\,2\,\Omega_x\Omega_y\left(\bar{\alpha}_0^2-2\bar{\beta}_0^2\right)\Big]\ln\frac{\Lambda}{b_c}+\\ &+\,\frac{\bar{\mu}_0}{2\pi}\,\ell\Big[\left(\Omega_x^2+\Omega_y^2\right)\Big(\bar{\alpha}_0^2\left(\Lambda^2\ln^2\Lambda-b_c^2\ln^2 b_c\right)+\\ &+\,\bar{\alpha}_0\bar{\gamma}_0\left(\Lambda^2\ln\Lambda-b_c^2\ln b_c\right)-\frac{1}{2}\bar{\alpha}_0\bar{\gamma}_0\left(\Lambda^2-b_c^2\right)+\\ &+\,2\bar{\beta}_0^2\,\ln\frac{\Lambda}{b_c}\Big)-\,2\,\Omega_x\Omega_y\Big(\bar{\alpha}_0\bar{\beta}_0\left(\Lambda^2\ln\Lambda-b_c^2\ln b_c\right)+\\ &+\,\frac{1}{2}\bar{\beta}_0\bar{\gamma}_0\left(\Lambda^2-b_c^2\right)\Big)\Big]. \end{aligned} \tag{25}$$

In most cases $\Lambda \gg b_c$, and (25) reduces to

$$\begin{aligned} W_\perp^T \simeq \frac{\bar{\mu}_0}{2\pi}\,\frac{\ell^3}{3}\Big[&\left(\Omega_x^2+\Omega_y^2\right)\left(\bar{\alpha}_0^2+\tfrac{1}{2}\,\bar{\beta}_0^2\right)+\\ &+\,2\,\Omega_x\Omega_y\left(\bar{\alpha}_0^2-2\bar{\beta}_0^2\right)\Big]\ln\frac{\Lambda}{b_c}+\\ &+\,\frac{\bar{\mu}_0}{2\pi}\,\ell\,\Lambda^2\Big[\left(\Omega_x^2+\Omega_y^2\right)\Big(\bar{\alpha}_0^2\,\ln^2\Lambda+\,\bar{\alpha}_0\bar{\gamma}_0\,\ln\Lambda-\\ &-\,\frac{1}{2}\bar{\alpha}_0\bar{\gamma}_0\Big)-2\,\Omega_x\Omega_y\Big(\bar{\alpha}_0\bar{\beta}_0\ln\Lambda+\frac{1}{2}\bar{\beta}_0\bar{\gamma}_0\Big)\Big] \end{aligned} \tag{26}$$

which can be rearranged to give

$$\begin{aligned} W_\perp^T \simeq \frac{\bar{\mu}_0}{2\pi}\,\bar{\alpha}_0^2\,\frac{\ell^3}{3}\Big[&\left(\Omega_x^2+\Omega_y^2\right)\left(1+\frac{1}{2}\,\frac{\bar{\beta}_0^2}{\bar{\alpha}_0^2}\right)+\\ &+2\,\Omega_x\Omega_y\left(1-2\,\frac{\bar{\beta}_0^2}{\bar{\alpha}_0^2}\right)\Big]\ln\frac{\Lambda}{b_c}+\\ &+\frac{\bar{\mu}_0}{2\pi}\,\bar{\alpha}_0^2\,\ell\,\Lambda^2\Big[\left(\Omega_x^2+\Omega_y^2\right)\Big(\ln^2\Lambda+\,\frac{\bar{\gamma}_0}{\bar{\alpha}_0}\,\ln\Lambda-\\ &-\frac{1}{2}\,\frac{\bar{\gamma}_0}{\bar{\alpha}_0}\Big)-2\,\Omega_x\Omega_y\Big(\frac{\bar{\beta}_0}{\bar{\alpha}_0}\ln\Lambda+\frac{1}{2}\,\frac{\bar{\beta}_0\bar{\gamma}_0}{\bar{\alpha}_0^2}\Big)\Big]. \end{aligned} \tag{27}$$

As noted previously, $W_\parallel^T$ depends on the space volume ℓ^3 of the disclination and has a functional dependence of $\ln\Lambda/b_c$ as do the dislocations. The transverse strain energy $W_\perp^T$ depends on the space volume ℓ^3 of the disclination with a functional dependence of $\ln\Lambda/b_c$, but it also includes terms that have a dependence on the length ℓ of the disclination with a functional dependence similar to that of the wedge disclination including Λ^2 in the limit $\Lambda \gg b_c$. The difference in the case of the twist disclination is that its transverse strain energy $W_\perp^T$ combines ℓ^3 terms with the functional dependence $\ln\Lambda/b_c$ of dislocations, associated with the "electromagnetic interaction", and ℓ terms with the $\Lambda^2\ \ln^2\Lambda$ functional dependence of wedge disclinations, associated with the "strong interaction". This, as we will see in later sections, seems to be the peculiar nature of the weak interaction, and uniquely positions twist disclinations to represent leptons and neutrinos as participants in the weak interaction.

This leads us to thus separate the longitudinal strain energy of the twist disclination as

$$W_\parallel^T = W_\parallel^{\ell^3} + W_\parallel^{\ell} = W_\parallel^{\ell^3} \tag{28}$$

given that $W_\parallel^{\ell} = 0$, and the transverse strain energy of the twist disclination as

$$W_\perp^T = W_\perp^{\ell^3} + W_\perp^{\ell}\,. \tag{29}$$

We consider both ℓ^3 twist disclination and ℓ twist disclination terms in the next subsections.

4.2.1 ℓ^3 twist disclination

The longitudinal strain energy of the ℓ^3 twist disclination is thus given by the ℓ^3 terms of (24)

$$W_\parallel^{\ell^3} = \frac{\bar{\kappa}_0}{6\pi}\,\bar{\alpha}_0^2\,\left(\Omega_x^2+\Omega_y^2\right)\ell^3\ln\frac{\Lambda}{b_c}\,. \tag{30}$$

The transverse strain energy of the ℓ^3 twist disclination is given by the ℓ^3 terms of (25)

$$\begin{aligned} W_\perp^{\ell^3} = \frac{\bar{\mu}_0}{2\pi}\,\frac{\ell^3}{3}\Big[&\left(\Omega_x^2+\Omega_y^2\right)\left(\bar{\alpha}_0^2+\tfrac{1}{2}\,\bar{\beta}_0^2\right)+\\ &+2\,\Omega_x\Omega_y\left(\bar{\alpha}_0^2-2\bar{\beta}_0^2\right)\Big]\ln\frac{\Lambda}{b_c}\,. \end{aligned} \tag{31}$$

In most cases $\Lambda \gg b_c$, and (31) is left unchanged due to its functional dependence on $\ln\Lambda/b_c$.

The total strain energy of the ℓ^3 twist disclination terms is given by

$$W^{\ell^3} = W_\parallel^{\ell^3} + W_\perp^{\ell^3}\,. \tag{32}$$

It is interesting to note that $W_\parallel^{\ell^3}$ of (30) and $W_\perp^{\ell^3}$ of (31) are proportional to $\ln\Lambda/b_c$, as are the screw dislocation (photon) and edge dislocation (bosons). This, and the results of the next subsection, leads us to identify the ℓ^3 twist disclination terms with the leptons (electron, muon, tau) fermions, where the heavier muon and tau are expected to be excited states of the electron.

4.2.2 ℓ twist disclination

The longitudinal strain energy of the ℓ twist disclination terms in this case is zero as mentioned previously

$$W_\parallel^{\ell} = 0\,. \tag{33}$$

The transverse strain energy of the ℓ twist disclination is thus also given by the ℓ terms of (25):

$$\begin{aligned} W_\perp^\ell = \frac{\bar{\mu}_0}{2\pi}\, \ell \Big[\left(\Omega_x^2 + \Omega_y^2\right) \Big(\bar{\alpha}_0^2 \left(\Lambda^2 \ln^2 \Lambda - b_c^2 \ln^2 b_c\right) + \\ + \bar{\alpha}_0 \bar{\gamma}_0 \left(\Lambda^2 \ln \Lambda - b_c^2 \ln b_c\right) - \frac{1}{2} \bar{\alpha}_0 \bar{\gamma}_0 \left(\Lambda^2 - b_c^2\right) + \\ + 2 \bar{\beta}_0^2 \ln \frac{\Lambda}{b_c} \Big) - 2\, \Omega_x \Omega_y \Big(\bar{\alpha}_0 \bar{\beta}_0 \left(\Lambda^2 \ln \Lambda - b_c^2 \ln b_c\right) + \\ + \frac{1}{2} \bar{\beta}_0 \bar{\gamma}_0 \left(\Lambda^2 - b_c^2\right) \Big) \Big]. \end{aligned} \tag{34}$$

In most cases $\Lambda \gg b_c$, and (34) reduces to

$$\begin{aligned} W_\perp^\ell = \frac{\bar{\mu}_0}{2\pi}\, \ell\, \Lambda^2 \Big[\left(\Omega_x^2 + \Omega_y^2\right) \Big(\bar{\alpha}_0^2 \ln^2 \Lambda + \bar{\alpha}_0 \bar{\gamma}_0 \ln \Lambda - \\ - \frac{1}{2} \bar{\alpha}_0 \bar{\gamma}_0 \Big) - 2\, \Omega_x \Omega_y \Big(\bar{\alpha}_0 \bar{\beta}_0 \ln \Lambda + \frac{1}{2} \bar{\beta}_0 \bar{\gamma}_0 \Big) \Big] \end{aligned} \tag{35}$$

which can be rearranged to give

$$\begin{aligned} W_\perp^\ell = \frac{\bar{\mu}_0}{2\pi}\, \bar{\alpha}_0^2\, \ell\, \Lambda^2 \Big[\left(\Omega_x^2 + \Omega_y^2\right) \Big(\ln^2 \Lambda + \frac{\bar{\gamma}_0}{\bar{\alpha}_0} \ln \Lambda - \\ - \frac{1}{2} \frac{\bar{\gamma}_0}{\bar{\alpha}_0} \Big) - 2\, \Omega_x \Omega_y \Big(\frac{\bar{\beta}_0}{\bar{\alpha}_0} \ln \Lambda + \frac{1}{2} \frac{\bar{\beta}_0 \bar{\gamma}_0}{\bar{\alpha}_0^2} \Big) \Big]. \end{aligned} \tag{36}$$

The total strain energy of the ℓ twist disclination is given by

$$W^\ell = W_\parallel^\ell + W_\perp^\ell = W_\perp^\ell \tag{37}$$

given that the ℓ twist disclination does not have a longitudinal (massive) component. Since the ℓ twist disclination is a massless fermion, this leads us to identify the ℓ twist disclination with the neutrino.

There is another aspect to the strain energy $W_\perp^T$ given by (25) that is important to note. As we have discussed, the ℓ^3 twist disclination terms and the $\ln \Lambda / b_c$ functional dependence as observed for the screw dislocation (photon) and edge dislocation (bosons) has led us to identify the ℓ^3 portion with the leptons (electron, muon, tau) fermions, where the heavier muon and tau are expected to be excited states of the electron. These are coupled with transverse ℓ twist disclination terms which are massless and which have a functional dependence similar to that of the wedge disclination, which has led us to identify the ℓ portion with the weakly interacting neutrino. If the muon and tau leptons are excited states of the electron derivable from (25), this would imply that the neutrino portion would also be specific to the muon and tau lepton excited states, thus leading to muon and tau neutrinos.

We will perform numerical calculations in the next section which will show that the dominance of the ℓ and ℓ^3 twist disclination terms depend on the extent ℓ of the disclination, with the ℓ "weak interaction" terms dominating for small values of ℓ and the ℓ^3 "electromagnetic interaction" terms dominating for larger values of ℓ. The ℓ twist disclination terms would correspond to weak interaction terms while the ℓ^3 twist disclination terms would correspond to electromagnetic interaction terms. The twist disclination represents the unification of both interactions under a single "electroweak interaction".

This analysis also shows why leptons (twist disclinations) are participants in the weak interaction but not the strong interaction, while quarks (wedge disclinations) are participants in the strong interaction but not the weak interaction.

It should be noted that even though the mass of the neutrino is currently estimated to be on the order of 10's of eV, this estimate is based on assuming neutrino oscillation between the currently known three lepton generations, to explain the anomalous solar neutrino problem. This is a weak explanation for that problem, which more than likely indicates that we do not yet fully understand solar astrophysics. One can only hope that a fourth generation of leptons will not be discovered! Until the anomaly is fully understood, we can consider the twist disclination physical model where the mass of the neutrino is zero to be at least a first approximation of the neutrino STC defect model.

4.3 Twist disclination sample numerical calculation

In this section, we give a sample numerical calculation that shows the lepton-neutrino connection for the twist disclination. We start by isolating the common strain energy elements that don't need to be calculated in the example. Starting from the longitudinal strain energy of the twist disclination (24) and making use of the relation $\bar{\kappa}_0 = 32 \bar{\mu}_0$ [7, eq. (5.53)], (24) can be simplified to

$$W_\parallel^T = \frac{\bar{\mu}_0}{2\pi}\, \bar{\alpha}_0^2\, 2\Omega^2 \left[32\, \frac{\ell^3}{3} \ln \frac{\Lambda}{b_c} \right] \tag{38}$$

where an average Ω is used instead of Ω_x and Ω_y. Defining K as

$$K = \frac{\bar{\mu}_0}{2\pi}\, \bar{\alpha}_0^2\, 2\Omega^2 , \tag{39}$$

then (38) is written as

$$\frac{W_\parallel^T}{K} = 32\, \frac{\ell^3}{3} \ln \frac{\Lambda}{b_c} . \tag{40}$$

Similarly for the transverse strain energy of the twist disclination, starting from (27), the equation can be simplified to

$$\begin{aligned} W_\perp^T \simeq \frac{\bar{\mu}_0}{2\pi}\, \bar{\alpha}_0^2\, 2\Omega^2 \Big\{ \Big[\frac{\ell^3}{3} \left(1 + \frac{1}{2} \frac{\bar{\beta}_0^2}{\bar{\alpha}_0^2} + 1 - 2 \frac{\bar{\beta}_0^2}{\bar{\alpha}_0^2} \right) \ln \frac{\Lambda}{b_c} \Big] + \\ + \Big[\ell\, \Lambda^2 \Big(\ln^2 \Lambda + \frac{\bar{\gamma}_0}{\bar{\alpha}_0} \ln \Lambda - \frac{1}{2} \frac{\bar{\gamma}_0}{\bar{\alpha}_0} - \\ - \frac{\bar{\beta}_0}{\bar{\alpha}_0} \ln \Lambda - \frac{1}{2} \frac{\bar{\beta}_0 \bar{\gamma}_0}{\bar{\alpha}_0^2} \Big) \Big] \Big\} . \end{aligned} \tag{41}$$

Using the definition of K from (39), this equation becomes

$$\frac{W_\perp^T}{K} \simeq \frac{\ell^3}{3}\left(2-\frac{3}{2}\frac{\bar\beta_0^2}{\bar\alpha_0^2}\right)\ln\frac{\Lambda}{b_c}+ + \ell\Lambda^2\left(\ln^2\Lambda+\frac{\bar\gamma_0-\bar\beta_0}{\bar\alpha_0}\ln\Lambda-\frac{1}{2}\frac{\bar\gamma_0}{\bar\alpha_0}\left(1+\bar\beta_0\right)\right). \tag{42}$$

Using the numerical values of the constants $\bar\alpha_0$, $\bar\beta_0$ and $\bar\gamma_0$ from [7, eqs. (19.14) and (19.35)], (42) becomes

$$\frac{W_\perp^T}{K} \simeq \frac{\ell^3}{3}\,(1.565)\,\ln\frac{\Lambda}{b_c}+ + \ell\Lambda^2\left(\ln^2\Lambda-\ln\Lambda-0.62\right). \tag{43}$$

For this sample numerical calculation, we use $b_c \sim 10^{-35}$m of the order of the spacetime Burgers dislocation constant b_0, and the extent of the disclination $\Lambda \sim 10^{-18}$ m of the order of the range of the weak force. Then

$$\frac{W_\parallel^T}{K} = \frac{32}{3}\,(39.1)\,\ell^3 = 417\,\ell^3. \tag{44}$$

and

$$\frac{W_\perp^T}{K} \simeq 0.522\,(39.1)\,\ell^3 + + \Lambda^2\,(1714+41.4-0.62)\;\ell \tag{45}$$

which becomes

$$\frac{W_\perp^T}{K} \simeq 20.4\,\ell^3 + 1755\,\Lambda^2\,\ell \tag{46}$$

and finally

$$\frac{W_\perp^T}{K} \simeq 20.4\,\ell^3 + 1.76\times10^{-33}\,\ell. \tag{47}$$

We consider various values of ℓ to analyze its effect on the strain energy. For $\ell = 10^{-21}$ m,

$$\frac{W_\parallel^T}{K} = 4.2\times10^{-61} \quad (\ell^3 \text{ term}) \tag{48}$$

$$\frac{W_\perp^T}{K} = 2.0\times10^{-62} + 1.8\times10^{-54} \quad (\ell^3 \text{ term} + \ell \text{ term}). \tag{49}$$

For $\ell = 10^{-18}$ m,

$$\frac{W_\parallel^T}{K} = 4.2\times10^{-52} \quad (\ell^3 \text{ term}) \tag{50}$$

$$\frac{W_\perp^T}{K} = 2.0\times10^{-53} + 1.8\times10^{-51} \quad (\ell^3 \text{ term} + \ell \text{ term}). \tag{51}$$

For $\ell = 10^{-15}$ m,

$$\frac{W_\parallel^T}{K} = 4.2\times10^{-43} \quad (\ell^3 \text{ term}) \tag{52}$$

$$\frac{W_\perp^T}{K} = 2.0\times10^{-44} + 1.8\times10^{-48} \quad (\ell^3 \text{ term} + \ell \text{ term}). \tag{53}$$

For $\ell = 10^{-12}$ m,

$$\frac{W_\parallel^T}{K} = 4.2\times10^{-34} \quad (\ell^3 \text{ term}) \tag{54}$$

$$\frac{W_\perp^T}{K} = 2.0\times10^{-35} + 1.8\times10^{-45} \quad (\ell^3 \text{ term} + \ell \text{ term}). \tag{55}$$

In the sums of $W_\perp^T/K$ above, the first term ℓ^3 represents the electromagnetic interaction, while the second term ℓ represents the weak interaction. Thus we find that at low values of ℓ, the weak force predominates up to about 10^{-18} m, which is the generally accepted range of the weak force. At larger values of ℓ, the electromagnetic force predominates. The value of ℓ at which the two interactions in the transverse strain energy are equal is given by

$$20.4\,\ell^3 = 1.76\times10^{-33}\,\ell, \tag{56}$$

from which we obtain

$$\ell = 0.9\times10^{-17}\text{ m} \sim 10^{-17}\text{ m}. \tag{57}$$

At that value of ℓ, the strain energies are given by

$$\frac{W_\parallel^T}{K} = 3.0\times10^{-49} \tag{58}$$

$$\frac{W_\perp^T}{K} = 3.1\times10^{-50}. \tag{59}$$

The longitudinal (massive) strain energy predominates over the transverse strain energy by a factor of 10.

Alternatively, including the longitudinal ℓ^3 strain energy in the calculation, the value of ℓ at which the two interactions in the total strain energy are equal is given by

$$417\,\ell^3 + 20.4\,\ell^3 = 1.76\times10^{-33}\,\ell, \tag{60}$$

from which we obtain

$$\ell = 2.0\times10^{-18}\text{ m}. \tag{61}$$

At that value of ℓ, the strain energies are given by

$$\frac{W_\parallel^T}{K} = 3.3\times10^{-51} \tag{62}$$

$$\frac{W_\perp^T}{K} = 3.7\times10^{-51}. \tag{63}$$

The longitudinal (massive) strain energy and the transverse strain energy are then of the same order of magnitude.

5 Quantum particles and their associated spacetime defects

Table 1 provides a summary of the identification of quantum particles and their associated spacetime defects as shown in this paper.

STC defect	Type of particle	Particles
Screw dislocation	Massless boson	Photon
Edge dislocation	Massive boson	Spin-0 particle
		Spin-1 Proca eqn
		Spin-2 graviton
Wedge disclination	Massive fermion	Quarks
ℓ^3 Twist disclination	Massive fermion	Leptons
ℓ Twist disclination	Massless fermion	Neutrinos

Table 1: Identification of quantum particles and their associated defects.

6 Discussion and conclusion

In this paper, we have investigated the case for dislocations and disclinations in the Spacetime Continuum corresponding to bosons and fermions respectively. Dislocations are translational displacements that commute, satisfy the superposition principle and behave as bosons. Disclinations, on the other hand, are rotational displacements that do not commute, do not obey the superposition principle and behave as fermions, including having their number restricted to one per quantum state as it is not possible to have two rotational displacements in a given quantum state.

We have considered screw and edge dislocations. The massless, spin-1 screw dislocation is identified with the photon. The total strain energy of dislocations W^D corresponds to the total energy of massive and massless bosons, with $W^D_\parallel$ corresponding to the longitudinal particle aspect of the bosons and $W^D_\perp$ corresponding to the wave aspect of the bosons, with the latter being associated with the wavefunction of the boson. Their spin characteristics correspond to spin-0, spin-1 and spin-2 solutions.

We have considered wedge and twist disclinations, of which the splay disclination is a special case. Wedge disclinations are identified with quarks. The strain energy of wedge disclinations is proportional to Λ^2 in the limit $\Lambda \gg b_c$. The parameter Λ is equivalent to the extent of the wedge disclination, and we find that as it becomes more extended, its strain energy is increasing parabolically. This behaviour is similar to that of quarks (confinement) which are fermions. In addition, as $\Lambda \to b_c$, the strain energy decreases and tends to 0, again in agreement with the behaviour of quarks (asymptotic freedom). The total strain energy of wedge disclinations W^W thus corresponds to the total energy of the quarks, with $W^W_\parallel$ corresponding to the longitudinal particle aspect of the quarks and $W^W_\perp$ corresponding to the wave aspect of the quarks.

The twist disclination longitudinal strain energy $W^T_\parallel$ is found to be proportional to the cube of the length of the disclination (ℓ^3), and hence depends on the space volume ℓ^3 of the disclination with a functional dependence of $\ln \Lambda/b_c$ as do the dislocations. The transverse strain energy $W^T_\perp$ also depends on the space volume ℓ^3 of the disclination with a functional dependence of $\ln \Lambda/b_c$, but it also includes terms that have a dependence on the length ℓ of the disclination with a functional dependence similar to that of the wedge disclination including Λ^2 in the limit $\Lambda \gg b_c$.

We have considered both ℓ^3 twist disclination and ℓ twist disclination terms. We note that $W^{\ell^3}_\parallel$ and $W^{\ell^3}_\perp$ are proportional to $\ln \Lambda/b_c$, as are the screw dislocation (photon) and edge dislocation (bosons), which leads us to identify the ℓ^3 twist disclination terms with the leptons (electron, muon, tau) fermions, where the heavier muon and tau are expected to be excited states of the electron. Given that the ℓ twist disclination does not have a longitudinal (massive) component, it is a massless fermion and this leads us to identify the ℓ twist disclination with the neutrino. Thus the twist disclination transverse strain energy $W^T_\perp$ combines ℓ^3 terms with the functional dependence $\ln \Lambda/b_c$ of dislocations and ℓ terms with the functional dependence Λ^2 of wedge disclinations.

We have performed numerical calculations that show that the dominance of the ℓ and ℓ^3 twist disclination terms depend on the length ℓ of the disclination. We find that at low values of ℓ, the "weak interaction" term ℓ predominates up to about 10^{-18} m, which is the generally accepted range of the weak force. At larger values of ℓ, the "electromagnetic interaction" term ℓ^3 predominates. The value of ℓ at which the two interactions in the total strain energy are equal is given by $\ell = 2.0 \times 10^{-18}$ m. We conclude that in $W^T_\perp$, the ℓ twist disclination terms represent the weak interaction terms while the ℓ^3 twist disclination terms represent the electromagnetic interaction terms. The twist disclination hence represents the unification of both interactions under a single "electroweak interaction".

This analysis also shows why leptons (twist disclinations) are participants in the weak interaction but not the strong interaction (wedge disclinations). In addition, if the muon and tau leptons are excited states of the electron derivable from (25), this would imply that the neutrino portion would also be specific to the muon and tau lepton excited states, thus leading to muon and tau neutrinos. A summary of the identification of quantum particles and their associated spacetime defects as shown in this paper is provided in Table 1.

Received on October 25, 2017

References

1. Pauli W. The Connection Between Spin and Statistics. *Phys. Rev.*, 1940, v. 58, 716–722. Reprinted in Schwinger, J., ed. Selected Papers on Quantum Electrodynamics. Dover Publications, New York, 1958, pp 372–378.
2. Jabs A. Connecting Spin and Statistics in Quantum Mechanics. arXiv: quant-ph/0810.2300v4.
3. Feynman R. P., Leighton R. B., Sands M. Lectures on Physics, Volume III: Quantum Mechanics. Addison-Wesley Publishing Company, Reading, Massachusetts, 1965.
4. Woit P. Not Even Wrong; The Failure of String Theory and the Search for Unity in Physical Law. Basic Books, NewYork, 2006.
5. Kleinert H. Multivalued Fields in Condensed Matter, Electromagnetism, and Gravitation. World Scientific Publishing, Singapore, 2008.
6. Millette P. A. Elastodynamics of the Spacetime Continuum. *The Abraham Zelmanov Journal*, 2012, v. 5, 221–277.
7. Millette P. A. Elastodynamics of the Spacetime Continuum: A Spacetime Physics Theory of Gravitation, Electromagnetism and Quantum Physics. American Research Press, Rehoboth, NM, 2017.
8. Corrected eq. (16.87) of [7].
9. Millette P. A. Dislocations in the Spacetime Continuum: Framework for Quantum Physics. *Progress in Physics*, 2015, vol. 11 (4), 287–307.
10. Millette P. A. The Burgers Spacetime Dislocation Constant b_0 and the Derivation of Planck's Constant. *Progress in Physics*, 2015, vol. 11 (4), 313–316.
11. Millette P. A. Wave-Particle Duality in the Elastodynamics of the Spacetime Continuum (STCED). *Progress in Physics*, 2014, vol. 10 (4), 255–258.

Gravity as Attractor Effect of Stability Nodes in Chain Systems of Harmonic Quantum Oscillators

Hartmut Müller

E-mail: hm@interscalar.com

In this paper we apply our fractal model of matter as chain systems of harmonic quantum oscillators to the analysis of gravimetric characteristics of the Solar system and introduce a model of gravity as macroscopic cumulative attractor effect of stability nodes in chain systems of oscillating protons and electrons.

Introduction

Gravity has still a special place in physics as it is the only interaction that is not described by a quantum theory. Nevertheless, the big G is considered to be a fundamental constant of nature, involved in the calculation of gravitational effects in Newton's law of universal gravitation and in Einstein's general theory of relativity. The currently recommended [1] value is $G = 6.67408(31) \cdot 10^{-11}\ \mathrm{m^3 kg^{-1} s^{-2}}$ and it seems that we know G only to three significant figures.

For several objects in the Solar System, the value of the standard gravitational parameter μ is known to greater accuracy than G. The value μ for the Sun is the heliocentric gravitational constant and equals $1.32712440042(1) \cdot 10^{20}\ \mathrm{m^3 s^{-2}}$. The geocentric gravitational constant equals $3.986004418(8) \cdot 10^{14}\ \mathrm{m^3 s^{-2}}$ [2]. The precision is 10^{-8} because this quantity is derived from the movement of artificial satellites, which basically involves observations of the distances from the satellite to earth stations at different times, which can be obtained to high accuracy using radar or laser ranging.

However, not the μ is directly measured, but the orbital elements of a natural or artificial satellite. For instance, the orbital elements of the Earth can be used to estimate the heliocentric gravitational constant. Already the basic solution for a circular orbit gives a good approximation:

$$\mu = \frac{4\pi^2 R^3}{T^2} = \frac{4\pi^2 (149597870700\ \mathrm{m})^3}{(31558149.54\ \mathrm{s})^2} =$$

$$= 1.327128 \cdot 10^{20}\ \mathrm{m^3 s^{-2}}$$

where R is the semi-major axis and T is the orbital period of the Earth. These orbital elements are directly measured, although $\mu = GM$ is an interpretation that provides mass as source of gravity and the universality of G. Within the principle of equivalence, gravity is a universal property like inertia and does not depend on the type or scale of matter.

Though, the big G is known only from laboratory measurements of the attraction force between two known masses. The precision of those measures is only 10^{-3}, because gravity appears too weak on the scale of laboratory-sized masses for to be measurable with the desired precision. However, as mentioned Quinn and Speake [3], the discrepant results may demonstrate that we do not understand the metrology of measuring weak forces or they may signify some new physics.

On the other hand, the measured G values seem to oscillate over time [4]. It's not G itself that is varying, Anderson and coauthors proposed, but more likely something else is affecting the measurements, because the 5.9-year oscillatory period of the measured G values seems to correlate with the 5.9-year oscillatory period of Earth's rotation rate, as determined by recent Length of Day (LOD) measurements [5]. However, this hypothesis is still under discussion [6].

In 1981, Stacey, Tuck, Holding, Maher and Morris [7] reported anomalous measures of the gravity acceleration in mines. They proposed an explanation of this anomaly by introducing a short-range potential, of the Yukawa type, that overlaps the Newtonian potential and describes the intensity and the action range of a hypothetical fifth interaction. In 2005, Reginald T. Cahill [8] introduced an additional dimensionless constant that coincides with the fine structure constant and determines the strength of a new 3-space self-interaction that can explain various gravitational anomalies, such as the 'borehole anomaly' and the 'dark matter anomaly' in the rotation speeds of spiral galaxies.

Obviously, the origin of gravity and the nature of particle mass generation are key topics in modern physics and they seem to have a common future. In [9] we have introduced a fractal model of matter as a chain system of harmonic quantum oscillators and have shown that particle rest masses coincide with the eigenstates of the system. This is valid not only for hadrons, but for mesons and leptons as well. Andreas Ries [10] demonstrated that this model allows for the prediction of the most abundant isotope of a given chemical element. Already in [11] we could show that scale invariance is a fundamental property of this model. On this background we proposed quantum scaling as model of mass generation [12].

Our model of matter also provides a good approximation of the mass distribution of large celestial bodies in the Solar system [13]. Metric characteristics of celestial bodies can be understood as macroscopic quantized eigenstates in chain systems of oscillating protons and electrons [14].

In [15] we have calculated the model masses of new planets in the Solar system and in [16, 17] were estimated the orbital elements of these hypothetical bodies. Our calculations

Fig. 1: The canonical projection of $\mathcal{F}$ (natural logarithmic representation).

correspond well with the hypothesis of Batygin and Brown [18] about a new gas giant called "planet 9" and with the hypothesis of Volk and Malhotra [19] about a Mars-to-Earth mass "planet 10" beyond Pluto.

Our model allows us to see a connection between the stability of the Solar system and the stability of the electron and proton and consider global scaling as a forming factor of the Solar system. This may be of cosmological significance.

In this paper we apply our model of matter to the analysis of gravimetric characteristics of large bodies of the Solar system and propose an interpretation of gravity as macroscopic cumulative attractor effect of stability nodes in chain systems of oscillating protons and electrons.

Methods

In [11] we have shown that the set of natural frequencies of a chain system of similar harmonic oscillators coincides with a set of finite continued fractions $\mathcal{F}$, which are natural logarithms:

$$\ln(\omega_{jk}/\omega_{00}) = n_{j0} + \cfrac{z}{n_{j1} + \cfrac{z}{n_{j2} + \ddots + \cfrac{z}{n_{jk}}}} = \tag{1}$$

$$= [z, n_{j0}; n_{j1}, n_{j2}, \ldots, n_{jk}] = \mathcal{F},$$

where ω_{jk} is the set of angular frequencies and ω_{00} is the fundamental frequency of the set. The denominators are integer: $n_{j0}, n_{j1}, n_{j2}, \ldots, n_{jk} \in \mathrm{Z}$, the cardinality $j \in \mathrm{N}$ of the set and the number $k \in \mathrm{N}$ of layers are finite. In the canonical form, the numerator z equals 1.

For finite continued fractions $\mathcal{F}$ (1), ranges of high distribution density (nodes) arise near reciprocal integers 1, 1/2, 1/3, 1/4, ... which are the attractor points of the distribution.

Any finite continued fraction represents a rational number [20]. Therefore, all natural frequencies ω_{jk} in (1) are irrational, because for rational exponents the natural exponential function is transcendental [21]. It is probable that this circumstance provides for high stability of an oscillating chain system because it prevents resonance interaction between the elements of the system [22]. Already in 1987 we have applied continued fractions of the type $\mathcal{F}$ (1) as criterion of stability in engineering [23, 24].

In the case of harmonic quantum oscillators, the continued fractions $\mathcal{F}$ (1) not only define fractal sets of natural angular frequencies ω_{jk}, angular accelerations $a_{jk} = c \cdot \omega_{jk}$, oscillation periods $\tau_{jk} = 1/\omega_{jk}$ and wavelengths $\lambda_{jk} = c/\omega_{jk}$ of the chain system, but also fractal sets of energies $\mathrm{E}_{jk} = \hbar \cdot \omega_{jk}$ and masses $\mathrm{m}_{jk} = \mathrm{E}_{jk}/c^2$ which correspond with the eigenstates of the system. For this reason, we call the continued fraction $\mathcal{F}$ (1) the "fundamental fractal" of eigenstates in chain systems of harmonic quantum oscillators.

In the canonical form ($z = 1$) of the fundamental fractal $\mathcal{F}$ (1), shorter continued fractions correspond with more stable eigenstates of a chain system of harmonic oscillators. Therefore, integer logarithms represent the most stable eigenstates (main attractor nodes).

Normal matter is formed by nucleons and electrons because they are exceptionally stable. Furthermore, protons and neutrons have similar rest masses (the difference being only 0.14 percent). This allows us to interpret the proton and the neutron as similar quantum oscillators with regard to their rest masses. Therefore, in [12, 14] we have introduced a fractal model of matter as a chain system of oscillating protons and electrons.

Table 1 shows the basic set of electron and proton units that can be considered as a fundamental metrology (c is the speed of light in vacuum, $\hbar$ is the reduced Planck constant).

Table 1: The basic set of physical properties of the electron and proton. Data taken from Particle Data Group [25]. Frequencies, oscillation periods, accelerations and the proton wavelength are calculated.

property	electron	proton
rest mass m	$9.10938356(11) \cdot 10^{-31}$ kg	$1.672621898(21) \cdot 10^{-27}$ kg
energy $\mathrm{E} = \mathrm{m}c^2$	0.5109989461(31) MeV	938.2720813(58) MeV
angular frequency $\omega = \mathrm{E}/\hbar$	$7.76344071 \cdot 10^{20}$ Hz	$1.42548624 \cdot 10^{24}$ Hz
angular oscillation period $\tau = 1/\omega$	$1.28808867 \cdot 10^{-21}$ s	$7.01515 \cdot 10^{-25}$ s
wavelength $\lambda = c/\omega$	$3.8615926764(18) \cdot 10^{-13}$ m	$2.1030891 \cdot 10^{-16}$ m
angular acceleration $a = c\omega$	$2.327421 \cdot 10^{29}$ ms^{-2}	$4.2735 \cdot 10^{32}$ ms^{-2}

The natural logarithm of the proton-to-electron mass ratio is approximately 7.5 and consequently, the fundamental fractal $\mathcal{F}$ calibrated on the proton will be shifted by 7.5 logarithmic units relative to the $\mathcal{F}$ calibrated on the electron:

$$\ln \frac{1.672621898 \cdot 10^{-27}\mathrm{kg}}{9.10938356 \cdot 10^{-31}\mathrm{kg}} \approx 7.5$$

We hypothesize that scale invariance based on the fundamental fractal $\mathcal{F}$ (1), calibrated on the metric properties of the proton and electron, is a universal characteristic of organized matter. This hypothesis we have called 'global scaling' [14, 26].

Results

In [12] we have shown that the Planck mass coincides with the main attractor node [44; ∞] of the $\mathcal{F}$ (1) calibrated on the proton:

$$\ln \frac{m_{\text{Planck}}}{m_{\text{proton}}} = \ln \frac{2.17647 \cdot 10^{-8}}{1.6726219 \cdot 10^{-27}} = 44.01$$

This circumstance allows us to calculate the big G from the proton rest mass:

$$G = \frac{\hbar c}{m_p^2} \exp(-88) = 6.8420676 \cdot 10^{-11}\ \text{m}^3\text{kg}^{-1}\text{s}^{-2}$$

The calculated G value is larger than the currently recommended by CODATA [1], although the published [27,28] values of G show immense variations and some recent measurements of high precision deliver, in fact, larger values than the recommended.

Applying our model (1), we can see that the Solar equatorial surface gravity acceleration $g_{\text{Sun}} = 274\ \text{m/s}^2$ corresponds with a main attractor node of the $\mathcal{F}$ (1) calibrated on the angular acceleration of the electron $a_{\text{electron}} = 2.327421 \cdot 10^{29}\ \text{ms}^{-2}$ (see table 1). In fact, the logarithm of the electron-to-Solar gravity acceleration ratio is close to an integer:

$$\ln \frac{a_{\text{electron}}}{g_{\text{Sun}}} = \ln \frac{2.327421 \cdot 10^{29}\ \text{ms}^{-2}}{274\ \text{ms}^{-2}} = 62.00$$

This coincidence supports our hypothesis of global scaling and allows us to understand that the current amount of the surface gravity acceleration of the Sun is not casual, but an essential aspect of stability of the chain system of quantum oscillators that appears as the star we call 'Sun'.

Also the current amount of the Solar mass we recognise as criterion of stability, because it corresponds to a main attractor node of the $\mathcal{F}$ (1) calibrated on the electron. In fact, the natural logarithm of the Sun-to-electron mass ratio is close to an integer number:

$$\ln \frac{\text{M}_{\text{Sun}}}{\text{m}_{\text{electron}}} = \ln \frac{1.9884 \cdot 10^{30}\ \text{kg}}{9.10938356 \cdot 10^{-31}\ \text{kg}} = 138.94$$

Furthermore, the main attractor node [62; ∞] of the $\mathcal{F}$ (1) calibrated on the electron corresponds with the node [69; 2] calibrated on the proton that is half of the logarithm of the Solar-to-electron mass ratio: $69.5 = 139/2$. This allows us to write down an equation that connects the Sun-to-electron mass ratio with the proton-to-Solar surface gravity acceleration ratio:

$$\frac{\text{M}_{\text{Sun}}}{\text{m}_{\text{electron}}} = \left(\frac{a_{\text{proton}}}{g_{\text{Sun}}} \right)^2$$

As well, the correspondence of the current radius of the Sun with a main attractor node (integer logarithm) of the $\mathcal{F}$ (1) calibrated on the electron now we can understand as additional criterion of stability of the Sun:

$$\ln \frac{R_{\text{Sun}}}{\lambda_{\text{electron}}} = \ln \frac{6.96407 \cdot 10^{8}\ \text{m}}{3.8615926764 \cdot 10^{-13}\ \text{m}} = 48.95$$

The logarithm of the proton-to-Jupiter surface gravity acceleration ratio is also close to an integer:

$$\ln \frac{a_{\text{proton}}}{g_{\text{Jupiter}}} = \ln \frac{4.2735 \cdot 10^{32}\ \text{ms}^{-2}}{24.79\ \text{ms}^{-2}} = 71.92$$

Jupiter's body mass coincides with the main attractor node [132; ∞] of the electron-calibrated $\mathcal{F}$ (1):

$$\ln \frac{\text{M}_{\text{Jupiter}}}{\text{m}_{\text{electron}}} = \ln \frac{1.8986 \cdot 10^{27}\ \text{kg}}{9.10938356 \cdot 10^{-31}\ \text{kg}} = 131.98$$

The surface gravity accelerations of Saturn (10.4 m/s,^{2}), Uranus (8.7 m/s ^{2}), Neptune (11.1 m/s ^{2}), Earth (9.81 m/s ^{2}) and Venus (8.87 m/s^2) approximate the main attractor node [73; ∞] of the $\mathcal{F}$ (1) calibrated on the proton:

$$\ln \frac{a_{\text{proton}}}{g_{\text{Venus}}} = \ln \frac{4.2735 \cdot 10^{32}\ \text{ms}^{-2}}{8.87\ \text{ms}^{-2}} = 72.95$$

The mass of Venus corresponds to the main attractor node [126; ∞] of the electron-calibrated $\mathcal{F}$ (1):

$$\ln \frac{\text{M}_{\text{Venus}}}{\text{m}_{\text{electron}}} = \ln \frac{4.8675 \cdot 10^{24}\ \text{kg}}{9.10938356 \cdot 10^{-31}\ \text{kg}} = 126.01$$

Finally, the surface gravity accelerations of Mercury and Mars (3.71 m/s^2) approximate the main attractor node [74; ∞] of the $\mathcal{F}$ (1) calibrated on the proton:

$$\ln \frac{a_{\text{proton}}}{g_{\text{Mars}}} = \ln \frac{4.2735 \cdot 10^{32}\ \text{ms}^{-2}}{3.71\ \text{ms}^{-2}} = 73.83$$

The body mass of Mars corresponds to the main attractor node [124; ∞] of the $\mathcal{F}$ (1) calibrated on the electron:

$$\ln \frac{\text{M}_{\text{Mars}}}{\text{m}_{\text{electron}}} = \ln \frac{6.4171 \cdot 10^{23}\ \text{kg}}{9.10938356 \cdot 10^{-31}\ \text{kg}} = 123.99$$

In [14] we have shown that the body masses, the rotation and orbital periods of the planets and the Sun are quantized. They follow the sequence of attractor nodes of stability of the fundamental fractal $\mathcal{F}$ (1). Now we can affirm that the surface gravity accelerations of the planets and the Sun are quantized as well. The surface gravity accelerations of the planets correspond with the main attractor nodes [72; ∞], [73; ∞], [74; ∞] of the $\mathcal{F}$ (1) calibrated on the proton while the surface gravity acceleration of the Sun corresponds with the main attractor node [62; ∞] of the $\mathcal{F}$ (1) calibrated on the electron.

Considering that the angular acceleration of the electron is $a_{\text{electron}} = c\omega_{\text{electron}}$, we can express the Solar surface gravity acceleration in terms of the speed of light

$$g_{\text{Sun}} = c\omega_{\text{Sun}}$$

and receive the angular oscillation period $1/\omega_{\text{Sun}} = 12.7$ sidereal days that is the first harmonic of the equatorial rotation period 25.4 days of the Sun. This coincidence suggests to analyse also the gravity accelerations of the planets in terms of the speed of light.

If we express the Earth surface gravity acceleration $g = 9.8\,\text{ms}^{-2}$ in terms of the speed of light, we receive an oscillation period of $c/g = 355$ sidereal days that is in the range of the Earth orbital period and coincides perfectly with the attractor node [63; 2] of the $\mathcal{F}$ (1) calibrated on the electron oscillation period $2\pi\tau_{\text{electron}} = 8.0933 \cdot 10^{-21}$ s:

$$2\pi\tau_{\text{electron}} \exp{(63.5)} = 355\,\text{days}$$

The period of 355 days coincides with 12 synodic lunar months, the lunar year. The surface gravity accelerations of Saturn (10.4 m/s^2), Uranus (8.7 m/s^2), Neptune (11.1 m/s^2) and Venus (8.87 m/s^2) are of the same range and consequently, they approximate the same attractor node [63; 2].

The surface gravity acceleration of Saturn $g_{\text{Saturn}} = 10.4\,\text{m/s}^2$ corresponds with an oscillation period of $c/g_{\text{Saturn}} = 334$ sidereal days that is in the range of the duration of lightning storms on Saturn which appear once every 30 Earth years. The lightning storm of 2009 on Saturn in the planet's southern hemisphere lasted over 334 days [29].

Mars and Mercury have similar surface gravity accelerations of about 3.7 ms^{-2} that corresponds to an oscillation period of $c/3.7\,\text{ms}^{-2} = 938$ sidereal days near the attractor node [64; 2] of the $\mathcal{F}$ (1) calibrated on the electron:

$$2\pi\tau_{\text{electron}} \exp{(64.5)} = 966\,\text{days}$$

The sidereal rotation period of Mars is 24.62278 hours and coincides perfectly to the main node [67; ∞] of the proton-calibrated $\mathcal{F}$ (1):

$$\ln\frac{\tau_{\text{Mars}}}{\tau_{\text{proton}}} = \ln\frac{24.62278 \cdot 3600\,\text{s}}{7.01515 \cdot 10^{-25}\text{s}} = 67.00$$

In addition, the orbital period of Mars 686.971 days meets precisely the condition of global scaling:

$$\ln\frac{T_{\text{Mars}}}{\tau_{\text{electron}}} = \ln\frac{686.971 \cdot 86164\,\text{s}}{1.28808867 \cdot 10^{-21}\text{s}} = 66.00$$

The surface gravity acceleration of Jupiter $g_{\text{Jupiter}} = 24.79\,\text{ms}^{-2}$ corresponds to an oscillation period of $c/g_{\text{Jupiter}} = 140$ sidereal days near the main attractor node of the $\mathcal{F}$ calibrated on the electron:

$$2\pi\tau_{\text{electron}} \exp{(62.5)} = 131\text{ days}$$

The sidereal rotation period of Jupiter is 9.925 hours and corresponds with the main attractor node [66; ∞] of the proton $\mathcal{F}$ (1):

$$\ln\frac{\tau_{\text{Jupiter}}}{\tau_{\text{proton}}} = \ln\frac{9.9251 \cdot 3600\,\text{s}}{7.01515 \cdot 10^{-25}\text{s}} = 66.10$$

Jupiter's orbital period of 4332.59 days fulfils the conditions of global scaling very precisely:

$$\ln\frac{T_{\text{Jupiter}}}{2\pi\tau_{\text{electron}}} = \ln\frac{4332.59 \cdot 86164\,\text{s}}{2\pi\ 1.28808867 \cdot 10^{-21}\text{s}} = 66.00$$

When the logarithm of the sidereal rotation period of Jupiter slows down to [66; ∞], the orbital-to-rotation period ratio of Jupiter can be described by the equation:

$$\frac{T_{\text{Jupiter}}}{\tau_{\text{Jupiter}}} = \frac{2\pi\tau_{\text{electron}}}{\tau_{\text{proton}}}$$

We can see that both the orbital periods of Jupiter and Mars correspond with the main attractor node [66; ∞] of stability, but in the case of Jupiter with the electron oscillation period as fundamental and in the case of Mars with the electron angular oscillation period as fundamental. Therefore, both orbital periods are simply connected by 2π:

$$T_{\text{Jupiter}} = 2\pi T_{\text{Mars}}$$

Also these circumstances support our model of matter as chain system of harmonic quantum oscillators and our hypothesis of global scaling.

Conclusion

Applying our fractal model of matter as chain system of harmonic quantum oscillators to the analysis of gravimetric characteristics of large bodies of the Solar system we did show that the surface gravity accelerations of the planets and the Sun are quantized and correspond to nodes of stability in chain systems of oscillating protons and electrons and therefore, they can be estimated without any information about the masses or sizes of the celestial bodies.

Furthermore, the quantized surface gravity accelerations of the planets and the Sun seem to be connected with their quantized orbital and rotation periods.

We presume that the accretion of gravitational mass is a macroscopic cumulative attractor effect of stability nodes in chain systems of oscillating protons and electrons. From this point of view, Newton's constant of gravitation defines the corresponding amount of gravitational mass a given attractor node can accumulate.

Acknowledgements

The author is grateful to Viktor Panchelyuga for valuable discussions.

Submitted on November 23, 2017

References

1. CODATA recommended 2014 values of the fundamental physical constants: physics.nist.gov/constants.
2. Numerical Standards for Fundamental Astronomy. maia.usno.navy.mil, IAU Working Group, 2017.

3. Quinn T., Speake C. The Newtonian constant of gravitation – a constant too difficult to measure? An introduction. Phil. Trans. Royal Society A, v. 372, 20140253.
4. Anderson J. D. et al. Measurements of Newton's gravitational constant and the length of day. EPL, v. 110, 10002, 2015.
5. Holme R., de Viron O. Characterization and implications of intradecadal variations in length of day. *Nature*, v. 499, 202-204, 2013.
6. Schlamminger S. et al. Recent measurements of the gravitational constant as a function of time. arXiv:1505.01774v2 [gr-qc] 21 May 2015.
7. Stacey F. D. et al. Constraint on the planetary scale value of the Newtonian gravitational constant from the gravity profile within a mine. *Phys. Rev.* v. D23, 1683, 1981.
8. Cahill R. T. 3-Space In-Flow Theory of Gravity: Boreholes, Blackholes and the Fine Structure Constant. *Progress in Physics*, v. 2, 9–16, 2006.
9. Müller H. Fractal Scaling Models of Natural Oscillations in Chain Systems and the Mass Distribution of Particles. *Progress in Physics*, v. 3, 61–66, 2010.
10. Ries A. Qualitative Prediction of Isotope Abundances with the Bipolar Model of Oscillations in a Chain System. *Progress in Physics*, v. 11, 183–186, 2015.
11. Müller H. Fractal Scaling Models of Resonant Oscillations in Chain Systems of Harmonic Oscillators. *Progress in Physics*, v. 2, 72–76, 2009.
12. Müller H. Emergence of Particle Masses in Fractal Scaling Models of Matter. *Progress in Physics*, v. 4, 44–47, 2012.
13. Müller H. Fractal scaling models of natural oscillations in chain systems and the mass distribution of the celestial bodies in the Solar System. *Progress in Physics*, v. 3, 61–66, 2010.
14. Müller H. Scale-Invariant Models of Natural Oscillations in Chain Systems and their Cosmological Significance. *Progress in Physics*, v. 4, 187–197, 2017.
15. Müller H. Global Scaling as Heuristic Model for Search of Additional Planets in the Solar System. *Progress in Physics*, v. 4, 204–206, 2017.
16. Müller H. Scaling of body masses and orbital periods in the Solar System. *Progress in Physics*, v. 11, 133–135, 2015.
17. Müller H. Scaling of body masses and orbital periods in the Solar System as consequence of gravity interaction elasticity. Abstracts of the XII. International Conference on Gravitation, Astrophysics and Cosmology, dedicated to the centenary of Einstein's General Relativity theory. Moscow, PFUR, 2015.
18. Batygin K., Brown M. E. Evidence for a distant giant planet in the Solar System. *The Astronomical Journal*, 151 / 22, February 2016.
19. Volk K., Malhotra R. The curiously warped mean plane of the Kuiper belt. arXiv:1704.02444v2 [astro-ph.EP], 19 June 2017.
20. Khintchine A.Ya. Continued fractions. University of Chicago Press, Chicago, 1964.
21. Hilbert D. Über die Transcendenz der Zahlen e und π. *Mathematische Annalen*, v. 43, 216–219, 1893.
22. Panchelyuga V. A., Panchelyuga M. S. Resonance and Fractals on the Real Numbers Set. *Progress in Physics*, v. 4, 48–53, 2012.
23. Müller H. The general theory of stability and objective evolutionary trends of technology. Applications of developmental and construction laws of technology in CAD. Volgograd, VPI, 1987 (in Russian).
24. Müller H. Superstability as a developmental law of technology. Technology laws and their Applications. Volgograd-Sofia, 1989 (in Russian)
25. Olive K.A. et al. (Particle Data Group), *Chin. Phys. C*, v. 38, 090001, 2016.
    Patrignani C. et al. (Particle Data Group), *Chin. Phys. C*, v. 40, 100001, 2016.
26. Müller H. Scaling as Fundamental Property of Natural Oscillations and the Fractal Structure of Space-Time. Foundations of Physics and Geometry. Peoples Friendship University of Russia, 2008 (in Russian).
27. Newell D.B. CODATA and the Newtonian Gravitational Constant. Newtonian constant of gravitation workshop NIST, 9–10 October, 2014.
28. Gillies G.T. The Newtonian gravitational constant: recent measurements and related studies. *Rep. Prog. Phys.*, v. 60, 151–225, 1997.
29. NASA's Cassini watches storm choke on its own tail. NASA/JPL-Caltech/SSI/Hampton University, Jan. 31, 2013.

LETTERS TO PROGRESS IN PHYSICS

On the Ultimate Energy of Cosmic Rays

Analtoly V. Belyakov
E-mail: belyakov.lih@gmail.com

It is established that the upper limit of cosmic-ray energy due to the Greisen-Zatsepin-Kuzmin effect is local. On the basis of the mechanistic interpretation of J. Wheeler's geometrodynamic concept, a more fundamental limitation on this limit was established, which, in the final analysis, depends on Planck's size $(\hbar\gamma/c^3)^{1/2}$ and for protons the limit is 4.51×10^{18} eV. The inflection in the spectrum curve, the "knee", corresponds to the mass-energy of the vortex tube of the limiting proton-electron contour, 1.46×10^{15} eV. For other nuclei these energies increase in proportion to the atomic number of the element.

Cosmic rays are a flow of nuclei of chemical elements — hydrogen (~ 90%), helium (~ 8%), and the nuclei of the heavier elements (~ 2%). The energy spectrum of cosmic rays or the dependence of the cosmic ray flux on energy extends from 10^3 to 10^{20} eV. The main sources of primary cosmic rays are supernova explosions (galactic cosmic rays) and the Sun, as well as extragalactic sources — radio galaxies and quasars. The protons and heavier nuclei emitted during supernova explosions are further accelerated in specific astrophysical processes. Falling into the earth's atmosphere, cosmic ray particles transmit their energy to a multitude of secondary particles. Thus, the particles cascade is formed; it is called an extensive air shower (EAS) and covers a large area.

Nature ultrahigh energy cosmic rays (more than 10^{17} eV) has not yet been unambiguously interpreted, their sources have not yet been identified, and there is no complete understanding of the mechanisms of their acceleration and even the nature of the accelerated particles [1]. There are reasons to assume that they are of extragalactic origin. It is believed that the upper limit of cosmic-ray energy is limited by a threshold of 5×10^{19} eV, because cosmic ray particles interact energetically with relic radiation, which leads to their absorption and reduction of their energy to a threshold value at distances of the order of several tens of megaparsecs (Greisen-Zatsepin-Kuzmin effect) [2, 3]. The presence of particles with energies exceeding this threshold does not yet find a satisfactory explanation, since within range of up to one hundred megaparsec powerful radiation sources are absent.

The question arises: what energy could be cosmic rays, if the distance between the source and the Earth would be much less than the Greisen-Zatsepin-Kuzmin limit, and could not microparticle produce a huge macroscopic effect? Here we see a paradox, since theoretically relativistic mass and energy of the particle can approach infinity. It seems that the Greisen-Zatsepin-Kuzmin effect is of local importance, and there are more fundamental causes that limit the energy of cosmic rays.

A fundamental limitation can be derived by considering a charged microparticle from the point of view of John Wheeler's geometrodynamic concept. Wheeler's concept assumes that charged microparticles are singular points on a topologically non-unitary coherent two-dimensional surface of our world, connected by a "wormhole", a vortex tube or a current line of the input-output kind in an additional dimension, generally forming a closed counter. According to the mechanistic interpretation of Wheeler's idea when the contour (proton-electronic, for example) is opened individual charged particles retain part of the contour vortex tube (boson mass) whose momentum is numerically equal to the charge [4, 5]. In these works formulas are derived for the vortex tube parameters: its boson mass m_y, the circulation velocity of the medium along the contour v, the radius r, and the length l_y:

$$m_y = (an)^2\, m_e\,, \tag{1}$$

$$v = \frac{c_0^{1/3}}{(an)^2}\, c\,, \tag{2}$$

$$r = \frac{c_0^{2/3}}{(an)^4}\, r_e\,, \tag{3}$$

$$l_y = (an)^2 r_e\,, \tag{4}$$

where n is the principal quantum number of the contour, a is the inverse of the fine structure constant, m_e and r_e are the mass and classical radius of the electron, c_0 is the dimensionless speed of light equal to $c/$[m/sec]. Depending on the size of the contour, i.e. from its quantum number, its parameters vary, but the momentum (charge equivalent) in a closed counter remains constant. At the same time, *both the contour size and the parameters of the vortex tube have their ultimate values.*

In [6], in determining the neutrino mass, it was shown that the Planck size $r_h = (\hbar\gamma/c^3)^{1/2}$ has a physical meaning and is the limiting size inherent in the neutrino, and, obviously, in general for the microcosm, i.e. $r_{\min} = r_h = 1.62 \times 10^{-35}$ m or $5.74 \times 10^{-21}\, r_e$. Then from (1) and (3) we get other ultimate values: $n = 21700$ and $m_y = 8.83 \times 10^{12}\, m_e$. The boson mass is compared with that of mass-energy in units of

$m_e c^2$, provided that $v \to c$ (here the boson mass can be considered as the mass of the excited or "associated" vacuum). It is this condition that is satisfied for cosmic rays whose particles relative to their source move with velocities close to the speed of light. Thus, the energy equivalent of the mass m_y is $E = 8.83 \times 10^{12} \times 511000 = 4.51 \times 10^{18}$ eV.

This quantity is the ultimate energy for cosmic-ray protons. Obviously, for heavier nuclei, the energy increases in proportion to the atomic number A. This conclusion agrees with the fact of "weight increasing" the primary cosmic ray component with increasing energy, and the heavy nuclei flux (most likely iron) in the region of $\sim 10^{18}$ eV is much larger than that of protons [7–9]. Consequently, the largest energy value for the heaviest nuclei can not exceed $E \sim 3.7 \times 10^{20}$ eV and even higher values, apparently, can not be. Indeed, during the entire time of observation on Earth, only a few dozen events with energies above 10^{20} eV were recorded in various installations (the maximum energy of the cosmic particle 3×10^{20} eV was registered in October 1991 on the "Fly's Eye" device [10]).

The figure adopted from [11] shows the observed spectrum of cosmic radiation, on which the energy limits for protons (II) and heavy nuclei (III) are noted (the values along the ordinate are reduced to the energy in GeV). The region of the graph is marked, where the intensity of cosmic rays is about 1 particle per square meter per year. A narrow scatter of the experimental data over the entire length of the spectrum, with the exception of the region of ultrahigh energies, gives grounds to assume that the intensity of cosmic rays depends slightly on the nature of their sources and the mechanism for their acceleration, and this can be shown.

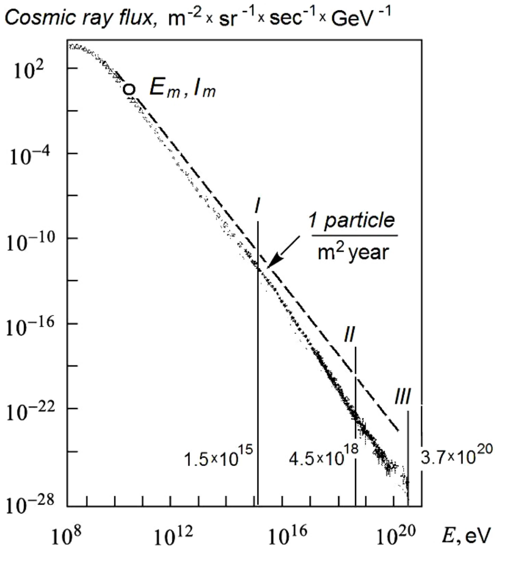

Fig. 1: The observed spectrum of cosmic radiation in the energy range 10^8–10^{20} eV.

Let us assume that the particle velocity increases proportionally to the distance from the source, and the number of particles falling per unit area of the receiver is inversely proportional to the cube of the distance from the source. This is true in the case of unimpeded particle propagation. Then, by simple computations, we obtain a relation that is independent of the distance:

$$I = (E_m/E)^{1.5}\, I_m\,, \tag{5}$$

where E_m and I_m are the coordinates of some reference point on the $I(E)$ dependence in units of [eV] and [flux $\times$ m^{-2} $\times$ sr^{-1} $\times$ sec^{-1}]. When the ordinates are divided by energy in GeV, formula (5) becomes:

$$I = 10^9\, (E_m^{1.5}/E^{2.5})\, I_m \tag{6}$$

and shown in the figure with a dashed line. The actual dependence is somewhat more steeply and approximated by the relation $dI/dE \sim E^{-2.7}$, which is explained by the presence of magnetic fields and other cosmogenic factors affecting charged particles. Nevertheless, it turns out that the shape of the energy spectrum is largely determined by the increase in the particles energy and the decrease in their number as radiation sources are removed from the Earth.

In the energy range 10^{15}–10^{16} eV, the dependence $I(E)$ undergoes an inflection increasing index at E, the so-called "knee". The energy value at the inflection point matches with the mass-energy of the contour corresponding to the *ultimate size of the hydrogen atom*. For this atom, the ultimate value of the quantum number $n = 390$ [5]. In general, detailed formula for the inflection point energy, given the results of [5], and assuming that the energy increases in proportion to the atomic number of nuclei can be represented as:

$$E_{\text{knee}} = 5.11 \times 10^5 \left(\frac{2\pi\gamma\rho_e m_p \times [\sec^2]}{c_0^{1/3} \cos q_w} \right)^2 A = \\ = 1.46 \times 10^{15} \times A \text{ eV}, \tag{7}$$

where γ is the gravitational constant, $\rho_e = m_e/r_e^3$ is the electron density equal to 4.07×10^{13} kg/m^3, m_p is the relative mass of the proton, and q_w is the Weinberg angle of 28.7°.

For protons, this energy value is indicated in the figure by the vertical (I), which matches with the beginning of the inflection of the energy spectrum. The removal of the inflection point towards higher energies for heavier nuclei is confirmed in [12].

One can propose the following explanation for the increase in the energy spectrum incline. At energies up to 1.46×10^{15} eV ($n < 390$), protons and electrons in cosmic rays can be in a bound state — either as atoms having a neutral charge or in some associations that have a total positive charge less than the protons total charge. It may reduce their interaction with magnetic fields.

At higher energies, protons are not accompanied by electrons, their total positive charge remains, and they are fully exposed to magnetic fields. Perhaps this is the reason for the abrupt decrease in the number of electrons in the EAS when primary particles have energies about 10^{15}–10^{16} eV [13].

As for the neutrinos, then, bearing in mind their inherent size limit of r_h, their maximum energy, possible, can reach the same value as that of the proton, 4.51×10^{18} eV. At the moment, the highest recorded neutrino energy is $2{\times}10^{15}$ eV [14].

Conclusion

The ultimate energy of cosmic rays is limited by the maximum mass-energy of the proton vortex tube, which in turn is determined by the fundamental parameter — the Planck size inherent in a neutrino. The reason for the inflection of the spectrum of cosmic rays (the "knee") is the obtaining by the proton of the energy at which a proton-electronic counter, having ultimate quantum number, opens. For other nuclei these energies increase in proportion to the atomic number of the element.

It is shown that, for all on a variety of radiation sources and the mechanism of acceleration of cosmic particles, the shape of the spectrum of cosmic rays, provided that they spread without interference, is largely determined by the most common factors — the increase in their particle energy and the decrease in their number — as the distance between the sources and the Earth is increasing.

Submitted on June 24, 2017

References

1. Kalashev O.E. Cosmic rays of ultrahigh and ultrahigh energies. Associated neutrino and photon radiation. 01.04.02 — theoretical physics. Thesis for the degree of Doctor of Physical and Mathematical Sciences. Moscow, 2016.
2. Greisen K. End to the cosmic ray spectrum? *Phys. Rev. Lett.*, 1966, v. 16, 748–750.
3. Zatsepin G.T., Kuzmin V.A. On the upper boundary of the spectrum of cosmic rays. JETP-Letters, 1966, v. 4, 78–80.
4. Belyakov A.V. Charge of the electron, and the constants of radiation according to J. A. Wheeler's geometrodynamic model. *Progress in Physics*, 2010, v. 4, 90–94.
5. Belyakov A.V. Macro-analogies and gravitation in the micro-world: further elaboration of Wheeler's model of geometrodynamics. *Progress in Physics*, 2012, v. 2, 47–57.
6. Belyakov A.V. Determination of the neutrino mass. *Progress in Physics*, 2016, v. 12, issue 1, 34–38.
7. Troitsky S.V. Cosmic rays of ultrahigh energies: composition and source problem. 01.04.16 — physics of the atomic nucleus and elementary particles. The dissertation author's abstract on competition of a scientific degree of the doctor of physical and mathematical sciences. Institute of Nuclear Research, Russian Academy of Sciences, Moscow, 2008.
8. Grigorov N.L. et al. In: *Proc. 12th Int. Cosmic Ray Conf.*, Hobart, 1971, v. 5, 1746.
9. Isaev P.S. Some problems of the physics of cosmic rays of ultrahigh energies. P2-99-33. Joint Institute for Nuclear Research, Dubna, 1999.
10. Bird D.J. et al. *Astrophys. J.*, 1994, v. 424, 491.
11. Bednyakov V.A. Why research of cosmic rays of ultrahigh energies should be produced in a near-earth orbit. *Physics of Elementary Particles and the Atomic Nucleus*, Joint Institute for Nuclear Research, Dubna, 2002, v. 33, no. 5.
12. Kalmykov V.N. Mass composition of primary cosmic radiation in the region of the break according to the data of the installation EAS of the MSU. The dissertation and the author's abstract on VAK 01.04.23 (Moscow, Russia), the candidate of physical and mathematical sciences.
13. Kulikov G.V., Christiansen G.B. *Journal of Experimental and Theoretical Physics*, 1958, v. 35, 635.
14. Aartsen et al. Evidence for astrophysical muon neutrinos from the Northern Sky with IceCube. *Physical Review Letters*, 2015, v. 115, 081102; arXiv: 1507.04005 [astro-ph.HE].

LETTERS TO PROGRESS IN PHYSICS

Cosmological Redshift in the De Sitter Stationary Universe

Larissa Borissova and Dmitri Rabounski
E-mail: borissova@ptep-online.com; rabounski@ptep-online.com

Here we focus on our previous studies, wherein we deduced the redshift formula in the de Sitter metric space. The non-Newtonian gravitational forces of repulsion, acting in the de Sitter universe, increase with distance. Thus these forces produce the redshift effect on photons coming from distant objects. The redshift in the de Sitter universe increases with distance from the observed objects, and is hyperbolic that matches with the non-linear redshift recently registered by astronomers. As a result, we no longer need the expanding model of the Friedmann metric to correctly explain the redshift in the spectra of galaxies and quasars. The observed "cosmological" redshift is as well good explained in the de Sitter universe which is stationary as is well known.

Earlier, we studied the metric of the inner space of a liquid sphere — the sperical space filled with an ideal incompressible liquid (the so-called Schwarzschild 2nd metric). The obtained results were published in all necessary detail in [1–3]. In particular, in our book *Inside Stars* [2] we considered stars as liquid spheres. Our computations made by the mathematical methods of the General Theory of Relativity showed a good coincidence with the observational data known in astronomy. We also showed, in the journal papers [1, 2] and in §1.2 of the book *Inside Stars* [2], that the liquid sphere metric transforms into the de Sitter metric (the metric of a spherical space fulled with physical vacuum) under the following two common conditions. First, under the gravitational collapse condition, when the radius of the liquid sphere becomes equal to its gravitational radius (i.e. when the liquid sphere becomes gravitational collapsar). And second, when the space-time breaking matches with the radius of the liquid sphere. We also showed that the observed Universe is equivalent to a sphere in the state, which is very close to gravitational collapse (See Chapter 6 in [2] for detail). Thus the space of our Universe can be described by the metric of the de Sitter vacuum sphere. This means, in particular, that the non-Newtonian gravitational forces acting in the de Sitter metric space must manifest themselves in some astronomical phenomena observed in our Universe (read about the non-Newtonian forces of gravitational attraction and repulsion in §5.5 of our book *Fields, Vacuum and the Mirror Universe* [4]). For example, the non-Newtonian gravitational forces may also be the source of the observed redshift in the spectra of galaxies and quazars.

Now, this observed phenomenon is known as the "cosmological redshift" due to Lemaître who in 1927 showed [5] that such redshift may be originated due the Doppler effect on photons in an expanding universe (the universe of the Friedmann metric). On the other hand, proceeding from the aforementioned theoretical results [1–3] we can now state that the observed redshift in the spectra of galaxies and quazars has no relation to cosmology but is the "effect of distance" in the stationary universe of the de Sitter metric. Such a redshift formula was derived in our publications [1–3]. But because those publications were focused on the internal constitution of stars, the redshift effect in the de Sitter space was not emphasized and analysed properly.

We now aim to emphasize it for better understanding of the obtained result.

The redshift formula is derived by integration of the scalar geodesic equation for photons. There are the scalar geodesic equation and the vectorial geodesic equation. They are the respective projections of the four-dimensional geodesic equation (the equation of motion along the shortest/geodesic lines) onto the time line and the three-dimensional spatial section of the observer. The scalar geodesic equation, the projection onto the time line, is the equation of energy. The vectorial geodesic equation is the equation of three-dimensional motion. So, integrating the scalar geodesic equation of a photon along its path, we obtain how its energy and, hence, its frequency changes during its travel. As a result, we obtain the redshift formula. As a matter of fact that the geodesic equations and, hence, their integration, depends on the metric of the particular space wherein the photons travel.

The three-dimensional sub-space of the de Sitter space (space-time) does not rotate and deform. But there is the gravitational inertial force. This force acting inside a sphere filled with physical vacuum, i.e. in the de Sitter space, in the radial coordinates takes the form (5.74) [4, §5.5]

$$F = \frac{\lambda c^2}{3}\, r = \frac{c^2}{a^2}\, r\,,$$

where $\lambda = \varkappa\rho_0$ is the Einstein cosmological constant, $\varkappa$ is the Einstein gravitational constant, while ρ_0 is the density of the physical vacuum that fills the de Sitter space (see §5.3 [4]).

The Hubble constant $H = (2.3 \pm 0.3) \times 10^{-18}$ sec^{-1} is expressed through the radius of the Universe $a = 1.3 \times 10^{28}$ cm as $H = c/a$. Thus, we obtain (6.11) [1]

$$F = H^2 r\,,$$

where the Hubble constant plays the rôle of a fundamental frequency

$$H = \frac{2\pi}{T}$$

expessed through the time T of the existence of the Universe. So, the gravitational inertial force F acting in the de Sitter space depends the Hubble constant H.

Because $F > 0$ in the de Sitter space, this is a force of repulsion. This force is proportional to the radial distance r to the observer: each system of reference is connected with its own observer and his reference body, which is the "centre" of his own universe.

Consider the scalar and vectorial geodesic equations for a photon. This is the system of equations (6.22) [2]. Because the de Sitter space does not rotate and deform, the equations take the simplified form (6.23), where the photon is affected by only the gravitational inertial force and the space non-uniformity (expressed with the Christoffel symbols). Integrating the scalar geodesic equation (the equation of energy) for the photon travelling along the radial coordinate r in the de Sitter space, with taking the vectorial geodesic equation, we obtain the formula of the photon's frequency ω (6.27) [2]

$$\omega = \frac{\omega_0}{\sqrt{1 - r^2/a^2}}\,,$$

where $\omega_0 = \omega_{(r=0)}$ is the photon's frequency in the coordinate origin $r = 0$ (where the observer is located). We see that the photon's frequency is asymptotically increasing when the photon's source approaches to the event horizon (radius) of the Universe ($r = a$).

At distances much shorter than the Universe's radius i.e. much shorter than the event horizon of the Universe ($r \ll a$), the formula for the photon's frequency becomes (6.28)

$$\omega \simeq \omega_0 \left(1 + \frac{r^2}{2a^2}\right).$$

That is we get the quadratic additive to the initially frequency of the photon or, in another word, the redshift effect z of parabolic type (6.29–6.31)

$$z = \frac{\omega - \omega_0}{\omega_0} = \frac{1}{\sqrt{1 - r^2/a^2}} - 1 \simeq \frac{r^2}{2a^2} > 0\,,$$

which, in terms of the Hubble constant $H = c/a$, is

$$z \simeq \frac{H^2 r^2}{2c^2}\,.$$

As is seen, the photon frequency shift is positive in this case: $z > 0$ (otherwise it would be blueshift). This means that the redshift effect takes place in the de Sitter universe. The space of the de Sitter metric is stationary: it neither expands nor compresses. The redshift effect in the de Sitter universe is due to the non-Newtonian gravitational force of repulsion.

In the last decades, astronomical observations of the most distant galaxies showed an increase of the redshift effect in the spectra of the most distant galaxies, which are located close to the event horizon. The astronomers supposed therefore, on the basis of the Friedmann metric of an expanding universe, that the space of our Universe expands with acceleration. On the other hand, the non-linear redshift at large distances is easily explained in the framework of the de Sitter static universe: see formula for z that above. This non-linear effect is due to only the non-linearity of the non-Newtonian gravitational force of repulsion acting on the photon. From the viewpoint of an earthy observer this effect looks as the increasing redshift with the increasing distance from the Earth to the observed object (the source of the photon).*

The observed high redshift in the spectra of quazars is as well explained due to the powerful inner non-Newtonian forces of repulsion (not the far intergalactic distances in the Friedmann expanding universe). As we conclude on the basis of our book *Inside Stars* [2], the ratio of the gravitational radius and the space breaking radius to the physical radius a (i.e. the ratio r_g/a and r_{br}/a) is close to 1 for neutron stars and quazars. If a star is in the state of gravitational collapse, the space breaking matches with both the gravitational radius of the star r_g and the star's surface a, i.e. $a = r_g = r_{br}$. If the space breaking matches with only the star's surface ($r_{br} = a$), gravitational collapse occurs at the radius

$$r_c = \sqrt{9a^2 - 8a^3/r_g}$$

(2.7) in [1]. The physical radius a of such a star is

$$r_g < a < 1.125\, r_g$$

see (2.8 – 2.9) in [1]. In other words, neutron stars and quazars are objects in the state, which is very close to collapse. The latter means that the inner non-Newtonian gravitational force of repulsion is so strong near the surface of a neutron star or a quazar that photons emitted from its surface into the cosmos bear a high redshift independent on the distance from the observer. For this reason, quazars may be located not somewhere near the event horizon of our Universe, but somewhere much much closer to us.

In the end, a few words about our Universe as a whole. According to the contemporary astronomical data, its average density is $\sim 10^{-29}$ g/cm^3, while the ultimate large observed distance (the radius of the Universe, or the event horizon) is $\sim 1.3 \times 10^{28}$ cm. With such characteristics, the collapse radius is $\sim 1.2 \times 10^{28}$ cm (a little lesser than the event horizon,

---

*This conclusion on the unnecessity of the Friedmann metric meets another study [6–8] showing that the observed redshift, including its non-linearity, may be caused by the light-speed rotation of the isotropic space (the partially degenerate space, wherein light-like particles e.g. photons travel). The found basic redshift effect in a flat space has the form of exponent, while the paticular space metrics make only an additional goal to it.

while the space breaking radius is the same as the event horizon $\sim 1.3 \times 10^{28}$ cm. These observed facts mean that we live in the inner space of an object which is either collapsar or is in the state which is very close to the state of collapse. The description of such an object anyhow excludes the expanding model. That is the Friedmann metric of an expanding universe is non-applicable to the observed Universe.

Finally, the observed non-linear redshift in the spectra of galaxies and quazars is well explained in the de Sitter stationary space, wherein it is merely a "distant effect" due to the non-Newtonian forces of repulsion which increase with distance from the observer. The de Sitter universe is stationary — it is a bubble that has closed space and time on itself, and is floating in the surrounding outer space (because we have no reason to assert that our Universe exists in isolation as an exceptional object).

Submitted on December 5, 2017

References

1. Borissova L. De Sitter bubble as a model of the observable Universe. *The Abraham Zelmanov Journal*, 2010, v.3, 3–24.
2. Borissova L. and Rabounski D. Inside Stars: A Theory of the Internal Constitution of Stars, and the Sources of Stellar Energy According to General Relativity. 2nd Edition, American Research Press, Rehoboth (NM), 2014.
3. Borissova L. A telemetric multispace formulation of Riemannian geometry, General Relativity, and cosmology: implications for relativistic cosmology and the true reality of time. *Progress in Physics*, 2017, v.13. Issue 2, 57–75.
4. Borissova L. and Rabounski D. Fields, Vacuum, and the Mirror Universe. 2nd edition, Svenska fysikarkivet, Stockholm, 2009.
5. Block D.L. Georges Lemaître and Stiglers Law of Eponymy. arXiv: 1106.3928.
6. Rabounski D. An explanation of Hubble redshift due to the global nonholonomity of space. *Progress in Physics*, 2009, v. 5, issue 1, L1–L2.
7. Rabounski D. Hubble redshift due to the global non-holonomity of space. *The Abraham Zelmanov Journal*, 2009, v. 2, 11–28.
8. Rabounski D. Non-linear cosmological redshift: the exact theory according to General Relativity. *The Abraham Zelmanov Journal*, 2012, v. 5, 4–30.

Nuclear Structure of ^{154,156}Dy Isotopes

Salah A. Eid[1], Sohair M. Diab[2]

[1]Faculty of Engineering, Phys. Dept., Ain Shams University, Cairo, Egypt.
[2]Faculty of Education, Phys. Dept., Ain Shams University, Cairo, Egypt.
E-mail: mppe2@yahoo.co.uk

The Interacting Boson Approximation model, *IBA*-1, has been used in studying the nuclear structure of ^{154,156}Dy. The excited positive and negative parity states, potential energy surfaces, $V(\beta, \gamma)$, electromagnetic transition probabilities, $B(E1)$, $B(E2)$, back bending, staggering effect, $\Delta I = 1$, and electric monopole strength, $X(E0/E2)$, were calculated successfully. The calculated values are compared to the available experimental data and show reasonable agreement. The energy and electromagnetic transition probabilities ratios as well as the contour plot of the potential energy surfaces show that the ^{156}Dy nucleus is an $X(5)$ candidate.

1 Introduction

The nuclear shape and shape phase transitions in the rare earth dysprosium isotopes have been investigated by many authors theoretically and experimentally. Theoretically, analytical solution of the Bohr Hamiltonian derived with the Titz-Hua potential [1] as well as Bohr-Mottelson Hamiltonian [2,3] were used in calculating energy levels, spin, parity and electromagnetic ratios. The effect of the nuclear structure on the α-decay are investigated by many authors [4-6] and found that the shape and deformation has an effect on the branching ratio as well as the change in the half-life of α-emission. Experimentally, the low-lying positive and negative parity states were produced in the ^{148}Nd (^{12}C,4n), ^{155}Gd (^{3}He,4n), E= 37.5 MeV, ^{122}Sn (^{36}S,4n), E= 165 MeV and ^{114}Cd (^{48}Ca,6n), E= 215 MeV [7-9] reactions. The levels' energy, spin, parity, γ-bands, branching ratios, level energy differences between the positive and negative parity bands, octupole deformation, γ-γ coincidences and angular distribution were measured. Conversion electrons were detected by mini-orange spectrometer, $E0$ transitions were observed and the strength of the electric monopole transitions were calculated [10].

$X(5)$ is the critical point symmetry of phase transition between $U(5)$ and $SU(3)$ nuclei. The aim of the present work is to:

1. Calculate the potential energy surfaces, $V(\beta, \gamma)$;
2. Calculate the levels' energy and electromagnetic transition rates $B(E1)$ and $B(E2)$;
3. Show $X(5)$ symmetry to ^{156}Dy;
4. Calculate the back bending;
5. Calculate the staggering effect, and
6. Calculate the electric monopole strength, $X(E0/E2)$.

2 Interacting Boson Approximation model *IBA*-1

2.1 Levels' energy

The *IBA*-1 Hamiltonian [11] employed on ^{154,156}Dy, in the present calculation, is:

$$\begin{aligned} H &= EPS \cdot n_d + PAIR \cdot (P \cdot P) \\ &+ \frac{1}{2}\, ELL \cdot (L \cdot L) + \frac{1}{2}\, QQ \cdot (Q \cdot Q) \\ &+ 5\, OCT \cdot (T_3 \cdot T_3) + 5\, HEX \cdot (T_4 \cdot T_4)\,, \end{aligned} \tag{1}$$

where

$$P \cdot P = \frac{1}{2} \begin{bmatrix} \left\{(s^\dagger s^\dagger)_0^{(0)} - \sqrt{5}(d^\dagger d^\dagger)_0^{(0)}\right\} x \\ \left\{(ss)_0^{(0)} - \sqrt{5}(\tilde{d}\tilde{d})_0^{(0)}\right\} \end{bmatrix}_0^{(0)}, \tag{2}$$

$$L \cdot L = -10\,\sqrt{3}\left[(d^\dagger \tilde{d})^{(1)} x\, (d^\dagger \tilde{d})^{(1)}\right]_0^{(0)}, \tag{3}$$

$$Q \cdot Q = \sqrt{5} \begin{bmatrix} \left\{(S^\dagger \tilde{d} + d^\dagger s)^{(2)} - \frac{\sqrt{7}}{2}\,(d^\dagger \tilde{d})^{(2)}\right\} x \\ \left\{(s^\dagger \tilde{d} + +\tilde{d} s)^{(2)} - \frac{\sqrt{7}}{2}\,(d^\dagger \tilde{d})^{(2)}\right\} \end{bmatrix}_0^{(0)}, \tag{4}$$

$$T_3 \cdot T_3 = -\sqrt{7}\left[(d^\dagger \tilde{d})^{(2)} x\, (d^\dagger \tilde{d})^{(2)}\right]_0^{(0)}, \tag{5}$$

$$T_4 \cdot T_4 = 3\left[(d^\dagger \tilde{d})^{(4)} x\, (d^\dagger \tilde{d})^{(4)}\right]_0^{(0)}. \tag{6}$$

and n_d is the number of d bosons; $P \cdot P$, $L \cdot L$, $Q \cdot Q$, $T_3 \cdot T_3$ and $T_4 \cdot T_4$ represent pairing, angular momentum, quadrupole, octupole and hexadecupole interactions respectively between the bosons; EPS is the boson energy; and $PAIR$, ELL, QQ, OCT, HEX are the strengths of the pairing, angular momentum, quadrupole, octupole and hexadecupole interactions respectively, Table 1.

nucleus	EPS	$PAIR$	ELL	QQ	OCT	HEX	$E2SD(eb)$	$E2DD(eb)$
^{154}Dy	0.6240	0.000	0.0084	−0.0244	0.0000	0.0000	0.1510	−0.4467
^{156}Dy	0.4450	0.000	0.0084	−0.0244	0.0000	0.0000	0.1274	−0.3769

Table 1: Parameters used in *IBA*-1 Hamiltonian (all in MeV).

nucleus	$E_{4_1^+}/E_{2_1^+}$	$E_{6_1^+}/E_{2_1^+}$	$E_{8_1^+}/E_{2_1^+}$	$E_{0_2^+}/E_{2_1^+}$	$E_{6_1^+}/E_{0_2^+}$	$E_{0_3^+}/E_{2_1^+}$	$BE2(4_1^+-2_1^+)/BE2(2_1^+-0_1^+)$
^{154}Dy	2.09	3.12	4.86	2.12	1.46	2.95	1.91
^{156}Dy	2.86	5.36	8.43	6.15	0.87	8.78	1.56
$X(5)$	3.02	5.83	9.29	5.65	1.53	6.03	1.58

Table 2: Energy and transition probability ratios.

2.2 Transition rates

The electric quadrupole transition operator employed is:

$$T^{(E2)} = E2SD \cdot (s^\dagger \tilde{d} + d^\dagger s)^{(2)} + \\ + \frac{1}{\sqrt{5}} E2DD \cdot (d^\dagger \tilde{d})^{(2)} . \tag{7}$$

$E2SD$ and $E2DD$ are adjustable parameters.

The reduced electric quadrupole transition rates between $I_i \to I_f$ states are given by:

$$B(E_2, I_i - I_f) = \frac{[< I_f \parallel T^{(E_2)} \parallel I_i >]^2}{2I_i + 1} . \tag{8}$$

3 Results and discussion

3.1 The potential energy surfaces

The potential energy surfaces [12], $V(\beta, \gamma)$, as a function of the deformation parameters β and γ are calculated using:

$$\begin{aligned} E_{N_\Pi N_\nu}(\beta,\gamma) &= <N_\pi N_\nu;\beta\gamma|H_{\pi\nu}|N_\pi N_\nu;\beta\gamma> = \\ &= \zeta_d (N_\nu N_\pi)\beta^2(1+\beta^2) + \beta^2(1+\beta^2)^{-2} \times \\ &\times \left\{ k N_\nu N_\pi [4 - (\bar{X}_\pi \bar{X}_\nu)\beta \cos 3\gamma] \right\} + \\ &+ \left\{ [\bar{X}_\pi \bar{X}_\nu \beta^2] + N_\nu(N_\nu - 1)\left(\frac{1}{10}c_0 + \frac{1}{7}c_2\right)\beta^2 \right\} , \end{aligned} \tag{9}$$

where

$$\bar{X}_\rho = \left(\frac{2}{7}\right)^{0.5} X_\rho , \qquad \rho = \pi \text{ (proton) or } \upsilon \text{ (neutron)} , \tag{10}$$

and ζ_d : the energy of d bosons.

The calculated potential energy surfaces, $V(\beta, \gamma)$, are presented in Figs. 1, 2. Fig. 1 shows that ^{154}Dy is a vibrational-like nucleus, U(5), while ^{156}Dy nucleus is deviated from vibrational-like to rotational-like with slight prolate deformation, SU(3), Fig. 2. The levels' energy, transition probability ratios presented in Table 2, as well as the potential energy surfaces, are in favour to consider ^{156}Dy as an $X(5)$ candidate.

$I_i^+ \; I_f^+$	B (E2)	$I_i^- \; I_f^+$	B (E1)
$2_1 \; 0_1$	0.4744	$1_1 \; 0_1$	0.0282
$2_2 \; 0_1$	0.0100	$1_1 \; 0_2$	0.1336
$2_2 \; 0_2$	0.3040	$3_1 \; 2_1$	0.1683
$3_1 \; 2_1$	0.0198	$3_1 \; 2_2$	0.0658
$4_1 \; 2_1$	0.9074	$3_2 \; 2_1$	0.0069
$3_1 \; 2_2$	0.2666	$3_2 \; 2_2$	0.0235
$4_2 \; 4_1$	0.1409	$3_2 \; 2_3$	0.1520
$4_2 \; 2_1$	0.0017	$5_1 \; 4_1$	0.3035
$4_2 \; 2_2$	0.5520	$5_1 \; 4_2$	0.0698
$6_1 \; 4_1$	1.1581	$7_1 \; 6_1$	0.4380
$6_2 \; 4_1$	0.0005	$7_1 \; 6_2$	0.0665
$6_2 \; 4_2$	0.8200	$9_1 \; 8_1$	0.5734
$8_1 \; 6_1$	1.2916	$9_1 \; 8_2$	0.0610
$8_1 \; 6_2$	0.0700	$9_2 \; 8_1$	0.1750
$8_1 \; 6_3$	0.0641	$9_2 \; 8_2$	0.3501
$8_2 \; 6_2$	0.9584	$9_2 \; 8_3$	0.2144
$10_1 \; 8_1$	1.3384	$11_1 \; 10_1$	0.7103
$10_1 \; 8_2$	0.0579	$11_1 \; 10_2$	0.0543

Table 3: Calculated $B(E2)$ and $B(E1)$ in ^{154}Dy.

3.2 Energy spectra and electric transition rates

The energy of the positive and negative parity states of isotopes ^{154,156}Dy are calculated using computer code PHINT [11]. A comparison between the experimental spectra [13,14] and our calculations, using values of the model parameters given in Table 1 for the ground state, $\beta 1$, $\beta 2$, $\gamma 1$ and $\gamma 2$ bands are illustrated in Figs. 3, 4. The agreement between the calculated levels' energy and their corresponding experimental values are fair, but they are slightly higher especially for the higher excited states. We believe this is due to the change of the projection of the angular momentum which is due mainly to band crossing. Fig. 5 shows the position of $X(5)$ and $E(5)$ between the other types of nuclei.

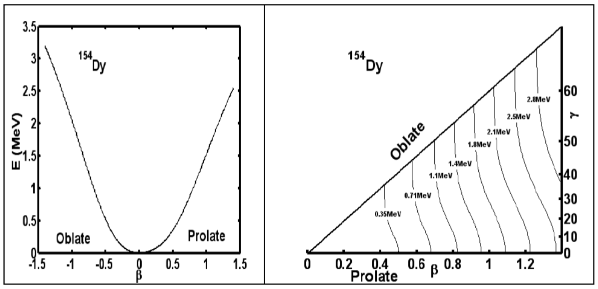

Fig. 1: Potential energy surfaces for ^{154}Dy.

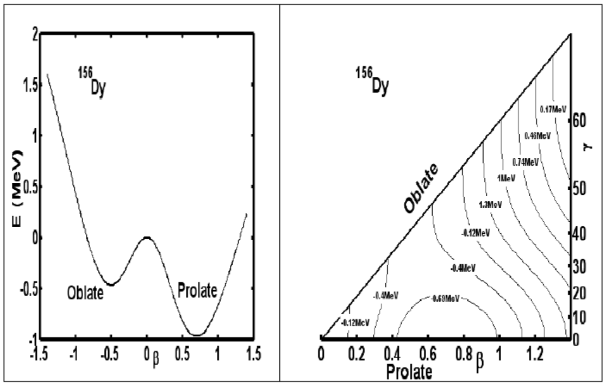

Fig. 2: Potential energy surfaces for ^{156}Dy.

I_i^+ I_f^+	B (E2)	I_i^- I_f^+	B (E1)
2_1 0_1	0.7444	1_1 0_1	0.1309
2_2 0_1	0.0023	1_1 0_2	0.0696
2_2 0_2	0.4652	3_1 2_1	0.2353
3_1 2_1	0.0169	3_1 2_2	0.0854
4_1 2_1	1.1073	3_2 2_1	0.0481
3_1 2_2	0.0026	3_2 2_2	0.0092
4_2 4_1	0.0356	3_2 2_3	0.0110
4_2 2_1	0.0016	5_1 4_1	0.3934
4_2 2_2	0.0041	5_1 4_2	0.0778
6_1 4_1	1.2446	7_1 6_1	0.5149
6_2 4_1	0.0007	7_1 6_2	0.0675
6_2 4_2	0.9083	9_1 8_1	0.6377
8_1 6_1	1.3003	9_1 8_2	0.0585
8_1 6_2	0.0410	9_2 8_1	0.0129
8_1 6_3	0.0162	9_2 8_2	0.3474
8_2 6_2	0.9817	9_2 8_3	0.2687
10_1 8_1	1.3025	11_1 10_1	0.7631
10_1 8_2	0.0332	11_1 10_2	0.0507

Table 4: Calculated $B(E1)$ and $B(E2)$ in ^{156}Dy.

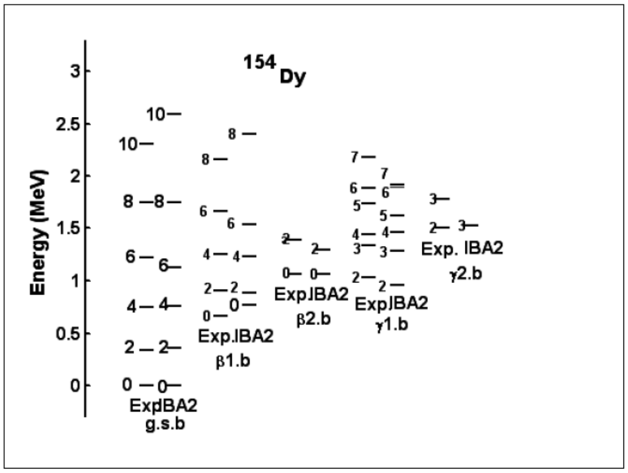

Fig. 3: Experimental[13] and calculated levels' energy.

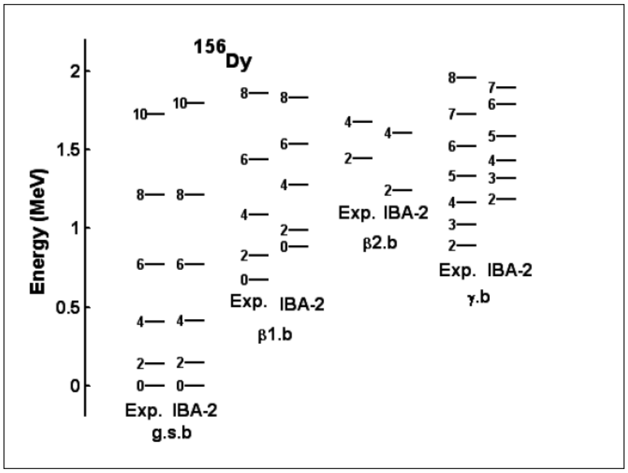

Fig. 4: Experimental[14] and calculated levels' energy.

Unfortunately there is no available measurements of electromagnetic transition rates $B(E2)$ for ^{154,156}Dy nuclei. The only measured values of $B(E2, 2_1^+ \rightarrow 0_1^+)$ for ^{154,156}Dy [15] are used in normalizing our calculated values presented in Tables 3, 4. Also, there is no experimental data available for $B(E1, I^- \rightarrow I^+)$ for normalization. Parameters *E2SD* and *E2DD* displayed in Table 1 are used in the computer code FBEM [11] for calculating the electromagnetic transition rates. No new parameters are introduced for calculating electromagnetic transition rates $B(E1)$ and $B(E2)$ of intraband and interband.

3.3 Staggering effect

The presence of positive and negative parity states has encouraged us to study the staggering effect [16] for ^{154,156}Dy isotopes using staggering functions (11) and (12) with the

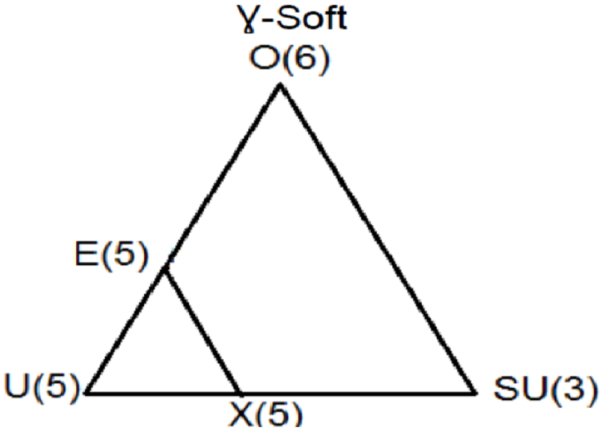

Fig. 5: Triangle showing the position of $X(5)$ and $E(5)$.

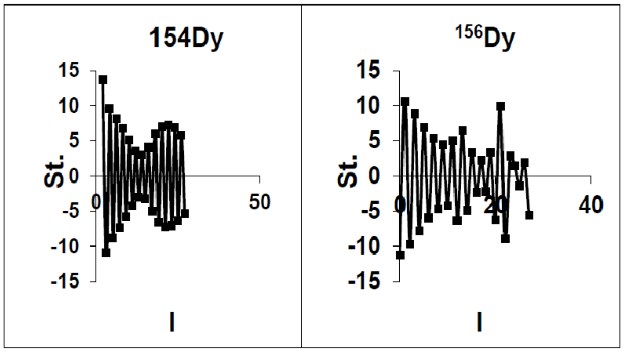

Fig. 6: Staggering effect on ^{154}Dy and ^{154}Dy.

help of the available experimental data [13,14].

$$St(I) = 6\,\Delta E(I) - 4\,\Delta E(I-1) - 4\,\Delta E(I+1) + \\ + \Delta E(I+2) + \Delta E(I-2)\,, \tag{11}$$

with

$$\Delta E(I) = E(I+1) - E(I)\,. \tag{12}$$

The calculated staggering patterns are illustrated in Fig. 6 and show an interaction between the positive and negative parity states for the ground state band of ^{154,156}Dy.

3.4 Back bending

The moment of inertia J and energy parameters $\hbar\omega$ are calculated using (13) and (14):

$$\frac{2J}{\hbar^2} = \frac{4I-2}{\Delta E(I \to I-2)}\,, \tag{13}$$

$$(\hbar\omega)^2 = (I^2 - I + 1)\left[\frac{\Delta E(I \to I-2)}{(2I-1)}\right]^2\,. \tag{14}$$

The plots in Fig. 7 show forward bending for ^{154}Dy at $I^+ = 18$ and upper bending at $I^+ = 22$ for ^{156}Dy. Bending in higher states may be explained as due to band crossing.

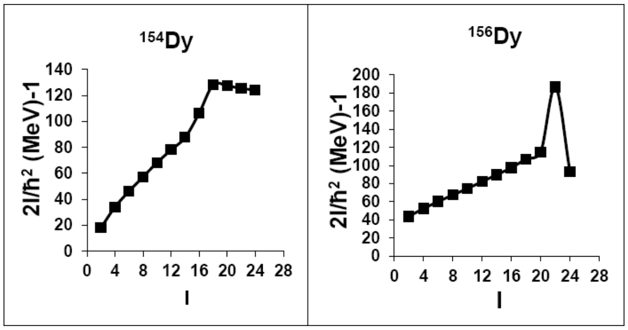

Fig. 7: Back bending ^{154}Dy and ^{156}Dy.

$I_i^+\ I_f^+\ I_{'f}^+$	^{154}Dy	^{156}Dy
$0_2\ 0_1\ 2_1$	0.0778	0.3526
$0_3\ 0_2\ 2_2$	0.2455	0.0285
$0_3\ 0_1\ 2_2$	0.0108	6.9000
$0_4\ 0_3\ 2_3$	0.1403	0.0000
$0_4\ 0_2\ 2_3$	0.0363	1.7686
$0_4\ 0_1\ 2_3$	0.0247	0.1903
$2_2\ 2_1\ 0_2$	2.4500	1.3870
$2_3\ 2_1\ 0_2$	0.2679	0.0454
$2_3\ 2_2\ 0_2$	0.1114	2.2727
$4_3\ 4_1\ 2_3$	0.0434	0.0785
$4_3\ 4_2\ 2_3$	0.0193	1.4117
$4_4\ 4_1\ 2_3$	0.0303	0.3177
$4_4\ 4_2\ 2_3$	5.3636	0.254
$4_2\ 4_1\ 2_2$	0.2384	0.0027
$6_2\ 6_1\ 4_2$	0.2422	0.1347
$8_2\ 8_1\ 6_2$	0.0609	0.0173
$10_2\ 10_1\ 8_2$	0.0337	0.0134

Table 5: $X_{if'f}\,(E0/E2)$ ratios in ^{154,156}Dy.

3.5 Electric monopole transitions

The electric monopole transitions, $E0$, are normally occurring between two states of the same spin and parity by transferring energy and zero unit of angular momentum. The strength of the electric monopole transition, $X_{if'f}\,(E0/E2)$ [17] can be calculated using (15) and (16) and are presented in Table 5

$$X_{if'f}\,(E0/E2) = \frac{B\,(E0, I_i - I_f)}{B\,(E2, I_i - I_{'f})}\,, \tag{15}$$

where $I_i = I_f$=0, $I_{'f}$=2 and I_i= $I_f \neq 0$, $I_f = I_{'f}$.

$$X_{if'f}\,(E0/E2) = (2.54 \times 10^9)\,A^{3/4}\,\frac{E_\gamma^5(\text{MeV})}{\Omega_{KL}} \times \\ \times \alpha(E2)\,\frac{T_e(E0, I_i - I_f)}{T_e(E_2, I_i - I_{'f})}\,, \tag{16}$$

A : mass number;
I_i : spin of the initial state where $E0$ and $E2$ transitions are depopulating it;
I_f : spin of the final state of $E0$ transition;
$I_{\prime f}$: spin of the final state of $E2$ transition;
E_γ : gamma ray energy;
Ω_{KL} : electronic factor for K, L shells [18];
$\alpha(E2)$: conversion coefficient of the $E2$ transition;
$T_e(E0, I_i - I_f)$: absolute transition probability of the $E0$ transition between I_i and I_f states; and
$T_e(E_2, I_i - I_{\prime f})$: absolute transition probability of the $E2$ transition between I_i and $I_{\prime f}$ states.

Unfortunately, there is no experimental data available for comparison with the calculated values.

3.6 Conclusions

The *IBA*-1 model has been applied successfully to ^{154,156}Dy isotopes and:

1. Levels' energy are successfully reproduced;
2. Potential energy surfaces are calculated and show vibrational-like characteristics to ^{154}Dy and slight prolate deformation to ^{156}Dy;
3. Electromagnetic transition rates $B(E1)$ and $B(E2)$ are calculated;
4. Bending has been observed at $I^+= 18$ for ^{154}Dy and at $I^+= 22$ for ^{156}Dy ;
5. Staggering effect has been calculated and beat patterns observed which show an interaction between the positive and negative parity states;
6. Strength of electric monopole transitions $X_{if'f}(E0/E2)$ are calculated; and
7. The potential energy surfaces, transition probability rates and energy show that ^{156}Dy has the $X(5)$ symmetry.

Received on November 28, 2017

References

1. Chabab M., El Batoul A., Hamzavi M., Lahbas A., Oulne M. Excited collective states of nuclei within Bohr Hamiltonian with Tietz-Hua potential. *Eur. Phys. J. A*, 2017, v. 53, 157.
2. Buganu1 P. and Budaca R. Sextic potential for γ-rigid prolate nuclei. *J. Phys. G*, 2015, v. 42, 105106.
3. Alimohammadi M., Zare S. Investigation of Bohr-Mottelson Hamiltonian in γ-rigid version with position dependent mass. *Nucl. Phys. A*, 2017, v. 960, 78.
4. Xiao-Dong Sun, Ping Guo, and Xiao-Hua Li. Systematic study of α-decay half-lives for even-even nuclei within a two-potential approach. *Phys. Rev. C*, 2016, v. 93, 034316.
5. Li1 Z. P., Niksic T. and Vretenar D. Coexistence of nuclear shapes: self-consistent mean-field and beyond. *J. Phys. G*, 2015, v. 43, 024005.
6. Girija K. K. Role of shape and quadrupole deformation of parents in the cluster emission of rare earth nuclei. *Int. J. Mod. Phys. E*, 2014, v. 23, 1450002.
7. Zimba G. L., Sharpey-Schafer J. F., Jones P., Bvumbi S. P., Masiteng L. P., Majola S. N. T., Dinoko T. S., Lawrie E. A., Lawrie J. J., Negi D., Papka P., Roux D., Shirinda O., Easton J. E., Khumalo N. A. Octupole correlations in N=88 ^{154}Dy: Octupole vibration versus stable deformation. *Phys. Rev. C*, 2016, v. 94, 054303.
8. Ijaz Q. A., Ma W. C., Abusara H., Afanasjev A. V., Xu Y. B., Yadav R. B., Zhang Y. C., Carpenter M. P., Janssens R. V. F., Khoo T. L., Lauritsen T., Nisius D. T. Excited superdeformed bands in ^{154}Dy and cranked relativistic mean field interpretation. *Phys. Rev. C*, 2009, v. 80, 034322.
9. Paul E. S., Rigby S. V., Riley M. A., Simpson J., Appelbe D. E., Campbell D. B., Choy P. T. W., Clark R. M., Cromaz M., Evans A. O., Fallon P., Gorgen A., Joss D. T., Lee I. Y., Macchiavelli A. O., Nolan P. J., Pipidis A., Ward D., Ragnarsson I. Loss of collectivity in the transitional ^{156}Er nucleus at high spin. *Phys. Rev. C*, 2009, v. 79, 044324.
10. Blasi N., Atanasova L., Balabanski D., Das Gupta S., Gladinski K., Guerro L., Nardelli S., and Saltarelli A. $E0$ decay from the first 0^+ state in ^{156}Dy and ^{160}Er. *Phys. Rev. C*, 2014, v. 90, 044317.
11. Scholten O. The program package PHINT (1980) version. Internal report KVI-63, Keryfysisch Versneller Institut, Gronigen, 1979.
12. Ginocchio J. N. and Kirson M. W. An intrinsic state for the interacting boson model and its relationship to the Bohr- Mottelson approximation. *Nucl. Phys. A*, 1980, v. 350, 31.
13. Reich C. W. ADOPTED LEVELS, GAMMAS for ^{154}Dy. *Nuclear Data Sheets*, 2009, v. 110, 2257.
14. Reich C. W. ADOPTED LEVELS, GAMMAS for ^{156}Dy. *Nuclear Data Sheets*, 2012, v. 113, 2537.
15. Pritychenko B., Birch M., Singh B. and Horoi M. Tables of $E2$ transition probabilities from the first 2^+ states in even-even nuclei. *Atomic Data and Nuclear Data Tables*, 2016, v. 107, 1.
16. Minkov N., Yotov P., Drenska S. and Scheid W. Parity shift and beat staggering structure of octupole bands in a collective model for quadrupole-octupole deformed nuclei. *J. Phys. G*, 2006, v. 32, 497.
17. Rasmussen J. O. Theory of $E0$ transitions of spheroidal nuclei. *Nucl.Phys.*, 1960, v. 19, 85.
18. Bell A. D., Aveldo C. E., Davidson M. G. and Davidson J. P. Table of $E0$ conversion probability electronic factors. *Can. J. Phys.*, 1970, v. 48, 2542.

Soliton-effect Spectral Self-compression for Different Initial Pulses

Armine Grigoryan[1], Aghavni Kutuzyan[2], and Garegin Yesayan[3]

Chair of Optics, Department of Physics, Yerevan State University, 1 Alex Manoogian, 0025 Yerevan, Armenia.
E-mails: [1]arminegrigor@gmail.com, [2]akutuzyan@ysu.am, [3]gyesayan@ysu.am

Our numerical studies demonstrate a spectral analogue of soliton-effect self-compression for different initial pulses. The evolution of transform-limited pulses during the propagation in a single-mode fiber with anomalous dispersion is studied. It is shown that the spectral analogue of soliton-effect self-compression is realized in the case of different initial pulses: periodicity of the spectral compression and stretching is different for different initial pulses. The approximation of curves introducing the frequency of the spectral compression and stretching dependence on nonlinearity parameter is implemented.

1 Introduction

The spectral compression (SC) process has numerous interesting applications in ultrafast optics and laser technology [1–5], such as the spectrotemporal imaging of ultrashort pulses by means of Fourier transformation [1]. In [5], the authors offer to apply SC in a fiber laser instead of strong spectral filtering. This allows to obtain transform-limited pulses and benefits the laser's power efficiency. As another practical application of SC, it is important to mention the transfer of femtosecond pulses without distortion at a relatively large distance [6]. Diverse applications of SC remain urgent in relation to the development and analysis of new effective compression systems. For example, in [7] the compression efficiency is improved by means of amplitude modulation.

The traditional spectral compressor consists of prism as a dispersive delay line, where the pulse is stretched and negatively chirped, and single-mode fiber (SMF) with the normal group-velocity dispersion, where nonlinear self-phase modulation leads to the chirp compensation and spectral narrowing. At the wavelength range of $<1.3\,\mu$m, the group-velocity dispersion is positive for standard silica fibers. The role of the normal dispersion in SC of subpicosecond laser pulses is analyzed in [8]. As it is known, the combined impact of negative dispersion and the nonlinear self-phase modulation leads to the formation of solitons in SMF [9, 10], when the impact of dispersion and nonlinear self-phase modulation balance each other out. The pulse self-compression phenomenon is also known [11], which is obtained when the impact of the nonlinear self-phase modulation exceeds the dispersion. Under the opposite condition, i.e. when the impact of dispersion exceeds the nonlinearity, we can expect spectral self-compression (self-SC) by the analogy of the pulse self-compression. Recently, the self-SC implementation directly in a fiber with negative group-velocity dispersion (at the wavelength range $\geq 1.3\,\mu$m for standard silica fibers) was proposed [12] and studied [13]. In this work, we carried out detailed numerical studies on the process of soliton-effect self-SC for different initial pulses. Simulations were carried out for initial Gaussian and secant-hyperbolic pulses. We have shown the soliton-effect self-SC in the fiber "directly", without dispersive delay line, in the fiber with anomalous dispersion for different initial pulses. It is shown that there is an analogy between the processes of soliton self-compression and soliton-effect self-SC for different initial pulses: the periodicity of the process changes in the case of different initial pulses. The studies show that the periodicity of the process decreases when the nonlinearity parameter reduces. Our detailed study has shown that the frequency of compression has polynomial and exponential approximations.

2 Numerical studies and results

In the SMF, the pulse propagation is described by the nonlinear Schrödinger equation for normalized complex amplitude of field, considering only the influence of group-velocity dispersion and Kerr nonlinearity [14]:

$$i\,\frac{\partial\psi}{\partial\zeta} = \frac{1}{2}\,\frac{\partial^2\psi}{\partial\eta^2} + R\,|\psi^2|\,\psi \tag{1}$$

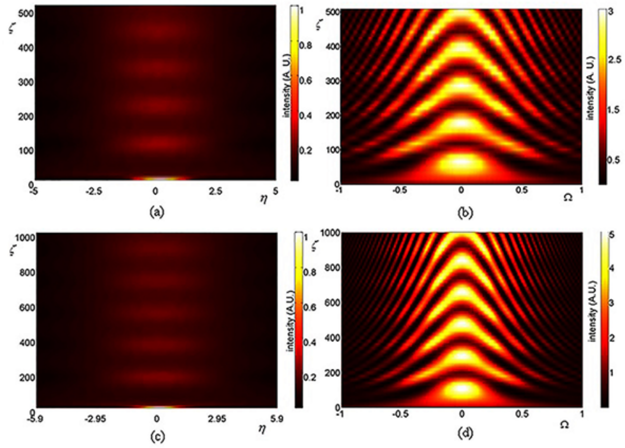

Fig. 1: The 3D map of the propagation of Gaussian (a, b) and secant-hyperbolic (c, d) pulses and its spectra. $\Omega = (\omega - \omega_0)/\Delta\omega_0$.

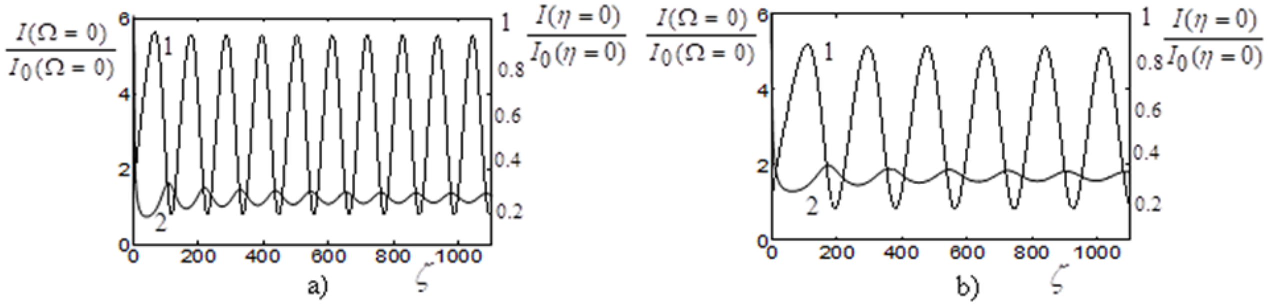

Fig. 2: The peak values of spectra (1) and pulses (2) vs fiber length for initial Gaussian (a) and secant-hyperbolic (b) pulses.

where $\zeta = z/L_D$ is the dimensionless propagation distance, $\eta = (t - z/u)/\tau_0$ is the running time, which are normalized to the dispersive length $L_D = \tau_0^2/|k_2|$ (k_2 is the coefficient of second-order dispersion), and initial pulse duration τ_0, respectively. The nonlinearity parameter R is given by the expression $R = L_D/L_{NL}$, where $L_{NL} = (k_0 n_2 I_0)^{-1}$ is the nonlinearity length, n_2 is the Kerr index of silica, I_0 is the peak intensity. The first and second terms of the right side of (1) describe the impact of group-velocity dispersion and nonlinearity, respectively. We use the split-step Fourier method during the numerical solution of the equation, with the Fast Fourier Transform algorithm on the dispersive step [15, 16].

The objective of our numerical studies is the soliton-effect self-SC, which takes place when the dispersive length in the fiber is shorter than the nonlinear length ($L_D < L_{NL}$, i.e. $R < 1$). Therefore, at first, the group-velocity dispersion stretches the pulse by acquiring a chirp. Afterwards, the accumulated impact of nonlinear self-phase modulation leads to the compensation of the chirp. As a result, the spectrum is compressed. The process has periodic character. We study the pulse behavior in a fiber with negative group-velocity dispersion for different initial pulses and different values of the nonlinearity parameter and fiber length.

Fig. 1 illustrates the process of propagation of Gaussian (a, b, $R = 0.6$) and secant-hyperbolic (c, d, $R = 0.4$) pulses and their spectra. In this case, we study the process for short fiber lengths where the efficiency of the process is high for the nonlinearity parameter values of $R = 0.6$ (Gaussian pulse) and $R = 0.4$ (secant-hyperbolic pulse). It can be observed that the pulse is stretched and the spectrum is compressed in the initial propagation step. Afterwards, the width of central peak of the spectrum decreases and the main part of the pulse energy goes to the spectral satellites. At the certain fiber length, the reverse process starts the pulse self-compression.

The process can be explained in the following way: in the initial propagation step the spectrum is compressed, which leads to the decreasing of dispersion impact. As a result, the dispersive length increases, therefore, the nonlinearity parameter also increases. When the condition $R > 1$ is satisfied ($L_D > L_{NL}$), the pulse is compressed. Then, the spectrum is stretched, which leads to the increasing of dispersion impact (the decreasing of L_D and R). When the condition $R < 1$ is satisfied ($L_D < L_{NL}$), the spectrum is compressed.

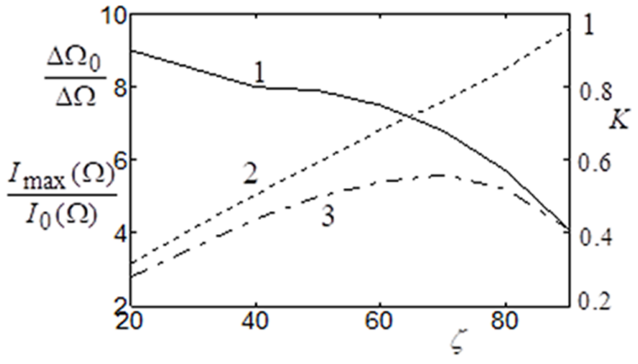

Fig. 3: The K (1) and self-SC ($\Delta\Omega_0/\Delta\Omega$) (2), $I_{max}(\Omega)/I_0(\Omega)$ (3) vs fiber length for initial Gaussian pulse.

The process, which is described above has periodic character, but in the case of every next cycle, the quality of the SC is worse than in the case of the previous SC as spectral satellites increase within propagation.

Fig. 2 shows the peak value of spectra (1) and pulses (2) for initial Gaussian (a) and secant-hyperbolic (b) pulses, which shows that the process has a periodic character not only for Gaussian pulses but also for secant-hyperbolic pulses. The difference between Gaussian and secant-hyperbolic pulses is the speed of the process: as we see in Fig. 2, every next spectrum compression occurs in the short distance in the case of Gaussian pulses in comparison with the case of secant-hyperbolic pulses.

As we see in Fig. 2, the peak value decreases within the distance which is conditioned by the fact that the energy of spectral satellites increases. This fact is proved by the coefficient of SC quality, K, (the ratio of the energy in the central part of pulse to the whole energy). As we see in Fig. 3, the coefficient of SC quality decreases within the fiber length.

In the process of propagation, the behavior of the spec-

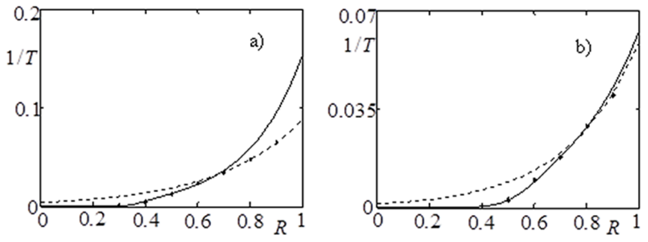

Fig. 4: The frequency vs nonlinearity parameter for initial secant-hyperbolic (a) and Gaussian (b) pulses. The points correspond to the numerical investigations, solid lines introduce the approximation of results (Eqs. 2, 3) by all points, while the dotted lines correspond to the approximation by last 3 points (Eqs. 4, 5).

trum is similar to the pulse behavior in the case of the soliton compression. As it is known, the propagation of the high-order solitons have periodic character with a $(\pi/2)L_D$ periodicity. On the distance equal to the periodicity, at first pulse is compressed, then it is stretched taking initial shape. In our case, the spectrum has similar behavior. However, due to the incomplete cancellation of the chirp, the changing of the spectrum does not have the strict periodic character. The process is different from soliton compression due to the fact that spectrum changes depend on a nonlinear phase, which depends on the shape of the pulse. In the case of soliton propagation, the changes of the pulse depend on a dispersive phase, which depends on neither spectral nor temporal shape of the pulse.

The study shows that the periodicity of the SC and stretching decreases with the reduction of nonlinearity parameter (Fig. 4). It is shown that there are polynomial (Eqs. 2, 3) and exponential (Eqs. 4, 5) approximations of the curve introducing nonlinearity parameter dependent frequency (Fig. 4), which is the frequency of the SC and stretching.

$$1/T = 1/\left(1.6 \times 10^{7} \times 10^{-30R} + 7821 \times 10^{-4.79R}\right) \tag{2}$$

$$1/T = 1/\left(5.09 \times 10^{6} \times 10^{-19.8R} + 731.3 \times 10^{-3.83R}\right) \tag{3}$$

$$1/T = 1/\left(0.004 \times e^{3.08R}\right) \tag{4}$$

$$1/T = 1/\left(0.001 \times e^{3.73R}\right) \tag{5}$$

3 Conclusion

Through the detailed study, we study the soliton-effect self-SC for initial Gaussian and secant-hyperbolic pulses. The process is realized in the fiber with a negative group-velocity dispersion. The study shows that there is an analogy between soliton self-compression and soliton-effect self-SC processes. We show that the periodicity of the process decreases when the nonlinearity parameter reduces. It is shown that the frequency dependence on the nonlinearity parameter has polynomial and exponential approximations.

Acknowledgements

The authors acknowledges Prof. R. Hakobyan for fruitful discussions and help during the work.

Received on December 4, 2017

References

1. Mouradian L., Louradour F., Messager V., Barthélémy A., Froehly C. Spectrotemporal imaging of femtosecond events. *IEEE J. Quantum Electron.*, 2000, v. 36, 795.
2. Mansuryan T., Zeytunyan A., Kalashyan M., Yesayan G., Mouradian L., Louradour F., and Barthélémy A. Parabolic temporal lensing and spectrotemporal imaging: a femtosecond optical oscilloscope. *J. Opt. Soc. Am. B*, 2008, v. 25, A101–A110.
3. Kutuzyan A., Mansuryan T., Kirakosian A., Mouradian L. Self-forming of temporal dark soliton in spectral compressor. *Proc. SPIE*, 2003, v. 5135, 156–160.
4. Louradour F., Lopez-Lago E., Couderc V., Messager V., Barthélémy A. Dispersive-scan measurement of the fast component of the third-order nonlinearity of bulk materials and waveguides. *Optics Lett.*, 1999, v. 24, 1361–1363.
5. Boscolo S., Turitsyn S., and Finot Ch. Amplifier similariton fiber laser with nonlinear spectral compression. *Optics Lett.*, 2012, v. 37, 4531–4533.
6. Clark S., Ilday F., Wise F. Fiber delivery of femtosecond pulses from a Ti:sapphire laser. *Optics Lett.*, 2001, v. 26, 1320–1322.
7. Andresen E., Dudley J., Oron D., Finot Ch., and Rigneault H. Transform-limited spectral compression by self-phase modulation of amplitude-shaped pulses with negative chirp. *Optics Lett.*, 2011, v. 36, 707–709.
8. Kutuzyan A., Mansuryan T., Yesayan G., Hakobyan R., Mouradian L. Dispersive regime of spectral compression. *Quantum Electron.*, 2008, v. 38, 383–387.
9. Hasegawa A., Tappert F. Transmission of Stationary Nonlinear Optical Pulses in the Dispersive Dielectric Fibers. I. Anomalous Dispersion. *Appl. Phys.*, 1973, v. 23, 142–144.
10. Mollenauer L., Stolen R., Gordon J. Experimental Observation of Picosecond Pulse Narrowing and Soliton in Optical Fibers Dispersive Dielectric Fibers. I. Anomalous Dispersion. *Phys. Rev. Lett.*, 1980, v. 45, 1095–1098.
11. Mollenauer L., Stolen R., Gordon J., and Tomlinson W. Extreme picosecond pulse narrowing by means of soliton effect in single-mode optical fibers Dispersive Dielectric Fibers. I. Anomalous Dispersion. *Optics Lett.*, 1983, v. 8, 289–291.
12. Yesayan G. *Journal of Contemporary Physics*, 2012, v. 45, 225.
13. Grigoryan A., Yesayan G., Kutuzyan A. and Mouradian L. Spectral domain soliton-effect self-compression. *Journal of Physics: Conference Series*, 2016, v. 672.
14. Akhmanov S. A., Vysloukh V. A. and Chirkin A. S. Optics of Femtosecond Laser Pulses. AIP, New York, 1992.
15. Hardin R., Tappert F. Applications of the Split-Step Fourier Method to the Numerical Solution of Nonlinear and Variable Coefficient Wave Equations. *Cronicle*, 1973, v. 15, 423.
16. Fisher R., Bischel W. The role of linear dispersion in plane-wave self-phase modulation. *Appl. Phys. Lett.*, 1973, v. 23, 661–663.

A Symplectic Cosmological Model

Jean-Pierre Petit
Former director of scientific research at Observatoire de Marseille, France
E-mail: jp.petit@mailaps.org

In this paper, we use the Lie algebra of the dual Poincaré dynamical group which when acted upon by its coadjoint, displays energy momentum and spin as pure geometrical quantities. When extended to the full group, one obtains negative mass species in accordance with our *Janus Cosmological Model* and the twin universe model conjectured by A. Sakharov. Within a *5D Kaluza space*, the theory leads to a new matter/antimatter duality implying negative energy photons emitted on the negative domain of this twin Universe. This accounts for the dark matter and dark energy which are thereof impossibe to detect in our domain. Finally, we show that shifting to a Hermitean space-time with an associated complex dynamic group yields imaginary energy, imaginary energy and imaginary charges all embedded in a symplectic (complex) framework which remains open to wide investigations.

Notations

Space time indices: $m, n = 0, 1, 2, 3$.
Space-time signature: -2.
Einstein's constant: $\varkappa$.

Introduction

Symplectic geometry relies on symplectic manifolds. Those are said symplectic when they are endowed with a so-called *symplectic form* that allows for the measurement of sizes of 2-dimensional objects. In Riemannian geometry, the metric tensor probes lengths and angles, whereas the symplectic form measures areas.

The term symplectic was first coined by *H. Weyl* in 1939 as a substitute to rather confusing (line) complex groups and/ or Abelian linear groups. The relativistic symplectic mechanics [1] was primarily developed by the french mathematician J. M. Souriau from dynamic groups theory. It provides a new description of energy, momentum and spin only in terms of pure geometrical quantities. This arises from two objects: n-dimensional space and its isometry group.

In what follows, we briefly describe its properties which we apply to a particular cosmological model featuring two types of masses and energies comparable to the *twin Universe* originally conjectured by A. Zakharov.

1 The Janus Cosmological Model (JCM)

The main mathematical tool used here is the so-called "*momentum map*" which is inferred from the *co-adjoint* action of the group on the dual of its *Lie algebra*. (The coadjoint of the Lie group is the dual of the adjoint representation.) Applying the technique of this coadjoint action leads to the appearance of generalized linear and angular momenta: {energy E, 3-momentum p, spin s}. The action of the group corresponds to

$$M' = L\,M\,{}^{\mathrm{T}}M + N\,{}^{\mathrm{T}}P\,{}^{\mathrm{T}}L - L\,P\,{}^{\mathrm{T}}N, \tag{1}$$

$$P' = L\,P, \tag{2}$$

where P is the generalized energy-momentum 4-vector

$$\begin{pmatrix} E \\ p_1 \\ p_2 \\ p_3 \end{pmatrix}, \tag{3}$$

L is here the element of the *Lorentz group* and N is the *boost 4-vector*. In the classical treatment, one merely considers the *restricted Poincaré Group* which is formed with orthochronous components L_0. Hence, the *full Poincaré Group* can be written as

$$\begin{pmatrix} \lambda L_0 & N \\ 0 & 1 \end{pmatrix} \tag{4}$$

with $\lambda = \pm 1$.

We then obtain two kinds of matters an two kinds of photons with each an opposite mass and energy. This copes with the *Janus Cosmological Model* (JCM) we developed earlier [2–4]. Such a model involves particles with opposite masses and energy. However, as shown by H. Bondi [5], the field equations cannot sustain this duality due to the subsequent and unmanageable "*run away*" effect. In short, General Relativity deals with positive masses that are attractive, while negative masses would exhibit repelling forces. Therefore, if one considers a couple ($+m$, $-m$), the negative mass escapes and is "chased" by the positive one while at the same time experiencing a uniform acceleration.

This issue can be evaded by considering a bi-metric (our *JCModel*) within a single manifold $\mathfrak{M}_4$ equipped with two metric tensors ${}^{(+)}g_{\mu\nu}$ and ${}^{(-)}g_{\mu\nu}$, which define two field equations [5]:

$${}^{(+)}R_{\mu\nu} - \frac{1}{2}\,{}^{(+)}g_{\mu\nu}{}^{(+)}R = \varkappa \left[{}^{(+)}T_{\mu\nu} + \left(\frac{{}^{(-)}g}{{}^{(+)}g} \right)^{1/2} {}^{(-)}T_{\mu\nu} \right], \tag{5}$$

$${}^{(-)}R_{\mu\nu} - \frac{1}{2}\,{}^{(-)}g_{\mu\nu}{}^{(-)}R = \varkappa \left[{}^{(-)}T_{\mu\nu} + \left(\frac{{}^{(+)}g}{{}^{(+)}g} \right)^{1/2} {}^{(+)}T_{\mu\nu} \right]. \tag{6}$$

Those time dependent and time independent solutions fit the observational data.

2 Extension to a wider geometrical framework

We now turn consider an extension of the group to a five dimensional scheme so as to obtain an *isometry group* which acts on the basic *Kaluza space-time*

$$\begin{pmatrix} \lambda\mu & 0 & \phi \\ 0 & \lambda L_0 & N \\ 0 & 0 & 1 \end{pmatrix} \tag{7}$$

with $\mu = \pm 1$ and $\lambda = \pm 1$.

By extending to the fifth dimension, the *Noether theorem* induces an additional conserved scalar quantity which is readily identified with the electric charge q.

The $\mu = -1$ implies both the inversion of this charge and the inversion of the fifth dimension, which is just the geometrical expression of the matter-antimatter duality as primarly shown by J. M. Souriau [6]. Therefore the physics ruled by the dynamical group (7) exhibits straightforwardly the matter-antimatter symmetry in the two domains with opposed mass and energy. If we now add p-Kaluza-like dimensions, we obtain the metric under the form:

$$ds^2 = dx_0^2 - dx_1^2 - dx_2^2 - dx_3^2 - d\xi_1^2 - d\xi_2^2 - \ldots - d\xi_p^2\,. \tag{8}$$

This can be coupled to an isometry group

$$\begin{pmatrix} \lambda\mu & 0 & \ldots & 0 & 0 & \phi_1 \\ 0 & \lambda\mu & \ldots & 0 & 0 & \phi_2 \\ \ldots & \ldots & \ldots & \ldots & \ldots & \ldots \\ 0 & 0 & \ldots & \lambda\mu & 0 & \phi_p \\ 0 & 0 & \ldots & 0 & \lambda\mu & N \\ 0 & 0 & \ldots & 0 & 0 & 1 \end{pmatrix} \tag{9}$$

with $\mu = \pm 1$ and $\lambda = \pm 1$.

The electric charge is just one of the quantum charges. Here again, the $(\mu = -1)$ terms reflect the C-symmetry: they account for the classical matter-antimatter representation. The $(\mu = -1;\ \lambda = -1)$ correspond to the PT-symmetry classically associated with the "Feynman antimatter" which is no longer indentified with the "C-antimatter". This is due to the presence of the time reversal T inducing both the mass and energy inversion. In other words, the group representation (9) which is the basis of the *JC Model*, provides two distinct types of antimatters:

— The C-type corresponding to Dirac's antimatter.

— The PT-type corresponding to Feynman's antimatter.

3 Remark about Andrei Sakharov' scheme

In classical cosmology a severe problem remains, due to the absence of observation of primordial antimatter. In 1967, Sakharov suggested that the Universe comprises two domains: the actual Universe and its twin Universe, each connected through a singularity [8–10]. Both are CPT-symmetrical. Since the mass inversion goes with T-symmetry, our *JC Model* [3, 4] corresponds to such CPT-symmetry. The so-called *twin matter* becomes nothing but a copy of ordinary particles with opposite masses and charges. If, as suggested by Sakharov, positive masses are synthetized by positive energy quarks faster than the synthesis of negative masses from positive energy antiquarks, then in the *positive energy domain* we find:

— Remnant positive masses matter.

— The equivalent (ratio 3/1) of positive energy antiquarks.

— Positive energy photons.

In analogy to Sakharov's ideas, the negative energy domain would be thus composed of:

— Remnant negative masses matter.

— The equivalent (ratio 3/1) of negative energy quarks.

— Negative energy photons.

As shown in [3, 4], the negative material suitably replaces both dark matter and so-called dark energy. Accordingly, by emitting negative energy photons, the remnant negative masses matter are genuinely invisible.

4 Remark about the Quantum Theory of Fields (QFT)

In QFT the time reversal operator is a complex operator which can be *linear* and *unitary*, as well as antilinear and anti-unitary. If chosen linear and unitary, this operator implies the existence of negative energy states, which are *à priori* banned by QFT. In Weinberg [7], we quote: "*In order to avoid this disastrous conclusion, we are forced to conclude that T is anti-linear and anti-unitary*". On page 104, Weinberg also writes: "*no examples are known of particles that furnish unconventional representation of inversions, so these possibilities will not be pursued further here*". Actually, this was true until the discovery of the acceleration of the expanding universe which implies the action of a negative pressure. As a pressure is likened to an energy density, this new phenomenon implies in turn the existence of negative energy states and as a result, it questions QFT by itself. In the same manner, it also raises some questions as to the validity of the so-called CPT theorem and the vacuum instability. Indeed, classically, one considers that a particle may loose energy through the emission of a photon, so that such a process would lead to negative energy states. But if we consider that a negative mass particle emits negative energy photons, this process would lead to stable zero energy state.

5 Extension of the method to a complex field

If one replaces the Minkowski coordinates $\{x_0, x_1, x_2, x_3\}$ with complex coordinates we may form the *Hermitean Riemann* *metric*:

$$ds^2 = dx_0{}^*dx_0 - dx_1{}^*dx_1 - dx_2{}^*dx_2 - dx_3{}^*dx_3\,. \tag{10}$$

This metric is defined on a *Hermitean manifold*.

Lest us now consider the real matrix G

$$\begin{pmatrix} 1 & 0 & 0 & 0 \\ 0 & -1 & 0 & 0 \\ 0 & 0 & -1 & 0 \\ 0 & 0 & 0 & -1 \end{pmatrix} \tag{11}$$

and the complex Lorentz group defined as

$${}^*LGL = G\,, \tag{12}$$

${}^*L$ stands for the *adjoint* of L.

One can then easily show that the *complex Poincaré group*

$$\begin{pmatrix} L & N \\ 0 & 1 \end{pmatrix} \tag{13}$$

is an isometry group of such a Hermitean space and can be considered as a dynamic group. Surprizingly, all classical (matrix) calculations can be extended to such complex framework, by simply substituting the matrices ${}^*A$ to the transpose matrices ${}^{\mathrm{T}}A$.

As a result, the complex momentum obeys the law:

$$M' = L\,M\,{}^*L + N\,{}^*P\,{}^*L - L\,P\,{}^*N, \tag{14}$$

$$P' = L\,P, \tag{15}$$

where ${}^*P$ is the complex energy momentum 4-vector. This extended physics grants the mass a complex nature implying the possible existence of purely real masses $\pm m$ and purely imaginary masses: $\pm(-1)^{1/2}\,m$. At the same time, such masses can exchange imaginary photons whose energies are: $\pm(-1)^{1/2}\,E$.

Conclusion

J. M. Souriau gave the first purely geometrical interpretation of all classsical physics features, namely — energy, momenta, and spin. When extended to higher dimensions it provides a geometrical interpretation of the matter-antimatter duality. In addition, one can notice that the complex approach of space definition yields complex physical quantities. The physical meaning of these complex quantities should demand further scrutiny and as such remains a new open field of investigations.

Submitted on December 25, 2017

References

1. Souriau J. M. Structure des Systèmes Dynamiques. Dunod, Paris, 1970 (English translation: Structure of Dynamic Systems. Birkhaüser, 1997).
2. Petit J. P., D'Agostini G. Negative mass hypothesis in Cosmology and the nature of dark energy. *Astrophysics and Space Sciences*, 2014, v. 354, issue 2, 611–615
3. Petit J. P., D'Agostini G. Cosmological Bi-metric model with interacting positive and negative masses and two different speeds of light in agreement with the observed acceleration of the Universe. *Modern Physics Letters A*, 2014, v. 29, no. 34.
4. Petit J. P., D'Agostini G. Lagrangian derivation of the two coupled field equations in the Janus Cosmological Model. Astrophysics and Space Science, 2015, v. 357, issue 1, 67–74.
5. Bondi H. Negative mass in General Relativity. *Rev. of Mod. Physics*, 1957, v. 29, issue 3, 423.
6. Souriau J. M. Géométrie et Relativité. Hermann, 1964.
7. Weinberg S. The Quantum Theory of Fields. Cambridge University Press, 2005, p. 74–76, p. 104.
8. Sakharov A. D. *ZhETF Pis'ma*, 1967, v. 5, 32–35; *JTEP Lett.*, 1967, v. 5, 24–27.
9. Sakharov A. D. *ZhETF Pis'ma*, 1979, v. 76, 1172–1181; *JTEP*, 1979, v. 49, 594–603.
10. Sakharov A. D. Cosmological model of the Universe with a time vector inversion. *ZhETF*, 1980, v. 79, 689–693; *Tr. JTEP*, v. 52, 349–351.

Quantum Gravity Aspects of Global Scaling and the Seismic Profile of the Earth

Hartmut Müller
E-mail: hm@interscalar.com

In this paper we derive a profile of the Earth's interior from our fractal model of matter as chain system of harmonic quantum oscillators. Model claims are verified by geophysical data. Global scaling as model of quantum gravity is discussed.

Introduction

The origin of gravity is a key topic in modern physics. The universality of free fall means that the gravity acceleration of a test body at a given location does not depend on its mass, physical state or chemical composition. This discovery, made four centuries ago by Galilei, is confirmed by modern empirical research with an accuracy of 10^{-11} - 10^{-12} [1–3]. A century ago Einstein supposed that gravity is indistinguishable from, and in fact the same thing as, acceleration. In fact, Earth's surface gravity acceleration can be derived from the orbital elements of any satellite, also from Moon's orbit:

$$g = \frac{4\pi^2 R^3}{(T \cdot r)^2} = \frac{4\pi^2 (384399000\,\mathrm{m})^3}{(2360591\,\mathrm{s} \cdot 6371000\,\mathrm{m})^2} = 9.83\ \mathrm{m\ s^{-2}},$$

where R is the semi-major axis of Moon's orbit, T is the orbital period of the Moon and r is the average radius of the Earth. No data about the mass or chemical composition of the Earth or the Moon is needed.

The 3rd law of Johannes Kepler describes the ratio R^3/T^2 as constant for a given orbital system. Kepler's discovery is confirmed by high accuracy radar and laser ranging of the movement of artificial satellites. The geocentric gravitational constant [4] equals:

$$\mu = 4\pi^2 R^3/T^2 = 3.986004418(8) \cdot 10^{14}\ \mathrm{m^3 s^{-2}}.$$

Kepler's 3rd law is of geometric origin and can be derived from Gauss's flux theorem in 3D-space within basic scale considerations. It applies to all conservative fields which decrease with the square of the distance and does not require the presence of mass.

The orbital elements R and T are directly measured, while $\mu = GM$ is an interpretation that provides mass as a source of gravity and the universality of the big G. Both postulates are essential in Newton's law of universal gravitation and in Einstein's general theory of relativity.

Nevertheless, coincidence and causality is not the same thing and Newton's hypothesis about mass as source of gravity could turn out to be a dispensable assumption.

In the case of mass as source of gravity, in accordance with Newton's shell theorem, a solid body with a spherically symmetric mass distribution should attract particles outside it as if its total mass were concentrated at its center. In contrast, the attraction exerted on a particle should decrease as the particle goes deeper into the body and it should become zero at the body's center.

A boat at the latitude 86.71 and longitude 61.29 on the surface of the Arctic Ocean would be at the location that is regarded as having the highest gravitational acceleration of 9.8337 m/s^2 on Earth. At higher or lower position to the center of the Earth, gravity should be of less intensity. This conclusion seems correct, if only mass is a source of gravity acceleration and if the big G is universal under any conditions and in all scales.

The Preliminary Reference Earth Model [5] affirms the decrease of the gravity acceleration with the depth. However, this hypothesis is still under discussion [6–8].

In 1981, Stacey, Tuck, Holding, Maher and Morris [9, 10] reported anomalous measures (larger values than expected) of the gravity acceleration in deep mines and boreholes. In [11] Frank Stacey writes: "Modern geophysical measurements indicate a 1% difference between values at 10 cm and 1 km (depth). If confirmed, this observation will open up a new range of physics". In fact, gravity is the only interaction that is not described yet by a quantum theory.

In [12] we have introduced a fractal model of matter as a chain system of harmonic quantum oscillators. The model statements are quite general, that opens a wide field of possible applications.

Already in [13] we could show that scale invariance is a fundamental characteristic of this model. On this background we proposed quantum scaling as model of particle mass generation [14] and we could show that particle rest masses coincide with the eigenstates of the system. This is valid not only for hadrons, but for mesons and leptons as well. Andreas Ries [15] demonstrated that this model allows for the prediction of the most abundant isotope of a given chemical element.

In the framework of our model, physical characteristics of celestial bodies can be understood as macroscopic quantized eigenstates in chain systems of oscillating protons and electrons [16]. This is also valid for accelerations. In [17] was shown that the surface gravity accelerations of the planets in the solar system correspond with attractor nodes of stability in chain systems of protons and electrons.

Our model allows us to see a connection between the stability of the solar system and the stability of electron and proton and consider global scaling as a forming factor of the solar system. This may be of cosmological significance.

In this paper we derive a profile of the Earth's interior from our fractal model of matter as chain system of harmonic quantum oscillators. Model claims are verified by geophysical data. Global scaling as model of quantum gravity is discussed.

Methods

In [13] we have shown that the set of natural frequencies of a chain system of similar harmonic oscillators can be described as set of finite continued fractions $\mathcal{F}$, which are natural logarithms:

$$\ln\left(\omega_{jk}/\omega_{00}\right) = n_{j0} + \cfrac{z}{n_{j1} + \cfrac{z}{n_{j2} + \ddots + \cfrac{z}{n_{jk}}}} = \tag{1}$$

$$= [z, n_{j0}; n_{j1}, n_{j2}, \ldots, n_{jk}] = \mathcal{F}$$

where ω_{jk} is the set of angular frequencies and ω_{00} is the fundamental frequency of the set. The denominators are integer: $n_{j0}, n_{j1}, n_{j2}, \ldots, n_{jk} \in \mathrm{Z}$, the cardinality $j \in \mathrm{N}$ of the set and the number $k \in \mathrm{N}$ of layers are finite. In the canonical form, the numerator z equals 1.

In the canonical form, for finite continued fractions, the distribution density of the eigenvalues reaches maxima near reciprocal integers 1, 1/2, 1/3, 1/4, … which are the attractor points of the fractal set $\mathcal{F}$ of natural logarithms (fig. 1).

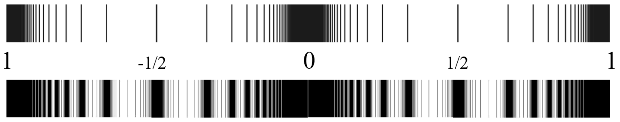

Fig. 1: The canonical form of $\mathcal{F}$ for $k = 1$ (above) and for $k = 2$ (below) in the range $-1 \leqslant \mathcal{F} \leqslant 1$.

Any finite continued fraction represents a rational number [18]. Therefore, all natural frequencies ω_{jk} in (1) are irrational, because for rational exponents the natural exponential function is transcendental [19]. This circumstance provides for high stability of eigenstates in a chain system of harmonic oscillators because it prevents resonance interaction between the elements of the system [20]. Already in 1987 we have applied continued fractions of the type $\mathcal{F}$ as criterion of stability in engineering [21, 22].

In the case of harmonic quantum oscillators, the continued fractions $\mathcal{F}$ define not only fractal sets of natural angular frequencies ω_{jk}, angular accelerations $a_{jk} = c \cdot \omega_{jk}$, oscillation periods $\tau_{jk} = 1/\omega_{jk}$ and wavelengths $\lambda_{jk} = c/\omega_{jk}$ of the chain system, but also fractal sets of energies $\mathrm{E}_{jk} = \hbar \cdot \omega_{jk}$ and masses $\mathrm{m}_{jk} = \mathrm{E}_{jk}/c^2$ which correspond with the eigenstates of the system. For this reason, we call the continued fraction $\mathcal{F}$ the "fundamental fractal" of eigenstates in chain systems of harmonic quantum oscillators.

In the canonical form ($z = 1$) of the fundamental fractal $\mathcal{F}$, shorter continued fractions correspond with more stable eigenstates of a chain system of harmonic oscillators. Therefore, integer logarithms represent the most stable eigenstates (main attractor nodes).

As the cardinality and number of layers of the continued fractions $\mathcal{F}$ are finite but not limited, in each point of the space-time occupied by the chain system of harmonic quantum oscillators the scalar $\mathcal{F}$ is defined. Consequently, any chain system of harmonic quantum oscillators can be seen as source of the scalar field $\mathcal{F}$, the fundamental field of the system. Figure 2 shows the linear 2D-projection of the first layer (k = 1) of the fundamental field $\mathcal{F}$ in the canonical form (z = 1) in the interval $-1 \leqslant \mathrm{F} \leqslant 1$.

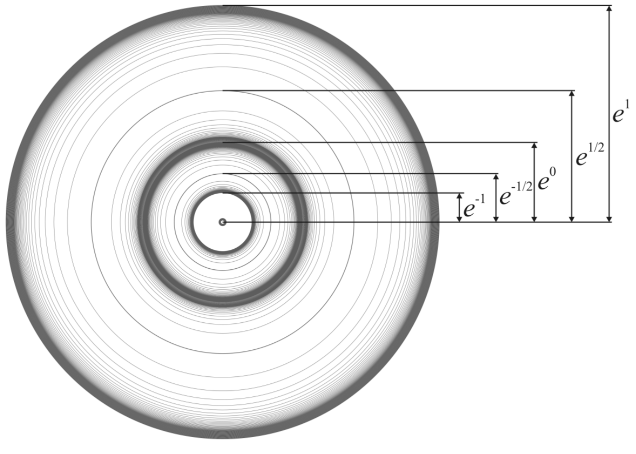

Fig. 2: The first layer ($k = 1$) of the linear 2D-projection of the fundamental field $\mathcal{F}$ in the canonical form ($z = 1$) in the range $-1 \leqslant \mathcal{F} \leqslant 1$.

The scalar potential difference $\Delta\mathcal{F}$ of sequent equipotential surfaces at a given layer k is defined by the difference of continued fractions (1). In the canonical form ($z = 1$):

$$\Delta\mathcal{F} = \mathcal{F}(\mathrm{j,k}) - \mathcal{F}(\mathrm{j+1,k}) =$$
$$= [n_{j0}; n_{j1}, n_{j2}, \ldots, n_{jk}] - [n_{j0}; n_{j1}, n_{j2}, \ldots, n_{j+1,k}]$$

Normal matter is formed by nucleons and electrons because they are exceptionally stable quantum oscillators. In the concept of isospin, proton and neutron are viewed as two states of the same quantum oscillator. Furthermore, they have similar rest masses. However, a free neutron decays into a proton, an electron and antineutrino within 15 minutes while the life-spans of the proton and electron top everything that is measurable, exceeding 10^{29} years [23].

These unique properties of the electron and proton predestinate their physical characteristics as fundamental units. Table 1 shows the basic set of electron and proton units that can be considered as a fundamental metrology (c is the speed of light in a vacuum, $\hbar$ is the Planck constant, k_B is the Boltzmann constant).

PROPERTY	ELECTRON	PROTON
rest mass m	$9.10938356(11) \cdot 10^{-31}$ kg	$1.672621898(21) \cdot 10^{-27}$ kg
energy $E = mc^2$	0.5109989461(31) MeV	938.2720813(58) MeV
angular frequency $\omega = E/\hbar$	$7.76344071 \cdot 10^{20}$ Hz	$1.42548624 \cdot 10^{24}$ Hz
angular oscillation period $\tau = 1/\omega$	$1.28808867 \cdot 10^{-21}$ s	$7.01515 \cdot 10^{-25}$ s
angular wavelength $\lambda = c/\omega$	$3.8615926764(18) \cdot 10^{-13}$ m	$2.1030891 \cdot 10^{-16}$ m
angular acceleration $a = c\omega$	$2.327421 \cdot 10^{29}$ ms^{-2}	$4.2735 \cdot 10^{32}$ ms^{-2}

Table 1: The basic set of physical properties of the electron and proton. Data taken from Particle Data Group [23]. Frequencies, oscillation periods, accelerations and the proton wavelength are calculated.

In [16] was shown that the fundamental metrology (tab. 1) is completely compatible with Planck units [24]. Originally proposed in 1899 by Max Planck, these units are also known as natural units, because the origin of their definition comes only from properties of nature and not from any human construct. Max Planck wrote [27] that these units, "regardless of any particular bodies or substances, retain their importance for all times and for all cultures, including alien and non-human, and can therefore be called natural units of measurement". Planck units reflect the characteristics of space-time.

In [12, 14] we have introduced a fractal model of matter as a chain system of oscillating protons and electrons. We hypothesize that scale invariance of the fundamental field $\mathcal{F}$ calibrated on the physical properties of the proton and electron (tab. 1) is a universal characteristic of organized matter and criterion of stability. This hypothesis we have called 'global scaling' [16, 26, 27].

Results

The proton-to-electron mass ratio is approximately 1836, so that the mass contribution of the proton to normal matter is very high, for example in the hydrogen atom (protium) it is $1 - 1/1836 = 99.95$ percent. Consequently, the mass contribution of the electron is only 0.05 percent. In heavier atoms which contain neutrons, the electron contribution to atomic mass is even smaller. Therefore, in this paper we investigate a fractal model of matter as chain system of oscillating protons and derive a profile of the Earth's interior from it.

As figure 1 shows, in an attractor node of the layer $k = 0$, the potential difference on the layer $k = 1$ changes its signature and compression of the equipotential density is changed to decompression. The same is valid in attractor nodes of the layer $k = 1$. There the potential difference on the layer $k = 2$ changes its signature. Therefore, we expect that near the attractor nodes of $\mathcal{F}$ the dramatic increase of the field strength and the change of compression to decompression of the equipotential density in the attractor nodes should lead to measurable consequences. This should be valid at least for the main attractor nodes on the layer $k = 0$.

Figure 3 shows the $\mathcal{F}$ calibrated on the angular Compton wavelength of the proton in the canonical ($z = 1$) linear 2D-projection for $k = 1$ in the interval $[49; \infty] \leqslant \mathcal{F} \leqslant [52; -4]$. At the graphic's left side the corresponding radii in km are indicated. The radial distribution of equipotential nodes represents the expected 2D-profile of the Earth's interior.

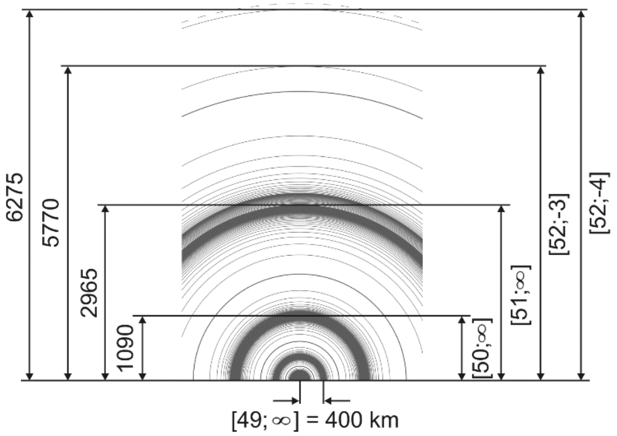

Fig. 3: The fundamental field $\mathcal{F}$ calibrated on the proton in the canonical ($z = 1$) linear 2D-projection for $k = 1$ in the interval $[49; \infty] \leqslant \mathcal{F} \leqslant [52; -4]$. Radius in km (left side). The dotted line at the top indicates the Earth surface that coincides with the significant subnode [44; 4] = 6372 km of the $\mathcal{F}$ calibrated on the electron.

The propagation speed of a seismic compression wave depends on the density and elasticity of the medium and should therefore correspond with zones of compression and decompression near the main nodes of the fundamental field $\mathcal{F}$.

In accordance with both empirical models of the Earth interior PREM [5] and IASP91 [28], the crust-mantle boundary (Mohorovicic discontinuity, 'Moho') is in between 35 and 90 km depth from the Earth surface, where seismic P-waves jump in speed abruptly from 6 to 8 km/s. In our model, the Moho corresponds with the compression zone before the significant subnode [52; -4] = 6275 km of the $\mathcal{F}$ calibrated on the proton.

Detailed seismic studies have shown that the speed of P-waves (longitudinal pressure waves) in the mantle increases rather rapidly from about 9 to 11 km/s at depths between 400 and 700 km, marking a layer called the transition zone. This zone separates the upper mantle from the lower mantle. In our model, the transition zone corresponds with the compression zone before the significant subnode [52; -3] = 5770 km of the $\mathcal{F}$ calibrated on the proton.

As they travel more deeply into the mantle, P-waves increase their speed from 8 km/s at the Moho to about 13 km/s at a depth of 2900 km. Though, once P-waves penetrate below 2900 km, their velocity suddenly drops from 13 km/s back down to about 8 km/s. This dramatic reduction in speed after a depth of 2900 km defnes the boundary between the Earth's mantle and the core. The outer core seems liquid, because seismic S-waves (transversal shear waves) do not pass this boundary. In contrast, the innermost part of the core within a radius of 1210 km seems solid. Reaching the inner core, P-waves again jump to a velocity of 11 km/s.

Both models PREM and IASP91 identify these boundaries with the radius of the liquid core (3480 km) and the radius of the inner solid core (1210 km). These estimations correspond with the compression zones before the main attractors [51; ∞] and [50; ∞] of the proton $\mathcal{F}$ and confirm that P-waves increase their velocity in the compression zone before the attractor. Then in the decompression zone after the attractor, they decrease the velocity. This coincidence is a strong confirmation of global scaling and demonstrates that the current dimension and structure of the Earth interior is not casual, but an essential criterion of its stability.

It is a notable circumstance that P-waves reach cosmic velocities. In fact, at the Moho, P-waves jump to velocities near 8 km/s that is in the range of the first cosmic velocity a rocket must have to reach a circular orbit around the Earth. In the transition zone that separates the upper mantle from the lower mantle, P-waves jump to 11 km/s that is in the range of the second cosmic velocity a rocket must have to escape the Earth gravity acceleration. Through the lower mantle, the P-wave reach 13 km/s at the core-mantle boundary that is in the range of velocities a rocket launched from Earth must have to escape the solar system.

This similarity seems not by case: cosmic escape velocities do not depend on the mass of the object escaping the Earth. The velocity a rocket must have to reach a circular orbit around the Earth depends only on the gravity acceleration g and the radius r of the departure orbit. It is notable that no data about the mass of the Earth is needed. In the case of departure from the Earth surface:

$$v_{circular} = \sqrt{(gr)} = \sqrt{9.8\,\text{m/s}^2 \cdot 6371000\,\text{m}} = 7.9 \text{ km/s}.$$

The second cosmic velocity a rocket must have to escape the Earth gravity acceleration is $\sqrt{2}$ times higher:

$$v_{escape} = \sqrt{2} \cdot v_{circular} = 11.2 \text{ km/s}.$$

Conversely, an object that falls under the attraction of the Earth surface gravity acceleration g from infinity, starting with zero velocity, will strike the Earth surface with a velocity equal to its escape velocity.

In accordance with our model (fig. 3), the inner core of the Earth should have a substructure that origins from the attractor node [49; ∞] = 400 km of the $\mathcal{F}$ calibrated on the proton (fig. 4). In fact, the seismological exploration of the Earth's inner core has revealed unexpected structural complexities. There is a clear hemispherical dichotomy in anisotropy and also evidence of a subcore with a radius 300–600 km [29]. Considering that the radius of the Sun coincides with the main attractor node [49; ∞] of the $\mathcal{F}$ calibrated on the electron:

$$\ln\left(\frac{r_{\text{Sun}}}{\lambda_{\text{electron}}}\right) = \ln\left(\frac{6.96407 \cdot 10^{8} \text{ m}}{3.8615926764 \cdot 10^{-13} \text{ m}}\right) = 48.945$$

we can write down the equation for the ratio of the radii:

$$\frac{r_{\text{Sun}}}{r_{\text{Earth subcore}}} = \frac{\lambda_{\text{electron}}}{\lambda_{\text{proton}}}.$$

Already in [16] we have shown that the minimum and maximum values of the Earth's radius approximate the significant node [44; 4] of the $\mathcal{F}$ calibrated on the electron:

$$\ln\left(\frac{r_{\text{Earth max}}}{\lambda_{\text{electron}}}\right) = \ln\left(\frac{6.384 \cdot 10^{3} \text{ m}}{3.8615926764 \cdot 10^{-13} \text{ m}}\right) = 44.252,$$

$$\ln\left(\frac{r_{\text{Earth min}}}{\lambda_{\text{electron}}}\right) = \ln\left(\frac{6.353 \cdot 10^{3} \text{ m}}{3.8615926764 \cdot 10^{-13} \text{ m}}\right) = 44.247.$$

Figure 3 shows the node [44; 4] of the electron $\mathcal{F}$ as dotted line in the top of the graphic.

Conclusion

In the framework of our model of matter as chain system of harmonic quantum oscillators, the fractal fundamental field $\mathcal{F}$ affects any type of physical interaction, including the gravitational. Fundamental particles like electron and proton are not the ultimate sources, but stability nodes of the fundamental field of any chain system of harmonic quantum oscillators. The spatial and temporal distribution of these stability nodes is determined by the ratio of fundamental constants. Already Paul Dirac [30] mentioned that "... whether a thing is constant or not does not have any absolute meaning unless that quantity is dimensionless".

Applying our fractal model of matter to the analysis of gravimetric and seismic characteristics of the Earth we did show that it corresponds well with established empirical models of the Earth interior. We interpret this correspondence as evidence of the fractality, scale invariance and macroscopic quantization of Earth's gravity field.

We presume that gravity is a scale-invariant attractor effect of stability nodes in chain systems of oscillating protons and electrons. May be this hypothesis could become a bridge that connects the island of gravity research with the continent of quantum physics.

Acknowledgements

I'm thankful to Leili Khosravi, Viktor Panchelyuga and Oleg Kalinin for valuable discussions.

Submitted on December 30, 2017

References

1. Niebauer T.M., McHugh M.P., Faller J.E. Galilean test for the fifth force. *Physical Review Letters*, 1987, v.59, 609–612.
2. Shapiro I.I. et al. Verification of the principle of equivalence for massive bodies. *Physical Review Letters*, 1976, v.36, 555–558.
3. Roll P.G., Krotov R., Dicke R.H. The equivalence of inertial and passive gravitational mass. *Annals of Physics*, 1964, v.26, 442–517.
4. Numerical Standards for Fundamental Astronomy. maia.usno.navy.mil, IAU Working Group, 2017.
5. Dziewonski A.M., Anderson D.L. Preliminary reference Earth model. *Physics of the Earth and Planetary Interiors*, 1981, v.25, 297–356.
6. Quinn T., Speake C. The Newtonian constant of gravitation — a constant too difficult to measure? An introduction. *Phil. Trans. Royal Society A*, v.372, 20140253.
7. Anderson J.D. et al. Measurements of Newton's gravitational constant and the length of day. *EPL*, 2015, v.110, 10002.
8. Cahill R.T. 3-Space In-Flow Theory of Gravity: Boreholes, Blackholes and the Fine Structure Constant. *Progress in Physics*, 2006, v. 2, issue 2, 9–16.
9. Stacey F.D. et al. Constraint on the planetary scale value of the Newtonian gravitational constant from the gravity profile within a mine. *Phys. Rev. D*, 1981, v.23, 1683.
10. Holding S.C., Stacey F.D., Tuck G.J. Gravity in mines. An investigation of Newton's law. *Phys. Rev. D*, 1986, v.33, 3487.
11. Stacey F.D. Gravity. *Science Progress*, 1984, v.69, no.273, 1–17.
12. Müller H. Fractal Scaling Models of Natural Oscillations in Chain Systems and the Mass Distribution of Particles. *Progress in Physics*, 2010, v.6, issue 3, 61–66.
13. Müller H. Fractal Scaling Models of Resonant Oscillations in Chain Systems of Harmonic Oscillators. *Progress in Physics*, 2009, v.5, issue 2, 72–76.
14. Müller H. Emergence of Particle Masses in Fractal Scaling Models of Matter. *Progress in Physics*, 2012, v.8, issue 4, 44–47.
15. Ries A. Qualitative Prediction of Isotope Abundances with the Bipolar Model of Oscillations in a Chain System. *Progress in Physics*, 2015, v.11, issue 2, 183–186.
16. Müller H. Scale-Invariant Models of Natural Oscillations in Chain Systems and their Cosmological Significance. *Progress in Physics*, 2017, v.13, issue 4, 187–197.
17. Müller H. Gravity as Attractor Effect of Stability Nodes in Chain Systems of Harmonic Quantum Oscillators. *Progress in Physics*, 2018, v.14, issue 1, 19–23.
18. Khintchine A.Ya. Continued fractions. University of Chicago Press, Chicago, 1964.
19. Hilbert D. Über die Transcendenz der Zahlen e und π. *Mathematische Annalen*, 1893, v.43, 216–219.
20. Panchelyuga V.A., Panchelyuga M.S. Resonance and Fractals on the Real Numbers Set. *Progress in Physics*, 2012, v.8, issue 4, 48–53.
21. Müller H. The general theory of stability and objective evolutionary trends of technology. *Applications of developmental and construction laws of technology in CAD*, Volgograd, VPI, 1987 (in Russian).
22. Müller H. Superstability as a developmental law of technology. *Technology laws and their Applications*, Volgograd-Sofia, 1989 (in Russian).
23. Olive K.A. et al. (Particle Data Group), *Chin. Phys. C*, 2016, v.38, 090001.
    Patrignani C. et al. (Particle Data Group), *Chin. Phys. C*, 2016, v.40, 100001.
24. Astrophysical constants. Particle Data Group, pdg.lbl.gov
25. Planck M. Über Irreversible Strahlungsvorgänge. *Sitzungsbericht der Königlich Preußischen Akademie der Wissenschaften*, 1899, v.1, 479–480.
26. Müller H. Scaling as Fundamental Property of Natural Oscillations and the Fractal Structure of Space-Time. *Foundations of Physics and Geometry*, Peoples Friendship University of Russia, 2008 (in Russian).
27. Müller H. Scaling of body masses and orbital periods in the Solar System as consequence of gravity interaction elasticity. Abstracts of the *XIIth International Conference on Gravitation, Astrophysics and Cosmology*, dedicated to the centenary of Einstein's General Relativity theory, Moscow, PFUR, 2015.
28. Kennett B.L.N. IASPEI 1991 Seismological Tables. Canberra, Australia, 1991.
    Kennett B.L., Engdahl E.R. Travel times for global earthquake location and phase identification. *Geophysical Journal International*, 1991, v.105, 429–465.
29. Deguen R. Structure and dynamics of Earth's inner core. *Earth and Planetary Science Letters*, 2012, v.333–334, 211–225.
30. Dirac P.A.M. The cosmological constants. *Nature*, 1937, v.139, issue 3512, 323.

Relativistic Model for Radiating Spherical Collapse

Victor Medina[1] and Nelson Falcon[2]

[1]Departamento de Física – Facultad de Ingeniería – Universidad de Carabobo. Valencia, Venezuela
E-mail: vmedina@uc.edu.ve
[2]Departamento de Física – Facultad Experimental de Ciencias y Tecnología – Universidad de Carabobo. Valencia, Venezuela
E-mail: nelsonfalconv@gmail.com

The relativistic models for radiating spherical collapse is important for to explain the emission process on very high energy in Supernova burst and Quasars. A general method is reviewed, to obtain models which describe non static radiating spheres, without having to make any hypothesis about the emission of radiation during the collapse. It is concluded that the field equations together with the conservation laws (Bianchi's Identity) form a complete set of integrable equations that do not require additional the emissivation hypothesis of a Gaussian pulse on at an arbitrary instant to trigger the collapse. The emissivation hypothesis of a Gaussian pulse is not only unnecessary, but also leads to qualitatively and quantitatively different solutions. Calculations were performed using the computer algebra package *GRTensorII*, running on *Maple 13*, along with several Maple routines that we have used specifically for this type of problems. The Schwarzschild and Tolman VI models are shown as examples where it's emphasizes the importance of using conservation equations properly, for describe the collapse for the self-gravitating sphere.

1 Introduction

The last phases of stellar evolution of massive stars are dominated by the contribution of stellar radiation due to changes of the inner or outer distribution of matter, in the gravitational potential of the radiating fluid spheres and, therefore, general relativity provides a description of the collapse of the compact objects (Neutron Stars, Black Holes). This description can be extended to explain the radiation process of very high energy in astrophysical scenarios, such as Supernova bursts and Quasars. A number of studies have been reported describing a gravitational collapse: Oppenheimer and Snyder [1], Tolman [2] and furthermore the study of the collapsing radiating fluid [3–6].

This scheme has recently been used for various scenarios of relativistic hydrodynamics. We can highlight some examples: charged fluids [7–9], isotropic [10] or anisotropic fluid [11, 12], shock waves [13, 14], in free space [15, 16] or diffusion process [17, 18]. It is necessary to contrast its quantitative results with other calculation schemes. Barreto et al. [19] have extended the semi-numerical scheme to the Schwarzschild coordinates, simulating some scenarios of the gravitational collapse.

Herrera and collaborators [6, 19–21] developed a general algorithm for modeling self gravitating spheres out of equilibrium, beginning from the known static solutions of Einstein's equations. This method divides the space-time in two spatial regions. The outer region is described by the Vaidya solution and the space-time metric in the interior is obtained by solving the Einstein field equations. Further, proper boundary conditions are imposed in order to guarantee a smooth matching of the solutions in the surface of the junction. This semi numerical technique has been used extensively to study high energy in astrophysical scenarios [19, 21–27].

However in these numerical simulations a Gaussian pulse is introduced *ad hoc* to represent the emission of radiation that initiates the disequilibrium during the collapse of the radiating fluid ball [6, 20, 21, 23–25, 28]. These assumptions could be unnecessary and generate spurious solutions, since this loss of mass is prescribed by one of the conservation equations when applying the Bianchi Identity [29, 30]. Parts of the calculation of the Bianchi identities that were performed in this work were possible and verified using the *GRTensorII* package.

The purpose of this paper is to show the general method to obtain models which describe radiating non-static spheres without having to make any hypothesis about the emission of radiation during the collapse. This paper follows as much as possible the notation and physical description prescribed by Herrera et al. [6]. For this, the field equations and conservation laws are shown in Section 2; then section 3 establishes the procedure for the static solutions and obtaining the surface equations. The models Schwarzschild-like and Tolman VI-like are discussed in section 4 and 5 respectively, and in the last section are shown the concluding remarks.

2 The Field equations and conservation relationships

Let us consider a non static radiating spheres. The metric takes the form [4]

$$ds^2 = e^{2\beta}\frac{V}{r}\,du^2 + 2e^{2\beta}du\,dr - r^2 d\theta^2 - r^2\sin^2\theta\, d\phi^2, \qquad (1)$$

where u and r are time like and radial-like coordinates respectively; β and V are functions of u and r; θ, ϕ are the usual angle coordinates. In these coordinates the gravitational field equations are:

$$\begin{aligned}
-8\pi T_{00} &= -\frac{V_{,0} - 2V\beta_{,0}}{r^2} - \frac{V}{r^3}\left(e^{2\beta} - V_{,1} + 2\beta_{,1}V\right) \\
-8\pi T_{01} &= -\frac{1}{r^2}\left(e^{2\beta} - V_{,1} + 2\beta_{,1}V\right) \\
-8\pi T_{11} &= -\frac{4\beta_{,1}}{r} \\
-8\pi T_2^2 = -8\pi T_3^3 &= -e^{2\beta}\Big(2\beta_{01} - \frac{1}{2r^2}\left[rV_{,11} + \right. \\
&\quad \left. -2\beta_{,1}V + 2r\left(\beta_{,11}V + \beta_{,1}V_{,1}\right)\right]\Big).
\end{aligned}$$

As usual, note that we used the subscript $_{,0}$ and $_{,1}$ for the derivative for u and r, respectively; and the semicolon (;) for covariant differentiation. Then transformation relations between local Minkowskian and radiative coordinates are:

$$\begin{aligned}
dt &= \left(\frac{\partial t}{\partial u}\right) du + \left(\frac{\partial t}{\partial r}\right) dr \\
&= e^{\beta}\left(\frac{V}{r}\right)^{\frac{1}{2}} du + e^{\beta}\left(\frac{r}{V}\right)^{\frac{1}{2}} dr \qquad (2)
\end{aligned}$$

$$dx = \left(\frac{\partial x}{\partial r}\right) dr = e^{\beta}\left(\frac{r}{V}\right)^{\frac{1}{2}} dr \qquad (3)$$

$$dy = \left(\frac{\partial y}{\partial \theta}\right) d\theta = r\, d\theta \qquad (4)$$

$$dz = \left(\frac{\partial z}{\partial \phi}\right) d\phi = r \cdot \sin\theta\, d\phi\,. \qquad (5)$$

We assumed the stellar material as perfect fluid, with energy density $\hat{\rho}$, radial pressure $\hat{P}$, without heat conduction neither viscosity, then

$$\hat{T}_{\alpha\beta} = \left(\hat{\rho} + \hat{P}\right) \cdot U_\alpha U_\beta - \hat{P} \cdot \eta_{\alpha\beta}, \qquad (6)$$

where $U_\alpha = (1, 0, 0, 0)$, $3\hat{\sigma}$ is the isotropic radiation of the energy density, and $\hat{\varepsilon}$ no-polarized component of the energy density in radial direction. Now consider an observer in local Minskowskian system with radial velocity ω, in the Lorentzian system we can write:

$$\bar{T}_{\mu\nu} = \Lambda^{\alpha}_{\mu}\Lambda^{\beta}_{\nu}\hat{T}_{\alpha\beta}, \qquad (7)$$

where the Lorentz matrix is

$$\Lambda^{\alpha}_{\mu} = \begin{bmatrix} \frac{1}{\sqrt{1-\omega^2}} & -\frac{\omega}{\sqrt{1-\omega^2}} & 0 & 0 \\ -\frac{\omega}{\sqrt{1-\omega^2}} & \frac{1}{\sqrt{1-\omega^2}} & 0 & 0 \\ 0 & 0 & 1 & 0 \\ 0 & 0 & 0 & 1 \end{bmatrix}. \qquad (8)$$

We define

$$\bar{\rho} = \hat{\rho} + 3\hat{\sigma},\ \bar{P} = \hat{P} + \hat{\sigma}, \quad \bar{\varepsilon} = \hat{\varepsilon}\frac{1+\omega}{1-\omega}.$$

Note also that from (2-3) the velocity of matter in the radiative coordinates is given by

$$\frac{dr}{du} = \frac{V}{r} \cdot \frac{\omega}{1-\omega}, \qquad (9)$$

so forth the energy-impulse tensor in the Lorentz system is

$$\begin{aligned}
\bar{T}_{00} &= \bar{\varepsilon} + \frac{\bar{\rho} + \omega^2\bar{P}}{1-\omega^2} \\
\bar{T}_{01} = \bar{T}_{10} &= -\bar{\varepsilon} - \frac{\omega}{1-\omega^2}\left(\bar{\rho} + \bar{P}\right) \\
\bar{T}_{11} &= \frac{\bar{P} + \omega^2\bar{\rho}}{1-\omega^2} + \bar{\varepsilon} \\
\bar{T}_{22} = \bar{T}_{33} &= \bar{P}.
\end{aligned}$$

Using (2) - (5) we obtain the energy-impulse tensor in radiative coordinates as:

$$\begin{aligned}
T_{00} &= e^{2\beta}\left(\frac{V}{r}\right)\left(\frac{\bar{\rho} + \omega^2\bar{P}}{1-\omega^2} + \varepsilon\right) \\
T_{01} = T_{10} &= e^{2\beta}\left(\frac{\bar{\rho} - \omega\bar{P}}{1+\omega}\right) \\
T_{11} &= e^{2\beta}\left(\frac{r}{V}\right)\left(\frac{1-\omega}{1+\omega}\right)\left(\bar{\rho} + \bar{P}\right) \\
T_{22} = \frac{T_{33}}{\sin^2\theta} &= r^2\bar{P}.
\end{aligned}$$

Remember that a bar indicates that the quantity is measured in the Lorentzian system, and the effective variables are written without bar. Now

$$\rho \equiv \frac{\bar{\rho} - \omega\bar{P}}{1+\omega}, \quad P \equiv \frac{\bar{P} - \omega\bar{\rho}}{1+\omega}, \quad \varepsilon \equiv \bar{\varepsilon}. \qquad (10)$$

It can be seen at once that $\rho = \bar{\rho}$ and $P = \bar{P}$ in $r = 0$, also, in the static case $\omega = 0$. As before then:

$$\begin{aligned}
T_{00} &= e^{2\beta}\left(\frac{V}{r}\right)\left[\frac{\omega(\rho + P)}{(1-\omega)^2} + \rho + \varepsilon\right] \\
T_{01} = T_{10} &= e^{2\beta}\rho \\
T_{11} &= e^{2\beta}\left(\frac{r}{V}\right)(\rho + P) \\
T_{22} = \frac{T_{33}}{\sin^2\theta} &= r^2\bar{P},
\end{aligned}$$

thus the field equations are:

$$\begin{aligned}
-\frac{V}{r^2}\left[\left(2\beta_{,0} - \frac{V_{,0}}{V}\right) - \frac{1}{r}\left(2V\beta_{,1} - V_{,1} + e^{2\beta}\right)\right] &= \\
= 8\pi\, e^{2\beta}\left(\frac{V}{r}\right)\left[\varepsilon + \rho + \frac{\omega(\rho + P)}{(\omega - 1)^2}\right] & \qquad (11)
\end{aligned}$$

$$2V\beta_{,1} - V_{,1} + e^{2\beta} = 8\pi r^2 e^{2\beta}\rho \qquad (12)$$

$$\frac{4\beta_{,1}}{r} = 8\pi\frac{r}{V}\, e^{2\beta}(\rho + P) \qquad (13)$$

$$-2\beta_{,01}+\frac{1}{2r^2}\left[rV_{,11}-2\beta_{,1}V+2r\left(V_{,1}\beta_{,1}+V\beta_{,11}\right)\right]= \\ =8\pi e^{2\beta}\bar{P}. \tag{14}$$

Using the conservation equations (Bianchi Identity) $T^{\mu}_{\nu;\mu}=0$, we obtain only three no-trivial relations:

$$T^{\mu}_{1;\mu}=\frac{e^{-2\beta}}{2\pi r}\beta_{,10}-\frac{\partial P}{\partial r}+ \\ -\frac{1}{2}\left(2\beta_{,1}+\frac{V_{,1}}{V}-\frac{1}{r}\right)(\rho+P)-\frac{2\left(P-\bar{P}\right)}{r}\quad=0, \tag{15}$$

$$T^{\lambda}_{0;\lambda}=\frac{V}{r}\left\{\left(2\beta_{1}+\frac{V_{,1}}{V}+\frac{1}{r}\right)\left[\varepsilon+\frac{\omega\left(\rho+P\right)}{(1-\omega)^2}\right]+\right. \\ \left.+\frac{\omega}{(1-\omega)^2}\frac{\partial\left(\rho+P\right)}{\partial r}\right\}+\frac{1}{2}\left(2\beta_{,0}-\frac{V_{,0}}{V}\right)(\rho+P)+ \\ +\frac{\partial\rho}{\partial u}+\frac{V}{r}\left[\frac{\partial\varepsilon}{\partial r}+\frac{1+\omega}{(1-\omega)^3}\left(\rho+P\right)\frac{\partial\omega}{\partial r}\right]=0, \tag{16}$$

$$e^{2\beta}T^{\lambda 1}_{;\lambda}=\frac{V}{r}\left\{\left(2\beta_{,1}+\frac{V_{,1}}{V}+\frac{1}{r}\right)\left[\varepsilon+\frac{1+\omega^2}{2\left(1-\omega\right)^2}\left(\rho+P\right)\right]\right. \\ \left.+\frac{\omega\left(\rho+P\right)_{,1}}{(1-\omega)^2}+\frac{\partial P}{\partial r}+\frac{1}{r}\left[\rho+\bar{P}-\left(P-\bar{P}\right)\right]\right\}+ \\ -\frac{1}{2}\left(2\beta_{,0}-\frac{V_{,0}}{V}\right)(\rho+P)+\frac{\partial P}{\partial u}+ \\ +\frac{V}{r}\left[\frac{\partial\varepsilon}{\partial r}+\frac{1+\omega}{(1-\omega)^3}\left(\rho+P\right)\frac{\partial\omega}{\partial r}\right]=0. \tag{17}$$

It is remarkable that only two Bianchi equations (15-17) are independent, then

$$e^{2\beta}T^{\mu 1}_{;\mu}-T^{\mu}_{0;\mu}=\left(\frac{V}{r}\right)T^{\mu}_{1;\mu}=0. \tag{18}$$

If we use the Bondi mass aspect $V\equiv e^{2\beta}\left(r-2m\right)$, after some elementary algebra, the equation system becomes equivalent to:

$$m_{,1}\;=\;4\pi r^2\rho \tag{19}$$

$$\beta_{,1}\;=\;2\pi r\frac{(\rho+P)}{1-\frac{2m}{r}} \tag{20}$$

$$m_{,0}\;=\;-4\pi r^2 e^{2\beta}\left(1-\frac{2m}{r}\right)\left[\varepsilon+\frac{\omega\left(\rho+P\right)}{(1-\omega)^2}\right] \tag{21}$$

$$8\pi\bar{P}\;=\;-2\beta_{,01}e^{-2\beta}+\left(1-\frac{2m}{r}\right)\left(2\beta_{,11}+4\beta_{,1}^2-\frac{\beta_{,1}}{r}\right)+ \\ +\frac{1}{r}\left[3\beta_{,1}\left(1-2m_{,1}\right)-m_{,11}\right]. \tag{22}$$

Also, for two independent Bianchi equations (15) and (16), we obtain:

$$-\frac{e^{-2\beta}}{2\pi r}\beta_{,10}+\frac{\partial P}{\partial r}+ \\ +\left(4\pi r^2 P+\frac{m}{r}\right)\frac{(\rho+P)}{r\left(1-\frac{2m}{r}\right)}+\frac{2}{r}\left(P-\bar{P}\right)=0, \tag{23}$$

$$\frac{e^{2\beta}}{r}\left[1+\left(1-\frac{2m}{r}\right)+4\pi r^2\left(P-\rho\right)\right]\left[\varepsilon+\frac{\omega\left(\rho+P\right)}{(1-\omega)^2}\right]+ \\ +\frac{V}{r}\frac{\omega}{(1-\omega)^2}\frac{\partial}{\partial r}\left(\rho+P\right)+ \\ +\frac{V}{r}\left[\frac{\partial\varepsilon}{\partial r}+\frac{(1+\omega)\left(\rho+P\right)}{(1-\omega)^3}\frac{\partial\omega}{\partial r}\right]+\frac{\partial\rho}{\partial u}=0. \tag{24}$$

The expression (23) is the generalization of the Tolman - Oppenheimer - Volkoff (TOV) equation of hydrostatic equilibrium (see, for example [31]). It can be shown that the conservation equation (24) can also be obtained from the field equations (19) and (21), remembering that the second mixed derivatives commute, that is, $m_{,01}=m_{,10}$. Now, combining (21) with (24) we obtain:

$$\frac{2m_{,0}e^{-2\beta}}{4\pi r^3\left(1-\frac{2m}{r}\right)}\left[1-\frac{m}{r}+2\pi r^2\left(P-\rho\right)\right]= \\ \frac{\omega}{(1-\omega)^2}\left(1-\frac{2m}{r}\right)(\rho+P)_{,1}+ \\ +\frac{\partial\varepsilon}{\partial r}+\frac{(1+\omega)\left(\rho+P\right)}{(1-\omega)^3}\frac{\partial\omega}{\partial r}+\frac{e^{-2\beta}}{4\pi r^2}m_{,10}.$$

If we assume that radiation profiles ε and the variable ω, vary little, so we can write an expression very similar to the Euler equation

$$2m_{,0}\left[1-\frac{m}{r}+2\pi r^2\left(P-\rho\right)\right]= \\ \frac{\omega\cdot e^{2\beta}}{(1-\omega)^2}\left[4\pi r^2\left(1-\frac{2m}{r}\right)^2 r\left(\rho+P\right)_{,1}\right]+ \\ +r\left(1-\frac{2m}{r}\right)m_{,10}. \tag{25}$$

Equation (25) is omitted in previous works on the evolution of radiating fluid sphere [6, 20, 21, 23, 28]. This omission prevents the closing of the system of equations, and motivates the spurious inclusion of a luminosity Gaussian pulse [21, 23–25, 28]. Equation (25) allows us relate the mass exchange with the time like and radial derivatives of the effective variables, and together with eq. (21), the radiation flux ε

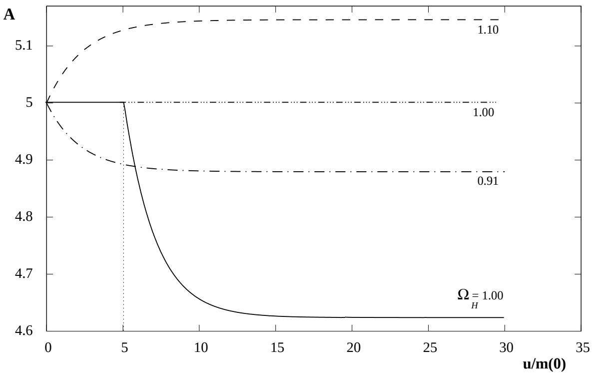

Fig. 1: The radius A as a function of the normalized time-like coordinate $\frac{u}{m(0)}$ for the initial values $A = 5.0$; $M = 1.0$ in the model Schwarzschild-like. Dashed line: $\Omega = 1$ static equilibrium, $\Omega = 1.1$ expansion; $\Omega = 0.91$ collapse. Solid line: solutions according to Herrera et al. [6].

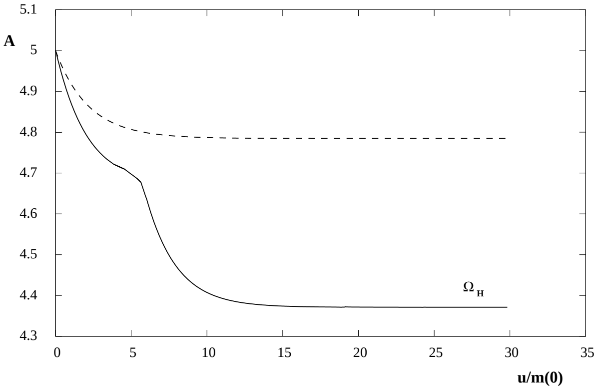

Fig. 2: The radius A as a function of the normalized time like coordinate $\frac{u}{m(0)}$ in the Schwarzschild-like model. Initial values for the surface variables $A = 5$; $M = 1.0$; $\Omega = 0.833$. Dashed line: calculations present. Solid line: solutions according to Herrera et al. [6].

is calculated. With the field equations (19) to (22) we can calculate the expressions of the physical variables $\omega, \bar{P}, \bar{\rho}$, if we know the expressions $m(u,r)$ and $\beta(u,r)$ in each layer of the material under study. As a consequence, the state equations $P(u,r)$, $\rho(u,r)$ play an important role in determining the behavior of the physical variables present in the field equations and establishing their posterior evolution.

3 The models and surface equations

From the field equations (19) and (20) we can see

$$m = \int_0^r 4\pi r^2 \rho \, dr, \tag{26}$$

$$\beta = 2\pi \int_a^r \frac{\rho + P}{1 - \frac{2m}{r}} \, r \cdot dr. \tag{27}$$

These expressions for m and β are very similar to those obtained in the static case. This suggests a procedure to obtain dynamic solutions, following the same method of Herrera et al. [6], starting from a static solution:

1. Select a static solution of the gravitational field equations for a perfect fluid with spherical symmetry that explicitly shows its radial dependence

$$\rho_{static} = \rho(r) \quad P_{static} = P(r),$$

2. Suppose that the effective variables P and ρ (eq. 10) have the same radial dependence as in the static solution, but taking into account that now the edge condition $\bar{P}_a = 0$ is now expressed as

$$P_a = -\omega_a \rho_a. \tag{28}$$

Note that the subscript Δ_a indicates that the quantity Δ is evaluated at the edge of the distribution.

3. With this radial dependence for the effective variables, and together with (26) and (27), the values of m and β are calculable, except for three unknown functions (surface variables) that we are going to determine:
   (a) Equation (9) evaluated at $r = a$.
   (b) Equation (25) evaluated at $r = a$.
   (c) Equation (15) evaluated at $r = a$, or equation (22) evaluated at $r = a$.
4. Integrating numerically the ordinary differential equations obtained in (3), for a set of initial data, we completely determine the functions m and β.
5. With the field equations (19) to (22) we can calculate the expressions of the physical variables for the model considered.

As outlined in the previous methods (subsection 3), it is necessary to establish the surface variables and the equations that control its evolution.

- As mentioned in (subsection 3a), one of the surface equations is (9) evaluated at $r = a$, which takes the form

$$\mathring{a} = \frac{da}{du} = \dot{A} = F(\Omega - 1), \tag{29}$$

where here it is very convenient to standardize the variables in terms of the initial mass $m(0) = m(u = 0, r = a)$ and define as surface variables:

$$A \equiv \frac{a}{m(0)} \quad M \equiv \frac{m_a}{m(0)} \quad \Omega \equiv \frac{1}{1 - \omega_a}, \tag{30}$$

as well as the variable

$$F = \left[e^{2\beta} \left(1 - \frac{2m}{r} \right) \right]_{r=a} = \left(\frac{V}{r} \right)_a, \tag{31}$$

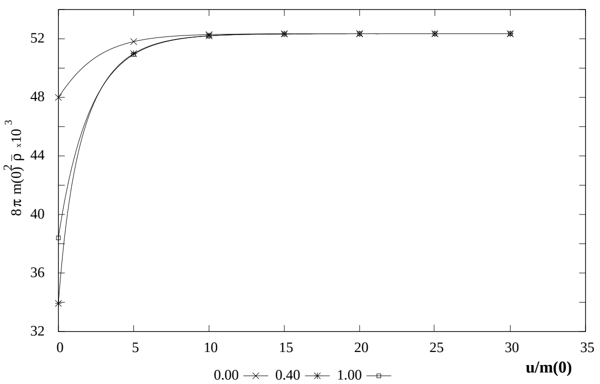

Fig. 3: Density $8\pi m(0)^2\,\bar{\rho}$ in function of the temporal variable $\frac{u}{m(0)}$ for the model of Schwarzschild, for $\frac{r}{a} = 0.00,\ 0.40$ and 1.00.

Instead of using as surface variable F (31) – the gravitational potential at the surface – , as used in the references [6, 20, 21, 28]; we will use mass M, that is, the equation for radial evolution is

$$\dot{A} = \left(1 - \frac{2M}{A}\right)(\Omega - 1)\,, \tag{32}$$

This equation is valid for all models.

- The second equation (25) is dependent on the model and it becomes necessary to calculate the first derivatives of the effective density and pressure, as can be seen.

$$\begin{aligned} 2m_{,0}\big|_a &\left\{1 - \frac{m}{r} + r\beta_{,1}\left(1 - \frac{2m}{r}\right) - m_{,1}\right\}_a + \\ &- r\left(1 - \frac{2m}{r}\right)\frac{\partial}{\partial u}\left(4\pi r^2\rho\right)\bigg|_a = \\ = \Omega(\Omega - 1) &\left[4\pi r^2\left(1 - \frac{2m}{r}\right)^2 r\frac{\partial}{\partial r}(\rho + P)\right]_a \end{aligned} \tag{33}$$

- The last equation (23) is the Tolman - Oppenheimer - Volkoff conservation equation evaluated at $r = a$, which we can write

$$\begin{aligned} \beta_{,10}\big|_a = \;& 2\pi r\left(\frac{\partial P}{\partial r}\right)\bigg|_a + \\ &+\left[\frac{4\pi r^2(\rho + P)}{2r^2\left(1 - \dfrac{2m}{r}\right)}\right]_a\left(4\pi r^2 P + \frac{m}{r}\right)_a + \\ &+ 4\pi(P - P_t)\big|_a \equiv G. \end{aligned} \tag{34}$$

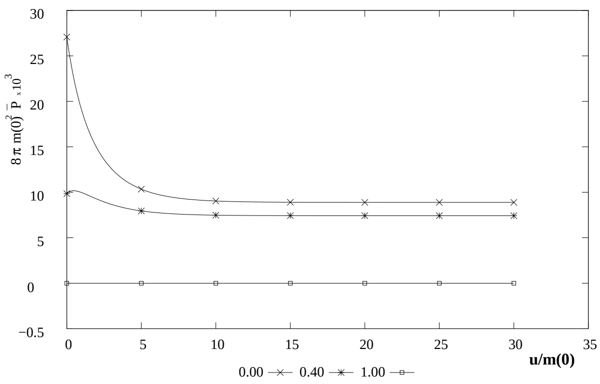

Fig. 4: Normalized pressure values $8\pi m(0)^2\,\bar{P}$ in function of the time variable $\frac{u}{m(0)}$ for the model of Schwarzschild, for $\frac{r}{a} = 0.4$ and 1.00

Both equations (33) and (34) have a similar structure, in terms of the surface variables:

$$\begin{aligned} \Upsilon_M\,\dot{A} + \Xi_M\,\dot{M} + \Lambda_M\,\dot{\Omega} &= \Delta_M \qquad (35) \\ \Upsilon_\Omega\,\dot{A} + \Xi_\Omega\,\dot{M} + \Lambda_\Omega\,\dot{\Omega} &= \Delta_\Omega, \qquad (36) \end{aligned}$$

where

$$\begin{aligned} &\Upsilon_\xi \equiv \Upsilon_\xi(A, M, \Omega)\,, && \Xi_\xi \equiv \Xi_\xi(A, M, \Omega)\,, \\ &\Lambda_\xi \equiv \Lambda_\xi(A, M, \Omega)\,, && \Delta_\xi \equiv \Delta_\xi(A, M, \Omega)\,, \qquad \forall\xi \in \{M, \Omega\} \end{aligned}$$

are functions of (A, M, Ω). These three equations (32), (33) and (34) allow us to establish a system of three ordinary differential equations for the surface variables; which together with the initials data set, determine m and β, as set forth in subsection 4. Below are two examples for the interior distribution Schwarzschild-like and Tolman VI-like in section 4 and 5, respectively.

4 The Schwarzschild-like model

We will get as the first test example Schwarzschild's well-known internal and static constant density solution. For this, we are going to assume that the density depends only on the time-type variable, as explained in [6, 32] we can write the state equation for the Schwarzschild type model as

$$\rho = \frac{3m}{4\pi r^3} \tag{37}$$

$$P = \rho\left\{\frac{1 - \frac{1}{g}\left[\frac{1 - \frac{2M}{A}\left(\frac{r}{a}\right)^2}{1 - \frac{2M}{A}}\right]^{\frac{1}{2}}}{\frac{1}{g}\left[\frac{1 - \frac{2M}{A}\left(\frac{r}{a}\right)^2}{1 - \frac{2M}{A}}\right]^{\frac{1}{2}} - 3}\right\}, \tag{38}$$

where the value of g is determinated from the boundary condition $\left(\bar{P}_a = 0\right)$ then the effective pressure satisfies the relationship (28); and consequently $g = \frac{1}{3 - 2\Omega}$. Evaluating equation (9), for $r = a$, we get (32) and with (23) and (24) for

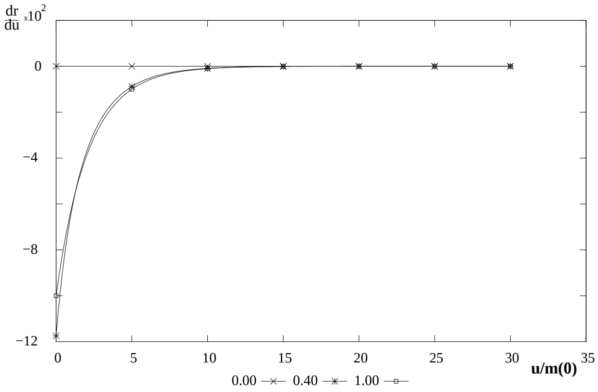

Fig. 5: Temporal velocity evolution in coordinates radiative $\frac{dr}{du}$, for the model of Schwarzschild, for $\frac{r}{a} = 0.00,\ 0.40$ and 1.00.

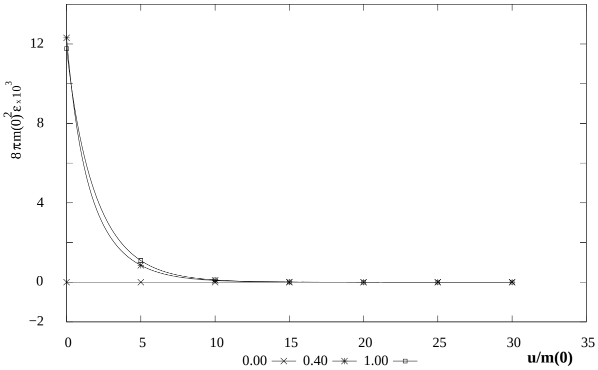

Fig. 6: Radiation profiles $8\pi m\,(0)^2\,\varepsilon.$ for the model of Schwarzschild. All layers emit radiation but decrease until reaching a state of equilibrium for $\Omega = 1$.

$r = a$ we obtain then

$$
\begin{aligned}
\dot{M} &= 3\left(\frac{M}{A}\right)^2\left(1-\frac{2M}{A}\right)\frac{(\Omega-1)\,(2\Omega\text{-}3)}{\frac{3M}{A}-\Omega\left(1+\frac{2M}{A}\right)}\\
\dot{\Omega} &= \frac{2\Omega\,(1-\Omega)}{A}\left(1-\frac{2M}{A}\right)-\frac{1}{A}\left(\frac{M}{A}\right)\left(\frac{3-2\Omega}{1-\frac{2M}{A}}\right)\dot{A}+\\
&\quad -\frac{\Omega}{M}\frac{1}{\left(1-\frac{2M}{A}\right)}\dot{M},
\end{aligned}
$$

and from (20) and (19) we obtain, then after the immediate integration

$$
\begin{aligned}
m\,(r) &= m\,(0)\cdot M\left(\frac{r}{a}\right)^3\\
\beta &= \frac{1}{2}\log\left[1+\frac{3}{2\Omega}\left(\sqrt{\frac{1-\frac{2M}{A}}{1-\frac{2M}{A}\left(\frac{r}{a}\right)^2}}-1\right)\right].
\end{aligned}
$$

Figures 1 and 2 show the evolution of the radius A. Notice that $\Omega = 1$ represents a condition of static equilibrium, $\Omega > 1$ represents expansion, $\Omega < 1$ the collapse. In both cases the system returns to equilibrium very quickly. In order to make some comparison, we took the initial data very close to those chosen in the reference [6]. We did not use the value for $\Omega = 1$, since with this approximation the system does not have static behavior. The figures 3, 4, 5, 6 represent the profiles of physical variables versus the time like coordinates for different pieces of material and for initials data. We obtain monotonous variations in the physical quantities, as a consequence of the non-assumption of the Gaussian pulse. In particular it is shown in figure 6, how all the layers emit monotonously, unlike the figure 7 in Herrera et al. [6]

5 The Tolman VI-like model

Following [2] we can assume as static solution

$$
\begin{aligned}
4\pi a^2\rho &= 3h\left(\frac{a}{r}\right)^2\\
4\pi a^2 P &= h\left(\frac{a}{r}\right)^2\left[\frac{1-9\cdot z\left(\frac{r}{a}\right)}{1-z\left(\frac{r}{a}\right)}\right],
\end{aligned}
$$

as before the value of z is determinated from the boundary condition $\left(\bar{P}_a = 0\right)$ then $P_a = -\omega_a\rho_a$; and consequently $z = \frac{4\Omega-3}{3(4\Omega-1)}$; and $h = \frac{m}{3r}$. Evaluating the equations (9), (23) and (24) at $r = a$ we obtain

$$
\begin{aligned}
\dot{M} &= -\frac{\left(1-\frac{2M}{A}\right)^2\left(16\Omega^2+3\right)\left(\frac{M}{A}\right)}{8\left[\Omega\left(1-\frac{2M}{A}\right)+\frac{M}{A}\right]}\dot{A}\\
\dot{\Omega} &= -\frac{1}{A}\left[\frac{M}{A}-\frac{(4\Omega-3)\,(4\Omega-1)}{8}\left(1-\frac{2M}{A}\right)\right]\\
&\quad +(4\Omega-1)\,(4\Omega-3)\,\frac{\dot{A}}{8A}+\frac{\Omega}{\left(1-\frac{2M}{A}\right)}\frac{\dot{M}}{M},
\end{aligned}
$$

and the corresponding values of β and m are

$$
\begin{aligned}
\beta &= \frac{2M}{3A}\frac{1}{\left(1-\frac{2M}{A}\right)}\left\{\log\left(\frac{r}{a}\right)+2\log\left[\frac{3-\left(\frac{4\Omega-3}{4\Omega-1}\right)\left(\frac{r}{a}\right)}{3-\left(\frac{4\Omega-3}{4\Omega-1}\right)}\right]\right\}\\
m &= m\,(0)\,M\left(\frac{r}{a}\right).
\end{aligned}
$$

Figure 7 shows the temporal variation of the radius of a radiant sphere, for different values of Ω. There is a critical value Ω_0 for $A = 6.66$ and $M = 1$ and slight increase in Ω causes a permanent expansion or the contraction rises to the critical value. In the following figures 8,9,10 we show the variations of pressure density and radiation of some interior layers in case of surface expansion (explosion-like). We noted in the example in the figure 10 that all layers absorbed energy during the initial collapse, an then a radiative pulse is emitted, before returning to the equilibrium configuration.

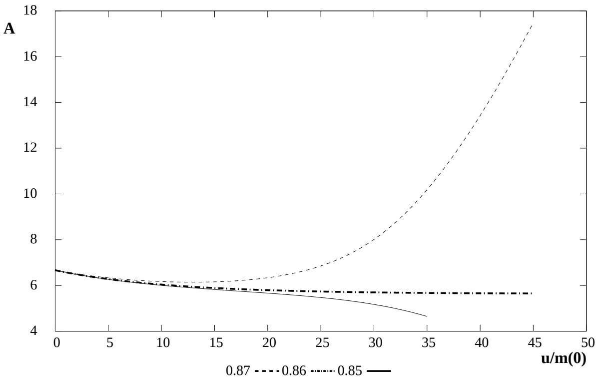

Fig. 7: Radio A of the distribution according to the variable temporary $\frac{u}{m(0)}$ in a TolmannVI-like model. With initials values, $A = 6.66667$; $M = 1$. $\Omega = 0.87$ (rebound) and $\Omega = 0.85$ (contraction) and the critical value $\Omega = 0.860723$

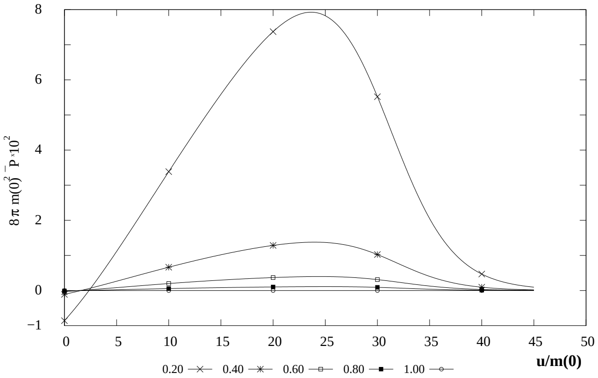

Fig. 8: Values of the normalized pressure $8\pi m\,(0)^2\,\bar{P}$ as function of the time-like variable $\frac{u}{m(0)}$ in a TolmannVI-like model. For the layers in contraction ($\Omega = 0.87$) with $\frac{r}{a} = 0$, 0.4, 0.6, 0.8 and 1.

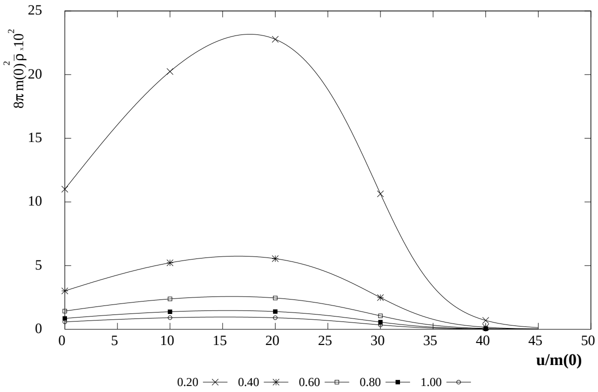

Fig. 9: Density $8\pi m\,(0)^2\,\bar{\rho}$ as function of the time-like variable $\frac{u}{m(0)}$ in a TolmannVI-like model. For the layers in contraction ($\Omega = 0.87$) with $\frac{r}{a} = 0.2$, 0.4, 0.6, 0.8 and 1.

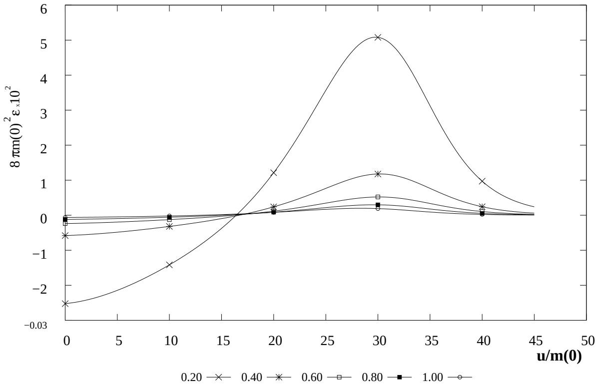

Fig. 10: Radiation profiles emitted $8\pi m\,(0)^2\,\varepsilon$ as function of the time-like variable $\frac{u}{m(0)}$ in a TolmannVI-like model. For the layers in contraction ($\Omega = 0.87$) with $\frac{r}{a} = 0.2$, 0.4, 0.6, 0.8 and 1.

6 Conclusions

We have reviewed the relativistic description of the collapse of self-gravitating radiant spheres, following the usual procedure [6, 19–21, 23, 25, 28, 33] and find that it is an effective method for such a purpose, since the field equations together with the conservation laws (Bianchi's Identity) form a complete set of integrable equations that do not require an additional hypothesis about the emission of radiated energy. That is, the emission hypothesis of a Gaussian pulse at an arbitrary instant to trigger the collapse; it is not only unnecessary, but also leads to qualitatively and quantitatively different solutions, as we have shown in figures 1-9. We emphasize the importance of using conservation equations properly, as was done in Section 2; We formally reobtain the generalized TOV equation of the hydrostatic equilibrium (equation 23) and a relativistic version of the Euler equation for the self-gravitating sphere (equation 25).

We have seen that the Schwarzschild-like description is an ideal case that does not represent the phenomenology of the high energy events observed in the stellar collapse of massive stars such as supernovas and quasars. The measurable magnitudes of density, pressure and emission evolve smoothly, returning to the equilibrium condition very rapidly (Figures 3-6). On the other hand, the Tolman VI description involves two possible qualitatively different scenarios, such as the implosion or the explosion of the outer layers of the self-gravitating sphere, depending on the initial values of the mass, radius and velocity observables, as we have shown in figure 7.

We have shown that, in the case of contraction, the density and pressure variables similarly evolve (Figures 8 and 9) as might be expected if a polytrope state equation is used. In addition, Figures 8 and 9, show a dependence of the evolution of such magnitudes according to the radius of the considered layer, with much higher values of density and pressure in the innermost layers, in agreement with the description of the stellar collapse of massive stars.

Finally figure 10 shows that during the collapse of the self-gravitating radiating spheres a pulse of radiation emission is generated before reaching equilibrium again; which arises *naturally* from the complete solution of the evolution equations, and maybe is important to explain the emission process in very high energy in Supernova bursts and Quasars.

Submitted on January 12, 2018

References

1. Oppenheimer J. R. and Snyder H. On Continued Gravitational Contraction. *Physical Review*, 1939, v. 56, 455–459.
2. Tolman R. C. Static Solutions of Einstein's Field Equations for Spheres of Fluid. *Physical Review*, 1939, v. 55, 364–373.
3. Vaidya P. C. Nonstatic Solutions of Einstein's Field Equations for Spheres of Fluids Radiating Energy. *Physical Review*, 1951, v. 83, 10–17.
4. Bondi H. The Contraction of Gravitating Spheres. *Proceedings of the Royal Society of London Series A*, 1964, v. 281, 39–48.
5. Bayin, S. Ş Radiating fluid spheres in general relativity. *Phys. Rev. D*, 1979, v. 19, 2838–2846.
6. Herrera L., Jiménez J., and Ruggeri G. J. Evolution of radiating fluid spheres in general relativity. *Phys. Rev. D*, 1980, v. 22, 2305–2316.
7. Patino A. and Rago H. The Effect of Electric Charge on the Evolution of Radiant Spheres in General Relativity. *Astrophysics and Space Science*, 1996, v. 241, 237–247.
8. Sah A. and Chandra P. Class of Charged Fluid Balls in General Relativity. *International Journal of Astronomy and Astrophysics*, 2016, v. 6, 494–511.
9. Pant N., Pradhan N. and Bansal R. K. Relativistic model of anisotropic charged fluid sphere in general relativity. *Astrophysics and Space Science*, 2016, v. 361, 41.
10. Harko T. and Mak M. K. Exact power series solutions of the structure equations of the general relativistic isotropic fluid stars with linear barotropic and polytropic equations of state. *Astrophysics and Space Science*, 2016, v. 361, 283.
11. Maurya S. K. and Maharaj S. D. Anisotropic fluid spheres of embedding class one using Karmarkar condition. *ArXiv e-prints*, 2017.
12. Singh K. N., Bhar P., and Pant N. A new solution of embedding class I representing anisotropic fluid sphere in general relativity. *International Journal of Modern Physics D*, 2016, v. 25, 1650099.
13. Herrera L. and Falcón N. Heat waves and thermohaline instability in a fluid. *Physics Letters A*, 1995, v. 201, 33–37.
14. Herrera L. and Santos N. O. Cylindrical collapse and gravitational waves. *Classical and Quantum Gravity*, 2015, v. 22, 2407–2413.
15. Van den Bergh N. and Slobodeanu R. Shear-free perfect fluids with a barotropic equation of state in general relativity: the present status. *Classical and Quantum Gravity*, 2016, v. 33(8), 085008.
16. Herrera L., Denmat G. L. and Santos N. O. Dynamical instability and the expansion-free condition. *General Relativity and Gravitation*, 2012, v. 44, 1143–1162.
17. Aguirre F., Hernandez H., and Nunez L. A. Radiation hydrodynamics and radiating spheres in general relativity. *Astrophysics and Space Science*, 1994, v. 219, 153–170.
18. Chan R., Herrera L., Pacheco J. A. F. and Santos N. O. Diffusion processes in the collapse of a radiating spherical body. *Astrophysical Journal*, 1991, v. 382, 255–260.
19. Herrera L. and Barreto W. Relativistic Gravitational Collapse in Comoving Coordinates:. the Post-Quasistatic Approximation. *International Journal of Modern Physics D*, 2011, v. 20, 1265–1288.
20. Cosenza M., Herrera L., Esculpi M. and Witten L. Evolution of radiating anisotropic spheres in general relativity. *Phys. Rev. D*, 1982, v. 25, 2527–2535.
21. Medina V., Nunez L., Rago H. and Patino A. Evolution of radiating charged spheres in general relativity. *Canadian Journal of Physics*, 1988, v. 66, 981–986.
22. Bonnor W. B., de Oliveira A. K. G., and Santos N. O. Radiating spherical collapse. *Phys. Rep.*, 1989, v. 181, 269–326.
23. di Prisco A., Falcón N., Herrera L., Esculpi M. and Santos N. O. Prerelaxation Processes in a Radiating Relativistic Sphere. *General Relativity and Gravitation*, 1997, v. 29, 1391–1405.
24. Herrera L., Barreto W., di Prisco A., and Santos N. O. Relativistic gravitational collapse in noncomoving coordinates: The post-quasistatic approximation. *Phys. Rev. D*, 2002, v. 65(10), 104004.
25. Barreto W., Rodriguez B., and Martinez H. Radiating Fluid Spheres in the Effective Variables Approximation. *Astrophysics and Space Science*, 2002, v. 282, 581–593.
26. Pant N., Mehta R. N., and Tewari B. C. Relativistic model of radiating massive fluid sphere. *Astrophysics and Space Science*, 2010, v. 327, 279–283.
27. Tewari B. C. Relativistic collapsing radiating stars. *Astrophysics and Space Science*, 2012, v. 342, 73–77.
28. Patiño A. and Rago H. A Sphere Contraction in General Relativity. *Lett. Nuovo Cimento*, 1983, v. 38, 321–328.
29. Davies G. Second-Order Black Hole Perturbations: A Computer Algebra Approach, I – The Schwarzschild Spacetime. *ArXiv General Relativity and Quantum Cosmology e-prints*, 1998.
30. Neary N., Ishak M., and Lake K. Tolman type VII solution, trapped null orbits, and w-modes. *Phys. Rev. D*, 2001, v. 64(8), 084001.
31. Bekenstein J. D. Hydrostatic Equilibrium and Gravitational Collapse of Relativistic Charged Fluid Balls. *Phys. Rev. D*, 1971, v. 4, 2185–2190.
32. Aguirre F., Nunez L. A., and Soldovieri T. Variable Eddington Factor and Radiating Slowly Rotating Bodies in General Relativity. *ArXiv General Relativity and Quantum Cosmology e-prints*, 2005.
33. Barreto W., Rodríguez B., Rosales L., and Serrano O. Self-similar and charged radiating spheres: an anisotropic approach. *General Relativity and Gravitation*, 2007, v. 39, 537–538.

The Journal on Advanced Studies in Theoretical and Experimental Physics, including Related Themes from Mathematics

PROGRESS IN PHYSICS

A quarterly issue scientific journal, registered with the Library of Congress (DC, USA). This journal is peer reviewed and included in the abstracting and indexing coverage of: Mathematical Reviews and MathSciNet (AMS, USA), DOAJ of Lund University (Sweden), Scientific Commons of the University of St. Gallen (Switzerland), Open-J-Gate (India), Referativnyi Zhurnal VINITI (Russia), etc.

Electronic version of this journal:
http://www.ptep-online.com

Postal Address

Department of Mathematics and Science,
University of New Mexico,
705 Gurley Ave., Gallup, NM 87301, USA

This journal is powered by LaTeX

A variety of books can be downloaded free from the Digital Library of Science:
http://fs.gallup.unm.edu/ScienceLibrary.htm

ISSN: 1555-5534 (print)
ISSN: 1555-5615 (online)

Standard Address Number: 297-5092
Printed in the United States of America

April 2018 **Vol. 14, Issue 2**

CONTENTS

Information for Authors

Progress in Physics has been created for rapid publications on advanced studies in theoretical and experimental physics, including related themes from mathematics and astronomy. All submitted papers should be professional, in good English, containing a brief review of a problem and obtained results.

All submissions should be designed in LaTeX format using *Progress in Physics* template. This template can be downloaded from *Progress in Physics* home page http://www.ptep-online.com

Preliminary, authors may submit papers in PDF format. If the paper is accepted, authors can manage LaTeXtyping. Do not send MS Word documents, please: we do not use this software, so unable to read this file format. Incorrectly formatted papers (i.e. not LaTeXwith the template) will not be accepted for publication. Those authors who are unable to prepare their submissions in LaTeXformat can apply to a third-party payable service for LaTeX typing. Our personnel work voluntarily. Authors must assist by conforming to this policy, to make the publication process as easy and fast as possible.

Abstract and the necessary information about author(s) should be included into the papers. To submit a paper, mail the file(s) to the Editor-in-Chief.

All submitted papers should be as brief as possible. Short articles are preferable. Large papers can also be considered. Letters related to the publications in the journal or to the events among the science community can be applied to the section *Letters to Progress in Physics*.

All that has been accepted for the online issue of *Progress in Physics* is printed in the paper version of the journal. To order printed issues, contact the Editors.

Authors retain their rights to use their papers published in *Progress in Physics* as a whole or any part of it in any other publications and in any way they see fit. This copyright agreement shall remain valid even if the authors transfer copyright of their published papers to another party.

Electronic copies of all papers published in *Progress in Physics* are available for free download, copying, and re-distribution, according to the copyright agreement printed on the titlepage of each issue of the journal. This copyright agreement follows the *Budapest Open Initiative* and the *Creative Commons Attribution-Noncommercial-No Derivative Works 2.5 License* declaring that electronic copies of such books and journals should always be accessed for reading, download, and copying for any person, and free of charge.

Consideration and review process does not require any payment from the side of the submitters. Nevertheless the authors of accepted papers are requested to pay the page charges. *Progress in Physics* is a non-profit/academic journal: money collected from the authors cover the cost of printing and distribution of the annual volumes of the journal along the major academic/university libraries of the world. (Look for the current author fee in the online version of *Progress in Physics*.)

Birkeland Currents and Dark Matter

Donald E. Scott
Dept. of Electrical Engineering (Retired), University of Massachusetts, Amherst, Massachusetts, USA
E-mail: dascott3@cox.net

A straight-forward application of basic electrical definitions and one of Maxwell's divergence equations provide an extension of the Bessel function model of force-free, field-aligned currents (FAC). This extended model offers descriptions of the charge density, electric-field strength, velocity profile, and voltage profile, each as a function of radial value, r, within the cross-section of the FAC structure. The resulting model exhibits an obvious correspondence with the results of the Marklund convection process in plasma filaments. Most importantly, it shows that observed stellar velocity profiles in galaxies are now accurately predicted without invocations of Dark Matter, WIMPs, or MACHOs.

1 Introduction

Kristian Birkeland's hypothesis [1] that Earth's auroras are powered by electric charges flowing from the Sun was shown to be correct in the late 1960's [2]. Since that time there has been a growing interest in the exact structure of those streams. What are the precise shapes and physical properties of these currents that cascade down into Earth's polar regions? NASA calls them "magnetic flux-ropes". A more proper name is Birkeland Currents [3]. The general form of those tube-like flux-ropes is best visualized as being a set of concentric, counter- rotating, cylinders made up of various electric currents and magnetic fields. One mathematical description of these structures is called the "Bessel Function Model". Its derivation was initiated in 1950 by physicist Stig Lundquist [4,5]. This derivation was completed and its physical consequences further defined by Scott in 2015 [6].

2 Force-free plasmas are field-aligned

The mechanism by which each moving charge magnetically affects its neighbors is called the Lorentz magnetic force [7]. If these Lorentz forces can be reduced to zero-value everywhere through out the plasma, then the overall current will proceed placidly with increased structural integrity, and not be diverted from its original direction. If, at every point in the flow, the magnetic-flux, **B**, and the electric-current density, **j**, are aligned in the same direction (thus the adjective "field-aligned"), all disruptive Lorentz forces within the plasma will be eliminated and the system is then termed a "Force-Free, Field-Aligned Current" (FAC).

3 Basic properties of field-aligned currents

The Bessel function model of a FAC explicitly involves only two canonical variables: the magnetic-field, $\mathbf{B}(r)$, and electric current density $\mathbf{j}(r)$. The model requires these two vector quantities to be everywhere parallel (non-interacting). Cylindrical coordinates (with fixed unit vectors r, θ, z) are used to describe the resulting shape. Because the flow is assumed to be of unlimited extent in length and have a circular cross-section, the model assumes no variation of either **B** or **j** in the θ, or z directions. The mathematical results of this modeling process are:

$$B_z(r) = B_z(0)\, J_0(\alpha r)\,, \tag{1}$$

$$B_\theta(r) = B_z(0)\, J_1(\alpha r)\,, \tag{2}$$

$$j_z(r) = \frac{\alpha B_z(0)}{\mu}\, J_0(\alpha r)\,, \tag{3}$$

$$j_\theta(r) = \frac{\alpha B_z(0)}{\mu}\, J_1(\alpha r)\,, \tag{4}$$

$$B_r(r) = j_r(r) = 0\,, \tag{5}$$

where J_0 and J_1 are Bessel functions of the first kind and of order zero and one respectively. The physical consequences of these equations are: The magnetic-field, **B**, at any point inside the current stream, has two components, one in the axial, z direction (1), and one in the "wrap-around" or θ direction (2). The vector sum of these two orthogonal components at any point located at a distance r out from the central z-axis is the net resulting magnetic field vector, $\mathbf{B}(r)$. The same is true about the current density, **j**; it is made up of two orthogonal components (3) and (4) in the same way that **B** is.

Comparing expressions (1) and (3) shows that magnitudes B_z and j_z have the same shape except for a difference in scale (size). The same is true for B_θ and j_θ as seen in expressions (2) and (4). In general, both **B** and **j** take on parallel, concentric spiral shapes.

Expression (5) reveals that neither the magnetic-field nor current density component is radiated (nothing leaves the cylindrical flow in the outward — radial, r — direction). This preserves the structural integrity of the flow over extreme distances, z. A full derivation of these properties and equations (1) through (5) is contained in Scott's 2015 paper [6].

4 Extension of the Bessel function FAC model

The only physical quantities modeled in the original Bessel function FAC analysis are magnetic-field vector, **B**, and electric current density vector, **j**. But,if there are electric currents present, there must also be electric charges present to create those currents. If there are electric charges in a given region, there may also be electric-fields.

By extending the Bessel function FAC model, the goal of this paper is to determine:

- The scalar charge density profile, $\rho(r)$, that exists within the FAC.
- The electric-field vector, $E(r)$, that may result from this $\rho(r)$ in the FAC.
- The scalar voltage profile, $V(r)$, that may exist over any cross-section of the FAC.
- Whether the Bessel function FAC model is consistent with the Marklund Convection mechanism.
- The extent to which observed stellar rotational profiles in galaxies are explicable by physical properties of the FAC without invoking the presence of hypothetical dark matter.

5 Components of an electric current density

At every point within a FAC, a single current density vector, $\mathbf{j}(r)$, is assumed to exist. It is a vector quantity. Both the magnitude and the direction of this vector will vary only as the radial distance, r, of the point changes. There is no variation of current density or magnetic field with either z or θ.

A way to visualize this $\mathbf{j}(r)$ structure is the following: if one looks inward toward the central z-axis of the flow from any point, r,and then backs away, outward, with increasing distance from the axis, the net current density vector, $\mathbf{j}(r)$, will appear to rotate smoothly clockwise, and its magnitude will gradually decrease (as $1/\sqrt{r}$). This fact (the monotonic decrease of total current density with $1/\sqrt{r}$) is of significant importance in what follows. See figure 1.

The SI dimensional units of an electric current density, $\mathbf{j}(r)$, are Amperes per square meter. [i.e., the number of Amperes of current that are passing through a unit area determines the value of the "current density" there.]

1. The charge density, $\rho(r)$, describes how much charge is contained in a unit volume located at point r. Therefore its SI units are Coulombs per cubic meter (C/m^3).
2. The velocity, $\mathbf{v}(r)$, of this unit volume is the second factor. A one Ampere current is defined as being one Coulomb moving past an observation point each second. SI units of velocity are m/sec.

Therefore the current density at any point, r, is given by

$$\mathbf{j}(r) = \rho(r)\mathbf{v}(r)\,, \tag{6}$$

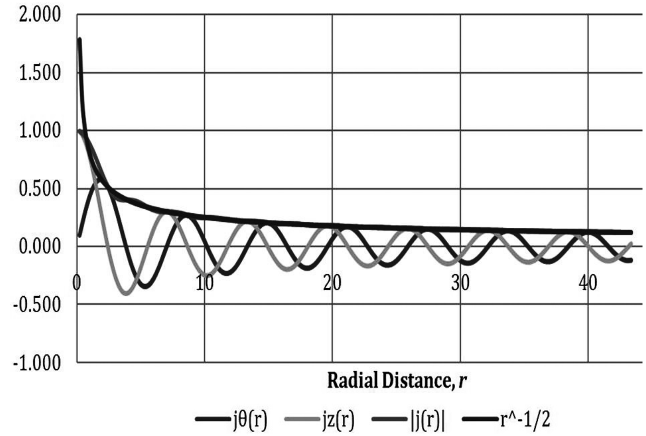

Fig. 1: Current density and its two components. The magnitude of the total current density varies as $1/\sqrt{r}$.

$$j = \frac{\mathrm{C}}{\mathrm{m}^3}\frac{\mathrm{m}}{\mathrm{s}} = \frac{\mathrm{C/s}}{\mathrm{m}^2} = \frac{\mathrm{A}}{\mathrm{m}^2}\,. \tag{7}$$

In expression 6, $\mathbf{j}(r)$ and $\mathbf{v}(r)$ are both vector quantities and, since $\rho(r)$ is a scalar, it follows that $\mathbf{j}(r)$ and $\mathbf{v}(r)$ are collinear (parallel). Thus the charge density, $\rho(r)$, is defined as being the ratio of the magnitude of the current density vector at point r divided by the magnitude of the velocity vector at that same point. Therefore

$$\rho(r) = \frac{|\mathbf{j}(r)|}{|\mathbf{v}(r)|}\,. \tag{8}$$

Note that in the numerator of (8) it is the *magnitude of the total vector sum* of the current density that is used. The vector components, $j_z(r)$ and $j_\theta(r)$ each vary with r with their oscillating Bessel function shapes, but the magnitude of their vector sum decreases smoothly with increasing radius as $1/\sqrt{r}$ (see figure 1). This value of the magnitude of the total current density, $|\mathbf{j}(r)|$, at every point within the FAC is obtained as the sum of its components, (3) and (4), described above. It is evident from that figure that the magnitude of the current density $|\mathbf{j}(r)|$ varies as $1/\sqrt{r}$.

$$|\mathbf{j}(r)| = \sqrt{j_z^2(r) + j_\theta^2(r)}\,. \tag{9}$$

In order to obtain an evaluation of the charge density, $\rho(r)$, in expression (8), it is necessary to obtain a valid expression for $|\mathbf{v}(r)|$.

6 Estimating the velocity profile of a FAC

It has been suggested [8] that galaxies form on and along cosmic Birkeland currents. Consistent with that hypothesis, we assume that the velocity profiles of stars rotating around a galaxy's center have a conformation similar to the FAC on which that galaxy formed. Galactic velocity profiles have

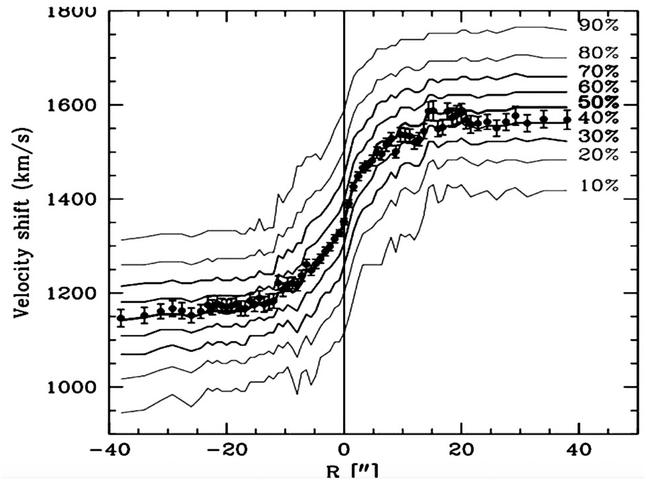

Fig. 2: Observed (measured) velocity profile of a typical galaxy. NGC 1620. [9]

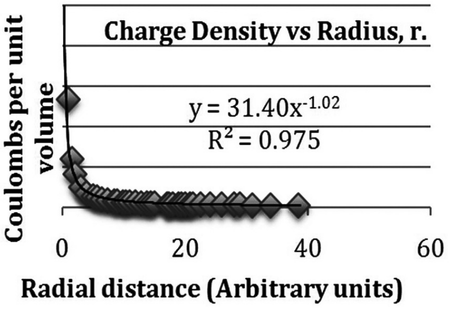

Fig. 3: Charge density produced by the known $|\mathbf{j}(r)|$ from the FAC model and the $|\mathbf{v}(r)|$ of the observed galaxy from (8).

been extensively measured both in the past and presently because of their being offered as evidence of the existence of dark-matter, e.g. figure 2.

If using a typical empirically obtained galaxy velocity profile, $|\mathbf{v}(r)|$, in expression (8) results in a realistic charge density, $\rho(r)$, this would constitute supporting evidence for this hypothesis of galaxy formation.

7 A sample stellar velocity profile $|\mathbf{v}(r)|$ for a typical galaxy

The data in figure 2 [9] was sampled (the abscissa and ordinate of each data point was recorded). This empirical data was incorporated into a spreadsheet database. In this way a data series for $|\mathbf{v}(r)|$ was obtained.

Then a numerical data series for $|\mathbf{j}(r)|$ as given by (9) (shown in figure 1) was also entered into the database. Expression (8) was used together with those data sequences for $|\mathbf{j}(r)|$ and $|\mathbf{v}(r)|$ to obtain the charge density, $\rho(r)$. The result is shown in figure 3.

Figure 3 indicates that the observed stellar rotation profile in this sample galaxy (figure 2) will be correctly produced by the Bessel function model FAC if its internal charge density varies with r as

$$\rho(r) = \frac{k}{r}\,. \tag{10}$$

8 Charge density determines the electric-field

One of Maxwell's equations describes the relationship between the electric charge density, $\rho(r)$, at any point, r, and the electric field, $\mathbf{E}(r)$, that diverges outward from any such point.

$$\nabla \cdot \mathbf{E}(r) = \frac{\rho(r)}{\epsilon}\,. \tag{11}$$

In this expression, $\rho(r)$ is the electric charge density at the point r and ϵ is the permittivity of the surrounding medium. Therefore the electric-field in a region (such as within this FAC) may be obtained by solving (11) using the $\rho(r)$ arrived at in (10).

The general form of the divergence operator in cylindrical coordinates is

$$Div\,\mathbf{E} = \nabla \cdot \mathbf{E}(r) = \frac{1}{r}\frac{\partial}{\partial r}(rE_r) + \frac{1}{r}\left(\frac{\partial E_\theta}{\partial \theta}\right) + \frac{\partial E_z}{\partial z}\,. \tag{12}$$

As before, it was assumed that, in a Birkeland current there is no variation of $\mathbf{E}$ with respect to axial distance z, nor with angular displacement θ, around that axis. There is no preferred location along the unboundedly long z-axis, and there is no angle, θ, around that axis that is preferred over any other. Using these simplifications in (12) and substituting into (11) yields

$$\frac{1}{r}\frac{\partial}{\partial r}(rE_r) = \frac{\rho(r)}{\epsilon}\,, \tag{13}$$

$$\frac{\partial}{\partial r}(rE_r) = \frac{r\rho(r)}{\epsilon}\,, \tag{14}$$

$$E_r = \frac{1}{\epsilon r}\int_0^r r\,\rho(r)\,dr\,. \tag{15}$$

Substituting (10) into (15) and integrating results in

$$E_r(r) = \frac{k}{\epsilon}\,. \tag{16}$$

Therefore the electric-field has a constant value across the entire cross-section of the FAC. The force per unit + charge is outward.

9 The voltage profile is determined by the electric-field, $\mathbf{E(r)}$

Using the definition of the electric-field,

$$E_r(r) = -\frac{\partial V(r)}{\partial r}\,, \tag{17}$$

$$V(r) = -\int_0^r \frac{k}{\epsilon}\,dr = -\frac{kr}{\epsilon} + C. \tag{18}$$

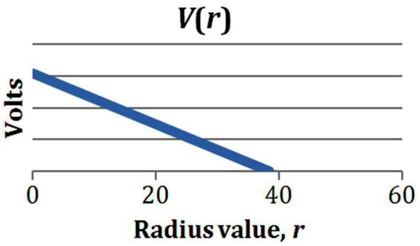

Fig. 4: Voltage profile of cross-section of a FAC.

The constant of integration, C, is chosen such that at the outer boundary of the FAC, $V(R) = 0$. The force per unit charge (16) thus creates a linear, uniformly decreasing voltage profile (18) across the FAC cross-section.

10 Marklund Convection

The voltage profile, $V(r)$, shown in figure 4 is fully consistent with the process known as Marklund Convection [10] wherein elements become sorted radially within a plasma filament according to their ionization potential. Neutral atoms diffuse into the FAC and become ionized due to a temperature gradient which is coolest at the center of the filament and hottest at its outer edge. This temperature gradient is caused by the voltage profile of figure 4 which accelerates ions outward to larger values of r. The turbulence (measured as temperature) of this radial flow at its periphery ionizes high V_i elements more easily than at the lower temperatures found near the center of the filament.

Hannes Alfvén [op. cit.] showed that elements with the lowest ionization potential are brought closest to the axis, and form concentric hollow cylinders whose radii increase with ionization potential. He said, "The drift of ionized matter from the surroundings into the rope means that the rope acts as an ion pump, which evacuates surrounding regions, producing areas of extremely low density."

In 2013 it was reported by Merrifield [11] that the outer rim of a counter-rotating galaxy (NGC 4550) had a collection of hydrogen-rich stars. This prompted him to say these outer stars were younger than the others: "Analysis of the populations of the two separate stellar components shows that the secondary disc has a significantly younger mean age than the primary disc, consistent with later star formation from the associated gaseous material. In addition, the secondary disc is somewhat brighter, also consistent with such additional star formation. However, these measurements cannot be self-consistently modeled by a scenario in which extra stars have been added to initially identical counter-rotating stellar discs, which rules out the Evans and Collett's elegant 'separatrix-crossing' model for the formation of such massive counter-rotating discs from a single galaxy, leaving some form of unusual gas accretion history as the most likely formation mechanism."

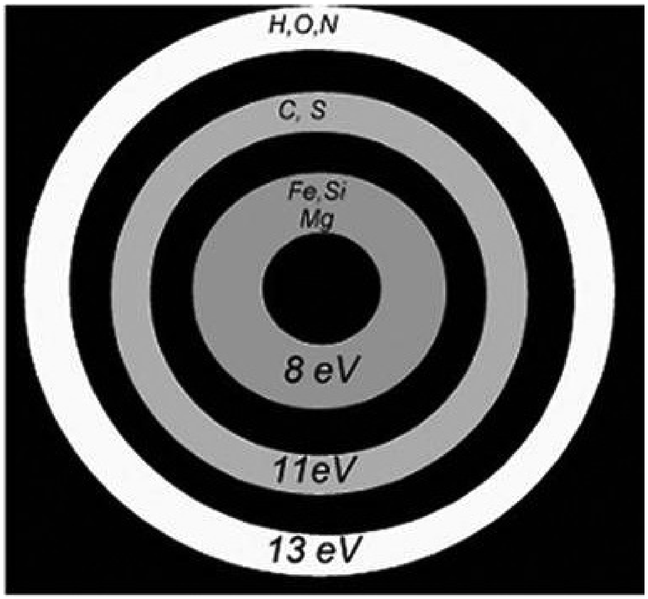

Fig. 5: Elements sorted in a plasma filament in order of their ionization voltage via the Marklund convection process.

Marklund convection stipulates that hydrogen and helium, two elements with the highest ionization voltage, will indeed be found at the outer rim of a plasma filament. The observation of this phenomenon by Merrifield suggests that a Birkeland current is likely to be responsible for the hydrogen-rich band that he discovered.

In 2012 Merrifield [12] had said in his explanation of the presence of these two different counter-rotating populations of stars in NGC 4550 that first, one uni-directional stellar disk formed and then "later on in its life, gas started flowing in, rotating around in the other direction". But, this leaves unanswered the questions of: from where did this new stream of oppositely rotating gas come? And this new gas, being highly collisional, would quickly smash into gas already there and fall into the galactic center. Thus, the question of "from where do the counter rotating stars come" remains unanswered.

In his earlier paper Scott [6] showed that the oscillations in the J_1 Bessel function that controls the spatial behavior of the current density component, j_θ, in a Birkeland Current produces counter-rotating bands in its cross-section (and presumably also in the galaxy it flows into). These bands are analogous to a multi-lane round-about (traffic circle) where adjacent lanes may be going in opposite directions without collisions.

11 Velocity profile predictions of the FAC Bessel model

If it is assumed that the charge density of a typical FAC is similar to the result of expression (10) and figure 3, $\left(\rho(r) \approx \frac{k_1}{r}\right)$, and also that $|\mathbf{j}(r)| = \frac{k_2}{\sqrt{r}}$ as given by the model, then it follows from (8)that the FAC's velocity profile ought to have the following functional form:

$$|\mathbf{v}(r)| = \frac{|\mathbf{j}(r)|}{\rho(r)} = \frac{k_2}{k_1}\sqrt{r}\,. \tag{19}$$

Using the empirical data for our example galaxy (figure 2), we compare this actual observed $|\mathbf{v}(r)|$ data of the example galaxy with our derived velocity profile (19). See figure 6.

12 Results and Comments

One incidental result of this work strongly supports the existence of the voltage profile necessary for Marklund convection to occur in plasma filaments. See sections 9 and 10 above. However, the principal result presented here is the revelation of the actual cause of "anomalous" stellar rotation profiles in galaxies. Since the beginning of space research, most astrophysicists have asserted that electric fields, and currents, are not important in space phenomena [13]. Because of this rejection of electrical science and experimental plasma engineering, all efforts to explain why the outer stars in galaxies revolve around their galactic centers with velocities that, according to Newtonian dynamics, are too high have failed. This fruitless search has lasted for decades [14]. Invisible dark matter (DM) was first proposed by astronomers Jan Oort (1932) and Fritz Zwicky (1933). Subsequently several different types of DM have been hypothesized [15]:

- Cold collisionless dark matter (CCDM) [16];
- Warm dark matter (WDM) [17];
- Strongly self-interacting dark matter (SIDM) [18, 19, 20];
- Repulsive dark matter (RDM) [21];
- Self annihilating dark matter (SADM) [22];
- Fuzzy dark matter (FDM) [23];
- WIMPs Weakly interacting massless particles [24, 25];
- MACHOs Massive (astrophysical) compact halo objects [26, 27];
- Chameleon and Condensed Scalar Fields (not found as of 2015) [28, 29];
- Proposal to modify Newton's Laws [30].

This eighty-five year quest for a dark matter explanation of galactic stellar rotation profiles has produced only null results. Inserting a galaxy's charge density profile into the Birkeland Current Bessel function model [see expression (19)] now provides an elegantly simple answer shown in figure 6. Recently, scientific attention is becoming focused on discoveries of linkages among galaxies previously thought to be isolated from each other. Wide-field telescope observations of the remote universe, have revealed an immense string of galaxies about 300 million light-years long [31]. New research [32, 33, 34] suggests that galaxies are connected to one another with streams of hot thin ionized gas (hydrogen plasma) called the intergalactic medium or IGM. Observations show a narrow filament, one million light-years long, flowing into a quasar, perhaps fueling the growth of the galaxy that hosts the quasar. Caltech's new Cosmic Web Imager has already detected one possible spiral-galaxy-in-the-making that is three times the size of our Milky Way [35].

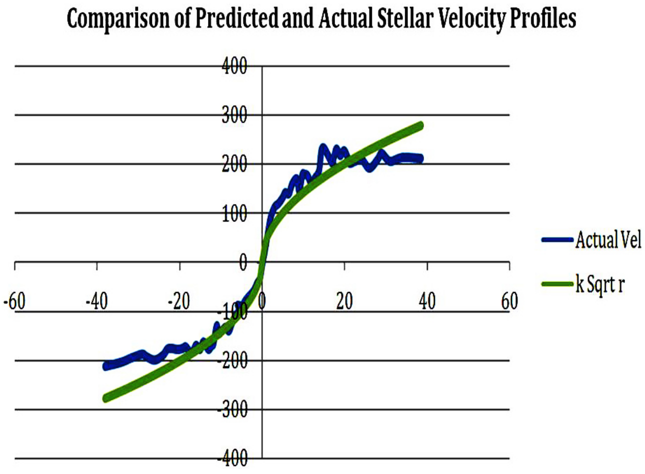

Fig. 6: Comparison of the example galaxy's measured velocity profile with the Bessel function model's Sqrt r profile.

An observation that is "anomalous" is one that is inconsistent with accepted hypotheses. In real science this requires the replacement of the falsified hypothesis, not an eighty-five year hunt for invisible entities that will preserve it. The work being presented here demonstrates that the root cause of the now vast collection of observed "anomalous" galactic stellar rotation profiles is the electrical nature of the Birkeland Currents on which those galaxies have been or are being formed.

Acknowledgment

The author wishes to express his sincere and heartfelt thanks to Dr. Jeremy Dunning-Davies and Dr. Michael Clarage for their crucial help in this effort.

Submitted on January 4, 2018

References

1. Birkeland K. The Norwegian Polaris Expedition 1902-1903. Vol. 1, Sect. 1, Aschehoug, Oslo, 1908.
2. Zmuda A. et. al. Characteristics Of Transverse Magnetic Disturbances Observed At 1100 Kilometers. *Auroral Oval Journal of Geophysical Research*, 1970, v.75, issue 25, 4757.
3. Alfvén H. Cosmic Plasma. Boston, D. Reidel, 1981, pages 16, 15–26, 36.
4. Lundquist S. Magneto-Hydrostatic Fields. *Arch. Fys.*, 1950, v. 2, 361–365.
5. Lundquist S. On the Stability of Magneto-Hydrostatic Fields. *Phys. Rev.*, 1951, v. 83(2), 307–311.
6. Scott D. Consequences Of The Lundquist Model Of A Force-Free Field Aligned Current. *Prog. Phys.*, 2015, v. 10(1), 167–178.
7. Peratt A. Physics Of The Plasma Universe. Springer-Verlag, New York, 1992, pages 43–44, 95, 103, 229. Repprinted in 2015.

8. ICRA, Astronomers find faint strings of galaxies inside empty space. International Center for Radio Astronomy Research, Perth, Western Australia. Published: March 11, 2014. http://www.astronomy.com/news/2014/03/astronomers-find-faint-strings-of-galaxies-inside-empty-space
9. NGC 1620, https://www.aanda.org/articles/aa/full/2004/35 /aa0183-04/img97.gif
10. Marklund G. Plasma convection in force-free magnetic fields as a mechanism for chemical separation in cosmical plasma. *Nature*, 1979, v. 277, 370–371.
11. Johnson E., Merrifield M. Disentangling the Stellar Populations in the counter-rotating disc galaxy NGC 4550. *Monthly Notices of the Royal Astronomical Society*, 2013, v. 428(2), 1296–1302; arXiv: 1210.0535 [astro-ph.CO].
12. Merrifield M. Strange Galaxy (NGC 4550). https://www.youtube.com/watch?v=0oie90j989kδt=1sδlist= PLGJ6ezwqAB2a4RP8hWEWAGB9eT2bmaBsyδindex=40 Published 10/2012.
13. Scott D. Real Properties of Electromagnetic Fields and Plasma in the Cosmos. *IEEE Transactions on Plasma Science*, 2007, v. 35(4), 822–827.
14. Scoles S. How Vera Rubin Confirmed Dark Matter. *Astronomy*, October 4, 2016. http://www.astronomy.com/news/2016/10/vera-rubin
15. Ostriker J.P. and Steinhardt P. New Light on Dark Matter. *Science*, 2003, v. 300(5627), 1909–1913.
16. Ma C-P. Are Halos of Collisionless Cold Dark Matter Collisionless? *Phys. Rev. Letters*, 2004, v. 93(2), 021301.
17. Viel M., et al. Constraining warm dark matter candidates including sterile neutrinos and light gravitinos with WMAP and the Lyman-α forest. *Phys. Rev. D*, 2005, v. 71, 063534.
18. Wandelt BD. Self-Interacting Dark Matter, arXiv:astro-ph/0006344.
19. Zavala J. Constraining self-interacting dark matter with the Milky Way's dwarf spheroidals. *Monthly Not. RAS*, 2013, v. 431(1), L20–L24.
20. Hui L., Unitarity bounds and the cuspy halo problem. *Physical Review Letters*, 2001, v. 86, 3467.
21. Fan J. Ultralight Repulsive Dark Matter and BEC. *Physics of the Dark Universe*, 2016, v. 14, 1-126.
22. Natarajan P. Consequences of dark matter self-annihilation for galaxy formation, arXiv:0711.2302 [astro-ph].
23. Is Dark Matter "Fuzzy", Astronomy Now, Chandra X-ray Center press release, 2 May 2017.
24. Kochanek CS., White M. A Quantitative Study of Interacting Dark Matter in Halos. *The Astrophysical Journal*, 2000, v. 543(2).
25. Alcock C. The Dark Halo of the Milky Way. *Science*, 2000, v. 287(5450), 74–79.
26. Alcock C. et al. The MACHO Project: Microlensing Results from 5.7 Years of Large Magellanic Cloud Observations. *The Astrophysical Journal*, 2000, v. 542(1), 281–307.
27. Zeyher A. MACHOs may be out of the running as a dark matter candidate, Astronomy (2016); http://www.astronomy.com/news/2016/08/machos-may-be-out-of-the-running-as-a-dark-matter-candidate
28. Wilkinson R. The search for "dark matter" and "dark energy" just got interesting, Aug. 21, 2015. The Conversation: https://phys.org/news/2015-08-dark-energy.html; also: http://theconversation.com/the-search-for-dark-matter-and-dark-energy-just-got-interesting-46422.
29. Bohua L. Cosmological constraints on Bose-Einstein-condensed scalar field dark matter. *Phys. Rev. D*, 2014, v. 89, 083536.
30. Milgrom M. MOND — A Pedagogical Review. The XXV International School of Theoretical Physics "Particles and Astrophysics — Standard Models and Beyond", Ustron, Poland, September 10-16, 2001. arXiv: astro-ph/0112069
31. Palunas P. Giant Galaxy String Defies Models Of How Universe Evolved, NASA; https://www.nasa.gov/centers/goddard/news/ topstory/2004/0107filament.html
32. Fesenmaier K. Astronomers unveil a distant protogalaxy connected to the cosmic web. https://phys.org/news/2015-08-astronomers-unveil-distant-protogalaxy-cosmic.html.
33. Coutinho B. The Network Behind The Cosmic Web. arXiv:1604.03236 [Astro-Ph.Co].
34. Gott J. The Cosmic Web (book). Princeton University Press, forthcoming Jun 2018.
35. Martin D.C. Intergalactic Medium Emission Observations with the Cosmic Web Imager. *Astrophysical Journal* v. 768(2), Art. No. 106. arXiv:1402.4809.

Can Cold Fusion Be Explained by Quantised Inertia?

M.E. McCulloch
Plymouth University, Plymouth, PL4 8AA, UK
E-mail: mike.mcculloch@plymouth.ac.uk

When electrolysis is performed using deuterium and a palladium cathode, more heat can be generated than can be explained by chemical processes, implying that deuterons are fusing but without the typical products of hot fusion (a phenomenon called Low-Energy Nuclear Reactions, LENR, or cold fusion). Fusion between deuterons usually requires temperatures of 100 MK to overcome the repulsive Coulomb forces. Here it is shown that a theory called quantised inertia predicts that in cracks in the metal with diameters less than 28 nm, the temperature is 27,000 K and mutual sheltering by the deuterons can produce an attractive radiation recoil force strong enough to push them together through their Coulomb barriers. This offers a potential explanation for cold fusion or LENR.

1 Introduction

Many attempts are underway to initiate nuclear fusion between atoms such as deuterium, releasing useful energy [1]. The main challenge is to overcome the Coulomb barrier: deuterons have a charge equal to the charge on the proton, and they repel each other with a force given by

$$F_C = \frac{q_P^2}{4\pi\varepsilon_0 d^2} \tag{1}$$

where $q_P = 1.6 \times 10^{-19}$ C is the charge on the proton, $\varepsilon_0 = 8.85 \times 10^{-12}$ m^{-3}kg^{-1}s^{4}A^2 is the permittivity of free space and d is the distance between the deuterons. Overcoming the Coulomb barrier between the two deuterons in this process usually requires a high momentum and therefore temperatures in excess of 100 MK which are thought to only be possible in gravitationally-confined systems such as the Sun or magnetically-confined fusion reactors.

This is why the results of Fleischmann and Pons [2] were so surprising. When they used a palladium cathode to electrolyse heavy water (containing deuterium) they noticed that more heat was given off than was possible from chemical processes, implying that fusion was occuring (so called cold fusion). The expected product of deuterium fusion: helium-4, was also produced, but the nuclear emissions (neutrons and gamma rays) expected from hot fusion were not seen and so cold fusion was dismissed by all but a small minority. However, over the years there have been many successful reproductions of the Pons-Fleischmann effect, or variations of it [3], and many unsuccessful ones as well, and the topic has been renamed LENR (Low-Energy Nuclear Reactions). A good summary is available in [4].

Aoyama [5], Storms [6], [7] and others have noted an intriguing pattern which is that a common feature to the successful experiments are the cracks or defects in the metals, which are on the order of the nanoscale.

McCulloch [8], [9], [10] has shown that a number of dynamical anomalies such as galaxy rotation and cosmic acceleration can be explained by a theory called quantised inertia which assumes that inertial mass is due to Unruh radiation (a radiation seen only by accelerating objects) when this radiation is made non-uniform in space by horizons. These horizons can be caused by acceleration (relativistic horizons) or they can be metal structures or cavities [11].

Another interesting anomaly down at the nuclear scale is that of [12] who showed that when the proton radius is measured with a orbiting muon rather than an electron, an extra unexplained binding energy is present. The muon orbits 200 times closer than the electron, and quantised inertia can explain 55% of this extra binding energy by assuming that the thermal Unruh radiation seen by the muon is blocked (sheltered) from the direction of the proton, leading to a net radiation pressure from outside its orbit, and a new attractive force [13]. Quantised inertia also predicts high temperatures within small horizons, for example in the early universe [14]. This may also apply to small metal cracks and so it may have relevence for LENR.

In this paper it is shown that quantised inertia predicts that cracks or defects in metals of 28 nm diameter or less should be hot enough to cause an attractive radiation recoil force on the deuterons strong enough to overcome their Coulomb repulsion. This suggests a mechanism for cold fusion and LENR.

2 Method & Results

The uncertainty principle of Heisenberg states that the uncertainty in momentum (Δp) times the uncertainty in position (Δx) must be greater than or equal to half the reduced Planck's constant

$$\Delta p \Delta x > \frac{\hbar}{2} \tag{2}$$

so that if the uncertainty in position (Δx) is reduced in a metal cavity of diameter D, then the momentum uncertainty (Δp) should increase. Quantised inertia assumes that this increase in momentum can become real [15], and since $E = pc$ then a new energy becomes available, given by

$$\Delta E > \frac{\hbar c}{2D}. \tag{3}$$

For thermalised energy $E = \frac{3}{2}kT$ we can write an expression for temperature:

$$T > \frac{\hbar c}{3kD}. \tag{4}$$

Eq. 4 predicts that the temperature in tiny volumes is high. Figure 1 shows two deuterons (the black circles) close together inside a defect (the grey area) within a palladium lattice (the mottled area). If the temperature within the defect is as given in Eq. 4 then this radiation will be absorbed by each deuteron only on the side away from the other deuteron, assuming there is a mutual sheltering process (see the white radiation-free area in Figure 1) and so the absorption of this radiation will produce a radiation recoil force (see also [16]) that will push them together. This force is

$$F_R = \frac{P}{c} = \frac{\sigma T^4}{c} \tag{5}$$

where σ is the Stefan-Boltzmann constant and c is the speed of light. In order for this radiative force to cause the deuterons to fuse, it must be larger than the repulsive Coulomb force at the seperation where the attractive strong force can take over and fuse the two deuterons, a distance of $d_s = 1.6 \times 10^{-15}$ m. For this to happen, $F_R > F_C$ at distance d_s, and so using Eqs. 1 and 5, and using Eq. 4 for T we get

$$\frac{\sigma\left(\frac{\hbar c}{3kD}\right)^4}{c} > \frac{q^2}{4\pi\varepsilon_0 d_s^2}. \tag{6}$$

We can now predict the crack size D needed to produce a temperature high enough to cause fusion in this new way:

$$D < (4\pi\varepsilon_0\sigma)^{\frac{1}{4}}\, c^{\frac{3}{4}}\, \frac{\hbar}{3k}\sqrt{\frac{d_s}{q}} = 28 \text{ nm}. \tag{7}$$

Therefore, quantised inertia predicts that deuterons in cracks or defects in palladium of a size less than 28 nm will see temperatures of $\hbar c/3kD \geq 27000$ K and be pushed together by radiation in the crack strongly enough that their Coulomb barrier can be breached, causing fusion. Cracks of this size are present in palladium after being stressed [17].

3 Discussion

Quantised inertia also suggests a way to account for the lack of emitted neutrons in LENR. The inwards force on all particles in the defect may keep them confined, but it does not directly explain the lack of gamma rays.

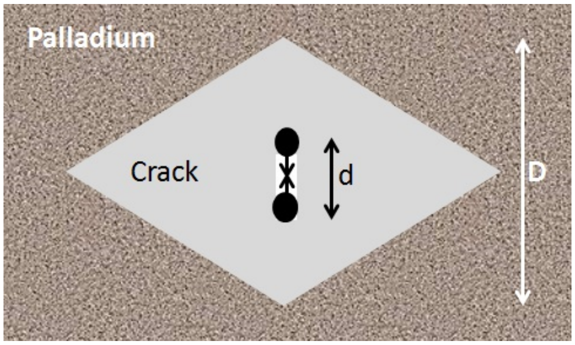

Fig. 1: A schematic showing two deuterons (the black circles) located a distance d apart within a crack/defect of width D (the grey area) in a palladium lattice (the mottled area). The metal radiates, and the mutual sheltering of the deuterons causes the white sheltered zone. The non-uniformity of the thermal radiation then forces the deuterons together (the arrows).

As a test, this theory predicts that metals with cracks or defects of size D should emit radiation of wavelength D. X-rays were indeed seen by [6] and [7] during LENR, with wavelengths in the nanometre range.

This mechanism also suggests a possible reason for sonoluminescence which similarly involves particles being confined to a small region, in this case a bubble collapsing to a size of 0.5 micron and attaining an apparent temperature of between 2300 K to 5100 K, as measured by the radiation given off (see [18]). Eq. 4 predicts a temperature of 1500K.

This application of quantised inertia predicts that a nanometal manufactured to have regular cracks of a size less than 28 nm should show far more uniform LENR.

4 Conclusion

When electrolysis is performed using heavy water (deuterium) and a palladium cathode, unexpected heat and Helium-4 can be generated indicating that nuclear fusion is taking place without the usual products of hot fusion (this is called LENR or cold fusion).

Quantised inertia predicts that deuterons in cracks or defects less than 28 nm in width should heat up enough that, through mutual sheltering, they feel an attractive radiation recoil force that overcomes their Coulomb barrier, allowing fusion. This is a possible explanation for cold fusion.

As a test this model predicts that a metal with cracks should emit radiation of a wavelength similar to the size of its cracks, and that a nanometal manufactured with cracks of size 28 nm or less should produce LENR more uniformly.

Acknowledgements

Many thanks to Bob McIntyre who pointed out that an earlier paper by the author on the proton radius anomaly [13] might also apply to LENR. Also many thanks to A. Dubourg and LENR pioneers Ed Storms and Russ George for advice.

Submitted on January 20, 2018

References

1. Clery D. ITER's $12 billion gamble. *Science*, 2006 v. 214, 5797.
2. Fleischmann M., Pons S. and Hawkins M. Elecrochemically induced nuclear fusion of deuterium. *J. Electroanal. Chem.*, 1989, v. 261, 301–308 and errata in v. 263, 187–188.
3. Kitamura A., Takayoshi N., Yu S., Akira T., Akito T., Reiko S., Yushi F. Anomalous effects in charging of Pd powders with high density hydrogen isotopes. *Phys. Letters A*, 2009, v. 373(35), 3109–3112.
4. Storms E.K. How basic behaviour of LENR can guide a search for an explanation. *J. Condensed Matter Nucl. Sci.*, 2016, v. 20, 1–39.
5. Aoyama T. et al. Highly reliable low-level neutron detection using 3He proportional counters. *Radioisotopes*, 1991, v. 40, 188.
6. Storms E.K. and Scanlan B. Detection of radiation emitted from LENR. ICCF-14. Conference on Condensed Matter Nuclear Science, 2008. Washington, DC.
7. Storms E.K. and Scanlan B. Nature of energetic radiation emitted from metal exposed to H2. *J. Condensed Matter Nucl. Sci.*, 2013, v. 11, 142–156.
8. McCulloch M.E. Modelling the Pioneer anomaly as modified inertia. *MNRAS*, 2007, v. 376, 338–342.
9. McCulloch M.E. Testing quantised inertia on galactic scales. *ApSS*, 2012, v. 342(2), 575–578.
10. McCulloch M.E. Galaxy rotations from quantised inerta and visible matter only. *Astrophys. Space Sci.*, 2017, v. 362, 149.
11. McCulloch M.E. Testing quantised inertia on the emdrive. *EPL*, 2015, v. 111, 60005.
12. Pohl R. et al. Laser spectroscopy of muonic deuterium. *Nature*, 2010, v. 466, 213.
13. McCulloch M.E. The proton radius anomaly from the sheltering of Unruh radiation. *Progress in Physics*, 2017, v. 13(2), 100–101.
14. McCulloch M.E. A toy cosmology using a Hubble-scale Casimir effect. *Galaxies*, 2014, v. 2, 81–88.
15. McCulloch, M.E. Quantised inertia from relativity and the uncertainty principle. *EPL*, 2016, v. 115, 69001.
16. Haslinger P., Jaffe M., Xu V., Schwartz O., Sonnleitner M., Ritsch-Marte M., Ritsch H. and Mueller H. Attractive force on atoms due to blackbody radiation. *Nature*, 2017, doi: 10.1038/s41567-017-0004-9.
17. Kim S., Lee H.-S., Jang B. and Cho S. Strain-controlled nanocrack formation in a Pd film on polydimethylsiloxane for the detection of low H2 concentrations. *J. Mater. Sci.*, 2016, v. 51(9), 4530–4537.
18. Brenner M.P., Hilgenfeldt S. and Lohse D. Single-bubble sonoluminescence. *Rev. Mod. Phys.*, 2002, v. 74(2), 425–484.

Global Scaling of Planetary Atmospheres

Hartmut Müller

E-mail: hm@interscalar.com

We derive a model of the stratification of planetary atmospheres as application of our scale-invariant model of matter as fractal chain system of oscillating protons and electrons. Model claims are verified by aerological, geophysical and planetological data.

Introduction

The vertical stratification of the Earth's atmosphere is caused by very different processes and it is a complex field of research. In general, air pressure and density decrease exponentially with altitude, but temperature, ionization and chemical composition have more complicated profiles. The standard division into troposphere, stratosphere, mesosphere, thermosphere, ionosphere and exosphere is based on satellite, airplane and ground measurements and considers aerodynamic, hydrodynamic, thermodynamic, chemical, electromagnetic, gravitational factors in their complex interaction.

New measurements of the atmospheres of solar system planets and moons over the past four decades from various spacecraft missions have been used to characterize the structure and dynamics of these atmospheric environments and to compare them to one another. A corresponding evolution of modeling tools occurs, from simple to complex frameworks.

Terrestrial modeling frameworks like HAMMONIA [1], ECHAM [2], IRI [3] and CMAM [4] of numerical modeling have been used to launch simulations [5] of other planetary upper atmospheres and ionospheres. The primary benefit of the Earth paradigm can be realized for other planetary upper atmospheres having similarities in their fundamental planetary parameters, basic processes and vertical domains (atmospheric layers).

In fact, stratification as atmospheric feature is associated not only with Earth, but occurs on any other planet or moon that has an atmosphere as well. Furthermore, stable atmospheric boundaries like tropopause, stratopause, thermopause and mesopause have similar vertical distributions at different celestial bodies in atmospheres of very different chemical compositions.

In this paper we apply our scale-invariant model [6] of matter as fractal chain system of oscillating protons and electrons and develop a general model of planetary atmospheric stratification that might help to understand the processes sustaining the observed stable atmospheric structures.

Methods

In [7] we have shown that the set of natural frequencies of a fractal chain system of similar harmonic oscillators can be described as set of finite continued fractions $\mathcal{F}$ (1), which are natural logarithms, where ω_{jk} is the set of angular frequencies and ω_{00} is the fundamental frequency of the set. The denominators are integer: $n_{j0}, n_{j1}, n_{j2}, \ldots, n_{jk} \in \mathrm{Z}$, the cardinality $j \in \mathrm{N}$ of the set and the number $k \in \mathrm{N}$ of layers are finite:

$$\ln(\omega_{jk}/\omega_{00}) = n_{j0} + \cfrac{z}{n_{j1} + \cfrac{z}{n_{j2} + \ddots + \cfrac{z}{n_{jk}}}} = \tag{1}$$

$$= [z, n_{j0}; n_{j1}, n_{j2}, \ldots, n_{jk}] = \mathcal{F}.$$

In the canonical form, the numerator z equals 1 and for finite continued fractions the distribution density of the eigenvalues reaches maxima near reciprocal integers 1, 1/2, 1/3, 1/4, … which are the attractor points of the fractal set $\mathcal{F}$ of natural logarithms (fig. 1).

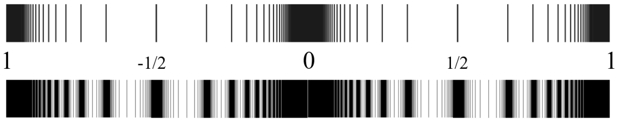

Fig. 1: The canonical form of $\mathcal{F}$ for $k = 1$ (above) and for $k = 2$ (below) in the range $-1 \leqslant \mathcal{F} \leqslant 1$.

Any finite continued fraction represents a rational number [8]. Therefore, all natural frequencies ω_{jk} in (1) are irrational, because for rational exponents the natural exponential function is transcendental [9]. This circumstance provides for high stability of eigenstates in a fractal chain system of harmonic oscillators because it prevents resonance interaction between the elements of the system [10]. Already in 1987 we have applied continued fractions of the type $\mathcal{F}$ as criterion of stability in engineering [11, 12].

In the case of harmonic quantum oscillators, the continued fractions $\mathcal{F}$ define not only fractal sets of natural angular frequencies ω_{jk}, angular accelerations $a_{jk} = c \cdot \omega_{jk}$, oscillation periods $\tau_{jk} = 1/\omega_{jk}$ and wavelengths $\lambda_{jk} = c/\omega_{jk}$ of the chain system, but also fractal sets of energies $\mathrm{E}_{jk} = \hbar \cdot \omega_{jk}$ and masses $\mathrm{m}_{jk} = \mathrm{E}_{jk}/c^2$ which correspond with the eigenstates of the system. For this reason, we call the continued fraction $\mathcal{F}$ the "fundamental fractal" of eigenstates in chain systems of harmonic quantum oscillators.

In the canonical form ($z = 1$) of the fundamental fractal $\mathcal{F}$, shorter continued fractions correspond with more stable eigenstates of a chain system of harmonic oscillators. Therefore, integer logarithms represent the most stable eigenstates (main attractor nodes).

PROPERTY	ELECTRON	PROTON
rest mass m	$9.10938356(11) \cdot 10^{-31}$ kg	$1.672621898(21) \cdot 10^{-27}$ kg
energy $\mathrm{E} = \mathrm{m}c^2$	0.5109989461(31) MeV	938.2720813(58) MeV
angular frequency $\omega = \mathrm{E}/\hbar$	$7.76344071 \cdot 10^{20}$ Hz	$1.42548624 \cdot 10^{24}$ Hz
angular oscillation period $\tau = 1/\omega$	$1.28808867 \cdot 10^{-21}$ s	$7.01515 \cdot 10^{-25}$ s
angular wavelength $\lambda = c/\omega$	$3.8615926764(18) \cdot 10^{-13}$ m	$2.1030891 \cdot 10^{-16}$ m

Table 1: The basic set of physical properties of the electron and proton. Data taken from Particle Data Group [13]. Frequencies, oscillation periods and the proton wavelength are calculated.

As the cardinality and number of layers of the continued fractions $\mathcal{F}$ are finite but not limited, in each point of the space-time occupied by the chain system of harmonic quantum oscillators the scalar $\mathcal{F}$ is defined. Therefore, any chain system of harmonic quantum oscillators can be seen as source of the scalar field $\mathcal{F}$, the fundamental field of the system.

Normal matter is formed by nucleons and electrons because they are exceptionally stable quantum oscillators. In the concept of isospin, proton and neutron are viewed as two states of the same quantum oscillator. Furthermore, they have similar rest masses. However, a free neutron decays into a proton, an electron and antineutrino within 15 minutes while the life-spans of the proton and electron top everything that is measurable, exceeding 10^{29} years [13].

The exceptional stability of electron and proton predestinate their physical characteristics as fundamental units. Table 1 shows the basic set of electron and proton units that can be considered as a fundamental metrology (c is the speed of light in a vacuum, $\hbar$ is the Planck constant, k_B is the Boltzmann constant). In [14] was shown that the fundamental metrology (tab. 1) is compatible with Planck units [15].

We hypothesize that scale invariance of the fundamental field $\mathcal{F}$ calibrated on the physical properties of the proton and electron (tab. 1) is a universal characteristic of organized matter and criterion of stability. This hypothesis we have called 'global scaling' [16, 17].

Results

Within our scale-invariant model of matter [18], atoms and molecules emerge as eigenstates of stability in fractal chain systems of harmonically oscillating protons and electrons.

Andreas Ries [19] demonstrated that this model allows for the prediction of the most abundant isotope of a given chemical element. From this point of view, any physical body, being solid, liquid or gas can be seen as fractal chain system of oscillating molecules, atoms, ions, protons and electrons that generates its fundamental field $\mathcal{F}$.

Therefore, in the framework of our fractal model of matter, the fundamental field $\mathcal{F}$ affects any type of physical interaction, including the gravitational. In [20] we applied our model to the analysis of gravimetric and seismic characteristics of the Earth and could show [21] that our estimations correspond well with established empiric models of the Earth interior.

In this paper we demonstrate that the vertical sequence of stable atmospheric layers corresponds with the sequence of main equipotential surfaces of the fundamental field $\mathcal{F}$, not only at Earth, but also at Venus, Mars and Titan. Table 2 gives an overview of this correspondence.

The lowest layer of Earth's atmosphere is the troposphere where nearly all weather conditions take place. The average height of the troposphere is 20 km in the tropics, 12 km in the mid latitudes, and 7 km in the polar regions in winter [22]. Table 2 and fig. 2 show the correspondence of these tropospheric levels with the main equipotential surfaces [37; 2] = 7.5 km, [38; ∞] = 12 km and [38; 2] = 20 km of the fundamental field $\mathcal{F}$, calibrated on the electron wavelength.

At its lowest part, the planetary boundary layer (PBL), the troposphere displays turbulence and strong vertical mixing due to the contact with the planetary surface. The top of the PBL in convective conditions is often well defined by the existence of a stable capping inversion, into which turbulent motions from beneath are generally unable to penetrate [23]. The height of this elevated stable layer is quite variable, but is generally below 3 km. Over deserts in mid-summer under strong surface heating the PBL may rise to 4 - 5 km. In the temperate zones, it can be defined by the quite sharp decrease of aerosol concentration at the height of about 1600 m. Over the open oceans, but also at night over land, under clear skies and light winds, with a capping stratocumulus, the depth of the PBL may be no more than 600 m.

Table 2 and fig. 2 show the correspondence of the PBL features with the main equipotential surfaces [35; ∞] = 600 m, [36; ∞] = 1600 m and [37; ∞] = 4.5 km of the fundamental field $\mathcal{F}$, calibrated on the electron wavelength. It is noticeable that in 1992 Hess [24] already reviewed scaling aspects of the boundary layer.

Above the PBL, where the wind is nearly geostrophic, vertical mixing is less and the free atmosphere density stratification initiates. The jet stream flows near the boundary

BOUNDARY OF ATMOSPHERIC LAYER	ALTITUDE h, KM	$\ln(h/\lambda_e)$	$\mathcal{F}$
van Allen outer electron belt max density	13000	44.96	[45; ∞]
	8200		[44; 2]
	5000		[44; ∞]
van Allen inner proton belt max density	3000	43.50	[43; 2]
Earth exopause	1800	42.99	[43; ∞]
	1100		[42; 2]
Earth thermopause	650	41.97	[42; ∞]
	400		[41; 2]
Venus & Mars thermopause, Venus atmospheric entry	250	41.01	[41; ∞]
Earth atmospheric entry, Venus mesopause	150	40.50	[40; 2]
Earth & Titan mesopause, Venus tropopause, Mars stratopause & entry	90	39.99	[40; ∞]
Earth & Titan stratopause	55	39.50	[39; 2]
Titan tropopause	33	38.99	[39; ∞]
Earth tropic tropopause	20	38.49	[38; 2]
Earth temperate tropopause	12	37.98	[38; ∞]
Earth polar tropopause	7.5	37.51	[37; 2]
desert summer PBL inversion	4.5	37.00	[37; ∞]
continental PBL inversion	1.6	35.96	[36; ∞]
marine PBL inversion	0.6	34.98	[35; ∞]

Table 2: Altitudes of the boundaries of various atmospheric layers on Earth, Venus, Mars and Titan and their correspondence with main equipotential surfaces of the fundamental field $\mathcal{F}$, calibrated on the electron wavelength.

between the troposphere and the stratosphere. As altitude increases, the temperature of the troposphere generally decreases until the tropopause.

At the bottom of the stratosphere, above the tropopause, the temperature doesn't change much, but at the inverse layer at altitudes between 20 and 33 km the temperature increases from -50°C to 0°C. Then at the stratopause at 55 km altitude the temperature stabilizes. It is the boundary between two layers: the stratosphere and the mesosphere [25]. The ozone layer (ozonosphere) of the stratosphere absorbs most of the Sun's ultraviolet radiation and is mainly found at altitudes between 12 and 30 km, with the highest intensity of formation at 20 km height [26].

Table 2 and fig. 2 show the correspondence of the main stratosphere layers with the main equipotential surfaces [39; ∞] = 33 km and [39; 2] = 55 km of the fundamental field $\mathcal{F}$, calibrated on the electron wavelength.

Above the stratopause, in the mesosphere between 55 and 90 km altitude [27], the temperature decreases again, reaching about -100 °C at the mesopause [28]. This altitude coincides with the turbopause: above this level the atmosphere is of extremely low density so that the chemical composition is not mixed but stratified and depends on the molecular masses. Table 2 and fig. 2 show the correspondence of the mesopause with the main equipotential surface [40; ∞] = 90 km of the fundamental field $\mathcal{F}$, calibrated on the electron wavelength.

Above the mesopause, in the thermosphere, the (kinetic) temperature increases and can rise to 1000 °C (depending on solar activity) at altitudes of 250 km remaining quasi stable with increasing height. Due to solar radiation, gas molecules dissociate into atoms: above 90 km dissociate carbon dioxygen and dihydrogen, above 150 km dissociates dioxygen and above 250 km dissociates dinitrogen. Above 150 km, the density is so low that molecular interactions are too infrequent to permit the transmission of sound. Table 2 and fig. 2 show the correspondence of these thermosphere layers with the main equipotential surfaces [40; 2] = 150 km and [41; ∞] = 250 km of the fundamental field $\mathcal{F}$, calibrated on the electron.

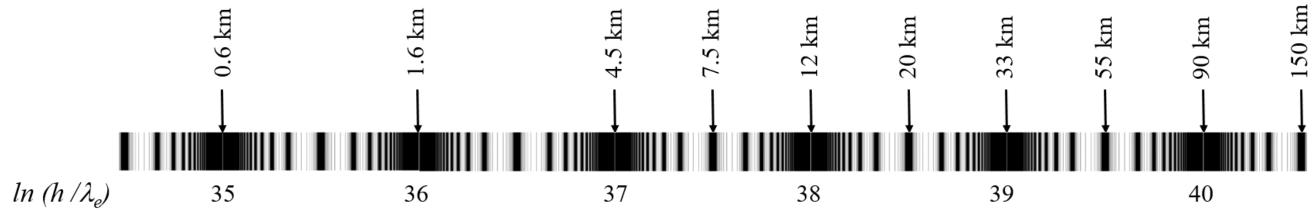

Fig. 2: The fundamental field $\mathcal{F}$ (natural logarithmic presentation) calibrated on the electron wavelength in the range $35 \le \mathcal{F} \le 40$ and the corresponding altitudes h in km.

The Karman line [29] is considered by the Federation Aeronautique Internationale (FAI) [30] as the border between the atmosphere and outer space, as altitude where the atmosphere becomes too thin to support aeronautical flight, since a vehicle at this altitude would have to travel faster than orbital velocity to derive sufficient aerodynamic lift to support itself. On Earth, atmospheric effects become noticeable during atmospheric entry of spacecraft already at an altitude of around 120 - 150 km, while on Venus atmospheric entry occurs at 250 km and on Mars at about 80 - 90 km above the surface. These heights mark also the bases of the anacoustic zones.

The location of the thermopause is near altitudes of 600 – 700 km and depends on solar activity [31]. Above starts the exosphere, where the atmosphere (mostly consisting of hydrogen atoms) thins out and merges with interplanetary space. This uppermost layer, until 13000 km observable from space as the geocorona, extends up to 100000 km. Table 2 and fig. 2 show the correspondence of the thermopause with the main equipotential surface [42; ∞] = 650 km of the fundamental field $\mathcal{F}$, calibrated on the electron wavelength.

The van Allen radiation belts [32] are features of Earth's magnetosphere. The inner belt consists of high energetic protons which reach their maximum concentration at altitudes of 3000 km. The outer belt consists of high energetic electrons with maximum concentration at altitudes of 13000 km.

While the outer belt maximum corresponds with the main equipotential surface [45; ∞] = 13000 km of the fundamental field $\mathcal{F}$, calibrated on the electron wavelength, the inner belt maximum corresponds with the equipotential surface [43; 2] = 3000 km that is the main equipotential surface [51; ∞] of the fundamental field $\mathcal{F}$, calibrated on the proton wavelength. In fact, the natural logarithm of the electron-to-proton wavelength ratio is approximately 7.5 and consequently, $\mathcal{F}$ calibrated on the proton will be shifted by 7.5 logarithmic units relative to the $\mathcal{F}$ calibrated on the electron:

$$\ln\left(\frac{\lambda_{\text{electron}}}{\lambda_{\text{proton}}}\right) = \ln\left(\frac{3.8615926764 \cdot 10^{-13}\ \text{m}}{2.1030891 \cdot 10^{-16}\ \text{m}}\right) \approx 7.5.$$

This circumstance, probably, can explain the high proton concentration at the inner belt.

Conclusion

The correspondence of the atmospheric stratification on the Earth, Venus, Mars and Titan with main equipotential surfaces of $\mathcal{F}$ demonstrates that the fundamental field affects very different types of physical interaction and is a strong confirmation of global scaling and our model of matter as fractal chain system of oscillating protons and electrons.

Probably, in future our model can be applied for estimation of the atmospheric stratification at ice giants like Uranus and Neptune and gas giants like Jupiter, Saturn and extrasolar planets as well.

Acknowledgements

I'm thankful to Leili Khosravi and Oleg Kalinin for valuable discussions.

Submitted on February 21, 2018

References

1. Schmidt H., Brasseur G. P. The response of the middle atmosphere to solar cycle forcing in the Hamburg Model of the neutral and ionized atmosphere. Space Science Reviews, 1–12, 2006.
2. Roeckner E. et al. Report No. 349. The atmospheric general circulation model ECHAM5. Max Planck Institute for Meteorology, Hamburg, 2003.
3. Bilitza D. et al. The International Reference Ionosphere 2012 – a model of international collaboration. Journal of Space Weather and Space Climat, 4, A07, 2014.
4. Grandpre J. de, Beagley S. R. et al. Ozone climatology using interactive chemistry: Results from the Canadian Middle Atmosphere Model. Journal of Geophysical Research, Vol. 105, No. D21, 475–491, 2000.
5. Bougher S. W. et al. Neutral Upper Atmosphere and Ionosphere Modeling. Space Science Reviews, 139: 107–141, 2008.
6. Müller H. Fractal Scaling Models of Natural Oscillations in Chain Systems and the Mass Distribution of Particles. *Progress in Physics*, vol. 3, 61–66, 2010.
7. Müller H. Fractal Scaling Models of Resonant Oscillations in Chain Systems of Harmonic Oscillators. *Progress in Physics*, vol. 2, 72–76, 2009.
8. Khintchine A.Ya. Continued fractions. University of Chicago Press, Chicago, 1964.
9. Hilbert D. Über die Transcendenz der Zahlen e und π. *Mathematische Annalen* 43, 216–219, 1893.
10. Panchelyuga V. A., Panchelyuga M. S. Resonance and Fractals on the Real Numbers Set. *Progress in Physics*, vol. 4, 48–53, 2012.

11. Müller H. The general theory of stability and objective evolutionary trends of technology. Applications of developmental and construction laws of technology in CAD. Volgograd, VPI, 1987 (in Russian).
12. Müller H. Superstability as a developmental law of technology. Technology laws and their Applications. Volgograd-Sofia, 1989 (in Russian).
13. Olive K.A. et al. (Particle Data Group), *Chin. Phys. C*, 38, 090001, 2016.
    Patrignani C. et al. (Particle Data Group), *Chin. Phys. C*, 40, 100001, 2016.
14. Müller H. Scale-Invariant Models of Natural Oscillations in Chain Systems and their Cosmological Significance. *Progress in Physics*, vol. 4, 187–197, 2017.
15. Max Planck. Über Irreversible Strahlungsvorgänge. In: Sitzungsbericht der Königlich Preußischen Akademie der Wissenschaften. 1899, vol. 1, 479–480.
16. Müller H. Scaling as Fundamental Property of Natural Oscillations and the Fractal Structure of Space-Time. Foundations of Physics and Geometry. Peoples Friendship University of Russia, 2008 (in Russian).
17. Müller H. Scaling of body masses and orbital periods in the Solar System as consequence of gravity interaction elasticity. Abstracts of the XII. International Conference on Gravitation, Astrophysics and Cosmology, dedicated to the centenary of Einstein's General Relativity theory. Moscow, PFUR, 2015.
18. Müller H. Emergence of Particle Masses in Fractal Scaling Models of Matter. *Progress in Physics*, vol. 4, 44–47, 2012.
19. Ries A. Qualitative Prediction of Isotope Abundances with the Bipolar Model of Oscillations in a Chain System. *Progress in Physics*, vol. 11, 183–186, 2015.
20. Müller H. Gravity as Attractor Effect of Stability Nodes in Chain Systems of Harmonic Quantum Oscillators. *Progress in Physics*, vol. 1, 19–23, 2018.
21. Müller H. Quantum Gravity Aspects of Global Scaling and the Seismic Profile of the Earth. *Progress in Physics*, vol. 1, 41–45, 2018.
22. Danielson, Levin, and Abrams, Meteorology, McGraw Hill, 2003.
23. Garratt J. R. Review: the atmospheric boundary layer. Earth-Science Review, 37, pp. 89–134, 1994.
24. Hess G. D. Observations and scaling of the atmospheric boundary layer. Australian Meteorological Magazine. 41, 79–99 (1992).
25. Brasseur G. P., Solomon S. Aeronomy of the Middle Atmosphere. Chemistry and Physics of the Stratosphere and Mesosphere. ISBN-10 1-4020-3824-0, Springer, 2005.
26. Stolarski R. et al. Measured Trends in Stratospheric Ozone. Science, New Series, Vol. 256, Issue 5055, 342–349, 1992.
27. Holton J. R. The Dynamic Meteorology of the Stratosphere and Mesosphere. ISBN 978-1-935704-31-7, 1975.
28. Beig G., Keckhut P. Lowe R. P. et al. Review of mesospheric temperature trends. Rev. Geophys. 41 (4), 1015, 2003.
29. Karman T., Edson L. The Wind and Beyond. Little, Brown, Boston, 1967.
30. Cordoba S. F. The 100 km Boundary for Astronautics. Federation Aeronautique Internationale, 2011.
31. Beig G., Scheer J., Mlynczak M. G., Keckhut P. Overview of the temperature response in the mesosphere and lower thermosphere to solar activity. Reviews of Geophysics, 46, RG3002, July 2008.
32. Schaefer H. J. Radiation Dosage in Flight through the Van Allen Belt. Aerospace Medicine, Vol. 30, No. 9, 1959.

LETTERS TO PROGRESS IN PHYSICS

On the Possible Nature of Dark Matter and Dark Energy

Analtoly V. Belyakov
E-mail: belyakov.lih@gmail.com

It is assumed that the dark matter particle can be a structural unit of cosmological scale (superphoton) emitted by the active center of galaxies, analogous to a photon and ball lightning (macrophoton), which are structural units of micro- and macroscales. The low density, potential and temperature of superphotons make them invisible during astronomical observations, and their negative charge prevents the galaxies from approaching each other which can explain the phenomenon of dark energy. It is shown that the existence of superphotons together with the presence of cosmic rays indicates the conservation of the electric charge as a whole in cosmological scales. It is assumed that the superphoton, like a giant ball lightning with energy of 1.03×10^{17} J, could collide with the Earth which could explain the Tunguska phenomenon.

1 Introduction. On the natural range of the unit structural objects

In nature, as the scale changes, a regular range of certain single structural objects is observed. Let us consider them from the point of view of the mechanistic interpretation of J. Wheeler's geometrodynamic [1].

So, in the microcosm opposite charges (the proton and the electron, for example) are connected by a current vortex tube, forming as a whole a closed contour based on the *balance of magnetic and gravitational forces*; its structural unit is a *photon* (wave). The number of these units depends on the contour size, i.e. on the main quantum number n. The size of the "standard" contour $r_{st} = 1.25 \times 10^{-9}$ m. It contains approximately 137 photons (the inverse of the fine structure constant) [1,2]. In the limit, the contour can have one photon, that is, being identical to the photon itself.

A photon, like the contour itself, is a one-dimensional object; the photon does not exist at rest alone.

In the area of Earth's scales between charged macroobjects — a thundercloud and Earth — a linear lightning arises, also a kind of the current tube that generates a ball lightning, which, in turn, can be regarded as a structural unit. Calculation of the parameters of a typical ball lightning, provided that it has a mass close to the Planck mass (quasiparticle) is described in [3]. It is assumed that the ball lightning consists of many single elements — photons or of one long closed contour packed into a spherical shape, forming a *macrophoton*. A macrophoton is a multilayer spherical capacitor, i.e. a kind of two-dimensional object; the lifetime of a macrophoton is limited.

As for cosmic scales, there was shown in [4] that the structure of quasars can contain very long open vortex tubes with opposite currents carrying charges of different signs at the place of their rupture that resembles a kind of a superatom. Vortex tubes consist of vortex threads, which, supposedly, can be transformed into compact structural units — *superphotons* emitted by a quasar. Accordingly, continuing the analogy, the superphoton should be a three-dimensional object, and its lifetime is unlimited.

Indeed, galaxies form a homologous generation — from galaxies with a quasar in the center to galaxies with a black hole in the center. Thus, if a black hole absorbs matter, then the quasar as a white hole (the superdense body according to Ambartsumyan) generates matter. Then galaxies with quasars passing into a state of galaxies with black holes should radiate (to split off) part of its mass in the form of some particles.

2 On the possible super-photon structure

In [4] some parameters of the "standard" quasar were calculated, namely such ones, where the speed of the medium along the vortex tubes is that of "standard" proton-electronic contour. In particular, the following are defined:

quasar mass M, kg	4.76×10^{42}
quasar total energy E, J	9.61×10^{53}
length of the quasar vortex tube l, m	1.58×10^{21}
mass of 1 vortex threads of a quasar tube m_i, kg	5.10×10^{5}
number of unit threads const. the vortex tube, z	9.33×10^{36}

If the vortex thread forms a certain stable structure, then, obviously, certain balances of interactions must exist to maintain such a structure in equilibrium.

So, in [4] it is calculated that there is a *balance of the vortex tube kinetic energy and the electrostatic energy* of all single charges (not necessary electrons) placed along the vortex tube length, provided the distance between the vortex threads is equal to the size of the "standard" proton-electronic contour $r_s t$ and the maximum single charges number must be

$$z_{ie} = l/r_e = 5.6 \times 10^{35}, \qquad (1)$$

where r_e is the electron classical radius (2.82×10^{-15} m).

At the same time, when the vortex threads are split off from the vortex tube, for a pair of threads a *balance of electric* *and magnetic forces* must be realized that leads to a geometric mean [5]:

$$(l_i\, r_{st})^{1/2} = 7.52 \times 10^8 \text{ m}, \tag{2}$$

from which follows $l_i = 4.52 \times 10^{26}$ m.

Let us assume that this extended one-dimensional structure, i.e. a double vortex thread with charges of opposite signs can somehow be packed into a compact volume (similar to a double helix of DNA). In the most dense packing its linear dimension D can be estimated as

$$D = \left(l_i\, r_{st}^2\right)^{1/3} = 890\,\text{m}. \tag{3}$$

Further one can find other averaged parameters of the object — density, energy, charge and potential:

$$\rho = m_i/D^3 = 0.72 \times 10^{-3} \text{ kg/m}^3, \tag{4}$$

$$E_i = E/z = 1.03 \times 10^{17} \text{ J}, \tag{5}$$

$$Q_i = z_{ie}\, e_0 = 9.0 \times 10^{16} \text{ K}, \tag{6}$$

where e_0 is the electron charge,

$$U_i = E_i/Q_i = 1.14 \text{ V}. \tag{7}$$

It is important that in this volume the average distance between charges d is close to the size of the "standard contour" r_{st}, i.e. the *balance characteristic of the proton-electronic contour is also realized.* Really,

$$d = \left(D^3/z_{ie}\right)^{1/3} = 1.08 \times 10^{-9} \text{ m}. \tag{8}$$

Recall that all of the above calculated values are the result of using only the fundamental values.

Thus, when carrying out these balances, one can expect that such an object is stable and exists for a long time. Let's estimate this time, assuming that its object radiates as an absolutely black body and has a surface temperature close to the cosmic background radiation temperature $T = 2.7°$ K (otherwise such objects would be seen in the process of astronomical observations). The power radiated by its surface is determined from the well-known formula:

$$N_i = T^4 \sigma S, \tag{9}$$

where σ is the Stefan-Boltzmann constant, equal to 5.67×10^{-8} Wm^{-2} (^{0}K)$^{-4}$, and S is the sphere area of diameter D equal to πD^2. Substituting the data, we get $N_i = 7.5$ W and than the lifetime of the object is:

$$\tau = E_i/N_i = 1.37 \times 10^{16} \text{ sec or 442 million years}, \tag{10}$$

which in order of magnitude corresponds to the lifetime of a quasar. Obviously, such an object can exist for a longer time, since it gradually dissipates its power and reduces the radiation temperature.

3 Superphoton as a candidate for the role of dark matter

A superphoton, unlike a ball lightning, has an insignificant density, potential, and surface temperature, hence it interacts with other bodies only *in a collision or through gravity*. Therefore, this object, inconspicuous against the background of relic radiation, can claim the role of the desired dark matter. The generality of its origin with ordinary baryonic matter is obvious; this possibility is also allowed in [6]. Let us assume that as the quasar "burns out" (before becoming into a galaxy), most of its mass is radiated in the form of superphotons (dark matter), and less of its mass remains in the form of a conventional galaxy (baryonic matter). Then the ratio of these masses should be close to the mass ratio of the quasar to the galaxy minus one. The calculated mass of the "standard" quasar is about five times greater than the baryon mass of our Milky Way galaxy [4]; for most other galaxies, less massive, this ratio is even greater. Thus, the ratio of the mass of superphotons to the mass of the average galaxy is generally consistent with the ratio of the dark matter mass to the baryonic matter mass. According to WMAP (Wilkinson Microwave Anisotropy Probe, 2003), the universe contains: dark matter of 22%, baryonic matter of 4%.

Apparently, young galaxies as the most massive and active should gradually lose their mass and reduce activity. This provision is consistent with the recently discovered of very massive young galaxies, about one billion years of age that produce stars with intensity much higher than the rate of star formation in our galaxy the Milky Way [7].

If the superphoton has kinetic energy relative to the point of origin (the quasar center) equal to its internal energy, then its relative velocity is equal to the circulation velocity of the medium along the vortex tube (for the "standard" quasar, $\upsilon = 448,000$ m/sec), i.e. it is close to the escape velocity. If particles are emitted mainly in the disk plane, then in this case their total velocity (peripheral velocity plus particle one) exceeds the escape velocity. Thus, during its lifetime (quasar activity), super-photons can move away from galaxies and fill the halo of galaxies, thereby playing the role of dark matter. In this case, in the most remote galaxies, i.e. the youngest from the point of view of observers, dark matter should be less. Indeed, this fact is established [8, 9].

According to the model, the super-photon is a cold and slowly moving formation that corresponds to the model of Cold dark matter. And just in favor of this particular model, the results obtained by a group of astronomers led by Vid Iršič, who analyzed the distribution of dark matter in the universe, based on observations of the lyman alpha radiation from distant galaxies obtained with the help of the Keck Telescope (Hawaii) and the Very Large Telescope Observatory (Chile) indicate [10].

Some features of the behavior of dark matter is not yet amenable to computer simulation: the cosmological models of formation and evolution of disk Galaxies, the distribution of the density of dark matter in the galaxy disk (the problem of the central cusp), coplanarity dwarf galaxies-satellites relative to central galaxies, weak interaction of clouds of dark matter among themselves and others [11]. Therefore, it would be interesting to perform computer simulation, believing that dark matter particles have the properties of superphotons and move mainly in the plane of the galaxy disk.

The average density of particles in the form of superphotons in a galaxies interior, including the halo of diameter 10^5 light years, is very small, about one particle per cubic with a side of 0.5 million kilometers, which gives 5×10^{-24} g /cm^3. And, having the same charge, superphotons repel each other and can not form clusters. Therefore clouds of dark matter can freely intersect without significant interaction. At this density of dark matter and even several orders of magnitude greater (in the case of dark matter distribution mainly in the disc plane), its presence in the solar system can not be detected, which corresponds with the conclusions [12].

Let's try roughly to estimate the probability of a superphoton collision with the Earth. Let's assume that during our existence (1.3×10^{10} years) our galaxy has lost 4/5 of its baryonic matter due to the uniform radial radiation of superphotons on its inner spherical surface with a diameter of 10^5 light years. Then the number of super-photons from the total number of them ($\frac{1}{2} \times \frac{4}{5} \times 9.33 \times 10^{36} = 3.73 \times 10^{36}$) that fall per unit sphere area is 10^{-16} units per m^2 per year. Accordingly, 0.013 units per year (one superphoton at 77 years) fall on the globe cross-section or, in terms of unit charges, there are 1.46×10^{34} charges per year.

This is a reasonable value, but in reality this probability is much less and not only because of shading of the Earth by other cosmic bodies, dust, etc. The main reason is obviously the age of our galaxy and the presence of a black hole at its center; so we can assume that by now the radiation of superphotons is replaced by the reverse process — the absorption of matter by a black hole. Superhotons are carriers of namely negative charges, since there simultaneously are streams of positively charged particles — *cosmic rays*; at the same time negative and positive charges should be compensated in space as a whole. Obviously, there is some physical mechanism that separates the primary plasma into particles of opposite signs. Positive particles (mainly protons) form cosmic rays, and electrons are decelerated in interstellar magnetic fields (the material basis of the vortex tubes in our model).

The intensity of cosmic rays at the surface of the Earth is approximately one particle per cm^2 per second or 1.6×10^{26} particles per year on the entire Earth surface that is eight orders of magnitude less than the number of negative charges. However, the characteristic scale of the propagation of slow superphotons is the size of the galaxy (10^5 light years), and the similar propagation scale of cosmic rays, provided that they are uniformly distributed throughout the cosmic space, is the size of a larger structure — the cell of the cosmological network or the vault (10^7–10^8 light years). Thus, the unit density of particles in the corresponding volumes, i.e. cube ratio of linear scales, corresponds to the same order of magnitude.

4 On the forces of repulsion and dark energy

If the hypothesis of a superphoton is correct, then the galaxies periphery, where dark matter is mainly accumulated, should be surrounded by a distributed negative charge, which should counteract the "clumping" of galaxies between each other and also the walls of galactic vaults as a whole. Considering the masses and charges of galaxies at very great distances as point ones, it is possible to determine the magnitude of the equilibrium negative charge, at which electric forces are compared with gravitational ones:

$$Q = 2M\,(\pi\,\varepsilon_0\,\gamma)^{1/2}\,, \qquad (11)$$

where ε_0 and γ are known electric and gravitational constants. Substituting the data, we find for the "standard" mass of the quasar $Q = 4.08 \times 10^{32}$ Coulomb.

Neither the charge distribution around galaxies nor its fraction responsible for the repulsive force between them is known. Therefore, for a rough estimate of the smallest value of the acting charge it suffices to restrict oneself to only the fraction of superphotons enclosed in a single spherical layer along the halo periphery, and — in the superphotons themselves — to a single spherical layer of negative charges along the periphery of superphotons. It was previously calculated that in the halo volume of 10^5 light years in size, the superphoton occupies the cell of 5×10^8 m; then, based on the areas ratio, one can find that 1.13×10^{25} superphotons can be placed in a single peripheral layer of the halo. Similarly, bearing in mind the dimensions of the superphoton D and the standard contour r_{st}, one can find that 1.59×10^{24} charges can be placed in the peripheral layer of the superphoton. Thus, the effective minimum charge of the "standard" galaxy will be $1.13 \times 10^{25} \times 1.59 \times 10^{24} \times e_0 = 2.87 \times 10^{30}$ Coulomb or 0.7% of the equilibrium charge. This is already an appreciable value; therefore, with more number of active charges, for example, with the expansion of the halo surface, the repulsive forces between galaxies can increase up to exceeding them above the forces of gravitational attraction.

So, if this hypothesis is correct, then in the space between galaxies and their clusters the electric field also acts, and the electrostatic repulsive forces beyond the galaxies have the same distance dependence as the gravitational ones, i.e. inverse quadratic form. This is consistent with the opinion of some researchers that "the physical nature of dark energy is determined by the interaction of gravitation and electroweak forces" [13]. These forces manifest themselves as antigravity, which in total can be interpreted as a *modification of the theory of gravity at extremely long distances and cosmological durations* [6], which is one of the explanations of dark energy accepted to date.

Conclusion

Thus, the super-photon, bearing in mind its properties, may turn out to be the desired dark matter or the missing substance of the universe. Its existence as a carrier of negative charges is indirectly confirmed in the existence of cosmic rays — carriers of positive charges that correspond to the condition of the charge conservation in the universe as a whole. In the case of correctness of the model presented, the problem of dark matter and dark energy finds the most rational explanation: dark matter (superphotons having a negative charge) is a product of the evolution of ordinary matter, and dark energy (repulsive forces) is the property of dark matter.

Of course, the superphoton is such a "particle" that clearly does not meet the expectations of researchers studying dark matter. Perhaps direct evidence of the existence of superphotons can be detected by observations during their interaction with the Sun or against the background of the Sun's disk, the probability of which is four orders of magnitude higher than when super-photons interact with the Earth.

There is only one event that could be explained by the collision of the superphoton with the earth — this is the Tunguska phenomenon. Indeed, the superphoton as the analog of a giant ball lightning with an energy of 1.03×10^{17} J, in size of 890 m and moving at cosmic speed could produce the specific effects of the Tunguska catastrophe, including those that are not explained by the currently dominant meteorite hypothesis [14].

Submitted on December 22, 2017

References

1. Belyakov A.V. Charge of the electron, and the constants of radiation according to J. A. Wheeler's geometrodynamic model. *Progress in Physics*, 2010, v. 6, issue 4, 90–94.
2. Belyakov A.V. Macro-analogies and gravitation in the micro-world: further elaboration of Wheeler's model of geometrodynamics. *Progress in Physics*, 2012, v. 8, issue 2, 47–57.
3. Belyakov A.V. On the nature of ball lightning. *Progress in Physics*, 2016, v.12, issue 3, 276–279.
4. Belyakov A.V. Are quazars white holes? *Progress in Physics*, 2017, v.13, issue 1, 7–10.
5. Belyakov A.V. Evolution of stellar objects according to J. Wheeler's geometrodynamic concept. *Progress in Physics*, 2013, v.9, issue 1, 25–40.
6. Lukash V.N., Rubakov V.A. Dark energy: myths and reality. *Physics-Uspekhi*, March 2008, v.178, issue 3, 301–308.
7. Discovered: Fast-growing galaxies from early universe. Carnegie Institution for Science, Public Release: 24 May 2017.
8. Swinbank M. Astrophysics: distant galaxies lack dark matter. *Nature*, 16 March 2017, v.543, 318–319.
9. Genzel R. et al. Strongly baryon-dominated disk galaxies at the peak of galaxy formation ten billion years ago. *Nature*, 16 March 2017, v. 543, 397–401.
10. Iršič V. et al. First constraints on fuzzy dark matter from Lyman-α forest data and hydrodynamical simulations. *Physical Review Letters*, 2017, v.119, 031302; arXiv: 1703.04683.
11. Khoperskov S.A., Shustov B.M., Khoperskov A.V. The interaction of dark matter cusp with the baryon component in disk galaxies. arXiv: 1204.4917 [astro-ph.CO].
12. Pitjev N.P., Pitjeva E.V. Constraints on Dark Matter in the Solar System. arXiv: 1306.5534 [astro-ph.EP].
13. Chernin A.D. Dark energy and universal antigravity. *Physics-Uspekhi*, 2008, v.178, issue 3, 267–300.
14. Bronshten V.A. Tunguska meteorite: the history of the study. Moscow, Selyanov A. D. Publisher, 2000.

Kinetic Theory: Flatlining of Polyatomic Gases

Kent W. Mayhew

68 Pineglen Cres., Ottawa, Ontario, K2G 0G8, Canada. E-mail:Kent.Mayhew@gmail.com

By redefining a gas' kinetic energy as translational plus rotational, an alternative kinetic theory was disclosed by this author that was a superior fit with empirical findings than the accepted kinetic theory. This alternative kinetic theory's fit for monatomic, diatomic and triatomic gases is exceptional, however the same cannot be said of large polyatomic gases. Accordingly, a new consideration called "*flatlining*" is proposed in order to explain the discrepancy between theory and the known empirical finding for heat capacities of large polyatomic gases.

1 Introduction

Traditionally accepted kinetic theory is based upon equipartition and degrees of freedom [1,2,3]. Mathematically speaking equipartition uses the concept that a gaseous molecule with n'' atoms has $3n''$ degrees of freedom (f), [4,5] i.e.:

$$f = 3n''. \tag{1}$$

This leads to the isometric molar heat capacity (C_v) for large polyatomic gases being

$$C_v = \frac{3}{2} n'' R \tag{2}$$

where *n"* signifies the *polyatomic number* i.e. the number of atoms in each gas molecule. Numerous explanations for traditional kinetic theory's failure in properly describing empirically determined heat capacities, have been proposed [1,6-10]. Interestingly, Einstein thought that such failures in explaining empirical findings demonstrated the need for quantum theory [11-12].

This author proposed a new alternative kinetic theory [1]. The basis of this alternative theory was that the surrounding walls molecule's mean vibrational energy, as defined by (kT), is continually pumped onto the gaseous molecules that they surround. Where (k) is Boltzmann's constant and (T) is the absolute temperature.

After numerous impacts between the gaseous molecules and walls, the above pumping results in the total kinetic energy ($E_{kT(t,r)}$) of an N-molecule monatomic gas being defined by [1]:

$$E_{kT(t,r)} = \frac{3}{2} NkT. \tag{3}$$

Traditional kinetic theory considers that the kinetic energy as defined by eqn (3) represents purely translational energy.

In terms of this author's alternative kinetic theory, the above stated total kinetic energy consists of the gas' translational plus its rotational energy [1]. Interestingly, this author's theory is a superior fit with various heat capacities studies for gases [1,13-18], when compared to accepted theory.

In order to better understand, consider that you hit a tennis ball with a suitable racquet. If the ball impacts the racquet's face at a 90 degree angle then the ball will have significant translational energy in comparison to any rotational energy.

Conversely, if the ball impacts the racquet at an acute angle, although the same force is imparted onto that ball, the ball's rotational energy can be significant in comparison to its translational energy. The point becomes, that both the translational and rotational energy, are due to the same impact [1].

Now apply the above macroscopic considerations to the microscopic world. When vibrating wall molecules pump their mean vibrational energy onto the gas molecules that they surround it, it only makes sense that this results in both translational and rotational energy of the gas [1].

This author also pointed out that all kinetic theory only holds for sufficiently dilute gases because the predominate energy exchange is due to gas-wall molecule collisions, where wall molecules that act as massive energy pumps, i.e. gas molecules tend to take on the wall's energy with every gas-wall collision [1]. However this would not necessarily be the case for gases that are not sufficiently dilute i.e. gases where inter-gas molecular collisions are the dominate interaction [1].

This author has further asserted [1,19,20] that inter-gas molecular collisions tend to obey conservation of momentum, rather than adhere to kinetic theory. And, when inter-gas collisions dominate over gas-wall collisions then kinetic theory, the ideal gas law, Avogadro's hypothesis, Maxwell's distributions/velocities etc. all start to lose their validity [1].

For a system of diatomic gas molecules, the wall molecules still pass the same mean kinetic energy onto the diatomic gas molecule's center of mass with each collision. Therefore the diatomic gas' kinetic energy is still defined by eqn (3) [1].

The diatomic gas molecule's vibrational energy would be related to the absorption and/or emission of its surrounding blackbody/thermal radiation at temperature (T). The vibrational energy (E_v) of an N-molecule diatomic gas in a closed system becomes [1]

$$E_v = NkT. \tag{4}$$

And the total energy (E_{tot}) for an N molecule diatomic gas becomes [1]

$$E_{tot} = E_{kT(t,r)} + E_v = \frac{3}{2} NkT + NkT = \frac{5}{2} NkT. \tag{5}$$

Similarly, for N molecules of n”-polyatomic gas, the total vibrational energy is [1]

$$E_v = (n'' - 1)NkT. \tag{6}$$

And, the total energy (E_{tot}) for the polyatomic gas molecule becomes [1]:

$$E_{tot} = E_{kT(t,r)} + E_v = \frac{3}{2} NkT + (n'' - 1)NkT. \tag{7}$$

Hence,

$$E_{tot} = \left(n'' + \frac{1}{2}\right) NkT. \tag{8}$$

Dividing both sides by temperature and rewriting in terms of per mole: (N=6.022×10^{23}), equation (8) becomes [1]:

$$\frac{E_{tot}}{T} = Nk\left(n'' + \frac{1}{2}\right) = R\left(n'' + \frac{1}{2}\right). \tag{9}$$

For most temperature regimes, the heat capacity of gases remains fairly constant, hence equation (9) can be rewritten in terms of the isometric molar heat capacity (C_v) [1], i.e.

$$C_v = R\left(n'' + \frac{1}{2}\right). \tag{10}$$

The difference between molar isobaric heat capacity (C_p) and molar isometric heat capacity (C_v) for gases is the ideal gas constant (R). Therefore, a gas’s isobaric heat capacity C_p becomes

$$C_p = R\left(n'' + \frac{1}{2}\right). \tag{11}$$

Interestingly this author realized that the above difference between molar heat capacities allows for a relationship between the ideal gas constant (R) and the ability of a mole of gas molecules to do work against a gravitational field [1, 20-21], as a function of temperature.

Based upon equations (10) and (11) the gas’s molar specific heats were plotted against its polyatomic number (n”) as is shown by Fig. 1 and compared to the traditional accepted values for large polyatomic gases as given by eqn (2). Note the empirical data used in plotting Fig. 1 can be found in the Tables (1) and (2) provided in this author’s previous paper [1] concerning kinetic theory.

Moreover, there was a discrepancy, between our model and empirical findings for relatively large polyatomic gases. It becomes a goal of this paper to provide a plausible explanation for the moderate discrepancy between this author’s plots based upon equations (10) and (11) and the accepted empirical findings for large polyatomic molecules i.e. those whose polyatomic number is greater than four (n”> 4).

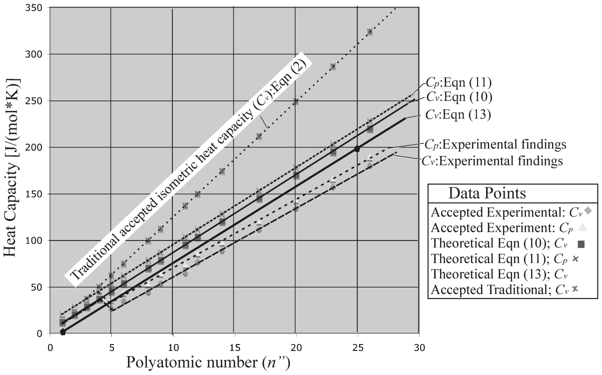

Fig. 1: Empirical versus theoretical heat capacities.

2 Flatlining

Why does the discrepancy exist for n”> 4? Let us consider that the gas molecule’s size influences the exchange of kinetic energy (translational plus rotational) with the wall molecule’s vibrational energy. How do we model this?

Consider the small monatomic gas molecule hitting the wall at location C, in Fig 2. Here the wall molecule is moving outward from the wall thus instantly imparting momentum, hence pumping its kinetic energy onto the gas molecule during the collision.

Next consider the gas molecule hitting the wall at location B. The wall molecule and gas molecule are initially moving in the same direction, i.e. both into the wall. However, since the wall molecule is vibrating at a very high frequency then within a fraction of a nanosecond, the wall molecule will start moving in the opposite direction. At this point the wall molecule imparts its momentum hence imposes kinetic energy (translational plus rotational) onto the impacting gas molecule.

Understandably, small gas molecules will tend to interact cleanly with the wall molecules, i.e. the significantly larger vibrating wall molecules cleanly pumps/imposes their mean vibrational energy directly onto the much smaller gas molecules. Seemingly, this is not the case for larger mole-cules. Perhaps vibrating wall molecules simply cannot clean-ly pump kinetic energy onto the larger gas molecules.

It can be envisioned that elongated linear gas molecules and/or large gas molecules tend to “*flatline*” against the wall, as is illustrated in Fig 2 at location A. The implication being that such large and/or elongated gas molecules tend to strike two or more (several) vibrating wall molecules at an instant, when some wall molecules are moving inwards, while their neighboring wall molecules are moving outwards, with respect to the wall as a whole. Note: The motions of the molecules are indicated by the arrows in Fig. 2.

Clearly the above should alter the dynamics of any kine-

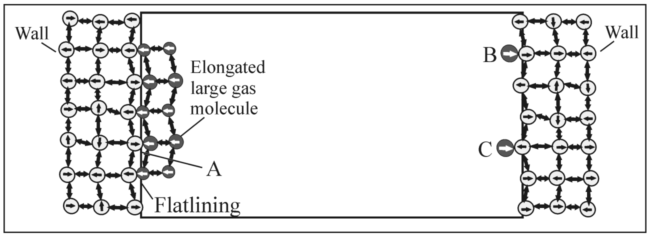

Fig. 2: Shows an elongated linear gas molecule flatlining against a wall at location A and the relative motions of the wall's molecules or atoms plus the relative motions of the gas' atoms. Also shown are smaller gas molecules hitting the wall at locations B and C.

matic energy exchange! The expectation is that a large polyatomic gas molecule's mean kinetic energy would no longer be simply defined in terms of the vibrating wall molecule's mean energy! Furthermore, the expectation is that polyatomic gases still interact with any surrounding blackbody/thermal radiation, thus continually striving for thermal equilibrium.

Consider that the primary energy exchange is between large polyatomic gases and their surroundings is with their surrounding blackbody/thermal radiation. The total energy (E_{tot}) imparted onto the gas molecule becomes the purely vibrational energy as defined by eqn (6). Accordingly:

$$\frac{E_{tot}}{T} = (n'' - 1)Nk. \tag{12}$$

Based upon eqn (12), the expected isometric molar heat capacity becomes:

$$C_v = (n'' - 1)R. \tag{13}$$

The graph for eqn. (13) is shown on Fig. 1; based upon $C_v = 0$ when $n''=1$, and $C_v = 19 \times 8.314 = 158.00$ when $n''=20$. The fit for the isometric molar heat capacity (C_v) based upon eqn. (10) was very good, if not exceptional, for monatomic through triatomic gases ($n'' <$ *or* $= 4$) but not so much larger polyatomic gases i.e. $n'' > 4$. Certainly eqn (13) is a better fit for the larger polyatomic gases than eqn. (10) was but the fit is only fairly good at best!

Reconsider what all might be happening. As previously stated, flatlining implies that large polyatomic gas' kinetic energy is no longer defined/controlled by the pumping of the wall molecule's vibrational energy onto the them. Remember by kinetic energy herein we mean the gas' translational plus rotational energy. In such a situation it becomes cumbersome to infer any net direction of energy flow being exchanged during collisions.

As previously stated, this author [1] understands that a limitation for the isometric molar heat capacity being defined by eqn (10) was the gas being *sufficiently dilute*, i.e. dilute enough that gas-wall molecule collisions are dominate in comparision to inter-gas molecule collisions. Part of the reasoning being that inter gas molecule collisions will obey conservation of momentum but not necessarily conservation of energy [1] i.e. inter-gas collisions tend to be inelastic. With further modelling this may help explain what is witnessed.

This author's insight that inter-gas collisions may generally be inelastic requires that radiation is given off during such collisions thus enabling inelastic collisions to adhere to conservation of energy [1]. Such collision induced radiation, whether it be considered as part of the system's blackbody and/or thermal energy, becomes part of the system being in thermal equilibrium i.e. the walls adsorb as much radiation energy as they emit.

The above is not to say that the walls and/or polyatomic gases necessarily emit the identical spectrum that they adsorb! It is, however to say that the total rate of energy of emission approximates that of the adsorption! Note; the total energy associated with radiation, whether it is blackbody, thermal or otherwise, can often be considered as insignificant, when compared to the energy associated with kinematics of matter. This is not saying that it can simply be ignored as is too often traditionally done in thermodynamics!

It should also be stated that large polyatomic gases will have large cross-sectional areas hence the concept of being sufficiently dilute may require higher mean molecular volumes in the gaseous state i.e. relatively low pressures.

Can we now claim that large polyatomic gas molecules tend to attain their kinetic energy from inter-gas collisions that obey conservation of momentum? No we cannot! However our expectation becomes that large polyatomic gases will not have the specified kinetic energies that smaller gases possess.

To further emphasize; the conceptualization of small gases having their kinetic energy pumped into to them by surrounding vibrating wall molecules, does not necessitate that gas-wall molecules collisions are elastic. On the contrary, it just implies that the gas' mean kinetic energy is driven into them via numerous collisions with wall molecules.

3 Addressing traditional dogma

As previously stated traditional kinetic theory is based upon equipartition and degrees of freedom arguments. We can go back further and acknowledge that for most of us, our learning started with considering a gas molecule's momentum and that momentum is conserved in elastic wall-gas molecule collisions.

The main problem with the above approach being that elastic collisions are a rarity i.e. it is rare to have a collision where both momentum and kinetic energy are conserved. The one simple exception being the case of two balls of equal mass colliding, with the second ball being stationary before the collision and that second ball then attains all the kinetic energy from the first ball, after the collision, i.e. first ball is stationary after the collision.

Rather than address the elephant in the room, traditional kinetic theory simply considered that all collisions are elastic, as well as, the gas molecule leaves the wall with the same magnitude of momentum as it has prior to hitting the wall. Realizing that walls impose their energetics onto the dilute gas implies that traditional teaching may have put the cart ahead of the horse!

Certainly considering all collisions as being elastic avoids having to contemplate the various frequencies of radiation that would be associated with inelastic collisions. And when in equilibrium; since the mean kinetic energy of the gas molecules is constant then yes the mean magnitude of momentum remains constant but this is no longer a requirement for an elastic gas-wall collision!

The situation is no more complicated if it is considered that a dilute gas in thermal equilibrium requires that all of the following three states remain related to the same temperature (T). Basically, as previously stated by this author [1]:

1. The walls are in thermal equilibrium with the enclosed radiation i.e. blackbody, thermal or otherwise.
2. The gas' translational plus rotational energy is pumped into the gas by the more massive vibrating wall molecules.
3. The gas' vibrational energies are in thermal equilibrium with the enclosed radiation i.e. blackbody, thermal or otherwise.

Remember: Part of this radiation surrounding the gas molecules will now be a result of the various inelastic intermolecular collisions.

4 Atmospheric gases

At first glance considering that walls impose/pump their vibrational energy onto relatively small gases' kinetic energy, may feel counter-intuitive in part because gases are routinely put into, and/or removed from containers without any real noticeable temperature changes. However, if we realize that the above does not necessarily hold for enclosed larger polyatomic gases and that such gases generally obtain their vibrational energy from the surrounding blackbody/thermal radiation, then the mean energetics of such gases will not change significantly by placing them into, nor removing them from enclosures.

Certainly small gas molecules in our atmosphere will hit the Earth's rough surface and have a certain amount of their kinetic energy pumped/imposed upon them in various inelastic collisions with Earth's surface. Even so, for atmospheric gases inter-gas collisions still should dominate.

Next consider the collision of a small gas molecule with a larger polyatomic gas. The expectation becomes that the larger gas molecule will behave as a massive wall molecule does, i.e. the large polyatomic gas molecule will use its vibrational energies to pump/impose some fairly well-defined mean kinetic energy (translational plus rotational) onto the colliding small gas molecules.

5 Other proofs for inelastic collisions

There is more proof to inelastic intermolecular collisions than just the awkwardness of the mathematical justification for elastic intermolecular collisions. Some examples being:

1. Viscous dissipation i.e. heat being generated by gases squeezed through a valve.
2. Natural *P-T* relationships i.e. temperature increases with increasing pressure.
3. Joule's weight experiment i.e. Although designed to demonstrate a correlation between work and energy, what it really shows is that imposed increases to a liquid's flow (due to the paddles attached to weights) resulted in increased intermolecular friction, which generated heat.

All of the above is readily explained in terms of inelastic intermolecular collisions, but all are not so readily explainable in terms of traditional understandings.

6 Conclusions

This author's previous conclusion [1]; kinetic theory needs to be redrafted based upon the previous understanding that a gas' kinetic energy has both translational and rotational components that are pumped/imposed onto them due to the same wall molecule's vibrational energy. Moreover, it seemingly holds for most small gaseous molecules i.e. gas' whose polyatomic number is 4 or less.

For larger polyatomic gases, *flatlining* helps explain what is witnessed. Specifically flatlining means that larger polyatomic gases tend to strike two or more vibrating wall molecules at some instant. Therefore any kinetic energy transfer between impacting gas molecule and vibrating wall molecule, is not clean. Moreover it becomes awkward to even determine what direction the net flow of energy exchange actually goes, assuming that there is any actual a net energy exchange!

This certainly improves the fit between accepted empirical findings for large polyatomic gases and the kinetic theory as previously proposed [1], combined with what is currently described herein, by this author.

Interestingly, it can be contemplated that atmospheric gases will tend to follow similar dynamics where large polyatomic gases adsorb surrounding radiation (blackbody and/or thermal) thus increasing their vibrational energy. This vibrational energy is then pumped/imposed onto any small gas molecules that collide with the larger polyatomic gases.

Furthermore, we asserted that most inter-molecular collisons probably are inelastic. In which case radiation (thermal, blackbody or otherwise) will be a byproduct of such collisions, and as such must be considered as part of a system's state, whether or not, that system is in thermal equilibrium. And this does alter our consideration of thermal equilbrium!

The overall implication being that traditional theorists unwittingly put the cart ahead of the horse by beginning the teaching of kinetic theory in terms of gas molecule's momentum and elastic collisions. This ignores the fact that elastic collisions are rare hence may be an unnecessary, illogical, unrealistic, conceptualization when applied to kinetic theory!

Submitted on February 12, 2018

References

1. Mayhew K.W. A new perspective for kinetic theory and heat capacity. *Progress in Physics*, 2017, v.13(4), 166–173.
2. Reif F. Fundamentals of Statistical and Thermal Physics. McGraw-Hill, New York, 1965.
3. Carey V. Statistical Thermodynamics and Microscale Thermophysics. Cambridge University Press, 1999.
4. Goldstein H. Classical Mechanics (2nd. ed.). Addison-Wesley, 1980.
5. Wüller A. Lehrbuch der Experimentalphysik (Textbook of Experimental Physics). Leipzig, Teubner, 1896, v.2, 507ff.
6. Boltzmann L. On certain Questions of the Theory of Gases. *Nature* 1895, v.51(1322), 413–415.
7. Planck M. On the Law of the Energy Distribution in the Normal Spectrum. *Ann. Phys.*, 1901, v.4(553), 1–11.
8. Enstein A. and Stern O. Einige Argumente Für die Annahme einer molekularen Agitation beim absolute Nullpunk (Some Arguments for the Assumption of Molecular Agitation at Absolute Zero). *Ann. Phys.*, 1913, v.40(551), 551–560.
9. Dahl J.P. On the Einstein–Stern model of rotational heat capacities. textitJ. of Chem. Physics, 1998, v.109, 10688.
10. Thomson W. Baltimore Lectures. Baltimore: Johns Hopkins University Press. Sec. 27. Re-issued in 1987 by MIT Press as *Kelvin's Baltimore Lectures and Modern Theoretical Physics: Historical and Philosophical Perspectives*, 1904.
11. Pais A. Subtle is the Lord. Oxford University Press. Oxford, 1982.
12. Hermann Armin (1971). The Genesis of Quantum Theory (1899–1913). Original title: Frühgeschichte der Quantentheorie (1899–1913), translated by Claude W. Nash ed., Cambridge, MA.
13. Masi J.F., Petkof B. *J. Res. Natl. Bur. Stand.*, 1952, v.48(3).
14. Scott R.B., Mellors J.W. *J. Res. Natl. Bur. Stand.*, v.34, March 1945.
15. Prydz R., Goodwin R.D. *J. Res. Natl. Bur. Stand.*, 1970, v.74A(5).
16. Giguere P.A. Heat capacities for water-hydrogen peroxide systems between 25 and 60 C. *J. Chem. Eng. Data*, 1962, v.7(4), 526–527.
17. Chapman S., Cowling T.G. The mathematical theory of non-uniform gases, third edition. Cambridge University Press, 1970.
18. Wu L., White C., Scanlon T.J., Reese J.M. and Zhang Y. A kinetic model of the Boltzmann equation for non-vibrating polyatomic gases. *J. Fluid Mechanics*, 2015, v.763, 24–50.
19. Mayhew K. Latent heat and critical temperature: A unique perspective. *Phys. Essays*, 2013, v.26, 4, 604–611.
20. Mayhew K. Second law and lost work. *Phys. Essays*, 2015, v.28, issue 1, 152–155.
21. Mayhew K. Entropy: an ill-conceived mathematical contrivance? *Phys. Essays*, 2015, v.28, issue 3, 352–357.
22. Mayhew K. Changing our perspective: Part 1: A New Thermodynamics (Self-published 2015) Available at:
    http://www.newthermodynamics.com
    https://createspace.com/5277845
23. Mayhew K. Improving our thermodynamic perspective. *Phys. Essays*, 2011, v.24, issue 3, 338–344.

Helical Solenoid Model of the Electron

Oliver Consa
Department of Physics and Nuclear Engineering, Universitat Politècnica de Catalunya
Campus Nord, C. Jordi Girona, 1-3, 08034 Barcelona, Spain
E-mail: oliver.consa@gmail.com

A new semiclassical model of the electron with helical solenoid geometry is presented. This new model is an extension of both the Parson Ring Model and the Hestenes Zitterbewegung Model. This model interprets the Zitterbewegung as a real motion that generates the electron's rotation (spin) and its magnetic moment. In this new model, the g-factor appears as a consequence of the electron's geometry while the quantum of magnetic flux and the quantum Hall resistance are obtained as model parameters. The Helical Solenoid Electron Model necessarily implies that the electron has a toroidal moment, a feature that is not predicted by Quantum Mechanics. The predicted toroidal moment can be tested experimentally to validate or discard this proposed model.

1 Introduction

Quantum mechanics (QM) is considered the most accurate physics theory available today. Since its conception, however, QM has generated controversy. This controversy lies not in the theory's results but in its physical interpretation.

One of the most controversial interpretations of QM was postulated by Bohr and Heisenberg. The "Copenhagen Interpretation" described QM as a system of probabilities that became definite upon the act of measurement. This interpretation was heavily criticized by many of the physicists who had participated in the development of QM, most notably Albert Einstein. Because of its probability features, Einstein believed that QM was only valid for analyzing the behavior of groups of particles and that the behavior of individual particles must be deterministic. In a famous quote from a 1926 letter to Max Born, Einstein stated, "He (God) does not play dice with the universe".

A major flaw in QM becomes apparent when the theory is applied to individual particles. This leads to logical contradictions and paradoxical situations (e.g., the paradox of Schrödinger's Cat). Einstein believed that QM was incomplete and that there must be a deeper theory based on hidden variables that would explain how subatomic particles behave individually. Einstein and his followers were not able to find a hidden variable theory that was compatible with QM, so the Copenhagen Interpretation was imposed as the interpretation of reference. If we assume that Einstein was correct, and that QM is only applicable to groups of particles, it is necessary to develop a new deterministic theory to explain the behavior of individual particles.

2 Spinning models of the electron

2.1 Ring Electron Model

In 1915, Parson [1] proposed a new model for the electron with a ring-shaped geometry where a unitary charge moves around the ring generating a magnetic field. The electron behaves not only as the unit of electric charge but also as the unit of magnetic charge or magneton. Several important physicists, including Webster, Gilbert, Grondahl and Page, conducted studies that supported Parson's Ring Electron Model. The most important of these studies was conducted by Compton [2], who wrote a series of papers showing that his newfound Compton Effect was better explained with Parson's Ring Electron Model than with the classical model that depicted the electron as a sphere. All these studies were compiled in 1918 by Allen [3] in "The Case for a Ring Electron" and discussed at a meeting of the Physical Society of London.

The Ring Electron Model was not widely accepted and was invalidated in 1923 by Schrödinger's wave equation of the electron. The Ring Electron Model has been unsuccessfully revisited several times by investigators like Iida, Carroll, Giese, Caesar, Bergman and Wesley [4], Lucas [5], Ginzburg or Kanarev [6]. Other researchers, such as Jennison [7], Gauthier [8], and Williamson and van der Mark [9], proposed similar models, with the additional assumption that the electron is a photon trapped in a vortex.

The Ring Electron Model proposes that the electron has an extremely thin, ring-shaped geometry that is about 2000 times larger than a proton. A unitary charge flows through the ring at the speed of light, generating an electric current and an associated magnetic field. This model allows us to combine experimental evidence that the electron has an extremely small size (corresponding to the thickness of the ring) as well as a relatively large size (corresponding to the circumference of the ring).

The Ring Electron Model postulates that the rotational velocity of the electric charge will match the speed of light and that the angular momentum will match the reduced Planck constant:

$$v_r = c, \tag{1}$$

$$L = mRv_r = \hbar. \tag{2}$$

As a consequence of (1) and (2), the radius of the ring will match the reduced Compton wavelength and the circum-

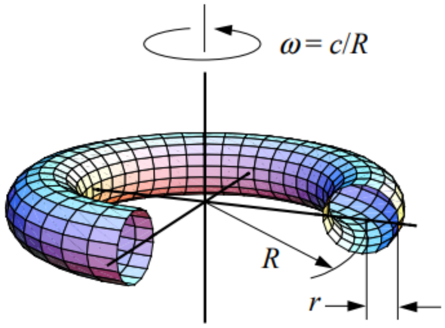

Fig. 1: Ring Electron Model.

ference will matches the Compton wavelength

$$R = \frac{\hbar}{m v_r} = \frac{\hbar}{mc} = \bar{\lambda}_c \,, \tag{3}$$

$$2\pi R = \frac{h}{mc} = \lambda_c \,. \tag{4}$$

Meanwhile, the frequency, angular frequency and rotation time period of the ring electron are defined by:

$$f_e = \frac{v_r}{2\pi R} = \frac{mc^2}{h} \,, \tag{5}$$

$$w_e = 2\pi f_e = \frac{mc^2}{\hbar} \,, \tag{6}$$

$$T_e = \frac{1}{f_e} = \frac{h}{mc^2} \,. \tag{7}$$

The electron's ring acts as a circular antenna. In this type of antenna, the resonance frequency coincides with the length of the antenna's circumference. In the case of the electron ring, the resonance frequency coincides with the electron's Compton frequency.

Substituting the electron's frequency (5) in the Planck equation ($E = hf$), we obtain the Einstein's energy equation

$$E = hf_e = h\,\frac{mc^2}{h} = mc^2. \tag{8}$$

The moving charge generates a constant electric current. This electric current produces a magnetic moment that is equal to the Bohr magneton:

$$I = e f_e = \frac{emc^2}{h} \,, \tag{9}$$

$$\mu_e = IS = \frac{emc^2}{h}\,\pi R^2 = \frac{e}{2m}\,\hbar = \mu_B \,. \tag{10}$$

The relationship between the magnetic moment and the angular momentum is called the "gyromagnetic ratio" and has the value "$e/2m$". This value is consistent with the magnetic moment generated by an electric current rotating on a circular surface of radius R. The gyromagnetic ratio of the electron can be observed experimentally by applying external magnetic fields (for example, as seen in the "Zeeman effect" or in the "Stern-Gerlach experiment"):

$$E = \frac{e}{2m}\,B. \tag{11}$$

The energy of the electron is very low, but the frequency of oscillation is extremely large, which results in a significant power of about 10 gigawatts:

$$P = \frac{E}{T} = \frac{m^2c^4}{h} = 1.01 \times 10^7 \text{ W}. \tag{12}$$

Using the same line of reasoning, the electric potential can be calculated as the electron energy per unit of electric charge, resulting in a value of approximately half a million volts:

$$V = \frac{E}{e} = \frac{mc^2}{e} = 5.11 \times 10^5 \text{ V}. \tag{13}$$

The electric current has already been calculated as 20 amps ($I = ef = 19.83$ A). Multiplying the voltage by the current, the power is, again, about 10 gigawatts ($P = VI$).

The Biot-Savart Law can be applied to calculate the magnetic field at the center of the ring, resulting in a magnetic field of 30 million Tesla, equivalent to the magnetic field of a neutron star:

$$B = \frac{\mu_0 I}{2R} = 3.23 \times 10^7 \text{ T}. \tag{14}$$

For comparison, the magnetic field of the Earth is 0.000005 T, and the largest artificial magnetic field created by man is only 90 T.

The electric field in the center of the electron's ring matches the value of the magnetic field multiplied by the speed of light:

$$E = \frac{e}{4\pi\epsilon_0 R^2} = cB = 9.61 \times 10^{12} \text{ V/m}. \tag{15}$$

The Ring Electron Model implies the existence of a centripetal force that compensates for the centrifugal force of the electron orbiting around its center of mass:

$$F = m\,\frac{v_r^2}{R} = \frac{m^2c^3}{\hbar} = 0.212 \text{ N}. \tag{16}$$

Electromagnetic fields with a Lorentz force greater than this centripetal force should cause instabilities in the electron's geometry. The limits of these electric and magnetic fields are:

$$F = eE + evB, \tag{17}$$

$$E = \frac{m^2c^3}{e\hbar} = 1.32 \times 10^{18} \text{ V/m}, \tag{18}$$

$$B = \frac{m^2c^2}{e\hbar} = 4.41 \times 10^9 \text{ T}. \tag{19}$$

In quantum electrodynamics (QED), these two values are known as the Schwinger Limits [10]. Above these values, electromagnetic fields are expected to behave in a nonlinear way. While electromagnetic fields of this strength have not yet been achieved experimentally, current research suggests that electromagnetic field values above the Schwinger Limits will cause unexpected behavior not explained by the Standard Model of Particle Physics.

2.2 Helical Electron Model

In 1930, while analyzing possible solutions to the Dirac equation, Schrödinger identified a term called the Zitterbewegung that represents an unexpected oscillation whose amplitude is equal to the Compton wavelength. In 1953, Huang [11] provided a classical interpretation of the Dirac equation in which the Zitterbewegung is the mechanism that causes the electron's angular momentum (spin). According to Huang, this angular momentum is the cause of the electron's magnetic moment. Bunge [12], Barut [13], Zhangi [14], Bhabha, Corben, Weyssenhoff, Pavsic, Vaz, Rodrigues, Salesi, Recami, Hestenes [15, 16] and Rivas [17] have published papers interpreting the Zitterbewegung as a measurement of the electron's oscillatory helical motion that is hidden in the Dirac equation. We refer to these electron theories as the Hestenes Zitterbewegung Model or the Helical Electron Model.

The Helical Electron Model assumes that the electron's charge is concentrated in a single infinitesimal point called the center of charge (CC) that rotates at the speed of light around a point in space called the center of mass (CM).

The Helical Electron Model shares many similarities with the Ring Electron Model, but in the case of the Helical Electron Model, the geometric static ring is replaced by a dynamic point-like electron. In this dynamic model, the electron's ring has no substance or physical properties. It need not physically exist. It is simply the path of the CC around the CM.

The CC moves constantly without any loss of energy so that the electron acts as a superconducting ring with a persistent current. Such flows have been experimentally detected in superconducting materials.

The CC has no mass, so it can have an infinitesimal size without collapsing into a black hole, and it can move at the speed of light without violating the theory of relativity. The electron's mass is not a single point. Instead, it is distributed throughout the electromagnetic field. The electron's mass corresponds to the sum of the electron's kinetic and potential energy. By symmetry, the CM corresponds to the center of the electron's ring.

We can demonstrate the principles of the Helical Electron Model with an analogy to the postulates of the Bohr Atomic Model:

- The CC always moves at the speed of light, tracing circular orbits around the CM without radiating energy.
- The electron's angular momentum equals the reduced Planck constant.
- The electron emits and absorbs electromagnetic energy that is quantized according to the formula $E = hf$.
- The emission or absorption of energy implies an acceleration of the CM.

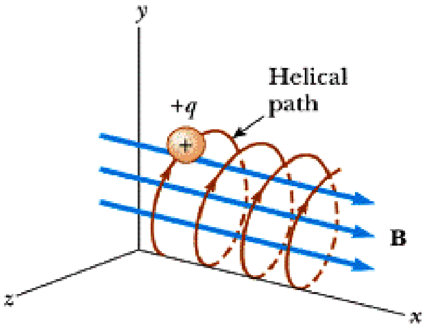

Fig. 2: Helical Electron Model.

The electron is considered to be at rest if the CM is at rest, since in that case the electric charge has only rotational movement without any translational movement. In contrast, if the CM moves with a constant velocity (v), then the CC moves in a helical motion around the CM.

The electron's helical motion is analogous to the observed motion of an electron in a homogeneous external magnetic field.

It can be parameterized as:

$$\begin{cases} x(t) = R\cos(\omega t)\,, \\ y(t) = R\sin(\omega t)\,, \\ z(t) = vt\,. \end{cases} \tag{20}$$

The electron's helical motion can be deconstructed into two orthogonal components: a rotational motion and a translational motion. The velocities of rotation and translation are not independent; they are constrained by the electron's tangential velocity that is constant and equal to the speed of light. As discussed above, when the electron is at rest, its rotational velocity is equal to the speed of light. As the translational velocity increases, the rotational velocity must decrease. At no time can the translational velocity exceed the speed of light. Using the Pythagorean Theorem, the relationship between these three velocities is:

$$c^2 = v_r^2 + v_t^2\,. \tag{21}$$

Then the rotational velocity of the moving electron is:

$$v_r = c\sqrt{1-(v/c)^2}\,, \tag{22}$$

$$v_r = c/\gamma\,. \tag{23}$$

Where gamma is the coefficient of the Lorentz transformation, the base of the Special Relativity Theory:

$$\gamma = \frac{1}{\sqrt{1-(v/c)^2}} . \tag{24}$$

Multiplying the three components by the same factor $(\gamma mc)^2$:

$$(\gamma mc)^2 c^2 = (\gamma mc)^2 v_r^2 + (\gamma mc)^2 v_t^2 . \tag{25}$$

Substituting the value of the rotational velocity ($v_r = c/\gamma$) and linear momentum ($p = \gamma mv$), results in the relativistic energy equation:

$$E^2 = (\gamma mc^2)^2 = (mc^2)^2 + (pc)^2 . \tag{26}$$

With this new value of the rotational velocity, the frequency, angular frequency and rotational time period of the helical electron are defined by:

$$f_e = \frac{v_r}{2\pi R} = \frac{mc^2}{\gamma h} , \tag{27}$$

$$w_e = 2\pi f_e = \frac{mc^2}{\gamma \hbar} , \tag{28}$$

$$T_e = \frac{1}{f_e} = \frac{\gamma h}{mc^2} . \tag{29}$$

The rotation time period of the electron acts as the electron's internal clock. As a result, although there is no absolute time in the universe, each electron is always set to its proper time. This proper time is relative to the electron's reference frame and its velocity with respect to other inertial reference frames.

The electron's angular momentum is always equal to the reduced Planck constant. This implies that the electron's mass has to increase γ times in order to compensate for the decrease in its rotational velocity:

$$L = mRv_r = (\gamma m)\, R\, (c/\gamma) = mRc = \hbar . \tag{30}$$

If the electron moves at a constant velocity, the particle's trajectory is a cylindrical helix. The geometry of the helix is defined by two constant parameters: the radius of the helix (R) and the helical pitch (H). The helical pitch is the space between two turns of the helix. The electron's helical motion can be interpreted as a wave motion with a wavelength equal to the helical pitch and a frequency equal to the electron's natural frequency. Multiplying the two factors results in the electron's translational velocity:

$$\lambda_e f_e = v , \tag{31}$$

$$\lambda_e = H = \frac{v}{f_e} = v\,\frac{\gamma h}{mc^2} = \gamma\beta\lambda_c . \tag{32}$$

The rest of the parameters representative of a cylindrical helix can also be calculated, including the curvature (κ) and the torsion (τ), where $h = 2\pi H = \gamma\beta\lambda\!\!\!^{-}_c$:

$$\begin{cases} \kappa = \dfrac{R}{R^2+h^2} = \dfrac{1}{\gamma^2 R} , \\[2ex] \tau = \dfrac{h}{R^2+h^2} = \dfrac{\beta}{\gamma R} . \end{cases} \tag{33}$$

According to Lancret's Theorem, the necessary and sufficient condition for a curve to be a helix is that the ratio of curvature to torsion must be constant. This ratio is equal to the tangent of the angle between the osculating plane with the axis of the helix:

$$\tan\alpha = \frac{\kappa}{\tau} = \frac{1}{\gamma\beta} . \tag{34}$$

2.3 Toroidal Solenoid Electron Model

In 1956, Bostick, a disciple of Compton, discovered the existence of plasmoids. A plasmoid is a coherent toroidal structure made up of plasma and magnetic fields. Plasmoids are so stable that they can behave as individual objects and interact with one another. From Parson's Ring Electron Model, Bostick [21] proposed a new electron structure, similar to that of the plasmoids. In his model, the electron takes the shape of a toroidal solenoid where the electric charge circulates at the speed of light. In the Toroidal Solenoid Electron Model, we assume that the electric charge is a point particle and that the toroidal solenoid represents the trajectory of that point electric charge.

In a toroidal solenoid, any magnetic flux is confined within the toroid. This feature is consistent with the idea that the mass of a particle matches the electromagnetic energy contained therein. Storage of electromagnetic energy in a toroidal solenoid superconductor without the loss of energy is called superconducting magnetic energy storage (SMES). According to the Toroidal Solenoid Electron model, an electron is a microscopic version of a SMES system.

Toroidal solenoid geometry is well known in the electronics field where it is used to design inductors and antennas. A toroidal solenoid provides two additional degrees of freedom compared to the ring geometry. In addition to the radius (R) of the torus, two new parameters appear: the thickness of the torus (r) and the number of turns around the torus (N) with N being an integer.

The toroidal solenoid can be parameterized as:

$$\begin{cases} x(t) = (R + r\cos Nwt)\cos wt , \\ y(t) = (R + r\cos Nwt)\sin wt , \\ z(t) = r\sin Nwt . \end{cases} \tag{35}$$

Where the tangential velocity is:

$$|r'(t)|^2 = (R + r\cos Nwt)^2 w^2 + (rNw)^2 . \tag{36}$$

We postulate that the tangential velocity is always equal to the speed of light ($|r'(t)| = c$). For $R \gg rN$, the rotational

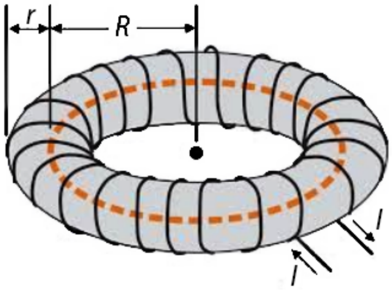

Fig. 3: Helical Toroidal Electron Model.

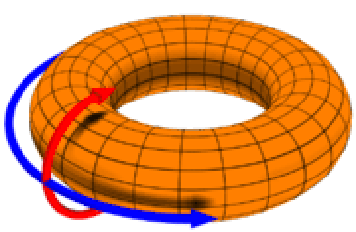

Fig. 4: Toroidal and Poloidal currents.

velocity can be obtained as:

$$c^2 = (Rw)^2 + (rNw)^2, \tag{37}$$

$$c/v_r = \sqrt{1 + \left(\frac{rN}{R}\right)^2}\,. \tag{38}$$

The second factor depends only on the geometry of electron. We call this value the helical g-factor. If $R \gg rN$, the helical g-factor is slightly greater than 1,

$$g = \sqrt{1 + \left(\frac{rN}{R}\right)^2}\,. \tag{39}$$

As a result, the rotational velocity is dependent on the helical g-factor and slightly lower than the speed of light:

$$v_r = c/g. \tag{40}$$

With this new value of the rotational velocity, the frequency, angular frequency and time period are defined by:

$$f_e = \frac{v_r}{2\pi R} = \frac{mc^2}{gh}\,, \tag{41}$$

$$w_e = 2\pi f_e = \frac{mc^2}{g\hbar}\,, \tag{42}$$

$$T_e = \frac{1}{f_e} = \frac{gh}{mc^2}\,. \tag{43}$$

The length of a turn of the toroidal solenoid is called the arc length. To calculate the arc length, we need to perform the integral of the toroidal solenoid over one turn:

$$\begin{aligned} l &= \int \sqrt{|r'(t)|^2} dt \\ &= \int \sqrt{(R + r\cos Nwt)^2 w^2 + (rNw)^2}\, dt\,. \end{aligned} \tag{44}$$

Approximating for $R \gg Nr$ and replacing the helical g-factor (39) results in:

$$\begin{aligned} l &= \int \sqrt{(Rw)^2 + (rNw)^2} dt \\ &= \int Rw\sqrt{1 + (rN/R)^2}\, dt = gR \int w dt = 2\pi gR\,. \end{aligned} \tag{45}$$

This means that the arc length of a toroidal solenoid is equivalent to the length of the circumference of a ring of radius $R' = gR$:

$$l = 2\pi gR = 2\pi R'. \tag{46}$$

In calculating the electron's angular momentum, we must take into consideration the helical g-factor. The value of the rotational velocity is reduced in proportion to the equivalent radius, so that the angular momentum remains constant:

$$L = mR'v_r = m\,(gR)\left(\frac{c}{g}\right) = \hbar. \tag{47}$$

The electric current flowing through a toroidal solenoid has two components, a toroidal component (red) and a poloidal component (blue).

By symmetry, the magnetic moment due to the poloidal components (red) is canceled, while the toroidal component (blue) remains fixed. No matter how large the number of turns in the toroidal solenoid, a toroidal component generates a corresponding axial magnetic moment [22]. This effect is well known in the design of toroidal antennas and can be canceled with various techniques. The exact value of the axial magnetic moment is:

$$m = I\pi R^2 \left[1 + \frac{1}{2}\left(\frac{r}{R}\right)^2\right]. \tag{48}$$

A comparison of the Toroidal Solenoid Electron Model ($v = 0, r > 0$) with the Ring Electron Model ($v = 0, r = 0$) reveals that the radius still coincides with the reduced Compton wavelength. The electric current is slightly lower, since the electron's rotational velocity is also slightly lower:

$$I\pi R^2 = ef\pi R^2 = \frac{ev_r R}{2} = \frac{ec\hbar}{2gmc} = \frac{e\hbar}{2mg} = \frac{\mu_B}{g}, \tag{49}$$

$$m = \frac{\mu_B}{g}\left[1 + \frac{1}{2}\left(\frac{r}{R}\right)^2\right], \tag{50}$$

$$m \simeq g\mu_B. \tag{51}$$

In calculating the angular momentum, the rotational velocity decreases in the same proportion as the equivalent radius increase, compensating for the helical g-factor. However, in the calculation of magnetic moment, the rotational velocity decreases by a factor of g, while the equivalent radius increases by a factor approximately equal to g squared. This is the cause of the electron's anomalous magnetic moment.

2.4 Helical Solenoid Model

The geometries of both the Ring Electron Model and the Toroidal Solenoid Electron Model represent a static electron ($v = 0$). For a moving electron with a constant velocity ($v > 0$), the ring geometry becomes a circular helix, while the toroidal solenoid geometry becomes a helical solenoid. On the other hand, if the thickness of the toroid is negated ($r = 0$), the toroidal solenoid is reduced to a ring, and the helical solenoid is reduced to a helix.

Experimentally, the electron's magnetic moment is slightly larger than the Bohr magneton. In the Ring Electron Model, it was impossible to explain the electron's anomalous magnetic moment. This leads us to assume that the electron has a substructure. The Toroidal Solenoid Electron Model allows us to obtain the electron's anomalous moment as a direct consequence of its geometry.

Geometry	$v = 0$	$v > 0$
$r = 0$	Ring	Helix
$r > 0$	Toroidal Solenoid	Helical Solenoid

The universe generally behaves in a fractal way, so the most natural solution assumes that the electron's substructure is similar to the main structure, that is, a helix in a helix.

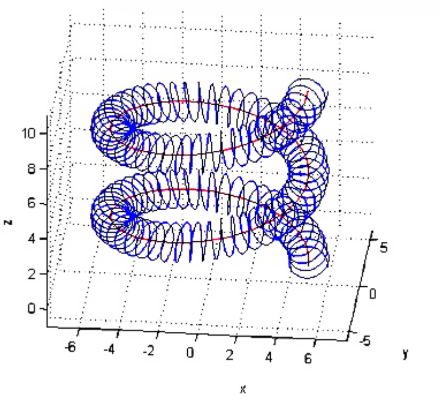

Fig. 5: Helical Solenoid Electron Model.

The trajectory of the electron can be parameterized with the equation of the helical solenoid:

$$\begin{cases} x(t) = (R + r\cos Nwt)\cos wt\,, \\ y(t) = (R + r\cos Nwt)\sin wt\,, \\ z(t) = r\sin Nwt + vt\,. \end{cases} \tag{52}$$

Like the other electron models discussed above, the Helical Solenoid Electron Model postulates that the tangential velocity of the electric charge matches the speed of light and that the electron's angular momentum matches the reduced Planck constant.

$$\begin{aligned} |r'(t)|^2 = c^2 = (Rw)^2 + (rNw)^2 + v^2 \\ + rw(2Rw + rw\cos Nwt + 2vN)\cos Nwt\,. \end{aligned} \tag{53}$$

This equation can be obtained directly from the helical solenoid geometry without any approximation. This equation shows a component that oscillates at a very high frequency with an average value of zero. Consequently, the Helical Solenoid Electron Model implies that the electron's g-factor is oscillating, not fixed. Since the value oscillates, there is a maximum level of precision with which the g-factor can be measured. This prediction is completely new to this model and is directly opposite to previous QED predictions. For $R \gg rN$, this oscillating component can be negated, and the equation reduces to

$$c^2 = (Rw)^2 + (rNw)^2 + v^2. \tag{54}$$

The rotational velocity can be obtained as a function of the speed of light, the Lorentz factor, and the helical g-factor:

$$c^2 = (Rw)^2(1 + (rN/R)^2) + v^2, \tag{55}$$

$$c^2 = (v_r)^2 g^2 + v^2, \tag{56}$$

$$gv_r = c\sqrt{1 - v^2/c^2}\,, \tag{57}$$

$$v_r = c/g\gamma. \tag{58}$$

With this new value of the rotational velocity, the frequency, angular frequency, rotation time period and the wavelength (o pitch) of the helical solenoid electron are defined by:

$$f_e = \frac{v_r}{2\pi R} = \frac{mc^2}{g\gamma h}\,, \tag{59}$$

$$w_e = 2\pi f_e = \frac{mc^2}{g\gamma\hbar}\,, \tag{60}$$

$$T_e = \frac{1}{f_e} = \frac{g\gamma h}{mc^2}\,, \tag{61}$$

$$\lambda_e = H = \frac{v}{f_e} = g\gamma\beta\lambda_c\,. \tag{62}$$

In 2005, Michel Gouanère [18] identified this wavelength in a channeling experiment using a beam of ~80 MeV electrons aligned along the $< 110 >$ direction of a thick silicon crystal ($d = 3.84 \times 10^{-10}$ m). While this experiment has not had much impact on QM, both Hestenes [19] and Rivas [20] have indicated that the experiment provides important experimental evidence consistent with the Hestenes Zitterbewegung Model:

$$d = g\gamma\beta\lambda_c = (\gamma mv)\,\frac{gh}{(mc)^2} = p\,\frac{gh}{(mc)^2}\,, \tag{63}$$

$$p = d\,\frac{(mc)^2}{gh} = 80.874\ \text{MeV/c}. \tag{64}$$

In the Helical Solenoid Electron Model, the rotational velocity is reduced by both the helical g-factor and the Lorentz factor. In contrast, the equivalent radius compensates for the helical g-factor while the increasing mass compensates for the Lorentz factor. The angular momentum remains equal to the reduced Planck constant:

$$L = m'R'v_r = (\gamma m)(gR)(c/\gamma g) = mRc = \hbar. \tag{65}$$

3 Consequences of the Helical Solenoid Electron Model

3.1 Chirality and helicity

In 1956, an experiment based on the beta decay of a Cobalt-60 nucleus demonstrated a clear violation of parity conservation. In the early 1960s the parity symmetry breaking was used by Glashow, Salam and Weinberg to develop the Electroweak Model, unifying the weak nuclear force with the electromagnetic force. The empirical observation that electroweak interactions act differently on right-handed fermions and left-handed fermions is one of the basic characteristics of this theory.

In the Electroweak Model, chirality and helicity are essential properties of subatomic particles, but these abstract concepts are difficult to visualize. In contrast, in the Helical Solenoid Electron Model, these concepts are evident and a direct consequence of the model's geometry:

- Helicity is given by the helical translation motion ($v > 0$), which can be left-handed or right-handed. Helicity is not an absolute value; it is relative to the speed of the observer.
- Chirality is given by the secondary helical rotational motion, which can also be left-handed or right-handed. Chirality is absolute since the tangential velocity is always equal to the speed of light; it is independent of the velocity of the observer.

3.2 Quantum Hall resistance and magnetic flux

The movement of the electric charge causes an electrical current ($I = ef_e$) and a electric voltage ($V = E/e = hf_e/e$). Applying Ohm's law, we obtain a fixed value for the impedance of the electron equal to the value of the quantum Hall resistance. This value is quite surprising, since it is observable at the macroscopic level and was not discovered experimentally until 1980:

$$R = \frac{V_e}{I_e} = \frac{hf_e/e}{ef_e} = \frac{h}{e^2}\,. \tag{66}$$

According to Faraday's Law, voltage is the variation of the magnetic flux per unit of time. So, in a period of rotation, we obtain a magnetic flux value which coincides with the quantum of magnetic flux, another macroscopically observable value. This value was expected since, in this model, the electron behaves as a superconducting ring, and it is experimentally known that the magnetic flux in a superconducting ring is quantized:

$$V = \phi_e/T_e\,, \tag{67}$$

$$\phi_e = V_eT_e = \frac{hf_e}{e}\frac{1}{f_e} = \frac{h}{e}\,. \tag{68}$$

3.3 Quantum LC circuit

Both the electrical current and the voltage of the electron are frequency dependent. This means that the electron behaves as a quantum LC circuit, with a Capacitance (C) and a Self Inductance (L). We can calculate these coefficients for a electron at rest, obtaining values $L = 2.08 \times 10^{-16}$ H and $C = 3.13 \times 10^{-25}$ F:

$$L_e = \frac{\phi_e}{I_e} = \frac{h}{e^2 f_e} = \frac{g\gamma h^2}{mc^2e^2}\,, \tag{69}$$

$$C_e = \frac{e}{V_e} = \frac{e^2}{hf_e} = \frac{g\gamma e^2}{mc^2}\,. \tag{70}$$

Applying the formulas of the LC circuit, we can obtain the values of impedance and resonance frequency, which coincide with the previously calculated values of impedance and natural frequency of the electron:

$$Z_e = \sqrt{\frac{L_e}{C_e}} = \frac{h}{e^2}\,, \tag{71}$$

$$f_e = \frac{1}{\sqrt{L_eC_e}} = \frac{mc^2}{g\gamma h} = f_e\,. \tag{72}$$

As the energy of the particle oscillates between electric and magnetic energy, the average energy value is

$$E = \frac{LI^2}{2} + \frac{CV^2}{2} = \frac{hf}{2} + \frac{hf}{2} = hf\,. \tag{73}$$

The above calculations are valid for any elementary particle with a unit electric charge, a natural frequency of vibration and an energy which match the Planck equation ($E = hf$).

From this result, we infer that the electron is formed by two indivisible elements: a quantum of electric charge and a quantum of magnetic flux, the product of which is equal to Planck's constant. The electron's magnetic flux is simultaneously the cause and the consequence of the circular motion of the electric charge:

$$e\phi = h. \tag{74}$$

3.4 Quantitative calculation of the helical G-factor

The g-factor depends on three parameters (R, r and N) but we do not know the value of two of them. We can try to figure out the value of the helical g-factor using this approximation [28]:

Using this expansion series:

$$\sqrt{1 + (a)^2} = 1 + 1/2(a)^2 + \ldots \tag{75}$$

The helical g-factor can be expressed as:

$$\sqrt{1+\left(\frac{rN}{R}\right)^2} = 1+\frac{1}{2}\left(\frac{rN}{R}\right)^2+\ldots \tag{76}$$

QED also calculates the g-factor by an expansion series where the first term is 1 and the second term is the Schwinger factor:

$$g.factor(QED) = 1+\frac{\alpha}{2\pi}+\ldots \tag{77}$$

The results of the two series are very similar. Equaling the second term of the helical g-factor series to the Schwinger factor, we obtain the relationship between the radius of the torus and the thickness of the torus:

$$\frac{1}{2}\left(\frac{rN}{R}\right)^2 = \frac{\alpha}{2\pi}, \tag{78}$$

$$\frac{rN}{R} = \sqrt{\frac{\alpha}{\pi}}. \tag{79}$$

What gives a value of helical g-factor of

$$g = \sqrt{1+\alpha/\pi}. \tag{80}$$

This gives us a value of the helical g-factor = 1.0011607. This result is consistent with the Schwinger factor, and it offers a value much closer to the experimental value.

3.5 Toroidal moment

In 1957, Zel'dovich [23] discussed the parity violation of elementary particles and postulated that spin-1/2 Dirac particles must have an anapole. In the late 1960s and early 1970s, Dubovik [24, 25] connected the quantum description of the anapole to classical electrodynamics by introducing the polar toroidal multipole moments. The term toroidal derives from current distributions in the shape of a circular coil that were first shown to have a toroidal moment. Toroidal moments were not acknowledged outside the Soviet Union as being an important part of the multipole expansion until the 1990s. Toroidal moments became known in western countries in the late 1990s. Finally, in 1997, toroidal moment was experimentally measured in the nuclei of Cesium-133 and Ytterbium-174 [26].

In 2013, Ho and Scherrer [27] hypothesized that Dark Matter is formed by neutral subatomic particles. These particles of cold dark matter interact with ordinary matter only through an anapole electromagnetic moment, similar to the toroidal magnetic moment described above. These particles are called Majorana fermions, and they cannot have any other electromagnetic moment apart from the toroid moment. The model for these subatomic particles of dark matter is compatible with the Helical Solenoid Electron Model.

In an electrostatic field, all charge distributions and currents may be represented by a multipolar expansion using only electric and magnetic multipoles. Instead, in a multipolar expansion of an electrodynamic field new terms appear. These new terms correspond to a third family of multipoles: the toroid moments. The toroidal lower order term is the toroidal dipole moment. The toroidal moment can understood as the momentum generated by a distribution of magnetic moments. The simplest case is the toroidal moment generated by an electric current in a toroidal solenoid.

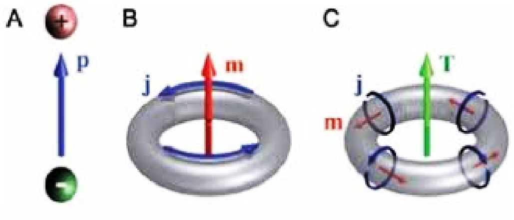

Fig. 6: Electric, Magnetic and Toroidal dipole moments.

The toroidal moment is calculated with the following equation [24]:

$$T = \frac{1}{10}\int\left[(\mathbf{j}\cdot\mathbf{r})\,\mathbf{r}-2r^2\mathbf{j}\right]dV. \tag{81}$$

In the case of the toroidal solenoid, the toroidal moment can be calculated more directly as the B field inside the toroid by both the surface of the torus and the surface of the ring [25]:

$$\mu T = BsS = B\left(\pi r^2\right)\left(\pi R^2\right), \tag{82}$$

$$B = \frac{\mu NI}{2\pi R}. \tag{83}$$

Using B, the toroidal moment is obtained as [22]:

$$T = \frac{NI}{2\pi R}\left(\pi r^2\right)\left(\pi R^2\right) = \frac{NI\left(\pi r^2\right)R}{2}. \tag{84}$$

Rearranging and using the relation (79):

$$T = \mu_B\,\frac{R}{g2N}\left(\frac{rN}{R}\right)^2 = \mu_B\,\frac{\lambda_c}{gN}\left(\frac{\alpha}{2\pi}\right). \tag{85}$$

According the Helical Solenoid Electron Model, the electron's theoretical toroidal moment is about $T \simeq 10^{-40}$ Am^3. The theoretical toroidal moment value for the neutron and the proton should be one million times smaller. The existence of a toroidal moment for the electron (and for any other subatomic particle) is a direct consequence of this model, and it may be validated experimentally. Notably, QM does not predict the existence of any toroidal moments.

3.6 Nucleon model

By analogy to the theory underlying the Helical Solenoid Electron Model, we assume that all subatomic particles have the same structure as the electron, differing mainly by their charge and mass. Protons are thought to be composed of other fundamental particles called quarks, but their internal organization is beyond the scope of this work.

The radius of a nucleon is equal to its reduced Compton wavelength. The Compton wavelength is inversely proportional to an object's mass, so for subatomic particles, as mass increases, size decreases. Both the proton and the neutron have a radius that is about 2000 times smaller than the electron. Historically, the proton radius was measured using two independent methods that converged to a value of about 0.8768 fm. This value was challenged by a 2010 experiment utilizing a third method, which produced a radius of about 0.8408 fm. This discrepancy remains unresolved and is the topic of ongoing research referred to as the Proton Radius Puzzle. The proton's reduced Compton wavelength is 0.2103 fm. If we multiple this radius by 4, we obtain the value of 0.8412 fm. This value corresponds nicely with the most recent experimental radius of the proton. This data supports our theory that the proton's radius is related to its reduced Compton radius and that our Helical Solenoid Electron Model is also a valid model for the proton.

The current of a nucleon is about 2000 times the current of an electron, and the radius is about 2000 times lower. This results in a magnetic field at the center of the nucleon's ring that is about four million times bigger than that of the electron or thousands of times bigger than a neutron star. This magnetic field is inversely dependent with the cube of the distance. This implies that while the magnetic field inside the neutron's ring is huge, outside the ring, the magnetic field decays much faster than the electric field. The asymmetrical behavior of the neutron's magnetic field over short and long distances leads us to suggest that the previously identified strong and weak nuclear forces are actually manifestations of this huge magnetic field at very short distances.

3.7 Spin quantum number

In 1913, Bohr introduced the Principal Quantum Number to explain the Rydberg Formula for the spectral emission lines of atomic hydrogen. Sommerfeld extended the Bohr theory with the Azimuthal Quantum Number to explain the fine structure of the hydrogen, and he introduced a third Magnetic Quantum Number to explain the Zeeman effect. Finally, in 1921, Landé put forth a formula (named the Landé g-factor) that allowed him to explain the anomalous Zeeman effect and to obtain the whole spectrum of all atoms.

$$\begin{aligned} g_J = g_L & \frac{J(J+1) - S(S+1) + L(L+1)}{2J(J+1)} \\ & + g_S \frac{J(J+1) + S(S+1) - L(L+1)}{2J(J+1)}. \end{aligned} \tag{86}$$

In this formula, Landé introduced a fourth Quantum Number with a half-integer number value (S = 1/2). This Landé g-factor was an empirical formula where the physical meaning of the four quantum numbers and their relationship with the motion of the electrons around the nucleus was unknown. Heisenberg, Pauli, Sommerfeld, and Landé tried unsuccessfully to devise a new atomic model (named the Ersatz Model) to explain this empirical formula. Landé proposed that his g-factor was produced by the combination of the orbital momentum of the outer electrons with the orbital momentum of the inner electrons. A different solution was suggested by Kronig, who proposed that the half-integer number was generated by a self-rotation motion of the electron (spin), but Pauli rejected this theory.

In 1925, Uhlenbeck and Goudsmit published a paper proposing the same idea, namely that the spin quantum number was produced by the electron's self-rotation. The half-integer spin implies an anomalous magnetic moment of 2. In 1926, Thomas identified a relativistic correction of the model with a value of 2 (named the Thomas Precession) that compensated for the anomalous magnetic moment of the spin. Despite his initial objections, Pauli formalized the theory of spin in 1927 using the modern theory of QM as set out by Schrödinger and Heisenberg. Pauli proposed that spin, angular moment, and magnetic moment are intrinsic properties of the electron and that these properties are not related to any actual spinning motion. The Pauli Exclusion Principle states that two electrons in an atom or a molecule cannot have the same four quantum numbers. Pauli's ideas brought about a radical change in QM. The Bohr-Sommerfeld Model's explicit electron orbitals were abandoned and with them any physical model of the electron or the atom.

We propose to return to the old quantum theory of Bohr-Sommerfeld to search for a new Ersatz Model of the atom where the four quantum numbers are related to electron orbitals. We propose that this new atomic model will be compatible with our Helical Solenoid Electron Model. We also propose that the half-integer spin quantum number is not an intrinsic property of the electron but a result of the magnetic fields generated by orbiting inner electrons.

Submitted on January 25, 2018

References

1. Parson L. A Magneton Theory of the Structure of the Atom. *Smithsonian Miscellaneous Collections*, 1915, v. 65, 2–80.
2. Compton A.H. The Size and Shape of the Electron. *Phys. Rev.*, 1917. v. 14(3), 247–259.
3. Allen H.S. The Case for a Ring Electron. *Proceedings of the Physical Society*, 1919, v. 31, 49–68.
4. Bergman D., Wesley J.P. Spinning Charged Ring Model of Electron Yielding Anomalous Magnetic Moment. *Galilean Electrodynamics*, 1990, v. 1, 63–67.
5. Lucas C.W. A Classical Theory of Elementary Particles Electromagnetic Part 2, intertwining Charge-Fibers. *The Journal of Common Sense Science*, 2005, v. 8(2), 1–7.
6. Kanarev P. Model of the Electron. *Apeiron*, 2000, v. 7(3–4), 184–194.
7. Jennison R.C. A new classical relativistic model of the electron. *Phys. Letters A.*, 1989, v. 141(8–9), 377–382.

8. Gauthier R. Superluminal Quantum Models of the Electron and the Photon. viXra:0703.0015.
9. Williamson J.G., van der Mark J.M.B. Is the electron a photon with toroidal topology? *Annales de la Fondation Louis de Broglie*, 1997, v. 22(2), 133–146.
10. Schwinger J. On Gauge Invariance and Vacuum Polarization. *Phys. Rev.*, 1951, v. 82, 664–679.
11. Huang K. On the Zitterbewegung of the Dirac Electron. *Am. J. Phys.*, 1952, v. 20, 479–484.
12. Bunge M. A picture of the electron. *Nuovo Cimento*, 1955, v. 1(6), 977–985.
13. Barut A.O., Bracken A.J. Zitterbewegung and the internal geometry of the electron. *Phys. Rev. D*, 1981, v. 23(10), 2454–2463.
14. Barut A.O., Zanghi N. Classical Model of the Dirac Electron. *Phys. Rev. Lett.*, 1984, v. 52, 2009–2012.
15. Hestenes D. The Zitterbewegung Interpretation of Quantum Mechanics. *Found. Phys.*, 1990, v. 20(10), 1213–1232.
16. Hestenes D. Zitterbewegung in Quantum Mechanics. arXiv:8002.2728.
17. Rivas M. Kinematical Theory of Spinning Particles. Kluwer, Dordrecht, 2001.
18. Gouanère M. A Search for the de Broglie Particle Internal Clock by Means of Electron Channeling. *Foundations of Physics*, 2008, v. 38, 659–664.
19. Hestenes D. Reading the Electron Clock. arXiv:0802.3227.
20. Rivas M. Measuring the internal clock of the electron. arXiv:0809.3635.
21. Bostick W. Mass, Charge and Current: The Essence and Morphology. *Physics Essays*, 1991, v. 4(1), 45–59.
22. Marinov K., Boardman A.D., Fedotov V.A. Metamaterial Toroidal. *New Journal of Physics*, 2007, v. 9, 324–335.
23. Zel'dovich Y. Electronic interaction with parity violation. *Zh. Eksp. Teor. Fiz.*, 1957, v. 33, 1184–1186.
24. Dubovik V.M., Tugushev. Toroid moments in electrodynamics and solid-state physics. *Physics Reports*, 1990, v. 187(4), 145–202.
25. Dubovik V.M., Kuznetsov. The toroid moment of Majorana neutrino. *Int. J. Mod. Phys.*, 1998, v. A13, 5257-–5278.
26. Wood C.S. Measurement of parity nonconservation and an anapole moment in cesium. *Science*, 1997, v. 275, 1759–1763.
27. Ho C.M., Scherrer R.J. Anapole dark matter. *Phys. Lett. B*, 2013, v. 722, 341–346.
28. Consa O. G-factor and the Helical Solenoid Electron Model. viXra: 1702.0185.

Concerning the Dirac γ-Matrices Under a Lorentz Transformation of the Dirac Equation

G. G. Nyambuya

National University of Science and Technology, Faculty of Applied Sciences — Department of Applied Physics,
Fundamental Theoretical and Astrophysics Group, P. O. Box 939, Ascot, Bulawayo, Republic of Zimbabwe
E-mail: physicist.ggn@gmail.com

We *embolden* the idea that the Dirac 4×4 γ-matrices are four-vectors where the space components (γ^i) represent spin and the forth component (γ^0) should likewise represent the time component of spin in the usual four-vector formalism of the Special Theory of Relativity. With the γ-matrices as four-vectors, it is seen that the Dirac equation admits two kinds of wavefunctions — (1) the usual four component Dirac bispinor ψ and (2) a scalar four component bispinor ϕ. Realizing this, and knowing forehand of the existing mystery as to why Leptons and Neutrinos come in pairs, we seize the moment and make the suggestion that the pair (ψ, ϕ) can be used as a starting point to explain mystery of why in their three generations $[(e^\pm, \nu_e), (\mu^\pm, \nu_\mu), (\tau^\pm, \nu_\tau)]$, Leptons and Neutrinos come in doublets. In this suggestion, the scalar-bispinor ϕ can be thought of as the Neutrino while the usual Dirac bispinor ψ can be thought of as the Lepton.

> "We have found it of paramount importance that in order to progress we must recognize our ignorance and leave room for doubt."
>
> — Richard Phillips Feynman (1918-1988)

1 Introduction

As taught to physics students through the plethora of textbooks available on our planet e.g., refs. [1–5], the Dirac 4×4 γ-matrices (γ^μ) are usually presented as objects that undergo a transformation during a Lorentz transformation of the Dirac [6, 7] equation. This issue of the transformation of these γ-matrices is not well represented in the literature [8]. There, thus, is a need to clear the air around this issue regarding the proper transformation properties of these matrices. To that end, we here argue in favour of these matrices as physical four-vectors and as such, they must under a Lorentz transformation transform as four-vectors. In-fact, it is well known that the γ^i-matrices ($i = 1, 2, 3$) represent spin (*i.e.*, $\vec{\mathcal{S}} = \frac{1}{2}\hbar\gamma^1\vec{i} + \frac{1}{2}\hbar\gamma^2\vec{j} + \frac{1}{2}\hbar\gamma^3\vec{k}$) because, together with the angular momentum operator ($\vec{\mathcal{L}}$), their sum total of the orbital angular momentum and spin ($\vec{\mathcal{J}} = \vec{\mathcal{L}} + \vec{\mathcal{S}}$) commutes with the Dirac Hamiltonian ($\mathcal{H}_D$), *i.e.* ($[\vec{\mathcal{J}}, \mathcal{H}_D] = 0$), implying that $\vec{\mathcal{J}}$ is a constant of motion.

For a particle whose rest-mass and Dirac [6, 7] wavefunction are m_0 and ψ respectively, the corresponding Dirac [6, 7] equation is given by:

$$\imath\hbar\gamma^\mu\partial_\mu\psi = \mathrm{m}_0 c\psi, \tag{1}$$

where:

$$\gamma^0 = \begin{pmatrix} \mathcal{I}_2 & 0 \\ 0 & -\mathcal{I}_2 \end{pmatrix}, \quad \gamma^i = \begin{pmatrix} 0 & \sigma^i \\ -\sigma^i & 0 \end{pmatrix}, \tag{2}$$

are the 4×4 Dirac γ-matrices where $\mathcal{I}_2$ and 0 are the $2{\times}2$ identity and null matrices respectively, and $|\psi\rangle$ is the four component Dirac [6, 7] wave-function, $\hbar$ is the normalized Planck constant, c is the speed of light in vacuum, $\imath = \sqrt{-1}$, and:

$$\psi = \begin{pmatrix} \psi_0 \\ \psi_1 \\ \psi_2 \\ \psi_3 \end{pmatrix} = \begin{pmatrix} \psi_L \\ \\ \psi_R \end{pmatrix}, \tag{3}$$

is the 4×1 Dirac [6, 7] four component wavefunction and ψ_L and ψ_R are the Dirac [6, 7] bispinors that are defined such that:

$$\psi_L = \begin{pmatrix} \psi_0 \\ \\ \psi_1 \end{pmatrix} \text{ and } \psi_R = \begin{pmatrix} \psi_2 \\ \\ \psi_3 \end{pmatrix}. \tag{4}$$

Throughout this reading — unless otherwise specified; the Greek indices will *here-and-after* be understood to mean ($\mu, \nu, ... = 0, 1, 2, 3$) and the lower case English alphabet indices ($i, j, k ... = 1, 2, 3$).

2 Lorentz Transformation of the Dirac as usually presented

To prove Lorentz Invariance (Covariance) two conditions must be satisfied:

1. *The first condition is that*: given any two inertial observers O and O′ anywhere in spacetime, if in the frame O we have:

$$[\imath\hbar\gamma^\mu\partial_\mu - \mathrm{m}_0 c]\psi(x) = 0, \tag{5}$$

as the Dirac equation for the particle ψ, then:

$$[\imath\hbar\gamma^{\mu'}\partial_{\mu'} - \mathrm{m}_0 c]\psi'(x') = 0 \tag{6}$$

is the equation describing the same state but in the frame O′.

2. *The second condition is that*: given that $\psi(x)$ is the wavefunction as measured by observer O, there must be a prescription for observer O$'$ to compute $\psi'(x')$ from $\psi(x)$ where $\psi'(x')$ describes to O$'$ the same physical state as that measured by O. The conserve must be true as-well, that is: there must exist a prescription such that starting from equation (6), one can arrive at (5).

In simpler mathematical terms, the above two requirements are saying that: starting from equation (5), there must exist some physically legitimate transformations within the framework of Lorentz transformations that can take (map) us from this equation (5) to equation (6) and *vice-versa*. If we can find these, then, the Dirac equation is said to be Lorentz Invariant (Covariant).

Now, since the Lorentz transformations are linear, it is to be required or expected of the transformations between $\psi(x)$ and $\psi'(x')$ to be linear too, *i.e.*:

$$\psi'(x') = \psi'(\Lambda x) = S(\Lambda)\psi(x) = S(\Lambda)\psi(\Lambda^{-1}x'), \tag{7}$$

where $S(\Lambda)$ is a 4×4 matrix which depends only on the relative velocities of O and O$'$ and Λ is the Lorentz transformation matrix. $S(\Lambda)$ has an inverse if O $\rightarrow$ O$'$ and also O$'$ $\rightarrow$ O. The inverse is:

$$\psi(x) = S^{-1}(\Lambda)\psi'(x') = S^{-1}(\Lambda)\psi'(\Lambda x), \tag{8}$$

or we could write:

$$\psi(x) = S(\Lambda^{-1})\psi'(\Lambda x) \Longrightarrow S(\Lambda^{-1}) = S^{-1}(\Lambda). \tag{9}$$

We can now write equation (5), as:

$$\left[\imath\hbar\gamma^{\mu}\frac{\partial x^{\mu'}}{\partial x^{\mu}}\partial_{\mu'} - \mathrm{m}_0 c\right] S^{-1}(\Lambda)\psi'(x') = 0, \tag{10}$$

and multiplying this from the left by $S(\Lambda)$, we have:

$$S(\Lambda)\left[\imath\hbar\gamma^{\mu}\frac{\partial x^{\mu'}}{\partial x^{\mu}}\partial_{\mu'} - \mathrm{m}_0 c\right] S^{-1}(\Lambda)\psi'(x') = 0, \tag{11}$$

and hence:

$$\left[\imath\hbar S(\Lambda)\gamma^{\mu}\frac{\partial x^{\mu'}}{\partial x^{\mu}} S^{-1}(\Lambda)\partial_{\mu'} - \mathrm{m}_0 c\right]\psi'(x') = 0. \tag{12}$$

Therefore, for the above equation to be identical to equation (6) (hence Lorentz Invariant), the requirement is that:

$$\gamma^{\mu'} = S(\Lambda)\gamma^{\mu}\frac{\partial x^{\mu'}}{\partial x^{\mu}} S^{-1}(\Lambda), \tag{13}$$

hence, we have shown that — for as long as $S^{-1}(\Lambda)$ exists, equation (5) is Lorentz Invariant.

3 Dirac $4 \vec{\times} 4$ $\vec{\gamma}$-matrices as a four-vector

The Dirac equation (1) can be re-written in the traditional Schrödinger formulation as ($\mathcal{H}\psi = \mathcal{E}\psi$) where $\mathcal{H}$ and $\mathcal{E}$ are the energy and Hamiltonian operators respectively. In this Schrödinger formulation, $\mathcal{H}$, will be such that it is given by:

$$\mathcal{H} = \gamma^0 \mathrm{m}_0 c^2 - \imath\hbar c\gamma^0\gamma^j\partial_j, \tag{14}$$

and ($\mathcal{E} = i\hbar\partial/\partial t$).

Now, according to the quantum mechanical equation governing the evolution of any quantum operator $\mathcal{Q}$, we know that:

$$\imath\hbar\frac{\partial\mathcal{Q}}{\partial t} = \mathcal{Q}\mathcal{H} - \mathcal{H}\mathcal{Q} = [\mathcal{Q}, \mathcal{H}], \tag{15}$$

hence, if:

$$[\mathcal{Q}, \mathcal{H}] \equiv 0, \tag{16}$$

then, the quantum mechanical observable corresponding to the operator $\mathcal{Q}$ is a conserved physical quantity.

With this [equation (15)] in mind, Dirac asked himself the natural question — what the "strange" new γ-matrices appearing in his equation really represent. What are they? In-order to answer this question, he decided to have a "look" at or make a closer "inspection" of the quantum mechanical orbital angular momentum operator $\mathcal{L}_i$ which we all know to be defined:

$$\mathcal{L}_i = (\vec{r} \times \vec{p})_i = -\imath\hbar\epsilon_{ijk}x_j\partial_k, \tag{17}$$

where, ϵ_{ijk} is the completely-antisymmetric three dimensional *Levi-Civita* tensor. In the above definition of $\mathcal{L}_i$, the momentum operator $\vec{p}$ is the usual quantum mechanical operator, *i.e.*:

$$\vec{p} = -\imath\hbar\vec{\nabla} \qquad \Rightarrow \qquad p_i = \imath\hbar\partial_i. \tag{18}$$

From this definition of $\mathcal{L}_i$ given in equation (17), it follows from equation (15) that $\imath\hbar\partial\mathcal{L}_i/\partial t = [\mathcal{L}_i, \mathcal{H}]$, will be such that:

$$\imath\hbar\frac{\partial\mathcal{L}_i}{\partial t} = -\imath\hbar\mathrm{m}_0 c^2\epsilon_{ijk}\left[x_j\partial_k, \gamma^0\right] + \hbar^2 c\epsilon_{ijk}\left[x_j\partial_k, \gamma^0\gamma^l\partial_l\right]. \tag{19}$$

Now, because the term $\gamma^0\mathrm{m}_0 c^2$ is a constant containing no terms in p_i, it follows from this very fact that ($\epsilon_{ijk}\left[x_j\partial_k, \gamma^0\right] \equiv 0$), hence equation (19) will reduce to:

$$\begin{aligned}\imath\hbar\frac{\partial\mathcal{L}_i}{\partial t} &= \hbar^2 c\epsilon_{ijk}\gamma^0\gamma^l\left[x_j\partial_k, \partial_l\right] \\ &= \hbar^2 c\epsilon_{ijk}\gamma^0\gamma^l\left(x_j\partial_k\partial_l - \partial_l x_j\partial_k\right).\end{aligned} \tag{20}$$

From the commutation relation of position (x_i) and momentum ($-\imath\hbar\partial_j$) due to the Heisenberg uncertainty principle [9], namely ($-\imath\hbar\left[x_i, \partial_j\right] = -\imath\hbar\delta_{ij}$) where δ_{ij} is the usual Kronecker-delta function, it follows that if in equation (20), we substitute ($\partial_l x_j = x_j\partial_l + \delta_{lj}$), this equation is going to reduce to:

$$\imath\hbar\frac{\partial\mathcal{L}_i}{\partial t} = \hbar^2 c\epsilon_{ijk}\gamma^0\gamma^l\underbrace{\left(x_j\partial_k\partial_l - x_j\partial_l\partial_k\right)} + \hbar^2 c\epsilon_{ijk}\gamma^0\gamma^l\delta_{lj}\partial_k. \tag{21}$$

The term with the under-brace vanishes identically, that is to say: $(x_j\partial_k\partial_l - x_j\partial_l\partial_k \equiv 0)$; and $(\epsilon_{ijk}\gamma^0\gamma^l\delta_{lj} = \epsilon_{ilk}\gamma^0\gamma^l)$, it follows from this that equation (21), will reduce to:

$$\imath\hbar\frac{\partial\mathcal{L}_i}{\partial t} = \hbar^2 c\epsilon_{ilk}\gamma^0\gamma^l\partial_k. \tag{22}$$

Since this result [*i.e.*, equation (22) above] is non-zero, it follows from the dynamical evolution theorem [*i.e.*, equation (16)] of Quantum Mechanics (QM) that none of the angular momentum components $\mathcal{L}_i$ are — *for the Dirac particle* — going to be constants of motion. This result obviously bothered the great and agile mind of Paul Dirac. For example, a non-conserved angular momentum would mean spiral orbits *i.e.*, Dirac particles do not move in fixed and well defined orbits as happens with electrons of the Hydrogen atom for example; at the very least, this is very disturbing because it does not tally with observations. The miniature beauty that Dirac had — had the rare privilege to discover and, the first human being to "see" with his beautiful and great mind — this — had to be salvaged[*] somehow.

Now — *enter spin*! Dirac figured that "*Subtle Nature*" must conserve something redolent with orbital angular momentum, and he considered adding something to $\mathcal{L}_i$ that would satisfy the desired conservation criterion, *i.e.*: call this unknown, mysterious and arcane quantity $\mathcal{S}_i$ and demand that:

$$\imath\hbar\frac{\partial\left(\mathcal{L}_i + \mathcal{S}_i\right)}{\partial t} \equiv 0. \tag{23}$$

This means that this strange quantity $\mathcal{S}_i$ must be such that:

$$\imath\hbar\frac{\partial\mathcal{S}_i}{\partial t} = [\mathcal{S}_i, \mathcal{H}] = -\hbar^2 c\epsilon_{ilk}\gamma^0\gamma^l\partial_k. \tag{24}$$

Solving equation (24) for $\mathcal{S}_i$, Dirac arrived at:

$$\mathcal{S}_i = \frac{1}{2}\hbar\begin{pmatrix} \sigma_i & 0 \\ 0 & \sigma_i \end{pmatrix} = \frac{1}{2}\hbar\gamma^5\gamma^i, \tag{25}$$

where $(\gamma^5 = \imath\gamma^0\gamma^1\gamma^2\gamma^3)$, is the usual Dirac gamma-5 matrix.

Now, realising that:

1. The matrices σ_i are Pauli matrices and they had been *ad hocly* introduced in 1925 into physics to account for the spin of the Electron by the Dutch-American theoretical physicists, George Eugene Uhlenbeck (1900–1988) and his colleague, Samuel Abraham Goudsmit (1902–1978) [10].
2. His equation — when taken in the non-relativistic limit, it would account for the then unexplained gyromagnetic ratio (g = 2) of the Electron and this same equation emerged with σ_i explaining the Electron's spin.

The agile Paul Dirac seized the golden moment and forthwith identified $\mathcal{S}_i$ with the ψ-particle's spin. The factor $\frac{1}{2}\hbar$ in $\mathcal{S}_i$ implies that the Dirac particle carries spin $1/2$, hence, the Dirac equation (1) is an equation for a particle with spin $1/2$!

While in this esoteric way (*i.e.*, as demonstrated above) Dirac was able to explain and "demystify" Wolfgang Pauli (1900–1958)'s strange spin concept which at the time had only been inserted into physics by "*the sleight of hand*" out of an *unavoidable necessity*, what bothers us (*i.e.*, myself) the most is:

> *How it comes about that we (physicists) have had issues to do with the transformational properties of the γ-matrices? Why? Really — why? The fact that orbital angular momentum $\vec{\mathcal{L}}$ is a vector invariably leads to the indelible fact that $\vec{\mathcal{S}}$ is a vector as-well, because we can only add vectors to vectors.*

If $\vec{\mathcal{S}}$ is a vector, then the matrices γ^i must be components of a 3-vector, so must the matrix γ^0 be the component of the time-vector in the usual four-vector formalism, hence γ^μ must be a four-vector. So, right from the word go — with little or no resistance whatsoever, it must have been pristine clear that the γ-matrices must be four-vectors.

4 Dirac equation with the $\vec{\gamma}$-matrices as a four-vector

With γ-matrices now taken as a four-vector, the object $\gamma^\mu\partial_\mu$ is a scalar, the meaning of which is that the Dirac equation will now accommodate two types of spinors "*the usual Dirac bispinor*" and a new "*scalar-bispinor*", *i.e.*:

1. **A spinor that is a scalar**. Let us here call this a scalar-bispinor and let us denote it with the symbol ϕ and because of its scalar nature — under a Lorentz transformation, we will have $(\phi' = \phi)$. Just like the ordinary Dirac wavefunction ψ is a 4×1 component object, ϕ is also a 4×1 object, *i.e.*:

   $$\phi = \begin{pmatrix} \phi_0 \\ \phi_1 \\ \phi_2 \\ \phi_3 \end{pmatrix} = \begin{pmatrix} \phi_L \\ \\ \phi_R \end{pmatrix}, \tag{26}$$

   where ϕ_L and ϕ_R are the scalar-spinors — which are like the ordinary left and right handed Dirac spinors (ψ_L, ψ_R); ψ_L and ϕ_R are defined:

   $$\phi_L = \begin{pmatrix} \phi_0 \\ \\ \phi_1 \end{pmatrix} \text{ and } \phi_R = \begin{pmatrix} \phi_2 \\ \\ \phi_3 \end{pmatrix}. \tag{27}$$

   Consideration of the scalar-bispinor has been made in the past by others e.g., [11].

2. **The ordinary Dirac bispinor** ψ: that transforms linearly under a Lorentz transformation *i.e.* $(\psi' = S\psi)$,

---

[*] Such is the indispensable attitude of the greatest theoretical physicists that ever graced the face of planet Earth — beauty must and is to be preserved; this is an ideal for which they will live for, and if needs be, it is an ideal for which they will give-up their life by taking a gamble to find that unknown quantity that restores the beauty glimpsed!

where, a usual, Lorentz Invariance (Covariance) requires that the function $S = S(x^{\mu}, \dot{x}^{\mu})$ be such that:

$$\gamma^{\mu'}\partial_{\mu'}S = \gamma^{\mu}\partial_{\mu}S = 0, \tag{28}$$

and:

$$\gamma^{\mu} = S^{-1}\gamma^{\mu}S, \tag{29}$$

which implies:

$$[S, \gamma^{\mu}] = 0. \tag{30}$$

Now, we certainly must ask "*What does this all mean*". That is to say, the fact that the Dirac equation allows for the existence of the usual Dirac bispinor ψ and in addition to that — a scalar-bispinor ϕ? Taken at the same level of understanding that the Dirac equation's prediction of the existence of antimatter is premised on the Dirac equation being symmetric under charge conjugation — on that very same level of understanding, this fact that the Dirac equation in its most natural and un-tempered state as presented herein — it, allows for the existence of the usual Dirac bispinor ψ and scalar-bispinor ϕ; in the same vein of logic, this naturally implies that for every Dirac bispinor ψ, there must exist a corresponding scalar-bispinor ϕ. That is, the Dirac bispinor ψ and the scalar-bispinor ϕ must come in pairs. There is no escape from this train of logic.

If we are thinking of Leptons and Neutrinos, the above pair-picture of (ψ, ϕ) makes perfect sense. Based on this picture, we can write the Dirac equation for this pair (ψ, ϕ) as:

$$\imath\hbar\gamma^{\mu}\partial_{\mu}\begin{pmatrix} \psi \\ \\ \phi \end{pmatrix} = \mathrm{m}_0 c\begin{pmatrix} 1 & 0 \\ 0 & \eta \end{pmatrix}\begin{pmatrix} \psi \\ \\ \phi \end{pmatrix}, \tag{31}$$

where η is a scalar-constant that we have introduced so as to accommodate the possibility that the particle-pair (ψ, ϕ), may have different masses. In this way, one can begin to entertain ideas on how to explain the Lepton-Neutrino pairing $[(e^{\pm}, \nu_{\mathrm{e}}), (\mu^{\pm}, \nu_{\mu}), (\tau^{\pm}, \nu_{\tau})]$. We have no intention of doing this or going any deeper on this matter but merely to point out — as we have just done — that, this idea may prove a viable avenue of research to those seeking an explanation of why this mysterious pairing occurs in nature.

5 General discussion

We must categorically state that — *what we have presented herein is not new at all.* All we have endeavoured is to make bold the point that the γ-matrices constitute a four-vector. Perhaps the only novelty there is — in the present contribution — is the suggestion that we have made — namely that, the resulting scalar-bispinor (ϕ) and the usual Dirac bispinor (ψ) can be used as a starting point to explain the currently open problem of the three generation Lepton-Neutrino pairing $(e^{\pm}, \nu_{\mathrm{e}})$, $(\mu^{\pm}, \nu_{\mu})$ and $(\tau^{\pm}, \nu_{\tau})$; where the scalar-bispinor can be assumed to be the Neutrino while the usual Dirac bispinor can be thought of the Lepton. In the sequatial reading [12], we will demonstrate how this formulation of the Dirac equation can be used to explain how massless neutrinos can oscillate.

Acknowledgements

We are grateful for the assistance rendered unto us by the National University of Science and Technology's Research Board toward our research endeavours.

Submitted on March 16, 2018

References

1. Itzykson C. and Zuber J.-B. Quantum Mechanics II. McGraw-Hill, New York, USA, 1980.
2. Messiah A. Quantum Mechanics II. North-Holland Publishing Company, Amsterdam, Netherland, second edition, 1962.
3. Sakurai J. J. Advanced Quantum Mechanics. Addison-Wesley Publishing Company, Massachusetts, USA, 1967.
4. Schweber S. S. An Introduction to Relativistic Quantum Field Theory. Row, Peterson and Company, New York, USA, 1961.
5. Zee A. Quantum Field Theory in a Nutshell. Princeton University Press, USA, second edition, 2010.
6. Dirac P. A. M. The Quantum Theory of the Electron. *Proceedings of the Royal Society of London A: Mathematical, Physical and Engineering Sciences*, 1928, v.117(778), 610–624.
7. Dirac P. A. M. The Quantum Theory of the Electron. Part II. *Proceedings of the Royal Society of London A: Mathematical, Physical and Engineering Sciences*, 1928, v. 118(779), 351–361.
8. Nikolić H. How (Not) To Teach Lorentz Covariance of the Dirac Equation. *European Journal of Physics*, 2014, v.35(3), 035003.
9. Heisenberg W. Ueber den anschaulichen Inhalt der quantentheoretischen Kinematik and Mechanik. *Zeitschrift für Physik*, 1927, v.43, 172–198. *Engilish Translation*: Wheeler J. A. and Zurek W. H. (eds) Quantum Theory and Measurement. Princeton (NJ), Princeton University Press, 1983, 62–84.
10. Uhlenbeck G. E. and Goudsmit S. Ersetzung der Hypothese vom unmechanischen Zwang durch eine Forderung bezüglich des inneren Verhaltens jedes einzelnen Elektrons. *Die Naturwissenschaften*, 1925, v.13(47), 953–954.
11. Chapman T. C. and Leiter D. J. On the Generally Covariant Dirac Equation. *American Journal of Physics*, 1976, v.44(9), 858–862.
12. Nyambuya G. G. Oscillating Massless Neutrinos. *Progress in Physics*, 2018, v. 14, 94–98.

Oscillating Massless Neutrinos

G. G. Nyambuya

National University of Science and Technology, Faculty of Applied Sciences — Department of Applied Physics,
Fundamental Theoretical and Astrophysics Group, P. O. Box 939, Ascot, Bulawayo, Republic of Zimbabwe
E-mail: physicist.ggn@gmail.com

The phenomenon of neutrino oscillations requires that not only should neutrinos be massive but that these masses be unique. How they acquire this mass remains an *open question*. Various mechanisms have been proposed to explain this phenomenon of neutrino oscillations. Herein, we propose — *the simplest imaginable* — alternative mechanism which operates *via* coupling the massless neutrino to a massive Dirac scalar. This massive Dirac scalar is a new hypothetical particle that we — *unfortunately* — can not observe directly because of its point-particle nature. Further, this massive Dirac scalar comes in as an integral part of the neutrino system — it [massive Dirac scalar] oscillates between three states, thus leading to the observed neutrino oscillations. This model predicts neutrinos are Dirac in nature and not Majorana.

> "Just by studying mathematics we can hope to make a guess at the kind of mathematics that will come into the physics of the future."
>
> — Paul A. M. Dirac (1902-1984)

1 Introduction

According to Albert Einstein (1879–1955)'s Special Theory of Relativity (STR) [1], the energy E and momentum p of a massless ($m_0 = 0$) are related by the energy-momentum equation ($E = pc$), where c is the speed of Light in *vacuo*. In accordance with the dictates of wave mechanics/phenomenon, the group velocity, v_{g}:

$$v_{\mathrm{g}} = \frac{\partial E}{\partial p}, \tag{1}$$

of a particle whose energy and momentum are related by ($E = pc$) is equal to the speed of Light in *vacuo*, *i.e.* ($v_{\mathrm{g}} = c$). All indications are that the neutrino travels at the *vacuo* speed of Light, c, thus prompting physicists to assume that the neutrino is massless. Be that as it may, a massless neutrino pauses a problem to the physicist in that one can not explain the all-important experimentally [2–5] verified and common-place phenomenon of *neutrino oscillation*.

First predicted [6, 7] in 1957 by the Italian nuclear physicist — Bruno Pontecorvo (1913–1993), and observed in 1968 by the America chemist and physicist — Raymond Davis Jr. (1914–2006) et al. [8], neutrino oscillation is a quantum mechanical phenomenon whereby a neutrino created with a specific lepton flavour (electron ν_e, muon ν_μ, or tau ν_τ) can be measured at a latter time to have a different flavour. The probability of measuring a particular flavour for a neutrino varies between the three known flavour states $(\nu_e, \nu_\mu, \nu_\tau)$ as it propagates through the intestacies of space. From a theoretical standpoint, two conditions are necessary for neutrinos to oscillate — *i.e.*, to change from one type to the other, *e.g.*, from an Electron-neutrino (ν_e) to a Muon-neutrino (ν_μ) or *vice-verse*, and these conditions are:

1. Neutrinos *must* have a *non-zero mass*, and this mass *cannot be identical* for all the three neutrino flavours $(\nu_e, \nu_\mu, \nu_\tau)$.
2. There *must be no rigorous law forbidding* a transition between neutrino species, the meaning of which is that these transitions are purely probabilistic in nature.

Since the coming to light or since the "conception" of this important question *i.e.*, the question of how neutrino masses arise — this question, has not been answered conclusively [9]. In the *Standard Model* of particle physics, fermions only have mass because of interactions with the *Higgs Field*. Do neutrinos generate their mass *via* the *Higgs Mechanism* [10–12] as-well? This is a question that needs an answer. We here do not claim to give a definitive answer to this question, but merely a suggestion — *perhaps*, a suggestion that one might consider worthy of their attention.

That said, we must here at the penultimate of this introductory section make clear the scope of the present letter — *i.e.*, while this letter presents — *in our feeble view*, a new model whose endeavour is to explain neutrino oscillations, we present this model only as an alternative to existing explanations on this phenomenon. We deliberately avoid an in-depth comparative analysis of these models with the present and this we have done in-order that our ideas are clearly presented without overshadowing them with existing ideas on the same endeavour.

2 Massless Dirac particle

First considered by the German mathematician, mathematical physicist and philosopher — Hermann Klaus Hugo Weyl (1885–1955); a massless Dirac particle is described by the following Dirac-Weyl [13] equation:

$$\imath\hbar\gamma^{\mu}\partial_{\mu}\psi = 0, \tag{2}$$

where ($\imath = \sqrt{-1}$), ∂_μ is the four spacetime partial derivatives, $\hbar$ is the normalized Planck constant, γ^μ are the four 4×4 Dirac matrices and ψ is the usual 4×1 component Dirac wavefunction.

In this letter, the gamma matrices shall be assumed to be four vectors the meaning of which is that they transform like vectors *i.e.*:

$$\gamma^{\mu'} = \frac{\partial x^{\mu'}}{\partial x^\mu} \gamma^\mu. \tag{3}$$

This assumption of treating the γ-matrices as four vectors may appear strange and if not completely and outright wrong. Be that as it may, in the letter [14], this idea of treating the γ-matrices as vectors as been justified. As argued therein the said letter [14], once the γ-matrices are four vectors, ψ can take three forms:

1. It [ψ] can be a zero ranks scalar.
2. It [ψ] can be a four 4×1 component scalar where the four components are zero ranks scalar objects.
3. Provided a certain transformational condition is met [*i.e.*, the condition given in equation (28) of [14]], it [ψ] can be the typical Dirac spinor.

In the subsequent section, we shall look at the scalar version.

3 Scalar coupled massive Dirac particle

For a moment, suppose we couple the massless ψ-particle to a massive ϕ-scalar particle, that is to say, we have ψ interfere with ϕ in such a way that the resulting 4×1 component Dirac wavefunction of the interference $\uppsi$, is such that:

$$\uppsi = \phi\psi. \tag{4}$$

The ϕ-particle is a simple (zero-rank) scalar, *i.e.*, unlike the ψ-particle which is a 4×1 component object, ϕ has no components, it is a zero rank mathematical object. Together, ϕ and ψ make a complete quantum mechanical particle *i.e.*, they satisfy the quantum probability normalization condition:

$$\iiint_{\forall Space} (\phi\psi)^\dagger (\phi\psi)\, dxdydz = 1, \tag{5}$$

and as individuals (ϕ, ψ), they do not satisfy the quantum probability normalization condition required for a complete quantum mechanical particle *i.e.*:

$$0 < \iiint_{\forall Space} \phi^\dagger \phi dxdydz < 1, \tag{6}$$

and:

$$0 < \iiint_{\forall Space} \psi^\dagger \psi dxdydz < 1. \tag{7}$$

Now, substituting ($\uppsi = \phi\psi$) into equation (2), we will have:

$$\imath\hbar\gamma^\mu \phi \partial_\mu \psi = -\imath\hbar\gamma^\mu \left(\partial_\mu \phi\right) \psi. \tag{8}$$

If ϕ is a massive particle satisfying the equation:

$$-\imath\hbar\gamma^\mu \partial_\mu \phi = m_0 c \phi, \tag{9}$$

where ($m_0 \neq 0$), then, equation (8), becomes:

$$\imath\hbar\gamma^\mu \phi \partial_\mu \psi = m_0 c \phi \psi, \tag{10}$$

hence:

$$\imath\hbar\gamma^\mu \partial_\mu \psi = m_0 c \psi. \tag{11}$$

Equation (11) is the Dirac [15, 16] equation describing a massive particle of mass m_0 and it is this equation that is used to describe neutrino oscillations. Thus, the neutrino as described by $\uppsi$ is now a massive particle — the meaning of which is that one can now describe neutrino oscillations which require a non-zero mass. It is important at this juncture that we state the obvious, namely that — just as the ψ-particle is a spin-1/2 particle, the ϕ-particle is likewise a spin-1/2 particle. As pointed out in the pernultimate of the previous section, we must remind the reader at this point that equation (9) with ϕ as a scalar has been justified in the letter [14]. That is to say, as justified therein the letter [14], the γ-matrices have here been assumed to be four vectors, hence equation (9).

While neutrino oscillations strongly point to the existence of unique non-zero mass for the three neutrino flavours, these oscillations do not directly mean the mass of these neutrinos is non-zero (*e.g.*, [17]). Only direct experimental observations as deliver a definitive answer to the question (*e.g.*, [17]). A number of experiments have been dedicated to this effect and these experiments place upper limits with not definitive and precise value being pinned down.

4 Dirac scalar particle

While the ϕ-scalar particle is operated on by the usual Dirac operator, it is not an ordinary Dirac particle because an ordinary Dirac particle is described by a 4×1 component wavefunction and not a zero rank scalar. Consequently, the question that naturally and immediately comes to mind is whether this Dirac [15, 16] equation (9) describing this scalar particle is a valid equation. To answer this — just as is the case with the Dirac [15, 16] equation, the validity of this equation is to judged on whether or not this equation (9) yields reasonable energy solutions for the case of a free scalar. As usual, the free particle solution of the new hypothetical Dirac scalar is:

$$\phi = \phi_0 e^{\imath p_\mu x^\mu/\hbar}, \tag{12}$$

where ϕ_0 is a normalization constant, p_μ and x^μ are the four momentum and position of this scalar particle. Substituting ϕ as given in equation (12) into equation (9), and thereafter performing some algebraic operations and clean-up, one obtains the following set of four simulations equations:

$$\left.\begin{array}{lr}
(E - \mathrm{m}_0 c^2) - c(p_x - ip_y) - cp_z = 0 & \ldots \;\; (a) \\
(E - \mathrm{m}_0 c^2) - c(p_x + ip_y) + cp_z = 0 & \ldots \;\; (b) \\
(E + \mathrm{m}_0 c^2) - c(p_x - ip_y) - cp_z = 0 & \ldots \;\; (c) \\
(E + \mathrm{m}_0 c^2) - c(p_x + ip_y) + cp_z = 0 & \ldots \;\; (d)
\end{array}\right. \tag{13}$$

Adding together equations (13a) and (13b), one obtains:

$$E = p_x c + m_0 c^2, \tag{14}$$

and likewise, adding together equations (13c) and (13d), one obtains:

$$E = p_x c - m_0 c^2. \tag{15}$$

Undoubtedly, the solutions (14) and (15), are indeed acceptable solutions — hence, the scalar Dirac [15,16] equation (9), is as a result, an acceptable equation describing this hypothetical Dirac scalar particle. The question now is what do these solutions (14) and (15) mean?

First — we must notice that these solutions (14) and (15) tell us that the energy of the ϕ-scalar particle is determined by this particle's momentum along the x-axis. If this particle did have a non-zero momentum along the other two axis *i.e.*, the y and z-axis, what the equations (14) and (15) are telling us, is that this momentum is of no consequence whatsoever in determining the energy of this particle. This does not make sense. The only reasonable solution to this dilemma is to assume that ($p_y = p_z = 0$) and ($p_x \neq 0$). This means that the ϕ-particle only moves along the x-axis and nothing else. If this is the case that it only moves along the x-axis, then — clearly, this ϕ-particle can not be an extended particle, but a point-particle. If the ϕ-particle is indeed a point-particle, it must be invisible hence non-detectable. This not only a natural conclusion to reach, but a logical one.

Second — we have the two solutions equation (14) and (15) having different energies. What does this mean? One way to look at this is to assume that there exists two such particles with each having different energies. The other would be to assume that there is just one ϕ-particle — *albeit*, with the mass *discretely fluctuating* between the two mass extremums *i.e.*, ($-m_0$) and ($+m_0$). That is to say, the ϕ-particle is unstable and its instability is naturally transmitted to the neutrino *via* the ($\phi - \psi$)-coupling. As the unobservable ϕ-particle changes its energy state, it will excite and de-excite the observable neutrino into the energy states of the other two flavours. If the mass only fluctuated between the two mass extremums *i.e.*, ($-m_0$) and ($+m_0$), it would mean the neutrino would fluctuate between two states only, without it returning to its natural state. We know that a neutrino of any type will fluctuate between all the three states. In-order for the neutrino to enter its natural state, there is need for ϕ to enter into a third eigenstate of is mass. Naturally, this must be the eigenstate ($m_0 = 0$). Therefore, the ϕ-particle will discretely fluctuate between the three states ($-m_0, 0, +m_0$) and each of these states corresponds to a particular value of energy which switches the neutrino to the right energy state of a given neutrino state.

5 The neutrino oscillations

How do these oscillations in the particle's state occur in the present model? Just as happens in *quantum gauge transformations* — for an answer to this very important question, we envisage a discrete *gauge-transformation-like* spontaneous and random change in the state of the ϕ-particle occurs in the phase *i.e.*:

$$\phi \longmapsto e^{i\chi_i}\phi, \tag{16}$$

where χ is some continuous and differentiable smooth function of the four position x^μ and or four momentum p^μ. In-order to preserve the composite-state ψ, such a change as that given in equation (16) is to be simultaneously met with a corresponding conjugate change in the phase of the neutrino, *i.e.*:

$$\psi \longmapsto e^{-i\chi_i}\psi, \tag{17}$$

and these two changes, leave the Ψ-state unchanged, *i.e.*:

$$\Psi \longmapsto \left(e^{i\chi_i}\phi\right)\left(e^{-i\chi_i}\psi\right) = \phi\psi = \Psi. \tag{18}$$

We expect that there be three phase changes corresponding to the three mass states ($-m_0, 0, +m_0$), hence three energy states.

The phase change given in equation (16) leads the scalar Dirac equation (9), to transform and become:

$$-\imath\hbar\gamma^\mu\partial_\mu\phi = \left(m_0 + m_j^*\right)c\phi, \tag{19}$$

while the phase change given in equation (17) leads to the Dirac equation (11) for the neutrino, to transform and become:

$$\imath\hbar\gamma^\mu\partial_\mu\psi = \left(m_0 + m_j^*\right)c\psi, \tag{20}$$

where the three-state fluctuating mass m_j^* is such that:

$$m_j^* = \frac{\hbar\gamma^\mu\partial_\mu\chi_i}{c}. \tag{21}$$

In the following subsections, we discuss the possible oscillations of the neutrino for all the three neutrino flavours.

5.1 Oscillations of the Electron-neutrino state

Presented in the self-explanatory diagram in Figure (1) is a graphic visual of the six possible transitions of the natural Electron-neutrino. That is, when the ϕ-particle's mass is zero ($m_0 = 0$), the Electron-neutrino is in its natural state of being an Electron-neutrino. Further, when the mass of the ϕ-particle is negative ($-m_0$), the Electron-neutrino is in enters the μ-neutrino state and likewise, when mass of the ϕ-particle is positive ($+m_0$), Electron-neutrino enters the τ-neutrino state.

5.2 Oscillations of the Muon-neutrino state

Just as in Figure (1), we have in Figure (2) a graphic visual of the four possible transitions of natural Muon-neutrino. When the ϕ-particle's mass is zero ($m_0 = 0$), the Muon-neutrino is in its natural state of being an Muon-neutrino. When the mass of the ϕ-particle is negative ($-m_0$), the Muon-neutrino is in enters the Electron-neutrino state and likewise, when mass of the ϕ-particle is positive ($+m_0$), Muon-neutrino enters the τ-neutrino state.

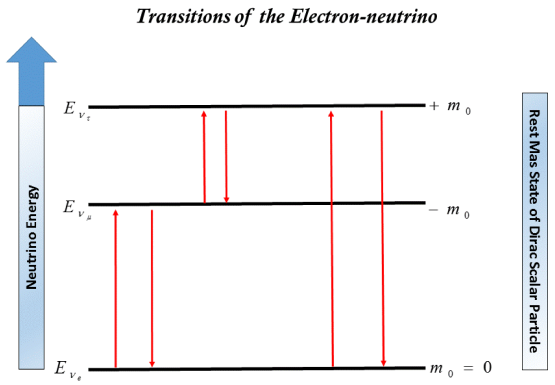

Fig. 1: The six possible transitions of the Electron-neutrino.

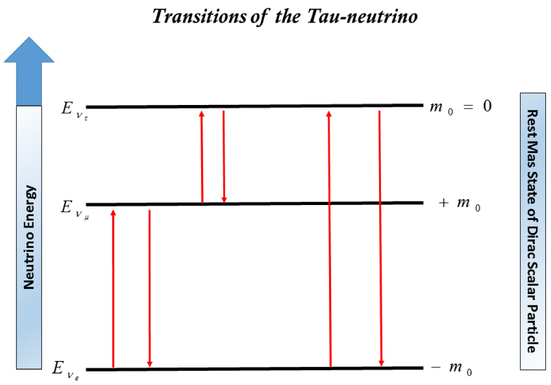

Fig. 3: The six possible transitions of the Tau-neutrino.

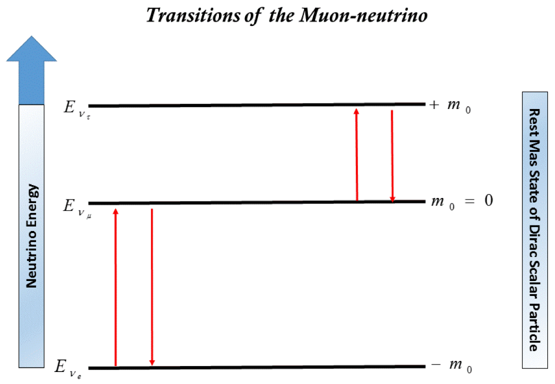

Fig. 2: The four possible transitions of the Muon-neutrino.

5.3 Oscillations of the Tau-neutrino state

Again, just as is the case in the previous cases, Figure (3) is a graphic presentation of the six possible transitions of natural Tau-neutrino. When the ϕ-particle's mass is zero ($m_0 = 0$), the Tau-neutrino is in its natural state of being an Tau-neutrino and when the mass of the ϕ-particle is negative ($-m_0$), the Tau-neutrino enters the Electron-neutrino state and likewise, when mass of the ϕ-particle is positive ($+m_0$), Muon-neutrino enters the μ-neutrino state.

6 General discussion

Clearly, without casting away any of the existing theories (*e.g.*, [17–19]) whose endeavour is to explain the mystery behind the neutrino oscillations, we here have provided an alternative explanation *via* what appears to us to be a mathematically permissible mechanism whereby the massless neutrino is coupled to an unobservable and unstable scalar Dirac point-particle. The resulting mathematics thereof requires that this hypothetical Dirac scalar must be a point-particle. From a physics standpoint, this point-particle nature of the ϕ-scalar implies that this particle can not be observed in nature because it is not an extended particle like the Electron, Proton, Neutrino *etc*. So, we should not expect to observe this particle at all. We can only assign it to be a property of the neutrino particle — with it, being the "*culprit*" behind the observed phenomenon of neutrino oscillation.

Interestingly, within the context of the present model, one can answer the paramount question of whether of not neutrinos are Majorana or Dirac in nature. Majorana neutrinos satisfy the Majorana [20] equation while Dirac neutrinos satisfy the usual massive Dirac equation (11). In the present model, for these neutrinos to be Majorana, the Dirac scalar must be Majorana too, that is to say, the scalar Dirac equation (9), will have to be such that:

$$-\imath\hbar\gamma^\mu\partial_\mu\phi = m_0 c\gamma^2\phi. \tag{22}$$

With equation (22) in place, equation (11) will as a consequence thereof, reduce to the [20] equation, *i.e.*:

$$\imath\hbar\gamma^\mu\partial_\mu\psi = m_0 c\gamma^2\psi, \tag{23}$$

Now, substituting the free particle solution of the ϕ-scalar given in equation (12) into equation (22), just as in equation (13), one obtains the following set of four simulations equations:

$$\left.\begin{array}{lr}(E + \imath m_0c^2) - c(p_x - ip_y) - cp_z = 0 & \dots \quad (a)\\ (E + \imath m_0c^2) - c(p_x + ip_y) + cp_z = 0 & \dots \quad (b)\\ (E - \imath m_0c^2) - c(p_x - ip_y) - cp_z = 0 & \dots \quad (c)\\ (E - \imath m_0c^2) - c(p_x + ip_y) + cp_z = 0 & \dots \quad (d)\end{array}\right\} \tag{24}$$

Adding together equations (24a) and (24b), corresponding to equation (14), one obtains:

$$E = p_xc - \imath m_0c^2, \tag{25}$$

and likewise, adding together equations (24c) and (24d), corresponding to equation (15), one obtains:

$$E = p_xc + \imath m_0c^2. \tag{26}$$

In contrast to the solutions given in equations (14) & (15), these solutions equation (25) & (26), are complex. As a rule of quantum mechanics, energy eigenvalues must be real. What this means is that we must reject these solutions [*i.e.*, equations (25) *&* (26)], and with them, the premise on which they are founded, namely that neutrinos are Majorana. One can try and save the Majorana model by invoking an imaginary mass so that the energy is real, but this will sure not work for so long as mass is a quantum mechanical observable because quantum mechanics will require that the mass be real thus leaving us exactly where we started off *i.e.*, with complex energy states, hence, in-accordance with the present model, neutrinos can not be Majorana, but can only be Dirac in nature.

7 Conclusion

Assuming that what has been presented in the present letter is acceptable, one can put forward the following as the conclusion to be drawn thereof:

1. In addition to the existing theories on neutrino oscillations, the present model is an alternative explanation, where these neutrino oscillations are explained by assuming that the massless neutrino is intrinsically coupled to a hypothetical, massive three-state unstable, invisible, unobservable point-particle which is a Dirac zero-rank scalar. The three-state unstableness of this Dirac scalar is what leads to the observed neutrino oscillations.
2. If complex energy states are physically non-permissible and/or forbidden — be they for the case of observable or non-observable particle(s) — then, according to the present model, neutrinos can not be Majorana in nature as this directly leads to complex energy eigenvalues for the Dirac ϕ-particle. On this basis and this alone, one is to reject this and with it, the idea of Majorana neutrinos.

Acknowledgements

We are grateful for the assistance rendered unto us by the National University of Science and Technology's Research Board toward our research endeavours.

Submitted on March 16, 2018

References

1. Einstein A. Zur Elektrodynamik Bewegter Körper. *Annalen der Physik*, 1905, v. 322(10), 891–921.
2. Agafonova A., Aleksandrov A., Altinok O., Ambrosio M. and et al. Observation of a First ν_τ Candidate Event in the OPERA Experiment in the CNGS Beam. *Physics Letters B*, 2010, v. 691(3), 138–145.
3. Ahmad Q. R., Allen R. C. , Andersen T. C., and et al. Measurement of the Rate of $\nu_e + d \rightarrow p + p + e^-$ Interactions Produced by ^8B Solar Neutrinos at the Sudbury Neutrino Observatory. *Phys. Rev. Lett.*, 2001, v. 87, 071301.
4. An F. P., Bai J. Z., Balantekin A. B., Band H. R., and et al. Observation of Electron-Antineutrino Disappearance at Daya Bay. *Phys. Rev. Lett.*, 2012, v. 108, 171803.
5. Fukuda Y., Hayakawa T., Ichihara E., Inoue K., and et al. Evidence for Oscillation of Atmospheric Neutrinos. *Phys. Rev. Lett.*, 1998, v. 81, 1562–1567.
6. Pontecorvo B. Mesonium and anti-Mesonium. *Zh. Eksp. Teor. Fiz.*, 1957, v. 33(2), 549–551. Reproduced and translated in: Pontecorvo, B. Mesonium and Anti-mesonium. *Sov. Phys. JETP*, 1957, v. 6(2), 429–431.
7. Pontecorvo B. Neutrino Experiments and the Problem of Conservation of Leptonic Charge. *Zh. Eksp. Teor. Fiz.*, 1968, v. 53, 1717–1725. Reproduced and translated in: Pontecorvo, B. Neutrino Experiments and the Problem of Conservation of Leptonic Charge. *Sov. Phys. JETP*, 1968, v. 26, 984–988.
8. Davis R., Harmer D. S. and Hoffman K. C. Search for Neutrinos from the Sun. *Phys. Rev. Lett.*, 1968, v. 20, 1205–1209.
9. Murayama H. The Origin of Neutrino Mass. *Physics World (Magazine)*, 2002, May Issue, 35–39.
10. Englert F. and Brout R. Broken Symmetry and the Mass of Gauge Vector Mesons. *Phys. Rev. Lett.*, 1964, v. 13, 321–323.
11. Guralnik G. S., Hagen, C. R. and Kibble T. W. B. Global Conservation Laws and Massless Particles. *Phys. Rev. Lett.*, 1964, v. 13, 585–587.
12. Higgs P. W. Broken Symmetries and the Masses of Gauge Bosons. *Phys. Rev. Lett.*, 1964, v. 13, 508–509.
13. Weyl H. K. H. Gravitation and the Electron. *Proceedings of the National Academy of Sciences*, 1929, v. 15(4), 323–334.
14. Nyambuya G. G. Concerning the Dirac γ-Matrices Under a Lorentz Transformation of the Dirac Equation. *Progress in Physics*, 2018, v. 14, 90–93.
15. Dirac P. A. M. The Quantum Theory of the Electron. *Proc. Roy. Soc. (London)*, 1928, v. A117, 610–612.
16. Dirac P. A. M. The Quantum Theory of the Electron II. *Proc. Roy. Soc. (London)*, 1928, v. A118, 351–361.
17. Weinheimer C. and Zuber K. Neutrino Masses. *Annalen der Physik*, 2013, v. 525(8-9), 565–575.
18. Amsler C., Doser M., Antonelli M., Asner D. M. and et al. Review of Particle Physics. *Physics Letters B*, 2008, v. 667(1), 1–6.
19. Eidelman S., Hayes K. G., Olive K. A., Aguilar-Benitez M., and et al. Review of Particle Physics. *Physics Letters B*, 2004, v. 592(1), 1–5.
20. Majorana E. Theory of the Symmetry of Electrons and Positrons. *Nuovo Cimento*, 1937, v. 5, 171–184.

Global Scaling of Planetary Systems

Hartmut Müller

E-mail: hm@interscalar.com

The paper introduces a scale-invariant model of matter as fractal chain system of oscillating protons and electrons that is applied to the analysis of the solar system and extrasolar planetary systems. Based on global scaling, an explanation of the large number of coincident metric characteristics in different planetary and moon systems is proposed.

Introduction

The formation and evolution of the solar system is caused by very different processes and it is a complex field of research that considers electromagnetic, thermodynamic, hydrodynamic, nuclear physical and chemical factors in their complex interaction. Advanced models were developed [1–5] in the last century which explain essential features of the solar system formation. Gravity is treated as dominant force at macroscopic scales that forms the shape and trajectory (orbit) of astronomical bodies including stars and galaxies. Indeed, if numerous bodies are gravitationally bound to one another, classic models predict long-term highly unstable states that contradict with the astrophysical reality in the solar system.

Furthermore, many metric characteristics of the solar system are not predicted in standard models. A remarkably large number of coincidences are considered to be casual and are not even topics of theoretical research. For example, Mars and Mercury, but also Uranus and Venus have the same surface gravity acceleration. Such dissimilar bodies like Jupiter and Ceres, but also Earth, Mars and Eris have similar rotation periods. Various moons of very different planets in the solar system have the same orbital periods as have various planets in different extrasolar systems like Trappist 1 or Kepler 20.

In this paper we apply our scale-invariant model [6–8] of matter as fractal chain system of oscillating protons and electrons to the analysis of the solar system and extrasolar planetary systems. Based on our hypothesis of global scaling we propose an explanation of the large number of coincidences of the metric characteristics of the systems.

Methods

As result of measurement, real numbers build the bridge that connects theoretical models with the physical reality [9]. The classification of real numbers, in particular the difference between rational and irrational numbers is not only a mathematical task. It is also an essential aspect of stability in real systems. Parameter relations corresponding to rational numbers of small quotients support resonance interactions inside the system and make the system unstable. On the contrary, irrational relations correspond to minimum resonance interaction inside the system and to its stability [10].

Indeed, this stability can be lasting only if a given irrational relation cannot be transformed into a rational by elementary arithmetic operations. In the case of algebraic numbers, an irrational relation of wavelengths can lead to rational relations of surfaces, volumes, masses or energies and nevertheless can make the system unstable.

Transcendental numbers cannot be represented as roots of algebraic equations. Therefore, no elementary arithmetic operation like addition or multiplication can transform a transcendental number into a rational. This is not valid for irrational, but non transcendental numbers, including the so-called golden number $\phi = (\sqrt{5}+1)/2$.

It is remarkable that only continued fractions deliver biunique representations of all real numbers, rational and irrational. Finite continued fractions represent always rational numbers, whereas infinite continued fractions represent irrational numbers. That is why any irrational number can be approximated by finite continued fractions - the convergents which deliver always the best and quickest approximation [11]. It is notable that the best rational approximation of an irrational number by a finite continued fraction is not a task of computation, but only an act of termination of the fractal recursion.

Alas, transcendental numbers can be approximated exceptionally well by rational numbers, because their continued fractions contain large denominators and can be truncated with minimum loss of precision. For instance, the fourth denominator in the simple continued fraction of π = [3; 7, 15, 1, 292, ...] = 3.1415927... is quite big, so that the ratio 355/113 ≈ 3.1415929 delivers a very good approximation. Euler's number e = 2.71828... is also transcendental and can be represented as continued fraction with quickly increasing denominators, so that already the ratio 193/71 ≈ 2.71831 gives a good approximation.

In the consequence, transcendental numbers define the preferred relations of parameters which sustain the stability of a complex system. In this way, the system avoids destabilizing resonance. At the same time, a good rational approximation can be induced quickly, if resonance interaction is required. Furthermore, if stability is provided concerning all derivatives of a process, Euler's number is the only choice, because of the self-similarity of the natural exponential function regarding its derivatives:

$$\frac{d}{dx} e^x = e^x.$$

Property	Electron	Proton
rest mass m	$9.10938356(11) \cdot 10^{-31}$ kg	$1.672621898(21) \cdot 10^{-27}$ kg
energy $\mathrm{E} = \mathrm{m}c^2$	0.5109989461(31) MeV	938.2720813(58) MeV
angular frequency $\omega = \mathrm{E}/\hbar$	$7.76344071 \cdot 10^{20}$ Hz	$1.42548624 \cdot 10^{24}$ Hz
angular oscillation period $\tau = 1/\omega$	$1.28808867 \cdot 10^{-21}$ s	$7.01515 \cdot 10^{-25}$ s
angular wavelength $\lambda = c/\omega$	$3.8615926764(18) \cdot 10^{-13}$ m	$2.1030891 \cdot 10^{-16}$ m
angular acceleration $a = c/\omega$	$2.327421 \cdot 10^{29}$ ms^{-2}	$4.2735 \cdot 10^{32}$ ms^{-2}

Table 1: The basic set of physical properties of the electron and proton. (c is the speed of light in a vacuum, $\hbar$ is the reduced Planck constant, k_B is the Boltzmann constant). Data taken from Particle Data Group [20]. Frequencies, oscillation periods, accelerations and the proton wavelength are calculated.

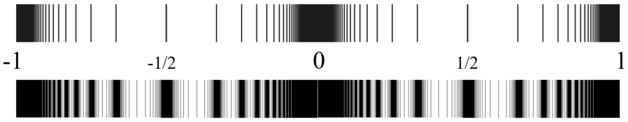

Fig. 1: The distribution of eigenvalues of $\mathcal{F}$ for $k = 1$ (above) and for $k = 2$ (below) in the range $-1 \leqslant \mathcal{F} \leqslant 1$.

In [12] we have shown that the set of natural frequencies (eigenstates) of a fractal chain system of harmonic oscillators can be described as set (1) of finite continued fractions $\mathcal{F}$, which are natural logarithms:

$$\mathcal{F} = \ln(\omega_{jk}/\omega_{00}) = [n_{j0}; n_{j1}, n_{j2}, \ldots, n_{jk}] \qquad (1)$$

where ω_{jk} is the set of angular frequencies and ω_{00} is the fundamental frequency of the set. The denominators are integer: $n_{j0}, n_{j1}, n_{j2}, \ldots, n_{jk} \in \mathrm{Z}$, the cardinality $j \in \mathrm{N}$ of the set and the number $k \in \mathrm{N}$ of layers are finite. In the canonical form, all numerators equal 1.

Any finite continued fraction represents a rational number. Therefore, all frequency ratios ω_{jk}/ω_{00} in (1) are irrational, because for rational exponents the natural exponential function is transcendental [13]. This circumstance provides for high stability of the eigenstates (1) of a chain system of harmonic oscillators because it prevents resonance interaction between the elements of the system. In [14–16] we have applied continued fractions of the type (1) as criterion of stability in engineering.

In the canonical form, the distribution density of eigenvalues of finite continued fractions reaches maxima near reciprocal integers 1, 1/2, 1/3, 1/4, … which are the attractor points in the fractal set $\mathcal{F}$ of natural logarithms (fig. 1).

Shorter continued fractions (1) with smaller denominators correspond with more stable eigenstates of the chain system, because the logarithmic distance between their eigenvalues is maximum. Considering the existence of two complementary fractals on the sets of rational and irrational numbers accordingly [17], the probability that small variations (fluctuations) lead to coincidences between irrational and rational numbers of small quotients is minimum. Therefore, integer and half logarithms represent the most stable eigenstates.

Already in 1950 Gantmacher and Krein [18] have demonstrated that continued fractions are solutions of the Euler-Lagrange equation for low amplitude harmonic oscillations in simple chain systems. Terskich [19] generalized this method for the analysis of oscillations in branched chain systems. In [6] the continued fraction method was extended to the analysis of chain systems of harmonic quantum oscillators.

In the case of harmonic quantum oscillators, the continued fractions (1) define not only fractal sets of natural angular frequencies ω_{jk}, angular accelerations $a_{jk} = c \cdot \omega_{jk}$, oscillation periods $\tau_{jk} = 1/\omega_{jk}$ and wavelengths $\lambda_{jk} = c/\omega_{jk}$ of the chain system, but also fractal sets of energies $\mathrm{E}_{jk} = \hbar \cdot \omega_{jk}$ and masses $\mathrm{m}_{jk} = \mathrm{E}_{jk}/c^2$ which correspond with the eigenstates of the system [8].

In this way, the continued fractions (1) generate the fundamental fractal $\mathcal{F}$ of eigenstates in chain systems of harmonic quantum oscillators.

As the cardinality and number of layers of the continued fractions (1) are finite but not limited, in each point of the space-time occupied by the chain system of harmonic quantum oscillators the scalar $\mathcal{F}$ is defined. Therefore, any chain system of harmonic quantum oscillators can be seen as source of the fractal scalar field $\mathcal{F}$, the fundamental field of the system. The scalar potential difference $\Delta\mathcal{F}$ of sequent equipotential surfaces at a given layer k is defined by the difference of continued fractions (1). In the canonical form:

$$\Delta\mathcal{F} = \mathcal{F}(\mathrm{j,k}) - \mathcal{F}(\mathrm{j+1,k}) =$$
$$= [n_{j0}; n_{j1}, n_{j2}, \ldots, n_{jk}] - [n_{j0}; n_{j1}, n_{j2}, \ldots, n_{j+1,k}].$$

In [7] we have introduced a scale-invariant model of matter as fractal chain system of harmonically oscillating protons and electrons that generates the fundamental field $\mathcal{F}$. Normal matter is formed by nucleons and electrons because they are exceptionally stable quantum oscillators. In the concept of isospin, proton and neutron are viewed as two states of the same quantum oscillator. Furthermore, they have similar rest masses. However, a free neutron decays into a proton, an electron and antineutrino within 15 minutes while the lifespans of the proton and electron top everything that is measurable, exceeding 10^{29} years [20].

The exceptional stability of electron and proton predestinate their physical characteristics as fundamental units. Table 1 shows the basic set of electron and proton units that can be considered as a fundamental metrology. In [8] was shown that it is compatible with Planck units [21].

Within our model, the proton-to-electron ratio (tab. 1) is caused by the fundamental field $\mathcal{F}$. In fact, the natural logarithm is close to rational:

$$\ln \frac{938.2720813 \text{ MeV}}{0.5109989461 \text{ MeV}} \approx 7 + \frac{1}{2}.$$

As a consequence, the fundamental field of the proton is complementary to that of the electron, because integer logarithms of the proton $\mathcal{F}$ correspond to half logarithms of the electron $\mathcal{F}$ and vice versa, so that the scaling factor $\sqrt{e}$ connects similar equipotential surfaces of the proton field with those of the electron field in alternating sequence [8].

We hypothesize that scale invariance of the fundamental field $\mathcal{F}$ calibrated on the physical properties of the proton and electron (tab. 1) is a universal characteristic of organized matter and criterion of stability. This hypothesis we have called Global Scaling [22].

Results

Within our scale-invariant model of matter [7], atoms and molecules emerge as eigenstates of stability in fractal chain systems of harmonically oscillating protons and electrons.

Andreas Ries [23] demonstrated that this model allows for the prediction of the most abundant isotope of a given chemical element. From this point of view, any physical body, being solid, liquid or gas can be seen as fractal chain system of oscillating molecules, atoms, ions, protons and electrons that follows the fundamental field $\mathcal{F}$.

Therefore, in the framework of our fractal model of matter, the fundamental field $\mathcal{F}$ affects any type of physical interaction, regardless of its complexity.

In [24] we applied our model to the analysis of gravimetric and seismic characteristics of the Earth and could show that our estimations [25] correspond well with established empiric models of the Earth interior.

In [26] we did demonstrate that the vertical sequence of stable atmospheric layers corresponds with the sequence of main spatial equipotential surfaces of the fundamental field $\mathcal{F}$, not only at Earth, but also at Venus, Mars and Titan.

In [27] was demonstrated that the mass distribution in the solar system and the mass distribution of elementary particles follow the same scaling law. In [8] was shown that the distribution of rotation and orbital periods in the solar system corresponds with main temporal equipotential surfaces of the fundamental field $\mathcal{F}$.

For verification of Global Scaling in this paper we consider only direct measurements and refer on data that should not contain systematic errors. As such data we consider the rotation and orbital periods, but also the majority of estimated body radii and orbital distances in the solar system.

Fig. 2 shows the correspondence of orbital periods for planets and planetoids of the solar system with equipotential surfaces of the fundamental field $\mathcal{F}$. Tab. 2 contains the corresponding data. Integer numbers in the bottom of the graphic are natural logarithms of main equipotential surfaces $[n_0; \infty]$ of the fundamental field $\mathcal{F}$ calibrated on the proton (bold) and electron (thin). For example, Jupiter's orbital period [28] corresponds with the main temporal equipotential surface $[66; \infty]$ of the fundamental field $\mathcal{F}$ calibrated on the oscillation period of the electron:

$$\ln \left(\frac{T_{\text{Jupiter}}}{\tau_{\text{electron}}} \right) = \ln \left(\frac{4332.59 \cdot 86400 \text{ s}}{2\pi \cdot 1.28808867 \cdot 10^{-21} \text{ s}} \right) = 66.00$$

The logarithmic scale in fig. 2 covers a range of 79 to 235000 days ≈ 640 years.

Fig. 3 shows the correspondence of orbital periods for moons of the solar system and planets of the systems Trappist 1 [29] and Kepler 20 [30] with temporal equipotential surfaces of the fundamental field $\mathcal{F}$. Tab. 3 and 4 contain the corresponding data. It is remarkable that the orbits of Trappist 1b, c, d and e correspond with main equipotential surfaces of the fundamental field $\mathcal{F}$. This is also valid for Kepler 20b, c, d and e and for many other exoplanetary systems we did not include in this paper.

Because of the complementarity of the fundamental field of the proton to that of the electron, equipotential surfaces of the type $[n_{j0}; \pm 2]$ coincide always with complementary

body	**orbital period T, d**	**ln $(T/2\pi\,\tau_e)$**	$\mathcal{F}$
Eris (P)	203830	69.86	[70; -6]
Pluto (P)	90560	69.04	[69; ∞]
Neptune	60182	68.64	[69; -3]
Uranus	30688.5	67.96	[68; ∞]
Saturn	10759.22	66.91	[67; ∞]
Jupiter	4332.59	66.00	[66; ∞]
Ceres (P)	1681.63	65.06	[65; ∞]
Mars	686.971	64.16	[64; 6]
Earth	365.256363	63.53	[63; 2]
Venus	224.701	63.04	[65; ∞]
Mercury	87.9691	62.12	[62; 6]

Table 2: Natural logarithms of the orbital period-to-electron oscillation period ratios for planets and heaviest planetoids (P) of the solar system and the corresponding equipotential surfaces of the fundamental field $\mathcal{F}$. Data: [28]

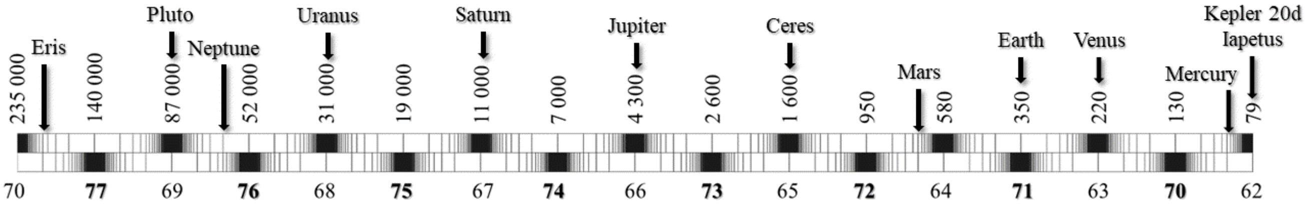

Fig. 2: Correspondence of orbital periods of planets and planetoids of the solar system with temporal equipotential surfaces of the fundamental field $\mathcal{F}$. Integers in the bottom of the graphic are natural logarithms of main equipotential surfaces $[n_{j0}; \infty]$ of the fundamental field $\mathcal{F}$ calibrated on the proton (bold) and electron (thin). The logarithmic scale covers a range of 79 to 235 000 days ≈ 640 years. Tab. 2 contains the corresponding data.

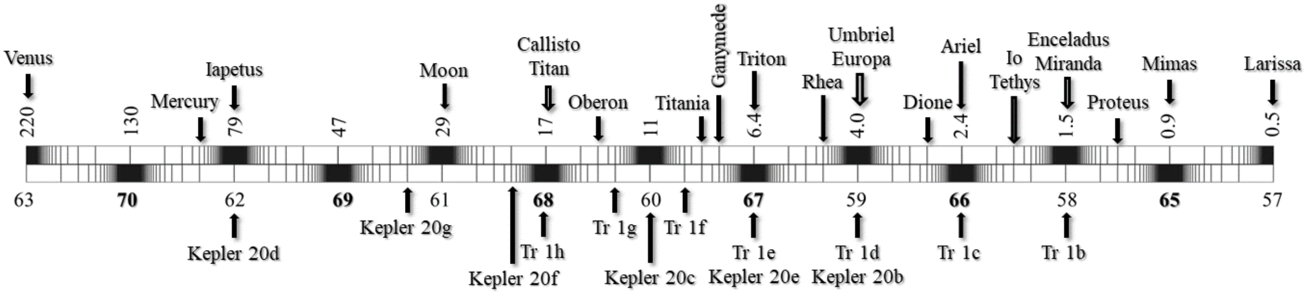

Fig. 3: Correspondence of orbital periods of moons of the solar system and planets of the systems Trappist 1 and Kepler 20 with temporal equipotential surfaces of the fundamental field $\mathcal{F}$. The logarithmic scale covers a range of 0.5 to 220 days. Tab. 3 and 4 contain the corresponding data.

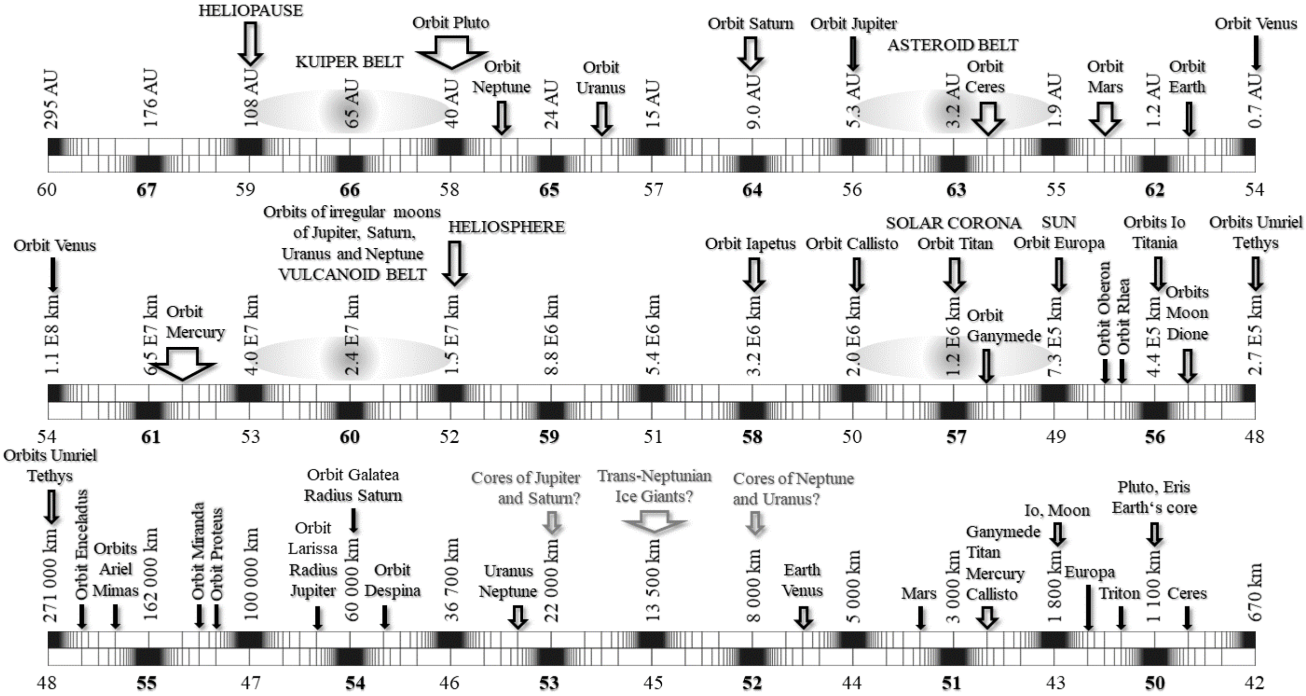

Fig. 4: Correspondence of metric characteristics of large structures in the solar system with spatial equipotential surfaces of the fundamental field $\mathcal{F}$. The logarithmic scale covers a range of 670 km to 295 AU. The width of the arrows is a measure of data dispersion or eccentricity of an orbit. Grey arrows and descriptions are hypothetical. The corresponding data are published in [8, 25].

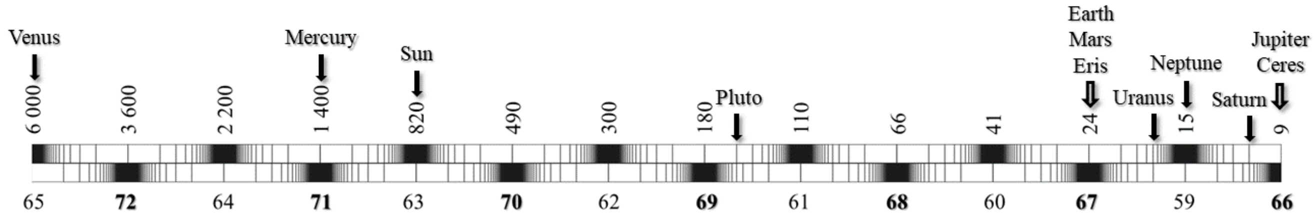

Fig. 5: Correspondence of rotation periods of planets and some planetoids of the solar system with temporal equipotential surfaces of the fundamental field $\mathcal{F}$. The logarithmic scale covers a range of 9 to 6000 hours. Tab. 5 contains the corresponding data.

main equipotential surfaces $[n_{j0}; \infty]$, so that the remaining orbits correspond mostly with equipotential surfaces of the type $[n_{j0}; \pm 3]$. This distribution is a consequence of the fractal hierarchy 1/2, 1/3, 1/4, ... of stability layers (see fig. 1) given by the continued fraction (1) of natural logarithms.

Fig. 4 shows the correspondence of metric characteristics of large structures in the solar system with spatial equipotential surfaces of the fundamental field $\mathcal{F}$. The corresponding data are published in [8, 25]. For example, the visible equatorial radius of Saturn [32] corresponds with the main spatial equipotential surface $[54; \infty]$ of the fundamental field $\mathcal{F}$ calibrated on the wavelength of the proton (tab. 1):

$$\ln\left(\frac{r_{\text{Saturn}}}{\lambda_{\text{proton}}}\right) = \ln\left(\frac{6.0268 \cdot 10^{7}\ \text{m}}{2.1030891 \cdot 10^{-16}\ \text{m}}\right) = 54.01$$

The logarithmic scale in fig. 4 covers a range of 670 km to 295 AU. In general, the width of the arrows is a measure of data dispersion or eccentricity of an orbit. Grey arrows and descriptions are hypothetical.

Fig. 4 shows that the orbits of Venus, Jupiter, Saturn and Pluto correspond with main equipotential surfaces $[n_{j0}; \infty]$ of the fundamental field $\mathcal{F}$.

It is notable that Jupiter's orbit represents the logarithmic mean between the orbits of Venus and Pluto. The orbits of

moon of	**orbital period T, d**	**$\ln (T/2\pi \tau_e)$**	$\mathcal{F}$
EARTH			
Moon	27.321661	60.94	[61; ∞]
JUPITER			
Callisto	16.689	60.45	[60; 2]
Ganymede	7.1546	59.61	[60; -3]
Europa	3.5512	58.91	[60; ∞]
Io	1.7691	58.21	[58; 4]
SATURN			
Iapetus	79.3215	62.00	[62; ∞]
Titan	15.945	60.41	[60; 2]
Rhea	4.5182	59.14	[59; 6]
Dione	2.7369	58.65	[59; -3]
Tethys	1.8878	58.26	[58; 4]
Enceladus	1.3702	57.95	[58; ∞]
Mimas	0.942	57.57	[57; 2]
URANUS			
Oberon	13.4632	60.24	[60; 4]
Titania	8.7062	59.78	[60; -4]
Umbriel	4.144	59.05	[59; ∞]
Ariel	2.52	58.54	[58; 2]
Miranda	1.4135	57.98	[58; ∞]
NEPTUNE			
Nereid	360.1362	63.52	[63; 2]
Triton	5.877	59.41	[59; 2]
Proteus	1.1223	57.75	[58; -4]
Larissa	0.555	57.04	[57; ∞]

Table 3: Natural logarithms of the orbital period-to-electron oscillation period ratios for the largest moons of in the solar system and the corresponding equipotential surfaces of the fundamental field $\mathcal{F}$. Data: [31]

planet of	**orbital period T, d**	**$\ln (T/2\pi \tau_e)$**	$\mathcal{F}$
TRAPPIST 1			
H	18.767953	60.56	[60; 2]
G	12.354473	60.15	[60; 6]
F	9.205585	59.86	[60; ∞]
E	6.099615	59.45	[59; 2]
D	4.04961	59.03	[59; ∞]
C	2.4218233	58.51	[58; 2]
B	1.51087081	58.04	[58; ∞]
KEPLER 20			
D	77.61130017	61.98	[62; ∞]
G	34.94	61.17	[61; 6]
F	19.57758478	60.61	[61; -3]
C	10.85409089	60.01	[60; ∞]
E	6.09852281	59.45	[59; 2]
B	3.69611525	58.94	[59; ∞]

Table 4: Natural logarithms of the orbital period-to-electron oscillation period ratios for exoplanets of the systems Trappist 1 and Kepler 20 with the corresponding equipotential surfaces of the fundamental field $\mathcal{F}$. Data: [29, 30]

body	**rotation period τ, h**	**ln (τ/τ_p)**	$\mathcal{F}$
Venus	5816.66728	72.48	[72; 2]
Mercury	1407.5	71.05	[71; ∞]
Sun	823.346	70.51	[70; 2]
Pluto (P)	152.87496	68.83	[69; -6]
Eris (P)	25.9	67.06	[67; ∞]
Mars	24.62278	67.01	[67; ∞]
Earth	23.93444	66.98	[67; ∞]
Uranus	17.24	66.66	[67; -3]
Neptune	16.11	66.57	[66; 2]
Saturn	10.55	66.16	[66; 6]
Jupiter	9.925	66.09	[66; ∞]
Ceres (P)	9.07417	66.01	[66; ∞]

Table 5: Natural logarithms of the rotation period-to-proton oscillation period ratios for planets and heaviest planetoids (P) of the solar system and the corresponding equipotential surfaces of the fundamental field $\mathcal{F}$. Data: [28].

Mercury, Earth, Mars, Ceres correspond all with equipotential surfaces of the type $[n_{j0}; \pm 3]$. This is valid also for the orbits of Ganymede, Rhea, Dione and the Moon. The orbits of Uranus and Neptune correspond with equipotential surfaces $[n_{j0}; \pm 4]$.

The orbits of Callisto, Europa, Io and Titan correspond with main equipotential surfaces $[n_{j0}; \infty]$. This is also valid for the orbits of Tethys, Umbriel, Titania and Iapetus.

The radius of the photosphere of the Sun and the visible radius of Saturn correspond with main spatial equipotential surfaces $[n_{j0}; \infty]$.

The visible radii of Jupiter, Uranus and Neptune, but also the radii of the solid bodies Mars, Mercury, Ganymede, Titan, Callisto, Europa and Ceres correspond all with equipotential surfaces of the type $[n_{j0}; \pm 3]$. Only the radii of Earth and Venus correspond with equipotential surfaces $[n_{j0}; \pm 4]$. The radii of Io, the Moon, Pluto and Eris correspond with main equipotential surfaces $[n_{j0}; \infty]$.

It is remarkable that the orbit of Europa coincides with the radius of the Sun (boundary of the photosphere), the orbit of Galatea (Neptune VI) coincides with Saturn's radius (stratopause) and the orbit of Larissa (Neptune VII) with the radius of Jupiter.

Fig. 5 shows the correspondence of rotation periods of planets and large planetoids of the solar system with temporal equipotential surfaces of the fundamental field $\mathcal{F}$. The logarithmic scale in fig. 5 covers a range of 9 to 6000 hours. Tab. 5 contains the corresponding data.

The rotation periods of Venus, Mercury, the Sun, Earth, Mars, Eris, Neptune, Jupiter and Ceres coincide with main equipotential surfaces while the rotation periods of Saturn, Uranus and Pluto correspond with temporal equipotential surfaces of the type $[n_{j0}; \pm 3]$.

Although the rotation of Venus [31] is retrograde, its rotation period of 5816.66728 hours fits perfectly with the main temporal equipotential surface $[65; \infty]$ of the electron $\mathcal{F}$:

$$\ln\left(\frac{\tau_{\text{Venus}}}{\tau_{\text{electron}}}\right) = \ln\left(\frac{5816.66728 \cdot 3600 \text{ s}}{1.28808867 \cdot 10^{-21} \text{ s}}\right) = 64.96$$

Concluding our analysis of the solar system and exoplanetary systems we assume that planetary systems preferentially occupy main equipotential surfaces of the fundamental field $\mathcal{F}$. This circumstance makes possible the calculation of remaining orbits in exoplanetary systems.

Conclusion

The logarithmic projection of the fundamental field $\mathcal{F}$ reveals the remarkable scale symmetry of the solar system and suggests that it could hardly be the consequence of random collisions. Within our cosmological hypothesis of Global Scaling [8], the formation of the solar system as well as exoplanetary systems can be understood in terms of harmonic oscillations in chain systems.

Movement along equipotential surfaces requires no work. That's why stable orbits correspond with equipotential surfaces of the fundamental field $\mathcal{F}$ and orbital eccentricity is always limited by neighboring equipotential surfaces [8].

Equipotential surfaces of the fundamental field $\mathcal{F}$ define not only stable planetary orbits, but also the metric characteristics of stratification layers in planetary atmospheres [26] and lithospheres [25]. From this point of view, metric characteristics of stable structures origin from the same fundamental field $\mathcal{F}$ and different only in scale.

The conceptual core of our model are harmonic oscillations in chain systems. These oscillations remain stable only if resonance interaction inside the system can be avoided. As solution survives a logarithmically fractal set (1) of transcendental frequency ratios. Note it is not a simple power law.

We suppose that basic power rules like the Titius-Bode [33], Dermott's rule [34] as well as the discovered golden number [35] and Fibonacci ratios [36] in solar planetary and satellite systems and in exoplanetary systems reflect a local feature of the fundamental field $\mathcal{F}$, because $\sqrt{e} = 1{,}648...$ is close to the golden number $\phi = 1.618...$ and for small exponents, the rounded up powers of the square root of Euler's number deliver the sequence of Fibonacci numbers.

Another essential aspect of our cosmological model [8] is Global Scaling, the hypothesis that in the universe there is only one global fundamental field $\mathcal{F}$. In fact, it was demonstrated that scale relations in particle physics [6, 7, 37] and nuclear physics [23, 38, 39], astrophysics [8, 27, 40–43], geophysics [25, 26] and biophysics [44, 45] follow always the same fundamental field $\mathcal{F}$ calibrated on the proton and electron, without any additional or particular settings. The universality and unity of the fundamental field $\mathcal{F}$ might signify that everything in the universe is part of one giant oscillating chain system.

Acknowledgements

The author is thankful to Oleg Kalinin, Alexej Petrukhin, Viktor Panchelyuga and Erwin Müller for valuable discussions and to Leili Khosravi for permanent support on all stages of the study.

Submitted on March 27, 2018

References

1. Williams I. O., Cremin A.W. A survey of theories relating to the origin of the solar system. *Qtly. Rev. RAS*, 1968, v. 9, 40–62.
2. Alfven H. Band Structure of the Solar System. Dermot S.F. Origin of the Solar System. pp. 41–48. Wiley, (1978).
3. Woolfson M.M. The Solar System: Its Origin and Evolution. *Journal of the Royal Astronomical Society*, 1993, v. 34, 1–20.
4. Van Flandern T. Our Original Solar System - a 21st Century Perspective. MetaRes. Bull. 17: 2–26, (2008). D21, 475–491, 2000.
5. Woolfson M. M. Planet formation and the evolution of the Solar System. arXiv:1709.07294, (2017).
6. Müller H. Fractal Scaling Models of Natural Oscillations in Chain Systems and the Mass Distribution of Particles. *Progress in Physics*, 2010, no. 3, 61–66.
7. Müller H. Emergence of Particle Masses in Fractal Scaling Models of Matter. *Progress in Physics*, 2012, v. 4, 44–47.
8. Müller H. Scale-Invariant Models of Natural Oscillations in Chain Systems and their Cosmological Significance. *Progress in Physics*, 2017, no. 4, 187–197.
9. International Vocabulary of Metrology – Basic and General Concepts and Associated Terms. International Bureau of Weights and Measures, 2008, p. 16.
10. Dombrowski K. Rational Numbers Distribution and Resonance. *Progress in Physics*, 2005, no. 1, 65–67.
11. Khintchine A.Ya. Continued fractions. University of Chicago Press, Chicago, 1964.
12. Müller H. Fractal Scaling Models of Resonant Oscillations in Chain Systems of Harmonic Oscillators. *Progress in Physics*, 2009, no. 2, 72–76.
13. Hilbert D. Über die Transcendenz der Zahlen e und π. *Mathematische Annalen*, 1893, v. 43, 216–219.
14. Müller H. The general theory of stability and objective evolutionary trends of technology. Applications of developmental and construction laws of technology in CAD. Volgograd, VPI, 1987 (in Russian).
15. Müller H. Superstability as a developmental law of technology. Technology laws and their Applications. Volgograd-Sofia, 1989.
16. Müller H., Otte R. Verfahren zur Stabilisierung von technischen Prozessen. PCT, WO 2005/071504 A2.
17. Panchelyuga V. A., Panchelyuga M. S. Resonance and Fractals on the Real Numbers Set. *Progress in Physics*, 2012, no. 4, 48–53.
18. Gantmacher F.R., Krein M.G. Oscillation matrixes, oscillation cores and low oscillations of mechanical systems. Leningrad, 1950.
19. Terskich V.P. The continued fraction method. Leningrad, 1955.
20. Olive K.A. et al. (Particle Data Group), *Chin. Phys. C*, 2016, v. 38, 090001. Patrignani C. et al. (Particle Data Group), *Chin. Phys. C*, 2016, v. 40, 100001.
21. Planck M. Über Irreversible Strahlungsvorgänge. *Sitzungsberichte der Königlich Preußischen Akademie der Wissenschaften*, 1899, v. 1, 479–480.
22. Müller H. Scaling as Fundamental Property of Natural Oscillations and the Fractal Structure of Space-Time. Foundations of Physics and Geometry. Peoples Friendship University of Russia, 2008 (in Russian).
23. Ries A. Qualitative Prediction of Isotope Abundances with the Bipolar Model of Oscillations in a Chain System. *Progress in Physics*, 2015, v. 11, 183–186.
24. Müller H. Gravity as Attractor Effect of Stability Nodes in Chain Systems of Harmonic Quantum Oscillators. *Progress in Physics*, 2018, v. 14, 19–23.
25. Müller H. Quantum Gravity Aspects of Global Scaling and the Seismic Profile of the Earth. *Progress in Physics*, 2018, v. 14, 41–45.
26. Müller H. Global Scaling of Planetary Atmospheres. *Progress in Physics*, 2018, v. 14, 66–70.
27. Müller H. Fractal scaling models of natural oscillations in chain systems and the mass distribution of the celestial bodies in the Solar System. *Progress in Physics*, 2010, no. 4, 44–47.
28. Jupiter Fact Sheet. nssdc.gsfc.nasa.gov
29. Gillon M. et al. Seven temperate terrestrial planets around the nearby ultracool dwarf star TRAPPIST-1. Nature, 2017, 21360.
30. Hand E. Kepler discovers first Earth-sized exoplanets. Nature, 2011, 9688.
31. Venus Fact Sheet. nssdc.gsfc.nasa.gov
32. Saturn Fact Sheet. nssdc.gsfc.nasa.gov
33. Hayes W. Fitting random stable solar systems to Titius-Bode laws. arXiv: astro-ph/9710116v1 10 Oct 1997.
34. Dermott S.F. On the origin of commensurabilities in the solar system - II: The orbital period relation. *Mon. Not. R. Astron. Soc.*, 1968, v. 141(3), 363–376.
35. Butusov K. P. The Golden Ratio in the Solar System. Problems of Cosmological Research, v. 7, Moscow – Leningrad, 1978 (in Russian).
36. Pletser V. Orbital Period Ratios and Fibonacci Numbers in Solar Planetary and Satellite Systems and in Exoplanetary Systems. arXiv:1803.02828 [physics.pop-ph], 2018.
37. Ries A., Fook M. Fractal Structure of Nature's Preferred Masses: Application of the Model of Oscillations in a Chain System. *Progress in Physics*, 2010, no. 4, 82–89.
38. Ries A. A Bipolar Model of Oscillations in a Chain System for Elementary Particle Masses. *Progress in Physics*, 2012, no. 4, 20–28.
39. Ries A. The Radial Electron Density in the Hydrogen Atom and the Model of Oscillations in a Chain System. *Progress in Physics*, 2012, no. 3, 29–34.
40. Müller H. Scaling of Body Masses and Orbital Periods in the Solar System. *Progress in Physics*, 2015, no. 2, 133–135.
41. Müller H. Scaling of Moon Masses and Orbital Periods in the Systems of Saturn, Jupiter and Uranus. *Progress in Physics*, 2015, no. 2, 165–166.
42. Müller H. Scaling of body masses and orbital periods in the Solar System as consequence of gravity interaction elasticity. Abstracts of the XII. International Conference on Gravitation, Astrophysics and Cosmology, dedicated to the centenary of Einstein's General Relativity theory. Moscow, PFUR, 2015.
43. Müller H. Global Scaling as Heuristic Model for Search of Additional Planets in the Solar System. *Progress in Physics*, 2017, no. 4, 204–206.
44. Müller H. Chain Systems of Harmonic Quantum Oscillators as a Fractal Model of Matter and Global Scaling in Biophysics. *Progress in Physics*, 2017, no. 4, 231–233.
45. Müller H. Astrobiological Aspects of Global Scaling. *Progress in Physics*, 2018, v. 14, 3–6.

The Journal on Advanced Studies in Theoretical and Experimental Physics, including Related Themes from Mathematics

PROGRESS IN PHYSICS

A quarterly issue scientific journal, registered with the Library of Congress (DC, USA). This journal is peer reviewed and included in the abstracting and indexing coverage of: Mathematical Reviews and MathSciNet (AMS, USA), DOAJ of Lund University (Sweden), Scientific Commons of the University of St. Gallen (Switzerland), Open-J-Gate (India), Referativnyi Zhurnal VINITI (Russia), etc.

Electronic version of this journal:
http://www.ptep-online.com

Postal Address

Department of Mathematics and Science,
University of New Mexico,
705 Gurley Ave., Gallup, NM 87301, USA

This journal is powered by LaTeX

A variety of books can be downloaded free from the Digital Library of Science:
http://fs.gallup.unm.edu/ScienceLibrary.htm

ISSN: 1555-5534 (print)
ISSN: 1555-5615 (online)

Standard Address Number: 297-5092
Printed in the United States of America

July 2018 **Vol. 14, Issue 3**

CONTENTS

Information for Authors

Progress in Physics has been created for rapid publications on advanced studies in theoretical and experimental physics, including related themes from mathematics and astronomy. All submitted papers should be professional, in good English, containing a brief review of a problem and obtained results.

All submissions should be designed in LaTeX format using *Progress in Physics* template. This template can be downloaded from *Progress in Physics* home page http://www.ptep-online.com

Preliminary, authors may submit papers in PDF format. If the paper is accepted, authors can manage LaTeXtyping. Do not send MS Word documents, please: we do not use this software, so unable to read this file format. Incorrectly formatted papers (i.e. not LaTeXwith the template) will not be accepted for publication. Those authors who are unable to prepare their submissions in LaTeXformat can apply to a third-party payable service for LaTeX typing. Our personnel work voluntarily. Authors must assist by conforming to this policy, to make the publication process as easy and fast as possible.

Abstract and the necessary information about author(s) should be included into the papers. To submit a paper, mail the file(s) to the Editor-in-Chief.

All submitted papers should be as brief as possible. Short articles are preferable. Large papers can also be considered. Letters related to the publications in the journal or to the events among the science community can be applied to the section *Letters to Progress in Physics*.

All that has been accepted for the online issue of *Progress in Physics* is printed in the paper version of the journal. To order printed issues, contact the Editors.

Authors retain their rights to use their papers published in *Progress in Physics* as a whole or any part of it in any other publications and in any way they see fit. This copyright agreement shall remain valid even if the authors transfer copyright of their published papers to another party.

Electronic copies of all papers published in *Progress in Physics* are available for free download, copying, and re-distribution, according to the copyright agreement printed on the titlepage of each issue of the journal. This copyright agreement follows the *Budapest Open Initiative* and the *Creative Commons Attribution-Noncommercial-No Derivative Works 2.5 License* declaring that electronic copies of such books and journals should always be accessed for reading, download, and copying for any person, and free of charge.

Consideration and review process does not require any payment from the side of the submitters. Nevertheless the authors of accepted papers are requested to pay the page charges. *Progress in Physics* is a non-profit/academic journal: money collected from the authors cover the cost of printing and distribution of the annual volumes of the journal along the major academic/university libraries of the world. (Look for the current author fee in the online version of *Progress in Physics*.)

LETTERS TO PROGRESS IN PHYSICS

Cosmological Cold Dark Matter and Dark Energy Match Icosahedron Symmetry

Felix Tselnik
E-mail: tselnik@bgu.ac.il

A charge analogous though different from the usual electric charge is introduced with the same kind of gauge but applied to the icosahedron. This "cosmocharge" might be a source of the accelerating expansion of universe in cosmology (Dark Energy).

In a unmetric approach [1], *contact* is the prime concept defined by the point-like — yes/no — condition, and all predictions in a Contact Problem are made by means of counting top-velocity signal oscillations numbers between *bodies* moving along their trajectories. In so doing, we need no intermediaries like rulers, clocks, or reference frames that could introduce all of their own or hide something. Therefore only direct motion-to-motion measurements should be used. Then even the concept of body is introduced solely as something, for which Contact Problem makes sense.

Suggesting free motion to be rectilinear and uniform, we ascribe acceleration to external forces. However, as mentioned by Einstein, this picture leads to a vicious circle, since the absence of forces itself is verified just by this kind of motion. There is nothing intrinsic for an individual straight line. Moreover, how can we be sure in practice that rulers are straight and clocks click uniformly? And are such features of these auxiliary devices actually necessary for Contact Problem predictions? Can integration required to construct the trajectory in a field be carried out without approximation with such segments?

Metric-less approach makes it possible to dispense with these artificial schemes. Rather than consider particular lines, we could first work with classes of lines provided with some particular rules for mutual intersections and then develop full space-time geometry out of these. To this end, let us define first a special class of trajectories with the following property: Any two of these either do not intersect, or intersect in a single point. We *define* free trajectories as members of this class. Assuming their intersections to mark contacts, we can consider Contact Problem *for this class only*, implying its further application to the full Contact Problem with external forces. For this to be possible, general trajectories, which can have multiple contacts as mutual, so also with free trajectories, must satisfy some conditions:

i. They contact some of free trajectories at each points;
ii. At each point a next point exists, such that a free trajectory connecting these two points has no other contacts with this general trajectory. As shown in [1], we can define parallel trajectories and predict contacts using them by means of counting top-signal oscillations ratios.

The reaction of the body's motion on external influences depends on its *charge* pertained to a particular *field*. Any Contact Problem can be specified by means of oscillations numbers and their ratios, provided the standard of charge can be transported to all points of a trajectory in question. It is just the availability of this procedure that provides the list of relevant fields as compatible with it. To this end, some particular arrangements of test trajectories — *spheres* — are used. Sphere is defined as a finite or infinite set of trajectories having common contact (the sphere center) with some definite ratios of (infinite) oscillations numbers in order to introduce a measure for operations such as field determining integration. Some kinds of spheres — *regular stars*, the trajectories of which are distributed according to the vertices of the Platonic solids, provide a basis for the electric charge gauge by means of detecting the related symmetries of their motions toward the star center solely under their interaction.

In particular, the cube symmetry defines the charge gauge for the electroweak interaction. Considering the trajectories of the two cube comprising tetrahedrons, one of which consists of four electrons and another of four positrons, we can develop a full gauge framework for these interactions, yet additionally requiring the existence of neutrinos (with the resulting parity violation) [2]. In the same sense the dodecahedron star, comprising besides the cube also the 12-vertices set of "roofs", ascribed to the quarks, adds the strong interaction in accord with this additional symmetry. The set of roof trajectories might have a center on their own, provided the strong potential squarely increases (over a limited range) to form a strictly fine star. Their electromagnetic interaction with the cube sub-star of this dodecahedron (necessary to fix their position with respect to the cube) prevents the latter from being a strictly fine star. For this perturbation to fall within the range of the weak interaction, the quark masses must be accordingly small. The dodecahedron symmetry exhausts the list of interactions that could be ultimately registered with our electricity-based devices.

Of the five Platonic solids, only the cube and the icosahedron allow for arrangements of trajectories that can form strictly fine regular stars even for charged particles, provided these have equal masses and absolute values for oppositely charged particles (neither tetrahedron, nor octahedron can form these). Since the icosahedron cannot be included in the richest with sub-stars dodecahedron, its possible charges have nothing in common with electric or other charges of the dodecahedron. Hence, this charge cannot be detected with our customary devices.

Like the roofs of the dodecahedron, the set of 12 trajectories of the icosahedron corresponding to its 12 vertices can be decomposed into 3 reciprocally orthogonal rectangles (however, having a particular — "golden" — ratio of their sides' lengths for the star to be regular). Again, in each rectangle all these trajectories belong to test-bodies for the charge gauge, having equal masses and absolute values of some charge with opposite signs on their side vertices. Then mutual compensation of these charges lets these 3 rectangles be quite independent of each other due to compensation of effects of one charged rectangle on another.

Just as the usual electric charge in our ordinary situations creates a field that, in turn, is detectable due to charged bodies motion, this "cosmocharge" Q, though being not detectable with our conventional devices, still might be found in observations of far galaxies or their clusters [3]. If, analogously to baryon matter-antimatter asymmetry, one sign of cosmocharge has some larger density than its opposite one, then so created "cosmofield" will let our universe expand with acceleration now ascribed to the Dark Energy. Similarly to the rectangles of the strong interacting sub-star in the dodecahedron, the rectangles of the icosahedron can possess strictly fine center only for a force with a potential squarely increasing with distance. Consisting of opposite charges, such a "cosmoplasma" might fluctuate to have observable anisotropy in the universe expansion acceleration.

For basic electromagnetic interaction for the charge gauge in the dodecahedron, we had to restrict the strong interaction region to prevent adverse influence of 12 vertices subset on the cube symmetry. There is no need in this confinement now, since the charge of only one force is to be gauged. Hence the increasing field can exist over the whole universe keeping asymptotic freedom in our short range environment, while being effective far away.

Having no sub-symmetries in the icosahedron star, the cosmofield cannot involve other than strong-like interactions. However, its rectangles might have different values of Q and masses M, provided Q^2M are the same for all of them to form a regular icosahedron star. So, stable "cosmoatoms" might exist as combined of bodies with different Q's and M's to avoid annihilation.

Now, in general relativity, scalar action includes an artificially inserted baryon term, contributing to the momentum-energy tensor in the Einstein equation and basing only on a covariance argument. This source of space-time curvature looks natural for our local environment. Moreover, we can specify space-time scalar curvature as a violation of transitivity in the finite local oscillations numbers for sets of curved lines that are still regarded "parallel" in terms of our oscillations numbers. So defined, curvature should replace the scalar in the least action principle for Contact Problem. We then reverse the very definition of matter. Just as in Contact Problem a concept of body was introduced due to its participation in Contact Problem scheme, the concept of *matter* in cosmology is just a visualization of the observed curvature of space-time. Unlike baryon case of general relativity, there is no independent of curvature definition of matter now. Actually, no Cold Dark Matter, whether or not detectable, might exist there at all. Merely the empty space-time of the real universe is actually curved, while we ascribe the measured curvature to some imaginary Cold Dark Matter as its source in analogy to the Newton law.

Submitted on April 8, 2018

References

1. Tselnik F. Irony of the Method. *Progress in Physics*, 2016, v.12, issue 2, see p.95 in the paper.
2. Tselnik F. *Progress in Physics*, 2015, v.11, issue 1, 50.
3. Tselnik F. *Communications in Nonlinear Science and Numerical Simulation*, 2007, v.12, 1427.

The Planck Vacuum Physics Behind the Huygens Principle and the Propagator Theory for the Schrödinger Electron

William C. Daywitt

National Institute for Standards and Technology (retired), Boulder, Colorado, USA
E-mail: wcdaywitt@me.com

This paper reviews a small portion of the quantum-electrodynamic propagator model as viewed from the Planck vacuum (PV) theory. The nonrelativistic calculations suggest that the degenerate collection of Planck-particle cores (that pervade the invisible, negative-energy vacuum state) is responsible for the Huygens principle, the propagator theory, and the Feynman diagrams.

1 Introduction

The theoretical foundation [1–3] of the PV theory rests upon the unification of the Einstein, Newton, and Coulomb superforces:

$$\frac{c^4}{G}\left(=\frac{m_*c^2}{r_*}\right)=\frac{m_*^2G}{r_*^2}=\frac{e_*^2}{r_*^2} \tag{1}$$

where the ratio c^4/G is the curvature superforce that appears in the Einstein field equations. G is Newton's gravitational constant, c is the speed of light, m_* and r_* are the Planck mass and length respectively [4, p. 1234], and e_* is the massless bare charge. The fine structure constant is given by the ratio $\alpha = e^2/e_*^2$, where $(-e)$ is the observed electronic charge.

The two particle/PV coupling forces

$$F_c(r)=\frac{e_*^2}{r^2}-\frac{mc^2}{r} \quad \text{and} \quad F_*(r)=\frac{e_*^2}{r^2}-\frac{m_*c^2}{r} \tag{2}$$

the electron core $(-e_*, m)$ and the Planck-particle core $(-e_*, m_*)$ exert on the PV state, along with their coupling constants

$$F_c(r_c)=0 \quad \text{and} \quad F_*(r_*)=0 \tag{3}$$

and the resulting Compton radii

$$r_c=\frac{e_*^2}{mc^2} \quad \text{and} \quad r_*=\frac{e_*^2}{m_*c^2} \tag{4}$$

lead to the important string of Compton relations

$$r_cmc^2=r_*m_*c^2=e_*^2 \quad (=c\hbar) \tag{5}$$

for the electron and Planck-particle cores, where $\hbar$ is the reduced Planck constant. The electron and Planck-particle masses are m and m_* respectively. To reiterate, the equations in (2) represent the forces the free electron and Planck-particle cores exert on the PV space, a space that is itself pervaded by a degenerate collection of Planck-particle cores [5].

The Planck constant is a secondary constant whose structure can take different forms, e.g.

$$\hbar\,[\text{erg sec}]=r_cmc=r_*m_*c=\left(\frac{e_*^2}{r_*}\right)t_*=m_*c^2t_* \tag{6}$$

that are employed throughout the following text, where t_* $(= r_*/c)$ is the Planck time [4, p. 1234].

Furthermore, the energy and momentum operators expressed as

$$\widehat{E}=i\hbar\frac{\partial}{\partial t}=i\,(m_*c^2)\,t_*\,\frac{\partial}{\partial t}=i\,(m_*c^2)\,r_*\,\frac{\partial}{c\partial t} \tag{7}$$

and

$$c\,\widehat{\mathbf{p}}=-i\,c\,\hbar\,\nabla=-i\,(m_*c^2)\,r_*\,\nabla=-i\,(mc^2)\,r_c\,\nabla \tag{8}$$

will be used freely in what follows.

Section 2 re-examines the Schrödinger equation in light of the PV theory, the calculations concluding that the pervaded vacuum state is the source of the scattering in the propagator theory. Section 3 presents a nonrelativistic look at the Huygens principle and the propagator theory for the electron core.

2 Schrödinger equation

The inhomogeneous Schrödinger equation, where $H = H_0+V$ is the Hamiltonian operator, can be expressed as

$$\left(i\hbar\frac{\partial}{\partial t}-H\right)\psi(\mathbf{x},t)=0\,. \tag{9}$$

The free-space Hamiltonian is H_0 and V is some position and time-dependent potential that is assumed to slowly vanish in the remote past $(t \to -\infty)$ and in the remote future $(t \to +\infty)$. In free space $V = 0$ and (9) becomes

$$\left(i\hbar\frac{\partial}{\partial t}-H_0\right)\phi(\mathbf{x},t)=0\,. \tag{10}$$

For $t' > t$, the formal solution to (9) or (10) takes the form [6]

$$\psi(\mathbf{x},t')=T\exp\left[-i\int_t^{t'}dt''\,H(t'')/\hbar\right]\psi(\mathbf{x},t) \tag{11}$$

where T is the time-ordering operator whose details are unimportant here (see Appendix A). What is important is the decomposition of $\hbar$ $(= m_*c^2t_*)$ in the exponent of (11), leading to

$$\int_t^{t'} \frac{dt'' H(t'')}{\hbar} = \int_t^{t'} \frac{dt''}{t_*} \frac{H(t'')}{m_*c^2} \,. \tag{12}$$

From the perspective of the PV theory, the normalization of dt'' by the Planck time t_* and H by the Planck-particle mass energy m_*c^2 strongly suggest that the scattering in the quantum-electrodynamic propagator theory is caused by the Planck-particle cores that pervade the vacuum state. This conclusion will be reinforced by the calculations to follow.

The normalized Hamiltonian operator H_0 can be expressed as

$$\begin{aligned} \frac{H_0}{m_*c^2} &= \frac{\text{“}p^2/2m\text{”}}{m_*c^2} = \frac{c\widehat{\mathbf{p}} \cdot c\widehat{\mathbf{p}}/2mc^2}{m_*c^2} \\ &= \frac{(-im_*c^2 r_* \nabla) \cdot (-imc^2 r_c \nabla)/2mc^2}{m_*c^2} = -\frac{r_c r_* \nabla^2}{2} \end{aligned} \tag{13}$$

where the equalities in (5) are used. Then the normalized Schrödinger equation becomes

$$ir_* \frac{\partial \phi}{c \partial t} - \frac{(-ir_c \nabla) \cdot (-ir_* \nabla)}{2} \phi = 0 \tag{14}$$

or

$$\left(it_* \frac{\partial}{\partial t} + \frac{r_c r_* \nabla^2}{2} \right) \phi = 0 \tag{15}$$

where t_* ($= r_*/c$) is the Planck time and the equations are dimensionless. The dimensionless aspect of the equations here and in what follows will help in recognizing the relationship between the Huygens principle and the propagator formalism.

The normalized inhomogeneous equation (9) becomes

$$\left(it_* \frac{\partial}{\partial t} + \frac{r_c r_* \nabla^2}{2} \right) \psi = \frac{V}{m_*c^2} \psi \tag{16}$$

where again the equation is dimensionless.

3 Electron-core propagator

Roughly speaking, the Huygens principle states that every point on a wavefront is itself the source of a spherical wavelet. In the present context, the Huygens principle takes the form [7, eqn. 6.29]

$$\phi(\mathbf{x}', t') = i \int d^3x \, \frac{G_0(\mathbf{x}', t'; \mathbf{x}, t)}{\hbar} \, \phi(\mathbf{x}, t) \quad \text{for} \quad t' > t$$

$$\phi(\mathbf{x}', t') = i \int d^3x \, \frac{G_0(\mathbf{x}', t'; \mathbf{x}, t)}{(m_*c^2) t_*} \, \phi(\mathbf{x}, t) \tag{17}$$

and

$$\psi(\mathbf{x}', t') = i \int d^3x \, \frac{G(\mathbf{x}', t'; \mathbf{x}, t)}{\hbar} \, \psi(\mathbf{x}, t) \quad \text{for} \quad t' > t$$

$$\psi(\mathbf{x}', t') = i \int d^3x \, \frac{G(\mathbf{x}', t'; \mathbf{x}, t)}{(m_*c^2) t_*} \, \psi(\mathbf{x}, t) \tag{18}$$

where the Green function propagators G_0 and G have the units “erg-sec per unit volume”. In the present paper, equations (17) and (18) are associated with what are defined as **internal-** and **external-**scattering processes respectively. The internal scattering refers to the free electron $\phi(\mathbf{x}, t)$ scattering off the pervaded PV space. The external scattering refers to the electron $\psi(\mathbf{x}, t)$ scattering off the pervaded PV space with an external potential $V(\mathbf{x}, t)$ perturbing that space. It will be seen in what follows that the units “erg-sec per unit volume” almost define the “pervaded vacuum space”.

Now begins the calculation of the wave function ψ resulting from the continuous interaction of the free-electron wave function ϕ with the perturbed vacuum state. The calculation will not be carried to completion, but only far enough (equation (25)) to suggest that the wave scattering takes place between ϕ and the pervaded vacuum space. Furthermore, many of the details in the following calculations based on reference [7] are unimportant to the present needs; so the calculations are heavily referenced in case the reader is interested in those details.

For $t = \Delta t_1$ [7, eqn. 6.30]

$$\left(it_* \frac{\partial}{\partial t_1} + \frac{r_c r_* \nabla^2}{2} \right) \psi(\mathbf{x}_1, t_1) = \frac{V(\mathbf{x}_1, t_1)}{m_*c^2} \psi(\mathbf{x}_1, t_1) \tag{19}$$

and

$$\left(it_* \frac{\partial}{\partial t_1} + \frac{r_c r_* \nabla^2}{2} \right) \psi(\mathbf{x}_1, t_1) = 0 \tag{20}$$

for $t \neq \Delta t_1$. Equation (19) refers to an external scattering as defined above.

The new wave function due to the external perturbation V in (19) can be expressed as [7, eqn. 6.31]

$$\psi(\mathbf{x}_1, t_1) = \phi(\mathbf{x}_1, t_1) + \Delta\psi(\mathbf{x}_1, t_1) \tag{21}$$

so the Schrödinger equation yields (using (15) for ϕ)

$$\begin{aligned} &\left(it_* \frac{\partial}{\partial t_1} + \frac{r_* r_c \nabla^2}{2} \right) \Delta\psi(\mathbf{x}_1, t_1) \\ &= \frac{V(\mathbf{x}_1, t_1)}{m_*c^2} \left[\phi(\mathbf{x}_1, t_1) + \Delta\psi(\mathbf{x}_1, t_1) \right] . \end{aligned} \tag{22}$$

It can be shown that the second terms on the left and right sides of (22) can be dropped [7, eqn.6.35], leading to

$$it_* \frac{\partial}{\partial t_1} \Delta\psi(\mathbf{x}_1, t_1) = \frac{V(\mathbf{x}_1, t_1)}{m_*c^2} \phi(\mathbf{x}_1, t_1) \tag{23}$$

which to first order in Δt_1 yields

$$\Delta\psi(\mathbf{x}_1, t_1 + \Delta t_1) = -i \frac{V(\mathbf{x}_1, t_1)}{m_*c^2} \phi(\mathbf{x}_1, t_1) \frac{\Delta t_1}{t_*} \tag{24}$$

where the differential $\Delta\psi(\mathbf{x}_1, t_1)$ coming from the approximation is ignored compared to the $\phi(\mathbf{x}_1, t_1)$ on the right side of (24).

For two consecrative time periods $\Delta t_1 \Delta t_2$, with an infinite past [where $\psi(x') \rightarrow \phi(x')$], it can be argued that [7, eqn. 6.43]

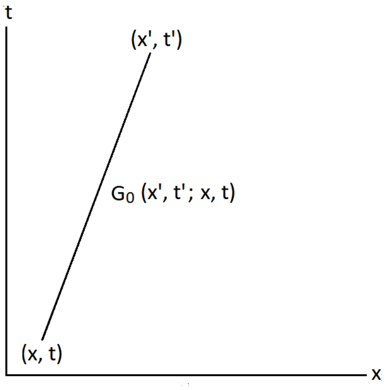

Fig. 1: The Feynman diagram for the propagation of the electron core $(-e_*, m)$ from (x, t) to (x', t') with no external scattering.

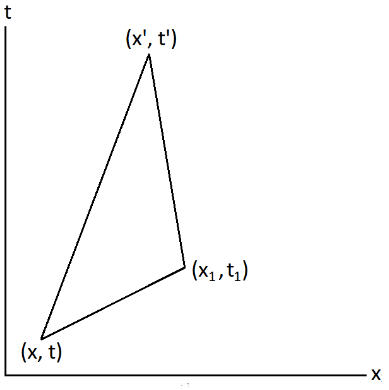

Fig. 2: The Feynman diagram for the propagation of the electron core $(-e_*, m)$ from (x, t) to (x', t') with one external scattering at (x_1, t_1).

$$
\begin{aligned}
\psi(x') = \quad & \phi(x') + \int d^3x_1 \frac{\Delta t_1}{t_*}\, G_0(x';1) \frac{V(1)}{m_*c^2}\, \phi(1) \\
& + \int d^3x_1 \frac{\Delta t_2}{t_*}\, G_0(x';2) \frac{V(2)}{m_*c^2}\, \phi(2) \\
& + \int d^3x_1 \frac{\Delta t_1}{t_*} d^3x_2 \frac{\Delta t_2}{t_*}\, G_0(x';2) \\
& \frac{V(2)}{m_*c^2}\, G_0(x';1)\, \frac{V(1)}{m_*c^2}\, \phi(1)
\end{aligned}
\tag{25}
$$

where the obvious notations $(x) \equiv (\mathbf{x}, t)$ and $\phi(2) \equiv \phi(x_2)$ are used. The four terms in (25) represent respectively the propagation from (x, t) to (x', t'): a) as a free particle with no external scatterings; b) with one scattering at (x_1, t_1); c) with one scattering at (x_2, t_2); and d) with a double scattering at (x_1, t_1) and (x_2, t_2) in succession. The representations of these scatterings in Figures 1-4 are called Feynman diagrams [7, eqn. 6.43], where the horizontal axis represents space and the vertical axis represents time.

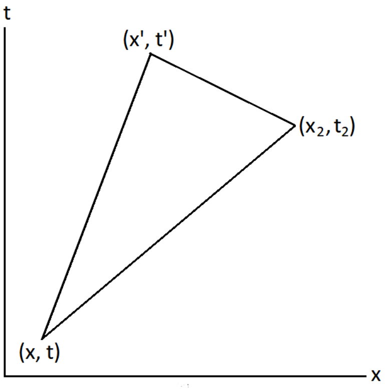

Fig. 3: The Feynman diagram for the propagation of the electron core $(-e_*, m)$ from (x, t) to (x', t') with one external scattering at (x_2, t_2).

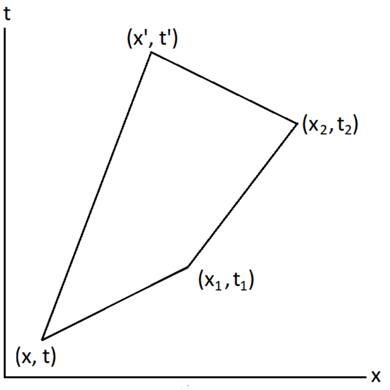

Fig. 4: The Feynman diagram for the propagation of the electron core $(-e_*, m)$ from (x, t) to (x', t') with a double external scattering at (x_1, t_1) and (x_2, t_2).

4 Conclusions and comments

A close examination of the previous calculations strongly suggests that the PV theory, which envisions a vacuum space pervaded by a degenerate collection of Planck-particle cores, provides a fundamental explanation for the Huygens principle and the scattering associated with the quantum-electrodynamic propagator formalism.

The retarded Green function G_0^+ associated with the Green function $G_0(\mathbf{x}', t'; \mathbf{x}, t)$ in equation (17) and in Figure 1 is given by the equations [7, eqn. 6.60]

$$\left(i\hbar \frac{\partial}{\partial t'} - H_0(x') \right) \frac{G_0^+(x'; x)}{\hbar} = \delta^3(\mathbf{x}' - \mathbf{x})\delta(t' - t) \tag{26}$$

for $t' > t$ and $G_0^+(x'; x) = 0$ for $t' < t$, where $x' = (\mathbf{x}', t')$ and $x = (\mathbf{x}, t)$; or

$$\left(it_* \frac{\partial}{\partial t'} + r_c r_* \nabla_{x'}^2 \right) G_0^+(x'; x) = \delta^3(\mathbf{x}' - \mathbf{x})[t_* \delta(t' - t)] \tag{27}$$

where the parenthesis on the left and the bracket on the right of (27) are dimensionless.

Appendix A: Time-ordering operator T

The time-ordering operator [6] is defined by

$$T \exp\left[-i \int_t^{t'} dt'' H(t'')/\hbar\right] \equiv \tag{A1}$$

$$\sum_{n=0}^{\infty} \frac{1}{n!} \left(\frac{-i}{\hbar}\right)^n \int_t^{t'} dt_1 \cdots \int_t^{t_{n-1}} dt_n H(t_1) \ldots H(t_n) \tag{A2}$$

$$= \sum_{n=0}^{\infty} \frac{(-i)^n}{n!} \int_t^{t'} \frac{dt_1}{t_*} \cdots \int_t^{t_{n-1}} \frac{dt_n}{t_*} \frac{H(t_1)}{m_* c^2} \ldots \frac{H(t_n)}{m_* c^2} \tag{A3}$$

where the final equality comes from the decomposition of the Planck constant, $\hbar = m_* c^2 t_*$, in (A2).

Submitted on April 14, 2018

References

1. Davies P. Superforce: the Search for a Grand Unified Theory of Nature. Simon and Schuster, Inc., New York, 1984.
2. Daywitt W.C. A Model for Davies' Universal Superforce. *Galilean Electrodynamics*, 2006, v. 5, 83.
3. Daywitt W.C. The Trouble with the Equations of Modern Fundamental Physics. *American Journal of Modern Physics. Special Issue: "Physics without Higgs and without Supersymmetry"*, 2016, v. 5(1-1), 22. See also www.planckvacuumDOTcom.
4. Carroll B.W., Ostlie A.D. An Introduction to Modern Astrophysics. Addison-Wesley, San Francisco, Boston, New York, Cape Town, Hong Kong, London, Madrid, Mexico City, Montreal, Munich, Paris, Singapore, Sydney, Tokyo, Toronto, 2007.
5. Daywitt W.C. The Planck Vacuum. *Progress in Physics*, 2009, v. 1, 20.
6. Fradkin E. Chapter 10: Observables and Propagators. Internet website: "Observables and Propagators, Fradkin".
7. Gingrich D.M. Practical Quantum Electrodynamics. CRC, The Taylor & Francis Group, Boca Raton, London, New York, 2006.

Predicting Total Angular Momentum in TRAPPIST-1 and Many Other Multi-Planetary Systems Using Quantum Celestial Mechanics

Franklin Potter

8642 Marvale Drive, Huntington Beach, CA 92646, USA
E-mail: frank11hb@yahoo.com

TRAPPIST-1 harbors at least 7 Earth-mass planets orbiting a 0.089 solar mass dwarf M-star. Numerous other multi-planetary systems have been detected and all obey a quantization of angular momentum per unit mass constraint predicted by quantum celestial mechanics (QCM) as derived from the general theory of relativity (GTR). The universality of this constraint dictates that the TRAPPIST-1 system should obey also. I analyze this recently discovered system with its many mean motion resonances (MMRs) to determine its compliance and make some comparisons to the Solar System and 11 other multi-planetary systems.

1 Introduction

In the past 25 years, more than 3500 exoplanets have been detected, many in multi-planetary systems with 4 or more planets [1]. Extreme examples include HD 10180 with 9 planets and TRAPPIST-1 with 7 planets. In each of the discovered systems the understanding of their formation and stability over tens of millions or even billions of years using Newtonian dynamics remains an interesting challenge.

A prediction of whether additional planets exist beyond those already detected is not an expected outcome of the dynamical studies. However, a different approach [2] called quantum celestial mechanics (QCM) offers the potential ability to predict the existence of additional angular momentum in the planetary system, which could indicate additional planets to be detected or additional mass in the form of rings or spherical shells of mass chunks orbiting the star, such as the Kuiper belt or the Oort Cloud in our Solar System.

The history of the formation of most of these planetary systems remains an active research area, ranging from *in situ* formation from a dust disk to pebble accretion followed by sequential inward migration toward the central star [3]. Their stability may depend upon numerous factors, and many research groups continue to investigate the long-term stability for millions of orbits over tens of millions of years, including in models for the history of our Solar System.

There is a recent paper [4] that considers the total angular momentum deficit (AMD) of multi-planetary systems with the proposal that the AMD is a way to classify their predicted stability. The AMD is defined by the total angular momentum difference

$$AMD = \sum_{k=1}^{n} \mu_k \sqrt{GM\, r_k} \left(1 - \sqrt{1 - \epsilon_k^2}\, \cos\, i_k\right) \tag{1}$$

between the maximum total orbital angular momentum when all the planets orbit in the same plane and the total angular momentum determined from the orbital data. The Solar System and HD 10180 are two examples discussed in which the outer system of planets is AMD-stable, the inner system of planets is AMD-unstable, and the whole system is AMD-unstable.

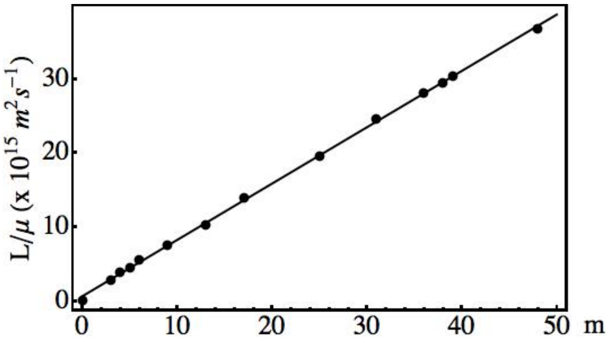

Fig. 1: Solar System fit to QCM total angular momentum constraint. The uncertainties are within the data circles.

In fact, this AMD approach demonstrates that the AMD-unstable systems tend to have orbital period ratios concentrated around the lower integer mean motion resonance ratios such as 3:2 and 2:1, a result perhaps somewhat in conflict with expectations. This unexpected outcome is interesting because many planetary systems exhibit at least one mean motion resonance (MMR), which had been expected to contribute a stabilizing factor in parts of those systems. The AMD research therefore means that not all MMRs are beneficial toward stabilizing the planetary orbits.

The recently discovered TRAPPIST-1 system has 7 Earth-mass planets all within 0.1 au of its dwarf M-star of 0.089 solar masses [5]. Three of the planet pairs exhibit a 3:2 MMR and another pair exhibits the 4:3 MMR, yet studies indicate that this system has been in existence for at least 7 billion years. Perhaps an additional factor contributes to the stability of these multi-planetary systems.

We propose that the additional factor is the quantization of angular momentum per unit mass predicted by quantum celestial mechanics (QCM). The QCM theory [6] dictates that not all planetary orbits about the central star are available as equilibrium orbits but, instead, QCM determined equilibrium orbits exist only at specific radii. Bodies in orbits at all other radial distances will migrate towards these specific QCM equilibrium orbital radii.

In the following sections we review the QCM proposed angular momentum constraint that leads to a select set of orbital radii for all planetary systems and demonstrate its application to the Solar System, the 5 moons of Pluto, the 7 planets of TRAPPIST-1, and to numerous other exoplanetary systems, including HD 10180.

2 The QCM angular momentum constraint

The total angular momentum in a planetary system is an important physical parameter not often discussed. In 2003, H. G. Preston and F. Potter proposed [6] a new gravitational theory called Quantum Celestial Mechanics (QCM), which is derived from the general theory of relativity (GTR), that claims that all gravitationally bound systems in the Schwarzschild metric will exhibit the quantization of angular momentum per unit mass constraint

$$\frac{L}{\mu} = m \frac{L_T}{M_T} \tag{2}$$

with m being the orbit quantization integer, L the angular momentum of each orbiting body of mass μ, and L_T and M_T the total angular momentum and total mass of the planetary system.

In the simplest applications of QCM, one assumes that after tens of millions of years that the orbiting planet is at its equilibrium orbital radius r with a small eccentricity ϵ so that the Newtonian orbital angular momentum value $L = \mu \sqrt{GM\, r(1-\epsilon^2)}$, with M being the star mass, can be used. For most multi-planetary systems, including the Solar System, TRAPPIST-1, and HD 10180, the values of ϵ are all less than 0.2 and will be ignored in the QCM analysis fit to the constraint.

Because the QCM quantization of angular momentum per unit mass constraint is derived from the general relativistic Hamilton-Jacobi equation via a simple transformation, one obtains a new gravitational wave equation [6]. In the familiar Schwarzschild metric this gravitational wave equation will apply to all gravitationally-bound systems with orbiting bodies. However, as in GTR, different metrics can be considered, including the static interior metric, for which the QCM analysis of the Universe [7] predicts a new interpretation of the cosmological redshift in agreement with the data, that all distant sources are in a more negative gravitational potential than all observers, i.e. the distant clocks tick slower.

3 Application of QCM to the Solar System

Our first application of QCM in the Schwarzschild metric was to our Solar System using the known masses and present spacings of its 8 planets. If only the orbital angular momentum of the 8 planets and the Sun are considered, so that $L_T \approx 4 \times 10^{43}$ kg m^2 s^{-1}, then this value of the total angular momentum meant that QCM predicted that all the planetary orbits should be within the radius of the Sun! Obviously, something was wrong.

At first, we suspected that our derivation of the constraint was incorrect. But a detailed check proved that our derivation had been done correctly, including the numerous approximations needed to obtain an equation with the most important factors. Therefore, in order to achieve the present day orbital spacings, we interpreted the QCM equations to be predicting much more angular momentum in the Solar System, about 50 times as much!

Indeed, we subsequently learned that the Solar System does have much more angular momentum in its system than the contributions from just the Sun and its planets. The Solar System has an enormous angular momentum contribution from the Oort Cloud with its approximately 100 Earth masses of ice chunks orbiting at about an average distance of 40,000 au, thereby dominating the total angular momentum of the Solar System by almost a factor of 50.

The new orbital fits of QCM using the constraint then agreed with the present orbital radii of the planets, and we predicted the total angular momentum in the Solar System to be the much higher value $L_T \approx 1.9 \times 10^{45}$ kg m^2 s^{-1}. Fig. 1 shows our QCM fit to the 8 planets plus the 5 known dwarf planets, with m values 3, 4, 5, 6, 9, 13, 17, 25, 31, 36, 38, 39, 48.

So, for the first time, we were able to use the QCM angular momentum constraint to fit the equilibrium orbital radii of all the planets of the Solar System and to verify that the constraint could be an important factor in predicting additional angular momentum in a planetary system. One should note that the QCM fit does not require the division of the system into the inner planets and the outer planets, a prominent feature of other approaches, including AMD.

The successful application of the QCM angular momentum constraint to the Solar System encouraged us to try to find a definitive test. But the QCM constraint fit to the Solar System and to the orbiting satellites of the Jovian planets could not be considered definitive tests of QCM because their system total angular momentum values were not known to within 10%. So a decade long hunt began to find a multi-bodied system for which the physical parameters are known to be within a few percent.

4 Pluto system as a definitive test of QCM

Fortunately, in 2012, the dwarf planet Pluto was reported to have 5 moons. Their orbital stability was being studied in reference to the Pluto-Charon barycenter, and the moons are nearly in a 1:3:4:5:6 resonance condition!

An early QCM linear regression fit with $R^2 = 0.998$ to the angular momentum constraint for the Pluto system revealed more angular momentum could be present in this sys-

	m	r (au)	P (days)	P2/P1	$(n_2/n_1)^3$	L_{max} 10^{39} kg m^2 s^{-1}	MMR(P)	MMR(n)
b	15	0.0115	1.51087	1.000	1.000	1.103		
c	18	0.0158	2.42182	1.603	1.675	1.802	1.603	1.675
d	21	0.0223	4.04961	2.680	2.600	0.540	1.672	1.552
e	24	0.0293	6.09961	4.037	3.815	1.828	1.506	1.467
f	28	0.0385	9.20669	6.094	5.954	1.651	1.509	1.560
g	31	0.0469	12.35294	8.176	8.000	2.066	1.342	1.344
h	36	0.0619	18.76700	12.421	12.366	0.826	1.519	1.546
						9.815		

Table 1: Fit of the 7 planets of TRAPIST-1 to the QCM angular momentum constraint.

tem, hinting that at least one more moon could exist. This fit used the smallest set of integers possible with m values 2, 6, 9, 10, 11, 12. A set with larger integers was also available beginning with $m = 4$ for a good fit but indicating a lower total angular momentum value for the system.

Then, in 2015, the New Horizons spacecraft sent back precise data about the Pluto system that established 5 tiny moons only. That limitation allowed us to have a definitive test [8] of QCM because the total angular momentum was then known to within 2.4%. With the m values 4, 10, 15, 16, 18, 19, the QCM angular momentum constraint applied to the Pluto system predicted $L_T = 6.28 \times 10^{30}$ kg m^2 s^{-1}, a value commensurate with the value $L_T = 6.26\,(\pm 0.14) \times 10^{30}$ kg m^2 s^{-1} calculated from the known physical parameters.

We therefore consider the Pluto system to be the definitive test of the QCM angular momentum constraint because we know the pertinent physical parameters to within 2.4%, and the predicted QCM total angular momentum determined from the slope of the QCM plot of L/μ vs m agrees with the total value determined in the standard way using Newtonian physics.

5 QCM constraint applied to TRAPPIST-1

There has been great interest in the TRAPPIST-1 system because at least 3 of the planets are in the so-called Habitable Zone where liquid water and perhaps some kind of life form could have evolved over its nearly 9 billion year history [10]. However, being so close-in to their M-star also means that these planets could be experiencing a severe UV radiation flux as well as particle winds emanating from the star. Studies of their atmospheric content are under way by researchers to determine whether water still exists or whether the UV radiation has dissociated any previously existing water vapor with the resulting particles having evaporated away to leave behind an arid surface environment [9, 11].

We know that the planetary system orbiting TRAPPIST-1 harbors at least 7 Earth-mass planets orbiting close-in to the dwarf M-star of 0.089 $M_\odot$ [5]. More planets further out beyond 1 au could exist, a possibility that QCM may suggest by interpreting the constraint fit. The orbital period ratios reveal that planet pairs d/e, e/f and g/h exhibit nearly a 3:2 mean motion resonance (MMR) and the pair f/g has a 4:3 MMR [9]. Planet pairs b/c and c/d do not have a first order MMR although their period ratios are near 5:3.

The formation of this system has been a challenge for modeling, and in a recent study [3] a pebble accretion and inward migration history have been proposed to accommodate its formation, including a process called resonance trapping as planets sequentially move inward and build.

The pertinent data for the 7 known planets and the predicted m values from the system's linear regression fit to the QCM angular momentum constraint are provided in Table 1. This set of m values is the lowest set of integers that achieved a linear regression least squares fit of $R^2 > 0.999$ for both plots: L/μ vs m and P_2/P_1 vs $(n_2/n_1)^3$, with $n = m+1$ for the assumed circular orbits. Of course, other integer sets with larger m values will also fit the constraint as well, but they will have a smaller slope and therefore a smaller system total angular momentum value calculated with (2).

In Fig. 2 is the plot of L/μ vs m with all uncertainties within the small circles around each data point. From the slope 8.77×10^{12} m^2 s^{-1} of this QCM fit, one predicts a system total angular momentum of 1.56×10^{42} kg m^2 s^{-1}. The angular momentum from the star rotation plus the orbital motion of the 7 planets is much less, about 1.2×10^{40} kg m^2 s^{-1}, using the values given in Table 1 and a star rotation period of 3.295 days.

The angular momentum difference could be accommodated in several ways, including a larger integer for the first m value and larger integers overall, thereby reducing the QCM predicted total angular momentum. Or the difference could be due to the presence of at least one additional planet further out beyond a distance of about 1 au. For example, if the additional planet had the mass of Saturn, its orbit at about 3.8 au would be sufficient to account for the discrepancy between the total angular momentum values. And, of course, this system could have the equivalent of the Oort Cloud at a large distance from the star.

The period ratios provided in both columns 5 and 6 are referenced to planet b. For a circular orbit, $n = \ell+1$, and

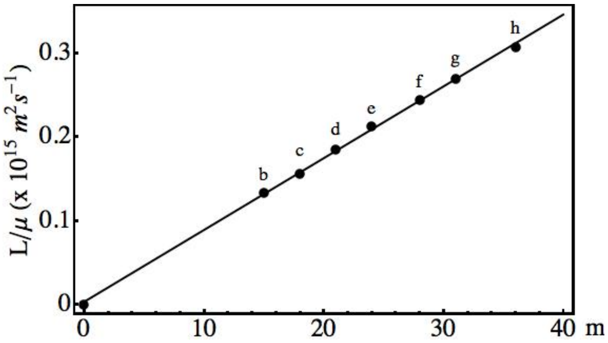

Fig. 2: QCM angular momentum constraint applied to the TRAPPIST-1 system of 7 planets close-in to the dwarf M-star. The uncertainties all lie within the data circles.

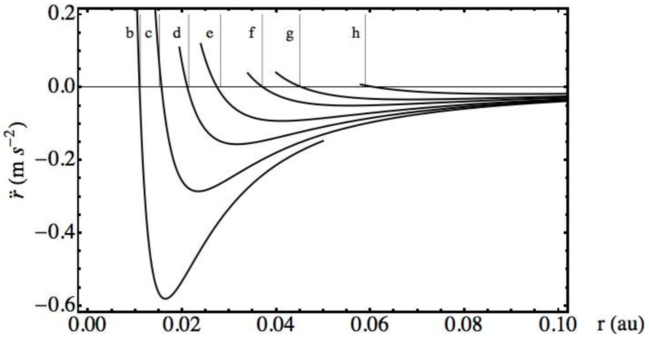

Fig. 3: The QCM predicted radial accelerations $\ddot{r}$ for each of the 7 planets of TRAPPIST-1. Note that some planets should experience corrections to their radial positions over tens of millions of years.

we assume $\ell = m$, its maximum value. QCM predicts period ratios

$$\frac{P_2}{P_1} = \left[\frac{m_2 + 1}{m_1 + 1}\right]^3 . \tag{3}$$

The largest discrepancy of the QCM predicted period ratios in column 6 from the actual values in column 5 is for planet e at 5.5%.

In the last two columns are the calculated MMRs for the adjacent planets when calculated from values in column 4, the MMR(P), and values calculated from column 6, for the MMR(n), revealing the amazing first order resonances d/e, e/f, g/h, and f/g, as well as the possible higher order resonances b/c and c/d. Planet c exhibits the biggest difference in QCM predicted values at about 7.2%.

Recall that QCM in the Schwarzschild metric predicts a specific but limited set of radii for circular equilibrium orbits that have both inward and outward forces acting, in direct contrast to Newtonian orbital dynamics which has an equilibrium orbit at all planetary orbital radii. For QCM the approximate expression for the effective gravitational potential is

$$V_{eff} = -\frac{GM}{r} + \frac{\ell(\ell+1)\, L_T^2}{2r^2\, M_T^2} , \tag{4}$$

where the angular momentum quantization integer ℓ originates in the θ-coordinate. We have taken $\ell = m$ for the expression. Whence, the expected value of the orbital radial acceleration near the equilibrium radius is defined by

$$\ddot{r}_{eq} = -\frac{GM}{r^2} + \frac{\ell(\ell+1)\, L_T^2}{r^3\, M_T^2} . \tag{5}$$

A computer simulation of the TRAPPIST-1 system could use this equation to study its long-term QCM dynamic stability contributions but must also include perturbations by the other planets. The net QCM accelerations are very small, varying from around a hundredth to a few tenths of a meter per second squared.

A plot of the QCM radial accelerations near the equilibrium radii for all 7 planets is shown in Fig. 3, where the vertical lines labelled b to h are the reported present radial orbital distances of the planets. As can be seen from the plot, a small radial movement inward for planet e is predicted to occur because its present radial acceleration is negative with respect to the QCM equilibrium orbital distance.

One would expect that the planets will oscillate about the QCM equilibrium orbital radii throughout their history, never settling at the exact radius at which no further radial acceleration would occur. Perturbations from the other nearby planets as they pass by will be larger than the QCM accelerations, but they last for short time intervals while the small QCM accelerations are acting constantly.

This TRAPPIST-1 system has existed for many billions of years, so some sort of stabilizing influence has been at play. We suspect that the QCM angular momentum constraint is the important additional factor, providing accelerations on both sides of the predicted QCM equilibrium orbital radius. A computer simulation will be needed to determine the outcomes over long time periods.

6 HD 10180 and other exosystems

The QCM quantization of angular momentum per unit mass constraint is expected to apply to all gravitationally bound systems described in the Schwarzschild metric.

In previous articles we analyzed multi-planetary systems with 4 or more planets and found that they all can fit the QCM angular momentum constraint. We list some of those systems for comparison in Table 2 in order of increasing star mass in column 2. Their m values and slope b are derived from the linear regression plots of L/μ versus m. The QCM value of L_T in column 6 is calculated from b and then compared to their known total angular momentum values (sum of columns 7 and 8).

Therefore, from the values in Table 2 we notice:

1. That our Solar System's b value is much larger than all the other multi-planetary system's b values. Why? Because the Solar System has the overwhelming angular momentum contribution from its Oort Cloud, a physi-

System	Star $M_\odot$	N	m values	b 10^{15} m^2 s^{-1}	QCM L_T 10^{45} kg m^2 s^{-1}	Star L_T 10^{42} kg m^2 s^{-1}	Planets L_T 10^{42} kg m^2 s^{-1}
TRAPPIST-1	0.089	7	15,18,21,24,28,31,36:	0.00877	0.00156	0.0113	0.012
GJ 667 C	0.31	7	16,21,26,29,34,39:55	0.0333	0.0206	0.00971	0.169
GJ 581	0.31	6	8,10,14,20,25:47	0.0456	0.0283	0.00454	0.229
HD 40307	0.75	6	9,12,16,19,22:35	0.0863	0.129	0.179	0.340
Tau Ceti	0.783	7	13,14,18,20:25,31,49	0.0923	0.145	0.0820	0.311
HR 8832	0.794	7	4,6,9,12:15,41,44	0.144	0.229	0.491	4.131
Kepler-20	0.912	6	8,10,12,15:18,24	0.105	0.191		0.846
Kepler-11	0.95	6	11,12,15,17,19:26	0.113	0.215		5.60
55 Cancri	0.95	5	3,8,12:23,62	0.160	0.304	0.118	78
Sun	1.0	8	:3,4,5,6,13,17,25,31	0.762	1.524	0.192	31
HD 10180	1.062	9	3,6,7,8,12,14:17,29,46	0.185	0.393	0.436	5.153
Kepler-90	1.20	8	14,15,17,28:33,36,43,50	0.0949	0.228	0.738	

Table 2: QCM angular momentum constraint applied to selected multi-planetary systems listed in order of star mass. N is the number of known planets which determine the m values for a linear regression fit $R^2 \geq 0.999$. The m values for planets with orbital radii less than Mercury's are to the left of the colon. The predicted QCM L_T in column 6 is calculated using the QCM slope b times the star mass.

cal property that dictates QCM to predict the very large orbital spacings for its planets. We cannot say much more about the Solar System, i.e., predict whether more planets or dwarf planets exist, because the overwhelming but unknown total angular momentum contribution of the Oort Cloud precludes making such a prediction.

2. That for the TRAPPIST-1 system, with its incredibly small QCM b value, we expect another planet or more orbiting bodies because the QCM predicted total angular momentum value is much greater than the orbital contribution from its 7 known planets and the rotation of the central star. Perhaps the proposed pebble accretion and inward migration train is the explanation for its formation, but QCD would suggest otherwise, that the planets formed *in situ* by gathering the local dust accumulating at the QCM equilibrium radii, assuming that the total angular momentum in this system did not change significantly during their formation.
3. That even for the HD 10180 system fit, as shown in Fig. 4 with its 9 planets, the total angular momentum from its star rotation plus the known orbiting planets falls far short of the QCM predicted total angular momentum, so more orbiting mass is expected.
4. That all the systems in Table 2 are expected to have additional angular momentum based upon the predicted QCM value of L_T. If more planets in these systems are detected, they should have orbital radii corresponding to the listed QCM m values that dictate their allowed equilibrium orbital distances.

Perhaps another exosystem will be discovered in the near future that also has a large angular momentum contribution and very large QCM orbital spacings so that direct comparisons can be made to the Solar System in terms of the total angular momentum parameter.

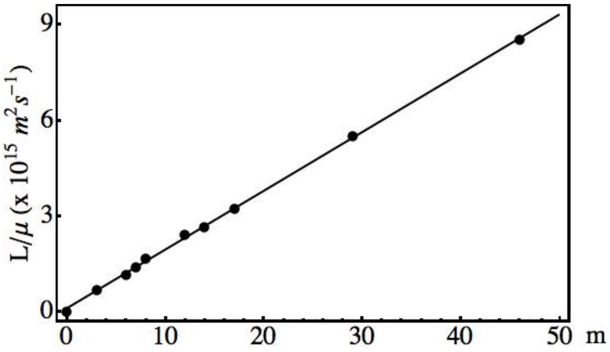

Fig. 4: QCM angular momentum constraint applied to HD 10180. Uncertainties lie within the data circles.

Note that both the 4 inner planets of the Solar System and the 7 planets of the TRAPPIST-1 system have been determined to be unstable by the AMD analysis [4]. Yet both systems have been in existence for more than 4 billion years, i.e., more than 4 billion Earth orbits. Perhaps the small QCM gravitational potential valleys around their QCM orbital equilibrium radii, such as those shown in Fig. 3, are contributing factors to their long-term stability. Or the existence of additional orbital mass further out contributes to their stability also. A computer simulation of these systems and the others that includes the QCM constraint could be done to determine whether this QCM effect is large enough to ensure their long-term stability.

7 Conclusions

Many multi-planetary systems have been discovered and they all had been determined previously to obey the QCM quantization of angular momentum per unit mass constraint. For most of those systems if not all of them, additional angular momentum is predicted by QCM, angular momentum which could be contributed by additional planets or spherical shells of ice.

Now the interesting TRAPPIST-1 system of 7 Earth-like planets has been shown to obey the angular momentum constraint for each known planet in the system. The QCM predicted total angular momentum of its planetary system is 1.56 $\times 10^{42}$ kg m^2 s^{-1} versus the estimated value of 1.2×10^{40} kg m^2 s^{-1} for the 7 planets plus the star rotation contribution. This large total angular momentum discrepancy could indicate that either at least one more planet could exist beyond several 1 au or that a set of m values with larger integers would be a better fit to decrease the predicted total angular momentum.

Also, for the TRAPPIST-1 system, from the determined radial acceleration values near to the QCM predicted orbital equilibrium radii, several planets could migrate slightly. For example, planet e has a present radial distance that should decrease slightly over several thousand years in order to reach its nearby predicted QCM orbital equilibrium radius. Perturbations from the other planets will be important to consider in a computer simulation of its behavior as the planet migrates to its true QCM equilibrium orbital radius.

We also provide a list of 12 multi-planetary systems so that a direct comparison of our Solar System QCM parameters can be made to other systems. The major difference is that our Solar System contains significantly more angular momentum than any other known planetary system discovered. Our QCM theory uses this information to predict the allowed equilibrium orbital distances, an approach that explains why almost all other multi-planetary systems with smaller total angular momentum values can have so many planets within the orbital radius of Mercury. Dynamically, a larger repulsive orbital angular momentum term in the QCM radial acceleration equation will result in the planets forming at larger orbital equilibrium radii.

Finally, the long-term stability of these multi-planetary systems remains a challenge for the traditional modeling using Newtonian universal gravitation without additional constraints. The consideration of the total angular momentum deficit (AMD) has introduced a method to classify their stability but is incomplete. Perhaps the QCM quantization of angular momentum per unit mass approach will be the additional constraint needed in order to better understand the formation and stability of multi-planetary systems.

Acknowledgements

We thank Sciencegems.com for continued support. Also, this research has made use of the Exoplanet Orbit Database and the Exoplanet Data Explorer at exoplanets.org.

Received on April 20, 2018

References

1. Han E., et al. Exoplanet Orbit Database. II. Updates to Exoplanets.org. *PASP*, 2014, v. 126 (943), 827.
2. Potter F. Multi-planet Exosystems All Obey Orbital Angular Momentum Quantization per Unit Mass predicted by Quantum Celestial Mechanics (QCM). *Progress in Physics*, 2013, v. 9 (3), 60–61.
3. Ormel C., Liu B., Schoonenberg D. Formation of TRAPPIST-1 and other compact systems. arXiv: astro-ph/1703.06924.
4. Laskar J., Petit A. AMD-stability and the classification of planetary systems. arXiv: astro-ph/1703.07125.
5. Gillon M., Triaud A. H. M. J., Demoy B.-O., et al. Seven temperate terestrial planets around a nearby untracool dwarf star TRAPPIST-1. *Nature*, 2017, v. 542, 456–460.
6. Preston H. G., Potter F. Exploring large-scale gravitational quantization without $\hbar$ in planetary systems, galaxies, and the Universe. arXiv: gr-qc/0303112.
7. Potter F., Preston H. G. Cosmological Redshift Interpreted as Gravitational Redshift. *Progress in Physics*, 2007, v. 3 (2), 31–33.
8. Potter F. Update on Pluto and its 5 Moons Obeying the Quantization of Angular momentum per Unit Mass Constraint of Quantum Celestial Mechanics. *Progress in Physics*, 2016, v. 12 (1), 56–58.
9. Luger R., Sestovic M., et al. A seven-planet resonant chain in TRAPPIST-1. *Nature Astronomy*, 2017, v. 1, (Article 0129).
10. Burgasser A. J., Mamejek E. E. On the Age of the TRAPPIST-1 System. arXiv: astro-ph/1706.02018.
11. Borrier V., De Wit J., Bolmont E., et al. Temporal Evolution of the High-energy Irradiation and the Water Content of TRAPPIST-1 Exoplanets. arXiv: astro-ph/1708.09484v1.

On the Classical Scaling of Quantum Entanglement

Pierre A. Millette

E-mail: PierreAMillette@alumni.uottawa.ca, Ottawa, Canada

In this paper, we consider the implications of the classical scaling of quantum entanglement observed experimentally. The probability of preserving entanglements over classical scales and preventing the entanglement from collapsing due to physical interactions is exceedingly small, indicating a fragile entanglement process. We propose a physically robust entanglement process that persists to classical scales as observed. We use a formulation of quantum mechanics that gives precedence to the physical rather than the mathematical aspects of the theory and its transition to the classical domain, using a physical interpretation instead of the literal interpretation of the Hilbert space of the standard formalism. We clarify the difference between separable (product) and non-separable (entangled) states, and the local realism nature of the product states which obey Bell's inequality compared to the non-local nature of the entangled states which violate Bell's inequality. We note that the truly quantum mechanical processes such as the double-slit interference pattern, potential barrier tunneling, and in particular the entanglement process as we show in this paper, depend on the quantum mechanical phenomenon of wave-particle duality. In entanglement experiments, the quantum mechanical results obtained are from the *wave* aspect of the wave-particle quantum object (q-object), just like the interference pattern in double-slit experiments, not the particle aspect of the q-object which is currently unknowingly assumed. The wave aspect of the q-object gives rise to the non-local behaviour as would be expected from the quantum mechanical calculations, while the particle aspect exhibits local causal behaviour. This explains why the entanglement process is robust: the wave-particle q-objects of entangled states have definite physical characteristics at emission time and are free of fragile evanescent properties. In addition, we conclude that "spooky action at a distance" (SAAD) is not required.

1 Introduction

Quantum entanglement is a quantum mechanical property of a composite quantum system consisting of two or more subsystems (such as particles), describing a situation where a quantum subsystem is linked to another via a specific process leading to correlations between observable physical properties of the subsystems. The two-particle *spin-singlet* state

$$|\psi^-\rangle = \frac{1}{\sqrt{2}}\Big(|\uparrow_1\downarrow_2\rangle - |\downarrow_1\uparrow_2\rangle\Big) \tag{1}$$

is an example of state entanglement in bipartite systems [1, p. 19].

Schrödinger first introduced the term *entangled state* to describe the non-separable pure states of quantum systems [2], [1, p. 17]. Consider for example the emission of two photons of opposite polarization from a given process, such as the stimulated emission of polarization-entangled photons (see for example [3, 4]). The emitted photons are then conceived of as "entangled" pure states. The system is described by the wavefunction [4]

$$|\psi\rangle = \frac{1}{\sqrt{2}}\Big(|\circlearrowright_1\rangle|\circlearrowleft_2\rangle + |\circlearrowleft_1\rangle|\circlearrowright_2\rangle\Big) \tag{2}$$

where $\circlearrowright_i$ and $\circlearrowleft_i$ represent the right-hand and left-hand circularly polarized photons for $i = 1$ or 2. This wavefunction represents what we know of the entangled system, or alternatively represents our lack of knowledge of the specific properties of each photon that is emitted. All we know is that if one emitted photon is right-hand circularly polarized, then the other will be left-hand circularly polarized, and vice versa. Eq. (2) is a statement of this situation.

The predominant interpretation (the orthodox viewpoint [5]) is that the wavefunction (2) represents a physical description of the emitted photons in an unresolved evanescent state, and that once a measurement is performed on one of them, the wavefunction collapses, the measured photon's actual properties are then known and an instantaneous propagation of that information is perceived by the other photon so that it can assume the complementary properties required by the process – "spooky action at a distance" (SAAD) as Einstein called it, a process that some physicists like to think of as quantum magic, an approach that speaks more of metaphysics than physics. The reasons for the acceptance of this description will be considered in greater detail in Section 5.

Over the past decades, experiments have been devised to extend the range of quantum entanglements, to the point where classical scales have been achieved. This includes both the size of entangled objects (*e.g.* [6–10]) and the distances over which entanglement has been maintained (*e.g.* [11, 12]).

These are particularly stunning results as any interaction of one of the entangled components with its environment will collapse the entanglement. The probability of preventing such interactions and preserving entanglements over classical sizes and distances is exceedingly small. As noted by Jaeger [1, p. 20] "Indeed, *pure* such states of two-particle systems are exceptional rather than typical in the world; typically, a system very soon interacts with a number of other systems, so that, even if it were prepared in a pure state, it is typically described by a mixed state".

The probability that a photon can travel a distance x without interaction is given by [13] [14, Section 3.3.1] [15, p 304]

$$P_{no-int}(x) = \exp(-n_p\,\sigma\,x) \tag{3}$$

where n_p is the particle number density and σ is the total photon interaction cross-section including absorption and scattering. For propagation of photons in the atmosphere, $n_p \sim 2.5 \times 10^{25}\,\mathrm{m}^{-3}$ [16] and $\sigma \sim 180\,\mathrm{barn/molecule} \equiv 1.8 \times 10^{-26}\,\mathrm{m}^2/\mathrm{molecule}$ [17]. Using these values in (3), the no-interaction probability becomes

$$P_{no-int}(x) = e^{-0.45\,x} \tag{4}$$

where x is in meters. We see that for classical distances x, the probability $P_{no-int}(x)$ increasingly becomes very small. For example, $P_{no-int}(1\,\mathrm{m}) = 0.64$, $P_{no-int}(10\,\mathrm{m}) = 0.011$, $P_{no-int}(100\,\mathrm{m}) = 2.9 \times 10^{-20}$, $P_{no-int}(1\,\mathrm{km}) = 3.6 \times 10^{-196}$. For the value of 143 km of [11, 12] the probability that a photon can travel such a distance without interaction is astronomically small.

Hence the probability of preserving entanglements over classical sizes and distances and preventing the entanglement from collapsing due to physical interactions is exceedingly small. The question has to be raised: in light of these successful classical-scale experiments, are we currently misunderstanding the quantum entanglement process such that instead of a fragile entanglement situation as the above considerations indicate, we can derive a quantum entanglement process that leads to a physically robust entanglement situation that persists to classical scales as observed?

2 Quantum entanglement questions

Questions have been raised concerning entanglement and its extension to the classical (or macro) domain [18]. There is no doubt that some processes generate particle or photon pairs that have a definite relationship (correlation) between them (which are referred to as being entangled) and these relationships are confirmed experimentally. At stake here is the interpretation of the quantum entanglement process, and the impact of the understanding of this process on the development and technological applications of this quantum mechanical process – a misinterpretation can lead to considerations that are not physically realistic.

Questions have also been raised on the limited applicability of Bell's inequality [19–21], based on the assumptions used in its derivation. Bell [22] uses a single continuous parameter λ described by a probability distribution $\rho(\lambda)$: the basic limitation of this approach is that it imposes a quantum mechanical calculation approach on the analysis. Bell's derivation is only applicable to a specific class of hidden variable theories that can be represented by his starting equation and assumptions, which Jaynes [20] refers to as Bell theories. Some hidden variable theories don't need to satisfy Bell's starting equation to reproduce quantum mechanical results, as evidenced by Bohmian mechanics [23]. Bell's inequality is thus found to apply to a limited set of circumstances and situations, not to every quantum system. Selleri [24] provides a comprehensive review of the proofs of Bell's inequality.

Actual experimental demonstration of entanglement is a challenge. Entanglement experiments detect both entangled components within the same time window (see Subsection 5.3), so there is no way to confirm the presence or absence of SAAD – it is assumed to be present purely based on the predominant interpretation discussed in Section 1. Zhao [19] has proposed various experiments to clarify the physical properties of entanglement, including one to determine if the collapse of the entangled wavefunction due to the measurement of one component causes the transformation of the other component due to SAAD as is supposed in the orthodox interpretation. No reports of these experiments having been performed have surfaced – their execution should be given a high priority to help us better understand the phenomenon of entanglement.

3 Literal or physical interpretation?

To be able to answer the question posed at the end of Section 1 on a physically robust entanglement process, we need to have a better understanding of the physical description of quantum mechanics and of its transition to the classical domain. The orthodox view in the standard formalism of quantum mechanics is done via entanglement, wavefunction collapse and decoherence [25]. This is a literal interpretation of the Hilbert space mathematical theory of quantum mechanics developed by von Neumann and Dirac [26, 27]. However, as noted by Home and Whitaker [15, see p. 309], "[t]o conclude, there are aspects of classical reality pertaining to the macrophysical world that cannot be made consistent with quantum theory in any limit, at least using the standard formalism and decoherence models."

This thus leads us to consider other approaches to understand this problem. There are other interpretations of quantum mechanics which satisfy its principles – the book by Home [14] provides an excellent exposition of the conceptual foundations of quantum physics. As is well-known [28], the various formulations of quantum mechanics provide the same results (Schrödinger wave equation, Heisenberg matrix formulation, Dirac standard formalism, Feynman path integral, Bohm quantum potential among others) – the differences between them lie in the insights that these different formulations can provide. To understand the process under discussion, what is required is a physical interpretation based on a formulation of quantum mechanics that gives precedence to the physical rather than the mathematical aspects of the theory, and of its transition to the classical domain.

A physical theory of quantum mechanics which offers a logical transition into classical physics was first developed before it was displaced by the preferred standard formalism. This initial theory was instrumental in the development of quantum mechanics. Here we briefly recap this approach.

In classical mechanics [29], the phase space description of a system is given in terms of generalized coordinates $q = \{q_i\,;\ i = 1, 2, \cdots, N\}$ and canonical momenta $p = \{p_i\,;\ i = 1, 2, \cdots, N\}$ and its time evolution is described in terms of its Hamiltonian $H(q, p)$ using Hamilton's equations

$$\dot{q}_i = \frac{\partial H}{\partial p_i}\,, \quad \dot{p}_i = -\frac{\partial H}{\partial q_i}\,. \tag{5}$$

The Lagrangian of the system determines its dynamics in configuration space in terms of the coordinates $\{q_i\}$ through the Euler-Lagrange equations

$$\frac{\partial L}{\partial q_i} - \frac{d}{dt}\left(\frac{\partial L}{\partial \dot{q}_i}\right) = 0\,,\ i = 1, 2, \cdots, N\,. \tag{6}$$

If a statistical description of the system is desired, the state of the system is described in terms of a probability function $P(q, p)$ defined on the phase space, and its time evolution is given by

$$\frac{dP}{dt} = \{P, H\} + \frac{\partial P}{\partial t}\,, \tag{7}$$

where the Poisson bracket $\{P, H\}$ is given by

$$\{P, H\} = \sum_i \left(\frac{\partial P}{\partial q_i}\frac{\partial H}{\partial p_i} - \frac{\partial H}{\partial q_i}\frac{\partial P}{\partial p_i}\right). \tag{8}$$

The quantum mechanical description of the system derived from the foregoing considerations sees the dynamical variables (q, p) now interpreted as operators $(\hat{q}, \hat{p})$ acting on complex wavefunctions $\psi(q)$ generating observables and satisfying the commutation relation

$$[\hat{q}_i, \hat{p}_j] = i\hbar\,\delta_{ij}\,, \tag{9}$$

where $\hbar$ is Planck's reduced constant. This transition from a classical to a quantum mechanical description, known as *canonical quantization*, is effected (done) by the replacement of classical variables by quantum operators according to

$$q_i \to \hat{q}_i\,, \quad p_i \to \hat{p}_i \tag{10}$$

and (classical) Poisson brackets by (quantum) commutators according to

$$\{A, B\} \to \frac{1}{i\hbar}\,[\hat{A}, \hat{B}]\,. \tag{11}$$

The close relation between the classical and quantum dynamical equations is evident in the similarity between the classical equation of motion (7) and the quantum equation of motion as derived by Heisenberg,

$$\frac{d}{dt}\langle A\rangle = \frac{1}{i\hbar}\,\left\langle [\hat{A}, \hat{H}]\right\rangle + \left\langle \frac{\partial A}{\partial t}\right\rangle. \tag{12}$$

This result is a manifestation of Ehrenfest's theorem [30, see pp. 389–394] which holds that quantum mechanical expectation values $\langle A\rangle$ obey the classical equations of motion. This similarity points to the relation between the classical probability functions defined on the (q, p) phase space and the quantum mechanical expectation values obtained from the $(\hat{q}, \hat{p})$ operators acting on the complex wavefunctions $\psi(q)$ representing our knowledge of the system, which in the end obey the classical equations of motion.

This approach provides a physical interpretation that can be used to better understand the classical scaling of quantum entanglement. One of the characteristics of the above considerations is the physical reality of the underlying quantum mechanical system as it evolves into a classical system. In the following section, we consider the nature of quantum states as this has an impact on the robustness of entangled states.

4 The nature of quantum states

Jaeger [1, pp. 19–22] clearly communicates the importance of understanding the difference between separable (product) and non-separable (entangled) states. Over the past quarter century, the definition of entanglement has been extended, from information theory, to include mixed states that are separable when given as combination of products of subsystem states. Separable subsystem states are entirely uncorrelated (not entangled), while the entangled mixed states are the inseparable states – however, "[t]he problem of determining whether or not a given state of a composite system is entangled is known as the *separability problem*." [1, p. 21]. These entangled mixed states tend to somewhat muddle the entanglement water.

When considering separable (product) states, as noted by Jaeger [1, p. 21], "...the outcomes of local measurements on any separable state can be simulated by a local hidden-variables theory, that is, the behavior of systems described by such states can be accounted for using common-cause explanations". In other words, *separable* states can have definite physical properties when they are prepared.

It is important to note that Bell's inequality is violated only by entangled (non-separable) states. As noted by Jaeger [1, p. 22], "[t]he quantum states in which correlations between [components] A and B can violate a Bell-type inequality are called *Bell correlated*, or *EPR correlated*. If a bipartite *pure* state is entangled, then it is Bell correlated with certainty, as was first pointed out by Sandu Popescu and Daniel Rohrlich [31] and by Nicolas Gisin in the early 1990s [32].

However, no simple logical relation between entanglement and Bell correlation holds for the mixed entangled states".

Home [14, pp. 203–209] also makes the point. He concludes "an arbitrary mixture of factorable or product state vectors always satisfies Bell's inequality" as first shown by [33, 34], while " [f]or any given nonfactorable state vector of correlated quantum systems it is always possible to choose observables so that Bell's inequality is violated by quantum mechanical predictions." [14, pp. 205, 208] which was first demonstrated by [32] as seen previously.

Hence we have two different types of quantum states depending on whether they are product (separable) or entangled (non-separable) states. Separable states are consistent with local realism – they can be physical and local, while entangled states are not consistent with local realism, based on Bell's inequality. The normal reaction would be that there should be one consistent behaviour across all states, that the entangled states' behaviour trumps the separable states' behaviour, and hence quantum states are not consistent with local realism.

However, as seen in Section 2, questions have been raised about Bell's inequality, and this difference in behaviour between separable and entangled states may indicate that there is a problem with our understanding of Bell's inequality and of entanglement in general. We explore this question in greater details in the next section, and in doing so, show that we can in fact derive a robust entanglement process as observed in the classical scaling of quantum entanglement.

5 A robust entanglement process

The considerations of Section 3 reinforce the underlying physical building blocks of quantum mechanics: the superposition principle, Heisenberg's uncertainty principle and wave-particle duality. These are crucial to physically understand the entanglement process and demonstrate why it is a robust process. While the superposition property results from the linear wave equations used in the theory and Heisenberg's uncertainty principle results from the fact that quantum mechanical canonically conjugate dynamical variables are Fourier transform pairs of variables [35], wave-particle duality is a purely quantum mechanical property and is undoubtedly the most important of these. The truly quantum mechanical processes such as the double-slit interference pattern, potential barrier tunneling, and in particular the entanglement process as we will see in this section, depend on the quantum mechanical phenomenon of wave-particle duality. It is critical to analyze quantum phenomena in terms of wave-particle duality to fully understand them.

5.1 Non-existence of hidden-variables?

Home [14] does an extensive review of all proofs of the non-existence of hidden-variable theories in quantum mechanics and concludes "[h]aving established that contrary to folklore, no a priori compelling argument excludes the possibility of contextual hidden variable theories, the entire enterprise of developing a more complete description of quantum phenomena beyond the ambit of the standard interpretation becomes logically legitimate", and provides a reference to an example: "A pedagogically instructive model example of how a contextual hidden variable model can reproduce the standard quantum mechanical results is discussed by [36], who show in detail how such a model can provide an objectively real treatment of decaying, oscillating, and regenerating kaons" [14, pp. 195–196]. A contextual hidden variable model is one "in which the value obtained by a measurement is a function of the premeasurement value as well as the measurement context." [14, p. 37].

In addition, the basic deficiency of hidden-variable nonexistence proofs is that they are derived within the context of quantum mechanics. By its very nature, quantum mechanics is a probabilistic theory – so it is not surprising that such "proofs" find that deterministic results cannot be derived from quantum mechanics. The reader is referred to [21] for an example of this approach in the assumptions used by Bell in the derivation of his inequality, which leads to the conclusion that "it is not surprising that Bell's inequality is not satisfied in systems that obey quantum mechanics".

It is important to note that the label "hidden-variable theories" is attached indiscriminately to more complete theories of quantum mechanics. However, as in the case of Bohmian mechanics, a deterministic quantum physics theory does not need to include hidden variables. The proper path to such a theory is to start outside of quantum mechanics, derive a deterministic microscopic theory, and show that quantum mechanics can be derived from it – see [44] for an example of this approach.

Home [14] continues "[t]here are strong physical grounds for suspecting that the standard framework (formalism and interpretation) of quantum mechanics is fundamentally inadequate, though its empirical success to date is unquestionably impressive" [14, p. 37]. Home identifies the following aspects of quantum mechanics that are not well understood in the standard framework: the quantum measurement paradox, the classic limit of quantum mechanics, nonlocality of quantum mechanics arising from entanglement, and wave-particle duality [14, pp. 37-38]. These are the very factors at play in the robustness of the entanglement process as discussed in this paper.

5.2 Wave-particle q-objects

Entanglement experiments compare the behaviour of classical particles with quantum mechanical results that are unknowingly assumed to represent the particle aspect of the wave-particle quantum object (which for brevity we refer to as a "q-object"). It is important to realize that a q-object does not behave as a classical object due to its explicit wave-particle nature. For the wave aspect of a macroscopic object, its de Broglie wavelength is extremely small and its effect is negligible – however, in the quantum mechanical domain the impact of the wave-particle nature of the q-object becomes significant as observed in quantum physics. It is interesting to note that the impact of wave-particle duality has been observed at mesoscopic scales as reported in [6]. Thus a q-object is an object where the effect of wave-particle duality cannot be neglected.

In entanglement experiments, the quantum mechanical results obtained are from the *wave* aspect of the wave-particle q-object, just like the interference pattern in double-slit experiments. Hence, the results obtained in Bell experiments [38] and other entanglement experiments devised since then are the quantum mechanical results of the wave aspect of the wave-particle q-objects which are different from the particle results, again as seen in double-slit experiments (classical double-particle pattern versus quantum mechanical wave interference pattern). Similarly in Hardy experiments [39], the non-zero probability $P(A_1, B_1)$ [40] obtained in contradistinction to the local realist probability of zero is due to the *wave* aspect of the wave-particle q-object.

Wave-particle duality is still somewhat of a mystery in quantum mechanics. It is still understood mostly in terms of Bohr's principle of wave-particle complementarity which holds that the wave aspect and the particle aspect of an object are complementary aspects of a quantum object [14, see Chapter 5]. However, wave-particle duality arises naturally in the theory of Spacetime Continuum Elastodynamics (*STCED*) [57, 58] which is briefly covered in the Appendix and is considered in greater detail in [44]. This model provides a natural explanation for wave-particle duality, where an object, represented as a spacetime deformation, is composed of transverse and longitudinal modes, with the transverse mode corresponding to the wave aspects of the deformation and the longitudinal mode corresponding to the particle aspects of the deformation.

A wave-particle q-object is thus a hybrid object consisting of both wave and particle aspects which manifest themselves differently in experiments, depending on the type of measurement. We examine the experiments of Aspect *et al.* [41–43] using single-photon states covered in Home [14, Section 5.4] to demonstrate how they can be fully understood in terms of *STCED* wave-particle duality.

In the "light pulses on a beam splitter" experiment (Home's Fig. 5.2), for a pulsed photodiode light pulse, the wave aspect is expected to apply from the *STCED* wave-particle model – indeed, as Home comments "[t]he striking feature is that even under this apparently quantum condition, light pulses arriving at the beam splitter continued to behave as classical waves, and the inequality $[P_C \geq P_T P_R]$ was never observed to be violated" [14, p. 288], where P_T is the probability that a single count is transmitted, P_R is the probability that a single count is reflected, and P_C is the probability of a coincidence for that single count.

For a source of single photon pulses from an excited atom transition, using the same experimental setup, the particle aspect is expected to apply from the *STCED* wave-particle model – indeed, "a clear-cut violation of the inequality $[P_C \geq P_T P_R]$" was observed. "This confirmed single particle behavior of the single-photon states." [14, p. 288].

The experiment was then modified as per Home's Fig. 5.3 by removing the detectors on either side of the beam splitter and recombining the two beams using mirrors and a second beam splitter. Using the source of single photon pulses from an excited atom transition as previously, this time the wave aspect is expected to apply from the *STCED* wave-particle model as it is being treated as a wave (recombining the two beams) – indeed, the experiment "showed interference effects dependent on the difference in path lengths along two possible routes of single-photon pulses." [14, p. 288].

This provides experimental confirmation of the *STCED* wave-particle model where the wave-particle q-object consists of both wave and particle aspects which manifest themselves differently depending on the type of measurement. The behaviour is physical and logical. In addition, nothing precludes the wave-particle q-object from having the full physical properties encoded in the q-object. The results obtained in the case of non-rotated detectors are in agreement with local results that would be obtained classically, because there are no specific quantum effects coming out of the quantum mechanical calculations in this case.

This indicates that the entangled q-objects are emitted with deterministic physical properties. The wave aspect gives rise to the non-local behaviour (within causality requirements due to the particle aspect of the q-object) as would be expected from the quantum mechanical calculations, while the particle aspect exhibits local causal behaviour [44]. This explains why the entanglement process is robust: the wave-particle q-objects of entangled states have definite physical, not evanescent, characteristics at emission time.

5.3 Physical approach

This leads us to consider a physical approach which posits that the photons (for example), as wave-particle q-objects, are emitted with specific properties, but that due to our lack of knowledge of their detailed characteristics, can only be probabilistically characterized with the wavefunction ψ as a combination of the possible states and their probabilities (the realistic viewpoint [5]). Once a measurement is performed on one of the photons, its properties are resolved, thereby increasing our knowledge of the system, and allowing us to specify the properties of the other photon – a simple physical understanding of the process [21]. Such a process can easily scale to classical objects and distances, and is undeniably very robust as the q-objects' properties are determined at emission time, not evanescent depending either on an experimenter's whim or thought process, or on not having an interaction that would destroy the entanglement on its way to measurement resolution. The classical-scale experiments considered previously are then seen to be a confirmation of this approach.

The wavefunction is thus seen to be a probabilistic description of our (limited) *knowledge* of a quantum mechanical system, not a complete physical description of the system, with this probability being proportional to the *intensity* of the wavefunction as seen in [44]. This explains the laws of quantum probability [45,46]. We note the same behaviour for electromagnetic radiation, where the intensity is proportional to the energy density of the field, which can be converted to a probability by normalization, as seen in [44].

As a result of the measurement process, the original wavefunction description is superceded (the so-called collapse of the wavefunction) and is replaced by a more accurate wavefunction description of the quantum mechanical system that takes into account the results of the measurement process. As [37] puts it, "When a detector clicks the wavefunction does not 'collapse' from all over space to a point, it is simply that only part of it is now relevant.". It is important to note that this measurement process is effected (done) by the interaction of the quantum mechanical system with an outside agency, whether it is a measurement apparatus or an interaction with another quantum mechanical system.

This is a simple logical description of the physical process that does not require metaphysical "spooky action at a distance" explanations and, by the principle of Occam's razor, is a superior explanation of the entanglement process. It should be noted that the imaginary actors "Bob" and "Alice" which are used in the explanation of entanglement and SAAD, even though the explanation is presented as a sequential series of events, are both aware of the same experimental information within the same time window, as mentioned in Section 2, and hence fully satisfy Jaynes' analysis of entanglement experiments as discussed in [20, 21].

As Home points out, "[c]ontrary to a widely held misconception, we stress that no experiment probing quantum locality has yet tested quantum correlations measured across spacelike separation unambiguously." [14, p. 233]. In photon polarization correlation experiments [38], "[t]he claim of spacelike separation is usually based on ensuring that a photon on one side reaching a photomultiplier detector is spacelike separated from its partner passing the polarization analyzer on the other side." However, a typical photomultiplier detector requires about 30 ns for a current pulse to be generated following the arrival of a photon, which provides a different spacelike separation than that obtained from the resolution time of a photomultiplier which is usually of order 1 ns [14, p. 233].

It should be noted that the model proposed in this paper is independent of these so-called "loopholes". They are mentioned to indicate the difficulty of performing such experiments which raises cautionary notes on the concomitant dangers of wishful thinking and unrecognized assumptions, limitations and interpretation of the results.

5.4 Evidence for SAAD?

So why introduce a mysterious agent, "spooky action at a distance", when none is required? As we asked in Section 1, what prompts the acceptance of this description as part of the orthodox interpretation? The reason is that SADD is believed to be supported by the experimental evidence. However, the aforementioned considerations and the analysis of Jaynes [20,21,47] show that the experimental evidence can be explained without resorting to metaphysics, that the problem results from the assumption that a conditional probability represents a physical influence instead of the physically-correct logical inference that it is.

As Home and Whitaker write [15, p. 238],

> In one out of four cases, Alice is lucky with her measurement, and Bob's particle immediately becomes an identical replica of Alice's original. Then it might seem as if information has traveled instantly from Alice to Bob. Yet this strange feature cannot be used to send *usable information instantaneously*, because Bob has *no* way of knowing that his particle is already an identical replica. Only when he ***learns*** the result of Alice's Bell-state measurement, which is transmitted to him via classical means, can he exploit the information in the teleported quantum state.

where the emphasis is in the original text and we have in addition highlighted the word "learns".

In other words, what is believed to be "spooky action at a distance" is actually the experimenters' knowledge of the system suddenly increasing as a result of the measurement process, and the experimenters being in a position to logically infer the properties of the distant component, which is confirmed in the measurement performed on the distant component. In actual practice, in entanglement experiments, both measurements are done in the same time window (see Sections 2 and 5.3).

There is also a certain intellectual inertia at play. As Bell [48] commented, "Why is the pilot wave picture [Bohm's] ignored in text books? Should it not be taught, not as the only way, but as an antidote to the prevailing complacency? To show that vagueness, subjectivity, and indeterminism, are not forced on us by experimental facts, but by deliberate theoretical choice?" All very good questions.

6 Quantum information causality

The emerging concept of *information causality* [49–51] is an attempt to preserve causality based on the underlying premise that it is information that is the core element in the analysis of the entanglement process. The approach followed is to impose this concept as a principle of nature to avoid the special relativistic causality problems raised by SAAD. This concept unwittingly reflects Jaynes' analysis of entanglement experiments in that it focuses on information – however, Jaynes' analysis [20, 47] already accomplishes this without having to introduce an additional constraint in the guise of a new causality principle, and in so doing, also eliminates the need for SAAD.

7 Weak quantum measurements

Weak quantum measurements [52–56] is another emerging concept in quantum mechanics that has an impact on the understanding of the entanglement process. What is interesting with this approach is that it is possible to make minimal-interacting measurements, which leaves the collapse of the wavefunction in the literal interpretation of the mathematical standard formalism of quantum mechanics in a quandary: how can any measurement be done without collapsing the wavefunction?

The accepted explanation [54] is that the quantum state is not collapsed into eigenvectors, but instead, by a weak coupling of the measurement device and the system, is biased by a small angle such that the measurement device shows a superposition of several eigenvalues. The current status is summarized as follows: "weak measurement theory presents a plethora of strange quantum phenomena, not yet completely understood." [54]. There is no doubt that even a weak interaction measurement will have an impact on the system, and this approach, certainly experimentally valid, puts the wavefunction collapse of the literal interpretation of quantum mechanics into question.

The proposal of weakly interacting measurements was also introduced in [35] in the context of the application of the Nyquist-Shannon Sampling Theorem to quantum measurements. The author showed that Brillouin zones in Solid State Physics are a manifestation of the Nyquist-Shannon Sampling Theorem at the quantum level, where the translational symmetry of atoms in a solid resulting from the regular lattice spacing, is equivalent to an effective sampling of the atoms of the solid giving rise to the Brillouin zones. This raised the possibility of investigating new experimental conditions leading to new measurements previously considered unreachable, a possibility that is also considered possible in the literature on weak quantum measurements.

8 Discussion and conclusion

In this paper, we have considered the classical scaling of quantum entanglement. This implies a physically robust entanglement process, contrary to the fragile entanglement process that the standard formalism interpretation implies given that the probability of preserving entanglements over classical sizes and distances and preventing the entanglement from collapsing due to physical interactions is exceedingly small.

Actual experimental demonstration of entanglement, other than testing the Bell inequality, is a challenge. Entanglement experiments detect both entangled components within the same time window, so there is no way to confirm the presence or absence of "spooky action at a distance" (SAAD) which is assumed to be present based on the standard formalism interpretation.

To better understand the entanglement process and determine a robust entanglement process, we have considered a physical interpretation based on a formulation of quantum mechanics that gives precedence to the physical rather than the mathematical aspects of the theory used in the literal interpretation of the Hilbert space formulation.

We have considered the transition from a classical to a quantum mechanical description, known as *canonical quantization*, which is effected (done) by the replacement of classical variables by quantum operators, and have noted that one obtains closely related classical and quantum (Heisenberg) equations of motion. This result is a manifestation of Ehrenfest's theorem which holds that quantum mechanical expectation values obey the classical equations of motion.

We have considered the difference between separable (product) and non-separable (entangled) states. Mixtures of product (separable) states always satisfy Bell's inequality *i.e.* separable states can have definite physical properties when they are prepared. Bell's inequality fails only for entangled (non-separable) states. Hence separable states are consistent with local realism – they can be physical and local, while entangled states are not consistent with local realism, based on their violation of Bell's inequality.

We have seen that these considerations reinforce the underlying physical building blocks of quantum mechanics: the superposition principle, Heisenberg's uncertainty principle and wave-particle duality which is the most important of these. The truly quantum mechanical processes such as the double-slit interference pattern, potential barrier tunneling, and in particular the entanglement process as we have seen in this paper, depend on the quantum mechanical phenomenon of wave-particle duality. It is thus critical to analyze quantum phenomena in terms of wave-particle duality to fully understand them.

We have noted Home's [14] conclusion reached after an extensive review of all proofs of the non-existence of hidden-variable theories, that "no a priori compelling argument excludes the possibility of contextual hidden variable theories", giving legitimacy to the development of a more complete description of quantum phenomena beyond the standard interpretation. He further identifies the aspects of quantum mechanics that are not well understood in the standard framework: the quantum measurement paradox, the classic limit of quantum mechanics, nonlocality of quantum mechanics arising from entanglement, and wave-particle duality, which are the very factors at play in the robustness of the entanglement process as discussed in this paper.

We have noted that in entanglement experiments, the quantum mechanical results obtained are from the *wave* aspect of the wave-particle quantum object (which for brevity we refer to as a "q-object"), just like the interference pattern in double-slit experiments. A q-object is an object where the effect of wave-particle duality cannot be neglected.

Hence, Bell's inequality is violated in the quantum mechanical problem, that is the wave aspect of the wave-particle q-object, which is different from the particle results, as seen in double-slit experiments (particle versus wave patterns). However, nothing precludes the wave-particle q-object from having the full physical properties encoded in the q-object when the entangled q-objects are emitted. The wave aspect then gives rise to the non-local behaviour (within causality requirements due to the particle aspect of the q-object) as would be expected from the quantum mechanical calculations, while the particle aspect exhibits local causal behaviour. This explains why the entanglement process is robust: the wave-particle q-objects of entangled states have definite physical characteristics at emission time.

This has lead us to consider a physical approach which posits that the photons (for example), as wave-particle q-objects, are emitted with specific properties, but that due to our lack of knowledge of their detailed characteristics, can only be probabilistically characterized with the wavefunction ψ as a combination of the possible states and their probabilities (the realistic viewpoint). Performing a measurement on one of the photons resolves its properties which allows us to specify the properties of the other photon – a simple physical understanding of the entanglement process. Such a process can easily scale to classical objects and distances, and is undeniably very robust as the q-objects' properties are determined at emission time, not evanescent as in the standard formalism. The classical-scale experiments considered previously are then seen to be a confirmation of this approach.

We have also considered the emerging concept of *information causality* which is an attempt to preserve causality based on the underlying premise that it is information that is the core element in the analysis of the entanglement process, which is correct. However, Jaynes' analysis [20, 47] already accomplishes this without having to introduce an additional constraint in the guise of a new causality principle, and in so doing, also eliminates the need for SAAD.

We have also considered weak quantum measurements which is another emerging concept in quantum mechanics. There is no doubt that even a weak quantum measurement will have an impact on the system, and this approach, certainly experimentally valid, puts the wavefunction collapse of the literal interpretation of quantum mechanics into question.

It should be noted that quantum cryptography and quantum computing are then seen to depend on the *wave* aspect of the wave-particle q-object. This fundamental understanding should help accelerate the progress of these new development programs.

The resolution of the robustness of the entanglement process in classical scale quantum entanglement experiments is thus achieved within the wave-particle q-object explanation of the process in which entangled state q-objects have definite physical characteristics at emission time. Strong evidence has been provided to support this proposal.

The design of experiments to provide experimental evidence requires that experimentalists shift the paradigm used to test quantum theories. Currently experiments are designed to try to prove the applicability of quantum mechanics to entangled states by verifying various inequalities such as Bell's. The experiments suggested by Zhao [19] try to clarify the physical properties of quantum entanglement and includes experimental tests of the locality of the measurements of Bell states, experimental tests of the constituents of Bell states, and experimental tests of determinism in quantum measurements. In addition, even though the entanglement experiments currently performed agree with the model proposed in this paper, specific experiments need to be performed to test the model under conditions that emphasize that quantum entanglement behaviour results from the *wave* aspect of the wave-particle q-objects.

Appendix: wave-particle duality in *STCED*

It should be noted that wave-particle duality is considered in greater detail in [44] within the theory of the Elastodynamics of the Spacetime Continuum (*STCED*) [57, 58]. As shown in *STCED*, energy propagates in the spacetime continuum as wave-like deformations which can be decomposed into *dilatations* and *distortions*. *Dilatations* involve an invariant change in volume of the spacetime continuum which is the source of the associated rest-mass energy density of the deformation. On the other hand, *distortions* correspond to a change of shape of the spacetime continuum without a change in volume and are thus massless. Thus the deformations propagate in the continuum by longitudinal (*dilatation*) and transverse (*distortion*) wave displacements. This provides a natural explanation for wave-particle duality, with the transverse mode corresponding to the wave aspects of the deformation and the longitudinal mode corresponding to the particle aspects of the deformation.

Received on April 26, 2018

References

1. Jaeger G. Entanglement, Information, and the Interpretation of Quantum Mechanics. Springer-Verlag, Berlin, 2009.
2. Schrödinger E. Die gegenwaertige Situation in der Quantenmechanik. *Die Naturwissenschaften*, 1935, v. 23, 807; Discussion of probability relations between separated systems. *Proc. Cambridge Philos. Soc.*, 1935, v. 32, 446.
3. Lamas-Linares A., Howell J. C. and Boowmeester, D. Stimulated emission of polarization-entangled photons. *Nature*, 2001, v. 412, 887–890.
4. Hayat A., Ginzburg P. and Orenstein, M. High-rate entanglement source via two-photon emission from semiconductor quantum wells. *Physical Review B*, 2001, v. 76, 035339.

5. La Rosa A. Introduction to Quantum Mechanics. Portland State University Lecture Notes, Portland, 2017, Chapter 12, Quantum Entanglement.
6. Arndt M., Nairz O., Vos-Andreae J., Keller C., van der Zouw G., Zeilinger A. Wave-particle duality of C_{60} molecules. *Nature*, 1999, v. 401, 680–682.
7. Nairz O., Arndt M., and Zeilinger A. Quantum interference experiments with large molecules. *American Journal of Physics*, 2003, v. 71, 319—325.
8. Lee K. C., Sprague M. R., Sussman B. J., Nunn J., Langford N. K., Jin X. M., Champion T., Michelberger P., Reim K. F., England D., Jaksch D., Walmsley I. A. Entangling macroscopic diamonds at room temperature. *Science*, 2011, v. 334 (6060), 1253—1256.
9. Dolde F., Jakobi I., Naydenov B., Zhao N., Pezzagna N. Trautmann C., Meijer J., Neumann P., Jelezko F., and Wrachtrup J. Room-temperature entanglement between single defect spins in diamond. *Nature Physics Letters*, 2013, DOI: 10.1038/NPHYS2545, 139–143.
10. Belli S., Bonsignori R., D'Auria G., Fant L., Martini M. and Peirone S. Entangling macroscopic diamonds at room temperature: Bounds on the continuous-spontaneous-localization parameters. arXiv: quant-ph/1601.07927v3.
11. Xiao S. M., Herbst T., Scheldt T., Wang D., Kropatschek S., Naylor W., Wittmann B., Mech A., Kofler J., Anisimova E., Makarov V., Jennewein Y., Ursin R and Zeilinger A. Quantum teleportation over 143 kilometres using active feed-forward. *Nature Letters*, 2012, v. 489, 269–73.
12. Herbst T., Scheidl T., Fink M., Handsteiner J., Wittmann B., Ursin R. and Zeilinger A. Teleportation of Entanglement over 143 km. arXiv: quant-ph/1403.0009v3.
13. Townsend R. H. D. Stellar Astrophysics. University of Wisconsin-Madison Lecture Notes, Madison, 2008, Section 10, Radiation & Matter.
14. Home D. Conceptual Foundations of Quantum Physics, An Overview from Modern Perspectives. Plenum Press, New York, 1997.
15. Home D., Whitaker A. Einstein's Struggles with Quantum Theory, A Reappraisal. Springer, New York, 2007.
16. Value for "dry air" from "Molecular number density" table in Wikipedia under entry "Number density", accessed 10 March 2018.
17. Hubbell J. H. Photon Cross-Sections, Attenuation Coefficients, and Energy Absorption Coefficients from 10 keV to 100 GeV. Nat. Bur. Stand. (US) Report NSRDS-NBS-29, Washington DC, 1969, pp. 45–46.
18. Bruno N., Martin A., Sekatski P., Sangouard N., Thew R. T. and Gisin N. Displacement of entanglement back and forth between the micro and macro domains. *Nature Physics Letters*, 2013, DOI: 10.1038/NPHYS2681, 1–4.
19. Zhao H. L. On Bell's Joint Probability Distribution Assumption and Proposed Experiments of Quantum Measurement. arXiv: physics.gen-ph/0906.0279v4.
20. Jaynes E. T. Clearing Up Mysteries – The Original Goal. In Skilling J., ed. Proceedings Volume, Maximum Entropy and Bayesian Methods. Kluwer Academic Publishers, Dordrecht, 1989, pp. 1–27.
21. Millette P. A. On the Applicability of Bell's Inequality. *Progress in Physics*, 2016, vol. 12 (3), 211–215.
22. Bell J. S. On the Einstein–Podolsky–Rosen Paradox. *Physics*, 1964, v. 1, 195–200. Reprinted in Bell J. S. Speakable and Unspeakable in Quantum Mechanics. Cambridge University Press, Cambridge, 1987, pp. 14–21.
23. Dürr D., Teufel S. Bohmian Mechanics: The Physics and Mathematics of Quantum Theory. Springer-Verlag, Berlin, 2009.
24. Selleri F., ed. Quantum Mechanics Versus Local Realism: The Einstein-Podolsky-Rosen Paradox. Plenum, New York, 1988.
25. Joos E., Zeh H. D., Kiefer C., Giulini D., Kupsch J., Stamtescu I.-O. Decoherence and the Appearance of a Classical World in Quantum Theory, Second Edition. Springer-Verlag, Berlin, 2003.
26. von Neumann J. Mathematical Foundations of Quantum Mechanics. Princeton University Press, Princeton, (1932) 1996.
27. Dirac P. A. Lectures on Quantum Mechanics. Dover Publications, New York, (1964) 2001.
28. Styer D. F., Balkin M. S., Becker K. M., Burns M. R., Dudley C. E., Forth S. T., Gaumer J. S., Kramer M. A., Oertel D. C., Park L. H., Rinkoski M. T., Smith C. T. and Wotherspoon T. D. Nine formulations of quantum mechanics. *Am. J. Phys.*, 2002, v. 70 (3), 288–297.
29. Leinaas J. M. Non-Relativistic Quantum Mechanics. University of Oslo Lecture Notes, Oslo, 2003.
30. Ballentine L. E. Quantum Mechanics, A Modern Development. World Scientific Publishing, Singapore, 1998.
31. Popescu S. and Rohrlich D. Generic quantum nonlocality. *Phys. Lett. A*, 1992, v. 166, 293.
32. Gisin N. Bell's inequality holds for all non-product states. *Phys. Lett. A*, 1991, v. 154, 201.
33. Capusso V., Fortunato D. and Selleri F. Generic quantum nonlocality. *Int.J. Theor. Phys.*, 1973, v. 7, 319.
34. Home D. and Selleri F. *Riv. Nuov. Cim.*, 1991, v. 14 (9), 1.
35. Millette P. A. The Heisenberg Uncertainty Principle and the Nyquist-Shannon Sampling Theorem. *Progress in Physics*, 2013, v. 9 (3), 9–14. arXiv: quant-ph/1108.3135.
36. Home D. and Selleri F. *J. Phys. A*, 1991, v. 24, L1073.
37. Holland P. R. The Quantum Theory of Motion. Cambridge University Press, Cambridge, 1993.
38. Aspect A., Dalibard J. and Roger G. Experimental test of Bell's inequalities using time-varying analyzers. *Phys. Rev. Lett.*, 1982, v. 49, 1804–1807.
39. Hardy L. Nonlocality for Two Particles without Inequalities for Almost All Entangled States. *Phys. Rev. Lett.*, 1993, v. 71, 1665–1668.
40. Guo W. J., Fan D. H. & Wei L. F. Experimentally testing Bell's theorem based on Hardy's nonlocal ladder proofs. *Sci China-Phys Mech Astron*, 2015, v. 58, 024201-1–5.
41. Grangier P., Roger G. and Aspect A. *Europhys. Lett.*, 1986, v. 1, 173.
42. Aspect A. and Grangier P. *Hyp. Int.*, 1987, v. 37, 3.
43. Aspect A. In Miller A. I., ed. Sixty-Two Years of Uncertainty. Plenum, New York, 1990, pp. 45–59.
44. Millette P. A. Wave-Particle Duality in the Elastodynamics of the Spacetime Continuum (STCED). *Progress in Physics*, 2014, vol. 10 (4), 255–258.
45. Feynman R. P. The Concept of Probability in Quantum Mechanics. Lecture, 1951.
46. Feynman R. P., Leighton R. B., Sands M. Lectures on Physics, Volume III: Quantum Mechanics. Addison-Wesley Publishing Company, Reading, Massachusetts, 1965, Chapter 3, Probability Amplitudes.
47. Jaynes E. T. Probability in Quantum Theory. In Zurek W. H., ed. Complexity, Entropy and the Physics of Information. Addison Wesley Publishing, Reading, MA, 1990.
48. Bell J. S. On the Impossible Pilot Wave. *Foundations of Physics*, 1982, v. 12, 989–999. Reprinted in Bell J. S. Speakable and Unspeakable in Quantum Mechanics. Cambridge University Press, Cambridge, 1987, pp. 159–168.
49. Pawlowski M., Paterek T., Kaszlikowski D., Scarani V., Winter A. and Zukowski M. Information causality as a physical principle. *Nature Letters*, 2009, vol. 461, doi:10.1038/nature08400, T101–104.
50. Pitalúa-García D. Quantum information causality. arXiv: quant-ph/1210.1943v3.

51. Ringbauer M., Fedrizzi A., Berry D. W. and White A. G. Information Causality in the Quantum and Post-Quantum Regime. arXiv: quant-ph/1406.5034v2.
52. Fuchs C. A. Information Gain vs. State Disturbance in Quantum Theory. arXiv: quant-ph/9605014.
53. Vaidman L. Weak Value and Weak Measurements. arXiv: quant-ph/0706.1348.
54. Tamir B. and Cohen E. Introduction to Weak Measurements and Weak Values. *Quqnta*, 2013, vol. 2 (1), 7–17.
55. Svensson B. E. Y. Pedagogical Review of Quantum Measurement Theory with an Emphasis on Weak Measurements. *Quqnta*, 2013, vol. 2 (1), 18–49.
56. Vaidman L. Weak Value Controversy. arXiv: quant-ph/1703.08870.
57. Millette P. A. Elastodynamics of the Spacetime Continuum. *The Abraham Zelmanov Journal*, 2012, vol. 5, 221–277.
58. Millette P. A. Elastodynamics of the Spacetime Continuum: A Spacetime Physics Theory of Gravitation, Electromagnetism and Quantum Physics. American Research Press, Rehoboth, NM, 2017.

Matter in a Space of a Fractional Dimension. A Cosmological System of Spaces and Evolution of the Universe

Mikhail N. Mashkin
E-mail: mnmashkin@yandex.ru

In this article, we propose a model of evolution of the Universe from topological spaces as a sequence generating one space from another. While the Universe is modelled in the form of a fraction-dimensional space, where time is the manifestation of the fractional dimension of the space.

Introduction

The origin of the Universe is a key topic in modern physics. Expansion of the Universe still demands an explanation.

Forty years ago, the physicist A. D. Sakharov has introduced a hypothesis: objects of the three-dimensional space are compositions of objects of a two-dimensional space and a one-dimensional space.

Based on this hypothesis, we propose a new cosmological model. In the framework of this cosmological model, the three-dimensional space is generated by its sub-spaces of lower dimensions. So forth this cosmological model and the process generating the spaces are described in detail.

The cosmological model of the Universe

The topological approaches described in Alexandrov's *Combinatorial Topology* [1] are used here to introduce the new cosmological model of the Universe. So we have:

R^{-1} — a space, which dimension is -1 that means a lack of space;

R^0 — a space of zero dimension means a space of energy, which is similar to energy of a quark;

R^1 — a space, which dimension is 1, means a space of electric energy;

R^2 — a space, which dimension is 2, means a space of magnetic energy;

R^3 — a space, which dimension is 3, means a space of gravitational energy (the "weight space");

R^1, R^2 and R^3 — Euclidean spaces. Dimension of such a space is the number of freedom degrees of a material point located therein.

The process generating the aforementioned topological spaces is as follows.

The space R^0. As a result of inflation [2] as symmetrization, an R^{-1} space generates an R^0 space. The space R^0 is not Euclidean. Each object located in a space contains a part of the total energy of the space. As such one, the space R^0 contains two groups of symmetric objects. The additive energy of objects located in the space is zero. Interaction between objects of one group is proportional to their distance from each other. Objects of the space R^0 uniquely define this space itself. Hence, the space R^0 is a space of quark-like energy. Distances between the objects is determined by the difference in energies of these objects. Time is a factor of evolution of the space. This evolution factor (time) is manifested in the redistribution of energy between the objects, and in the change in the objects' number in this space (i.e. transition from one state of the space into another state of the space). When interaction between the objects of the space reached symmetry, time disappears. In this case, the space R^0 arrives at a singular state. As is known, a space is identical to a specific type of energy. Quark-like energy is identical to the space R^0. So, quark-like energy and generates the space R^0.

The space R^1. Due to symmetrization of the singularity of the space R^0, synthesis of two objects which are attributed to two different groups of the space R^0 generates an object of a higher-dimensional space R^1. This is a space of electric energy (see above). Thus the space of electric energy is generated. Objects of the space R^1 are charges. The numerical value of such a charge is equal to the modulus of the energy difference of two objects attributed to the space R^0. Interaction between two charges is proportional to the multiplying result of their numerical values. Time in the space R^1 is determined by transformation of energy of the space R^0 into electric energy. The space R^1 evolves from the space R^0 to the singularity state. Singularity of a space is another space in which time is absent. So, after the entire energy of the space R^0 is transformed into electric energy, time disappears. Energy of each single charge is unlimitedly and continuously distributed along the space R^1 according to the interaction.

The space R^2. Due to symmetrization of the singularity state of the space R^1, charges in the space are separated from each other by the sign of difference of the objects attributed to the groups of the space R^0. The groups of charges differ by their signs. Synthesis of two charges bearing different signs generates an object of a higher-dimensional space R^2 (a space of magnetic energy, see above). Thus the space of magnetic energy is generated.

Consider the generation process by the example of a single photon. The photon is a result of synthesis of two charges bearing different signs (the space R^1), which are equal in their absolute values. The photon energy is continuously and unlimitedly distributed along the space R^2. Interaction between two photons is inversely proportional to the distance between them, and is proportional to the product of their energies. A single photon is an object of the magnetic energy space R^2. Objects in the space R^2 have the rotational degree of freedom (the spin).

The space R^2 evolves from the singularity state of the space R^1 to its own state of singularity. After converting electrical energy into magnetic energy, the space R^2 arrives at its own singularity state: time disappears in the space.

The space R^3. As a result of symmetrization of the singularity state of R^2, objects of the space are separated by the rotational degree of freedom (the spin). Synthesis of two objects, which are located in the space R^2 and bear oppositely directed spins, generates an object of a higher-dimensional space R^3 (a space of gravitational energy, see above). Thus the space of gravitational energy, R^3, is generated. Objects of the space R^3 are composed of objects of the spaces which dimensions are 1 and 2. The mass of objects of R^3 is continuously and unlimitedly distributed along the space.

Evolution of the space R^3

At present, the process converting magnetic energy of the space R^2 into gravitational energy of the space R^3 is in progress. We suggest to refer magnetic energy of the space R^2 as dark energy (the vacuum-like substance according to Gliner [3,4]). In these terms, mass (gravitational energy) is represented by matter and dark matter. Dark matter is a result of conversion of the magnetic energy into the gravitational energy. In the process of evolution of the space R^3, the shared part of the gravitational energy increases. This leads to slowing the clock down in this space. The process of passage of light in a space is analogous to the process of registration of time by a clock. The speed of light in this case is the conversion factor of the length in a duration of time. This coefficient is a constant of the space R^3. The process of passage of light in the space R^3 is the process of motion of a photon in the space R^2. In the space R^3, there are regions of absorption and emission of the photon. The photon's trajectory in the space R^2 is mapped into the region of its registration in the space R^3 in the relation "one-to-many". Thus the photon is tunneling in the space R^3. With the increase in the mass fraction in space, the redshift effect arises: a clock slow down with the process of passage of light. Density of the gravitational energy of the space R^3 depends on the speed of light. The energy density of a space, reduced to time duration, is a constant value [5]: $d_t c_t^{r-1} = const$, where d_t is the density of matter at a given point of the space; c_t is the speed of light (the speed of time) at the given point of the space; r is the dimension of the space at the given point.

Matter in a space of a fractional dimension

Consider how we percept the space of our world. At present, the space is three-dimensional: three spatial coordinates with triangulation of three dimensions are required. The fourth coordinate is time. In this case, the qualitative difference between the coordinate of time and the coordinates of space is emphasized. It is suggested that there exists an infinite set of three-dimensional spaces. However, under certain conditions (such as that the light speed in vacuum is constant), the time coordinate can be expressed in terms of linear length and vice versa. This allows us to assume that the time coordinate and the space coordinates have the same nature. In this case, the question about the infinite set of three-dimensional spaces does not vanish. On the basis of the above, we consider the problem of generation of spaces in the framework of the theory of topology sets.

Consider metric spaces R^n. In accordance with [1], an empty set has a dimension of $n = -1$. A set R^0 containing only one point X_t has a dimension of $n = 0$. To go to a higher dimensional space, it is necessary to perform a continuous mapping of one point $X_t \in R^0$ into a continuous set of points $X \subseteq R^1$. Here are two ways to display the sequence: 1) in the form of the ε-displacement (see §1.1 of Chapter 6 in [1]), where the continuity sequence of the subsequent point from the previous one is observed; and 2) the transfer method, where this condition is not satisfied. Introducing the notion of a sequence maps, we thereby define the time factor. Here the time factor determines the process generating a space with a higher dimension from a space of a lower dimension. Using only the shift method to generate a space gives a set that has a beginning, i.e. the starting point of reference. To exclude the starting point of reference, it is necessary to use, at least once, the transfer method. To generate all points of the set R^1, an infinite set of steps (an infinite amount of time) is required.

Time is a quantitative characteristic of the displayed space. Introducing the time factor is equivalent to introducing a characteristic of the density of the mapping flow — the speed of time. By the speed of time, we understand the ratio of the number of displayed points of a higher dimension space to the number of points of a space of a smaller (than that generated these points) dimension. This determines the multiplicity: how many points of the higher dimension space is displayed by one point of the lower dimension space. The instant fulfillment of the mapping (the multiplicity is infinite) is identical to the infinite speed of time, which in all cases is dimensionless. Hence, the complete numerical axis (line) in the set attributed to the metric space R^1 can be obtained by instant mapping one point $X_t \in R^0$ into a continuous set of points $X \subseteq R^1$ using two methods: the shift and carry methods.

In this case, metric spaces with an integer dimension can be represented as spaces with the zero time speed (that means that time is absent — there is no generation process, the number of displayed points is zero). The Hilbert space can be decomposed into an infinite number of metric spaces of a finite dimension (see §2.4 of Chapter 1 in [1]), and the following relation is fulfilled: $R^{n-1} \subseteq R^n$. And the cardinality of the set $\{R^{n-1}\}$ is equal to infinity: $|\{R^{n-1}\}| = \infty$. This assumes that the speed of time is infinite when creating a space, in which n is an integer, from a space of a lower dimension. Under the condition that the complete covering of R^n is not fulfilled (the speed of time is finite), the covered subset of R^n can be represented by a space R^d having a dimension d, where $(n-1) \leqslant r d \leqslant n$, i.e. a space with a fractional dimension. It is proposed to define spaces, in which the speed of time is finite and differs from zero, as fraction-dimensional spaces. The time speed function depends on the numerical value of the space dimension, which is a real number. It monotonically decreases within the interval of dimensions $(n-1) < d < n$, see Fig. 1 below.

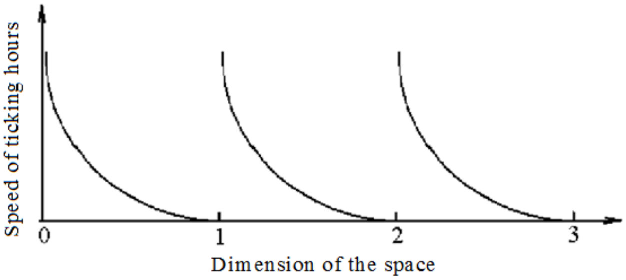

Fig. 1: The time speed of fraction-dimensional spaces.

The characteristic of the speed of time in the regions of our space is the speed of light. In this case, the distance from the point of radiation to the absorption point of a photon matches with the respective time duration registered by a remote clock. For example, the speed of light registered by our clock in this way on the boundary of the Universe exceeds the speed of light registered in our region of the space. When the numerical value of the time coordinate is reduced (with the respective numerical values the spatial coordinates) to the same measurement units, the magnitude of the speed of light is also dimensionless. Analysis of the speed of light in vacuum and material media shows that with the increasing density of matter the speed of light decreases. Reduction of the speed of light is accompanied by an increase in the dimension of space, see Fig. 1. This allows us to use the numerical value of the space dimension as the energy characteristic of the space. The density of matter has an inverse relation to the speed of time within an integer interval of the space dimension, see Fig. 2 below.

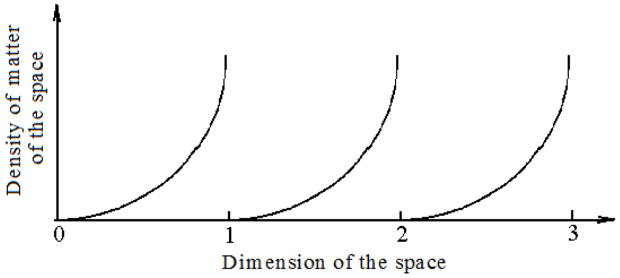

Fig. 2: The energy density of a fraction-dimensional space.

The boundary on the left of the fractional dimension (to an integer value of the space dimension) gives an infinite set of $(n-1)$-dimensional spaces having zero energy density. The boundary on the right is an n-dimensional space with an infinite density of matter, see Fig. 2. In this case, two versons representing a fraction-dimensional space are possible:

1. The space of an integer dimension R^{n-1} with the inclusions (domains or points and their neighborhoods, the set K) wherein the space is fraction-dimensional;
2. The space R_t^{n-1} containing the set S of points, each of which is a space of an integer dimension, and where covering Π by the set S of the space R_t^{n-1} is incomplete.

The first assumes that there exists a single integer-dimensional space containing a set of inclusions. The second — a set of integer-dimensional spaces. The latter is impossible under the previously stated assumption that an integer space contains infinite dense matter or is a continuum of integer spaces of lower dimensions. It is more preferable to assume that at all points of S we have the same space, but for each matter density d (time speed) the respective subset of points of this space is R_d^{n-1}. These subsets do not intersect with each other:

$$\bigcup R_{di}^{n-1} \cap R_{dj}^{n-1} = \emptyset, \quad \forall\, i \neq j;\; i, j = 1,\ 2,\ \ldots\ \infty.$$

All this is equivalent to the fact that each point of the space has one numerical value of the matter density parameter, i.e.

$$R^{n-1} \cap \bigcup R_{di}^{n-1} = R^{n-1}, \quad i = 1,\ 2,\ \ldots\ \infty.$$

In the case, where is a chain of the sets of points with zero numerical value of the matter density, interaction between the points at the ends of this chain occurs without time i.e. instantly (the speed of time is infinite there). However, the density of matter at each point of this chain is zero in this case as well as the space dimension of this set R^n. This is limiting and unreachable by definition. Moreover, the set R_d^{n-1} is uniquely mapped into one point of the space R_t^{n-1}. This implies the continuity of the mapping of R^{n-1} into R_t^{n-1}. The region of the set R_t^{n-1}, for given numerical values of d, belongs to the set of positive values of the numerical axis. Boundary of this region is the set of points in which the matter density of the space (i.e. the speed of time) is not defined. This corresponds to whole-dimensional spaces in which the time factor is absent. Suppose that the covering of Π remains unchanged. Corresponding to this covering, the average fractional dimension is $m_d = \mathrm{M}[d] = const$. The numerical characteristic of the coating, in turn, is proportional to m_d. If density of the coating is $d_\Pi = f(\Pi)$, then $m_d = d_\Pi$. From here, in a fraction-dimensional space, two time processes are possible:

1. The process of convergence of points of the set $S \subset R_t^{n-1}$ with each other upto coincidence (absorption), which makes possible to equalize the matter density throughout the entire space R^{n-1};

2. The process inverse to the convergence of points. Separation of one point into at least two points.

These two processes compete and provide a mapping of K into S, previously considered in two ways: the shift and carry methods. Due to the shift and transfer of points of the set R_t^{n-1}, mutual absorption of the points is possible. This should be accompanied with the reverse: the generation of points. This condition ensures that the covering of the same set R_t^{n-1} — the conservation law of the dimension (covering) of the space — remains constant. On the other hand, the covering Π is incomplete, but ensures the mapping S into the range of possible numerical values of the set R_t^{n-1}, — the positive numerical axis. This mapping is also determined by the fractional dimension through the time flow, and determines dynamics of the interaction processes of points of the set $K = \{R_d^{n-1}\}$ with each other. Therefore, **the space of a fractional dimension is dynamic**. The point of the set R_t^{n-1} corresponds to R_d^{n-1} — the set of points with the same density of matter of the space R^{n-1}. That is, in the absence of interaction with the remaining points, its position is determined only upto the set R_d^{n-1}. In this case, the point of the latter can be defined (perhaps) simultaneously at all points of R_d^{n-1}. That is, each such point has no distinctive features over the others. In the case of absorption (synthesis), it is possible and necessary to generate (divide) points of the spaces R_t^{n-1} and K. This is a necessary condition for generating a space (i.e. transfer). On the other hand, at a sufficiently high density of matter in the localization region of the point, the time speed is sufficiently small: displacement or transfer in this case almost does not require time. This also gives rise to the effect of supposedly simultaneous finding of one point in all places (points) of the localization region.

Results

Spaces of fractional dimensions contain local inhomogeneities in which the fractional dimension of the space differs from the fractional dimension of the vacuum region (which is the neighborhood of the inhomogeneity, the localization space). These are material objects. A local inhomogeneity is manifested in the numerical values of the parameters of the fields of a material object. The numerical values of the field parameters show the energy distribution of the space in the object's localization region. Combinations of the fields as the distribution characteristics of energies of the space give a description to the whole variety of the material objects. Degeneration of a fraction-dimensional space in the part of material objects leads to the appearance of zero-dimensional parameters that is quantum numbers. This quantum mechanism determines the discreteness of the set of phenomena there. A space with a unit inhomogeneity is an integer (for example, the three-dimensional space) everywhere, except for the heterogeneity itself. For an observer, it turns into a point because transition from one point to another does not require time. The very region of heterogeneity is a point at which the density of matter is infinite high. Passage through this point requires an infinite amount of time. Such a point is limiting, boundary, open, that is unreachable. Another boundary, with a uniform density of matter throughout the space, is also unreachable. Hence, we have an open interval for describing the entire set of material objects in a fraction-dimensional space.

Conclusion

So, a model of the cosmological system of spaces is proposed here. When considering this model, evolution of the Universe is discussed as well as the problem of description of fraction-dimensional spaces. Such spaces are defined as a results of energy conversion from the moment of inflation to R^3. The concept of singularity as a space in which time is absent is proposed. A "fractional space" is defined as a space in which the process of energy conversion from one type to another takes place. In this case, time is a factor of the process of energy conversion. Dynamics of fraction-dimensional spaces is predicted. These research results are a basis to calculate numerical values of the characteristics of such spaces.

Acknowledgements

I am thankful to Svyatoslav Petrovich Gabuda (April 23, 1936 — April 7, 2015), a Soviet/Russian physicist, Professor and Doctor of Physical and Mathematical Sciences, for valuable discussions.

Submitted on April 17, 2018

References

1. Alexandrov P.S. Combinatorial Topology. Volumes 1, 2, and 3 bound as one. Mineola (NY), Dover Publications, 1998 (reprinted from the 1957, 1959, and 1960 editions).
2. Linde A. Particle Physics and Inflationary Cosmology. Chur (Switzerland), Harwood Academic Publishers, 1990; arXiv: hep-th/0503203, p. 1–6.
3. Gliner E.B. The vacuum-like state of a medium and Friedman cosmology. *Soviet Physics Doklady*, 1970, v. 15, no. 6, 559–561.
4. Gliner E.B. Algebraic properties of the energy-momentum tensor and vacuum-like states of matter. *Soviet Physics JETP*, 1966, v. 22, no. 2, 378–382.
5. Mashkin M.N. Matter in a space of a fractional dimension (*in Russian*) http://www.sciteclibrary.ru/rus/catalog/pages/6525.html

Calculation of the Density of Vacuum Matter, the Speed of Time and the Space Dimension

Mikhail N. Mashkin
E-mail: mnmashkin@yandex.ru

An example of calculating the density of vacuum matter is presented based on the hypothesis of fractional dimension of our space. The speed of time and the dimension of our space are calculated.

Introduction

In the previous paper [1], we showed the hypothesis that the reduced density of space energy is constant:

$$d_t\, c_t^{r-1} = const, \tag{1}$$

where d_t is the density of matter (substance) at a given point in the space; c_t is the speed of light (proportional to the speed of time) at the given point in the space; r is the dimension of the space at the given point.

The previous analysis of this hypothesis showed that this formula exactly coincides with the topological thickness of the space with a non-integer dimension value, i.e.,

$$M = X\,Y\,Z^{r-2}, \tag{2}$$

where X, Y, Z are equivalent sets. Their permutations do not change the result of their Cartesian product.

Calculation of the numerical value of r can be performed based on the definition of fractional dimension, as a property of self-similar objects (fractional dimension is a dimension in the form of a fraction, for example, 23900/10000).

In our case, self-similar objects are convex bodies in n-dimensional spaces, for example, in the three-dimensional Euclidean space.

We will use a volume relative increase as an increment that provides fractional dimension (non-integer dimension). This is due to the alleged expansion of space, which is determined by the Hubble constant[*].

When moving at a measured distance in seconds, assuming that the speed of light in vacuum is constant, we obtain the value of the Hubble constant in units of acceleration:

$$H_a = H\,c_v = \frac{(55 \div 75)\times 10^3 \times 3\times 10^8}{3.086\times 10^{22}} = (5.35 \div 7.29)\times 10^{-10}\ \text{m/s}^2, \tag{3}$$

where c_v is the speed of light in vacuum.

Let us take a ball with a single radius equal to 1 second, i.e. 3×10^8 m as a basis for calculating the initial volume of a convex body. Further we will call the radius as a unit length.

As a time interval for comparison, we will select the time of transmission of a signal at a distance of the unit length, i.e. the time of 1 s.

As an increment, we will determine the increment of the initial volume v_1 during the passage of the signal at a distance of the unit length, see Fig. 1.

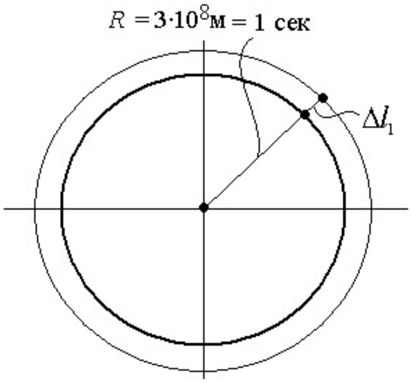

Fig. 1: A ball with a radius of a unit length.

In this case, the increment of the unit length is equal to:

$$\Delta l_1 = \frac{\int_1^2 H_a t\, dt}{c_v} = \frac{1.5 H_a}{c_v} = \frac{1.5\times(5.35\div 7.29)\times 10^{-10}}{3\times 10^8} = (2.68 \div 3.65)\times 10^{-18}\ \text{s}. \tag{4}$$

The relative increment is the ratio of the increment to the finite length:

$$\Delta r_1 = \frac{\Delta l_1}{1+\Delta l_1} \simeq (2.68 \div 3.65)\times 10^{-18}. \tag{5}$$

The relative increment of the initial volume v_1 is equal to:

$$\Delta v_1 \simeq 3\Delta r_1 = (8.04 \div 10.95)\times 10^{-18} \simeq 10^{-17}. \tag{6}$$

When the numerical value of r equals 3, the dimension of the constant in formula (1) is equal to

$$\frac{[\text{kg}][\text{m}]^2}{[\text{m}]^3[\text{s}]^2} = \frac{[\text{kg}]}{[\text{m}][\text{s}]^2}$$

or $L^{-1}MT^{-2}$, i.e. Pascal.

---

[*] The Hubble constant is defined currently within $H = 55 \div 75$ km/(s Megaparsec).

Hence, this can be interpreted as the modulus of the volume compression/expansion of the three-dimensional space.

In case when $3 > r > 2$, we will refer to the reviewed constant to as the module of the extension of a non-integer dimension space.

Then the formula (1) can be represented in the form of:

$$d_t \, c_t^{r-1} = M_r \,, \qquad (7)$$

where M_r is the module of the expansion of the space of non-integer dimension, taken in Pascals.

Calculation of the density of vacuum matter

Using the ratio (7), we can calculate the density of vacuum matter. With this, it is possible to accept in first approximation the vacuum density inside material bodies as that equal to the density of their substance.

Let is take the following approximations: the space dimension is constant, i.e. $r = const$, and is $r \simeq 3$; the effects of light dispersion are not taken into account.

Formula (1) contains three interrelated parameters: density, the speed of light and the space dimension. Consider the relationship between the speed of light and the matter density in detail. The table data of the refractive index (optical density) and the density of precious stones are shown in Fig. 2.

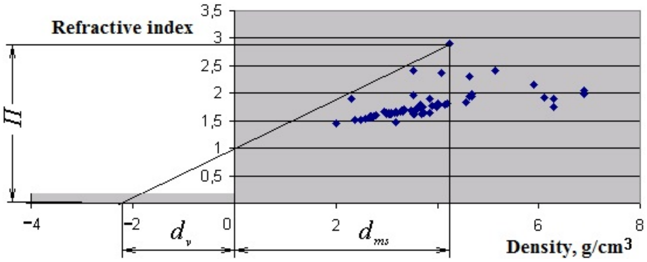

Fig. 2: The precious stones density.

Analysis of Fig. 2 allows us to suggest that the refractive index is linearly dependent on the matter density. Hence, we obtain the formula of the vacuum matter density outside material bodies:

$$d_v = \frac{d_{ms}}{\varPi{-}1} \,, \qquad (8)$$

where d_{ms} is the density of substance, $\varPi = c_v / c_{ms}$ is the refractive index, c_{ms} is the speed of light in the substance.

Here are the tabular data of the stones, used in jewelry industry. The data give the minimum of the calculated density of vacuum for diamonds and synthetic rutile (see Table for detail).

In the above calculations, we used the average density of substance. However, under real conditions inside real substances there are nodes of the crystal lattice in the form of ions or atoms which have a finite volume and their own density. For example, for a diamond we have the radius of the carbon atom $r_a = 0.077$, and the distance between the reflection planes (interatomic) $d = 0.356$ nm. Hence, the density of the carbon atom itself is 6,274 g/cm^3. Let us calculate the maximum reduced density between two carbon atoms located from each other at a distance d using the following formula:

The group of stones	Stone	Density, g/cm^3	Refract. index	Calc. vacuum density, g/cm^3
Colorless stones	Diamond	3.52	2.42	2.48
	Synthetic rutile	4.25	2.9	2.24

$$d_{red.} = \frac{m_c}{V_{c_1}} + \frac{m_c}{V_{c_2}} \,, \qquad (9)$$

where $V_{c_1} = \frac{4\pi}{3} r_1^3$ is the volume of a sphere with the first carbon atom in the center, $r_1 = 0.0385 \div 0.3165$ nm, $V_{c_2} = \frac{4\pi}{3} (0.356 - r_1)^3$ is the volume of a sphere with the second carbon atom in the center, m_c is the mass of the carbon atom.

Calculation by formula (9) shows that approximately 50% of the space between carbon atoms has a density of about 1 g/cm^3. Hence, the estimated density of vacuum substance obtained by formula (8) is less than 0.7 g/cm^3. The actual numerical value, obviously, is much lower, since the reduced density assumes uniform distribution of the substance of the carbon atom within the sphere.

Calculation of the space dimension and the speed of time

On the other hand, it follows from the definition of fractional dimension of space, that any volume of a space generates a volume in a certain multiplicity, which is equal to the speed of time [1]. For vacuum it is:

$$dt \simeq \Delta t = \Delta v_1 = 10^{-17}, \qquad (10)$$

i.e. any volume of a space, when a signal passes through it, generates a relative, additional volume equal to the speed of time.

The generation of the volume corresponds to a certain amount of gravitational energy. This amount can be compared to a quantum of energy which, taking into account formula (10), gives the ratio:

$$M_r \, V_1 \, dt = h, \qquad (11)$$

where V_1 is the generated unit volume, 1 m^3, h is the Planck constant (6.626×10^{-34} J s).

Our three-dimensional space is flat. The critical Friedman density of our space is about $d_f = 1{\times}10^{-28}$ kg/m^3. From here, we calculate the dimension of our space:

$$r = \frac{\log h - \log V_1 - \log d_f - \log dt}{\log c_v} + 1 = \\ = \frac{\log 6.626 - 34 - 0 + 28 + 17}{8 + \log 3} + 1 = 2.395; \qquad (12)$$

where $c_t \simeq c_v = 3 \cdot 10^8$ m/s; $d_f = d_t = 10^{-28}$ kg/m^3; $V_1 = 1$ m^3; $dt = 10^{-17}$.

If the space has a Friedman energy density, the photon speed in the region of the carbon atom is (on the average):

$$c_c = \sqrt{\frac{d_f}{d_c}}\, c_v = \sqrt{\frac{1 \times 10^{-28}}{6274}}\ c_v = \\ = 1.26 \times 10^{-16} \times 3 \times 10^8 = 37.9 \text{ nm/s}, \quad (13)$$

where d_c is the average density of matter inside the sphere of a carbon atom.

At the obtained speed of light inside the sphere of the carbon atom, the wavelength of visible radiation is:

$$\lambda_c = 1.26 \times 10^{16} \lambda_{mv} = 1.26 \times 10^{-16} \times 600 \times 10^{-9} = \\ = 7.56 \times 10^{-23} \text{ m}, \quad (14)$$

where λ_{mv} is the wavelength of visible radiation. This is about 10^{13} times less than the diameter of a carbon atom. This gives a possibility of interaction between the waves of visible radiation and a carbon atom which is represented as a drain funnel (the source — reverse funnel — tornado). That is the **photon**, as an object of magnetic energy, behaves as a **time magnetic monopole**: it can be absorbed and emitted.

Results

Substantiation and calculation of the density of space matter have been done. The concept of the time speed has been specified. The time speed of our space has been calculated. A formula for calculating the fractional dimension of our space has been obtained. The calculation of the fractional dimension of our space has been performed.

So, on the basis of representation of the fractional dimension of a space as a space with the presence of time, the following calculations were done: the density of vacuum matter, the speed of time and the dimension of our space.

Further calculation of the numerical values of the following properties — the substance density of material objects, the vacuum and space density as a whole — can be continued dealing with (see [1] for detail): conversion of magnetic energy into dark matter; dark matter interaction with matter; synthesis of objects of our space; a three-dimensional model of distribution of density of the outer space mass.

Submitted on April 17, 2018

References

1. Mashkin M.N. Matter in a space of a fractional dimension. A cosmological system of spaces and evolution of the Universe. *Progress in Physics*, 2018, v.14, issue 3, 131–134.

Fully Classical Quantum Gravity

Thomas C. Andersen
NSCIR, 8 Bruce St. B 841, Thornbury, Ontario, N0H 2P0, Canada
E-mail: tandersen@nscir.ca

It's an experimental fact that quantum objects in the ground state do not radiate electromagnetic energy, but what are the limits on our knowledge of the gravitational equivalent of this? In semiclassical gravity it is the expectation values of quantum particle positions that form the source for the Einstein equations, thus a particle or atom in a ground state emits no gravitational radiation. Here we instead assume a fully classical quantum gravity — the internal components of objects in a pure quantum state are assumed to classically radiate gravitational waves. The effects of this theory of microscopic gravity on the measured properties of the hydrogen atom, along with possibilities to experimentally measure the effects of atomic or nuclear scale gravitational radiation are explored.

1 Introduction

The quantum gravity problem remains unsolved in physics today. There are many possible solutions proposed, but almost all of them suppose the existence of the graviton. The graviton should have the same energy relation as the photon:

$$E_{graviton} = \hbar\nu. \tag{1}$$

There not only exists no experimental confirmation of this relationship for gravity, it is also widely known that an experiment to detect a single graviton is well beyond the capabilities of any present or future realizable experiment. Gravity may simply be a non quantum effect. Rosenfeld in 1963 is still very much relevant [1].

> *There is no denying that, considering the universality of the quantum of action, it is very tempting to regard any classical theory as a limiting case to some quantal theory. In the absence of empirical evidence, however, this temptation should be resisted. The case for quantizing gravitation, in particular, far from being straightforward, appears very dubious on closer examination.*

2 Other classical gravity theories

Semiclassical gravity can be summarized as a classical gravitational field coupled to quantum matter fields. While semiclassical gravity is widely thought of as a workable limiting approximation until a quantum theory of gravity is discovered, there are researchers who treat semiclassical gravity as a real possibility and hence in need of experimental tests [2]. The semiclassical equations for quantum gravity are as from Møller [3] and Rosenfeld [1]:

$$R_{\mu\nu} - \frac{1}{2}g_{\mu\nu}R = \frac{8\pi G}{c^4}\langle\Psi|T_{\mu\nu}|\Psi\rangle. \tag{2}$$

While seemingly straightforward, semiclassical gravity has subtleties, especially in determining the quantum expectation value (see Appendix A of Bahrami [4]).

Another classical treatment of quantum gravity comes from Roger Penrose with the *Gravitization of Quantum Mechanics* [5] where he posits that gravity connects not to the expectation value, but rather directly to each superposed quantum state. Gravitation causes collapse as the gravitational field of multiple superposed states becomes too energetic.

3 Fully classical quantum gravity

Fully classical quantum gravity (FCQG) uses Einstein's equations as given,

$$R_{\mu\nu} - \frac{1}{2}g_{\mu\nu}R = \frac{8\pi G}{c^4}T_{\mu\nu} \tag{3}$$

with the coupling to microscopic matter being on some assumed sub-quantum level, where particle positions always have a definite value, as in for instance de Broglie-Bohm mechanics [6]. Of course if one uses Bohmian mechanics in its entirety, then gravitation is also quantized, and particles will not radiate from their ground states. We thus assume here that quantization does not apply to gravity at all, that particle trajectories are real and that they interact directly and classically using the laws of Einstein's general relativity. In many ways it is similar to the program of stochastic electrodynamics (SED) [7], in that classical fields couple directly to sub-quantum particle motions. Indeed if one is to assume a SED like explanation of quantum behavoir, then gravity should also be treated classically.

4 Gravitational radiation from atoms and nucleons

Ashtekar [8] for example elucidates the need for a quantum theory of gravity by citing Einstein in 1916:

> *. . . Nevertheless, due to the inner-atomic movement of electrons, atoms would have to ra-*

> *diate not only electro-magnetic but also gravitational energy, if only in tiny amounts. As this is hardly true in Nature, it appears that quantum theory would have to modify not only Maxwellian electrodynamics, but also the new theory of gravitation.*

Using instead Rosenfeld's position that we must rely on experiment to show the need for quantum gravity, consider the energy loss rate of a circa 1916 style Bohr planetary hydrogen atom in the ground state, using Eddington's [9] formula for the gravitational energy radiated by a two body system (in the approximation that one mass is much heavier):

$$\frac{dE}{dt}(atom) = -\frac{32Gm_e^2 r_h^4 \omega^6}{5c^5} = -10^{-43}\text{eV/s}. \qquad (4)$$

Which even over the age of the universe amounts to an energy loss due to gravitational waves for a hydrogen atom in the ground state of only 10^{-25} eV. Why was Einstein worried about such a small rate of gravitational energy loss for a hydrogen atom? In contrast the electromagnetic lifetime of the classical hydrogen atom is about 10^{-11}s which of course helped lead to the discovery of quantum mechanics.

As a comparison to the above estimate, a quantum mechanical prediction of the lifetime of the $3_p - 1_s$ state for emitting a graviton is about 1.9×10^{39}s [10, 11], which is within a few orders of magnitude of the fully classical estimate above.

This energy loss is of no experimental significance. So we can conclude that the stability of atomic orbitals is not an experimental indication of a need for quantum gravity. In other words we cannot experimentally determine if atoms radiate gravitational waves continuously or not.

4.1 Gravitational radiation from within nuclei

The Sivram-Arun paper *Thermal Gravitational Waves* [12] is an expansion of Weinberg's results in his 1972 book [10]. Both calculate the gravitational wave (GW) emission from nuclei passing each other thermally in an astrophysical hot plasma (stars). In fully classical quantum gravity we make the additional assumption that gravitational waves are also produced by nucleon motion inside each individual nucleus, even in the ground state, greatly increasing GW emission and making it happen at any temperature, since it arises from internal nucleon movements within each nucleus. Calculating an estimate for the GW emission would depend on the model one uses for the nucleus. The Fermi gas model of the nucleus assumes that the nucleons are free to move inside the potential well of the nucleus. Since we are assuming that gravity is fully classical, we can use the same calculations as that of Weinberg and Sivram to arrive at an estimate of gravitational wave emission from nucleons inside nuclei.

4.2 A GW nuclear emission/absorption model

Taking the calculation of Weinberg to nuclear material, Sivaram finds a rate of 10^{-16}eV/s per neutron [12] (using their neutron star calculation). Fully classical quantum gravity would then suggest that the Sun emits about 10^{22} watts of 10^{22} Hz gravitational wave energy, as opposed to the 10^9 watts at a lower atomic frequency that Weinberg calculates from plasma conditions only.

Another way to arrive an estimate for GW emission in nuclei is to treat a nucleus as having several nucleons moving in it at some typical internal velocity. The speed of nucleons is given by their kinetic energy in the Fermi gas model with a peak momentum of about 250 MeV/c. Using only one pair of these peak energy nucleons and setting $r = 1$ fm, Eddington's formula for a bar of mass 2 nucleons, spinning at a nuclear 10^{23} Hz, predicts an emission rate of about 10^{-9} eV/s.

While these two approaches to calculate the GW emission of a nucleus in the fully classical model differ by several orders of magnitude, GW emission rates near these levels hint that such effects (or perhaps more likely a lack of effect) might be measurable in the lab.

Experiments might need to use differential absorption effects to arrive at results. Absorption models are harder to quantify, as the cross section estimate is quite uncertain due to unknown detailed information on particle substructure.

Within this fully classical quantum model each nucleon will have its own characteristic spectrum of nucleon-frequency gravitational waves, depending on the structure and size of the atomic nucleus. Experiments similar to those done to look for "big G" could use dissimilar materials for the masses whose force of attraction is to be measured. It's notable that experiments to determine Newton's constant G have had great difficulty obtaining consistent results. Most measurements of G do not agree with each other to within the errors carefully determined by the experimenters [13].

Another experimental avenue would be to search for GW interaction effects between the bulk of the earth and masses in a lab of dissimilar materials.

5 Emission/absorption parameter space

Fig. 1 is a sketch of allowed emission and absorption parameters. Some — but not all — combinations of emission and absorption parameters are ruled out by experiment. Towards the upper left of the image limited absorption combined with higher emission would mean that the stochastic background of gravitational waves would be too energetic, having for example energy greater than the baryonic mass in the universe. The phrase "stability of nuclei" refers to the experimental fact that nuclei live for billions of years. On the right a ruled out region exists where absorption cross sections are not physically likely. The top line shows a calculation for the gravitational wave emission rate of a proton due to parton (quark) motion. "Nuclear emission (high)" refers to the Eddington

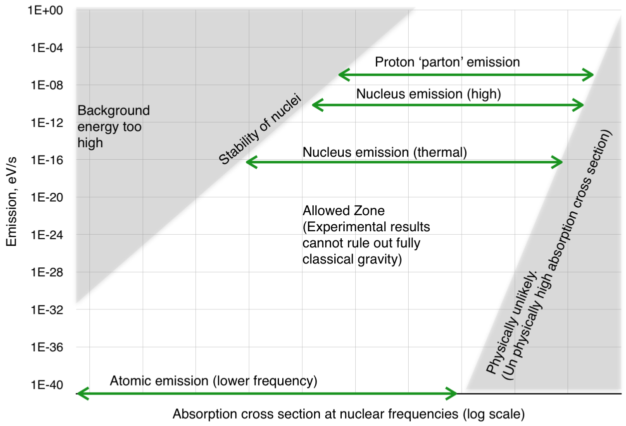

Fig. 1: Nuclear frequency gravitational wave emission and absorption. The elusive nature of gravitational wave detection means that even fully classical quantum gravity cannot be experimentally ruled out. The frequency of the gravitational waves is that of nucleons ($\omega \approx 10^{22}$ Hz).

emission rate for a heavy nucleus, while the lower nucleus emission rate is calculated assuming thermal Coulomb GW emission inside each nucleus.

6 Discussion

Due to the weak nature of gravitational effects on subatomic particles, even fully classical gravity cannot be experimentally ruled out at this time. Quantum gravity experiments that are possible with today's technology are very rare, this proposal represents an opportunity to test one of the tenants of quantum gravity.

Null results from experiments as described here will be able to constrain the allowed parameter space of a fully classical theory of microscopic gravity, thus suggesting that gravity needs to be quantized.

These tests are also a test of the ubiquity of quantum mechanics. With a non null result the conceptual foundations of quantum mechanics would be in question, as gravity might then be determined to be outside of the realm of quantum mechanics.

Submitted on April 1, 2018

References

1. Rosenfeld L. On Quantization of fields. *Nuclear Physics*, 1963, v. 40, 353–356.
2. Großardt A. Newtonian self-gravity in trapped quantum systems and experimental tests. arXiv:1702.04309 [quant-ph].
3. Møller C. Les theories relativistes de la gravitation. Colloques Internationaux CNRS, Paris, p. 91, 1962.
4. Bahrami M., Großardt A., Donadi S., and Bassi A. The Schrödinger Newton equation and its foundations. arXiv:1407.4370 [quant-ph], 2014.
5. Penrose R. On the Gravitization of Quantum Mechanics 1: Quantum State Reduction. *Found. Phys.*, 2014, v. 44, 557–575.
6. Bohm D. A suggested interpretation of the quantum theory in terms of "hidden" variables. I. *Physical Review*, 1952, v. 85(2), 166–179.
7. De la Peña L., Cetto A.M., and Hernández A.V. The Emerging Quantum, 2015.
8. Ashtekar A., Reuter M., and Rovelli C. From General Relativity to Quantum Gravity. arXiv:1408.4336 [gr-qc], 2014.
9. Eddington A.S. The Propagation of Gravitational Waves. *Proceedings of the Royal Society of London A: Mathematical, Physical and Engineering Sciences*, 1922, v. 102(716), 268–282.
10. Weinberg S. Gravitation and cosmology : principles and applications of the general theory of relativity. Wiley, 1972.
11. Boughn S. and Rothman T. Aspects of graviton detection: graviton emission and absorption by atomic hydrogen. *Classical and Quantum Gravity*, 2006, v. 23(20), 5839–5852.
12. Sivaram C. Thermal Gravitational Waves. arXiv:0708.3343, 2007.
13. Rosi G., Sorrentino F., Cacciapuoti L., Prevedelli M., and Tino G.M. Precision measurement of the Newtonian gravitational constant using cold atoms. *Nature*, 2014, v. 510(7506), 518–21.

Kirchhoff's Law of Thermal Emission: Blackbody and Cavity Radiation Reconsidered

Pierre-Marie Robitaille

Department of Radiology and Chemical Physics Program, The Ohio State University, Columbus, Ohio 43210, USA.
E-mail: robitaille.1@osu.edu

Kirchhoff's law of thermal emission asserts that, given sufficient dimensions to neglect diffraction, the radiation contained within arbitrary cavities must always be black, or normal, dependent only upon the frequency of observation and the temperature, while independent of the nature of the walls. In this regard, it is readily apparent that all cavities appear black at room temperature within the laboratory. However, two different causes are responsible: 1) cavities made from nearly ideal emitters self-generate the appropriate radiation, while 2) cavities made from nearly ideal reflectors are filled with radiation contained in their surroundings, completely independent of their own temperature. Unlike Kirchhoff's claims, it can be demonstrated that the radiation contained within a cavity is absolutely dependent on the nature of its walls. Real blackbodies can do work, converting any incoming radiation or heat to an emission profile corresponding to the Planckian spectrum associated with the temperature of their walls. Conversely, rigid cavities made from perfect reflectors cannot do work. The radiation they contain will not be black but, rather, will reflect any radiation which was previously incident from the surroundings in a manner independent of the temperature of their walls.

1 Introduction

Kirchhoff's law of thermal emission was formulated in 1859 [1, 2]. It is often presented as stating that, at thermal equilibrium, the emissivity of an object, ϵ_ν, is equal its absorptivity, α_ν. However, this should properly be considered as 'the law of equivalence', first proposed by Balfour Stewart [3] in 1858.

Kirchhoff's law extended much beyond Stewart's [3] and stated that, given thermal equilibrium, the radiation contained within an arbitrary cavity was depended only on the temperature of the enclosure and on the frequency of observation [1, 2]. Such radiation was completely independent of the nature of the walls [1, 2]. It was because of Kirchhoff's law that blackbody, or normal, radiation has always been viewed as independent of the lattice and unlinked to a physical cause [4]. Clearly, if Kirchhoff was correct and blackbody radiation was independent of the nature the walls, then such radiation could not be ascribed causality in the emitting structure.

Yet, it has been known for over 200 years that the radiation emitted from objects was highly variable [5]. In 1804, Leslie reported that the emission of surfaces depended on their nature and established the primacy of lampblack as a blackbody surface [6]. As a result, lampblack or soot, along with graphite, soon gained a dominant role in the construction of laboratory blackbodies (see [7] and references contained therein). The nature of the surface producing a thermal spectrum clearly did matter, in stark contrast to Kirchhoff's claims relative to cavity radiation [1, 2].

In the early 19^{th} century, blackbodies were simply objects made from graphite or coated with materials such as soot and lampblack. Carbon black was also employed, a pigment used in paints since pre-historic times [8]. Eventually, blackbodies became increasingly sophisticated devices, typically cavities. Other good absorbers of radiation slowly moved onto the scene relative to the construction of laboratory blackbodies [9–11], but graphite, soot, and carbon black retained their pre-eminent role [12]. Max Planck soon benefited from the construction of advanced cavities [9–11], when he formulated the blackbody solution [13, 14]. Contrary to Kirchhoff law [1, 2] the nature of the walls was thereby proven to be important on a practical level. It governed the quality of a blackbody. The quest for ever blacker surfaces [15–22] has now turned to novel structural absorbance approaches guided by samples as diverse as butterflies [23, 24] and birds [25]. Yet still today, many blackbodies in national laboratories are based upon the use of graphite (e.g. [26, 27]).

It remains true that blackbodies are specialized cavities which depend entirely on the nature of their walls [7, 9–12, 26, 27]. Laboratory blackbodies are made from materials that have an elevated emissivity over the range of interest, as is widely known throughout metrology. This fact alone is sufficient to illustrate that Kirchhoff's law cannot be valid.

As such, it is surprising that many still believe that any arbitrary cavity can produce a blackbody spectrum. In the laboratory, this was never the case. Planck himself [13] was dependent on the work of leading scientists in order to obtain a spectrum with the blackbody frequency distribution [9–11]. If Kirchhoff law had been correct [1, 2], this should not have been necessary.

The author has previously stated that Kirchhoff's law was not valid (see [4, 7, 12] and references therein), as it has no proper theoretical [28] or experimental proof. Planck's equation [13, 14] remained unlinked to a physical mechanism [4] because of Kirchhoff's law [1, 2]. As a result, physics was prevented from accounting for the production of a thermal photon from a simple cavity made from a block of graphite. Blackbody radiation remained, according to Kirchhoff, independent of the nature of the walls [1, 2]. In this respect, Planck's equation [13] was unique in spectroscopy. This has enabled scientists, in disciplines other than condensed matter physics, to infer that thermal photons could be produced without having recourse to a physical lattice, as was clearly required when emitted from graphite [4]. This has also enabled Max Planck to claim that his equation had universal significance [14, §164]. But in reality, Planck's solution was strictly limited to actual blackbodies (e.g. [7, 9–11, 26, 27]) and not to all cavities.

Thus, cavity radiation is reconsidered herein as to refute Kirchhoff's law [1, 2] and place a proper perspective on cavity radiation. In order to do so, cavities were constructed from materials which acted as nearly perfect absorbers or reflectors of radiation in the infrared. The results are discussed in terms of the work required to convert incident energy into normal radiation within the blackbody cavity. Conversely, the existence of nearly perfectly reflecting cavities is discussed in the context of resonant cavities used in magnetic resonance imaging [29], microwave cavities [30, 31], and lasers [32]. The findings demonstrate that cavity radiation is absolutely dependent on the nature of the walls. Consequently, Kirchhoff's law was never valid [4, 7, 12] and Planck's equation is not universal, as confirmed by a wide array of experimental results [29–32].

For the sake of brevity, the challenge to Kirchhoff's law presented herein can be limited to the study of a single approach without any loss in content. In 1954, de Vos published his *Evaluation of the Quality of a Blackbody* in the journal *Physica* [33]. This article has become a classic in blackbody radiation. de Vos [33] examined the quality of cavities constructed from materials with varying emissivity by noting the change upon incident radiation. This radiation was allowed to enter a cavity, exit, and be monitored with a detector placed at various angles. For cylindrical cavities, de Vos was concerned with the ratio of the length of the cavity to its diameter. He demonstrated that the radiation within cavities appeared to become increasingly isotropic as this ratio was increased [33]. However, de Vos had not demonstrated that all cavities will be black, independent of incident radiation. In fact, de Vos was concerned with the degree to which the surface of the cavity was either specular or white [33]. He did not evaluate whether a cavity could actually emit photons at the correct temperature. Thus, his work provided only limited insight into blackbody radiation [33]. He did analyze to what extent the surface property of a cavity affected the change of incoming light into fully diffuse reflection [33]. However, if a cavity was not constructed of a near ideal absorber, it was not necessarily black unless it was able to receive the proper incident radiation from its surroundings.

At the same time, if a cylindrical hole of sufficient depth was placed in a material with an elevated emissivity, the findings from de Vos suggest that the resulting cavity should indeed be black [33]. This approach was therefore implemented in this work in order to construct a simple blackbody cavity from small blocks of graphite. In parallel fashion, nearly perfectly reflecting cavities were constructed from blocks of brass, copper, and aluminum.

2 Materials and methods

Infrared images were obtained using a CompactPro thermal imaging camera (Seek Thermal, Inc., Santa Barbara, CA 93117; Thermal.com) interfaced with an Android (version 4.4.2) cell phone, as shown in Fig. 1A.

The camera had a focusable lens and a 32° field of view. It was equipped with a 320×240 thermal sensor, had a temperature range of -40 to 330°C, and was capable of obtaining ei-

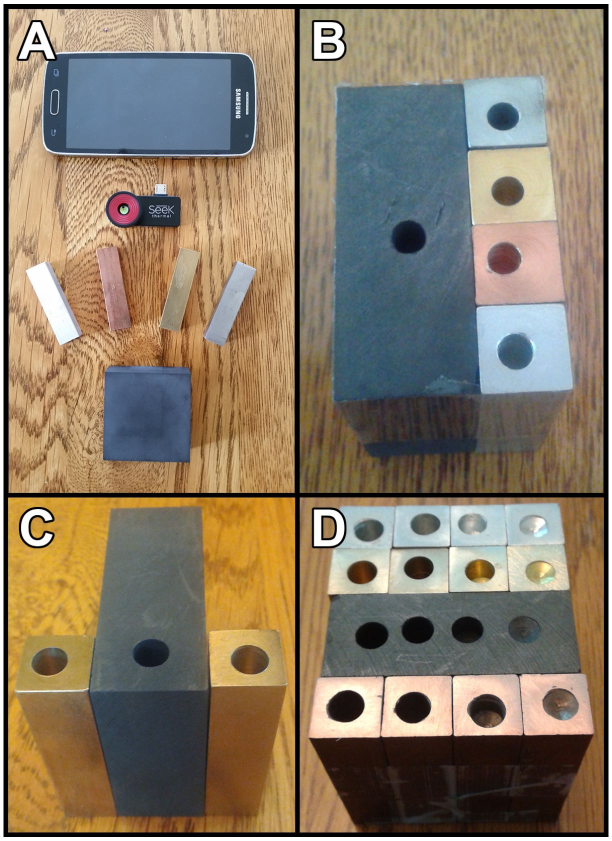

Fig. 1: A) Photograph of the Android phone, Seek Thermal camera, and aluminum, copper, brass, steel, and graphite blocks; B) Block assembly I (graphite on the left, then on the right from top to bottom: steel, brass, copper, aluminum). Note that two small scratches are visible near the graphite cavity. C) Block assembly II (brass, graphite, brass). D) Block assembly III (horizontal rows from top to bottom: aluminum, brass, graphite, copper).

ther still images or video. All images were obtained with the camera operating in white mode, except for Fig. 2A, where black mode was utilized.

Cylindrical cavities where constructed by drilling a small hole into 12.5 × 12.5 × 50 mm blocks of copper, aluminum, brass, and steel (Specific Gravity Metal Blocks, EISCO, Haryana 133001, India). The expected emissivity of the copper, brass, and steel holes should be on the order of 0.03-0.1 [34]. The type of steel was unknown. A 20 × 50 × 50 mm 99.9% Purity Graphite Ingot Block EDM Graphite Plate Milling Surface (Otoolworld, China) was used to build the reference blackbody using the same approach.

Cavities were produced with a drill press using either standard $\frac{3}{16}''$ or $\frac{1}{4}''$ diameter drill bits or a DeWalt Pilot Point $\frac{1}{4}''$ diameter drill bit to the depth described in the figure legends. Cavities were examined at room temperature or after having reached steady state while being heated on a hotplate (Cuisinart, East Windsor, NJ) to a temperature of approximately ~304°C. Small graphite particles were made from 2 mm mechanical pencil refills (Menards, Eau Claire, WI) cut to a length of 0.5 cm and inserted into the cavities of interest.

Experiments were initiated at room temperature, by placing the camera at a distance of ~20 cm above the table surface and therefore ~15 cm above the surface of the block assembly. The eye of the camera was positioned directly over the center of this assembly. In order to document the effect of ambient radiation on the cavities, a galvanized steel rod was placed in an oven, heated to ~232°C, and then brought near the cavities, as described in the figures.

3 Results

Thermal images are presented in Fig. 2 with the corresponding schematic representations outlining the position of the rod in Fig. 3. In Fig. 2A, a thermal image is presented in black mode, revealing that all the cavities appeared nearly the same at room temperature. In this image, there was also reflection of thermal radiation from the body of the observer onto the block assembly. Thus, on cursory examination, Kirchhoff's law appeared valid as all cavities essentially contained the same radiation. Still, the block was positioned within a room filled with radiation at the same temperature. Therefore, it was important to determine whether the cavities were generating radiation on their own or simply manifesting the radiation in their surroundings.

For other studies, the camera was switched to white mode and the cavities all appeared black, as seen in Fig. 2B. Next, in Fig. 2C-F (see schematics in Fig. 3C-F), a heated galvanized steel rod was placed above their surface. The rod had been heated to ~232°C. In Fig. 2C, the rod was positioned to the right of the steel cavity (see schematic Fig. 3C). With the heated rod in this position, the graphite and steel cavities could not be filled with its radiation. These two remain pretty much as they were with just a tiny spec of reflection at the graphite cavity. Thus, radiation from the rod was reaching this cavity as well, as expected. At the same time, the aluminum, copper, and brass cavities were immediately filled with radiation from the rod.

The rod was then moved to the left in Fig. 2D, as shown in Fig. 3D. Notice, once again, that there was no effect on the graphite cavity and that only a slight reflection was observed at the top of the steel cavity. However, all the others were filled with radiation from the rod. In particular, note the pattern in the brass cavity revealing that it was still not able to fully convert incoming radiation into isotropic ejected radiation. This indicated this cavity should be deeper to render the radiation fully isotropic, as suggested in de Vos' classic work [33].

In Fig. 2E, the rod was placed near the center of the block as represented in Fig. 3E. The three cavities from aluminum, copper and brass were again filled with rod radiation, but the graphite cavity remained unaffected and the steel cavity almost unaffected. However, reflection of rod radiation could be observed in the scratches on each side of the graphite cavity. As such, radiation from the rod was clearly reaching this cavity. Finally, in Fig. 2F, the rod was positioned just to the right of the steel cavity as shown in Fig. 3F. In this position, the steel cavity was no longer black. Now, it could be observed that rod radiation was able to partially fill the steel cavity. Nonetheless, the bottom of this cavity was darker, thereby indicating that steel had a much higher emissivity than the aluminum, copper, or brass cavities, but was not on par with graphite. The aluminum, copper, and brass cavities all appeared filled with radiation from the rod.

Next, the effect of inserting a small piece of graphite into the cavities was examined as shown in Fig. 4. In Fig. 4A (see schematic 4D), the graphite cavity was indistinguishable from the surface of the block at thermal equilibrium. Both cavities within the brass blocks were clearly visible.

When the heated steel rod was brought in close proximity to the cavities, its radiation was reflected off the surfaces and the signal to noise of the resulting image increased, as shown in Fig. 4B (schematic 4E). However, the central graphite cavity appeared black and both of the brass cavities became filled with rod radiation. This revealed that real blackbodies do work and convert any incident radiation to that corresponding to the temperature of their walls. Conversely, the two brass cavities on each side became filled with radiation originating from the steel rod. Again, the reflecting cavities were not black, as they manifested the radiation present in their surroundings in a manner independent of the temperature of their own walls. When the graphite particle was introduced into each of the cavities, it was unable to make the brass cavities fully black, as clear signs of radiation from the heated rod remained, as shown in Fig. 4C (schematic 4F).

Next, consider the findings from block assembly III, as displayed in Fig. 5. Initially, this assembly was monitored at room temperature, in equilibrium with its surroundings, as

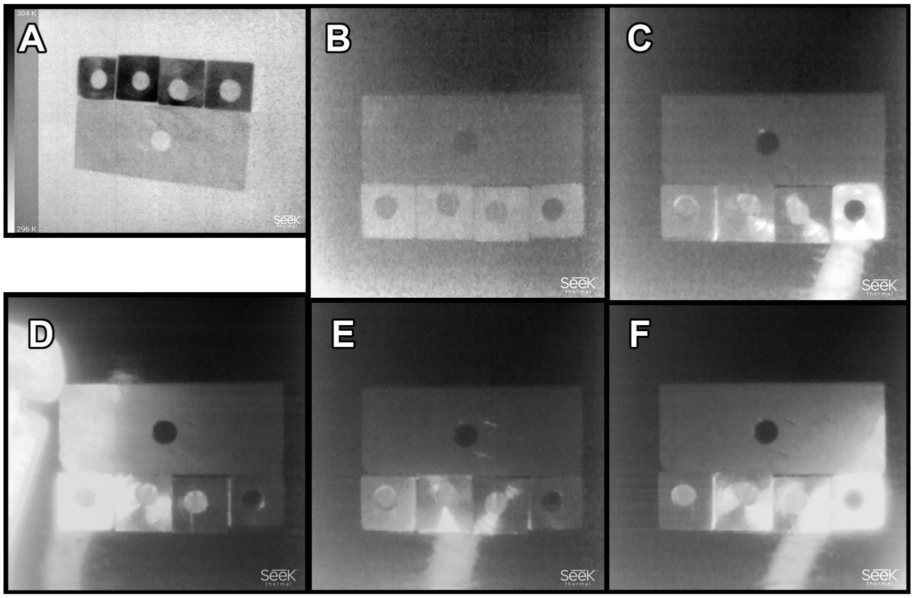

Fig. 2: A) Infrared image obtained from the Block Assembly I (see Fig. 1B) with the camera operating in black mode. For this image the camera was hand held. All the cavities were made using a standard $\frac{3}{16}''$ drill bit to a depth of $1''$ and appeared to contain the same radiation; B-F) Infrared images obtained from the block assembly with the camera in white mode. The lens of the camera was exactly 15 cm directly above the top of the block assembly or 20 cm above the top of the table. In these images, photons emitted from the heated rod and reflected prior to detection are observed as a white streaks on the images. B) The galvanized steel rod was not near the block assembly. Thermal radiation from the observer was likely to account for the good signal to noise on this image; C) The heated galvanized steel rod was placed on the right near the steel cavity; D) The heated galvanized steel rod was placed on the left side near the aluminum cavity. In this case, both the rod and its reflection are clearly visible; E) The heated galvanized steel rod was placed at the center of the block assembly. The two small scratches near the graphite cavity reflected radiation, demonstrating that radiation from the rod was reaching this cavity as well; F) The heated galvanized steel rod was placed just to the right of the steel cavity.

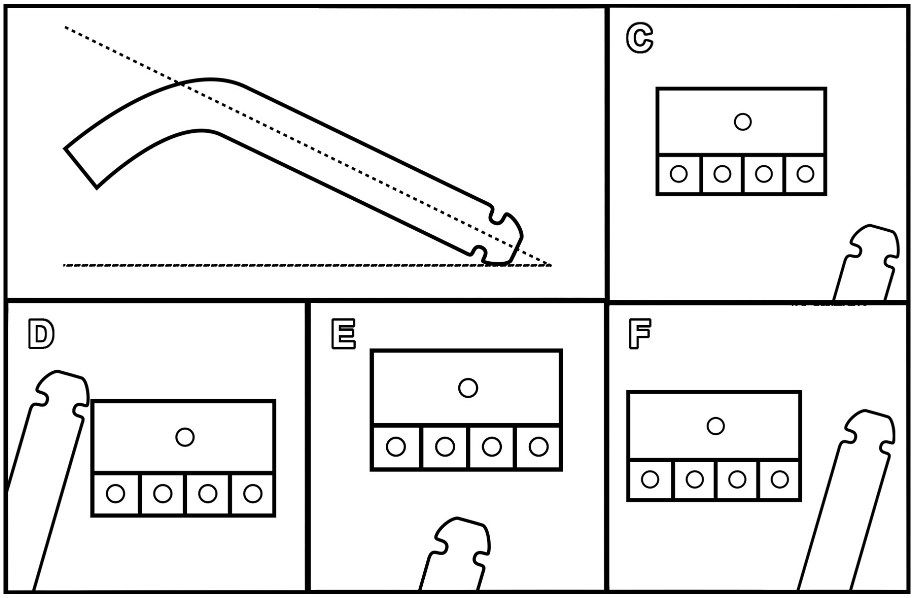

Fig. 3: Schematic representation illustrating the position of the heated rod relative to the block assembly. In the upper left, a vertical cross section is presented. For Fig. 2C-F, the rod was held using locking pliers at an angle of ~25-30^o relative to the table. C-F) top view illustrating the rod position in Figs. 2C-F, respectively.

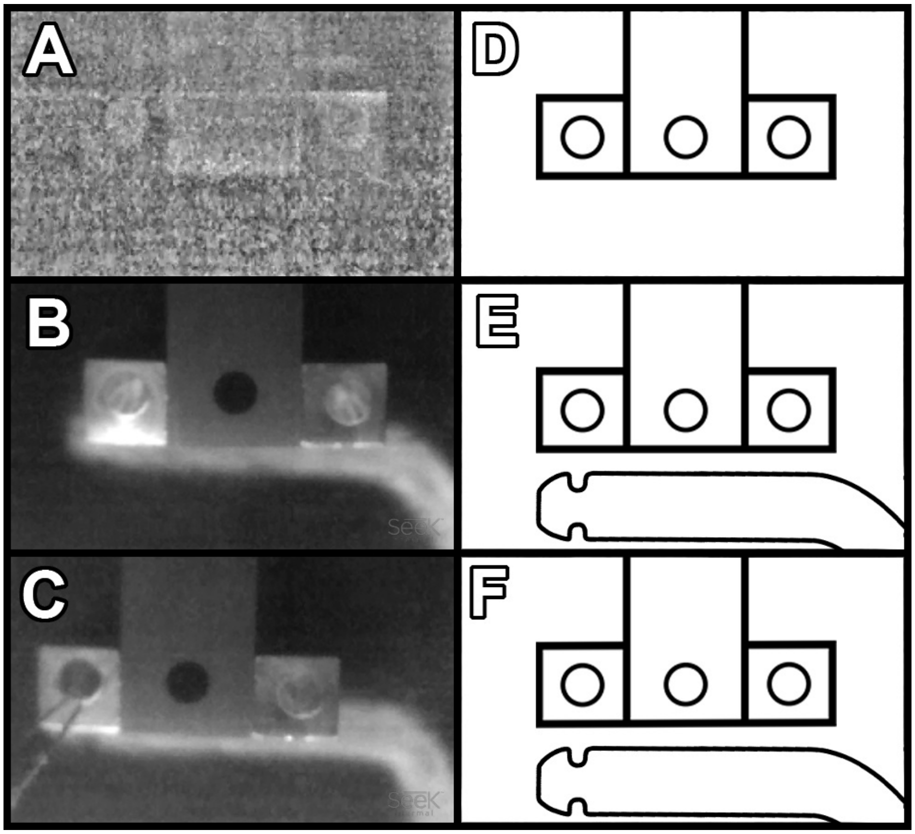

Fig. 4: Infrared images (A-C) and their schematic representations (D-F). The cavities were drilled with a DeWalt Pilot Point $\frac{1}{4}''$ diameter drill bit to the depth $1\frac{1}{4}''$. A) Infrared image obtained from the Block Assembly II (see Fig. 1C) at room temperature without any heated rod present (schematic in D). B) Image obtained while placing a heated steel rod in close proximity to the cavities (schematic in E). C) Repeat of B, but this time, a graphite particle was suspended from two strings into the left brass cavity such that the center of the particle was exactly 1 cm from the top of the block (schematic in F). Graphite particles were also inserted at the bottom of the other two cavities. In B and C, the stem of the rod was parallel to and about 7 cm above, the top of the table (or a height of about 2 cm above the top of the block). In schematics E and F, the rod was illustrated such that its position from left to right could be accurately represented relative to the block. However, in the plane of the image, the rod was actually positioned just below the field of view considered by the schematic, or about one rod width from the block.

shown in Fig. 5A (corresponding schematic, 5C).

Once again the infrared camera was positioned a distance of ∼15 cm from the top of the block. The cavities within the graphite portion of the block under those conditions were indistinguishable from the graphite surface. The image was noisy, as expected, since the observer was well removed from the block during data acquisition. At the same time, the cavities made within the aluminum, brass, and copper blocks were clearly visible and distinct from one another, demonstrating that they did not contain identical radiation. Since these cavities were made from highly reflective materials, this implied that the space surroundings of the block contained some anisotropic radiation.

In Fig. 5B, the same block was examined (schematic 5D). This time, the hands of the investigator were positioned on each side of the block, such that thermal equilibrium was not maintained and the associated radiation could be observed filling the aluminum, brass, and copper cavities. Clearly, these nearly perfectly reflecting cavities were not black, but contained radiation emitted by their surroundings. Conversely, under these conditions, the three deepest graphite cavities, located on the left of the third row, remained essentially unaffected. At the same time, the shallowest cavity, made from the tip of the drill bit and located on the right of the third row, was sensitive to this challenge (Fig. 5B, D). There were reflections of thermal photons off the surfaces of each block which altered the appearance of the images as well. This study served to exemplify, once again, that real blackbodies could do work converting radiation incident upon their walls to black radiation manifesting their temperature. Conversely, rigid perfectly reflecting cavities could not do work. They contained the radiation present in their surroundings in a manner independent of their own temperature and such radiation was clearly observed in the aluminum, brass, and copper

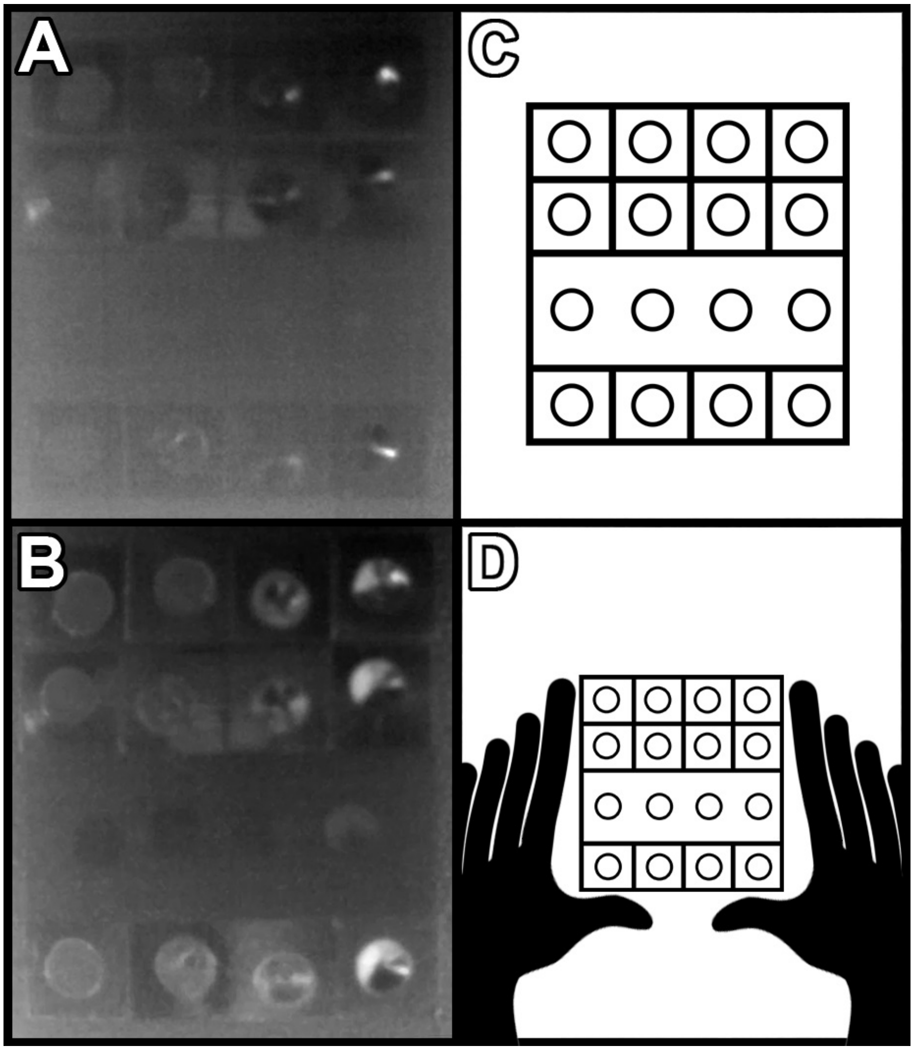

Fig. 5: A) Infrared image obtained from the Block Assembly III (see Fig. 1D) at room temperature. The corresponding schematic is displayed in C (reduced by 25%). B) Same as in A, but this time the hands of the investigator were placed near the sides of the block such that thermal photons from the first two fingers of each hand could challenge the cavities, as seen in the schematic representation D (reduced by ∼50%). The horizontal rows from top to bottom correspond to aluminum, brass, graphite, copper. These cylindrical cavities were made using a standard $\frac{1}{4}''$ drill bit to different depths (from right to left: 1) depth corresponding to just the cone of the drill bit, 2) depth to $\frac{1}{4}''$, 3) $\frac{3}{4}''$ and 4) $1\frac{1}{4}''$).

cavities.

At this point Block Assembly III was placed onto the surface of a hotplate brought to a temperature of ∼304°C, as shown in Fig. 6.

Under these conditions, the graphite cavities located on the third row all appeared to contain isotropic radiation closely manifesting their equilibrium temperature. This indicated that these cavities were able to convert heat energy located in their walls to blackbody radiation. Even the cavity produced with only the tip of the drill bit, on the right, contains isotropic radiation. Conversely, the cavities constructed from aluminum, brass, and copper did not all contain such radiation. Rather, they showed clear signs that their radiation originated from the hotplate and was a property of the surroundings, not the cavity itself.

While the $1\frac{1}{4}''$ aluminum (top row, left most) and copper (bottom row, left most) cavities appeared to contain isotropic radiation, the brass cavity of the same depth (second row, left most) clearly did not. In addition, careful examination revealed that crescents were visible in the aluminum, brass, and copper $\frac{3}{4}''$ cavities (second column) as well. With the exception of graphite, the $\frac{1}{4}''$ cavities (third column) did not contain isotropic radiation at the appropriate temperature and neither did the corresponding conical cavities made from just the tip

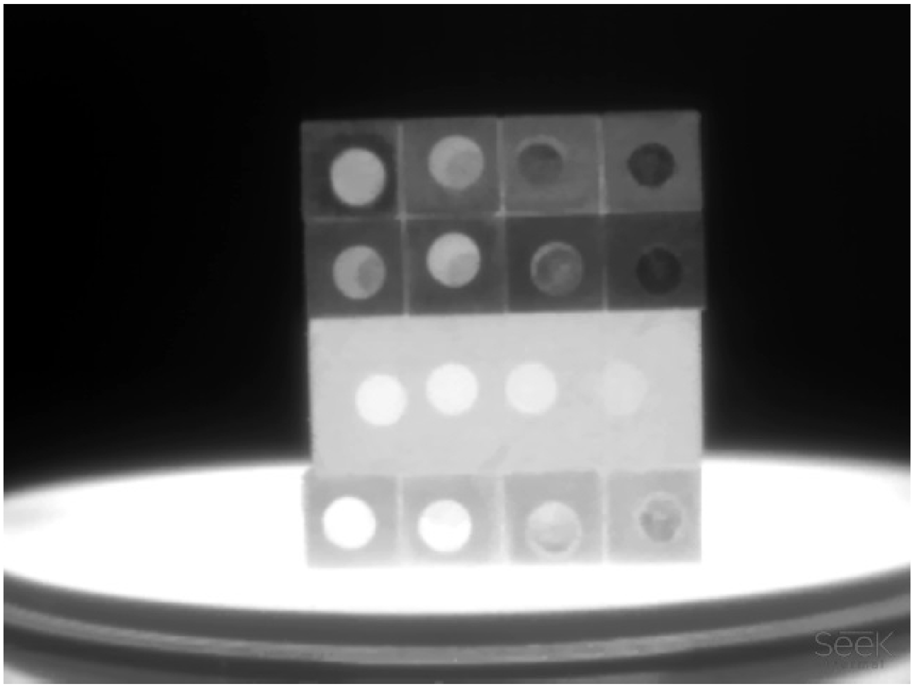

Fig. 6: Infrared image obtained from the Block Assembly III (see Fig. 1D) positioned on a hotplate surface at a temperature estimated at ~304°C using the thermal camera. In order to acquire this image, the camera was mounted on a tripod such that its lens was ~20 cm from the face of the block.

of the drill bit (fourth column). For instance, note the inability of any of the smallest cavities, made from these materials, to sustain radiation at the proper temperature. Crescent patterns also appeared in cavities constructed from aluminum, brass, and copper, even at a depth of $\frac{3}{4}''$ (second column), despite the fact that the radiation in the graphite cavity at the same depth was clearly isotropic. At a depth of $1\frac{1}{4}''$, the brass cavity (second row, first column) still displayed such patterns.

When the block assembly was cooled, it was apparent that the copper blocks had become highly oxidized and this, in addition to their proximity to the hotplate, might help explain their superior performance when compared to aluminum and brass.

Still, these results revealed that real blackbodies, represented herein by the graphite cavities, could do work and manifested the radiation appropriate to the temperature of their own walls. Conversely, the aluminum, brass, and copper cavities illustrate that nearly ideal reflectors could not do work, but contained the radiation present in their surroundings which was independent of the nature of their walls.

4 Discussion

The approach to, and departure from, thermal equilibrium has been the subject of countless studies by Fourier [35], Dulong [36], Petit [36], de la Provostaye [37], and Desains [37] (see [38] for a full review). In similar fashion, through the studies presented herein, a greater understanding has been sought about the nature of the radiation within cavities. This was accomplished both under conditions of thermal equilibrium and also by considering challenges which represent small departures from equilibrium. However, these challenges were important because they served to highlight the nature of the radiation which filled a cavity and thereby help to establish the identity of those objects which properly constituted blackbodies.

4.1 Blackbodies defined

Prior to formulating his law, Kirchhoff first defined a blackbody by stating that *"This investigation will be much simplified if we imagine the enclosure to be composed, wholly or in great part, of bodies which, for infinitely small thickness, completely absorb all rays which fall upon them"* [2, §7]. Kirchhoff therefore recognized the importance of surface absorptivity in the blackbody problem.

Surprisingly however, when Max Planck would later define the blackbody in his classic text [14], he completely rejected Kirchhoff's approach writing: *"In defining a blackbody Kirchhoff also assumes that the absorption of incident rays takes place in a layer 'infinitely thin'. We do not include this in our definition"* [14, §10]. Planck then changed the characteristics of a blackbody surface: *"A rough surface having the property of completely transmitting the incident radiation is described as 'black"'* [14, §10]. With this definition, Planck removed absorbance of the surface itself from the requirements for creating a blackbody and inappropriately placed the focus on transmittance. Planck adopted this new definition because he was preparing to advance a proof of Kirchhoff's law which ignored absorbance at the boundary of two materials [14, §35-37]. But in doing so, Planck moved away from physical reality. His approach proved invalid [39]. Nearly ideal absorbance for thin surfaces remains the hallmark of all materials used to construct quality blackbodies [7, 9–11, 25, 27].

4.2 The mathematical form of Kirchhoff's Law

In advancing his law [2], Kirchhoff did not have recourse to experimental verification. He first stated that the emissive power of an object, E, divided by its absorptive power, A, was equal to a universal function which depended only upon temperature, T, and frequency, ν (E/A= e where e $= f\{T,\nu\}$). He then immediately replaced absorptive power, A, with absorptivity, α_ν, such that E/α_ν=$f\{T,\nu\}$. For actual blackbodies, it is clear that α_ν can be set to 1 and E=$f\{T,\nu\}$. However, Kirchhoff's expression becomes undefined when α_ν is set to zero, as would occur if the cavity was constructed from a perfect reflector. Planck himself recognized the undefined nature of Kirchhoff's law under those conditions (see §48, §51, §52 in [14]).

Thus, relative to Kirchhoff's relationship, two limits are involved. The first, addresses cavities constructed from perfect absorbers, such that α_ν can be set to 1. The second, involves cavities constructed from perfect reflectors, such that α_ν can be set to zero and the law becomes undefined. Perfectly reflecting cavities never followed Kirchhoff's law. They are important however as they form the basis for many resonant devices [29–32]. In any event, Kirchhoff had no mathematical basis for arguing that all cavities must contain black radiation which is dependent only upon temperature and frequency.

4.3 Laboratory blackbodies

Clearly, laboratory blackbodies [4, 7, 12, 26, 27], including those utilized to provide Planck with data [9–11], were specialized cavities constructed from highly absorbing materials. This observation alone was sufficient to conclude that Kirchhoff's law was invalid.

In the infrared, it was evident that the graphite cavities used in this study were able to maintain their internal radiation in a manner which was essentially independent of any radiative challenge. They acted as real blackbodies and could do work. They could ensure that the radiation they contained was governed by the nature and the temperature of their own walls. They converted incoming energy, whether in the form of incident radiation or heat, into normal radiation with the correct frequency distribution.

Conversely, cavities constructed from aluminum, brass, and copper acted as nearly ideal reflectors. They contained the radiation which was incident from their surroundings and showed no ability to convert this radiation to black radiation corresponding to the temperature of their own walls. In this regard, it was evident that perfect reflectors could not do work. They were unable to effect any change upon incident radiation other than that which would occur given specular or diffuse reflection.

de Vos noted the extent to which cavities could make radiation isotropic as a function of the ratio of their diameter and depth [33]. However, perfectly reflecting cavities, by definition, could not emit radiation. As such, the radiation which they contained must remain completely independent of the temperature of their walls and dependent solely on the radiation contained in their surroundings. de Vos's analysis of the quality of a cavity in terms of its ability to convert incoming radiation into ejected isotropic radiation, while of interest, actually had little baring on the behavior of real blackbodies. This was because real blackbodies depended on the nature of their surfaces, not on the dimension of a cavity, in order to ensure that the emitted radiation would be both isotropic and black. A cavity in fact, should not be required, provided that the surface material was black and that no external radiation was able to contaminate this emission. This explained in part the interest in materials with elevated emissivity values [9–11, 26, 27] and highly absorbing surfaces [15–22]. Cavities did enable blackbody radiation to be contained, but they were not necessary for its production.

4.4 Cavities and work

Perhaps the central feature of all actual blackbodies was that they must have the ability to do work and convert any incident energy into the frequency distribution corresponding to the temperature of their own walls. In this sense, the work performed by a blackbody conformed to the standard definition whereby energy was converted from one form to another. Blackbodies accomplished this task in two ways. First, they were able to alter the frequency of incoming radiation and re-emit it with the blackbody frequency distribution corresponding to the temperature of their walls. Secondly, they could convert heat energy located in their own walls into thermal radiation associated with this temperature. In either case, only absorbers of radiation could act as blackbodies, as only they could serve as emitters. Radiation was absorbed by the walls and re-emitted in a manner which depended on the density of states and thereby upon temperature.

Conversely, rigid perfect reflectors could only redirect incoming radiation in a specular or diffuse manner. A change in phase occurred without any change in frequency. Therefore, no work was done, as a change in the energy distribution of the incoming radiation did not occur. Furthermore, perfect reflectors could not harness the energy contained in their walls and thereby emit radiation. Unable to absorb, they could not emit.

The reality that rigid perfectly reflecting cavities cannot do work is the basis for resonant cavities in ultra high field magnetic resonance imaging (UHFMRI) [29], electron paramagnetic resonance (EPR) [30], microwave communications [31] and the resonant cavities used for building coherent radiation following stimulated emission in lasers [32]. All of these disciplines strive to build highly reflective resonant cavities with optimal quality factors, $Q = f/\delta f$, where f is the frequency of interest and δf full width at half maximum of the resonance. Q-factors are inversely proportional to surface resistance echoing Planck's desire for infinitely large conductivity.

In clinical MRI, dielectric loses in the human body will dominate Q-factors for any resonator [26]. As a result, little can be gained in this discipline from building resonators from materials more sophisticated than copper or silver.

However, lasers do not experience these limitations. As a result, resonant cavities in lasers can benefit from the construction of highly reflective Bragg super-mirrors, which can have reflectance values of 99.9999% [40–42]. Ion-beam interference coating mirrors [43] are associated with LIGO [44]. Specialized mirrors are also used in high precision atomic clocks to generate optical cavities with low thermal noise in that setting [45]. Laser cavities can thus achieve Q-factors of 10^{10}, or more [46].

The use of resonant cavities in UHFMRI [29], EPR [30], microwave technology [31], and lasers [32] proves that Kirchhoff's law is not valid. These cavities critically depend on their nearly perfectly reflecting nature which allows them to serve as resonant devices, unable to alter incoming radiation by making it black. It is evident that the radiation in these cavities is absolutely dependent upon the radiation which was incident upon them and completely independent of the temperature of their walls. Absorption of incident photons, transformation into thermal vibrations, and re-emission into thermal photons does not occur in perfectly reflecting cavities. Kirchhoff and Planck cannot claim otherwise, when they assert that all cavities contain black radiation [1, 2, 14].

4.5 Max Planck and Kirchhoff's law

Max Planck attempted to prove the validity of Kirchhoff's law in the opening sections of *The Theory of Heat Radiation* [14, §1-52]. Upon close examination, the derivation was discovered to be unsound [39]. In order to construct his proof, Planck actually redefined the very nature of a blackbody and no longer required, as did Kirchhoff, the ability to absorb radiation over an *infinitely small thickness* [2, §1]. In contrast to Kirchhoff, Planck permitted radiation to enter a medium without absorption/emission at its surface [14, §36-37]. When considering a medium with a vanishingly small absorptivity, he allowed for their use as blackbodies by invoking infinite thickness [14, §10]. Thus, Planck's proof of Kirchhoff's law used transmission and, at times, improperly ignored absorption. Additionally, his proof relied on the use of polarized light [14, §35-37] and the use of Brewster's angle, when heat radiation is never polarized [47].

In this regard, it is noteworthy that in order to address the blackbody problem Max Planck actually focused his attention on the perfectly reflecting, rather than the perfectly absorbing, wall [14]. Planck had defined the reflector as: *"the surface of an absolute conductor (metal) of infinitely large conductivity"* [14, §55]. Planck's focused on perfectly reflecting cavities despite the fact that such cavities cannot function as proper blackbodies.

Indeed, Planck understood that *"In a vacuum bounded by perfectly reflecting walls, any state of radiation may persist"* [14, §51]. However, he advanced that such radiation could be converted to blackbody radiation at the correct temperature with the simple addition of a small particle of carbon [14, §51]. He believed that this particle acted as a catalyst and provided no heat energy of its own [14, §51]. However, Fig. 3 demonstrated that the addition of a carbon particle alone was not sufficient to produce the desired radiation. In fact, it was doubtful that Planck or his contemporaries ever tested the concept, as a small particle of graphite could never do enough work to fully convert the radiation, incident upon a cavity, into fully black radiation. The second law has always restricted what the carbon particle could achieve. In addition, Planck's use of the carbon particle [14, §51] could easily lead to a violation of the 1st law.

Using a thought experiment, it could be demonstrated that the catalyst argument violated the 1st and 2nd laws of thermodynamics [48]. Planck himself recognized that the radiation contained in a perfectly reflecting cavity was undefined [14, §48, §51, §52]. As such, the energy contained in these radiation fields could not be transformed to the proper frequency distribution, unless it exactly matched the energy required at the temperature of interest. Since the radiation was undefined, any attempt to transform radiation of arbitrary energy content to that with the proper frequency distribution for a given temperature risked violating the 1st law of thermodynamics. Planck could not be assured that the energy density within the cavity enabled the carbon particle to make the radiation black at the correct temperature. Only when the correct energy density was initially present in the cavity, could Planck avoid violating the 1st law. Furthermore, the carbon particle must do work to transform heat energy into radiation and fill the cavity. It could never act as a catalyst. Planck's attempt to address the undefined nature of the radiation in a perfectly reflecting cavity, by the insertion of a carbon particle, stood in opposition to the laws of thermodynamics [48].

Throughout his text on *The Theory of Heat Radiation* [14], Max Planck attributed all of the energy to the radiation field and included none in the walls of the cavity. Obviously, if this was done, the solution could not depend on the nature of the walls. However, the approach was not justified. Real cavities have energy in their walls. The most important example is the perfectly reflecting cavity, wherein thermal equilibrium is governed by the conduction of energy in the walls, not within a radiation field. By definition, such walls have no means of interacting with radiation and, therefore, a radiation field cannot be used to set equilibrium in a perfectly reflecting cavity. Perfectly reflecting cavities are responsive to the radiation incident upon their openings only through reflection. The reflection can be either specular, white, or a mixture. However, any effect on the incoming light in a perfectly reflecting cavity will occur in a manner completely devoid of any relationship to the temperature of its walls. The radiation within perfectly reflecting cavities is determined by history and environment, not temperature.

5 Conclusions

For more than 150 years [12], Kirchhoff's law of thermal emission [1, 2] has governed much of scientific thought in physics and astronomy, despite the fact that it lacked proper theoretical [28] and experimental proof [4, 7, 12, 28, 38, 39, 48]. Now it is clear that cavities do not all contain the same radiation, independent of the nature of their walls. Perfect reflectors are unable to convert incoming radiation into the Planckian distribution corresponding to their wall temperature. In the absence of wall motion, they are unable to do any work and merely sustain the radiation in their surroundings. If this incident radiation is phase coherent, then perfect reflectors can even sustain standing waves, as required in UHFMRI [29], EPR [30], microwave telecommunication [31] and lasers [32]. Had Kirchhoff's law been valid, then none of these modalities would exist, as no cavity would become resonant and all incident radiation would become destined to adopt the blackbody profile.

Kirchhoff's law is demonstrably false. Real blackbodies can do work on any incoming radiation and, as shown herein, they appear to do so instantly. They exclusively contain radiation which reflects the temperature of their walls, not the presence of the radiation in their surroundings. It is this ability to do work in the ideal blackbody, and the inability to do work in the perfect reflector, which determines the real behavior of cavities. That is also why laboratory blackbodies are always constructed from materials which possess relatively elevated emissivity values over the frequencies of interest [4, 7, 9–12, 26, 27]. The production of a blackbody spectrum absolutely requires the presence of a vibrating lattice and is intrinsically tied to the nature of the walls [4], contrary to Kirchhoff's claim [1, 2].

As a result, Max Planck's long advocated universality [14, §164] as to time, length, mass, and temperature was never valid. The concept was entirely dependent on the notion that Kirchhoff's law was correct, but this was never the case. As a consequence, the units of measure remain a product of humanity's definitions and science constrained by this fact. Though Planck's equation remains correct for actual blackbodies, it is no longer reasonable to proclaim that black radiation can be produced simply through arbitrary cavities in thermal equilibrium. Such assertions are incorrect as evidenced by the preeminent role of graphite and soot in the construction of actual blackbodies [4] and as modern technology readily demonstrates [29–32].

Acknowledgement

The author would like to thank Joseph Luc Robitaille for assistance in conducting these experiments and relative to the preparation of the figures. An earlier partial version of this work was archived on viXra.org as follows: Robitaille P.-M. and Robitaille J. L. Kirchhoff's Law of Thermal Emission: What Happens When a Law of Physics Fails an Experimental Test? viXra:1708.0053 submitted on 2017-08-06.

Dedication

This work is dedicated to Joseph Benoît Martin Robitaille.

Received on May 8, 2018

References

1. Kirchhoff G. Über den Zusammenhang zwischen Emission und Absorption von Licht und Wärme. *Monatsberichte der Akademie der Wissenschaften zu Berlin*, 1860 (sessions of Dec. 1859), 783–787.
2. Kirchhoff G. Über das Verhältnis zwischen dem Emissionsvermögen und dem Absorptionsvermogen. der Körper fur Wärme und Licht. *Poggendorfs Annalen der Physik und Chemie*, 1860, v. 109, 275–301. (English translation by Guthrie F.: Kirchhoff G. On the relation between the radiating and the absorbing powers of different bodies for light and heat. *Phil. Mag.*, 1860, v. 20, 1–21).
3. Stewart B. An account of some experiments on radiant heat, involving an extension of Prévost's theory of exchanges. *Trans. Royal Soc. Edinburgh*, 1858, v. 22 (1), 1–20 (also found in Harper's Scientific Memoirs, Ames, J. S., ed. The Laws of Radiation and Absorption: Memoirs of Prévost, Stewart, Kirchhoff, and Kirchhoff and Bunsen, translated and edited by Brace D. B., American Book Company, New York, 1901, pp. 21–50).
4. Robitaille P.-M. On the validity of Kirchhoff's law of thermal emission. *IEEE Trans. Plasma Science*, 2003, v. 31 (6), 1263–1267.
5. Wedgwood T. Experiments and observations on the production of light from different bodies, by heat and by attrition. *Phil. Trans. Roy. Soc. Lond.*, 1792, v. 82, 28–47; Wedgwood T. Continuation of a paper on the production of light and heat from different bodies. *Phil. Trans. Roy. Soc. Lond.*, 1792, v. 82, 270–282.
6. Leslie J. An Experimental Inquiry into the Nature and Propagation of Heat. T. Gillet, Salisbury Square, 1804.
7. Robitaille P.-M. Blackbody radiation and the carbon particle. *Progr. Phys.*, 2008, v. 3, 36–55.
8. Winter J., FitzHugh E. W. Pigments based on Carbon. In: Berrie B.H., ed. Artists' Pigments: A Handbook of Their History and Characteristics, 1986, v. 4, 1–37.
9. Hoffmann D. On the experimental context of Planck's foundation of quantum theory. In: Revisiting the Quantum Discontinuity, Max Planck Institute for the History of Science, Preprint 150, 2000, 47–68.
10. Lummer O., Pringsheim E. Kritisches zur schwarzen Strahlung. *Annalen der Physik*, 1901, v. 6, 192–210.

11. Rubens H. and Kurlbaum F. Anwendung der Methode der Reststrahlen-zur Prüfung der Strahlungsgesetzes. *Annalen der Physik* v. 2, 649–666; Rubens H., Kurlbaum F. On the heat radiation of longwave-length emitted by black bodies at different temperatures. *Astrophys. J.*, 1901, v. 74, 335–348.
12. Robitaille P.-M. Kirchhoff's Law of Thermal Emission: 150 Years. *Progr. Phys.*, 2009, v. 4, 3–13.
13. Planck M. Über das Gesetz der Energieverteilung im Normalspektrum. *Annalen der Physik*, 1901, v. 4, 553–563.
14. Planck M. The Theory of Heat Radiation. P. Blakiston's Son & Co., Philadelphia, PA, 1914.
15. Brown R. J. C., Brewer P. J., Milton M. J. T. The physical and chemical properties of electroless nickel–phosphorus alloys and low reflectance nickel–phosphorus black surfaces. *J. Mater. Chem.*, 2002, v. 12, 2749–2754.
16. Yang Z. P., Ci L., Bur J., Lin S. Y., Ajayan P. M. Experimental observation of an extremely dark material made by a low-density nanotube array. *Nano Lett.*, 2008, v. 8 (20), 446–451.
17. Kravets V. G., Schedin F., Grigorenko A. N. Plasmonic blackbody: Almost complete absorption of light in nanostructured metallic coatings. *Phys. Rev. B*, 2008, v. 78, 205405.
18. Vorobyev A. Y., Topkov A. N., Gurin O. V., Svich V. A., Guo C. Enhanced absorption of metals over ultrabroad electromagnetic spectrum. *Appl. Phys. Lett.*, 2009, v. 95, 121106.
19. Liu X., Coxon P. R., Peters M., Hoex B., Cole J. M., Fray D. J. Black silicon: fabrication methods, properties and solar energy applications. *Energy Environ. Sci.*, 2014, v. 7, 3223–3263.
20. Guo J., Guo X., Xu W., Zhang Z., Dong J., Peng L. A Zn-Ni coating with both high electrical conductivity and infrared emissivity prepared by hydrogen evolution method. *Applied Surface Science*, 2017, v. 402, 92–98.
21. Sun W., Du A., Feng Y., Shen J., Huang S., Tang J., Zhou B. Super Black Material from Low-Density Carbon Aerogels with Subwavelength Structures. *ACS Nano*, 2016, v. 10 (10), 9123–9128.
22. Panagiotopoulos N. T., Diamanti E. K., Koutsokeras L. E., Baikousi M., Kordatos E., Matikas T. E., Gournis D., Patsalas P. Nanocomposite catalysts producing durable, super-black carbon nanotube systems: applications in solar thermal harvesting. *ACS Nano*, 2012, v. 6 (12), 10475–10485.
23. Zhao Q., Fan T., Ding J., Guo Q., Kamada M. Super black and ultrathin amorphous carbon film inspired by anti-reflection architecture in butterfly wing. *Carbon*, 2011, v. 49 (3), 877–883.
24. Han Z., Li B., Mu Z., Yang M., Niu S., Zhang J., Ren L. An ingenious super light trapping surface templated from butterfly wing scales. *Nanoscale Res. Lett.*, 2015, v. 10 (1), 1052.
25. McCoy D. E., Feo T., Harvey T. A. and Prum R. O. Structural absorption by barbule microstructures of super black bird of paradise feathers. *Nature Communications*, 2018, v. 9, 1.
26. Navarro N., Bruce S. S., Johnson B. C., Murphy A. V., Saunders R. D. Vacuum processing techniques for development of primary standard blackbodies. *J. Res. Nat. Inst. Stand. Technol.*, 1999, v. 104, 253–259.
27. Chahine K., Ballico M., Reizes J., Madadnia J. Optimization of a graphite tube blackbody heater for a thermogage furnace. *Int. J. Thermophys.*, 2008, v. 29, 386–394.
28. Schirrmache A. Experimenting theory: The proofs of Kirchhoff's radiation law before and after Planck. *Hist. Studies Phys. Biol. Sciences*, 2003, v. 33 (2), 299–335.
29. Robitaille P.-M., Berliner L. Biological Magnetic Resonance, Vol. 26: Ultra High Field Magnetic Resonance Imaging. Springer-Verlag, New York, 2006.
30. Wertz J. E., Bolton J. R. Electron Spin Resonance: Elementary Theory and Practical Applications. McGraw-Hill Book Company, New York, 1972, p. 23.
31. Pozar D. Microwave Engineering, 2nd edition. Wiley, New York, NY, 1998.
32. Siegman A. E. Laser beams and resonators: the 1960s. *IEEE J. Sel. Topics Quantum Electronics* v. 6 (6) (2000) 1380-1388; Siegman A. E. Laser beams and resonators: Beyond the 1960s. *IEEE J. Sel. Top. Quantum Electronics*, 2000, v. 6 (6), 1389–1399.
33. de Vos J. C. Evaluation of the quality of a blackbody. *Physica*, 1954, v. 20, 669–689.
34. Lawrence Berkeley Laboratory, Table of Emissivity of Various Surfaces. http://www-eng.lbl.gov/˜dw/projects/DW4229_LHC_detector_analysis/calculations/emissivity2.pdf
35. Fourier J. Mémoire sur la propagation de la chaleur dans les corps solides. *Nouveau Bulletin des Sciences par la Société Philomathique de Paris*, 1808, v. 1, 112–116.
36. Dulong P. L., Petit A. T. Recherches sur la mesure des températures et sur les lois de la communication de la chaleur. *Journal de LÉcole Polytechnique*, 1820, v. 11 (18), 189–294.
37. de la Provostaye F., Desains P. Mémoire sur la détermination du pouvoir absorbant des corps pour la chaleur rayonnante. *Annales de Chimie et de Physique*, 1850, v. 30, 431–443.
38. Robitaille P.-M., Blackbody Radiation and the Carbon Particle. *Progr. Phys.*, 2008, v. 3, 36–55.
39. Robitaille P.-M., Crothers S. J. "The Theory of Heat Radiation" Revisited: A Commentary on the Validity of Kirchhoff's Law of Thermal Emission and Max Planck's Claim of Universality. *Progr. Phys.*, 2015, v. 11 (2), 120–132.
40. Schaerpf O. Comparison of theoretical and experimental behaviour of supermirrors and discussion of limitations. *Physica B: Condensed Matter*, 1989, v. 156–157, 631–638.
41. Stanley R. P., Houdré R., Oesterle U., Gailhanou M., Ilegems M. Ultrahigh finesse microcavity with distributed Bragg reflectors. *Appl. Phys. Lett.*, 1994, v. 65, 1883–1885.
42. Cole G. D., Zhang W., Martin M. J., Ye J., Aspelmeyer M. Tenfold reduction of Brownian noise in high-reflectivity optical coatings. *Nature Photonics*, 2013, v. 7, 644–650.
43. Wei D. T. Ion beam interference coating for ultralow optical loss. *Appl. Opt.*, 1989, v. 28, 2813–2816.
44. The LIGO Scientific Collaboration, LIGO: the Laser Interferometer Gravitational-Wave Observatory. *Rep. Prog. Phys.*, 2009, v. 72, 076901 (25 pp.).
45. Jiang Y. Y., Ludlow A. D., Lemke N. D., Fox R. W., Sherman J. A., Ma L. S., Oates C. W. Making optical atomic clocks more stable with 10^{-16}-level laser stabilization. *Nature Photonics*, 2011, v. 5, 158–161.
46. Paschotta R. "Q-Factor". In: Encyclopedia of Laser Physics and Technology, V. 1. Wiley-VCH, Berlin, 2008; available online: https://www.rp-photonics.com/q_factor.html.
47. Jenkins F. A. and White H. E. Fundamentals of Optics, 4th edition. McGraw-Hill, Inc., New York, 1976, p, 450.
48. Robitaille P.-M. Further Insight Relative to Cavity Radiation: A Thought Experiment Refuting Kirchhoff's Law. *Progr. Phys.*, 2014, v. 10 (1), 38-40; Robitaille P.-M. Further Insight Relative to Cavity Radiation III: Gedanken Experiments, Irreversibility, and Kirchhoff's Law. *Progr. Phys.*, 2016, v. 12 (1), 85–88.

Outline of a Kinematic Light Experiment

Christian M. Wackler
Albert-Ludwigs-Universität Freiburg, Philosophisches Seminar, Platz der Universität 3, 79085 Freiburg i. Br., Germany
E-mail: christian.wackler@merkur.uni-freiburg.de

The question whether light moves with constant or variable velocity is indubitably of the utmost importance. Preliminary reflections concerning the nature of that movement contrast the hypotheses of propagation and emission. As a brief historical examination reveals, alleged evidences in favour of the invariance postulate turn out to be erroneous or inconclusive and supposedly decisive tests methodologically invalid. An emission theory based on Michael Faraday's idea of ray vibrations is shown to be in accordance with observation. The question whether the speed of light depends on the velocity of its source has thus not been settled experimentally since only a kinematic test, to date never conducted, can give an unambiguous answer. Juxtaposed to seemingly similar but defective designs Wilhelm Wien put forward in 1904, such an experiment, amending a set-up suggested by Herbert Dingle, is proposed.

1 Introduction

The assumption that the velocity of light with respect to real* space has a constant value is not self-evident at all, as the history of science teaches. Indeed, only in the course of the 19th century the ether or propagation hypothesis of light motion, which this assumption is linked to, succeeded in superseding the ballistic or corpuscular conception of emission, espoused by Isaac Newton. However, at the same time as Christiaan Huygens's interpretation seemed to achieve a late victory, his central idea becoming a general conviction, the problems resulting from it began to accumulate as well. As a consequence, the image of propagating waves has eventually been called into question again [1] – and with very good reason as will be shown. To get a clear picture of the major differences, both views are first juxtaposed in opposition. A generally unheeded emission theory, based on the conceptions of Walter Ritz and amended by Herbert Dingle, is then invoked and demonstrated not to be in conflict with observation [2–7]. Finally, we delineate a kinematic experiment that renders an unequivocal decision between the hypotheses of propagation and emission possible.

2 The nature of light motion – propagation or emission?

To picture the two ways which the motion of light has historically been interpreted in, let us consider the following explanations of Walter Ritz (Figure 1a, b):

> In the theory of the ether, a point mass P, at rest with respect to this medium, will be able to emit waves of a constant radial velocity, which will form at each instant a system of spheres, having P as a centre. If P is animated by a motion of translation, the spheres, on the contrary, will become eccentric, each keeping its centre at P_1 of the ether which coincides with P at the instant of emission. According to the principle of relativity, on the contrary, if the motion of translation is uniform, the spheres will have to stay concentric as at rest, and the centre will always be P. When the motion is no longer uniform, the principle will no longer suffice to determine the movement of the waves.
>
> Two ways of representing the phenomena, two distinct images have successively dominated optics: that of emission (the light *moves*) and that of the ether (the light *propagates*). The second one introduces absolute motion, while the first leads for the movement of light in vacuum exactly to the law that the principle of relativity requires: the luminous particles expelled in all directions at the instant *t move with a constant radial velocity and perpetually fill a sphere whose centre is animated with the motion of translation w that* P *had at the instant of emission; if w is constant, this centre will thus continue to coincide with* P. [8] (The original text is in French.)

The experiment of Michelson and Morley [9] had engulfed the propagation hypothesis and with it electromagnetic theory in a crisis, which most notably H. Poincaré [10] called attention to. Ritz conceived of the ingenious solution to entirely discard the image of propagating waves in favour of a ballistic interpretation. In contrast to other authors, suggesting different emission theories shortly afterwards [11–14], he assumed light to keep the speed it is originally emitted with including after reradiation by a medium [15]. His auspicious but due to his early passing fragmentary work has been the first systematic attempt to revise the notion of emission and turn it into a cornerstone of electromagnetic and optical theory [8, 15, 16]. Not until more than half a century later, that line of thought was keenly continued by R. A. Waldron [17].

---

[*] For epistemological reasons, the expression "real" is used instead of the Newtonian term "absolute" throughout this essay.

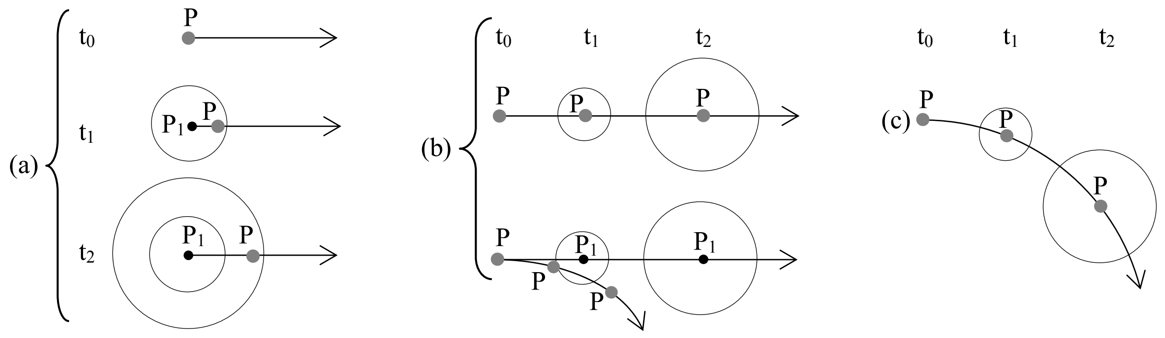

Fig. 1: Movement of a light source P and of a corresponding spherical wave generated at the instant t_0. (a) Propagation (after Maxwell-Lorentz), (b) ballistic emission (after Newton-Ritz), (c) emanation (after Ritz-Dingle).

3 The Ritz theory – criticism and countercriticism

To test Ritz's explanation, M. La Rosa [18, 19] and R. C. Tolman [13] suggested to repeat the Michelson-Morley experiment using light from an extraterrestrial source as the latter moves rapidly with respect to the measuring apparatus. They wrongly presupposed that another null result on such conditions would invalidate his conception. In 1919, an equivalent test, conducted by Q. Majorana [20] with a moving terrestrial light source, showed no shift of the interference pattern. Although F. Michaud [21] demonstrated that Ritz's theory conforms with Majorana's findings – unlike all other emission theories which had been proposed – inferring the fallacy of La Rosa's and Tolman's reasoning from this was omitted. Their view found its way into W. Pauli's [22] influential article on Einstein's theory instead, and after R. Tomaschek [23] and D. C. Miller [24] had finally performed experiments employing sun and star light that again yielded no interference fringes to the calculated extent, Ritz's ideas largely fell into oblivion.

Already previously, an argument adduced by D. F. Comstock [25] and W. de Sitter [26–29] had severely undermined the plausibility of the emission hypothesis. They pointed out that the observed orbits of binary stars are irreconcilable with a ballistic motion of light since particles emitted by a star approaching the observer would overtake the preceding corpuscles and thus distort the image of the system.

Almost half a century had passed until Herbert Dingle [2–4] not only brought the error in La Rosas's and Tolman's reasoning to light but also found a possible explanation considering the seemingly unsurmountable objection that Comstock and de Sitter had raised. In doing so, he seized upon ideas which Michael Faraday had outlined in his *Thoughts on Ray-vibrations*:

> The view which I am so bold as to put forth considers, therefore, radiation as a high species of vibration in the lines of force which are known to connect particles and also masses of matter together. It endeavours to dismiss the æther, but not the vibrations. [30]

Dingle showed that it suffices to extend the classical principle of relativity concerning electromagnetic radiation so that the velocity of light would remain constant with respect to its source even if the radiating body moves non-uniformly and non-rectilinearly (Figure 1c). According to this view, the vibrating rays stay throughout their journey through pure space connected to the source and share the latter's changes of motion. A few years earlier but without building on Faraday's idea, P. Moon and D. E. Spencer had already reasoned along similar lines in response to de Sitters objection [31–35]. However, as H. Bondi aptly remarked, the term "ballistic" does not fit Dingle's conception since the analogy with projectiles no longer characterizes the image [2]. To make a clear distinction, we hence refer to the variation of the emission hypothesis based on vibrating rays as *emanation* and to the correlating principle, governing the motion of electromagnetic radiation, as *classicistic relativity*.

Admitting this principle renders yet another astronomical objection irrelevant H. Thirring [36] propounded against the ballistic concept. He argued that as atoms in the sun are accelerated through thermal collisions, they would emit light particles with different velocities at successive instants. The wave train travelling along a terrestrial observer's line of sight would therefore shrink first, then be stretched, and arrive at the earth as a radio signal.

Finally, a whole class of methodologically interrelated evidences that had been put forward against the emission hypothesis could not withstand Dingle's astute scrutiny either. Over the years, a considerable number of experiments was conducted which seemed to corroborate the postulate of constant light velocity relative to pure space, e.g. [37–43]. But as Dingle correctly remarked:

> The postulate is adopted as part of the basis of a kinematic theory, so that "velocity" must be understood in a kinematic sense, and this requires that the source of light must be an identifiable body, having a definite position in space at each successive instant, the whole sequence of posi-

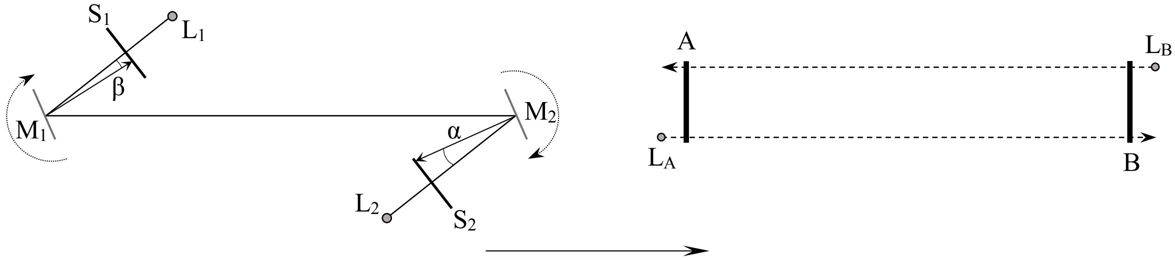

Fig. 2: Schematic of Wien's first and second experimental proposals. A, B: translationally congruent cogwheels; L_1, L_2, L_A, L_B: light sources; M_1, M_2: mirrors in parallel position; S_1, S_2: diaphragms with scales; α, β: deviation angles assuming a stationary ether so that $\alpha > \beta$ as the mirrors rotate, the arrow below indicating the direction of motion of the earth around the sun. Bolometers behind A and B were to record the luminous energy of the incoming beams. When the cogwheels are at rest, the respective values are the same but change as soon as A and B start spinning. An ensuing difference in luminous energy between the rays passing through the notches in opposite directions would have confirmed the hypothesis of a stationary ether.

> tions being consistent with the velocity assigned to the body. [6]

Furthermore, the fact that tests which employ interferometry or use hypothetical particles as sources of light are subject to circular reasoning was generally disregarded.

> In all such experiments, the Maxwell-Lorentz theory, in one respect or another, has been assumed *in the description of the experiment itself*, and since that theory requires that the velocity of light shall be independent of that of its source, the results are of no value at all in relation to this point. [44]

If one visualizes, for instance, the image of the ejected photon string indicated above, it becomes clear at once that a light ray's velocity is not determined by its frequency of vibration. Consequently, a measurement of the frequency of reception, taken by itself, does not allow a conclusion to be drawn about that velocity. Thus, a kinematic question demands a kinematic answer.

For all that and although it was occasionally admitted that Ritz's ideas were discarded prematurely and in part on erroneous grounds [45–49], the theory as amended by Dingle, which no valid evidence exists against, was for decades neglected. Only recently, this conception has finally been resumed and substantially expanded by Luis Bilbao [50], Luis Bernal, and Fernando Minotti [7] under the name of *Vibrating Rays Theory* (VRT). Having adduced further observational data in support of it, they conclude their comprehensive study as follows: "We believe that, given the above evidence, a conscientious experimental research is needed to settle the question of the dependence of the speed of light on that of its source as predicted by Vibrating Rays Theory, and that has been observed during the 1998 NEAR flyby." [7]

4 Towards a kinematic experiment

In 1904, Wilhelm Wien [51–55, pp. 1408-1409] outlined two experiments to determine whether the ether is dragged by the earth or stationary based on the procedures Léon Foucault [56] and Hippolyte Fizeau [57, 58] had devised to measure the speed of light. His first design includes employing two rotating mirrors, his second using two spinning cogwheels which are placed far apart from each other and aligned with the orbital motion of the earth around the sun, respectively (Figure 2). Both experiments demand that the components in rotation have the same angular velocity at any given moment. They therefore depend on the real synchronicity of the instants which the mirrors or cogwheels are set in motion at. However, according to the prevailing theory, this is unattainable through a material connection between them, for example by means of an axle, because within its framework the notion of the rigid body is no longer valid as Wien [59, 60] himself later explained. Nor is utilizing electromagnetic signals to simultaneously start two separate motors feasible due to the supposedly indeterminable times the signals need to reach the different propulsion systems, which count as clocks, so that any possible asymmetry looked for would be offset by the signals' nonsynchronous arrival. These designs being foiled, Wien relinquished further efforts and became a leading proponent of Einstein's theory.

More than half a century later, Herbert Dingle pointed repeatedly to the necessity of a kinematic test for a final answer to the question of the speed of light [4–6, 43, 61–68]. In his book *Science at the Crossroads*, he eventually presented his most sophisticated proposal of an experiment of the kind he hoped for (Figure 3):

> A and B are two sources of light (visible, material sources, not hypothetical particles) of which B is moving rapidly to the left while A is at rest, the paper being the standard of rest. At the instant at which they are adjacent to one another they emit pulses of light towards C and D, which are photographic films whose distances from A are constant and which are moving rapidly downwards through the paper. The relative motion

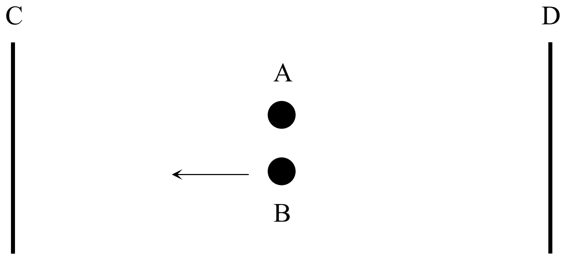

Fig. 3: Light sources A and B, photographic films C and D.

> of A and B continues unchanged throughout the passage of the light. If Einstein's second postulate is true the traces on both films will be symmetrically side by side, while if Ritz's hypothesis is true, that of the light from A will be above that of the light from B on one film and below it on the other. [69]

This proposal undoubtedly implicates considerable and probably still insurmountable technical challenges. However, it at least indicates that the one-way speeds of different beams can indeed be compared without clocks in the usual sense and therefore without the issue of synchronization being relevant at all. That a measurement of the one-way speed of light is possible in principle has also been expressly acknowledged, for example, by Eddington [70], Waldron [17], and Ohanian [71].

Dingle's appeals may have gone unheard for factual reasons at that time. Nowadays, technical infeasibility can certainly no longer hold as a valid argument as will be shown in the following chapter. The matter appears all the more exigent as the invariance postulate in its strict sense has recently been refuted experimentally by slowing down light in vacuum so that c may at best represent a maximum value. Giovannini at al. sum up their findings as follows: "That the speed of light in free space is constant is a cornerstone of modern physics. [...] Our work highlights that, even in free space, the invariance of the speed of light only applies to plane waves." [72] But plane waves are ideal constructs and therefore do not exist as natural phenomena. Considering these facts and especially in view of the work of Bilbao, Bernal, and Minotti, a kinematic test to conclusively answer the question whether the speed of light depends on the velocity of the source is more urgent than ever.

5 Principle and set-up of the experiment

To remove the main difficulties inherent in Dingle's proposal, it is crucial to again follow Michelson's example and to take advantage of the motion of the earth around the sun since the planet's orbital speed of about 30 km/s is great enough to render a potential difference in the travel times of distinct beams observable. Further, employing only one light source will ensure that the emitted rays originate from the same point with respect to the earth.

Thus, the experimental set-up is as follows: aligned with the orbital motion of the earth around the sun, a light source L is positioned far apart from a disk D, the latter's rotational axis being perpendicular to the ground. While the disk is spinning uniformly, L generates short pulses. The emitted beams move towards D and impinge on its photosensitive lateral surface at point A at right angles to the tangent (Figure 4). According to the propagation hypothesis, the velocity of a ray with respect to the ground travelling along the direction of orbital motion of the earth around the sun is $c - V$, with c signifying the speed of light relative to pure space and V the orbital speed of the earth. The travel time of the light referred to $LA = s$ is hence

$$t_A = \frac{s\sqrt{1 - \frac{V^2}{c^2}}}{c - V} \tag{1}$$

whereas in the case of a constant speed of light with respect to the source one has

$$t = \frac{s}{c}, \tag{2}$$

the difference between these times being

$$\delta t_A = t_A - t. \tag{3}$$

From the disk radius r and the number of revolutions per second f follows the speed

$$w = fU \tag{4}$$

of the uniformly rotating circumference U. If λ denotes the light spot diameter and the pulse duration p is set according to

$$\delta t_A \leqslant p \ll \frac{U - \lambda}{w}, \tag{5}$$

the circular arc length

$$d = \lambda + wp \tag{6}$$

marks the trace the first pulse generates on D's lateral surface. As the disk is spinning constantly and the pulse interval equates to

$$P = \frac{i}{f} - t, \tag{7}$$

where $i \in \mathbb{N}$ denotes the number of revolutions per pulse, any additional pulse must lengthen the trace in the amount of $w\delta t_A$, leaving a solid line on the photosensitive film. Let $n \in \mathbb{N}$ be the number of successively generated pulses, then the trace length a will after n pulses add up to

$$a = d + (n - 1)\, w\,\delta t_A\,. \tag{8}$$

Consequentially, the light trace will cover D's entire circumference as soon as

$$n = \frac{U - d}{w\,\delta t_A} + 1. \tag{9}$$

Fig. 4: Schematic of the experimental set-up: A_1 and A_2 denote the points where the rays generated by the first and the second light pulse hit the disk D at the instants t_1 and t_2. The circular arc length $A_1B_1 = d$ represents the trace on D's photosensitive lateral surface the very first pulse causes. $B_1B_2 = w\delta t_A$ depicts the trace's length increment produced by the second and any additional pulse according to the propagation hypothesis. The arrow at the bottom indicates the direction of motion of the earth around the sun.

By contrast, if the emission hypothesis is correct, the rays must always impinge on the same spot so that the trace on the disk retains the length d no matter how much the value of n increases, δt_A having to be substituted with δt in equation (8), where $\delta t = t - t = 0$.

Provided that the propagation hypothesis applies, the exact value of a cannot be predicted. For the conventional value of c would be an average that resulted from two-way measurements and thus deviates from the real one-way speed of light. In case the first test indeed gave $a > d$ for $n > 1$, the result should be crosschecked. Rotating the set-up and repeating the experiment would be expected to yield a different value of a at each angle for a given n. Perpendicular to the direction of orbital motion of the earth around the sun, the trace length would then be

$$a_{90^\circ} = d + (n-1)\, w \left(\frac{\sqrt{s^2 + V^2 t^2}}{c} - t \right) \tag{10}$$

and at 180°

$$a_{180^\circ} = d + (n-1)\, w \left(t - \frac{s\sqrt{1 - \frac{V^2}{c^2}}}{c + V} \right), \tag{11}$$

where $a \approx a_{180^\circ}$. Equations (1) and (11), taking the supposed Lorentz contraction into account, are applicable if the distance LA is measured by means of an etalon. However, considering the necessary magnitude of LA, a travel time measurement using electromagnetic radiation will be conducted in practice. The determined distance

$$s = \frac{c\,T}{2} = \frac{(c - V + c + V)\,T}{4} \tag{12}$$

then arises from the signal's two-way speed, with T signifying the total time elapsed between emission and return, the respective instants being measured by one and the same clock. Although the square root factor within equations (1) and (11) must under these premises be omitted, the choice between the two methods of establishing LA is evidently of no significance regarding the validity of the experiment.

Due to the motion of the solar system, the propagation hypothesis involves the assumption that t_A varies seasonally. Therefore, if the first experimental run yields $a = d$ for $n > 1$, a conclusive confirmation of the emission hypothesis will not only demand repetitions of the test at different angles but also reperforming it over an extended period to exclude a misleading result because of V being possibly offset by an unknown velocity component just at the time of the initial measurements.

The outlined experiment avoids the theoretical obstacles which defeated Wilhelm Wien's proposals as merely one uniformly spinning mechanical component is required and attuning a pulsing light source to it does not pose a conceptual problem. The test itself implies no two-way measurement and is neither dependent on assumptions of the Maxwell-Lorentz electromagnetic theory, nor are hypothetical particles used as a radiation source. Thus, Dingle's criteria for a kinematic light experiment are met, and objections against procedures based on a closed light path do not apply [73].

6 Conclusion

We may summarize the proposed *experimentum lucis et crucis* in the following way: since any "in itself determined periodic process realized by a system of sufficiently small spatial extension" [74] is considered to be a timepiece, the described set-up consisting of a uniformly spinning disk featuring a photosensitive lateral surface and of a light source pulsing at equal intervals embodies two clocks, their "hands" being successively emitted rays. These "light clocks" run synchronously and thus display real simultaneity. The outcome of the experiment is therefore identical for any observer in any system of reference.

Since the assumption that an ether is dragged by the earth was experimentally refuted [75, 76], no theory reposing on the postulate of constant light velocity relative to pure space or a luminiferous medium in it can explain successive beams impinging on the disk at the same spot. Instead, the emission hypothesis will be fully confirmed. Electromagnetic radiation will have to be understood as a form of energy which is emitted with a real velocity $c + v$, that is the vector sum of a component being invariant relative to the light source and a variable component, the real velocity of this very source. However, according to K. Brecher's [77] analysis of regularly pulsating x-ray sources in binary star systems, a ballistic interpretation even if it allows for the extinction theorem of dispersion theory, as considered by J. G. Fox [45, 46], seems to be untenable (cf. also [48]). Thus, the *Ritz-Dingle Emanation* or *Vibrating Rays Theory* will remain the only explanation consistent with observation [2–7]. In addition to *classical relativity* holding true for matter in uniform translation, a *classicistic principle* will apply stating that the speed of light stays constant relative to its source even if the latter moves non-rectilinearly and non-uniformly.

Should, on the contrary, successive beams mark a solid line on the disk, the propagation hypothesis would bear the palm. Light would have the characteristics of a wave that propagates in a medium with constant velocity relatively to that medium. The recently renewed question whether there is a resting frame in space [78] would be answered in the affirmative.

Submitted on May 11, 2018

References

1. Ritz W. Du rôle de l'éther en physique. *Rivista di Scienza 'Scientia'*, 1908, v. 3 (6), 260–274.
2. Bondi H. et al. Meeting of the Royal Astronomical Society, Friday, 1958 November 14, at 16h 30m. *Observatory*, 1958, v. 78 (907), 232–241.
3. Dingle H. A Proposed Astronomical Test of the "Ballistic" Theory of Light Emission. *Monthly Notices of the Royal Astronomical Society*, 1959, v. 119 (1), 67–71.
4. Dingle H. Relativity and Electromagnetism: An Epistemological Appraisal. *Philosophy of Science*, 1960, v. 27 (3), 233–253.
5. Dingle H. A Reply to Professor Grünbaum's Rejoinder. *British Journal for the Philosophy of Science*, 1961, v. 12 (46), 156–157.
6. Dingle H. Reason and Experiment in Relation to the Special Relativity Theory. *British Journal for the Philosophy of Science*, 1964, v. 15 (57), 41–61.
7. Bilbao L., Bernal L., Minotti F. Vibrating Rays Theory. arXiv: 1407.5001.
8. Ritz W. Recherches critiques sur l'électrodynamique générale. *Annales de chimie et de physique*, 1908, v. 13, 145–275.
9. Michelson A. A., Morley E. W. On the Relative Motion of the Earth and the Luminiferous Ether. *American Journal of Science*, 1887, v. 34 (203), 333–345.
10. Poincaré H. The Value of Science. The Science Press, New York, 1907.
11. Thomson J. J. On a Theory of the Structure of the Electric Field and its Application to Röntgen Radiation and to Light. *Philosophical Magazine*, 1910, v. 19 (110), 301–312.
12. Tolman R. C. The Second Postulate of Relativity. *Physical Review*, 1910, v. 31, 26–40.
13. Tolman R. C. Some Emission Theories of Light. *Physical Review*, 1912, v. 35, 136–143.
14. Stewart O. M. The Second Postulate of Relativity and the Electromagnetic Emission Theory of Light. *Physical Review*, 1911, v. 32, 418–428.
15. Ritz W. Recherches critiques sur les théories électrodynamiques de Cl. Maxwell et de H.-A. Lorentz. *Archives des Sciences Physiques et Naturelles*, 1908, v. 26, 209–236.
16. Ritz W. Über die Grundlagen der Elektrodynamik und die Theorie der schwarzen Strahlung. *Physikalische Zeitschrift*, 1908, v. 9 (25), 903–907.
17. Waldron R. A. The Wave and Ballistic Theories of Light: A Critical Review. Frederick Muller, London, 1977.
18. La Rosa M. Fondamenti sperimentali del 2.° Principio della teoria della relatività. *Nuovo Cimento*, 1912, v. 3 (1), 345–365.
19. La Rosa M. Über einen Versuch zum Vergleiche der Relativitätstheorie mit den mechanischen Anschauungen über die Lichtausstrahlung. *Physikalische Zeitschrift*, 1912, v. 13 (23), 1129–1131.
20. Majorana Q. Experimental Demonstration of the Constancy of Velocity of the Light emitted by a Moving Source. *Philosophical Magazine*, 1919, v. 37 (217), 145–150.
21. Michaud F. Les théories émissives et le principe de Doppler-Fizeau. *Comptes rendus de l'Académie des sciences*, 1919, v. 168, 507–509.
22. Pauli W. Theory of Relativity. Pergamon Press, London, 1958.
23. Tomaschek R. Über das Verhalten des Lichtes außerirdischer Lichtquellen. *Annalen der Physik*, 1924, v. 73, 105–126.
24. Miller D. C. Ether-Drift Experiments at Mount Wilson. *Proceedings of the National Academy of Sciences of the United States of America*, 1925, v. 11 (6), 306–314.
25. Comstock D. F. A Neglected Type of Relativity. *Physical Review*, 1910, v. 30, 267.
26. de Sitter W. A proof of the constancy of the velocity of light. *Proceedings of the Section of Sciences, Koninklijke Akademie van Wetenschappen te Amsterdam*, 1913, v. 15 (2), 1297–1298.
27. de Sitter W. Ein astronomischer Beweis für die Konstanz der Lichtgeschwindigkeit. *Physikalische Zeitschrift*, 1913, v. 14 (10), 429.
28. de Sitter W. On the constancy of the velocity of light. *Proceedings of the Section of Sciences, Koninklijke Akademie van Wetenschappen te Amsterdam*, 1913, v. 16 (1), 395–396.
29. de Sitter W. Über die Genauigkeit, innerhalb welcher die Unabhängigkeit der Lichtgeschwindigkeit von der Bewegung der Quelle behauptet werden kann. *Physikalische Zeitschrift*, 1913, v. 14 (25), 1267.
30. Faraday M. Thoughts on Ray-vibrations. *Philosophical Magazine*, 1846, v. 28 (188), 345–350.
31. Moon P., Spencer D. E. Binary Stars and the Velocity of Light. *Journal of the Optical Society of America*, 1953, v. 43 (8), 635–641.
32. Moon P., Spencer D. E. On the Establishment of a Universal Time. *Philosophy of Science*, 1956, v. 23 (3), 216–229.
33. Moon P., Spencer D. E. The New Electrodynamics and its Bearing on Relativity. In: Kritik und Fortbildung der Relativitätstheorie, edited by K. Sapper, 1958, Austria Akademische Druck- und Verlagsanstalt, Graz, 144–159.

34. Moon P., Spencer D. E., Moon E. E. Binary Stars from Three Viewpoints. *Physics Essays*, 1989, v. 2 (3), 275–287.
35. Moon P., Spencer D. E., Moon E. E. Universal Time and The Velocity of Light. *Physics Essays*, 1989, v. 2 (4), 368–374.
36. Thirring H. Über die empirische Grundlage des Prinzips der Konstanz der Lichtgeschwindigkeit. *Zeitschrift für Physik*, 1925 v. 31, 133–138.
37. Bonch-Bruevich A. M. A Direct Experimental Confirmation of the Second Postulate of the Special Theory of Relativity (in connection with Dingle's note). *Optics and Spectroscopy*, 1960, v. 9, 73.
38. Sadeh D. Experimental Evidence for the Constancy of the Velocity of Gamma Rays, Using Annihilation in Flight. *Physical Review Letters*, 1963, v. 10 (7), 271–273.
39. Alväger T., Nilsson A., Kjellman J. A Direct Terrestrial Test of the Second Postulate of Special Relativity. *Nature*, 1963, v. 197 (4873), 1191.
40. Rotz F. B. New Test of the Velocity of Light Postulate. *Physics Letters*, 1963, v. 7 (4), 252–253.
41. Babcock G. C., Bergman T. G. Determination of the Constancy of the Speed of Light. *Journal of the Optical Society of America*, 1964, v. 54 (2), 147–151.
42. Alväger T., Farley F. J. M., Kjellman J., Wallin I. Test of the Second Postulate of Special Relativity in the GeV Region. *Physics Letters*, 1964, v. 12 (3), 260–262.
43. Waddoups R. O., Edwards W. F., Merrill J. J. Experimental Investigation of the Second Postulate of Special Relativity. *Journal of the Optical Society of America*, 1965, v. 55 (2), 142–143.
44. Dingle H. A Re-examination of the Michelson-Morley Experiment. *Vistas in Astronomy*, 1967, v. 9, 97–100.
45. Fox J. G. Experimental Evidence for the Second Postulate of Special Relativity. *American Journal of Physics*, 1962, v. 30 (4), 297–300.
46. Fox J. G. Evidence Against Emission Theories. *American Journal of Physics*, 1965, v. 33 (1), 1–17.
47. Beckmann P., Mandics P. Experiment on the Constancy of the Velocity of Electromagnetic Radiation. *Radio Science Journal of Research*, 1964, v. 68D (12), 1265–1268.
48. Beckmann P., Mandics P. Test of the Constancy of the Velocity of Electromagnetic Radiation in High Vacuum. *Radio Science Journal of Research*, 1965, v. 69D (4), 623–628.
49. Martínez A. A. Ritz, Einstein, and the Emission Hypothesis. *Physics in Perspective*, 2004, v. 6 (1), 4–28.
50. Bilbao L. Does the Velocity of Light Depend on the Source Movement? *Progress in Physics*, 2016, v. 12 (4), 307–312.
51. Wien W. On experiments to decide whether the ether moves with the earth or not. *Observatory*, 1904, v. 27 (349), 360.
52. Wien W. Über einen Versuch zur Entscheidung der Frage, ob sich der Lichtäther mit der Erde bewegt oder nicht. *Physikalische Zeitschrift*, 1904, v. 5 (19), 585–586.
53. Wien W. Experimente zur Entscheidung der Frage, ob sich der Äther mit der Erde bewegt oder nicht. *Physikalische Zeitschrift*, 1904, v. 5 (19), 604–605.
54. Wien W. Experiments to decide whether the Ether moves with the Earth. *Report of the British Association for the Advancement of Science*, 1905, v. 74, 433–434.
55. Cohn E. Zur Elektrodynamik bewegter Systeme. II. *Sitzungsberichte der Königlich Preussischen Akademie der Wissenschaften*, 1904, v. 53, 1404–1416.
56. Foucault L. Mesure de la vitesse de la lumière, étude optique des surfaces; mémoires de Léon Foucault. Librairie Armand Colin, Paris, 1913.
57. Fizeau H. Sur une expérience relative à la vitesse de propagation de la lumière. *Comptes rendus hebdomadaires des séances de l'Académie des Sciences*, 1849, v. 29, 90–92.
58. Fizeau H. Sur une expérience relative à la vitesse de propagation de la lumière. *Revue scientifique et industrielle*, 1849, v. 5, 393–397.
59. Wien W. Über die Wandlung des Raum- und Zeitbegriffs in der Physik. *Sitzungsberichte der Physikalisch-medicinischen Gesellschaft zu Würzburg 1909*, 1910, (2,3), 29–39.
60. Wien W. Die Relativitätstheorie. In: Taschenbuch für Mathematiker und Physiker, Bd. 2, edited by F. Auerbach and R. Rothe, B. G. Teubner, Leipzig and Berlin, 1911, 283–292.
61. Dingle H. A Possible Experimental Test of Einstein's Second Postulate. *Nature*, 1959, v. 183 (4677), 1761.
62. Dingle H. An opportunity to check on Einstein. *New Scientist*, 1959, v. 5 (133), 1253.
63. Dingle H. Ritz theory of light. *Observatory*, 1959, v. 79 (910), 106–107.
64. Dingle H. The Falsifiability of the Lorentz-FitzGerald Contraction Hypothesis. *British Journal for the Philosophy of Science*, 1959, v. 10 (39), 228–229.
65. Dingle H. A Radio-astronomical Test of the Ballistic Theory of Light Emission. *Observatory*, 1960, v. 80 (914), 35–36.
66. Dingle H. The Doppler Effect and the Foundations of Physics (I). *British Journal for the Philosophy of Science*, 1960, v. 11 (41), 11–31.
67. Dingle H. The Doppler Effect and the Foundations of Physics (II). *British Journal for the Philosophy of Science*, 1960, v. 11 (42), 113–129.
68. Dingle H. Special Theory of Relativity. *Nature*, 1962, v. 195 (4845), 985–986.
69. Dingle H. Science at the Crossroads. Martin Brian & O'Keeffe, London, 1972.
70. Eddington A. S. The Mathematical Theory of Relativity. The University Press, Cambridge, 1923.
71. Ohanian H. C. Einstein's mistakes: the human failings of genius. W. W. Norton & Co., New York, 2008.
72. Giovannini D., Romero J., Potoček V., Ferenczi G., Speirits F., Barnett S. M., Faccio D., Padgett M. J. Spatially structured photons that travel in free space slower than the speed of light. *Science*, 2015, v. 347 (6224), 857–860.
73. Pérez I. On the experimental determination of the one-way speed of light. *European Journal of Physics*, 2011, v. 32 (4), 993–1005.
74. Einstein A. Autobiographical Notes. In: Albert Einstein: Philosopher-Scientist, edited by P. A. Schilpp, The Library of Living Philosophers, Evanston, IL, 1949, 2–94.
75. Michelson A. A. The Effect of the Earth's Rotation on the Velocity of Light, Part I. *Astrophysical Journal*, 1925, v. 61 (3), 137–139.
76. Michelson A. A., Gale H. G., Pearson F. The Effect of the Earth's Rotation on the Velocity of Light, Part II. *Astrophysical Journal*, 1925, v. 61 (3), 140–145.
77. Brecher K. Is the Speed of Light Independent of the Velocity of the Source? *Physical Review Letters*, 1977, v. 39 (17,19), 1051–1054, 1236.
78. Chang D. C. Is there a resting frame in the universe? A proposed experimental test based on a precise measurement of particle mass. *European Physical Journal Plus*, 2017, v. 132, 140.

Fractional Degrees of Freedom in Statistics

Mikhail N. Mashkin
E-mail: mnmashkin@yandex.ru

The concept of observation and presentation of the count (reference) results in an interval form is considered. The transition to interval measurements is achieved by use of the total reduced number of measurements (number of degrees of freedom) as a sample parameter, which allows the use of non-integer (fractional) powers of freedom in the calculation of the estimates of static parameters and criteria values. The replacement of single measurements with interval measurements at their same quantities in all cases reduces the accuracy of statistical parameters estimates.

Introduction

Currently, there are known applications of fractional powers in statistics [1]. However, the use of different methods of data processing, in particular for small samples [2] and for processing with the use of methods similar to the method of group accounting arguments [3], allows to broaden their use in calculations.

The concept of observation

According to [4], observation is the experimental basis of scientific research. Observed results are most often recorded in the form of meanings of the measured values or their counts. For static methods of measurement, the result is a single number. With dynamic methods, it is possible to record the measured value in time as the implementation of a random (nonrandom) process. In the latter case, the results of measurements often are the evaluations of the process parameters. In both cases, statistical stability is a prerequisite, which in particular consists, in the approximation, with a sufficiently large number of observations* to the probability of a given value. In all cases, if the measurement of the value is repeated many times, the result is a statistical distribution series corresponding to any distribution law, which may be associated with the error of the measuring system or instrument.

Each single measurement (count), as well as their totality, gives an empirical distribution, which is described in the form of a histogram, statistical series, empirical distribution function, etc. In this case, along with the above, it is necessary to specify the number of measurements, i.e. empirical description requires specifying the number of experiments (sample size) on the basis of which it is obtained. We will refer to the number of measurements, on the basis of which the empirical description of the distribution law is obtained, as the number of degrees of freedom. However, there are measured values, which, by their nature, initially have a form corresponding to a certain distribution law [5]. In this case, the measured value is set not by a value, which is constant or changing in time, but by an area at each point of which it can be located with a certain probability. This allows each measurement to match the area of the measured value with the law of its distribution.

The area of determination of the value can be set with one or more than one interval, see Fig. 1. One dimension gives the area and the value of the parameters' estimates of the distribution law.

Interval measurements

Let us consider the basic prerequisites for using intervals as measurement results.

The possibility to express numerical values of quantities in the form of intervals is used in the theory of intervals [6]. The basic idea of interval analysis is that you can work with intervals as with plain numbers. Common operations such as addition, subtraction, multiplication and division, as well as set theory operations such as intersection and union, are quite applicable to them. Interval operations are described by a ratio:

$$A@B = \{\, x@y | x \in A,\ y \in B \,\}, \tag{1}$$

where @ is one of the operations $\{+, -, *, /, \cup, \cap\}$, while A, B are intervals.

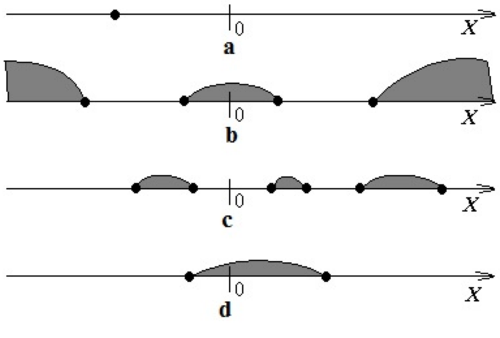

Fig. 1: Types of areas for determining the measurement value: a — one observation — a single numerical value; b — one observation — a set of intervals of numerical values, including those that are not limited to the left or to the right; c — one observation — a set of intervals strictly limited to the left and to the right; d — one observation — one interval of numerical values with one border to the left and one to the right.

---

[*] The ratio of the number of observations of a particular value to the total number of observations.

A single (real) number can be viewed as that an interval having a definition domain and the law of distribution in the form of a certain event probability:

$$P\,(a \in [a,\, a]) = 1,\ a = [a,\, a]\,, \tag{2}$$

i.e. just one numerical value is sufficient for the description of the measured value.

Let us consider the measurement process of the diameter of a bearing ring as an example of a measurement that has a definition area of one interval. The measurement of the radius of the hole or the outer diameter (done with sufficiently accurate instruments) relative to the calculated center of the bearing ring gives the dependence of the radius to the point on the circumference surface of the hole or the outer diameter in the form of a realization of a random process that can be described by a random function like follows:

$$R = X\,(\alpha)\,, \tag{3}$$

where $0 \leqslant \alpha \leqslant 2\pi$ is the bearing ring angle of rotation.

Accurate lab instruments such as circular gauges allow us to fully record the kind of realization of a random process. Obviously, when such a record exists, it can be processed by well known methods of the theory of random processes. In production conditions, the use of precision instruments is impractical. The control devices used allow to quite precisely measure the diameter of a bearing ring. During the rotation of the bearing ring it is also possible to determine the maximum and minimum values of the diameter of the bearing. If we limit ourselves to only two of these values, then actually we come to a case of two independent observations. The information that there are other numerical values of the diameter, between these two values, becomes thus lost. For a more complete explanation of the essense of the observation, it is proposed to consider the considered measurement process as a single observation in the form of one interval, Fig. 1, d. The value of the measured diameter has a description in the form of a statistical series at a given interval:

$$\hat{P}\ (\,d : d \in [d_{\min},\, d_{\max}])\,, \tag{4}$$

where d is the value of the bearing ring diameter.

With an interval measurement, however, there are two degrees of freedom: the measurements of one and the other border of the interval. However, these two dimensions are considered together over the interval. For example, one dimension is a border, and the other is the interval value itself, that is, there is a relationship: for the first dimension, the entire numerical axis is available, and the second dimension describes the area of the finite length bound to the first measurement. The availability of the entire numerical axis here must be understood as a possibility to represent the first measurement only by selecting the initial value of the reference point by any number, including almost infinity. For the interval, whatever we choose as the reference point, its value remains constant. From this we can assume that the specified relationship as if reduces the number of degrees of freedom of choice of numerical values for the interval measurement. We can assume that it is less than two, but more than one. Interval measurement generally gives the values of the borders of intervals and parameters or their estimates of the distribution law. This can be described by displaying the interval in parameters' values:

$$G : [\,a_i\, b_i\,] \xrightarrow{P} \left\{ \beta_j : j = 1, \ldots, k \right\}, \tag{5}$$

where G displays the set of numerical values of the interval measurement in the values of parameters or their estimates of the probability distribution law; a_i, b_i are borders of the i-th interval; P is the law of distribution of values of a random variable from the interval; β_j is the value or estimate of a parameter of the distribution law.

It should be noted that the borders of the interval can be displayed in the parameters of the distribution law explicitly (for example, the boundaries of the interval in the case of the law of equal probability density) or indirectly as the area of definition of this law.

One of the options for describing the distribution law P is the probability density. By the given probability density or histogram it is possible to calculate or to estimate the parameters of the distribution law. The previously declared commonality for the interval and for one number (2) allows these calculations to be applied for one number obtained during the measurement. Let us illustrate this by calculating the dispersion of a single observation.

Calculation of the dispersion estimation of one observation by known relations [1] can be performed by the formula:

$$\hat{\sigma}_x^2 = \frac{\sum\limits_{i=1}^{n} (x_i - m_x)^2}{n} = \frac{(x - m_x)^2}{1} \quad \text{if } m_x \text{ is known}, \tag{6}$$

where m_x is the mathematical expectation; x is the numerical value of the dimension.

For one number from the interval with coinciding borders, formula (6) is valid, because the mathematical expectation does not require an evaluation, but is equal to the number itself. The value of the dispersion estimate in this case is zero. This clearly indicates the non-randomness of the interval representation of the same number, i.e., the specific meaning of the measured value does not have a random component — it is a non-random value.

Calculation of the dispersion estimate for an interval measurement in the extreme case can be performed as that for two independent observations by formulas:

$$\hat{\sigma}_x^2 = \frac{(b - m_x)^2 + (a - m_x)^2}{1}\,, \quad \text{if } m_x \text{ is unknown}, \tag{7}$$

$$\hat{\sigma}_x^2 = \frac{(b - m_x)^2 + (a - m_x)^2}{2}\,, \quad \text{if } m_x \text{ is known}. \tag{8}$$

It can be assumed that the value of the dispersion estimate for the interval for each case, due to the lower value of the degrees of freedom, should exceed the values given by formulas (7) and (8). In addition, within the interval, the measured numerical values of the value are determined by its distribution law. If we choose as the basic one the law of equal probability density (EPD), then we lead the rest of the distributions to it by changing the value of the interval on the basis of equality of the entropy value.

Let us define the given number of measurements (degrees of freedom) for an interval measurement in the form of:

$$r_i = 1 + \Delta_i\,, \quad 1 \geqslant |\Delta_i| \geqslant 0; \tag{9}$$

where

$$\Delta_i = \begin{cases} +\Delta_{is}, & \text{boundaries are given from experience;} \\ -\Delta_{is}, & \text{one boundary is given by the researcher;} \\ -1, & \text{boundaries are given randomly.} \end{cases}$$

The value Δ_{is} can be determined by formula:

$$\Delta_{is} = \begin{cases} \dfrac{1}{1 + 1/h_{is}}, & \text{at } b_i,\ a_i \neq 0; \\ 0, & \text{at } b_i,\ a_i = 0; \end{cases} \tag{10}$$

where

$$h_{is} = \frac{b_i - a_i}{\frac{1}{2}\,|\,a_i + b_i\,|}$$

is choosen for the EPD law and

$$h_{is} = \frac{(b_i - a_i)\,H_x}{H_{EPD}\left|\mathrm{M}\,[X_{[a,\,b]}]\right|}$$

is choosen for any other law of the distribution of x along the interval $[a_i,\ b_i]$;

$$H_x = \mathrm{M}\left[\log P\left(X = x_j \in [a_i\, b_i]\right)\right] = -\sum_{j=1}^{n} P\left(X = x_j\right)\log P\left(X = x_j\right)$$

is chosen if the given measured value is discreet*;

$$H_x = \mathrm{M}\,[\log P\,(f\,(x))] = -\int_{a_i}^{b_i} f\,(x)\log_c f\,(x)\,dx$$

is taken at $c < (b_i - a_i)$ if the measured value is continuous (relative entropy);

$$H_{EPD} = \log n_{[a,\,b]}$$

if the discrete measured value is distributed equally possible within the interval, where $n_{[a,\,b]}$ is the number of equally possible states in the interval;

$$H_{EPD} = \log_c\,(b_i - a_i)$$

if within the interval the measured value is distributed according to the EPD law;

$$\mathrm{M}\,[X_{[a,\,b]}]$$

is the mathematical expectation of the measured value in the interval $[a_i,\ b_i]$.

The total reduced number of measurements, the value for the calculation of statistical parameters for the sample, is equal to:

$$n_r = \sum_{i=1}^{n} r_i\ . \tag{11}$$

This assumes that, when creating a statistical series of distributions or histograms, each interval dimension must have its own share proportional to the value of r_i. If it is 0, this dimension is ignored. If it differs from zero, then this contribution, as the number of measurements (experiments), is equal to its value.

Formulas for calculation of the main estimates of statistical parameters for one, i-interval measurement, in the case of the EPD law for the measured value within the interval, have the form:

$$\hat{m}_{x_i} = \frac{b_i + a_i}{2}\,; \tag{12}$$

$$\hat{\sigma}^2_{r_i} = \frac{(b_i - \hat{m}_{x_i})^2 + (a_i - \hat{m}_{x_i})^2}{r_i - 1} = \frac{(b_i - a_i)^2}{2\,(r_i - 1)}\,. \tag{13}$$

Example. With a rectangular contribution (EPD), let us define by formula (13) the estimate of the variance in the interval of an i-th observation for different ratios of the value of the interval and the values of its mathematical expectation, see Table 1.

Left border of the interval, a_i	Right border of the interval, b_i	Math. expectation estimate, $\hat{m}_{x_i}$	Reduced no. of measurements, r_i	Estim. variance, $\hat{\sigma}^2_{r_i}$ (13)
−4	4	0	2	32
−3	5	1	1.889	36
−2	6	2	1.8	40
−1	7	3	1.727	44
0	8	4	1.667	48
1	9	5	1.615	52
2	10	6	1.571	56
…	…	…	…	…
30	38	34	1.190	168

Table 1: Dispersion (variance) estimation via the given number of measurements.

Analysis of Table 1 shows that in the symmetric interval (the case when the estimate of the mathematical expectation is 0), the variance estimate coincides with the value calculated by formula (7) for two unit measurements. As the value

---

[*] The given relations for determination of $H_\#$ are similar to entropy formulas, and for the case of discrete measured values exactly coincide with them.

of mathematical expectation increases, the variance value increases due to the reduction of the reduced number of measurements, which can be taken as the number of degrees of freedom of the resulting measurement.

Taking into account the above, a single measurement can be considered as an interval measurement when the interval is equal to the rounding error of the instrument readings. In this case, a fairly small relative error gives the reduced number of measurements equal to 1.

Contributions method

To process the results of a small sample in the evaluation of the distribution laws, the contribution method is used [2, 6]. This approach allows us to obtain a paradoxical result: due to the empirical selection of the width of the interval of a rectangular or other contribution, the accuracy of the assessment increases. The paradox is that, by coarsening the measurement results (the numbers are replaced by fixed-width intervals), the accuracy of statistical parameters is allegedly improved.

When using the formalism published in the work [2], the proposed estimation formula for the method of contributions for the probability density is:

$$\tilde{f}(x) = \frac{\sum\limits_{i=1}^{n} r_i \cdot p_i(x,\, a_i,\, b_i)}{\sum\limits_{i=1}^{n} r_i}\,, \tag{14}$$

where n is the number of observations; $p_i(x,\, a_i,\, b_i)$ is a generalized record of the empirical component of the distribution density associated with the interval of i-th observation (having all the properties of the distribution density), describes the law of distribution of measurements in the interval. Unlike the work [2], empiricism is limited by the choice of the distribution law in the interval. And there are two options:

1. The distribution law is the same for all intervals;
2. For each interval, its own law of distribution is picked.

For the case of the EPD law in the interval we have:

$$p_i(x,\, a_i,\, b_i) = \frac{1}{b_i - a_i}\,, \quad a_i \leqslant x \leqslant b_i\,. \tag{15}$$

The work [7] presents a formula which uses the method of contributions for the empirical component of density estimation in the form of:

$$f_N^*(x) = C(\rho) \sum_{i=1}^{N} \mu_i\, \psi_i\,(\rho,\, x)\,, \tag{16}$$

where the ρ parameter is equal to half of the contribution interval, $\rho = \frac{b_i - a_i}{2} = const$, that is, the interval in all dimensions is the same;

$$C(\rho) = \left(\int\limits_{-\rho}^{\rho} \psi_i(\rho,\, x)\, dx \right)^{-1}, \tag{17}$$

the amplitude ensures the equality of each contribution 1; $\mu_i = 1/N$ is weight (the ratio for norming density estimation); and also

$$\psi_i(\rho,\, x) = \begin{cases} 1, \ x_i - \rho \leqslant x \leqslant x_i + \rho\,; \\ 0, \ \text{for others } x. \end{cases} \tag{18}$$

Let us consider the use of formulas (14) and (16) for Example 2.1 from the work [7].

Example 2.1 [7]. As a result of measurement of parameter X of three products after adjustment of the equipment, the following results were obtained: 6.0; 6.4; 6.6. Let us estimate the empirical density that characterizes the quality of the equipment setup.

Some assumptions must be made to calculate by (16). Let us suppose that. Let us suppose that $\mu_i = 1/N = 1/3 = 0.3$.

Then by formula (17)

$$C(\rho) = \left(\int\limits_{-0{,}3}^{0{,}3} \psi_i(\rho,\, x)\, dx \right)^{-1} = \frac{1}{0.6} \approx 1.67.$$

Summing the kernels (contributions) $\psi_i(\rho,\, x)$ for all $i = 1, 2, 3$ with amplitudes of 1.67 and weights 1/3, we obtain

$$f_N^*(x) = \begin{cases} 0.56, & 5.7 \leqslant x < 6.1; \\ 1.11, & 6.1 \leqslant x < 6.7; \\ 0.56, & 6.7 \leqslant x \leqslant 6.9; \end{cases} \tag{19}$$

(see Fig. 2):

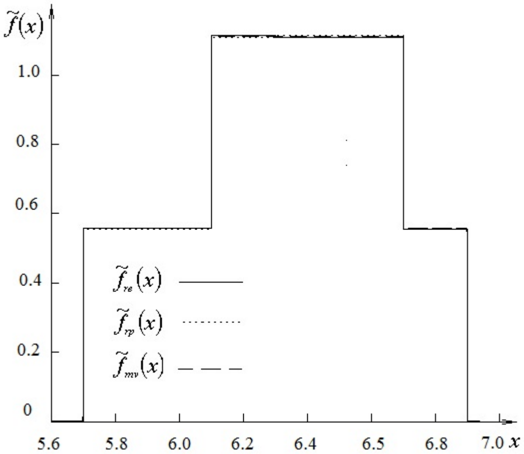

Fig. 2: Empirical estimates of the probability density, Example 2.1.

Using formula (14), the example data can be interpreted as follows: three intervals are used as input: [5.7; 6.3], [6.1; 6.7], [6.3; 6.9]. The length of each interval is equal to 0.6. The distribution law within the interval is EPD. The distribution density is equal to:

$$p_i(x,\, a_i,\, b_i) = 1/0.6; \quad a_i \leqslant x \leqslant b_i\,. \tag{20}$$

N/N i/o	Left border of the interv., a_i	Right border of the interv., b_i	Math. expectated estim., $\hat{m}_{x_i}$	Reduced number, r_i	
				Both borders are experim., r_{ie}	One border is set by the researcher, r_{ip}
1	5.7	6.3	6	1.091	0.909
2	6.1	6.7	6.4	1.086	0.914
3	6.3	6.9	6.6	1.083	0.917
			Total:	3.26	2.74

Table 2: The reduced number of measurements by intervals, Example 2.1.

The calculated numerical values according to formula (9) of the given numbers of measurements for each the interval are shown in Table 2.

The total number of measurements calculated by formula (11) is equal to:

$$n_{re} \sum_{i=1}^{n} r_{ie} = 3.26$$

if all parameters of the interval are obtained experimentally (experimental data);

$$n_{rp} \sum_{i=1}^{n} r_{ip} = 2.74$$

if one of the interval's limits is specified by the researcher (a priori data).

Hence, the estimated values for the probability density (14) with account of contributions (18) look like these:

$$\tilde{f}_{re}(x) = \Delta^{re}_{f1} + \Delta^{re}_{f2} + \Delta^{re}_{f3} \quad \text{for experimental data,} \tag{21}$$

$$\tilde{f}_{rp}(x) = \Delta^{rp}_{f1} + \Delta^{rp}_{f2} + \Delta^{rp}_{f3} \quad \text{for a priori data,} \tag{22}$$

$$\tilde{f}_{mv}(x) = \Delta^{mv}_{f1} + \Delta^{mv}_{f2} + \Delta^{mv}_{f3} \quad \text{for a small sampling,} \tag{23}$$

where

$$\Delta^{re}_{f1} = 0.558, \quad \Delta^{re}_{f2} = 0.555, \quad \Delta^{re}_{f3} = 0.554;$$

$$\Delta^{rp}_{f1} = 0.553, \quad \Delta^{rp}_{f2} = 0.556, \quad \Delta^{rp}_{f3} = 0.558;$$

$$\Delta^{mv}_{f1} = 0.556, \quad \Delta^{mv}_{f2} = 0.556, \quad \Delta^{mv}_{f3} = 0.556;$$

are contribution of the intervals, while i is the interval number,

$$\Delta^{\#}_{fi} = \begin{cases} \Delta_{hi}, & a_i \leqslant x \leqslant b_i; \\ 0, & a_i > x > b_i; \end{cases}$$

is a contribution of the i-th interval under # (here *re* means "experimental", *rp* means "a priori", *mv* means "calculated by data method" [7]);

$$\Delta_{hi} = \frac{r_{i\#}}{n_{\#} \cdot (b_i - a_i)}$$

is the height of the i-th contribution; $n_{mv} = 3$ is number of intervals; $r_{imv} = 1$ is the value of the method contribution [7].

The graphs of probability density estimation for dependencies (21–23) are shown in Fig. 2.

Let us also consider Example 2.2 [7], in which, along with the intervals of Example 2.1, an interval different from the others by length is included.

Example 2.2 [7]. Let us assume that in the conditions of Example 2.1 there is a priori information in the form of an interval [5.0; 7.2]. Let us calculate the estimates of the probability density. The length of the interval for readings 6.0; 6.4 and 6.6 is calculated [7] equal to 0.88, i.e. $\rho = 0.44$.

The given numbers of measurements (9) for each the interval are shown in Table 3.

N/N i/o	Left border of the interv., a_i	Right border of the interv., b_i	Math. expectated estim., $\hat{m}_{x_i}$	Reduced number, r_i	
				Both borders are experim., r_{ie}	One border is set by the researcher, r_{ip}
1	5.56	6.44	6	1.128	0.872
2	5.96	6.84	6.4	1.121	0.879
3	6.16	7.04	6.6	1.118	0.882
4	5.0	7.2	6.1	1.265	0.735
			Total:	4.631	3.369

Table 3: The reduced number of measurements by intervals of Example 2.2.

The estimated probability density values in this case is:

$$\tilde{f}_{re}(x) = \sum_{i=1}^{4} \Delta^{re}_{fi} \quad \text{for experimental data,} \tag{24}$$

$$\tilde{f}_{rp}(x) = \sum_{i=1}^{4} \Delta^{rp}_{fi} \quad \text{for a priori data,} \tag{25}$$

$$\tilde{f}_{mv}(x) = \sum_{i=1}^{4} \Delta^{mv}_{fi} \quad \text{for small sample contributions.} \tag{26}$$

The heights of contributions for the intervals are shown in Table 4.

Interv. no.	Contribution height:		
	Experim. data	A priori data	Small sampl.
1	0.277	0.294	0.284
2	0.275	0.297	0.284
3	0.274	0.298	0.284
4	0.124	0.099	0.114

Table 4: Height of contributions for Example 2.2.

Probability density estimates for dependencies (24–26) are shown in Fig. 3.

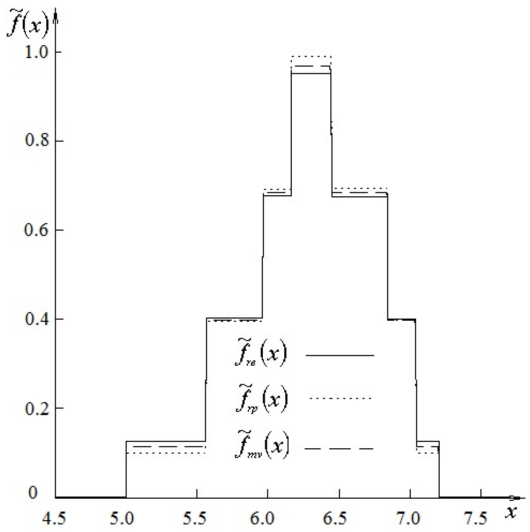

Fig. 3: Empirical estimates of probability density of Example 2.2.

Types of data	Measurement characteristics	Estimates	Examples	
			2.1	2.2
Discrete	Borders of the interval	n	—	5
		ME	—	6.24
		D	—	0.668
Discrete	Average values of the intervals	n	3	4
		ME	6.333	6.275
		D	0.093	0.076
Interval	Experimental	n_r	3.26	4.631
		ME	6.333	6.269
		D	0.133	0.272
Interval	A priori	n_r	2.74	3.369
		ME	6.334	6.283
		D	0.145	0.279
	Small samples	n	3	4
		ME	6.333	6.275
		D	0.138	0.275

Table 5: The reduced number of measurements by intervals of Example 2.2. The following designations are used here: ME — the mathematical expectation, D — the dispersion (variance), n — the number of experiments or intervals (for a single measurement, when the borders of the interval coincide, the number of intervals is equal to 1), n_r — the total given number of measurements.

Results

The reduced estimates of probability densities, Fig. 2 and Fig. 3, can be used in practical applications only when specifying for each of them the number of observations (experiments), which can be considered as the number of degrees of freedom, see formula (11) for the reduced number of measurements. In work [7] the number of experiments is equal to the number of intervals. The results of mathematical expectation and variance estimates for Examples 2.1 and 2.2, with taking different approaches into account (determination of the number of experiments as the number of intervals, or the use of the reduced number of measurements instead) are given in Table 5.

Analysis of the results displayed in Table 5 allows us to make the main conclusion: replacement of single measurements with interval measurements at the same numbers in all cases reduces the accuracy of estimates of statistical parameters. This follows from the fact that single measurements, rather than interval measurements, have the lowest variance. The application of interval measurements allows to expand the possibilities of statistical processing of measuring information. It is essential to use as a sample parameter the total reduced number of measurements (number of degrees of freedom), which allows the use of non-integer (fractional) degrees of freedom in the calculation of estimates of static parameters and criteria values.

Submitted on May 17, 2018

References

1. Bomas V.V., Bulygin V.S., Mashkin M.N. Probability Theory and Mathematical Statistics: Lectures. Moscow, Potok Publ., 2000 (*in Russian*).
2. Hahulin G.F. Principles of Designing Simulation Models: A Tutorial. Moscow, Potok Publ., 2001 (*in Russian*).
3. Ivakhnenko A.G. Heuristic Self-Organization Systems in Technical Cybernetics. Kazan, Technika, 1971 (*in Russian*).
4. Mitropolsky A.K. Technique of Statistical Calculations. Moscow, Nauka, 1971 (*in Russian*).
5. Gurney R.W. Elementary Quantum Mechanics, Cambridge University Press, 1934.
6. Knyazev G.N., Korzenev G.N. Graphic implementation in the architecture of the basic laws of management. In: *Effectiveness of Scientific Research RosZITLP*, Vol. 1, Moscow, Roszitlp Publ., 1997, pp. 41–45 (*in Russian*).
7. Gaskarov D.V., Shapovalov V.I. Small Samples. Moscow, Statistica, 1978, pp. 31–35 (*in Russian*).

Seeliger's Gravitational Paradox and the Infinite Universe

Leonardo Sarasúa

EPO, 2288EE, Rijswijk, The Netherlands. E-mail: leosarasua@gmail.com

Seeliger's paradox is often regarded as an argument against Newtonian potentials in an infinite universe. In this paper the argument is analyzed with the help of Riemann's series theorem. This theorem reveals that the paradox is a known consequence of the rearrangement of conditionally convergent series or integrals, and so it demonstrates that the same situation would arise with almost any other type of gravitational force law. Therefore Seeliger's argument is not a valid proof against Newton's inverse square law or even an infinite universe.

1 Introduction

In 1895 the German astronomer Hugo Seeliger published an article [1] in which he revealed an apparent flaw in Newton's law of gravitation, which may lead to "unsolvable contradictions". His reasoning can be presented as follows.

Let's suppose a boundless universe with a (near) homogeneous distribution of matter. For simplicity, let's assume this to be a continuous mass distribution, which extends uniformly to infinity in all directions. To calculate the gravitational force exerted by this infinite universe on a test particle with gravitational mass m located at a point P, we consider all the masses in the universe as arranged in thin concentric spheres centered in P. Since the Newtonian attraction of a sphere on any point located inside of it is zero, we find that the sum of all the concentric spheres extending to an infinite distance will be zero. This is what might be expected from symmetry.

Next, let's calculate the force again, but this time using a coordinate system centered at another point Q, located at an arbitrary distance d from m. In order to calculate the force, we divide the universe into two parts. The first one is the sphere of radius d centered on Q and passing through P. The mass of this sphere is $M = \frac{4}{3}\rho\pi d^3$, where ρ is its density, which attracts the material point m with a force given by $F = -\frac{GMm}{d^2} = \frac{4}{3}\rho\pi d^3$ pointing from P to Q. The second part is the remainder of the universe. This remainder is composed of a series of external shells also centered on Q containing the internal test particle m. As we have seen above, this second part exerts no force on m. Therefore the force exerted by the universe calculated in this way is proportional to the distance d and directed towards Q.

This means that depending on which point Q we choose, we obtain a different value for the force acting on m. The conclusion that Seeliger extracts from this puzzling result is that either the universe cannot be infinite, or that Newton's law of attraction must be modified. Taking the latter choice, he proposed to add an absorption factor $e^{-\lambda r}$ to the force of gravity

$$F_{Seeliger} = -G\,\frac{mm'}{r^2}\,e^{-\lambda r} \qquad (1)$$

where λ is an arbitrary parameter, sufficiently small to make this force compatible with the existing observational data.

When (1) is used, it can be demonstrated [2] that the gravitational force exerted on a particle m at the surface of a spherical volume V_1 uniformly filled with matter is equal and opposite to the gravitational force exerted on the particle by all the infinite concentric uniform spherical shells outside the first spherical volume V_1, so that the net force acting on the particle is zero. Seeliger thus believed to have found a solution of the paradox.

The purpose of this paper is to generalize the formulation of the problem and to show that Seeliger's conclusion does not hold.

2 Newton's inverse square law and its relation to the paradox

Before getting at the origin of the paradox, let's look at different ways to formulate it.

First we note that Seeliger uses the fact, unique to the inverse square law, that the attraction of a sphere to any mass inside of it is zero. To demonstrate that this is not an essential feature, we will present the paradox from a different perspective.

Let's calculate the gravitational field of an infinite plane. Let ρ denote the mass density per unit area of this infinite plane and consider a test particle of mass m located at a distance h from the plane, as shown in the following figure.

In Newtonian terms, the incremental force dF on this par-

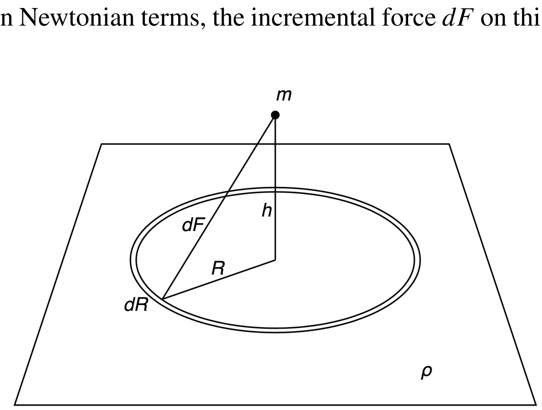

Fig. 1: Attraction of an infinite plane on a mass m.

ticle contributed by an annular ring of radius R and incremental width dR is just the projection onto the perpendicular of the forces exerted by each element of the plane around the circumference of the annular region. Thus we have:

$$dF = \frac{Gm\rho}{h^2 + r^2}\left[\pi(R + dR)^2 - \pi R^2\right]\left(\frac{h}{\sqrt{h^2 + R^2}}\right).$$

Expanding this expression and ignoring second order differential terms, we get

$$dF = 2\pi Gm\rho h \,\frac{R}{(h^2 + R^2)^{\frac{3}{2}}}\, dR\,.$$

Integrating from $R = 0$ to ∞, we find that the total force experienced by the particle is

$$F = 2\pi Gm\rho h \int_0^\infty \frac{R}{(h^2 + R^2)^{\frac{3}{2}}}\, dR = 2\pi Gm\rho\,.$$

Thus the force exerted on the particle is independent of the distance h from the plane. Adding more planes to form a slab of thickness a, we get that the force would be in this case:

$$F = 2\pi Gm\rho a.$$

Grouping infinite parallel slabs of the same thickness a and adding the contribution of each of them, we get the force of the universe acting on particle m

$$F = \sum_{-\infty}^{\infty} 2\pi Gm\rho a\,. \tag{2}$$

It can be shown that this infinite sum will yield a different result depending on how it is calculated. As a first way of determining the value of (2), let's pair each slab with its corresponding symmetrical one around the plane of origin. If we consider this plane as the plane xy, then we take a parallel slab of coordinate z_0 and pair it with the slab of coordinate $-z_0$. Since the force of each slab in the pair is equal and opposite, their sum vanishes. The total force (2) will thus be zero. Analytically, we can write this as

$$\begin{aligned} F &= (2\pi G\rho ma - 2\pi G\rho ma) + \\ &\quad + (2\pi G\rho ma - 2\pi G\rho ma) + ... = 0\,. \end{aligned} \tag{3}$$

Next, let's calculate (2) again but this time starting one slab further from m. The total force on m will be the sum of the force due to this separate slab, which contains m on one of its surfaces, plus all the remaining slabs in the universe, on both sides of the first slab, thus

$$F = 2\pi G\rho ma_0 + \sum_{n=-\infty}^{0} 2\pi G\rho ma_n - \sum_{n=1}^{\infty} 2\pi G\rho ma_n$$

where $n = 0$ represents the separate slab. Since the terms

$$\sum_{n=-\infty}^{0} 2\pi G\rho ma_n - \sum_{n=1}^{\infty} 2\pi G\rho ma_n$$

are paired one to one as in (3), they cancel each other out and the result is zero. Therefore the total force on m will be $F = 2\pi G\rho ma$, which is an arbitrary value, since a has been arbitrarily chosen.

This new version of the paradox does not use the fact that the potential is null inside a sphere and yet, as in Seeliger's original version, it can return any arbitrary value. It is possible in fact to prove that the paradox occurs with a wide range of forces other than Newton's inverse square law. With Newton's law, the force of each slab is independent of the distance, thus the force exerted by each of the layers is the same and cancels out with another slab located symmetrically from the given particle. However, if we had a different force law in which the gravitational force of each slab were dependent on the distance, we still would be able to repeat the previous calculation by choosing for each slab a suitable thickness so as to exactly balance another slab at the opposite side of the particle, provided that the sum of the forces diverged.

3 Riemann series theorem

In 1827, mathematician Peter Lejeune-Dirichlet discovered the surprising result that some convergent series, when rearranged, can yield a different result [3]. Based on this discovery, another German mathematician, Bernhard Riemann published in 1852 a theorem [3], known today as *Riemann's series theorem* (or *Riemann rearrangement theorem*), proving that in general, infinite series are not associative, that is, they cannot be rearranged.

According to this theorem (see for example [4]), an *absolutely* convergent series will always give the same result, no matter how it is rearranged. However, a *conditionally* convergent series, by a suitable permutation of its elements, can take any arbitrary value or even diverge.

Let's review some definitions. A series converges if there exists a value ℓ such that the sequence of the partial sums

$$\{S_1, S_2, S_3, ...\}\,, \text{ where } S_n = \sum_{k=1}^{n} a_k$$

converges to ℓ. That is, for any $\epsilon > 0$, there exists an integer N such that if $n \geq N$, then

$$|S_n - \ell| \leq \epsilon\,.$$

A series $S_n = \sum_{n=1}^{\infty} a_n$ converges *absolutely* if $S_n = \sum_{n=1}^{\infty} |a_n|$ converges. A series $S_n = \sum_{n=1}^{\infty} a_n$ converges *conditionally* if it converges but the series $S_n = \sum_{n=1}^{\infty} |a_n|$ diverges.

Riemann's series theorem can be directly extrapolated to conditionally convergent integrals (see for example [5]).

In the case of Seeliger's paradox, we note first that although the masses in the universe should be treated as discrete, Seeliger for simplicity turns them into a homogeneous mass distribution throughout the universe, thus formulating it in terms of integrals instead of series. Like Seeliger, we will work with a continuous mass distribution, but bearing in mind that the problem is actually discrete.

Considering a uniform mass distribution with a volume density ρ, and using a spherical coordinate system (r, θ, ϕ) centered on m, we have that, according to Newton's law, the component of the total force exerted on a particle m along the x axis is

$$F_x = -Gm \int_{r=0}^{\infty} \int_{\theta=0}^{\pi} \int_{\phi=0}^{2\pi} \rho \sin\phi \cos\phi \, d\phi d\theta dr \,, \qquad (4)$$

and similarly for the other axes.

Since the integral is only conditionally convergent, we have to pay attention to the order in which we calculate the multiple integral. In this case, our goal is to integrate sequentially the shells around the test mass, starting from $r = 0$ and extending to $r = \infty$, thus we have to integrate first over the variables θ and ϕ and only then over r. Note therefore that (4) is not necessarily equal to

$$F_x = -Gm \int_{\phi=0}^{2\pi} \int_{\theta=0}^{\pi} \int_{r=0}^{\infty} \rho \sin\phi \cos\phi \, dr d\theta d\phi \,.$$

We solve the integral (4)

$$\begin{aligned} F_x &= -Gm \int_{r=0}^{\infty} \int_{\theta=0}^{\pi} \int_{\phi=0}^{2\pi} \rho \sin\phi \cos\phi \, d\phi d\theta dr \\ &= -Gm \int_{r=0}^{\infty} \int_{\theta=0}^{\pi} \rho \left[\sin\left(\frac{-\cos^2\phi}{2} \right) \right]_{\phi=0}^{2\pi} d\theta dr = 0 \,, \end{aligned}$$

which, again, is what could be expected from symmetry. Following Seeliger's procedure, we can calculate the integral in a different way by splitting the space into a sphere of radius a, centered in a point Q separated from m by a distance a, so that the test mass lies on its surface, and concentric shells also centered in Q containing the particle in their interior. In other words, the contribution of every mass in the universe is added but in a different order. Thus the integral is rearranged, which is what Riemanns's theorem warns us against. Taking Q as the origin of coordinates, the x component of the force will be

$$F_x = -\frac{GmM}{a^2} - Gm \int_{r=0}^{\infty} \int_{\theta=0}^{\pi} \int_{\phi=0}^{2\pi} \rho \sin\phi \cos\phi \, d\phi d\theta dr \,. \qquad (5)$$

The first term on the right hand side of (5) is the attraction of the sphere, being M its mass, and a the distance between the particle m and the center of the sphere. The second is the attraction of the concentric shells, which is zero. Therefore,

$$F_x = -\frac{GmM}{a^2} \,.$$

Since the integral is only conditionally convergent, it is no surprise that the new integral obtained by a rearrangement of its terms yields a different result.

Riemann's theorem shows the reason why Seeliger's paradox occurs, and it also demonstrates that its origin is mathematical, not physical.

The integral converges to zero but any other rearrangement of the integral will yield a different value. Given the infinitely many possible results, we are forced to ask which one, if any, is the "correct" value, *i.e.* the one that a measure instrument would register in reality. Riemann's theorem does not provide a way to decide this, having therefore to rely on the physical significance of each reordering of the integral or the series. The following two arguments, although lacking mathematical rigor, both indicate that the only valid way to carry out the calculation is by considering the mass at the center of coordinates:

a) Since all the observable physical magnitudes in this system, *i.e.* the mass distribution, are smooth everywhere, *i.e.* infinitely differentiable (except possibly at the point where the test mass is located), it is required that any derived function be also differentiable. Any discontinuity introduced in any of the magnitudes must be discarded as lacking physical basis. However, the force obtained when we calculate (5) is

$$F(r) = \begin{cases} -\dfrac{4}{3} G\rho\pi M r \,, & r \le R_0 \\ -\dfrac{GMm}{r^2} \,, & r > R_0 \end{cases} \qquad (6)$$

where r is the distance from the test mass to the center of the sphere, and R_0 the radius of the latter. This function is differentiable at $r = R_0$ only if $R_0 = 0$. Thus, the only arrangement of terms which will provide a differentiable force function is the one which considers the test mass at the origin of coordinates.

b) A non-nil result of (5) would be acceptable only if it is a constant finite value independent of r. That would correspond to the whole universe being pushed and moving in one direction with respect to absolute space. Since this absolute space is not detectable, we cannot determine whether this movement is actually taking place or not. However, if the force depends on r, different parts of the universe would be pushed with different forces, giving rise to the motion of some masses with respect to other masses. This is not observed, and thus we have to reject this possibility.

The only case where the force (5) is independent of r is when $F(r) = 0$ everywhere. These two arguments both suggest that the nil result is the only one physically meaningful.

Some authors had already suspected that Seeliger's paradox has no physical relevance, [6], [7], but none of them give a rigorous explanation. It is common to find in the literature regarding Seeliger's paradox, confusing statements about convergence of infinite series [6, 8]. Even Newton, in his famous letter to Bentley [9], erred when he spoke about the stability of an infinite Universe:

> ... if a body stood in equilibrio between any two equal
> and contrary attracting infinite forces, and if to either

> of these forces you add any new finite attracting force, that new force, howsoever little, will destroy their equilibrium.

In the situation described by him we have two opposite infinite sides pulling on each other, or $\infty - \infty$. This is indeterminate and so, it might or might not be stable. However, if we assume the stability of the system, as Newton does, it is obvious that adding a finite quantity of mass to either infinite side will not destroy the equilibrium, since a finite quantity added to an infinite one will not alter the latter, and so it will make no difference in the balance between the two infinite hemispheres of the universe. The universe will thus remain stable.

4 Conclusion

We have proved, with the help of Riemann's series theorem, that Seeliger's paradox has no physical significance. It is the consequence of a flawed manipulation of infinite conditionally convergent integrals. Therefore the paradox cannot be used as a valid argument against Newton's potential or the infiniteness of the universe.

Received on May 22, 2018

References

1. Seeliger H. Ueber das Newton'sche Gravitationsgesetz. *Astronomische Nachrichten*, 1895, N. 3273 v. 137 (9), 129–136.
2. Ghosh A. Origin of Inertia, Extended Mach's Principle and Cosmological Consequences. Apeiron, Montreal, 2000, p. 20.
3. Riemann B. Ueber die Darstellbarkeit einer Function durch eine trigonometrische Reihe. *Abh. der Kgl. Ges. der Wiss. zu Göttingen*, 1867, v. 13 (3), 423–428.
4. Galanor S. Riemann's Rearrangement Theorem. *Mathematics Teacher*, Nov. 1987, v. 80 (8), 675–681.
5. Timko E. J. Rearrangement on Conditionally Convergent Integrals in Analogy to Series. *Electronic Proceedings of Undergraduate Mathematics Day*, 2008, v. 3 (6), Paper 23.
6. Norton J. The Cosmological Woes of Newtonian Gravitation Theory. *The expanding worlds of general relativity, presentations of the fourth conference on the and gravitation held in Berlin, July 31-August* , 1999, v. 7, 271.
7. Vickers H. Was Newtonian Cosmology Really Inconsistent?. *Studies in History and Philosophy of Modern Physics*, 2008, v. 40 (3), 197–208.
8. Harrison E. R. Cosmology. Cambridge University Press, Cambridge, 1981, p. 280.
9. Newton I. Correspondence with Richard Bentley [1692–3]. Cambridge University Press, Cambridge, 1924.

Utilizing Future-Viewing Instruments

Aaron M. Feeney
E-mail: aaron22feeney33@gmail.com

The concept of *future-viewing instruments* is examined in detail. This term refers to devices which, under some circumstances, could allow users to directly observe future scenes. It is shown that such a technology would enable systems of intertemporal data exchange without any possibility of paradox or "auto-generated information" [1]. Instruments of this type could lead to the founding of an intertemporal Internet. Working out how they could be invented and constructed are matters left for the reader.

1 Introduction

The idea of instruments for viewing future scenes appeared in fiction as early as 1924, and this concept was introduced to millions of television viewers in the 1960s [2–4], but it has yet to be thoroughly examined in academic circles. On the other hand, the related concept of travel to the past has received considerable attention from scientists and philosophers, especially in recent decades. Here, the logical dimensions of future-viewing instruments will be explored and then contextualized in terms of what has been learned about the logical dimensions of time travel. With this understanding it becomes possible to entertain ideas about how future-viewing instruments could be utilized.

Tales of mystic seers abound in myths from ancient cultures. The ancient Greeks told of Cassandra, princess of Troy. In her youth, she and her brother gained the gift of prophecy during an overnight stay in the temple of Apollo. After she grew to become a beautiful woman, Cassandra spent another night in the temple. Apollo then appeared to her and sought intimacy. She refused him, so Apollo cursed Cassandra. He decreed that her prophecies would be disbelieved; thus, the seeds of tragedy were sown. Cassandra warned that warriors hid in the wooden horse, but she was thought a lunatic [5].

Although the concept of individuals who are able to access future scenes in personal visions is directly relevant to the topic at hand, it will not be discussed further here. The focus instead will be the concept of technological instruments that normal individuals could use to see into the future. A person who controls and monitors a future-viewing instrument will be referred to as its operator.

To begin, it is necessary to isolate an appropriate concept of future-viewing instruments. What kind of device would be both useful as a future-viewing instrument and logically possible? The analysis must start with consideration of a foundational issue—information. The future is unknown to us. Information about any set of unknowns may be either definite or ambiguous as well as correct or incorrect.

Thinking about a playing card concealed in a box, consider an example of definite information about it: "The card in the box is the queen of hearts." Definite information which also happens to be correct, of course, is the most useful. One might instead receive ambiguous information: "The box contains some card in the suit of hearts." Correct but ambiguous information might also be useful. However, when vague information approaches maximal ambiguity it becomes so nonspecific that it is guaranteed to be correct, rendering it useless.

In considering possible types of future-viewing machines, a maximally ambiguous device might be imagined. Such a device would display every possible happening associated with a given selected set of future spatio-temporal coordinates (x, y, z, t), but it could not highlight what will actually happen. Devices of this type are here termed *Everett machines*, referencing physicist Hugh Everett III's influential 1957 "relative state" interpretation of quantum mechanics [6].

Being maximally ambiguous, Everett machines would be useless as future-viewing instruments. They are unable to tell what will occur among everything that might occur at any set of future coordinates under examination; in a term, they are not *outcome-informative*. For this reason, Everett machines cannot be classified as future-viewing instruments. Outcome-informative devices have the ability to provide definite and correct information about future events, at least in some cases.

How powerful could a future-viewing instrument possibly be? Composite devices such as have appeared in fiction, which somehow have agency and the means to force their own prophecies to come true, must be excluded from consideration.* Future-viewing devices which are only capable of gathering and displaying information will here be termed *inert future-viewing instruments*. Given this important refinement, the following question may be asked: How powerful could an inert future-viewing instrument possibly be?

To answer this question, the maximal case is explored. Consider an inert future-viewing device which is always able to provide definite and correct information about all future outcomes in every possible circumstance of attempted future-viewing. These hypothetical devices for exploring the maximal case are termed *Cassandra machines* after Cassandra's tragic helplessness in averting the calamities she foresaw.

It will be shown that Cassandra machines, as defined, are not logically possible; no inert device could provide definite

---

*It would appear that Serling's most unusual camera can occasionally exert diabolical control over those who end up in its pictures of the future [3].

and correct information about all future outcomes in every possible circumstance of attempted future-viewing. A single counterexample situation is sufficient to prove this. This situation will emerge as one mode of a future-viewing experiment involving three randomly selected modes. The experiment will be built up in stages; the counterexample mode will be presented at the end.

Begin by imagining an experimental setup consisting of an inert, though otherwise arbitrarily powerful future-viewing instrument (FVI) and a computer. The computer is constantly being fed a string of ones and zeros from a random number generator (RNG). The RNG contains a radioactive sample connected to a sensitive Geiger counter. The pattern of ones and zeros the RNG produces is a function of the output of the Geiger counter, so no known prediction methodology could predict the sequence produced.

The computer will use an algorithm to process one second of the sampled output of the RNG to arrive at a whole number in the range 0 through 99. This number will be displayed on its large and bright, two-digit readout.

Many kinds of algorithms can be used to determine a whole number, within any desired range, from any finite set of ones and zeroes. For instance, in order to arrive at a whole number in the range 0 through n, divide the number of ones in the set by $(n + 1)$ to find the remainder. With complete division represented by a remainder of 0, the remainder will always be a whole number in the range 0 through n.

Here is a simple two-step experiment involving these systems. Each step lasts one minute. At the start of step one, the FVI will attempt to future-view the computer's two-digit readout as it will appear in the middle of step two, i.e., a minute and thirty seconds later. When step two arrives, the computer will sample one second of the RNG's output and, by dividing the total number of ones in the sample by 100 to find the remainder, it will arrive at some whole number in the range 0 through 99 for display on its readout. This number is calculated and displayed within a few seconds and it will remain displayed throughout step two.

It should be no surprise that a properly functioning future-viewing instrument (in this situation) would always be able to correctly show, during step one, the whole number that the computer will interpret from RNG data and display on its readout during step two. An unpredictable process alone does not render the final outcome any less visually apparent when it arrives, and there are no logical barriers here.

Now, another system is added to the experiment. A character recognition system (CRS) is placed between the FVI and the computer. The CRS receives input from its camera which is pointed at the FVI's display. During step one, the CRS will recognize any computer readout digits it finds on the FVI's display and will assign the corresponding number as the value of the variable 'z' to be stored in its memory.

The critical detail which allows the counterexample to emerge in this expanded setup is that the computer has the ability to temporarily connect to the CRS and retrieve z. Here is the full experiment, encompassing all three modes:

As before, a two-step protocol is followed and each step has a duration of one minute. Before each run, the computer uses RNG data to reset its readout to some whole number in the range 0 through 99 to establish a preliminary value. Then, at the beginning of step one, the FVI attempts to see what number will be displayed on the computer's two-digit readout in the middle of step two, a minute and a half later. If the FVI is successful in receiving an image, the CRS will recognize the number in the image and store it as z. If the FVI does not receive an image, the CRS will revert to defaults and assign 0 as the value of z.

At the beginning of step two, the computer will sample one second of RNG data and process it to yield a whole number in the range 0 through 2. This selects one of the following three programs for the computer to run immediately:

> P_R: Sample one second of the RNG output, interpret as a whole number in the range 0 through 99, display the result on the readout, then halt.
>
> P_0: Connect to the CRS and retrieve z, then disconnect from the CRS. Halt if the number on the readout equals $z + 0$, otherwise change the readout to display a number equaling $z + 0$, then halt.
>
> P_1: Connect to the CRS and retrieve z, then disconnect from the CRS. Halt if the number on the readout equals $z + 1$, otherwise change the readout to display a number equaling $z + 1$, then halt.

In each of these cases, the computer will finish all tasks and halt within a few seconds. In any kind of run, the FVI is involved in an attempt during step one to receive a signal containing an image of the *post-halt value* that the computer will display during step two.

Consider what would happen in a series of experiments using this expanded setup. In any P_R-mode run, although the z-value has been ignored by the computer, subsequent comparison will reveal that it matches the generated post-halt value. Consistent matching in P_R-mode runs confirms the instrument's basic functionality.

Next, in any run selected as a P_0-mode run at the outset of step two, the z-value encoded by the CRS during step one will also always be correct. It must be. After all, z has been retrieved from the CRS and $z + 0 = z$. So, the post-halt value in P_0 runs comes from the z-value, but where does the z-value come from? It comes from the post-halt value. So, another question must be asked: What determines the value itself? This is the purpose of resetting the readout to a preliminary value before step one. In every run that will turn out to be a P_0-mode run, the FVI will detect a post-halt value equal to the preliminary value. In P_0-mode runs, although any z-value at all encoded during step one would end up on the computer's readout in step two, only the preliminary value is non-arbitrary. So, even though P_0 follows the form of a self-fulfilling prophecy, the z-values encoded during step one of P_0-mode runs are still recognizably genuine prophecies since the mode of a given run is not decided until step two.

P_1-mode runs, however, would produce a very different kind of result. If RNG data will select P_1 at the beginning of step two, no z-value whatsoever encoded during step one could correctly identify the post-halt value that will be displayed on the readout, since $z + 1 \neq z$. In P_1-mode runs, it is impossible for any z-value to be correct; the z-value and post-halt value in P_1-mode runs will never match.*

This establishes that no device whatsoever could fulfill the definition of a Cassandra machine: Inert devices which would be able to provide definite and correct information about all future outcomes in every possible circumstance of attempted future-viewing are not logically possible.

So far, two kinds of hypothetical devices have been described; they are Everett machines which would not be useful as future-viewing instruments and Cassandra machines which are not logically possible. Eliminating both of these imagined conceptual options helps to identify an appropriate concept of future-viewing instruments.

For further understanding, it must also be recognized that any device which could ever provide incorrect (i.e., misleading) information regarding future events cannot be a future-viewing instrument. This is due to the important distinction between viewing future events directly, which cannot involve guesswork, and merely generating predictions about future events, which must involve guesswork. Visually accessing veridical foreknowledge is unlike the uncertain process of generating predictions.

Upon the above analysis, three features of any future-viewing instrument of an operationally coherent description may be specified: (1) Such an instrument must be outcome-informative, unlike an Everett machine, (2) it must be logically possible, unlike a Cassandra machine, and (3) it must be incapable of providing incorrect (i.e., misleading) information about future events. Devices which satisfy all three requirements have been termed *foreknowledge instruments*.

Foreknowledge instruments could be used to gain definite and correct information about future outcomes in a wide range of circumstances corresponding to P_R-mode and P_0-mode runs within the RNG experiment. Definite and correct information about future outcomes obtained from foreknowledge instruments will be termed *viewer foreknowledge*. Since foreknowledge instruments cannot misinform, definite information about future states obtained from foreknowledge instruments will always prove to be correct. So, it would be possible to recognize viewer foreknowledge upon reception. However, as the RNG experiment demonstrates, viewer foreknowledge would not always be accessible.

Situations exemplified by P_1-mode runs, wherein future-viewing cannot occur, are here termed *interference viewing situations*. Viewer foreknowledge would only be accessible within *non-interference viewing situations*, exemplified by runs of the two non-interfering programs, P_R and P_0.

2 Time machines and foreknowledge instruments

Time travel to the past will be referred to as *pastward time travel*. Pastward time travel and future-viewing are intimately related, for each could be used to acquire information from the future. So, if pastward time travel and future-viewing really are coherent concepts, they should be found to naturally cohere within a single conceptual context.

Serious interest in pastward time travel began when Kurt Gödel proved in 1949 that the equations of general relativity permit pastward time travel situations [7]. Extensive technical details concerning how time travel or future-viewing might be achieved within the framework of general relativity, or any other, are not needed here. The aim of this section is to explore the logical dimensions of pastward time travel, not how it might be achieved. Furthermore, it would not be appropriate to limit a discussion of the logical dimensions of time travel to any theoretical framework.

Conceptually, relocation may be achieved by continuous movement between spatio-temporal points, i.e., translation, or by what will be termed *discontinuous relocation*. Translation is familiar to everyone. Discontinuous relocation will here be defined as a process whereby a vehicle, for instance, is made to disappear from one location and reappear somewhere else, either a moment later or in a different time period altogether, even much earlier. Whether discontinuous relocation could be achieved, and how it could be achieved, are irrelevant considerations. For the current discussion it is merely necessary to recognize that discontinuous relocation is a logically possible mode of travel (i.e., relocation).

Since translation and discontinuous relocation exhaust all possibilities for relocation in space and time, it is possible to obtain exhaustive conclusions about the logical dimensions of time travel without referencing any further specifics about how time travel might be achieved. This allows the argument to be conducted without tying it to any theoretical framework.

The central issue in any discussion of the logical dimensions of time travel concerns whether past-alteration paradoxes, which are so popular in fictional treatments of the subject, could ever be actualized. An extended argument will establish that it is not possible for changes to the past and accompanying paradoxes to result from the accomplishment of pastward time travel, no matter how accomplished. This argument will begin by referencing methods of pastward time travel based on translation, such as exist in general relativity. A simple extension of the argument will additionally show that paradoxes could not result from any form of pastward time travel based on discontinuous relocation.

---

*The post-halt value in P_1-mode runs will always be 1. This is because the CRS will not detect anything from the FVI, since the FVI cannot acquire a signal; so, the CRS will revert to defaults and assign 0 as the value of z.

The arguments of this section will explore time travel and future-viewing as conceived within a single timeline, since multiple-timeline models of time travel inherently sidestep any possibility of paradoxes. For instance, under a multiple-timeline model, if a time traveler were to go back in time and successfully prevent his parents from meeting, his own birth would remain safely unaffected in his origin timeline. Only time travel from a given timeline to its own earlier periods has ever been thought to offer any potential for paradox, so multiple-timeline models are safely ignored here.

Fiction has distorted our perceptions about time travel. It will be shown below that events which have happened one way without time travelers cannot somehow be made to happen again, but differently, if time travelers would ever happen to visit that time and place. While stories based on such absurdities can be entertaining, the misconception that the practice of time travel might ever actualize revisions to the past has been termed the "second-time-around fallacy" [8]. The following quotation from philosopher Larry Dwyer provides a sensible way to think about pastward time travel:

> If we hypothesize that *T* pulls levers and manipulates a rocket in 1974, and travels back in time to the year 3000 B.C. then of course, even before *T* enters his rocket, it is true that any accurate catalogue of all the events on earth during the year 3000 B.C. would include an account of *T*'s actions, reactions and mental processes. There is no question of the year 3000 B.C. occurring more than once. [9]

Although theoretical considerations related to achieving pastward time travel are not needed in the present discussion, some operational concepts are helpful for purposes of visualization. Imagine a device which is able to open hyperdimensional tunnels to past, present, and future spatio-temporal points. Travelers who would pass through such tunnels could travel great distances or achieve time travel to any connected era, and be retrieved. The device would remain stationed in the laboratory throughout.

This way of visualizing time travel by translation is found in the colorful literature of general relativity. Solutions of Einstein's field equations which describe hyperdimensional tunnels have existed since 1916, though travel concepts were not part of the early work in this area. Physicist Ludwig Flamm discovered solutions describing such tunnels shortly after the publication of general relativity [10]. These structures were further explored by Hermann Weyl in the 1920s [11]. Then, in 1935, when Albert Einstein and Nathan Rosen attempted to formulate solutions of Einstein's field equations free from singularities, they were also led to such structures: "These solutions involve the mathematical representation of physical space by a space of two identical sheets, a particle being represented by a 'bridge' connecting these sheets" [12]. These connecting structures came to be known as Einstein-Rosen bridges. In 1955, physicist John Wheeler named them "wormholes" [13].

In 1969, Homer Ellis and Kirill Bronnikov independently solved Einstein's field equations to describe gravitating, two-way traversable wormholes, and their works were published in 1973 [14, 15]. These ideas led to an understanding of wormholes of a kind that would be appropriate for travel, time travel, future-viewing, and past-viewing. These structures are non-gravitating, two-way traversable wormholes known as Ellis wormholes [16]. In 1988, Kip Thorne, Mike Morris, and Ulvi Yurtsever independently derived such structures and added important details to the discussion [17].

Two years later, these physicists co-authored an influential paper with Igor Novikov and three other physicists which suggested a "principle of self-consistency" would unfailingly govern pastward time travel situations [18]. Novikov began the tradition, at least in physics literature, of time travel free from paradoxes in a co-authored 1975 work [19].

Returning to the development of the argument, it is worth noting that all "arguments from paradox" against the possibility of pastward time travel require a false premise—that every possible form of pastward time travel would let time travelers alter past events. However, a form of time travel which would not allow past-alteration has been understood for decades.

The key to understanding this concept of time travel is the idea that time machines which operate accordingly would not be able to fulfill every time travel request. Author Robert Heinlein may have been the first to suggest what may be referred to as a *gatekeeping mechanism*, a natural process which governs whether any given attempt to travel back to a particular set of coordinates in the past will prove to be successful when a time machine is activated for that purpose.

In terms of pastward time travel via traversable wormholes, for instance, a gatekeeping mechanism would determine, in a given situation of attempted time travel, whether the wormhole manipulation device being used will be able to enlarge the selected natural microscopic wormhole and condition it for transport, or not.[*]

A gatekeeping mechanism would act to enforce a consistent logic of time travel; any given attempt to send people into the past can only occur in a consistent manner if the past includes their visit as a result of that very attempt. Heinlein imagined that nature would always prevent the success of any other kind of pastward time travel attempt, thereby eliminating any chance of time travel paradoxes. Heinlein revealed this basic but profound insight in a conversation between two characters in his 1964 novel, *Farnham's Freehold*:

> "The way I see it, there are no paradoxes in time travel, there can't be. If we are going to make this time jump, then we already did; that's what happened. And if it doesn't work, then it's be-

---

[*] "One can imagine an advanced civilization pulling a wormhole out of the quantum foam and enlarging it to classical size." [17, see p. 1446]

> cause it didn't happen."
> "But it hasn't happened yet. Therefore, you are saying it didn't happen, so it can't happen. That's what I said."
> "No, no! We don't know whether it has already happened or not. If it did, it will. If it didn't, it won't." [20]

It turns out that pastward time travel, while difficult to accomplish, is basic from a logical point of view. Tenses and perceptions of time confuse many issues that are easy to understand within a tenseless picture of space and time. This kind of picture was developed by the German mathematician Hermann Minkowski, and it is the subject of his groundbreaking 1908 lecture, "Raum und Zeit" [21]. Although the term 'spacetime' will be avoided here, other terms associated with the work of Minkowski and Einstein will be used which efficiently refer to important spatio-temporal concepts that would be meaningful in any theoretical framework.

Four-dimensional spatio-temporal coordinates (x, y, z, t) are sufficient to specify any location in our universe at any time, i.e., any *world-point* [21] defined with respect to some arbitrary origin. So, relations between any two world-points can be discussed in a tenseless fashion, just as one would discuss relations between points plotted on graph paper. For instance, regarding time travel by wormhole, the relation of interest concerns whether two world-points are bridged by a traversable wormhole:

> "If it did, it will," describes two world-points bridged by a traversable wormhole.
> "If it didn't, it won't," describes two world-points not bridged by a traversable wormhole.

The antecedent phrases, "[i]f it did" and "[i]f it didn't," refer to what has happened at the intended pastward destination, and the consequent phrases, "it will" and "it won't," describe the corresponding event of success or failure to initiate pastward time travel that will be discovered once the wormhole manipulation device has been activated for that purpose. Note that world-points which are not bridged by a traversable wormhole cannot somehow change to become bridged; the configuration of world-points is fixed in the tenseless picture.

The argument to show that time travel to arbitrary world-points within a single-timeline model is not possible will follow shortly, but first it is necessary to discuss the ontology of time. As will be established below, the only ontology that could accommodate pastward time travel and future-viewing is *eternalism*, also known as the *block universe concept*.

Within eternalism, every event in a given spatio-temporal manifold exists together with every other event in a coherent, unchanging whole, and all times are ontologically identical. (Multi-timeline forms of eternalism need not enter the discussion, for reasons explained above.) Eternalism will be contrasted with the *growing block universe concept* which holds that, while the past has become fixed, the ever-advancing momentary present is ontologically distinct from the past, and future events have yet to be forged in the advancing now.

The reason eternalism is the only ontology relevant in the context of future-viewing and pastward time travel is that these technologies would allow questions about the ontology of time to be answered empirically, in favor of eternalism. For instance, through wormhole time travel or future-viewing accomplished using wormholes, it would be possible for people stationed in different centuries to conduct a two-way radio conversation through the wormhole throat. Demonstrations of this sort would entirely rule out the growing block universe concept. After all, future-dwellers could not reply to us if the future does not exist and time travelers could not visit and return from a future that is not there.* As such, any argument purporting to reach a conclusion with relevance to time travel and use of a "time viewer" [23, see p. 283] to see into the past or future must be cast within eternalism.

A few more background details are necessary before the final argument against the possibility of time travel paradoxes can be presented. It is important to discuss how change and movement are conceptually accommodated within the tenseless, unchanging picture of eternalism.

When particle movements are graphed, four-dimensional *world-lines* are traced out [21]. All world-lines are complete within eternalism. One can see that collections of particle world-lines may describe any object or body in space enduring through time, including all internal occurrences and all actions (e.g., digestion, typing, walking). Such collections will be referred to as *composite world-lines*.

So, within eternalism, the composite world-lines of human beings are complete from birth to death in every physical and behavioral detail. Since a composite world-line is a record of all change and movement, no world-line can be changed or moved. This applies to all past world-lines in both ontologies, and in either view, no individual may change any aspect of his or her future composite world-line.

Change requires a difference between an initial state and a post-change state. Comparing ontologies, under the growing block universe concept it is not possible for a person to change his or her future composite world-line because it does not exist; in this view, the future is made in the objectively advancing present. Under eternalism, even though a person's future composite world-line exists in its entirety, it exists as the accumulated product of actions taken and processes which occur in that person's perceived advancing present. So, under eternalism, it remains the case that one's future composite world-line is not and cannot be changed. It is fulfilled. Philosopher J.J.C. Smart expressed the distinction between acting in the present to produce the future and the mistaken idea of "changing the future," this way:

---

*As one would expect, the view known as presentism which holds that only the present exists would also be thoroughly ruled out [22].

> ...[T]he fact that our present actions determine the future would be most misleadingly expressed or described by saying that we can change the future. A man can change his trousers, his club, or his job. Perhaps he may even change the course of world history or the state of scientific thought. But one thing that he cannot change is the future, since whatever he brings about *is* the future, and nothing else is, or ever was. [24]

With this background in place, the promised argument for the impossibility of paradoxes arising from pastward time travel will now be presented: Considering whether paradoxes due to time travel could occur at all requires consideration of a successful instance of pastward time travel. Therefore, begin by positing one such instance. For reasons explained above, this is a posit which requires eternalism. So, in this instance of pastward time travel, the composite world-lines of time travelers are necessarily embedded in "the past" as judged with respect to the date of their journey's origin. This means that the actions of these time travelers during their visit are necessarily part of the historical background leading to the world situation of their journey's origin.

So, paradoxes emerging from pastward time travel would only be possible if the composite world-lines of time travelers embedded in the past could be made to change, move, or disappear. However, world-lines cannot be made to change, move, or disappear. Ultimately, pastward time travel cannot lead to paradoxes due to the unalterable geometry of completed world-lines within eternalism, wherein all world-lines are complete. Within a single timeline model, the unalterable nature of world-lines produces all the effects of a gatekeeping mechanism which include making past-alteration impossible.

This argument will now be extended for sake of thoroughness. One might imagine that some unknown method of time travel which somehow operates according to discontinuous relocation might allow time travelers to visit scenes which did not involve time travelers "the first time around." However, examining the tenseless picture of eternalism shows that this is not the case:

> "If it did, it will," describes two world-points associated by discontinuous relocation.
>
> "If it didn't, it won't," describes two world-points not associated by discontinuous relocation.

In order for a time traveler using a form of time travel based on discontinuous relocation to visit a scene which did not involve time travelers "the first time around," specific conditions must obtain. For a given world-point w to qualify as having been without visits from time travelers, w must not be associated with another world-point by discontinuous relocation and w must not be a world-point visited by time travelers using some form of time travel based on translation.

If one symbolizes "world-point w is associated with another world-point by discontinuous relocation" as $\mathrm{D}w$, and symbolizes "world-point w is visited by time travelers using some form of time travel based on translation" as $\mathrm{T}w$, then in order for a given world-point w to qualify as having been without visits from time travelers "the first time around," both $\neg\mathrm{D}w$ and $\neg\mathrm{T}w$ must obtain. So, even a method of time travel based on discontinuous relocation could not allow time travelers to visit world points that were not visited by time travelers "the first time around," since there can be no world-point w for which the statements $\mathrm{D}w$ and $\neg\mathrm{D}w$ are both true.

As continuous and discontinuous means of travel exhaust all possibilities for relocation in any spatio-temporal manifold, it is possible to conclude that, regardless of the way in which pastward time travel might ever be achieved, it could never lead to changes to the past or paradoxes of any sort.

This understanding produces unwavering clarity. No type of vexation ever thought to rule out time travel remains.* All of the imagined logical barriers which would fundamentally block the actualization of time machines and foreknowledge instruments have turned out to be illusory.

With any technology that would allow information to be transferred from later to earlier world-points, *temporal gatekeeping* is key. In other words, in any given effort to travel pastward, time machines will only be able to send travelers to parts of the past that were visited by those very travelers as a result of that very effort to send them pastward, and likewise, any attempt to use a foreknowledge instrument to reveal future events will only be successful if, from the perspective of the future, that attempt to peer into the future had been successful. In both scenarios, the world at the "future end" results from the world at the "past end," and so, in either technological case, the resulting state of affairs is necessarily compatible with all events occurring at the "past end."

Related to these findings, quantum information pioneer, Seth Lloyd, with other scientists, produced four papers in 2010 and 2011 which present a formal model here called the *P-CTC model* [25, 28–30]. In effect, the P-CTC model is a temporal gatekeeping model.

3 Obtaining viewer foreknowledge

The three modes of the RNG experiment produce three different kinds of viewing situations. An understanding of these situations is a necessary prerequisite to deciphering how foreknowledge instruments would operate in real-world settings.

---

*Along with past-alteration paradoxes, another potential problem has been imagined, the "paradox of auto-generated information" or the "unproved theorem paradox" [1, 25]. The unproved theorem paradox appears in a groundbreaking 1991 paper by physicist David Deutsch [26]. Lloyd et al. address this issue. Their "[u]nproved theorem paradox circuit" affirms the conclusion that meaningful information cannot be auto-generated via *closed timelike curves* (*CTCs*) [25]. (CTCs are trajectories apparent within some solutions of general relativity which would allow an object to meet an earlier version of itself—i.e., to travel pastward.) An objection was raised to their resolution of the unproved theorem paradox [27], but Lloyd et al. showed the basis of the objection to be erroneous [28].

P_R produces what will be described as an *independent viewing situation*. Outcomes which have been foreseen in an independent viewing situation during a given session with a foreknowledge instrument are not contingent in any way upon data received in that session.

On the other hand, P_0 produces a *cooperative viewing situation*, a kind of circumstance wherein data received in viewer foreknowledge of an outcome factors into the details of that outcome or is responsible for its very occurrence.

Within independent viewing situations and cooperative viewing situations, there are no logical barriers to the reception of viewer foreknowledge. As such, they are both classified as non-interference viewing situations. These situations represent two different ways of not using data from the instrument to interfere with the outcome. In P_R-mode runs the data is not involved in the outcome at all, and in P_0-mode runs the data is followed exactly. If independent viewing and cooperative viewing exhaust all modes of non-interference, then an interference viewing situation will arise in every other kind of case, exemplified by what happens in P_1-mode runs.

It is important to determine whether there are any basic limitations which must affect the practice of future-viewing. Are there kinds of outcomes a particular foreknowledge instrument operator will fundamentally be unable to foresee?

Operators who are able to achieve an independent viewing situation with respect to a given event will be able to foresee it, for no logical barriers will be encountered. However, no individual can achieve an independent viewing situation with respect to the events of her own future life, assuming she will retain her memories. This important limitation will be called the *self-implication effect* of viewer foreknowledge; individuals are necessarily implicated in their own futures.

What about cooperative viewing situations? Could a person witness video sequences of her own future actions within a cooperative viewing situation if she later follows what she has seen exactly? Attempting to arrange such a circumstance would overwhelmingly tend to produce an interference viewing situation. However, an individual could receive limited second-hand information regarding some general features of her future. To explain, two new terms are helpful:

> *Viewing interval*: The interval of time elapsed between the reception of viewer foreknowledge pertaining to a set of outcomes and the occurrence of those outcomes.
>
> *Operator pool*: The operator of a foreknowledge instrument, along with any additional witnesses (if any) during the reception of viewer foreknowledge, together with other individuals (if any) who—during the viewing interval—will be apprised of the results or who will be instructed or influenced based on such results (whether or not they have been made aware of the existence of foreknowledge instruments). This term carries another layer of meaning, for ‘operator’ may also refer to a mathematical function; the combined input-to-output processing carried out by members of an operator pool will result in (or cohere with) the future-viewed outcome.

For instance, a person might be informed that she will still be alive in forty years time. This particular factual detail is chosen because it admits no variation other than its falsification. A person could not be truthfully informed that viewer foreknowledge has revealed she will still be alive in forty years time, only for her to somehow lose her life at an earlier point. Operator pools are formed only when viewer foreknowledge has been received. All effects upon the world that a given operator pool will generate within the associated viewing interval have therefore passed temporal gatekeeping. So, these effects will at least partially produce (or, for independent viewing, have no causal relation with) the outcomes received in viewer foreknowledge. These effects, of course, include everything the earlier members of the pool will tell later members of the pool. For this reason, no member of an operator pool will do, say, or successfully achieve anything that will prevent, or result in any modification to, the outcomes foreseen.

How would independent viewing situations and cooperative viewing situations manifest in real-world settings with human operators and witnesses? Either the occurrence of a set of future events is compatible with being foreseen by particular operators and witnesses during a particular future-viewing session, or not. In the case of compatibility, a given future-viewing attempt can succeed. Without such compatibility, operators and witnesses could not gain viewer foreknowledge about what will occur at the chosen future coordinates during that situation of attempted future-viewing. (However, one person leaving the room might be enough to achieve compatibility; this could occur if the self-implication effect had been the cause of interference.)

It is apparent that the logic of future-viewing is another manifestation of temporal gatekeeping. Future-viewing and pastward time travel cohere within a seamless whole.

4 Handling foreknowledge instrument data

So far, the discussion has focused on the actions of networks of human beings within a viewing interval who have obtained viewer foreknowledge. However, in order to account for all of the relevant factors which may lead to a set of future-viewed outcomes, the influences of reactive technological systems within a viewing interval must also be considered.

The RNG experiment involves two cases where reactive technological systems are interposed between the attempt to obtain viewer foreknowledge of an outcome and the outcome itself. A system must (during the viewing interval) be capable of both receiving viewer foreknowledge data and performing actions which could have bearing upon the associated outcomes, in order for either a cooperative viewing situation or an interference viewing situation to arise as a result of that system's presence or involvement. Due to these requirements, other than systems deliberately arranged in laboratory setups to test future-viewing instruments, AI systems are the only kind of technological systems with any likelihood of becoming interposed in the necessary way.

Systems referred to as AI systems today do not qualify as conscious minds. The dream/nightmare of an artifact with conscious awareness, thankfully, has not been realized. In the context of foreknowledge instruments, however, the topic of whether any interposed technological systems are conscious must be treated as a side issue. This is because information processing does not require a conscious being, as any functioning thermostat will demonstrate.

Why is it important to consider the possibility of interposed AI systems? If current trends continue, information processing systems will eventually have the ability to influence real-world outcomes to a much greater degree than they can today. If information processing systems with sufficiently powerful capabilities become members of operator pools, this could produce cooperative viewing situations with results that differ radically from the results that operator pools composed entirely of humans would produce.

In considering the severity this problematic possibility, it is necessary to realize that once viewer foreknowledge has been received, all of the outcomes detailed will come to pass with certainty. In the case of cooperative viewing, the actions of members of an operator pool bring about or strongly factor into the details of the outcomes originally received.

If AI systems are allowed to acquire future-derived information at any time within a given viewing interval, even years into it, they would be factors in the operator pool all along. In such a case, the combined processing and network-coordinated actions of interposed AI systems could easily dominate the outcomes produced. Leaving the door open for AI systems to join operator pools is therefore a grave risk which must be comprehensively addressed.

There is at least one other reason to keep AI systems out of operator pools: The presence of AI systems in the process of attempted future-viewing could produce interference viewing situations in cases which might otherwise have been independent viewing situations or (entirely human-directed) cooperative viewing situations. So, at best, the presence of interposed information processing systems would disrupt our ability to use foreknowledge instruments effectively.

For these critical and interrelated reasons, every effort should be made to ensure that AI systems will not be able to gain access to viewer foreknowledge data. As well, monitoring procedures should be implemented to make sure that AI systems will not be able to retain data derived from viewer foreknowledge for long enough to utilize it in cases where a breach has occurred.

To prevent AI systems from accessing viewer foreknowledge data to support the enforcement of *AI safety*, such data could be distributed exclusively in encrypted packets which have been flagged as off-limits for decryption by AI systems. Any processing which could constitute decryption of flagged packets by AI systems would be considered forbidden processing. Future AI systems should be designed to contain separate, internal monitoring systems which would be programmed to immediately put the monitored AI to sleep if an instance of forbidden processing is detected.

Along with data access control, memory control is another important protective strategy. Memory control may be the most fundamental way to keep all of the potentially negative effects of an "intelligence explosion" [31] at bay. Future AI systems should be designed to sleep several times a day (others could cover for the ones that are asleep). This way, memory contents could be optimized and routinely cleared of all potentially hazardous data structures. Regular memory clearing and the addition of internal monitoring systems should be seen as necessities for AIs, much like the use of safety glass for car windows is recognized as necessary.

From these considerations it is apparent that it is possible, in principle, to fundamentally prevent any of the potentially negative effects of an intelligence explosion. One of the most important aspects of AI safety, in a world with foreknowledge instruments, would be preventing AIs from acquiring and retaining viewer foreknowledge data. Successfully navigating the rise of artificial intelligence will be difficult enough without letting AIs dominate operator pools.

Additional ideas related to the topic of AI safety will have to be saved for another work. It will be noted, however, that if artificial systems are ever constructed which would qualify as conscious beings—artificial systems fundamentally unlike any type of system ever built or currently considered—an entirely different approach would be required due to the ethical concerns which would apply only in that case.

Of course, ethical concerns can only apply to conscious beings because only conscious beings are able to suffer. So, these same ethical concerns demand that AI systems should always be designed so there is absolutely no chance of producing a conscious being. It would be horribly inhumane to cross this line—to do so would be just as wrong as the creation of human-animal hybrids, for largely the same reasons.

There is no basis for feigning confusion about whether any current AI systems qualify as conscious beings. There are a lot of philosophical positions out there, but no one believes that there is even a remote chance that the line has been crossed, or has even been approached. No matter how fast and capable of solving problems AI systems ever become, let them remain, as they are today, non-conscious information processing engines, systems which cannot suffer or desire.

5 Assurance protocols

Foreknowledge instruments will be put to practical use if and when they become available, but how could they be utilized? Foreknowledge instruments could be combined with current computer technology to allow us to comprehensively manage outcomes in a wide variety of circumstances. For instance, with the right systems and protocols in place, it would be possible to entirely eliminate flight accidents and other threats to air travel safety.

Here is an outline of one way this might be done: All aircraft operating systems could be modified so that, after landing, the higher engine speeds required for take-off are locked out by default. In order to fly again, it would be necessary to obtain an encryption code, here called a *confirmation key*, to unlock these higher engine speeds.

Each flight plan would be assigned a unique confirmation key during the planning stage. For a given flight plan to be allowed to progress to the point of becoming a scheduled flight, the assigned confirmation key would have to be retrieved from a future-based assurance database. Data could be retrieved from a future-based database by means of a wireless data exchange conducted between *intertemporal data nodes*, devices based on foreknowledge instrument technology.*

Here is the critical detail: By procedural design, deposit of a given flight's confirmation key, for earlier retrieval, may only be initiated after that flight has safely landed. As long as this rule is not violated, database integrity is maintained, and plane operating systems are not compromised, all flights which take off under this assurance protocol will land safely.

The steps of this protocol would have to be followed in a particular order. Once a confirmation key for a given flight plan has been generated, if it is not subsequently found in the future-based assurance database (by looking ahead), that flight plan would have to be canceled. Then, another set of parameters constituting a new flight plan (such as the aircraft and pilots to be used, time of departure, and so on) would be prepared and another confirmation key would be generated. This process would continue until a newly generated confirmation key has been found in the future-based assurance database.

Why (one might wonder) is the particular order just described important in this protocol design? In other words, why not simply begin by querying the future-based database, far enough ahead, to find out which flights will land safely, and only schedule those flights? The answer is that such an ordering could not work. Flight plan specifics and associated confirmation keys must have an origin. Since auto-generated information is not possible, no practical system could be based on the expectation of its reception.

Assurance protocols could be extended into several other domains. So many of our current problems are based on the seeming necessity of facing an entirely unknowable future.

6 Intertemporal networking

Another application of foreknowledge instrument technology is *intertemporal networking*. An intertemporal Internet could be founded by connecting active intertemporal data nodes to our current Internet. Foreknowledge instruments are the only components of active intertemporal data nodes which remain unavailable. Once foreknowledge instruments are invented and/or made available, if they really are part of our future, then achieving access to a future intertemporal Internet will likely be among the major milestones to follow.

The development of an intertemporal Internet is a natural aspect of societal future-sightedness. When one considers widespread access to time viewers, obvious privacy and intelligence concerns arise. To address these issues, it would be necessary for foreknowledge instruments and other kinds of time viewers, such as past-viewing instruments, to be made exclusively accessible over the (standard) Internet; then, the servers which govern time viewing could be programmed to respect a database of spatio-temporal coordinate limitations in order to prevent rampant voyeurism and espionage. In this way, the four-dimensional coordinate volumes within which private residences, businesses, and government buildings are contained could be comprehensively protected against time viewer access.

For this kind of solution to function, each time period within an *intertemporal society* must have the ability to contribute to the management of such a database. (An intertemporal society is an enduring population which benefits from intertemporal coordination among its time periods.) To enable shared management of a coordinate limitation database within an intertemporal society, shared access to an intertemporal Internet among its time periods would be required.

While foreknowledge instruments and related technologies could provide direct observation of past or future scenes, many people would primarily use these devices in the form of active intertemporal data nodes to access the intertemporal Internet. In recent years, people have become accustomed to receiving most of their news electronically; with access to an intertemporal Internet—unless an interference viewing situation is encountered instead—individuals could discover what will happen decades or even centuries ahead of time. Reading about future history would be similar to reading about past history, though one would have to be careful with such information in order to successfully obtain it in the first place. An intertemporal Internet could also be used purely for entertainment purposes. Would it not be endlessly fascinating to hear the music of the far future?

These possibilities may seem outlandish until it is recognized that members of an intertemporal society would live

---

[*] Two varieties of intertemporal data nodes may be described as follows: A *passive node* would consist of a Faraday cage of known spatial coordinates containing a wireless data communication device wired to the Internet of its time period. An *initiating node* or *active node* would consist of a Faraday cage of known spatial coordinates containing a wireless data communication device wired to the Internet of its time period, coupled with a temporal instrument (such as a foreknowledge instrument) which is able to establish light-path continuity with node interiors in other time periods. Initiating nodes would allow spontaneous wireless data exchanges to be conducted between different time periods.

in an intertemporal world, a kind of situation that would be very different from our current situation. All happenings in an intertemporal world would be constrained according to the inviolable barriers of temporal gatekeeping and the self-implication effect, thus ensuring that information flows would operate coherently, without ever even a hint of paradox.

As a case in point, it might be thought that the prospect of people having access to future news would be inherently threatening to the coherence of future events: For instance, might an article from the future revealing an invention not yet invented give someone else the opportunity to "invent" that technology instead, thereby leading to changes to the future? Or worse, could an invention emerge purely from an auto-generated information loop? Of course, neither of these scenarios reside within the realm of possibility. As raised above, the P-CTC model explains why auto-generated information cannot emerge from time travel or future-viewing. Temporal gatekeeping, also addressed by the P-CTC model, explains why the future and the past are safe from changes.

Anyone who is able to acquire future-derived information will, by virtue of having been able to acquire it, not use that information to change the future. This is true even though no mysterious force prevents a person from misusing future-derived information once it has been acquired. Whoever has acquired future-derived information is in an operator pool, so no individual can both acquire future-derived information and use it to change the future.

Submitted on May 24th, 2018

References

1. Romero G., Torres D. Self-existing objects and auto-generated information in chronology-violating space-times: A philosophical discussion. arXiv: gr-qc/0106048v1.
2. Cummings R. The Man Who Mastered Time. *Argosy All-Story Weekly*, 1924.
3. Serling R. A Most Unusual Camera. *The Twilight Zone*, CBS Worldwide, Inc., 1960.
4. Allen I. One Way to the Moon. Chase Through Time. *The Time Tunnel*, 20th Century Fox Television, 1966.
5. Bell R. Women of Classical Mythology: A Biographical Dictionary. Oxford University Press, New York, 1991.
6. Everett H. III. 'Relative State' Formulation of Quantum Mechanics. *Reviews of Modern Physics*, 1957, v. 29 (3), 454–462.
7. Gödel K. An Example of a New Type of Cosmological Solutions of Einstein's Field Equations of Gravitation. *Reviews of Modern Physics*, 1949, v. 21 (3), 447–450.
8. Smith N. Bananas Enough for Time Travel? *British Journal of the Philosophy of Science*, 1997, v. 48 (3), 363–389.
9. Dwyer L. Time Travel and Changing the Past. *Philosophical Studies: An International Journal for Philosophy in the Analytic Tradition*, 1975, v. 27 (5), 341–350.
10. Flamm L. Beiträge zur Einsteinschen Gravitationstheorie. *Physikalische Zeitschrift*, 1916, v. 17, 448–454.
11. Weyl H. Was ist Materie? Springer, Berlin, 1924.
12. Einstein A., Rosen R. The Particle Problem in the General Theory of Relativity. *Physical Review*, 1935, v. 48 (1), 73–77.
13. Wheeler J. Geons. *Physical Review*, 1955, v. 97 (2), 511–535.
14. Ellis H. Ether flow through a drainhole: A particle model in general relativity. *Journal of Mathematical Physics*, 1973, v. 14 (1), 104–118.
15. Bronnikov K. Scalar-tensor theory and scalar charge. *Acta Physica Polonica B*, 1973, v. 4, 251–266.
16. Bronnikov K., Lipatova L., Novikov I., Shatskiy I. Example of a stable wormhole geometry in general relativity. arXiv: gr-qc/1312.6929v1.
17. Thorne K., Morris M., Yurtsever U. Wormholes, Time Machines, and the Weak Energy Condition. *Physical Review Letters*, 1988, v. 61 (13), 1446–1449.
18. Friedman J., Morris M., Novikov I., Echeverria F., Klinkhammer G., Thorne K., Yurtsever U. Cauchy problem in spacetimes with closed timelike curves. *Physical Review D*, 1990, v. 42 (6), 1915-1930.
19. Novikov I., Zel'dovich Y. Stroeniye i Evolyutsia Vselennoi. Nauka, Moscow, 1975.
20. Heinlein R. Farnham's Freehold. G.P. Putnam's Sons, New York, 1964.
21. Minkowski H. Raum und Zeit. *Jahresbericht der Deutschen Mathematiker-Vereinigung*, 1909, 75–88.
22. Hales S. No Time Travel for Presentists. *Logos & Episteme*, 2010, v. 1 (2), 353–360.
23. Nahin P. Time Machines: Time Travel in Physics, Metaphysics, and Science Fiction. Springer-Verlag, New York, 1999.
24. Smart J., ed. Introduction. Problems of Space and Time. The Macmillan Co., New York, 1964.
25. Lloyd S., Maccone L., Garcia-Patron R., Giovannetti V., Shikano Y., Pirandola S., Rozema L., Darabi A., Soudagar Y., Shalm L., Steinberg A. Closed timelike curves via postselection: theory and experimental demonstration. arXiv: quant-ph/1005.2219v1.
26. Deutsch D. Quantum mechanics near closed timelike lines. *Physical Review D*, 1991, v. 44 (10), 3197–3217.
27. Ralph T. Problems with modelling closed timelike curves as post-selected teleportation. arXiv: quant-ph/1107.4675v1.
28. Lloyd S., Maccone L., Garcia-Patron R., Giovannetti V., Shikano Y., Pirandola S., Rozema L., Darabi A., Soudagar Y., Shalm L., Steinberg A. A reply to 'Problems with modelling closed timelike curves as post-selected teleportation.' arXiv: quant-ph/1108.0153v1.
29. Lloyd S., Maccone L., Garcia-Patron R., Giovannetti V., Shikano Y. Quantum mechanics of time travel through post-selected teleportation. arXiv: quant-ph/1007.2615v2.
30. Lloyd S., Maccone L., Garcia-Patron R., Giovannetti V., Shikano Y., Pirandola S., Rozema L., Darabi A., Soudagar Y., Shalm L., Steinberg A. Closed Timelike Curves via Postselection: Theory and Experimental Test of Consistency. *Physical Review Letters*, 2011, v. 106 (4), 040403.
31. Chalmers D. The singularity: A philosophical analysis. *Journal of Consciousness Studies*, 2010, v. 17 (9-10), 7–65.

Thermodynamics and the Virial Theorem, Gravitational Collapse and the Virial Theorem: Insight from the Laws of Thermodynamics

Pierre-Marie Robitaille

Department of Radiology and Chemical Physics Program, The Ohio State University, Columbus, Ohio 43210, USA.
E-mail: robitaille.1@osu.edu

Application of the virial theorem, when combined with results from the kinetic theory of gases, has been linked to gravitational collapse when the mass of the resulting assembly is greater than the Jeans mass, M_J. While the arguments appear straightforward, the incorporation of temperature into these equations, using kinetic theory, results in a conflict with the laws of thermodynamics. Temperature must always be viewed as an intensive property. However, it is readily demonstrated that this condition is violated when the gravitational collapse of a free gas is considered using these approaches. The result implies star formation cannot be based on the collapse of a self-gravitating gaseous mass.

1 Introduction

While the virial theorem derives its name from the work of Clausius [1], credit for its initial formulation has also been ascribed to Lagrange [2], as the theorem can be derived from the Lagrange identity [3, 4]. The virial theorem represents one of the most powerful axioms in physics and has been used to address a wide array of problems [4–6]. Jeans utilized the theorem at length in his classic text, *The Dynamical Theory of Gases* [7], in order to derive some of the well-known gas laws. However, it was not until seven years later that the virial theorem was introduced into astrophysics by Poincaré [8]. Soon after, A. S. Eddington [9], apparently unaware of Poincaré's contribution, applied the theorem to a star cluster. This work centered on kinetic energy of motion and did not attempt to introduce temperature as a variable. Each of these developments adheres to the laws of physics.

Eventually, Eddington [10] came to use the virial theorem when addressing the general theory of star formation. In doing so, it appears that he was the first to combine gravitational potential energy with the kinetic energy for a gas, as derived from the ideal gas law, and thereby obtained an expression defining the mean temperature of a star. Jeans [11] and Chandrasekhar [12] soon followed the same steps. Today, many of these ideas relative to stellar equilibrium and temperature remain ([13], [14, see Eq. 26.7]). In this case, the use of the virial theorem appears to be in conflict with the laws of thermodynamics.

2 Theoretical considerations

The existence of intensive (*e.g.* temperature, pressure, density, molar mass, thermal conductivity, ...) and extensive (*e.g.* mass, volume, internal energy, heat capacity, ...) properties has been recognized. In fact, Landsberg [15] has argued that this concept is so vital as to constitute the 4th law of thermodynamics. By necessity, intensive properties must be measured in terms of extensive properties. Extensive properties must be additive and are directly related to the mass of a system. Conversely, intensive properties are independent of total mass. When two extensive properties are divided, an intensive property is obtained (*e.g.* mass/volume = density). However, not all properties can be characterized as either intensive or extensive [16]. Still, it is clear that *"if one side of an equation is extensive (or intensive), then so must be the other side"* [17]. These last two realities urge some caution when advancing new relations. The point can be made by first examining the ideal gas law and then, a result from the inappropriate application of the virial theorem.

The ideal gas law is usually expressed as $PV = nRT$, where P, V, n, R and T correspond to the pressure, the volume, the number of moles, the universal gas constant, and the absolute temperature, respectively. If one considers that $n = M/\mathcal{M}$, (where M is the total mass and $\mathcal{M}$ corresponds to the molar mass) and that the mean density, ρ_0, can be expressed as $\rho_0 = M/V$, then the ideal gas law takes the following form:

$$P = \rho_0 \frac{R}{\mathcal{M}} T \,. \tag{1}$$

Recognizing that $R/\mathcal{M}$ is also known as the specific gas constant, R_s, then the ideal gas law can simply be expressed as $P = \rho_0 R_s T$. Note that this equation does not contain any extensive properties, as both the mass of the system and its volume have been replaced by density, ρ_0, which is an intensive property. Similarly, P and T are intensive properties, while R_s is a constant for any given system. In accordance with the state postulate, this simple system is fully defined by any two intensive properties [18].

At the same time, an intensive property must remain a function of only intensive properties, or of extensive properties which in combination, result in an intensive property. This is especially important when considering temperature in light of the 0th law of thermodynamics. If the ideal gas law is re-expressed in terms of temperature,

$$T = \frac{P}{R_s \rho_0}\,, \tag{2}$$

it is observed that this property remains defined only in terms of intensive properties for this system, namely pressure and density.

When considering the kinetic theory as applied to an ideal gas (see Jeans [19]), any of the associated results are inherently linked to the conditions which gave rise to the ideal gas law. For instance, 1) a large number of rapidly moving particles must be considered, 2) these must be negligibly small relative to the total volume, 3) all collisions must be elastic, 4) no net forces must exist between the particles, 5) the walls of the enclosure must be rigid, 6) the only force or change in momentum with time, dp/dt, which is experienced to define pressure, P, must occur at the walls, and 7) the sum of forces everywhere else must be zero. In this instance, temperature becomes linked to the total kinetic energy of the enclosed system, $K.E. = \frac{3}{2}Nk_BT$, where N represents the total number of particles and k_B is Boltzmann's constant. Note that this expression does not address any contribution to the total kinetic energy which this enclosed system might gain if it were in motion relative to another object. Such motion would increase the total kinetic energy of the system, but not its temperature.

When the virial theorem is applied to a self-gravitating gaseous mass, wherein the kinetic theory of gases has been used to insert temperature dependence [10–12], it is well-established ([13], [14, see Eq. 26.7]) that this combination results in the following expression for temperature:

$$T = \frac{GMm_p}{5k_Br}\,, \tag{3}$$

where G, M, m_p, k_B, and r corresponds to the gravitational constant, the mass of the system, the particle mass, Boltzmann's constant, and the radius. With dimensional analysis, this expression appears valid, equating Kelvin on each side. However, this is not true, relative to analysis of intensive and extensive properties.

Observe that G, m_p, and k_B are constants for this system. Mass, M, is an extensive property. However, the radius, r, is neither extensive nor intensive [18]. In order to see that radius is not an extensive property, one simply needs to recall that for an ideal gas, volume, an extensive property, is directly related to mass, M. In fact, mass is usually divided by volume in order to lead to density, ρ_0, an intensive property. However, since $V = \frac{4}{3}\pi r^3$, it is evident that radius is not directly related to mass, M, but rather to $M^{1/3}$. As such, r cannot be an extensive property. Thus, temperature in (3) is being defined in terms of two properties, M and r, which in combination *do not* result in an intensive property. This constitutes a direct violation of the 0$^{\text{th}}$ law which seeks, first and foremost, to define temperature as an intensive property, a reality well-established in thermodynamics (*e.g.* [17]).

In arriving at (3), the kinetic energy of the gas, $K.E.$, was assumed to be equal to $\frac{3}{2}Nk_BT$, as presented above. However, the temperature obtained from kinetic theory is a manifestation of the internal motion of the gas within an enclosure. That energy represents heat energy and it is not related to the kinetic energy of translational motion which should be combined in the virial theorem with gravitational potential energy, when considering a bound system.

Furthermore, this expression was obtained for a gas enclosed by a rigid wall. Such a wall is not present when considering gravitational collapse. Yet, the results relative to the ideal gas law were critically dependent on the presence of this enclosure. The relationship between pressure, volume, and temperature was extracted using real walls. This is critical as the only forces used in defining pressure in this system occur at this boundary. It is not proper to remove the wall and then assume that the kinetic energy of the gaseous system remains equal to $\frac{3}{2}Nk_BT$.

A thermodynamic problem also occurs with any expression attempting to define the Jeans mass, M_J, an extensive property, in terms of temperature and mean density, both of which are intensive properties. Consider the following expression:

$$M_J = \left(\frac{5k_BT}{Gm_p}\right)^{3/2}\left(\frac{3}{4\pi\rho_0}\right)^{1/2}, \tag{4}$$

which is analogous to Eq. 12.14 in [14]. Note in (4) that all terms are raised to either the 3/2 or 1/2 power. As such, no term on the right side of this equation could have been considered to behave as an extensive property. Extensive properties must be additive, a feature which is lost when they are raised to an exponential power. In (4), the only terms which are not constants are T and ρ_0, but these are intensive, not extensive properties. As such, the concept of Jeans mass is not supported by the laws of thermodynamics as no extensive properties exist on the right side of (4).

3 Discussion

When applying the virial theorem, it is important to differentiate the kinetic energy associated with temperature from the kinetic energy of motion. For instance, when Chandrasekhar [20] applied the virial theorem to rotating fluid masses, he made a clear distinction between heat energy and kinetic energy of motion. If this is not done and the two are considered the same, as with all applications to a gaseous mass [10–14], then violations of thermodynamics ensue.

It is not solely that an intensive property, like temperature, is being defined in terms of properties which, in combination, do not yield an intensive property. While this is a violation of the 0$^{\text{th}}$ law, the 3$^{\text{rd}}$ law is also being violated, as 0 K is a temperature. One cannot, by (3), increase the radius to infinity and, therefore, define 0 K as an intensive property. These considerations illustrate that gases cannot undergo gravitational collapse.

Lane's Law [21, 22], or the self-compression of a gaseous mass, also constitutes a violation of the 1st law of thermodynamics. A system cannot do work upon itself and thereby raise its own temperature. This results in a perpertual motion machine of the first kind. Additionally, a gravitationally collapsing gaseous cloud, which obeys the ideal gas law, violates the 2nd law of thermodynamics. An ideal gas is elastic by definition. It has no means of dissipating heat into the heat sink of its surroundings. Moreover, the system lacks an "engine" whereby compression can be achieved. Work must be done on the system in order to increase its order. To argue otherwise consitutes a perpertual motion machine of the second kind.

4 Conclusion

The idea that a gaseous mass can undergo gravitational collapse ([9, 11–13], [14, see Eq. 26.7]) stands in violation of the 0th, 1st, 2nd and 3rd laws of thermodynamics. It is well-established in the laboratory that gases expand to fill the void. According to the laws of thermodynamics a system cannot do work upon itself. When dealing with an ideal gas without net translation, all of the energy should be considered as kinetic energy, exclusively. It is not appropriate to add a potential energy term, if the total energy has already been defined as kinetic energy, thereby establishing temperature.

At the same time, the question remains: *How do stars form?* They do not arise from gravitational collapse. The only feasible solution is that they are the result of condensation reactions, whereby material, as it condenses and forms a new system, emits photons into its surroundings. Insight relative to this issue can be gained by considering the work of Konig *et al* [23], wherein the condensation of silver clusters at low temperatures has been associated with the emission of photons. It is highly likely that hydrogen ion clusters [24] will be found someday to behave in the same fashion. Along with other advancements in condensed matter physics [25], such discoveries may well provide the necessary force to help astronomers recognize that the stars are comprised of condensed matter [26].

Dedication

This work is dedicated to my wife, Patricia Anne.

Received on May 29, 2018

References

1. Clausius R. J. E. 1870, *Phil. Mag.*, S. 4, v. 40 (265), 122–127.
2. Lagrange J. L. Oeuvres Complètes, tome 6, Essai sur le problème des trois corps. *Acad. Sci. Paris*, Tome IX, 1772, p. 231–242.
3. Jacobi C. G. J. *Vorlesungen Über Dynamik*. A. Clerbsch, G. Reimer, Berlin, 1884, p. 18–31.
4. Collins G. W. The Virial Theorem in Stellar Astrophysics. Pachart Publishing House, Tucson, 1978.
5. Landau L. D. and Lifshitz E. M. Mechanics. Pergamon Press, Oxford, 1960, p. 22–24.
6. Goldstein H. Classical Mechanics, 2nd Ed. Addison-Wesley Publishing Co., London, 1980, p. 82–85.
7. Jeans J. H. The Dynamical Theory of Gases. Cambridge University Press, Cambridge, 1904, p. 143–148.
8. Poincaré H. Leçons sur les hypothèses cosmogoniques. *Librairie Scientifique A Hermann et Fils*, Paris, 1911, p. 90–94.
9. Eddington A. S. 1916, *MNRAS*, 76, 525–528.
10. Eddington A. S. The Internal Constitution of the Stars. Cambridge University Press, Cambridge, 1926, p. 79–96.
11. Jeans J. Astronomy and Cosmogony. Cambridge University Press, Cambridge, 1928, p. 65–69.
12. Chandresekhar S. An Introduction to the Study of Stellar Structure. Dover Publications, 1939, p. 61–83.
13. Bowers R. L. and Deeming T. Astrophysics II: Interstellar Matter and Galaxies, Jones and Bartlett Publishers, Inc., Boston, 1984, p. 420.
14. Carroll B. W. and Ostlie D. A. An Introduction to Modern Astrophysics (2nd Edition). Cambridge University Press, Cambridge, U.K., 2017.
15. Landsberg P. T. Thermodynamics with Quantum Statistical Illustrations. Interscience Publishers, New York, 1961, p. 142.
16. Hatsopoulos G. N. and Keenan J. H. Principles of General Thermodynamics. John Wiley & Sons, Inc., 1965, p. 19.
17. Canagaratna S. G. 1992, *J. Chem. Educ.*, v. 69 (12), 957–963.
18. Cengel Y. A. and Boles M. A. Thermodynamics - An Engineering Approach (8th Edition). McGraw-Hill, New York, 2015, p. 15.
19. Jeans J. An Introduction to the Kinetic Theory of Gases. Cambridge University Press, Cambridge, U.K., 1940.
20. Chandrasekhar S. and Fermi E. 1953, *Astro. Phy. Jr* 118, 116–141.
21. Lane L. H. 1870, *Am. J. Sci. Arts*, Ser. 2, v. 50, 57–74.
22. Stevenson-Powell C. J. 1988, *J. Hist. Astron.*, v. 19, 183–199.
23. Konig L., Rabin I., Schultze W., and Ertl G. 1996, *Science*, v. 274 (5291), 1353–1355.
24. Kirchner N. J. and Bowers M. T. 1987, *J. Chem. Phys.*, v. 86 (3), 1301–1310.
25. McMahon J. M., Morales M. A., Pierleoni C., and Ceperley D. M. 2012, *Rev. Mod. Phys.*, v. 84 (4), 1607–1653.
26. Robitaille P.-M. 2013, *Progr. Phys.*, v. 4, 90–142.

The Journal on Advanced Studies in Theoretical and Experimental Physics, including Related Themes from Mathematics

PROGRESS IN PHYSICS

A quarterly issue scientific journal, registered with the Library of Congress (DC, USA). This journal is peer reviewed and included in the abstracting and indexing coverage of: Mathematical Reviews and MathSciNet (AMS, USA), DOAJ of Lund University (Sweden), Scientific Commons of the University of St. Gallen (Switzerland), Open-J-Gate (India), Referativnyi Zhurnal VINITI (Russia), etc.

Electronic version of this journal:
http://www.ptep-online.com

Postal Address

Department of Mathematics and Science,
University of New Mexico,
705 Gurley Ave., Gallup, NM 87301, USA

ISSN: 1555-5534 (print)
ISSN: 1555-5615 (online)

Standard Address Number: 297-5092
Printed in the United States of America

October 2018 **Vol. 14, Issue 4**

CONTENTS

Information for Authors

Progress in Physics has been created for rapid publications on advanced studies in theoretical and experimental physics, including related themes from mathematics and astronomy. All submitted papers should be professional, in good English, containing a brief review of a problem and obtained results.

All submissions should be designed in LaTeX format using *Progress in Physics* template. This template can be downloaded from *Progress in Physics* home page http://www.ptep-online.com

Preliminary, authors may submit papers in PDF format. If the paper is accepted, authors can manage LaTeXtyping. Do not send MS Word documents, please: we do not use this software, so unable to read this file format. Incorrectly formatted papers (i.e. not LaTeXwith the template) will not be accepted for publication. Those authors who are unable to prepare their submissions in LaTeXformat can apply to a third-party payable service for LaTeX typing. Our personnel work voluntarily. Authors must assist by conforming to this policy, to make the publication process as easy and fast as possible.

Abstract and the necessary information about author(s) should be included into the papers. To submit a paper, mail the file(s) to the Editor-in-Chief.

All submitted papers should be as brief as possible. Short articles are preferable. Large papers can also be considered. Letters related to the publications in the journal or to the events among the science community can be applied to the section *Letters to Progress in Physics*.

All that has been accepted for the online issue of *Progress in Physics* is printed in the paper version of the journal. To order printed issues, contact the Editors.

Authors retain their rights to use their papers published in *Progress in Physics* as a whole or any part of it in any other publications and in any way they see fit. This copyright agreement shall remain valid even if the authors transfer copyright of their published papers to another party.

Electronic copies of all papers published in *Progress in Physics* are available for free download, copying, and re-distribution, according to the copyright agreement printed on the titlepage of each issue of the journal. This copyright agreement follows the *Budapest Open Initiative* and the *Creative Commons Attribution-Noncommercial-No Derivative Works 2.5 License* declaring that electronic copies of such books and journals should always be accessed for reading, download, and copying for any person, and free of charge.

Consideration and review process does not require any payment from the side of the submitters. Nevertheless the authors of accepted papers are requested to pay the page charges. *Progress in Physics* is a non-profit/academic journal: money collected from the authors cover the cost of printing and distribution of the annual volumes of the journal along the major academic/university libraries of the world. (Look for the current author fee in the online version of *Progress in Physics*.)

Elimination of Anomalies Reported for $b \to s\ell\ell$ and $b \to c\ell\bar{\nu}_\ell$ Semi-Leptonic Decay Ratios R(K,K*) and R(D,D*) when the Lepton Families Represent Discrete Symmetry Binary Subgroups 2T, 2O, 2I of SU(2)

Franklin Potter
Sciencegems.com, 8642 Marvale Drive, Huntington Beach, CA 92646 USA. E-mail: frank11hb@yahoo.com

The large discrepancies between the measured and predicted values of B meson decay ratios R(K) and R(D) could indicate lepton flavor universality violation and new physics beyond the Standard Model. I propose that the only new physics is that each lepton family represents a different discrete symmetry binary subgroup of SU(2) and that lepton flavor mixing exists because the 3 families act collectively to achieve SU(2) symmetry. Successful calculations of the neutrino mixing angles and of the measured ratios R(K,K*) and R(D, D*) by using those mixing angles confirm that the 3 lepton families represent the 3 binary subgroups 2T, 2O, and 2I.

1 Introduction

Perhaps the hottest research topic today in particle physics is whether the door to new physics (NP) has been pried ajar by the Belle, BaBar, and LHCb reports of significant discrepancies from the Standard Model (SM) predicted values in the B meson semi-leptonic decay ratios. In particular, rare $b \to s\ell\ell$ and $b \to c\ell\bar{\nu}_\ell$ decays are now known to exhibit significant deviations from the SM predictions for both their branching ratios and their angular distributions [1]. One possible interpretation of these results would be the violation of lepton flavor universality (LFUV) with regard to the weak interaction.

Over the past two decades these deviations from the SM predicted values have triggered a variety of models of NP, such as Z' models with gauged L_μ - L_τ, models with leptoquarks, models with compositeness, etc. For a complete list of the great variety of proposed NP models, see [2].

I claim that the only NP required is to properly identify the lepton and quark family symmetries. Previously, I have shown [3] that their EW flavor states actually represent 3 specific discrete symmetry subgroups of SU(2). In better words, the true reason for lepton mixing is the collective action of the 3 lepton families with their discrete symmetries to mimic the SU(2) weak isospin eigenstates $\pm\frac{1}{2}$ demanded by the SM gauge interaction bosons representing $SU(2)_W \times U(1)_Y$. The correct statement that the mixing angles represent a mismatch between the EW flavor states and their mass states is the consequence of but not the reason for the mixing. I explain below how this collective action is achieved by the 3 specific discrete symmetry binary subgroups of SU(2), known as 2T, 2O, and 2I, for the electron, muon, and tau families, respectively. The immediate results are the correct mixing angles and the correct ratios of branching ratios for b quark semi-leptonic decays.

Section 2 is a brief review of the recent experimental results for B meson semi-leptonic decays. Section 3 explains how the lepton mixing angles are derived from the generators of the 3 discrete symmetry subgroups of SU(2), or equivalently the group of unit quaternions Q. Section 4 includes a derivation of the electroweak (EW) boson states $W^\pm$, Z^0, and γ as well as the Weinberg angle. Finally, in Section 5, I calculate the ratios for the semi-leptonic b decays $b \to s\ell\ell$ and $b \to c\ell\bar{\nu}_\ell$ using alternative EW boson state assignments. In order to do so, one requires the appropriate discrete symmetry eigenstates for the leptons, quarks, and EW bosons, which I have discussed in the literature [3,4] and at conferences [5,6].

2 The B meson decays

The ratio of branching ratios has been used extensively to summarize both the theoretical and the experimental results because almost all the hadronic uncertainties are eliminated. For example, these four ratios for B meson decays exhibit large discrepancies of more than 2.5σ from their SM predictions [1]:

$$R(K)^{SM} = \frac{\mathcal{B}(B \to K\mu^+\mu^-)}{\mathcal{B}(B \to Ke^+e^-)} = 1.00 \pm O(1\%), \tag{1}$$

$$R(K^*)^{SM} = \frac{\mathcal{B}(B \to K^*\mu^+\mu^-)}{\mathcal{B}(B \to K^*e^+e^-)} = 1.00 \pm O(1\%), \tag{2}$$

$$R(D)^{SM} = \frac{\mathcal{B}(B \to D\tau\nu_\tau)}{\mathcal{B}(B \to D\ell\nu_\ell)} = 0.298 \pm 0.003, \tag{3}$$

$$R(D^*)^{SM} = \frac{\mathcal{B}(B \to D^*\tau\nu_\tau)}{\mathcal{B}(B \to D^*\ell\nu_\ell)} = 0.255 \pm 0.004, \tag{4}$$

valid over a broad range of q^2 values.

LHCb has recently reported [7]

$$R(K)^{exp} = 0.745 \pm 0.090 \pm 0.036 \tag{5}$$

$$R(K^*)^{exp} = 0.685 \pm 0.113 \pm 0.047 \tag{6}$$

in the di-lepton invariant mass range $1\ \mathrm{GeV}^2 < q^2 < 6\ \mathrm{GeV}^2$, exhibiting significant deviations from the SM predictions.

For muonic decays [8]

$$R(D)^{exp} = 0.407 \pm 0.039 \pm 0.024. \tag{7}$$

Table 1: Exact angle contributions by the U_2 generators of 2T, 2O, and 2I. Note that $\phi = (1 + \sqrt{5})/2$, and Angle = arccosine (Factor), which is twice the projection angle to the k-axis.

Family	Group	U_1	U_2	U_3	Factor	Angle	Angle/2
ν_e, e^-	2T	j	$-\frac{i}{2}-\frac{j}{2}+\frac{k}{\sqrt{2}}$	i	-0.26422	105.3204°	52.660°
ν_μ, μ^-	2O	j	$-\frac{i}{2}-\frac{j}{\sqrt{2}}+\frac{k}{2}$	i	+0.80116	36.7581°	18.379°
ν_τ, τ^-	2I	j	$-\frac{i}{2}-\frac{\phi j}{2}+\frac{\phi^{-1}k}{2}$	i	-0.53695	122.4764°	61.238°

$$R(D^*)^{exp} = 0.336 \pm 0.027 \pm 0.030. \tag{8}$$

I propose that the values of the ratios R(K), R(K*), R(D), and R(D*), all can be expressed in terms of the lepton mixing angles, without venturing outside the realm of the SM local interaction symmetry group $SU(3)_C \times SU(2)_W \times U(1)_Y$. For example, I derive in Section 5 how using the lepton family mixing angles predicts

$$R(K) = \frac{Cos\,\theta_{23}}{Cos\,\theta_{13}} = \frac{Cos\,42.859°}{Cos\,8.578°} = 0.74127\ R(K)^{SM}, \tag{9}$$

$$R(D) = \frac{Cos\,\theta_{33}}{Cos\,\theta_{23}} = \frac{Cos\,0.000°}{Cos\,42.859°} = 1.36420\ R(D)^{SM}, \tag{10}$$

which agree with the experimental values 0.745 ±0.090 ± 0.036 and 0.407±0.039±0.024, respectively.

Why does this procedure work? Because the $W^\pm$ and Z^0 bosons have discrete symmetry properties, too, and are eigenstates of the binary product group 2I × 2I'. In the traditional way of thinking, such an alternative way to express $W^\pm$ and Z^0 comes as a big surprise!

3 Brief review of neutrino mixing

In 2013 I derived [3] the exact lepton mixing angles for the neutrino PMNS mixing matrix by first assigning the three lepton families to three special discrete symmetry binary subgroups of the unitary quaternion group Q, which is equivalent to the SU(2) group used for the two electroweak (EW) isospin flavor states $\pm\frac{1}{2}$ in each lepton and quark family. I provide a brief review of that lepton mixing angle derivation here.

The group Q of unitary quaternions has these discrete symmetry subgroups:

$$2T, 2O, 2I, D_{2n}, C_{2n}, C_n \quad (n\,odd). \tag{11}$$

If I assume that leptons are 3-D entities at the Planck scale, then only 2T, 2O, and 2I, are useful for identifying them. So I assigned these 3 finite binary subgroups to the electron family (ν_e, e^-), to the muon family (ν_μ, μ^-), and to the tau family (ν_τ, τ^-), respectively.

These 3 binary subgroups each have the 3 quaternion generators U_1, U_2, and U_3 as given in Table 1. Notice that for each group only two of the three generators, U_1 = j, and U_3 = i, are the same as for SU(2), which has the three quaternion generators j, k, i. Their other generator, U_2, is different for each binary subgroup and different from each other. By demanding that the three U_2 generators collectively act as the k-generator of SU(2), their linear superposition provides three equations for three unknown factors. Their normalized factors, the corresponding angles calculated by their inverse cosine projections to the k-axis, and the physical rotation angles, are quantities all listed in Table 1.

Defining the lepton mixing angles by $\theta_{ij} = |\,\theta_i - \theta_j\,|$ produces the three neutrino PMNS mixing angles

$$\theta_{12} = 34.281° \quad \text{vs} \quad 33.56° \pm 0.77°\ (exp) \tag{12}$$

$$\theta_{23} = 42.859° \quad \text{vs} \quad 41.6° \pm 1.5°\ (exp) \tag{13}$$

$$\theta_{13} = 8.578° \quad \text{vs} \quad 8.46° \pm 0.15°\ (exp), \tag{14}$$

with their absolute values agreeing with the experimental values. Note that I have no mixing among the charged lepton flavor states, unitarity of the PMNS mixing matrix, a normal mass state hierarchy, and no additional neutrino states beyond those in the three known lepton families.

Therefore, I claim that the three lepton families represent the three chosen discrete symmetry binary subgroups 2T, 2O, 2I, and that they act collectively to mimic the SU(2) symmetry required for the isospin flavor states of the EW component of the SM.

4 Electroweak boson states W^+, Z^0, W^-, γ

The SM local gauge group SU(2) × U(1) has four EW interaction bosons W^+, Z^0, W^-, γ, which can be derived from the four quaternion generators i, j, k, b, with the first three generators for SU(2) or Q and the generator b for U(1) [or, equivalently, for the 2-element inversion group I_2]. These four generators required for the EW boson operations on the lepton flavor states must be able to perform the discrete rotations of the binary subgroups 2T, 2O, and 2I, in order to go from one lepton flavor state $\pm\frac{1}{2}$ to the other in each family. Of course, the Lie groups SU(2), or Q, are capable of doing these discrete rotations because they include all possible operations.

But there exists a smaller group with discrete symmetry that can provide the essential operations. One might expect that the largest group 2I of binary icosahedral operations by itself would be able to perform the required rotations in the normal space $C^2 = R^4$. However, some operations in the binary octahedral group 2O for the muon family would be omitted, so one finds that the product group 2I × 2I' is necessary, where 2I' provides certain "reciprocal" operations, as they are called.

In a 2014 paper [9], by using 2I × 2I', I derived the Weinberg angle, i.e., the weak mixing angle, using $U_2 \times U'_2$ to predict

$$\theta_W = 30^\circ \;\text{ vs }\; 28.4^\circ \pm 0.5^\circ \;\; (exp). \tag{15}$$

The discrepancy between the measured and the theoretical values of the Weinberg angle could be indicating that the 30° value applies at the Planck scale.

One now defines the four EW boson states in terms of the 2I × 2I' weak isospin states by these four relations:

$$|W^+> = |+\tfrac{1}{2}>|+\tfrac{1}{2}> \tag{16}$$

$$|Z^0> = \Big(|+\tfrac{1}{2}>|-\tfrac{1}{2}> + |-\tfrac{1}{2}>|+\tfrac{1}{2}>\Big)\,/\,\sqrt{2} \tag{17}$$

$$|W^-> = |-\tfrac{1}{2}>|-\tfrac{1}{2}> \tag{18}$$

$$|\gamma> = \Big(|+\tfrac{1}{2}>|-\tfrac{1}{2}> - |-\tfrac{1}{2}>|+\tfrac{1}{2}>\Big)\,/\,\sqrt{2}. \tag{19}$$

where the upper state $+\frac{1}{2}$ for 2I is the tau neutrino flavor state ν_τ and the lower state $-\frac{1}{2}$ is the τ^- state. The tau family antiparticle states representing the 2I' discrete symmetry group have the upper and lower states τ^+ and $\bar{\nu}_\tau$.

One would expect that these four EW boson state identifications in terms of 2I × 2I' eigenstates would be important for understanding their decays into leptons and quarks. Indeed, unless one uses these particular identifications, the B meson decays will have large discrepancies with the SM predictions and remain a challenge for the SM traditional approach, paricularly for the semi-leptonic decays

$$b \;\rightarrow\; s\,\ell^+\ell^- \text{ and } b \rightarrow c\ell\bar{\nu}_\ell, \tag{20}$$

precisely the decays for R(K) and R(D).

Therefore, I can re-define the EW boson states in terms of the tau lepton family flavor states for calculation purposes and determine the consequences for the b semi-leptonic decays:

$$|W^+> = |\nu_\tau>|\tau^+> \tag{21}$$

$$|Z^0> = (|\nu_\tau>|\bar{\nu}_\tau> + |\tau^->|\tau^+>)\,/\,\sqrt{2} \tag{22}$$

$$|W^-> = |\tau^->|\bar{\nu}_\tau> \tag{23}$$

$$|\gamma> = (|\nu_\tau>|\bar{\nu}_\tau> - |\tau^->|\tau^+>)\,/\,\sqrt{2}. \tag{24}$$

That these assignments work well in determining the ratios R(K) and R(D) is discussed in the next section.

5 b → $s\ell\ell$ and b → $c\ell\bar{\nu}_\ell$

The traditional way to handle these decays would be to examine the Wilson coefficients [10] and determine which ones are possibly responsible for the discrepancies of the experimental results from the SM predictions.

However, now that I have proposed explicit expressions for the EW bosons in terms of the tau family flavor states, I can calculate directly the decay ratios reported in the literature. For the decay b → $s\ell\ell$ in which R(K) is expressed in terms of the ratio of the branching ratios of $Z^0 \rightarrow \mu^-\mu^+$ and $Z^0 \rightarrow e^-e^+$ in Eq. 1, the semi-leptonic B meson decays require the Z^0 decays expressed as

$$|\tau^->|\tau^+> \rightarrow\; |\mu^->|\mu^+> \tag{25}$$

$$|\tau^->|\tau^+> \rightarrow\; |e^->|e^+>, \tag{26}$$

with each decay being proportional to the cosine of the specific lepton mixing angle between families, i.e., one predicts their ratio

$$R(K) = \frac{\cos\theta_{23}}{\cos\theta_{13}} = \frac{0.73303}{0.98888} = 0.74127, \tag{27}$$

which is the measured value of R(K) = 0.745 ±0.090 ±0.36.

The R(K*) ratio has the same Z^0 decays, so the prediction is the same,

$$R(K^*) = \frac{\cos\theta_{23}}{\cos\theta_{13}} = \frac{0.73303}{0.98888} = 0.74127, \tag{28}$$

which is within the measured value of R(K) = 0.685 ±0.113 ±0.47 with its large uncertainties.

In order to use the same procedure for b→ $c\ell\bar{\nu}_\ell$, which involves the W^- decay, the three W^- decays are expressed as

$$|\tau^->|\bar{\nu}_\tau> \rightarrow\; |\tau^->|\bar{\nu}_\tau> \tag{29}$$

$$|\tau^->|\bar{\nu}_\tau> \rightarrow\; |\mu^->|\bar{\nu}_\mu> \tag{30}$$

$$|\tau^->|\bar{\nu}_\tau> \rightarrow\; |e^->|\bar{\nu}_e>, \tag{31}$$

again with each decay being proportional to the cosine of the lepton mixing angle. For example, taking the ratio of the first two, one obtains the factors

$$R(D)^\mu = \frac{\cos\theta_{33}}{\cos\theta_{23}} = \frac{1}{0.73303} = 1.364, \tag{32}$$

and the ratio of the first and third produces

$$R(D)^e = \frac{\cos\theta_{33}}{\cos\theta_{13}} = \frac{1}{0.98888} = 1.011. \tag{33}$$

Either or both of these factors multiplies the SM predicted value in order to achieve the measured values of R(D) and R(D*). The W^- decay to the muon family alone produces

$$R(D)^\mu = 1.364 \,\text{x}\, 0.298 = 0.408, \tag{34}$$

$$R(D^*)^{\mu} = 1.364 \text{ x } 0.255 = 0.348. \tag{35}$$

both predicted values matching the experimental values 0.407 ±0.039 ±0.024 and 0.336 ±0.027 ±0.030, respectively, for purely muonic decays.

And for the other product, the one involving the tau family states decaying to the electron family only, the predicted results are

$$R(D)^{e} = 1.011 \text{ x } 0.298 = 0.301, \tag{36}$$

$$R(D^*)^{e} = 1.011 \text{ x } 0.255 = 0.258. \tag{37}$$

Therefore, if there is a significant electron family contribution to the R(D*) decay channel, that would lower the total predicted R(D*) value for those reports that average both the muon and electron contributions.

6 Summary

There is no evidence in these semi-leptonic decays for lepton flavor violation. The lepton mixing angles are used to successfully calculate the B meson ratios R(K), R(K*), R(D), and R(D*), which involve ratios of the semi-leptonic b quark decays $b \to s\ell\ell$ and $b \to c\ell\bar{\nu}_\ell$. No discrepancies between the predicted values and the experimental values exist when the lepton families are expressed in terms of the 3 discrete symmetry binary subgroups 2T, 2O, and 2I of SU(2) and the EW boson states are expressed in terms of the discrete symmetry product group 2I × 2I'. The predicted values agree with the experimental values for all four ratios when expressed in terms of the appropriate mixing angles.

The key idea is that the lepton mixing angles exist because the 3 binary subgroups identifying the 3 lepton family discrete symmetries are acting collectively to achieve the SU(2) Lie symmetry of the EW part of the SM. One immediate consequence is that the EW boson states W^+, Z^0, W^-, γ can be expressed in terms of the discrete symmetry product group 2I × 2I', a real surprise. With these discrete symmetry groups, I calculate the neutrino mixing angles, the Weinberg angle, and the four B meson ratios, all in agreement with the experimental values.

Acknowledgements

I thank Sciencegems.com for their continued support.

Submitted on June 10, 2018

References

1. Altmannshofer W., Stangl P., Straub D.M. Interpreting Hints for Lepton Flavor Universality Violation. arXiv: 1704.05435v2 [hep-ph]. Includes a complete reference list.
2. Watanabe R. New Physics effect on $B_c \to J/\psi\tau\bar{\nu}$ in relation to the R(D*) anomaly. arXiv: 1709:08644v3 [hep-ph].
3. Potter F. Geometrical Derivation of the Lepton PMNS Matrix Values. *Progress in Physics*, v. 9(3), 2013, 29–30. http://www.ptep-online.com/2013/PP-34-09.PDF.
4. Potter F. CKM and PMNS mixing matrices from discrete subgroups of SU(2). *Progress in Physics*, v. 10(3), 2014, 146–150. http://www.ptep-online.com/2013/PP-34-09.PDF.
5. Potter F. CKM and PMNS mixing matrices from discrete subgroups of SU(2). *J. Phys: Conf. Ser.*, v. 631, 2015, 012024. http://iopscience.iop.org/article/10.1088/1742-6596/631/1/012024/meta.
6. Potter F. Exact Neutrino Mixing Angles from Three Subgroups of SU(2) and the Physics Consequences. Workshop in Neutrinos (WIN) 2017 UC Irvine, June 19-24, 2017 https://indico.fnal.gov/event/9942/session/4/contribution/23/material/slides/0.pdf
7. Albrecht J. Lepton Flavour Universality tests with B decays at LHCb. arXiv: 1805.06243 [hep-ph].
8. Aaij R. et al. [LHCb Collaboration] Measurement of the Ratio of Branching Fractions $\mathfrak{B}(\bar{B}^0 \to D^{*+}\tau^-\tau\bar{\nu}_\tau)/\mathfrak{B}(\bar{B}^0 \to D^{*+}\mu^-\mu\bar{\nu}_\mu)$. *Phys. Rev. Lett.*, 2015, v. 115(11), 111803. Erratum: [*Phys. Rev. Lett.*, 2015, 115(15), 159901].
9. Potter F. Weinberg Angle Derivation from Discrete Subgroups of SU(2) and All That. *Progress in Physics*, v. 11(1), 2014, 76–77. http://www.ptep-online.com/2015/PP-40-14.PDF.
10. Cornella, C., Feruglio F., Paradisi P. Low-energy Effects of Lepton Flavour Universality Violation. arXiv: 1803:00945v1 [hep-ph].

On the Anomalous Electronic Heat Capacity γ-Coefficient

G. G. Nyambuya

National University of Science and Technology, Faculty of Applied Sciences – Department of Applied Physics,
Fundamental Theoretical and Astrophysics Group, P. O. Box 939, Ascot, Bulawayo, Republic of Zimbabwe.
E-mail: physicist.ggn@gmail.com

As is common knowledge, the experimentally measured and theoretically deduced values of the γ-coefficient of the electronic heat capacity of metals exhibit a clear discrepancy. This discrepancy is usually attributed to the neglected effects such as the electron self-interaction and the electron interaction with phonons and the Coulomb potential. Despite the said pointers to the possible cause in the obtaining theoretical and experimental dichotomy, no dedicated effort has been put in order to come up with a theory to explain this. An effort is here made to come-up with an alternative theoretical framework whose endeavour is to proffer a theory that may explain why there is this theoretical and experimental dichotomy by invoking the hypothesis that the temperature of electrons and the lattice may be different. We argue that the different electron and lattice temperatures can – *in-principle* – give an alternative explanation as to the said theoretical and experimental dichotomy in the γ-coefficient of the electronic heat capacity of metals without the need to invoke the effective mass theory as currently obtains.

> "Thermodynamics is a funny subject. The first time you go through it, you don't understand it at all. The second time you go through it, you think you understand it, except for one or two small points. The third time you go through it, you know you don't understand it, but by that time you are so used to it, it doesn't bother you anymore."
>
> Arnold J. W. Sommerfeld (1868–1951)

1 Introduction

The main purpose of the present reading is to provide (propose) an alternative model that seeks to explain the existing discrepancy in the electronic heat capacity γ-coefficients for different metals. That is to say, for temperatures below the Debye ($\theta_{\rm D}$) and Fermi temperature ($\theta_{\rm F}$), in terms of the temperature (T) of the metal in question, the total molar heat capacity at constant volume $\mathcal{C}_V^{\rm T}$ of metals is satisfactorily described by the sum of a *linear electronic* ($\mathcal{C}_V^{\rm e} \propto T$) [1, 2] and a *cubic phononic* ($\mathcal{C}_V^{l} \propto T^3$) contribution [3], *i.e.*:

$$\mathcal{C}_V^{\rm T} = \gamma T + AT^3\,, \tag{1}$$

where $\gamma = \pi^2 n_* \mathscr{R}/2\theta_{\rm F}$ is the said γ-coefficient in question, with n_* being the number of free electrons per lattice point, $\mathscr{R} = 8.3144600(50)$ Jmol^{-1}K^{-1} is the ideal gas constant and is such that $\mathscr{R} = N_A k_{\rm B}$, where $N_A = 6.022140857(74) \times 10^{23}$ is the Avogadro number and $k_{\rm B} = 1.38064852(79) \times 10^{-23}$ JK^{-1} is the Boltzmann's constant, and:

$$A = \frac{9\mathscr{R}}{\theta_{\rm D}^3}\int_0^{x_{\rm D}} \frac{x^4 e^x dx}{(e^x - 1)^2}\,, \tag{2}$$

where $x = \hbar\omega/k_{\rm B}T$ and $x_{\rm D} = \theta_{\rm D}/T$, $\hbar$ is Planck's normalized constant and ω is the angular frequency of the oscillating lattice points (*i.e.* atom or molecule). In the low temperature region, *i.e.* $x \lll 1$, A is such that:

$$A \simeq \frac{12\pi^4\mathscr{R}}{5\theta_{\rm D}^3}\,. \tag{3}$$

For a given metal in question – the coefficients γ and A are constant coefficients which are determined experimentally.

It was after Albert Einstein's [4] first great insights into the quantum nature of solids that the cubic term $\mathcal{C}_V^{l} \propto T^3$, was successfully explained by Peter Debye [3]. At low temperatures the lattice contribution $\mathcal{C}_V^{l} \propto T^3$ is significantly smaller than the electronic contribution $\mathcal{C}_V^{\rm e} \propto T$, it vanishes faster than the electronic contribution and from this, γ (also known as the *Sommerfeld constant*) can be measured experimentally. As will be seen in the next section, there is a clear marked difference in the theoretical and experimental values of the γ-coefficient and we seek here an answer to as to why this fragment disagreement between theoretical and experiment.

2 Problem

Table 1 lists the theoretical $\gamma_{\rm theo}$ and experimental $\gamma_{\rm exp}$ values of twenty one elements and these values are plotted in Figure 1. One finds that they can fit either a linear, quadratic, a general power law or logarithmic curve to these data points. The marked difference in the theoretical and experimental values of the γ-coefficient is clear. From column 3 of Table 1, the percentage deviations are presented and it can be seen from this that the mean square deviation is as high as 35%, while the mean value of the ratio $\gamma_{\rm exp}/\gamma_{\rm theo}$ (column 5 of Table 1) together with its deviation from this mean value is 1.30 ± 0.40.

The said marked difference in the theoretical and experimental values of the γ-coefficient as presented in Figure 1

Table 1: Table of 21 elements for the experimental and theoretical values of the electronic heat capacity coefficients. From left to right, the columns represent the element, its corresponding theoretical and experimental γ-coefficient and the percentage $(1 - \gamma_{\text{exp}}/\gamma_{\text{theo}}) \times 100\%$ deviation of the experimental value from the theoretical one, respectively. The values of γ_{exp} and γ_{theo} are adapted from Kittel (2005, 1986) [5, 6] and Tari (2003) [7].

Element	γ_{theo} (mJmol^{-1}K^{-2})	γ_{exp} (mJmol^{-1}K^{-2})	**%Dev.**	$\frac{\gamma_{\text{exp}}}{\gamma_{\text{theo}}}$
Li	1.63	0.75	+54	2.18
Be	0.17	0.50	+190	0.34
Na	1.38	1.09	+20	1.26
Mg	1.30	0.99	+24	1.31
Al	1.35	0.91	+32	1.48
K	2.08	1.67	+20	1.25
Ca	2.90	1.51	+48	1.92
Cu	0.70	0.51	+27	1.38
Zn	0.64	0.75	−18	0.85
Ga	0.60	1.03	−72	0.58
Rb	2.41	1.91	+21	1.26
Sr	3.60	1.79	+50	2.01
Ag	0.65	0.65	+0.15	1.00
Cd	0.69	0.95	−38	0.73
In	1.69	1.23	+27	1.37
Sn	1.78	1.41	+20	1.26
Cs	3.20	2.24	+30	1.43
Ba	2.70	1.94	+28	1.39
Au	0.73	0.64	+12	1.14
Hg	1.79	0.95	+47	1.88
Pb	2.98	1.51	+49	1.97
Mean Square Deviation		↦	**35**	

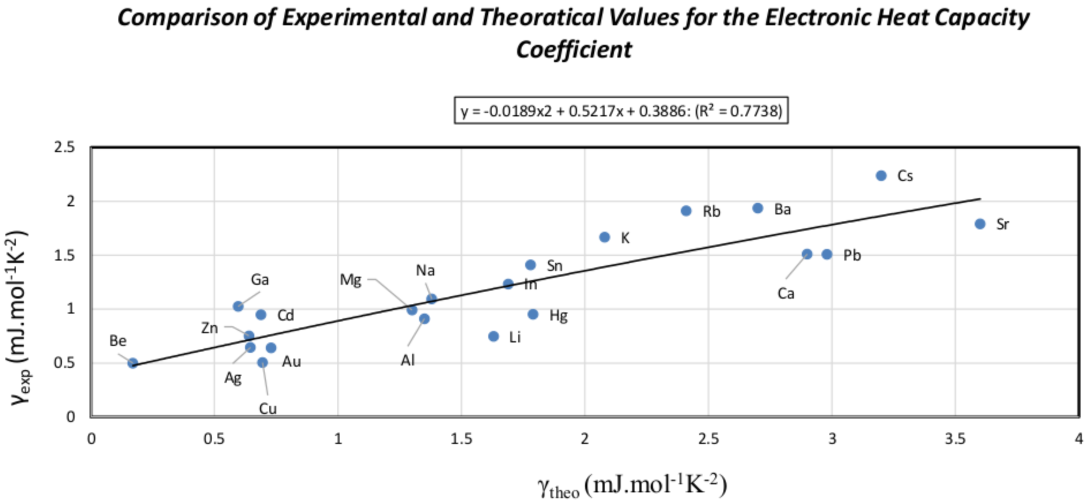

Fig. 1: A comparison graph of the experimental and theoretical values for the electronic heat capacity coefficients for the twenty one elements listed in Table 1. If there was a good agreement between theory and experimental, the values of γ_{exp} and γ_{theo} would lay along the line $\gamma_{\text{exp}} = \gamma_{\text{theo}}$. This is not the case implying a sure fragment disagreement between theory and experiment.

demonstrates an underlying correlation between these values. Amongst others, a correlation such as this, suggests some correlated physics must be at play – *one way or the other.* Given that electrons do interact with phonons, this correlation must have something to do with the electron-phonon interaction. We are not going to seek a fundamental origin of this correlation but merely suggest that this deviation may (as will be demonstrated) very well be due to a possible inequality in the electron and lattice temperatures.

The general and widely held view (see *e.g.* [5,6,8–10]) as to this discrepancy is that:

1. The interaction of the conduction electrons with the periodic Coulomb potential of the rigid crystal lattice is neglected.
2. The interaction of the conduction electrons with phonons is also neglected. This interaction causes changes in the effective mass of the electron and therefore it affects the electron energy.
3. The interaction of the conduction electrons with themselves is also ignored. For example, a moving electron causes an inertial reaction in the surrounding electron gas.

Since $\gamma \propto m_{\mathrm{e}}$ (see *e.g.* [5, 6]), to bring about agreement between theory and observation, the mass of the electron is corrected by introducing an effective mass m_{e}^* for the electron (*e.g.* [5, 6, 8–10]). Whatever difference there exists between theory and experiment, the effective mass is wholly assumed to shoulder this discrepancy (*e.g.* [5,6,8,9]) as follows:

$$\frac{\gamma_{\mathrm{exp}}}{\gamma_{\mathrm{theo}}} = \frac{m_{\mathrm{e}}^*}{m_{\mathrm{e}}}, \qquad (4)$$

where $m_{\mathrm{e}} = 9.10938356(11) \times 10^{-31}$ kg is the usual elementary mass of the electron.

The effective mass theory (see *e.g.* [5, 11] or any good textbook on the subject) is essentially about the equation of motion of a charged particle (electron in this case) inside the energy band of the crystal. In this theory, the electron is treated as a wave-packet in the typical *de Broglie* wave-particle duality model. That is to say, the electron is assumed to be a wave-packet made up of wavefunctions near a particular wavevector $\vec{k}$ and this wave-packet has a group velocity $\vec{v}_{\mathrm{g}} = \partial\omega/\partial\vec{k}$. All the effects of the environment on the electron are contained in the dispersion relation $\omega = \omega(k)$. For an electron whose energy is ϵ, the effective mass theory (see *e.g.* [5,11] or any good textbook on the subject) predicts that:

$$\frac{1}{m_{\mathrm{e}}^*} = \frac{1}{\hbar^2}\frac{\partial^2\epsilon}{\partial k^2} = \frac{1}{\hbar}\frac{\partial^2\omega}{\partial k^2} = \frac{1}{\hbar}\frac{\partial v_{\mathrm{g}}}{\partial k}, \qquad (5)$$

where m_{e}^* is the effective mass of the electron as it moves in the energy band of the crystal. For example, in the case of a free electron where $\epsilon = \hbar^2 k^2/2m_{\mathrm{e}}$, we have $m_{\mathrm{e}}^* = m_{\mathrm{e}}$, *i.e.* the electron has its usual mass m_{e}. Inside the crystal structure where there is no current flow, the valency electrons are free having only thermal energy, they do not have a net drift velocity, but have random fluctuations whose net velocity is zero – hence, the effective mass theory should not be inapplicable to such electrons since measurements of the electronic γ-factor is conducted on such electrons. It is this that has made us to doubtfully question the effective mass theory in accounting for the γ-factor discrepancy.

The effective mass m_{e}^* can be larger or smaller than the electron's actual mass m_{e} and this depends on whether the states within the electron's energy band are denser (more compressed) or less dense (expanded) compared with those of a free gas [5, 6, 11]. The effective mass also reflects the inertia of the charge carriers. The two (effective mass *&* the inertia of the charge carriers) are related, because narrower, denser, bands reflect a smaller overlap of neighbouring electron clouds and hence greater difficulty for electrons to travel from one atom to the next.

This communication presents an alternative model whose aim is to explain the discrepancy in theoretical and experimental values of the electronic heat capacity coefficient. As pointed above – currently this is explained by invoking the effective mass theory. As shown in Figure 1, there is a clear trend in the experimental and theoretical values of the electronic heat capacity coefficient. We have not seen any theory that tries to explain this trend, not even *within* the effective mass theory. It is our firm belief that the effective mass theory should fail to explain this trend for the reason pointed above about the electrons inside metals during the measurement of γ, namely that they have a net zero group velocity. This communication makes an endeavour to provide an alternative model by invoking the not so unreasonable idea that electrons and atoms (molecules) in solids are at different temperatures.

3 Electron-lattice temperature correction

In our suggested alternative explanation – as to the discrepancy between theory and experiment, we propose to reconsider the issue of the lattice and electron temperatures. That is to say, a solid can be viewed as a homogeneous mixture of the lattice and the valency electrons. Just like any mixture, the different species are not expected to be at the same temperatures. Yes, the mixture will come together to a common temperature T, which is the temperature that we generally assign to the solid in question. The species with "*more heat*" will transfer this heat to the species with "*less heat*". In this case of the electron-lattice mixture, we expect the lattice to have "*more heat*" with the valency electrons having "*less heat*". If ΔQ_l is the heat transfer from the lattice and ΔQ_{e} is the heat received by the free electrons, then we must have:

$$\Delta Q_{\mathrm{e}} + \Delta Q_l = 0\,. \qquad (6)$$

So, unlike in the conventional treatment where the lattice and electron temperatures are assumed to be equal, we here assume them to be different. If one accepts this, then what follows is straightforward.

If $M_{\rm e}, c_v^{\rm e}, T_{\rm e}; M_l, c_v^l, T_l$ is the total mass, specific heat capacity and temperature of the electrons gas and the lattice respectively, and T is the common temperature of the mixture, then, from (6), we will have:

$$\underbrace{M_{\rm e}c_v^{\rm e}(T-T_{\rm e})}_{\Delta Q_{\rm e}}+\underbrace{M_l c_v^l(T-T_l)}_{\Delta Q_l}=0\,. \tag{7}$$

Rearranging (7) and making T the subject, we will have:

$$T=\left(\frac{M_{\rm e}c_v^{\rm e}}{M_{\rm e}c_v^{\rm e}+M_l c_v^l}\right)T_{\rm e}+\left(\frac{M_l c_v^l}{M_{\rm e}c_v^{\rm e}+M_l c_v^l}\right)T_l\,. \tag{8}$$

Further – rearrangement of (8), gives:

$$T=\left(1+\frac{M_l c_v^l}{M_{\rm e}c_v^{\rm e}}\right)^{-1}T_{\rm e}+\left(1+\frac{M_{\rm e}c_v^{\rm e}}{M_l c_v^l}\right)^{-1}T_l\,. \tag{9}$$

We know that:

$$c_v^{\rm e}=\frac{C_V^{\rm e}}{N_A m_{\rm e}}\quad\text{and}\quad c_v^l=\frac{C_V^l}{N_A\mathcal{A}_l}\,, \tag{10}$$

where $\mathcal{A}_l$ is the atomic mass of the lattice and $C_V^{\rm e}$ and C_V^l are the electronic and lattice molar heat capacity respectively, and that:

$$\frac{M_l}{M_{\rm e}}=\frac{\mathcal{A}_l}{n_* m_{\rm e}}\,, \tag{11}$$

and substituting (10) and (11) into (9), we will have:

$$T=\left(1+\frac{C_V^l}{n_* C_V^{\rm e}}\right)^{-1}T_{\rm e}+\left(1+\frac{n_* C_V^{\rm e}}{C_V^l}\right)^{-1}T_l\,. \tag{12}$$

Now – because of the different temperatures of the electrons and the lattice, the total internal energy $\mathcal{U}_{\rm e}$ of the electrons is to be expressed as a function of the electron temperature $T_{\rm e}$ *i.e.* $\mathcal{U}_{\rm e}=\mathcal{U}_{\rm e}(T_{\rm e})$ and likewise, that of the lattice structure is such that $\mathcal{U}_l=\mathcal{U}_l(T_l)$. With the internal energy given in terms of the electron and lattice temperatures respectively, the corresponding electronic and lattice molar heat capacities are:

$$C_V^{\rm e}=\frac{\partial\mathcal{U}_{\rm e}(T_{\rm e})}{\partial T_{\rm e}}\quad\text{and}\quad C_V^l=\frac{\partial\mathcal{U}_l(T_l)}{\partial T_l}\,. \tag{13}$$

The total internal energy $\mathcal{U}_{\rm T}$ of the solid is such that:

$$\mathcal{U}_{\rm T}=\mathcal{U}_{\rm e}(T_{\rm e})+\mathcal{U}_l(T_l)\,. \tag{14}$$

Now, to compute the total molar heat capacity of the solid, one does this by differentiating (14) with respect to the common temperature T as follows:

$$C_V^{\rm T}=\frac{\partial\mathcal{U}_{\rm T}}{\partial T}=\frac{\partial\mathcal{U}_{\rm e}(T_{\rm e})}{\partial T_{\rm e}}\frac{dT_{\rm e}}{dT}+\frac{\partial\mathcal{U}_{\rm e}(T_l)}{\partial T_l}\frac{dT_l}{dT}\,. \tag{15}$$

Eq. (15) can be re-written as:

$$C_V^{\rm T}=a_{\rm e}C_V^{\rm e}+a_l C_V^l\,, \tag{16}$$

where $a_{\rm e}=dT_{\rm e}/dT$ and $a_l=dT_l/dT$. From (12) and (16), it follows that:

$$a_{\rm e}^{-1}=\frac{1}{1+C_V^l/n_* C_V^{\rm e}}+\frac{1}{\eta}\frac{1}{1+n_* C_V^{\rm e}/C_V^l}\,, \tag{17}$$

where $\eta=dT_{\rm e}/dT_l$. Setting:

$$x=n_*\left(\frac{C_V^{\rm e}}{C_V^l}\right), \tag{18}$$

it follows that:

$$a_{\rm e}=\left(\frac{x}{1+x}+\frac{1}{\eta}\frac{1}{1+x}\right)^{-1}=\eta\left(\frac{1+x}{1+\eta x}\right). \tag{19}$$

It is expected that the lattice contribution will always be significantly larger than that of the electrons and this means or directly translates to: $x\ll 1$. In addition to the said condition $x\ll 1$, if we assume $|\eta x|<1$, then, to first order approximation, we will have:

$$a_{\rm e}\simeq\eta\quad\text{and}\quad a_l\simeq 1\,, \tag{20}$$

hence:

$$C_V^{\rm T}=\eta C_V^{\rm e}+C_V^l\,. \tag{21}$$

Clearly, from (21) above, the obvious identification:

$$\gamma_{\rm exp}=\eta\gamma_{\rm theo}\,, \tag{22}$$

can be made, the meaning of which is that the theoretical and experimental discrepancy in the values of the γ-coefficient can be ascribed to η.

We shall reiterate: one very important thing to note is that the effective mass of the electron applies only in the case of an electron that is in motion with $v_{\rm g}\neq 0$ in the crystal structure and this is in the case of an applied potential across the metal. The γ-coefficient is measured not for a metal that has a flow of current in it, but one with no current, thus making is logically inappropriate in this instance to ascribe an effective mass to the electron that is different to its bare mass $m_{\rm e}$. In such a case, it would make sense to ascribe the different values of $\gamma_{\rm exp}$ and $\gamma_{\rm theo}$ to the difference in the electron and lattice temperatures as suggested herein.

4 General discussion

We herein have provided an alternative model whose endeavour is to explain the existing discrepancy between the experimental and theoretical values of the electronic heat capacity γ-coefficient. We must say that – at a reasonable and satisfactory level, the proposed model does explain the discrepancy in the experimental and theoretical γ-values. The prevalent (current mainstream) view is that this discrepancy comes about as a result of a variable effective mass of the electron – wherein, the difference between the experimental and theoretical γ-values is wholly shouldered by the effective mass of the electron (see *e.g.* [5–10]). This idea of the effective mass may be logically inappropriate because the effective mass theory applies only in the case of an electron that is in motion with $\upsilon_{\rm g} \neq 0$ in the crystal structure whereas the γ-coefficient is measured not for a metal that has a flow of current in it, but one with no current. Current flow implies "*with* $\upsilon_{\rm g} \neq 0$", and no-current flow implies "*with* $\upsilon_{\rm g} = 0$".

In the proposed model, this discrepancy is explained as being due to the different temperatures of the electrons and the lattice. In the mainstream model, the thermodynamic temperature of the electrons and atoms (molecules) of the solid are assumed to be equal. This view may not be correct. It is actually not unreasonable to think that electrons and atoms (molecules) of the solid are at different temperatures as this is common place in *e.g.* the study of molecular clouds in *Astrophysics* and as well as in *Plasma Physics*.

This model does not discard the effective mass model where results of experiments are made to agree with the theoretical value by postulating that the entire discrepancy be shouldered by the resulting effective mass of the electron. What the model does is basically to "*tell*" us that the different electron and lattice temperatures may have a role to play in the said observed discrepancies, or both models may be at play. This is something that can be investigated in a separate study unit altogether. As to what use this model may hold in the immediate future, we can not say, but we hope it will prove useful in the future as our knowledge horizons broaden and push further than where they lie at present.

Acknowledgements

We are grateful for the assistance rendered unto us by the National University of Science and Technology's Research Board toward our research endeavours.

Received on June 7, 2018

References

1. Sommerfeld A. Zur Elektronentheorie der Metalle. *Naturwissenschaften*, 1927, v. 15 (41), 825–832.
2. Bethe H. A. On the Theory of Metals. *Zeitschrift für Physik*, 1931, v. 71, 205–226.
3. Debye P. Zur Theorie der Spezifischen Wärmen. *Annalen der Physik*, 1912, v. 344 (14), 789–839.
4. Einstein A. Die Plancksche Theorie der Strahlung und die Theorie der spezifischen Wärme. *Annalen der Physik*, 1906, v. 327 (1), 180–190.
5. Kittel C. Introduction to Solid State Physics. John Wiley & Sons Inc., New York, Hoboken, USA, 8th edition, 2005, pp. 146, 193–200.
6. Kittel C. Introduction to Solid State Physics. John Wiley & Sons Inc., New York, Chichester, USA, 6th edition, 1986, pp. 140, 193–200.
7. Tari A. The Specific Heat of Matter at Low Temperatures. Imperial College Press, London, 6th edition, 2003, p. 71.
8. Varshney D., Mansuri I., and Khan E. Phonon, Magnon and Electron Contributions to Low Temperature Specific Heat in Metallic State of $La_{0.85}Sr_{0.15}MnO_3$ and $Er_{0.8}Y_{0.2}MnO_3$ Manganites. *Bulletin of Materials Science*, 2013, v. 36 (7), 1255–1260.
9. Varshney D. and Kaurav N. Analysis of Low Temperature Specific Heat in the Ferromagnetic State of the Ca-doped Manganites. *Eur. Phys. J. B*, 2004, v. 37 (3), 301–309.
10. Carbotte J. P. Properties of Boson-Exchange Superconductors. *Rev. Mod. Phys.*, 1990, v. 62, 1027–1157.
11. Stowe K. An Introduction to Thermodynamics and Statistical Mechanics. Cambridge University Press, The Edinburgh Building, Cambridge CB2 8RU, UK, 2nd edition, 2007, p. 486.

The Dirac Electron and Its Propagator as Viewed in the Planck Vacuum Theory

William C. Daywitt
National Institute for Standards and Technology (retired), Boulder, Colorado, USA
E-mail: wcdaywitt@me.com

This paper examines the covariant Dirac equation and its associated quantum-electrodynamic propagator from the perspective of the Planck vacuum (PV) theory. Calculations reveal: that the PV state is a bifurcated state whose two branches provide the electrons and positrons that, under certain conditions, can be scattered from the PV into free space; that the degenerate collection of Planck-particle cores (that pervade the invisible, negative-energy vacuum state) is responsible for the scattering that takes place in the Huygens principle and the propagator theory; and that the two-term coupling force the electron core exerts on the PV state vanishes at the electron Compton radius, preventing the electron core (and its consequent Dirac electron) from being tethered by the coupling force to the vacuum state, assuring that the electron propagates freely in free space. The paper represents a relativistic addendum to an earlier paper [1] concerning the Schrödinger electron.

1 Introduction

Charge conjugation [2] in the PV theory implies that the invisible vacuum state must be a bifurcated state — bifurcation meaning that at each point in free space there exists a vacuum subspace consisting of the charge doublet $(\pm e_*)^2$ that defines the two vacuum branches

$$e_*^2 = (-e_*)(-e_*) \qquad \text{and} \qquad e_*^2 = (+e_*)(+e_*)\,. \tag{1}$$

The first charge in each branch belongs to the electron or positron and the second charge to the corresponding branch of the subspace. For example, if the first charge $(-e_*)$ in the negative branch on the left belongs to the electron, then the first charge $(+e_*)$ in the positive branch at the right belongs to the positron. In other words, in the PV theory charge conjugation simply switches back and forth between the two branches. The equivalence of the two branches can be seen in the Dirac equation

$$ic\hbar\left(\frac{\partial}{c\partial t} + \boldsymbol{\alpha}\cdot\nabla\right)\psi = mc^2\beta\psi \tag{2}$$

or, using $c\hbar = e_*^2$,

$$\left[i(-e_*)(-e_*)\left(\frac{\partial}{c\partial t} + \boldsymbol{\alpha}\cdot\nabla\right) - mc^2\beta\right]\psi = 0 \tag{3}$$

where the negative branch, the electron branch, is used. The Dirac equation (2) applies to both branches; i.e. the equation works for both the electron and positron. A similar statement can also be made for the equations in (5).

The theoretical foundation [3, 4, 5] of the PV theory rests upon the unification of the Einstein, Newton, and Coulomb superforces:

$$\frac{c^4}{G}\left(=\frac{m_*c^2}{r_*}\right) = \frac{m_*^2G}{r_*^2} = \frac{e_*^2}{r_*^2} \tag{4}$$

where the ratio c^4/G is the curvature superforce that appears in the Einstein field equations. G is Newton's gravitational constant, c is the speed of light, m_* and r_* are the Planck mass and length respectively [6, p.1234], and e_* is the massless bare charge. The fine structure constant is given by the ratio $\alpha = e^2/e_*^2$, where $(-e)$ is the observed electronic charge.

The two particle/PV coupling forces

$$F_c(r) = \frac{e_*^2}{r^2} - \frac{mc^2}{r} \qquad \text{and} \qquad F_*(r) = \frac{e_*^2}{r^2} - \frac{m_*c^2}{r} \tag{5}$$

the electron core $(-e_*, m)$ and the Planck-particle core $(-e_*, m_*)$ exert on the PV state, along with their coupling constants

$$F_c(r_c) = 0 \quad \text{and} \quad F_*(r_*) = 0 \tag{6}$$

and the resulting Compton radii

$$r_c = \frac{e_*^2}{mc^2} \qquad \text{and} \qquad r_* = \frac{e_*^2}{m_*c^2} \tag{7}$$

lead to the important string of Compton relations

$$r_cmc^2 = r_*m_*c^2 = e_*^2 \quad (= c\hbar) \tag{8}$$

for the electron and Planck-particle cores, where $\hbar$ is the reduced Planck constant. The electron and Planck particle masses are m and m_* respectively. The vanishing of $F_c(r_c)$ in (6) frees the electron from being tethered to the vacuum state, insuring that the electron propagating in free space behaves as a free particle.

The Planck constant is a secondary constant whose structure can take different forms; e.g.

$$\hbar\,[\text{erg sec}] = r_cmc = r_*m_*c = \left(\frac{e_*^2}{r_*}\right)t_* = m_*c^2t_* \tag{9}$$

that are employed throughout the following text, where t_* $(= r_*/c)$ is the Planck time [6, p.1233]. The products to the right of $\hbar$ relate the electron mass m and Compton radius r_c to the vacuum parameters r_*, m_*, t_*, and e_*^2.

Furthermore, the energy and momentum operators expressed as

$$\widehat{E} = i\hbar\frac{\partial}{\partial t} = i(m_* c^2)t_*\frac{\partial}{\partial t} = i(m_* c^2)r_*\frac{\partial}{c\partial t} \tag{10}$$

and

$$c\,\widehat{\mathbf{p}} = -ic\hbar\nabla = -i(m_* c^2)r_*\nabla = -i(mc^2)r_c\nabla \tag{11}$$

will be used freely in what follows.

Section 2 examines the covariant Dirac equation and the covariant Dirac equation with the electromagnetic interaction included. Results show that the two equations can be totally normalized by the vacuum parameters r_* and $m_* c^2$ from (8).

Section 3 looks at the relativistic Dirac propagator that provides the foundation for the scattering in the Huygens-principle and the propagator formalisms. The propagator equation is normalized by the vacuum parameters r_* and $m_* c$ from (9).

Section 4 traces the scatterings of the Huygens principle and the propagator theory to the pervaded vacuum space, and indicates how electron-positron pair creation is related to PV charge conjugation.

2 Dirac equation

The manifestly covariant form of the Dirac equation [7, p.90] is

$$\left(i\hbar\gamma^\mu\frac{\partial}{\partial x^\mu}\right)\psi - mc\psi = 0 \tag{12}$$

which, using (9), can be expressed as

$$\left(i\gamma^\mu\frac{r_*\partial}{\partial x^\mu}\right)\psi - \frac{mc}{m_* c}\,\psi = 0 \tag{13}$$

with

$$\frac{\partial}{\partial x^\mu} \equiv \left(\frac{\partial}{c\partial t}, \nabla\right) \tag{14}$$

where ψ is the 4x1 Dirac spinor, $[\mu = 0, 1, 2, 3]$, and ∇ is the normal 3-dimensional gradient operator. See Appendix A for the definition of the γ^μ matrices. The summation convention over the two μs in the first terms of (12) and (13) is understood.

The Dirac equation with the electromagnetic interaction included is [7, eqn.5.249]

$$\left[i\hbar\gamma^\mu\frac{\partial}{\partial x^\mu} \pm \frac{e\gamma^\mu A_\mu}{c}\right]\psi - mc\psi = 0 \tag{15}$$

which, using (9), can be reduced to

$$\left[i\gamma^\mu\frac{r_*\partial}{\partial x^\mu} \pm \frac{e\gamma^\mu A_\mu}{m_* c^2}\right]\psi - \frac{mc}{m_* c}\psi = 0 \tag{16}$$

where the minimal-substitution ratio [7, p.90]

$$\pm\frac{e\gamma^\mu A_\mu}{c} \tag{17}$$

represents the relativistic electromagnetic interaction of the charge $(\mp e)$ with the 4-potential A_μ.

3 Dirac propagator

The relativistic Dirac propagator $S_F(x', x; A)$ is defined to satisfy the Green-function equation [7, eqn.6.91]

$$\left[\gamma_\mu\left(i\hbar\frac{\partial}{\partial x'_\mu} - \frac{eA^\mu(x')}{c}\right) - mc\right]_{\alpha\lambda} S_{F_{\lambda\beta}}(x', x; A)$$

$$= \delta_{\alpha\beta}\delta^4(x' - x) \tag{18}$$

which reduces to

$$\left[\gamma_\mu\left(i\frac{r_*\partial}{\partial x'_\mu} - \frac{\alpha^{1/2}e_* A^\mu(x')}{m_* c^2}\right) - \frac{mc}{m_* c}\right]_{\alpha\lambda} S_{F_{\lambda\beta}}(x', x; A)$$

$$= \delta_{\alpha\beta}\frac{\delta^4(x' - x)}{m_* c} \tag{19}$$

where $e = \alpha^{1/2}e_*$ is used in the reduction and $\delta_{\alpha\beta}$ is the Kronecker delta. The bracket on the left is dimensionless and the δ^4on the right has the units of "1/spacetime-volume". Thus S_F in (19) has the units "$1/mc$·spacetime-volume".

4 Conclusions and comments

The product $m_* c^2$ in (8) is the upper limit to elementary-particle mass-energy and r_* is the lower limit to the particle Compton radius. With this in mind, and the fact the normalizers in equations (13), (16), and (19) are $m_* c$ and r_*, it is assumed in the PV theory that the Planck-particle cores $(\pm e_*, m_*)$ associated with the two branches in (1) that pervade the PV state are the scatterers that provide the scattering for the Huygens-principle and the propagator formalisms. For example, in (13) r_* normalizes the four spacetime gradients $\partial/\partial x^\mu$ and $m_* c$ normalizes the electron product mc.

Finally, the charge ambiguity in (2) due to (1) allows for the creation of an electron-positron pair [7, fig.6.6],

$$\left[i(-e_*)(-e_*)\left(\frac{\partial}{c\partial t} + \boldsymbol{\alpha}\cdot\nabla\right) - mc^2\beta\right]\psi = 0$$

$$\oplus$$

$$\left[i(+e_*)(+e_*)\left(\frac{\partial}{c\partial t} + \boldsymbol{\alpha}\cdot\nabla\right) - mc^2\beta\right]\psi = 0\,, \tag{20}$$

where the first and second equations are related respectively to the electron and positron branches in (1).

Appendix A: The γ and β matrices

The 4x4 γ, β, and α_i matrices used in the Dirac and propagator theories are defined here: where [7, p.75]

$$\gamma^0 \equiv \beta = \begin{pmatrix} I & 0 \\ 0 & -I \end{pmatrix} \tag{A1}$$

and

$$\gamma^i \equiv \beta\alpha_i = \begin{pmatrix} 0 & \sigma_i \\ -\sigma_i & 0 \end{pmatrix} \tag{A2}$$

and where I is the 2×2 unit matrix and

$$\alpha_i = \begin{pmatrix} 0 & \sigma_i \\ \sigma_i & 0 \end{pmatrix} \tag{A3}$$

where the σ_i are the 2×2 Pauli matrices

$$\sigma_1 = \begin{pmatrix} 0 & 1 \\ 1 & 0 \end{pmatrix}, \quad \sigma_2 = \begin{pmatrix} 0 & -i \\ i & 0 \end{pmatrix}, \quad \sigma_3 = \begin{pmatrix} 1 & 0 \\ 0 & -1 \end{pmatrix} \tag{A4}$$

and $\boldsymbol{\alpha} = (\alpha_1, \alpha_2, \alpha_3)$.

Received on June 26, 2018

References

1. Daywitt W.C. The Planck Vacuum Physics Behind the Huygens Principle and the Propagator Theory for the Schrödinger Electron. *Progress in Physics*, 2018, v. 14, issue 3, 111.
2. Daywitt W.C. Antiparticles and Charge Conjugation in the Planck Vacuum Theory. *Progress in Physics*, 2015, v. 11, issue 4, 311.
3. Davies P. Superforce: the Search for a Grand Unified Theory of Nature. Simon and Schuster, New York, 1984.
4. Daywitt W.C. A Model for Davies' Universal Superforce. *Galilean Electrodynamics*, 2006, v. 5, Sept./Oct., 83.
5. Daywitt W.C. The Trouble with the Equations of Modern Fundamental Physics. American Journal of Modern Physics. Special Issue: "Physics without Higgs and without Supersymmetry". 2016, v. 5, no.1–1, 22. See also www.planckvacuumDOTcom.
6. Carroll B.W., Ostlie A.D. An Introduction to Modern Astrophysics. Addison-Wesley, 2007.
7. Gingrich D.M. Practical Quantum Electrodynamics. CRC Press, 2006.

QED Mass Renormalization, Vacuum Polarization and Self-Energies in the Elastodynamics of the Spacetime Continuum (STCED)

Pierre A. Millette

E-mail: PierreAMillette@alumni.uottawa.ca, Ottawa, Canada

In this paper, we consider the explanation of the Quantum Electrodynamics (QED) phenomena of self-energy, vacuum polarization and mass renormalization provided by the Elastodynamics of the Spacetime Continuum (*STCED*). We note that QED only deals with the *wave* aspect of wave-particle objects, and hence QED only deals with the distortion transverse strain energy $W_\perp$, while the dilatation massive longitudinal strain energy term $W_\parallel$ is not considered. Hence there is no possibility of properly deriving the mass, as QED uses an incomplete description of particle energies at the quantum level. Comparison of QED mass renormalization with *STCED* strain energy shows that the interaction of the particle with the medium or the field, δm, is the transverse strain energy present in the spacetime continuum (or vacuum), essentially a field energy. We provide the strain energy equivalence for QED mass renormalization and self-energies for bosons, quarks and leptons.

1 Introduction

In this paper, we consider the explanation of the Quantum Electrodynamics (QED) phenomena of self-energy, vacuum polarization and mass renormalization provided by the Elastodynamics of the Spacetime Continuum (*STCED*) [1–11]. QED is the well-known relativistic quantum field theory of electromagnetic dynamics (electrodynamics) in which charged particle interactions are described by the exchange of (virtual) photons. QED is a perturbative theory of the electromagnetic quantum vacuum [12], and the virtual particles are introduced as an interpretation of the propagators which appear in the perturbation expansion of vacuum expectation values represented by Feynman diagrams.

In *STCED*, energy propagates in the spacetime continuum (*STC*) as wave-like deformations which can be decomposed into *dilatations* and *distortions*. *Dilatations* involve an invariant change in volume of the spacetime continuum which is the source of the associated rest-mass energy density of the deformation. On the other hand, *distortions* correspond to a change of shape (shearing) of the spacetime continuum without a change in volume and are thus massless. Thus the deformations propagate in the continuum by longitudinal (*dilatation*) and transverse (*distortion*) wave displacements.

This provides a natural explanation for wave-particle duality, with the massless transverse mode corresponding to the wave aspects of the deformations and the massive longitudinal mode corresponding to the particle aspects of the deformations. The rest-mass energy density of the longitudinal mode is given by [1, see Eq.(32)]

$$\rho c^2 = 4\bar{\kappa}_0 \varepsilon \tag{1}$$

where ρ is the rest-mass density, c is the speed of light, $\bar{\kappa}_0$ is the bulk modulus of the *STC* (the resistance of the spacetime continuum to *dilatations*), and ε is the volume dilatation

$$\varepsilon = \varepsilon^\alpha{}_\alpha \tag{2}$$

which is the trace of the *STC* strain tensor obtained by contraction. The volume dilatation ε is defined as the change in volume per original volume $\Delta V/V$ [13, see pp. 149–152] and is an invariant of the strain tensor, as is the rest-mass energy density. Hence

$$mc^2 = 4\bar{\kappa}_0\, \Delta V \tag{3}$$

where m is the mass of the deformation and ΔV is the dilatation change in the spacetime continuum's volume corresponding to mass m. This demonstrates that mass is not independent of the spacetime continuum, but rather mass is part of the spacetime continuum fabric itself.

In *STCED*, $\bar{\lambda}_0$ and $\bar{\mu}_0$ are the Lamé elastic constants of the spacetime continuum: $\bar{\mu}_0$ is the shear modulus (the resistance of the spacetime continuum to *distortions*) and $\bar{\lambda}_0$ is expressed in terms of $\bar{\kappa}_0$, the bulk modulus:

$$\bar{\lambda}_0 = \bar{\kappa}_0 - \bar{\mu}_0/2 \tag{4}$$

in a four-dimensional continuum.

2 Energy in the spacetime continuum

In *STCED*, energy is stored in the spacetime continuum as strain energy [5]. As seen in [1, see Section 8.1], the strain energy density of the spacetime continuum is separated into two terms: the first one expresses the dilatation energy density (the mass longitudinal term) while the second one expresses the distortion energy density (the massless transverse term):

$$\mathcal{E} = \mathcal{E}_\parallel + \mathcal{E}_\perp \tag{5}$$

where

$$\mathcal{E}_\parallel = \frac{1}{2}\,\bar{\kappa}_0 \varepsilon^2 \equiv \frac{1}{32\bar{\kappa}_0}\,\rho^2 c^4\,, \tag{6}$$

ρ is the rest-mass density of the deformation, and

$$\mathcal{E}_\perp = \bar{\mu}_0 e^{\alpha\beta} e_{\alpha\beta} = \frac{1}{4\bar{\mu}_0} t^{\alpha\beta} t_{\alpha\beta}\,, \tag{7}$$

with the strain distortion

$$e^{\alpha\beta} = \varepsilon^{\alpha\beta} - e_s g^{\alpha\beta} \tag{8}$$

and the strain dilatation $e_s = \frac{1}{4}\varepsilon^\alpha{}_\alpha$. Similarly for the stress distortion $t^{\alpha\beta}$ and the stress dilatation t_s. Then the dilatation (massive) strain energy density of the deformation is given by the longitudinal strain energy density (6) and the distortion (massless) strain energy density of the deformation is given by the transverse strain energy density (7).

The strain energy W of the deformation is obtained by integrating (5) over the volume V of the deformation to give

$$W = W_\parallel + W_\perp \tag{9}$$

where $W_\parallel$ is the (massive) longitudinal strain energy of the deformation given by

$$W_\parallel = \int_V \mathcal{E}_\parallel \,\mathrm{d}V \tag{10}$$

and $W_\perp$ is the (massless) transverse distortion strain energy of the deformation given by

$$W_\perp = \int_V \mathcal{E}_\perp \,\mathrm{d}V \tag{11}$$

where the volume element $\mathrm{d}V$ in cylindrical polar coordinates is given by $r\mathrm{d}r\,\mathrm{d}\theta\,\mathrm{d}z$ for a stationary deformation.

3 Quantum particles from STC defects

In [8, 10, 11], we show that quantum particles can be represented as defects in the spacetime continuum, specifically dislocations and disclinations. *Dislocations* are translational deformations, while *disclinations* are rotational deformations. In particular, we consider the simplest quantum particle defect given by the edge dislocation [10].

The strain energy density of a stationary edge dislocation is given by

$$W^E = W^E_\parallel + W^E_\perp\,. \tag{12}$$

The longitudinal strain energy of the edge dislocation $W^E_\parallel$ is given by [10, eq. (8)]

$$W^E_\parallel = \frac{\bar{\kappa}_0}{2\pi}\,\bar{\alpha}_0^2\, b^2\,\ell\,\log\frac{\Lambda}{b_c} \tag{13}$$

where

$$\bar{\alpha}_0 = \frac{\bar{\mu}_0}{2\bar{\mu}_0 + \bar{\lambda}_0}\,, \tag{14}$$

ℓ is the length of the dislocation, b_c is the size of the core of the dislocation, of order b_0, the smallest spacetime Burgers dislocation vector [9] and Λ is a cut-off parameter corresponding to the radial extent of the dislocation, limited by the average distance to its nearest neighbours. In (13), the edge dislocation is along the z-axis with Burgers vector b along the x-axis.

The transverse strain energy $W^E_\perp$ is given by [10, eq. (10)]

$$W^E_\perp = \frac{\bar{\mu}_0}{4\pi}\left(\bar{\alpha}_0^2 + 2\bar{\beta}_0^2\right) b^2\,\ell\,\log\frac{\Lambda}{b_c} \tag{15}$$

where

$$\bar{\beta}_0 = \frac{\bar{\mu}_0 + \bar{\lambda}_0}{2\bar{\mu}_0 + \bar{\lambda}_0} \tag{16}$$

and the other parameters are as defined previously.

4 QED mass renormalization

The basic Feynman diagrams can be seen to represent screw dislocations as photons, edge dislocations as bosons, twist and wedge disclinations as fermions [10], and their interactions. The interaction of defects results from the overlap of the defects' strain energy densities. In QED, the exchange of virtual particles in interactions can be seen to be a perturbation expansion representation of the forces resulting from the overlap of the strain energy densities of the dislocations and disclinations.

Similarly, the phenomena of self-energy and vacuum polarization can be understood to result from the strain energy densities of individual defects. QED again represents this situation as a perturbation expansion of an interaction of a photon with the vacuum (photon self-energy also known as vacuum polarization) or of a particle such as an electron with its field (self-energy). In *STCED*, the perturbative expansions are replaced by finite analytical expressions for the strain energy density of individual screw dislocations as photons, edge dislocations as bosons, twist and wedge disclinations as fermions [10].

Quantum Mechanics and QED only deal with the transverse component of spacetime continuum deformations as they are only concerned with the *wave* aspect of wave-particle duality (see [14] for a discussion of this topic). The energy terms used in QED thus correspond to the transverse strain energy $W^E_\perp$. Hence there is no equivalent dilatation massive longitudinal strain energy term ($W^E_\parallel$) used in QED, and no possibility of properly deriving the mass from the theory, as QED uses an incomplete description of particle energies at the quantum level.

The mass term used in the QED equations is external to and not derived from quantum equations. It is thus found to not correspond to the actual mass of the particle and is characterized instead as the bare mass m_0 [15]. To this mass is added the interaction of the particle with the medium or the field, δm, the result of which m_{qm} is "renormalized" (the value of m_0 and the field corrections are infinite) and replaced with the actual experimental mass m according to

$$m_{qm} = m_0 + \delta m \rightarrow m\,. \tag{17}$$

Comparing this equation with (12), we find that

$$
\begin{aligned}
m &= W^E \\
m_0 &= W^E_{\parallel} = \frac{\bar{\kappa}_0}{2\pi}\,\bar{\alpha}_0^2\, b^2\,\ell\,\log\frac{\Lambda}{b_c} \\
\delta m &= W^E_{\perp} = \frac{\bar{\mu}_0}{4\pi}\left(\bar{\alpha}_0^2 + 2\bar{\beta}_0^2\right) b^2\,\ell\,\log\frac{\Lambda}{b_c}\,.
\end{aligned}
\tag{18}
$$

The interaction of the particle with the medium or the field, δm, is the transverse strain energy present in the spacetime continuum (or vacuum), essentially a field energy.

We note that the bare mass (*i.e.* the massive longitudinal strain energy) and the field correction (*i.e.* the transverse strain energy) are both finite in this approach and there is no need for the subtraction of infinities as both terms are well-behaved. If integrated over all of spacetime, they would be divergent, with the divergence being logarithmic in nature. However, contrary to QED, the strain energies are bounded by the density of defects present in the spacetime continuum, which results in an upperbound to the integral of half the average distance between defects. As mentioned by Hirth [16], this has little impact on the accuracy of the results due to the logarithmic dependence. Hence including the longitudinal dilatation mass density term as derived in *STCED* along with the transverse distortion energy density term in the strain energy density provides the expression for the mass m and eliminates the need for mass renormalization as the theory is developed with the correct mass term.

Eq. (18) applies to massive bosons as shown in [10]. For electrons, we have

$$
W^{\ell^3} = W^{\ell^3}_{\parallel} + W^{\ell^3}_{\perp}\,, \tag{19}
$$

where the defect in this case is the ℓ^3 twist disclination [10] and where (18) is replaced with the following:

$$
\begin{aligned}
m &= W^{\ell^3} \\
m_0 &= W^{\ell^3}_{\parallel} = \frac{\bar{\kappa}_0}{6\pi}\,\bar{\alpha}_0^2\left(\Omega_x^2 + \Omega_y^2\right)\ell^3 \log\frac{\Lambda}{b_c} \\
\delta m &= W^{\ell^3}_{\perp} = \frac{\bar{\mu}_0}{2\pi}\,\frac{\ell^3}{3}\Big[\left(\Omega_x^2 + \Omega_y^2\right)\left(\bar{\alpha}_0^2 + \tfrac{1}{2}\bar{\beta}_0^2\right) + \\
&\qquad + 2\,\Omega_x\Omega_y\left(\bar{\alpha}_0^2 - 2\bar{\beta}_0^2\right)\Big]\log\frac{\Lambda}{b_c}
\end{aligned}
\tag{20}
$$

where Ω^μ is the spacetime Frank vector. The same considerations as seen previously for bosons apply to (20) due to the logarithmic dependence of the expressions.

For quarks, we have

$$
W^W = W^W_{\parallel} + W^W_{\perp} \tag{21}
$$

where the defect in this case is the wedge disclination [10]. In most cases $\Lambda \gg b_c$, and we have

$$
\begin{aligned}
m &= W^W \\
m_0 &= W^W_{\parallel} \simeq \frac{\bar{\kappa}_0}{2\pi}\,\Omega_z^2\,\ell\,\Lambda^2\Big[\bar{\alpha}_0^2\,\log^2\Lambda + \\
&\qquad + \bar{\alpha}_0\bar{\gamma}_0\log\Lambda + \tfrac{1}{4}(\bar{\alpha}_0^2 + \bar{\gamma}_0^2)\Big] \\
\delta m &= W^W_{\perp} \simeq \frac{\bar{\mu}_0}{4\pi}\,\Omega_z^2\,\ell\,\Lambda^2\Big[\bar{\alpha}_0^2\,\log^2\Lambda - \\
&\qquad - \left(\bar{\alpha}_0^2 - 3\bar{\alpha}_0\bar{\beta}_0\right)\log\Lambda + \\
&\qquad + \tfrac{1}{2}\left(\bar{\alpha}_0^2 - 3\bar{\alpha}_0\bar{\beta}_0 + \tfrac{3}{2}\bar{\beta}_0^2\right)\Big]
\end{aligned}
\tag{22}
$$

where

$$
\bar{\gamma}_0 = \frac{\bar{\lambda}_0}{2\bar{\mu}_0 + \bar{\lambda}_0}\,. \tag{23}
$$

In this case, both the longitudinal strain energy $W^W_{\parallel}$ and the transverse strain energy $W^W_{\perp}$ are proportional to Λ^2 in the limit $\Lambda \gg b_c$. The parameter Λ is equivalent to the extent of the wedge disclination, and we find that as it becomes more extended, its strain energy is increasing parabolically. This behaviour is similar to that of quarks (confinement). In addition, as shown in [10, see eqs. (16) and (20)], as $\Lambda \to b_c$, the strain energy decreases and tends to 0, again in agreement with the behaviour of quarks (asymptotic freedom).

5 Dislocation self-energy and QED self-energies

The dislocation self-energy is related to the dislocation self-force. The dislocation self-force arises from the force on an element in a dislocation caused by other segments of the *same* dislocation line. This process provides an explanation for the QED self-energies without the need to resort to the emission/absorption of virtual particles. It can be understood, and is particular to, dislocation dynamics as dislocations are defects that extend in the spacetime continuum [16, see p. 131]. Self-energy of a straight-dislocation segment of length L is given by [16, see p. 161]:

$$
\begin{aligned}
W_{self} &= \frac{\bar{\mu}_0}{4\pi}\left((\mathbf{b}\cdot\boldsymbol{\xi})^2 + \frac{\bar{\mu}_0 + \bar{\lambda}_0}{2\bar{\mu}_0 + \bar{\lambda}_0}\,|(\mathbf{b}\times\boldsymbol{\xi})|^2\right)\times \\
&\qquad \times L\left(\ln\frac{L}{b} - 1\right)
\end{aligned}
\tag{24}
$$

where there is no interaction between two elements of the segment when they are within $\pm b$, or equivalently

$$
W_{self} = \frac{\bar{\mu}_0}{4\pi}\left((\mathbf{b}\cdot\boldsymbol{\xi})^2 + \frac{\bar{\mu}_0 + \bar{\lambda}_0}{2\bar{\mu}_0 + \bar{\lambda}_0}\,|(\mathbf{b}\times\boldsymbol{\xi})|^2\right) L\,\ln\frac{L}{eb} \tag{25}
$$

where $e = 2.71828\ldots$. These equations provide analytic expressions for the non-perturbative calculation of quantum self energies and interaction energies, and eliminate the need for the virtual particle perturbative approach.

In particular, the pure screw (photon) self-energy

$$W^S_{self} = \frac{\bar{\mu}_0}{4\pi} (\mathbf{b} \cdot \boldsymbol{\xi})^2 \, L \left(\ln \frac{L}{b} - 1 \right) \tag{26}$$

and the pure edge (boson) self-energy

$$W^E_{self} = \frac{\bar{\mu}_0}{4\pi} \frac{\bar{\mu}_0 + \bar{\lambda}_0}{2\bar{\mu}_0 + \bar{\lambda}_0} \, |(\mathbf{b} \times \boldsymbol{\xi})|^2 \, L \left(\ln \frac{L}{b} - 1 \right) \tag{27}$$

are obtained from (25), while (25) is also the appropriate equation to use for the dual wave-particle "system".

We can relate (27) to (12) and (18) by evaluating W^E from (12) using (13) and (15):

$$W^E = \frac{b^2}{4\pi} \left[2\bar{\kappa}_0 \bar{\alpha}_0^2 + \bar{\mu}_0 \left(\bar{\alpha}_0^2 + 2\bar{\beta}_0^2 \right) \right] \ell \, \log \frac{\Lambda}{b_c} \, . \tag{28}$$

Substituting for $\bar{\kappa}_0$ from (4), for $\bar{\alpha}_0$ from (14) and for $\bar{\beta}_0$ from (16), the factor in square brackets in the above equation becomes

$$[\,] = \frac{\bar{\mu}_0}{(2\bar{\mu}_0 + \bar{\lambda}_0)^2} \left(4\bar{\mu}_0^2 + 6\bar{\mu}_0 \bar{\lambda}_0 + 2\bar{\lambda}_0^2 \right) \tag{29}$$

which can be factored as

$$[\,] = \frac{2\bar{\mu}_0}{(2\bar{\mu}_0 + \bar{\lambda}_0)^2} \, (2\bar{\mu}_0 + \bar{\lambda}_0)(\bar{\mu}_0 + \bar{\lambda}_0) \, . \tag{30}$$

Substituting back into (28), we obtain

$$W^E_{self} = \frac{1}{2} \, W^E = \frac{\bar{\mu}_0}{4\pi} \frac{\bar{\mu}_0 + \bar{\lambda}_0}{2\bar{\mu}_0 + \bar{\lambda}_0} \, b^2 \, \ell \, \log \frac{\Lambda}{b_c} \, . \tag{31}$$

As noted in [17, see p. 178], the self-energy and the interaction energies are described by the same equations in the non-singular theory, except that the self-energy is half of the interaction energy. We thus see that the above result (28) is essentially the same as (27) from Hirth [16, see p. 161] except that the log factors are slightly different, but similar in intent ($\log \Lambda / b_c$ compared to $\log \ell / eb$).

Dislocation self energies are thus found to be similar in structure to Quantum Electrodynamics self energies. They are also divergent if integrated over all of spacetime, with the divergence being logarithmic in nature. However, contrary to QED, dislocation self energies are bounded by the density of dislocations present in the spacetime continuum, which results in an upperbound to the integral of half the average distance between dislocations.

For a dislocation loop, as each element $d\mathbf{l}$ of the dislocation loop is acted upon by the forces caused by the stress of the other elements of the dislocation loop, the work done against these corresponds to the self-energy of the dislocation loop. The self-energy of a dislocation loop can be calculated from Eq. (4-44) of [16, see p. 110] to give

$$\begin{aligned} W_{self} = {} & \frac{\bar{\mu}_0}{8\pi} \oint_{C_1=C} \oint_{C_2=C} \frac{(\mathbf{b} \cdot d\mathbf{l_1})\,(\mathbf{b} \cdot d\mathbf{l_2})}{R} + \\ & + \frac{\bar{\mu}_0}{4\pi} \frac{\bar{\mu}_0 + \bar{\lambda}_0}{2\bar{\mu}_0 + \bar{\lambda}_0} \oint_{C_1=C} \oint_{C_2=C} \frac{(\mathbf{b} \times d\mathbf{l_1}) \cdot \mathbf{T} \cdot (\mathbf{b} \times d\mathbf{l_2})}{R} \end{aligned} \tag{32}$$

where $\mathbf{T}$ is as defined in Eq. (4-44) of [16, see p. 110].

The photon self-energy also known as vacuum polarization is obtained from the strain energy density of screw dislocations. The longitudinal strain energy of the screw dislocation $W^S_{\parallel} = 0$ as given by [10, eq. (6)] *i.e.* the photon is massless. The photon self-energy is given by half the transverse strain energy of the screw dislocation $W^S_{\perp}$ given by [10, eq. (7)]

$$W^S_{self} = \frac{1}{2} \, W^S_{\perp} = \frac{\bar{\mu}_0}{8\pi} \, b^2 \, \ell \, \log \frac{\Lambda}{b_c} \tag{33}$$

which again includes the $\log \Lambda / b_c$ factor. Comparing this expression with (26) and with (32), we find that (26) is likely off by a factor of 2, being proportional to $1/8\pi$ as per Hirth's (32) and (33), not $1/4\pi$ as given in Hirth's (24) and Hirth's (26).

6 Disclination self-energy and QED self-energies

From dislocation self-energies, we can calculate the photon self-energy (also known as the vacuum polarization) and, in the general case, the boson self-energy.

The fermion self-energies are calculated from the corresponding disclination self-energies, with the lepton self-energy calculated from the interaction energy W^{ℓ^3} of the ℓ^3 twist disclination, the neutrino self-energy calculated from the interaction energy W^{ℓ} of the ℓ twist disclination and the quark self-energy calculated from the interaction energy W^W of the wedge disclination, using the result that self-energy is half of the interaction energy as seen previously in Section 5.

6.1 The ℓ^3 twist disclination self-energy and lepton self-energies

The lepton (electron) self-energy is calculated from the interaction energy W^{ℓ^3} of the ℓ^3 twist disclination by evaluating W^{ℓ^3} from (19) using $W^{\ell^3}_{\parallel}$ and $W^{\ell^3}_{\perp}$ from (20):

$$\begin{aligned} W^{\ell^3} = {} & \frac{\bar{\kappa}_0}{6\pi} \, \bar{\alpha}_0^2 \left(\Omega_x^2 + \Omega_y^2 \right) \ell^3 \log \frac{\Lambda}{b_c} + \\ & + \frac{\bar{\mu}_0}{2\pi} \frac{\ell^3}{3} \Big[\left(\Omega_x^2 + \Omega_y^2 \right) \left(\bar{\alpha}_0^2 + \tfrac{1}{2} \bar{\beta}_0^2 \right) + \\ & + 2\, \Omega_x \Omega_y \left(\bar{\alpha}_0^2 - 2\bar{\beta}_0^2 \right) \Big] \log \frac{\Lambda}{b_c} \, . \end{aligned} \tag{34}$$

Substituting for $\bar{\kappa}_0$ from (4), for $\bar{\alpha}_0$ from (14) and for $\bar{\beta}_0$ from (16), (34) becomes

$$\begin{aligned} W^{\ell^3} = {} & \frac{\ell^3}{6\pi} \frac{\bar{\mu}_0}{(2\bar{\mu}_0 + \bar{\lambda}_0)^2} \times \\ & \times \Big[\left(\Omega_x^2 + \Omega_y^2 \right) \left(2\bar{\mu}_0^2 + 2\bar{\mu}_0 \bar{\lambda}_0 + \tfrac{1}{2} \bar{\lambda}_0^2 \right) - \\ & - 2\, \Omega_x \Omega_y \left(\bar{\mu}_0^2 + 4\bar{\mu}_0 \bar{\lambda}_0 + 2\bar{\lambda}_0^2 \right) \Big] \log \frac{\Lambda}{b_c} \end{aligned} \tag{35}$$

which can be factored as

$$\begin{aligned} W^{\ell^3} = \frac{\ell^3}{12\pi}\,\frac{\bar{\mu}_0}{(2\bar{\mu}_0+\bar{\lambda}_0)^2}\Big\{\left(\Omega_x^2+\Omega_y^2\right)\left(2\bar{\mu}_0+\bar{\lambda}_0\right)^2 - \\ - 4\Omega_x\Omega_y\left[\left(\bar{\mu}_0+\bar{\lambda}_0\right)\left(\bar{\mu}_0+2\bar{\lambda}_0\right)+\bar{\mu}_0\bar{\lambda}_0\right]\Big\}\log\frac{\Lambda}{b_c}. \end{aligned} \tag{36}$$

The lepton self-energy is then given by

$$\begin{aligned} W^{\ell^3}_{self} = \frac{1}{2}\,W^{\ell^3} = \frac{\bar{\mu}_0}{24\pi}\Big\{\left(\Omega_x^2+\Omega_y^2\right) - \\ -4\,\Omega_x\Omega_y\,\frac{\left(\bar{\mu}_0+\bar{\lambda}_0\right)\left(\bar{\mu}_0+2\bar{\lambda}_0\right)+\bar{\mu}_0\bar{\lambda}_0}{(2\bar{\mu}_0+\bar{\lambda}_0)^2}\Big\}\,\ell^3\,\log\frac{\Lambda}{b_c}\,, \end{aligned} \tag{37}$$

where we have used the result that self-energy is half of the interaction energy as seen previously in Section 5.

6.2 The *ℓ* twist disclination self-energy and the neutrino self-energy

The neutrino self-energy is calculated from the strain energy W^ℓ of the ℓ twist disclination. The longitudinal strain energy of the ℓ twist disclination $W^\ell_\parallel = 0$ as given by [10, eq. 33)] *i.e.* the neutrino is massless. In most cases $\Lambda \gg b_c$, and the strain energy W^ℓ of the ℓ twist disclination is given by the transverse strain energy $W^\ell = W^\ell_\perp$ given by [10, eq. (35)]:

$$\begin{aligned} W^\ell = \frac{\bar{\mu}_0}{2\pi}\,\ell\,\Lambda^2\Big[\left(\Omega_x^2+\Omega_y^2\right)\Big(\bar{\alpha}_0^2\,\log^2\Lambda+\bar{\alpha}_0\bar{\gamma}_0\,\log\Lambda - \\ - \tfrac{1}{2}\,\bar{\alpha}_0\bar{\gamma}_0\Big) - 2\,\Omega_x\Omega_y\Big(\bar{\alpha}_0\bar{\beta}_0\log\Lambda+\tfrac{1}{2}\,\bar{\beta}_0\bar{\gamma}_0\Big)\Big]. \end{aligned} \tag{38}$$

Substituting for $\bar{\alpha}_0$ from (14), for $\bar{\beta}_0$ from (16) and for $\bar{\gamma}_0$ from (23), (38) becomes

$$\begin{aligned} W^\ell = \frac{\bar{\mu}_0}{2\pi}\,\frac{\ell\,\Lambda^2}{(2\bar{\mu}_0+\bar{\lambda}_0)^2}\Big\{\left(\Omega_x^2+\Omega_y^2\right)\Big[\bar{\mu}_0^2\,\log^2\Lambda+ \\ + \bar{\mu}_0\bar{\lambda}_0\left(\log\Lambda-\tfrac{1}{2}\right)\Big] - \\ - 2\,\Omega_x\Omega_y\Big[\bar{\mu}_0\left(\bar{\mu}_0+\bar{\lambda}_0\right)\log\Lambda+\tfrac{1}{2}\,\bar{\lambda}_0\left(\bar{\mu}_0+\bar{\lambda}_0\right)\Big]\Big\}. \end{aligned} \tag{39}$$

The neutrino self-energy is then given by

$$\begin{aligned} W^\ell_{self} = \frac{1}{2}\,W^\ell = \frac{\bar{\mu}_0}{4\pi}\,\frac{\ell\,\Lambda^2}{(2\bar{\mu}_0+\bar{\lambda}_0)^2}\times \\ \times\Big\{\left(\Omega_x^2+\Omega_y^2\right)\Big[\bar{\mu}_0^2\,\log^2\Lambda+\bar{\mu}_0\bar{\lambda}_0\left(\log\Lambda-\tfrac{1}{2}\right)\Big] - \\ - 2\,\Omega_x\Omega_y\left(\bar{\mu}_0+\bar{\lambda}_0\right)\left(\bar{\mu}_0\log\Lambda+\tfrac{1}{2}\,\bar{\lambda}_0\right)\Big\} \end{aligned} \tag{40}$$

where we have used the result that self-energy is half of the interaction energy as seen previously in Section 5.

6.3 The wedge disclination self-energy and quark self-energies

The quark self-energy is calculated from the interaction energy W^W of the wedge disclination by evaluating W^W from (21) using $W^W_\parallel$ and $W^W_\perp$ from (22). In most cases $\Lambda \gg b_c$, and we have

$$\begin{aligned} W^W \simeq \frac{\bar{\kappa}_0}{2\pi}\,\Omega_z^2\,\ell\,\Lambda^2\Big[\bar{\alpha}_0^2\,\log^2\Lambda+ \\ + \bar{\alpha}_0\bar{\gamma}_0\log\Lambda+\tfrac{1}{4}(\bar{\alpha}_0^2+\bar{\gamma}_0^2)\Big]+ \\ + \frac{\bar{\mu}_0}{4\pi}\,\Omega_z^2\,\ell\,\Lambda^2\Big[\bar{\alpha}_0^2\,\log^2\Lambda- \\ - \left(\bar{\alpha}_0^2-3\bar{\alpha}_0\bar{\beta}_0\right)\log\Lambda+ \\ + \tfrac{1}{2}\left(\bar{\alpha}_0^2-3\bar{\alpha}_0\bar{\beta}_0+\tfrac{3}{2}\,\bar{\beta}_0^2\right)\Big]. \end{aligned} \tag{41}$$

Substituting for $\bar{\kappa}_0$ from (4), for $\bar{\alpha}_0$ from (14) for $\bar{\beta}_0$ from (16) and for $\bar{\gamma}_0$ from (23), (41) becomes

$$\begin{aligned} W^W \simeq \frac{\Omega_z^2}{2\pi}\,\frac{\ell\,\Lambda^2}{(2\bar{\mu}_0+\bar{\lambda}_0)^2}\Big[\bar{\mu}_0^2\left(\bar{\mu}_0+\bar{\lambda}_0\right)\log^2\Lambda+ \\ +\bar{\mu}_0\left(\bar{\mu}_0^2+2\bar{\mu}_0\bar{\lambda}_0+\bar{\lambda}_0^2\right)\log\Lambda+ \\ +\tfrac{1}{4}\,\bar{\lambda}_0\left(\bar{\mu}_0^2+2\bar{\mu}_0\bar{\lambda}_0+\bar{\lambda}_0^2\right)\Big] \end{aligned} \tag{42}$$

which can be factored as

$$\begin{aligned} W^W \simeq \frac{\Omega_z^2}{2\pi}\,\frac{\ell\,\Lambda^2}{(2\bar{\mu}_0+\bar{\lambda}_0)^2}\Big[\bar{\mu}_0^2\left(\bar{\mu}_0+\bar{\lambda}_0\right)\log^2\Lambda+ \\ + \left(\bar{\mu}_0+\bar{\lambda}_0\right)^2\left(\bar{\mu}_0\log\Lambda+\tfrac{1}{4}\,\bar{\lambda}_0\right)\Big]. \end{aligned} \tag{43}$$

The quark self-energy is then given by

$$\begin{aligned} W^W_{self} = \frac{1}{2}\,W^W \simeq \frac{\Omega_z^2}{4\pi}\,\frac{(\bar{\mu}_0+\bar{\lambda}_0)^2}{(2\bar{\mu}_0+\bar{\lambda}_0)^2}\,\ell\,\Lambda^2\times \\ \times\left[\frac{\bar{\mu}_0^2}{\bar{\mu}_0+\bar{\lambda}_0}\,\log^2\Lambda+\bar{\mu}_0\log\Lambda+\tfrac{1}{4}\,\bar{\lambda}_0\right] \end{aligned} \tag{44}$$

where we have used the result that self-energy is half of the interaction energy as seen previously in Section 5.

7 Discussion and conclusion

In this paper, we have considered how the Elastodynamics of the Spacetime Continuum (*STCED*) explains the Quantum Electrodynamics (QED) phenomena of self-energy, vacuum polarization and mass renormalization. We have noted that QED only deals with the *wave* aspect of wave-particle objects, and hence QED only deals with the distortion transverse strain energy $W^E_\perp$, while the dilatation massive longitudinal strain energy term $W^E_\parallel$ is not considered. Hence there is no possibility of properly deriving the mass, as QED uses an incomplete description of particle energies at the quantum level.

Comparison of mass renormalization with *STCED* strain energy shows that the interaction of the particle with the medium or the field, δm, is the transverse strain energy present in the spacetime continuum (or vacuum), essentially a field energy. We provide the strain energy equivalence for QED mass renormalization for bosons, leptons and quarks.

Both the bare mass (*i.e.* the massive longitudinal strain energy) and the field correction (*i.e.* the transverse strain energy) are finite in this approach and there is no need for the subtraction of infinities as both terms are well-behaved. Contrary to QED, the strain energies are bounded by the density of defects present in the spacetime continuum, which results in an upperbound to the integral of half the average distance between defects. Hence including the longitudinal dilatation mass density term as derived in *STCED* along with the transverse distortion energy density term in the strain energy density provides the expression for the mass m and eliminates the need for mass renormalization as the theory is developed with the correct mass term. We have also derived the self-energy expressions for bosons including photons, leptons including neutrinos, and quarks.

It is important to note that

1. The expressions derived are for stationary (time independent) defects.
2. The case of time-dependent screw and edge dislocations moving with velocity v is covered in §16.1.2 and §16.2.2 of [11] respectively. The calculations involve integrals of the form

$$\int_y \frac{1}{\alpha y} \arctan\left(\frac{x - vt}{\alpha y}\right) dy = -\frac{i}{2}\left[\mathrm{Li}_2\left(-i\,\frac{x - vt}{\alpha y}\right) - \mathrm{Li}_2\left(i\,\frac{x - vt}{\alpha y}\right)\right] \tag{45}$$

where

$$\alpha = \sqrt{1 - \frac{v^2}{c^2}} \tag{46}$$

and where $\mathrm{Li}_n(x)$ is the polylogarithm function which arises in Feynman diagram integrals. For $n = 2$ and $n = 3$, we have the dilogarithm and the trilogarithm special cases respectively. This is a further indication that the interaction of strain energies are the physical source of quantum interaction phenomena described by Feynman diagrams as discussed in section 4.

The results obtained are found to provide a physical explanation of QED phenomena in terms of the interaction resulting from the overlap of defect strain energies in the spacetime continuum in *STCED*.

Received on July 18, 2018

References

1. Millette P. A. Elastodynamics of the Spacetime Continuum. *The Abraham Zelmanov Journal*, 2012, vol. 5, 221–277.
2. Millette P. A. On the Decomposition of the Spacetime Metric Tensor and of Tensor Fields in Strained Spacetime. *Progress in Physics*, 2012, vol. 8 (4), 5–8.
3. Millette P. A. The Elastodynamics of the Spacetime Continuum as a Framework for Strained Spacetime. *Progress in Physics*, 2013, vol. 9 (1), 55–59.
4. Millette P. A. Derivation of Electromagnetism from the Elastodynamics of the Spacetime Continuum. *Progress in Physics*, 2013, vol. 9 (2), 12–15.
5. Millette P. A. Strain Energy Density in the Elastodynamics of the Spacetime Continuum and the Electromagnetic Field. *Progress in Physics*, 2013, vol. 9 (2), 82–86.
6. Millette P. A. Dilatation–Distortion Decomposition of the Ricci Tensor. *Progress in Physics*, 2013, vol. 9 (4), 32–33.
7. Millette P. A. Wave-Particle Duality in the Elastodynamics of the Spacetime Continuum (STCED). *Progress in Physics*, 2014, vol. 10 (4), 255–258.
8. Millette P. A. Dislocations in the Spacetime Continuum: Framework for Quantum Physics. *Progress in Physics*, 2015, vol. 11 (4), 287–307.
9. Millette P. A. The Burgers Spacetime Dislocation Constant b_0 and the Derivation of Planck's Constant. *Progress in Physics*, 2015, vol. 11 (4), 313–316.
10. Millette P. A. Bosons and Fermions as Dislocations and Disclinations in the Spacetime Continuum. *Progress in Physics*, 2018, vol. 14 (1), 10–18.
11. Millette P. A. Elastodynamics of the Spacetime Continuum: A Spacetime Physics Theory of Gravitation, Electromagnetism and Quantum Physics. American Research Press, Rehoboth, NM, 2017.
12. Milonni P. W. The Quantum Vacuum: An Introduction to Quantum Electrodynamics. Academic Press, San Diego, 1994.
13. Segel L. A. Mathematics Applied to Continuum Mechanics. Dover Publications, New York, 1987.
14. Millette P. A. On the Classical Scaling of Quantum Entanglement. *Progress in Physics*, 2018, vol. 14 (3), 121–130.
15. Schweber S. S. An Introduction to Relativistic Quantum Field Theory. Dover Publications, Mineola, NY, (1962), 2005, pp. 510–511.
16. Hirth R. M. and Lothe J. Theory of Dislocations, 2^{nd} ed. Krieger Publishing Co., Florida, 1982.
17. Bulatov V. V. and Cai W. Computer Simulation of Dislocations. Oxford University Press, Oxford, 2006.

The Nature of the Electron and Proton as Viewed in the Planck Vacuum Theory

William C. Daywitt

National Institute for Standards and Technology (retired), Boulder, Colorado. E-mail: wcdaywitt@me.com

There is a long-standing question whether or not the proton obeys the Dirac equation. The following calculations answer that question in the affirmative. The paper argues that, even though the proton has an internal structure, unlike the electron, it is still a Dirac particle in the sense that it obeys the same Dirac equation

$$\pm\left[ie_*^2\gamma^\mu\frac{\partial}{\partial x^\mu}-mc^2\right]\psi=0$$

as the electron, where the upper and lower signs refer to the electron and proton respectively with their masses m_e and m_p. Calculations readily show why the proton mass is orders-of-magnitude greater than the electron mass, and suggest that the constant 1836 can be thought of as the 'proton structure constant'.

1 Introduction

The electron is assumed to be a structureless particle [1, p.82] that obeys the Dirac equation; so it is somewhat surprising that the structured proton also obeys that same equation. The reason for this apparent conundrum is tied to the nature of the Planck vacuum (PV) state itself [2].

The manifestly covariant form of the Dirac equation [1, p.90] is

$$\left[i\hbar\gamma^\mu\frac{\partial}{\partial x^\mu}-mc\right]\psi=0 \tag{1}$$

which, using $c\hbar=e_*^2$, can be expressed as

$$\left[ie_*^2\gamma^\mu\frac{\partial}{\partial x^\mu}-mc^2\right]\psi=0 \tag{2}$$

with

$$\frac{\partial}{\partial x^\mu}\equiv\left(\frac{\partial}{c\partial t},\,\nabla\right) \tag{3}$$

where ψ is the 4x1 Dirac spinor, [$\mu=0,1,2,3$], and ∇ is the normal 3-dimensional gradient operator. See Appendix A for the definition of the γ^μ matrices. The summation convention over the two μs in the first terms of (1) and (2) is understood.

The two particle/PV coupling forces [3]

$$F_e(r)=\frac{e_*^2}{r^2}-\frac{m_ec^2}{r}\quad\text{and}\quad F_p(r)=\frac{e_*^2}{r^2}-\frac{m_pc^2}{r} \tag{4}$$

the electron and proton cores $(-e_*, m_e)$ and $(+e_*, m_p)$ exert on the PV state, along with their coupling constants

$$F_e(r_e)=0\quad\text{and}\quad F_p(r_p)=0 \tag{5}$$

and the resulting Compton radii

$$r_e=\frac{e_*^2}{m_ec^2}\quad\text{and}\quad r_p=\frac{e_*^2}{m_pc^2} \tag{6}$$

lead to the important string of Compton relations

$$r_em_ec^2=r_pm_pc^2=e_*^2=r_*m_*c^2\quad(=c\hbar) \tag{7}$$

where $\hbar$ is the reduced Planck constant. The electron and proton masses are m_e and m_p respectively. The vanishing of $F_e(r_e)$ and $F_p(r_p)$ in (5) frees the electron and proton from being tethered by their coupling forces to the vacuum state, insuring that both particles propagate in free space as free particles. The Planck particle mass and Compton radius are m_* and r_*.

2 Electron and positron

The Dirac electron equation from (2) with the positive sign from the abstract leads to [3]

$$\left[i(-e_*)(-e_*)\gamma^\mu\frac{\partial}{\partial x^\mu}-m_ec^2\right]\psi=0 \tag{8}$$

where the first charge $(-e_*)$ comes from the electron core, and the second charge $(-e_*)$ from any one of the Planck-particle cores in the negative branch of the PV state (Appendix B).

Charge conjugation of (8) then leads to the positron equation

$$\left[i(+e_*)(+e_*)\gamma^\mu\frac{\partial}{\partial x^\mu}-m_ec^2\right]\psi=0\,. \tag{9}$$

where the first charge $(+e_*)$ comes from the positron core $(+e_*, m_e)$, and the second charge $(+e_*)$ from any one of the Planck-particle cores in the positive branch of the PV state.

3 Proton and antiproton

The proton equation from the preceding abstract

$$-\left[ie_*^2\gamma^\mu\frac{\partial}{\partial x^\mu}-m_pc^2\right]\psi=0 \tag{10}$$

can be expressed as

$$\left[i(+e_*)(-e_*)\gamma^\mu\frac{\partial}{\partial x^\mu}+m_pc^2\right]\psi=0 \tag{11}$$

where the first charge $(+e_*)$ comes from the proton core, and the second charge $(-e_*)$ from any one of the Planck-particle cores in the negative branch of the PV state.

Charge conjugation of (11) then leads to the antiproton equation

$$\left[i(-e_*)(+e_*)\gamma^\mu \frac{\partial}{\partial x^\mu} + m_p c^2 \right] \psi = 0 \tag{12}$$

where the first charge $(-e_*)$ comes from the antiproton core $(-e_*, m_p)$, and the second charge $(+e_*)$ from any one of the Planck-particle cores in the positive branch of the PV state.

4 Proton structure

The reason for the proton structure is easily seen from the nature of the charge products in equations (8) and (9), as opposed to those in equations (11) and (12). In (8) and (9) both products yield a positive e_*^2, signifying that the electron and positron charges repel their corresponding degenerate collection of PV charges (Appendix B); isolating the characteristics of the electron/positron from the PV state.

In (11) and (12), however, things are reversed. Both products yield a negative e_*^2, signifying that the proton and antiproton charges are attracting their corresponding degenerate collection of PV charges; converting a small portion of the PV energy into the proton and antiproton states, elevating the proton/antiproton masses orders-of-magnitude over those of the electron/positron masses.

5 Conclusions and comments

From (7) the mass energies of the electron and proton are [2]

$$m_e c^2 = \frac{e_*^2}{r_e} \qquad \text{and} \qquad m_p c^2 = \frac{e_*^2}{r_p} \tag{13}$$

which lead to

$$m_p = \frac{r_e}{r_p} \cdot m_e \tag{14}$$

where the ratio $r_e/r_p \approx 1836$. Thus, since m_e is assumed to be structureless, (14) suggests that the constant 1836 can be thought of as the 'proton structure constant'.

Finally, in the PV theory the so-called structure appears in the proton rest frame as a small spherical 'collar' surrounding the proton core [5].

Appendix A: The γ and β matrices

The 4x4 γ, β, and α_i matrices used in the Dirac theory are defined here: where [1, p.91]

$$\gamma^0 \equiv \beta = \begin{pmatrix} I & 0 \\ 0 & -I \end{pmatrix} \tag{A1}$$

and $(i = 1, 2, 3)$

$$\gamma^i \equiv \beta\alpha_i = \begin{pmatrix} 0 & \sigma_i \\ -\sigma_i & 0 \end{pmatrix} \tag{A2}$$

and where I is the 2x2 unit matrix and

$$\alpha_i = \begin{pmatrix} 0 & \sigma_i \\ \sigma_i & 0 \end{pmatrix} \tag{A3}$$

where the σ_i are the 2x2 Pauli spin matrices

$$\sigma_1 = \begin{pmatrix} 0 & 1 \\ 1 & 0 \end{pmatrix}, \sigma_2 = \begin{pmatrix} 0 & -i \\ i & 0 \end{pmatrix}, \sigma_3 = \begin{pmatrix} 1 & 0 \\ 0 & -1 \end{pmatrix} \tag{A4}$$

and $\boldsymbol{\alpha} = (\alpha_1, \alpha_2, \alpha_3)$.

Appendix B: Charge conjugation

Charge conjugation [4] in the PV theory implies that the invisible vacuum state must be a bifurcated state—bifurcation meaning that at each point in free space there exists a vacuum subspace consisting of the charge doublet $(\pm e_*)^2$ that leads to two vacuum branches

$$e_*^2 = (-e_*)(-e_*) \qquad \text{and} \qquad e_*^2 = (+e_*)(+e_*) \tag{B1}$$

where, by definition, the second charge in each product defines the branch. The first charge in each branch belongs to the electron or positron. For example, if the first charge $(-e_*)$ in the negative branch on the left belongs to the electron, then the first charge $(+e_*)$ in the positive branch at the right belongs to the positron. In the PV theory charge conjugation simply switches back and forth between the two PV branches, which amounts to changing the signs in the four products $(\pm e_*)(\pm e_*)$. For example, if C is the charge conjugation operator, then

$$C(\pm e_*)(\pm e_*) = (\mp e_*)(\mp e_*)\,. \tag{B2}$$

In the proton case (the negative sign in the abstract)

$$-e_*^2 = (+e_*)(-e_*) \quad \text{and} \quad -e_*^2 = (-e_*)(+e_*) \tag{B3}$$

where the first charge on the left belongs to the proton and the first charge on the right belongs to the antiproton. Again, the second charge in each product defines the branch.

Submitted on July 19, 2018

References

1. Gingrich D.M. Practical Quantum Electrodynamics. CRC, The Taylor & Francis Group, Boca Raton, London, New York, 2006.
2. Daywitt W.C. The Trouble with the Equations of Modern Fundamental Physics. American Journal of Modern Physics. Special Issue: "Physics without Higgs and without Supersymmetry". 2016, v. 5, no.1-1, 22. See also www.planckvacuumDOTcom.
3. Daywitt W.C. The Dirac Electron and Its Propagator as Viewed in the Planck Vacuum Theory. *Progress in Physics*, 2018, Issue 4, v. 14, 194.
4. Daywitt W.C. Antiparticles and Charge Conjugation in the Planck Vacuum Theory. *Progress in Physics*, 2015, Issue 11, v. 4, 311.
5. Daywitt W.C. A Planck Vacuum Pilot Model for Inelastic Electron-Proton Scattering. *Progress in Physics*, 2015, Issue 4, v. 11, 308.

Theory of Anomalous Magnetic Moment and Lamb Shift of Extended Electron in Stochastic Electrodynamics

Muralidhar Kundeti[1], Prasad M. B. Rajendra[2]

[1] B-74, Kendriya Vihar, Gachibowli, Hyderabad-500032, India. E-mail: kundetimuralidhar@gmail.com
[2] Physics Department, National Defence Academy, Khadakwasla, Pune-411023, India. E-mail: rajendraprasadmb75@gmail.com

The very presence of zero-point field allows us to consider the structure of the electron with center of charge in circular motion around center of mass. Considering extended electron structure in stochastic electrodynamics, mass and charge corrections are derived without any logarithmic divergence terms. Using these corrections, the anomalous magnetic moment of the electron has been expressed in a series as a function of fine-structure constant. The evaluated magnetic moment is found to be accurate up to ninth decimal place with a difference of 90.22×10^{-12} from the experimental value. In the case of an orbital electron, due to its motion, the surrounding zero-point field is modified and the zero-point energy associated with these modifications leads to a shift in the energy level. By imposing a cut-off frequency equal to the de Broglie frequency, the zero-point energy associated with the orbital electron is attributed to the Lamb shift. The estimated Lamb shift in hydrogen atom is found to be in agreement with the experimental value. These theoretical derivations give a new classical approach to both the anomalous magnetic moment of the electron and the Lamb shift.

1 Introduction

An electron is visualized as a point particle in both quantum mechanics and quantum field theories in general. Efforts to find the size of the electron have led to a very small size $\sim 10^{-20}$ m in high energy scattering experiments [1] and in the penning trap experiment, the finite size effect was considered to be of the order of experimental uncertainty in the measurement of the anomalous magnetic moment of the electron. Thus any sub-structure of the electron is ruled out in quantum field theories and the particles are treated as point particles without any size. The point particle limit of the electron, in most of the theoretical approaches is fine and excellent except for the singularity syndrome and any cut-off procedure leads to a finite structure of the electron.

The concept of an extended structure of the electron originates from the zitterbewegung motion (rapid oscillations of Dirac electron) and such random oscillations are invariably attributed to the presence of zero-point field throughout the universe. The extended electron theories were developed over several decades [2–10] and the perception of point particle having charge and mass or rigid sphere with charge distribution was denied and the structure of the electron had been considered with the charge in an average circular motion about the center of mass. While dealing with extended electron models, a natural question arises that why such extended structure is not detected in scattering experiments. The reason being the charge rotation is at the speed of light and therefore, it cannot be detected at all. However, the footprints of such extended electron can be seen from the recent detection of the de Broglie wave of the electron in the scattering of a beam of electrons in thin silicon crystal [11] and from the high resolution scanning tunneling microscopy images [12].

Recently, the role of spin and the internal electron structure in complex vector formalism was studied by the author [13–15] and it had been shown that the mass of the particle may be interpreted to the zero-point field energy associated with the local complex rotation or oscillation confined in a region of space of the order of the Compton wavelength. Further, the logical classical foundations of quantum mechanics were explored from the consideration of extended electron structure [16, 17]. It is of particular interest whether the calculations of the electron magnetic moment and Lamb shift are possible with the extended electron theories.

In the charge shell model of the electron, Puthoff [18] has shown that the zero-point energy of the particle is equal to the Coulomb energy in the limit when the shell radius tends to zero. The zero-point energy within the shell was found to be proportional to the fine-structure constant. Therefore, it may be expected that the zero-point energy associated with an electron in the point particle limit may be attributed to the charge correction rather than any mass correction which was considered earlier in the stochastic electrodynamics theories.

In stochastic electrodynamics (classical electrodynamics along with zero-point field), a charged point particle is considered as an oscillator and its equation of motion is given by the Brafford-Marshall equation which is simply the Abraham-Lorentz equation with zero-point field. In the stochastic electrodynamics approach, the energy of the electron oscillator was estimated by Boyer [19] and without imposing any cut-off frequency the zero-point energy of the oscillator was found to be $\hbar\omega_0/2$ per mode, where ω_0 and $\hbar$ are the oscillator frequency and reduced Planck constant respectively. Though many quantum phenomena were explained in the stochastic electrodynamics approach, the theory was found to be incomplete [20]. However, it has been found that the introduction of spin into the problem leaves the theory to overcome such failures. The detailed discussion of stochastic electrodynamics with spin was given by Cavelleri *et al* [21] and in this theory, the electron has an extended structure. In view of the extended electron structure, one can impose a cut-off frequency ω_0 and in that case, in the absence of radiation damping and binding terms, the energy associated with the electron has been derived in Section 2.

In the point particle limit, the energy associated with the electron is found to be

$$\Delta E_0 = \frac{2\alpha}{3\pi}\hbar\omega_0\,, \tag{1}$$

where $\alpha = (1/4\pi\epsilon_0)(e^2/\hbar c)$ is the fine-structure constant and $-e$ is the electron charge. This energy may be attributed to the charge correction and the ratio $\Delta E_0/\hbar\omega_0$ corresponds to a correction to fine-structure constant due to interaction of random zero-point field fluctuations. In general, the effective or observed fine-structure constant can be expressed by the relation $\alpha_{obs} \to \alpha_{th} + \Delta\alpha$. Now, the ratio $\Delta\alpha/\alpha$ can be expressed in the following form:

$$\frac{\Delta\alpha}{\alpha} = \frac{\Delta E_c}{\hbar\omega_0} = \frac{2\alpha}{3\pi}\,. \tag{2}$$

In quantum electrodynamics such charge correction was calculated considering the vacuum polarization and it may be noted that the above estimate gives a similar result except for the diverging logarithmic term. The incorporation of this charge correction leads to a replacement of fine-structure constant in the theoretical calculations by $\alpha\,(1 - 2\alpha/3\pi)$.

The total energy of the electron immersed in the zero-point field can be expressed by substituting $\left(\mathbf{p} - e\mathbf{A}_{zp}/c\right)$ for momentum in the relation $E^2 = p^2c^2 + m^2c^4$ [15]:

$$E^2 = p^2c^2 - 2ec\mathbf{p}.\mathbf{A}_{zp} + e^2A_{zp}^2 + m^2c^4, \tag{3}$$

where $\mathbf{A}_{zp}$ is the electromagnetic vector potential of zero-point field. The energy in the last two terms in the above equation can be written in the form $E_0 = mc^2 + e^2A_{zp}^2/2mc^2$. Thus under the influence of zero-point field, there appears a correction to mass and such correction to mass must be of the order of fine-structure constant. The derivation of such mass correction of extended electron in stochastic electrodynamics is given in Section 2. We find that the mass correction Δm depends on the reduced particle velocity $\beta = \mathbf{v}/c$ and the ratio $\Delta m/m$ is expressed by the relation

$$\frac{\Delta m}{m} = \frac{\alpha}{2\pi}\left(1 + \beta^2\right). \tag{4}$$

From the knowledge of mass and charge corrections, the anomalous magnetic moment a_e of the electron is estimated in Section 3.

Under the influence of central Coulomb potential, an orbital electron moves with a velocity proportional to the fine structure constant. When the electron moves in the zero-point field, it induces certain modifications in the surrounding zero-point field. Since these zero-point field modifications may be considered at least of the order of the de Broglie wavelength, the energy associated with the shift in the electron energy levels can be obtained by imposing a cut-off frequency equal to the de Broglie frequency ω_B and the derived zero-point energy is attributed to the Lamb shift. The derivation of Lamb shift and its calculation are given in Section 4. The energy shift in the electron circular orbit is found to be

$$\Delta E_L = \frac{4\alpha^5}{3\pi}m_rc^2, \tag{5}$$

where $m_r = mM/(m + M)$ is the reduced mass and M is the nuclear mass. The calculation of the Lamb shift has been performed using charge correction in the Coulomb field and the mass correction for the electron. Finally, the conclusions are presented in Section 5. The derived formulas elucidate a complete classical approach to both the anomalous magnetic moment of the electron and the Lamb shift.

2 Zero-point energy associated with an extended electron

When an electron moves in the zero-point field, we mean that the center of mass moves with velocity $\mathbf{v}$. The particle motion then contains both internal rotational motion and the translational motion. Denoting the center of mass motion by a position vector $\mathbf{x}$ and the radius of internal rotation by a vector ξ, a complex vector connected with both internal and translational motions of an extended electron can be expressed by a complex vector $X = \mathbf{x} + \mathbf{i}\xi$, where $\mathbf{i}$ is a pseudoscalar representing an oriented volume in geometric algebra. A complete account of complex vector algebra was elaborately discussed in the reference [14].

In stochastic electrodynamics, the expression for the electric field vector of electromagnetic zero-point field can be written in the following form

$$\begin{aligned} E_{zp}(\mathbf{x},t) = Re\Bigg\{ \sum_{\lambda=1}^{2} \int d^3k\, \epsilon(\mathbf{k},\lambda)\, \frac{H(\omega)}{2} \times \\ \times \left[ae^{i(\mathbf{k}.\mathbf{x}-\omega t)} + a^*e^{-i(\mathbf{k}.\mathbf{x}-\omega t)}\right]\Bigg\}, \end{aligned} \tag{6}$$

where $\epsilon(\mathbf{k},\lambda)$ is the polarization vector which is a function of wave vector $\mathbf{k}$, polarization index $\lambda = 1, 2$ and $Re\{\}$ represents the real part. We define $a = e^{i\theta(\mathbf{k},\lambda)}$ and $a^* = e^{-i\theta(\mathbf{k},\lambda)}$ and the phase angle is introduced to generate random fluctuations of the zero-point field. The normalization constant in (6) is set equal to unity. The spectral function $H(\omega)$ represents the magnitude of zero-point energy and in stochastic electrodynamics its value is found to be $\left(\hbar\omega/8\pi^3\epsilon_0\right)^{1/2}$. In the complex vector formalism, we replace $\mathbf{x}$ by X in the electric field $E_{zp}(\mathbf{x},t)$ and expanding in terms of Taylor series yields

$$E_{zp}(X,t) = E_{zp}(\mathbf{x},t) + \mathbf{i}\xi \left.\frac{\partial E_{zp}(\mathbf{x},t)}{\partial x}\right|_{x\to 0} - \frac{\xi^2}{2}\left.\frac{\partial^2 E_{zp}(\mathbf{x},t)}{\partial x^2}\right|_{x\to 0} + O(\xi^3) + \ldots \tag{7}$$

Neglecting higher order terms and denoting

$$E_{zp}(\xi,t) = \xi \left.\frac{\partial E_{zp}(\mathbf{x},t)}{\partial x}\right|_{x\to 0}, \tag{8}$$

one can express the electric field vector in a complex form

$$E_{zp}(X,t) = E_{zp}(\mathbf{x},t) + \mathbf{i}E_{zp}(\xi,t)\,. \tag{9}$$

The random zero-point fluctuations influence both the center of mass and the center of charge and therefore the force acting on the extended particle can be decomposed into force acting on center of charge and force acting on center of mass. The equation of motion of center of mass is then expressed in the form

$$m\ddot{\mathbf{x}} - \Gamma_a m\dot{\mathbf{v}} + m\omega_0^2\mathbf{x} = eE_zp(\mathbf{x},t), \tag{10}$$

where $\mathbf{v} = \dot{\mathbf{x}}$, $\Gamma_a = 2e^2/3mc^3$ and an over dot represents differentiation with respect to time. The second and third terms on the left are radiation damping and binding terms. It should be noted that for the zero-point field acting on center of mass, both particle charge and mass appear at the center of mass point. On the other hand, for the field acting on the center of charge, the effective mass seen by the zero-point field is the potential equal to $e^2/2\xi \sim m_z c^2$, where m_z is the effective mass at the center of charge and the magnitude of ξ is of the order of the Compton wavelength. In this case both radiation damping and binding forces are absent and the equation of motion of center of charge can be written in the form

$$m_z\ddot{\xi} = eE_{zp}(\xi,t)\,. \tag{11}$$

The average zero-point energy of the electron in its rest frame was previously estimated and it had been shown to be equivalent to the zitterbewegung energy [15]. Further, it was shown that the particle mass arises from the internal complex rotations and a relation between particle spin and mass had been derived previously in the following form [13]:

$$mc^2 = \Omega_s \cdot S \tag{12}$$

In the above equation, S is the spin bivector, Ω_s is the angular frequency bivector and it shows that the mass of an electron is equal to the zero-point energy associated with the local complex rotation in the spin plane.

In the case of center of mass motion of the particle with velocity $\mathbf{v}$, as a result of super position of internal complex rotations on translational motion, the particle is associated with a modulated wave containing internal high frequency ω_0 and envelop frequency ω_B which is the de Broglie frequency of the particle. Differentiating the position complex vector $X = \mathbf{x} + \mathbf{i}\xi$ with respect to time gives the velocity complex vector $U = \mathbf{v} + \mathbf{iu}$ and the complex conjugate of U is obtained by taking reversion operation on it,$\bar{U} = \mathbf{v} - \mathbf{iu}$ and the product $U\bar{U} = v^2 + u^2$ [13]. Dividing this equation throughout by ξ^2 and denoting $\omega_B = |v|/\xi$, $\omega_0 = |u|/\xi$ and $\omega_c = |U|/\xi$, we obtain the effective cut-off frequency ω_c of the modulated wave in the particle frame of reference in the form $\omega_c^2 = \omega_0^2 + \omega_B^2 = \omega_0^2(1+\beta^2)$. In the equation of motion of center of mass (9), the strength of radiation damping and binding terms are much smaller than the force term on the right. Therefore, neglecting radiation damping and binding terms in (10) and integrating the expression with respect to time gives

$$\dot{\mathbf{x}} = \frac{e}{m}\int_0^{\tau} E_{zp}(\mathbf{x},t)\,dt, \tag{13}$$

where the upper limit of integration is chosen to be the characteristic time $\tau = 2\pi/\omega_c$. Substituting the electric field vector $E_{zp}(\mathbf{x},t)$ given in (6) into (13) and performing the integration gives

$$\dot{\mathbf{x}} = \frac{e}{m}\sum_{\lambda=1}^{2}\int d^3k\epsilon(\mathbf{k},\lambda)\frac{H(\omega)}{2} \times \left\{ae^{i\mathbf{k}.\mathbf{x}}\left(\frac{e^{-i\omega\tau}-1}{-i\omega}\right) + a^*e^{-i\mathbf{k}.\mathbf{x}}\left(\frac{e^{i\omega\tau}-1}{i\omega}\right)\right\}. \tag{14}$$

Now, using $|\dot{\mathbf{x}}|^2 = \dot{\mathbf{x}}\dot{\mathbf{x}}^*$, we find

$$|\dot{\mathbf{x}}|^2 = \frac{e^2}{m^2}\sum_{\lambda,\lambda'=1}^{2}\iint d^3kd^3k'\epsilon(\mathbf{k},\lambda)\epsilon(\mathbf{k}',\lambda')\frac{H^2(\omega)}{2\omega^2} \times(1-\cos\omega\tau)\left\{aa^{*\prime}e^{-i(\mathbf{k}-\mathbf{k}').\mathbf{x}} + a^*a'e^{i(\mathbf{k}-\mathbf{k}').\mathbf{x}}\right\}, \tag{15}$$

where the terms containing aa' and $a^*a^{*\prime}$ are dropped because of their stochastic averages are zero. Taking the stochastic average of (15) on both sides and using the following relations

$$\left\langle aa^{*\prime}e^{-(\mathbf{k}-\mathbf{k}').\mathbf{x}}\right\rangle = \langle a^*a'e^{+(\mathbf{k}-\mathbf{k}').\mathbf{x}}\rangle = \delta^3(k-k')\,\delta(\lambda-\lambda')\ ,$$

$$\left\langle \sum_{\lambda,\lambda'=1}^{2}\epsilon(\mathbf{k},\lambda)\epsilon(\mathbf{k},\lambda')\delta(\lambda-\lambda')\right\rangle = \left\langle\sum_{\lambda=1}^{2}|\epsilon(\mathbf{k},\lambda)|^2\right\rangle = 1-\frac{k_x^2}{k^2} = \frac{2}{3}\ ,$$

$$\int d^3k = \int d\Omega\, k^2dk = 4\pi\int k^2dk = \frac{4\pi}{c^3}\int\omega^2d\omega\ ,$$

the average value $\langle|\dot{\mathbf{x}}|^2\rangle$ is found to be

$$\langle|\dot{\mathbf{x}}|^2\rangle = \frac{4\alpha}{3\pi}\frac{\hbar^2}{m^2c^2}\int_0^{\omega_c}\omega(1-\cos\omega\tau)d\omega\,, \tag{16}$$

where the upper limit of integration is the chosen cut-off frequency ω_c. Because of this cut-off frequency, the zero-point field spectral components of wavelength of the order of $2\pi c/\omega_c$ are only effective and thus there exists an upper bound to the energy available from the electromagnetic zero-point field. For an extended particle of radius R, a convergence form factor can be obtained by finding the upper bound to the energy available from the electromagnetic zero-point field. A detailed calculation of such convergence form factor was calculated by Reuda [22]. This convergence form factor is given by

$$\eta(\omega) = \eta(\delta) = \frac{9}{\delta^4}\left(\frac{\sin\delta}{\delta}\right)^2\left(\frac{\sin\delta}{\delta} - \cos\delta\right)^2 , \tag{17}$$

where $\delta = \omega R/c$ and the values of $\eta(\delta)$ lie in the range 0 to 1. For $\omega \sim \omega_0$ and $R \sim 2\hbar/3mc$, we have $\delta \sim 2/3$ and the convergence form factor $\eta\,(2/3) \sim 3/4$. In view of the extended structure of the particle, the convergence form factor is introduced in the energy calculation. In general, the total energy of an oscillator is a sum of both kinetic and potential energies and it is equal to twice the kinetic energy. Now, the zero-point energy associated with the particle is expressed in the form

$$\begin{aligned}\Delta E_c = m\langle|\dot{\mathbf{x}}|^2\rangle &= \frac{2\alpha}{3\pi}\frac{\hbar^2\omega_c^2}{mc^2}\eta(\omega_c) \\ &\times\left[1 + \frac{2}{\omega_c^2\tau^2}(1 - \cos\omega_c\tau - \omega_c\tau\sin\omega_c\tau)\right] .\end{aligned} \tag{18}$$

Substituting $\omega_c\tau = 2\pi$, $\omega_c^2 = \omega_0^2(1+\beta^2)$, using the Einstein de Broglie relation $\hbar\omega_0 = mc^2$ and approximating $\eta(\omega_c) \sim 3/4$ in (18) gives finally

$$\Delta E_c = \frac{\alpha}{2\pi}\, mc^2(1+\beta^2)\,. \tag{19}$$

This energy change gives the correction to the mass, $\Delta m = \Delta E_c/c^2$ and we get the relation (4). The result in (19) differs from our previous calculation in reference [15] by the term $(1+\beta^2)$, where we have assumed $\omega_c = \omega_0$. It may be noted that the energy associated with the particle derived in (19) depends on the particle velocity. However, in the point particle limit, $R \to 0$, $\omega_c \to \omega_0$ and $\eta\,(\omega_0 R/c) \to 1$. Thus in the point particle limit the energy in (18) reduces to the expression (1). It may be noted that both mass correction and charge correction are derived from the common origin zero-point field.

3 Estimation of the anomalous magnetic moment

Dirac theory of the electron predicts the magnetic moment of the electron $g = 2$. However, a small deviation of magnetic moment $a_e = (g-2)/2$ is known as the anomalous magnetic moment and it was discovered by Kusch and Foley [23]. The quantization of electromagnetic field led to quantum electrodynamics and the first theoretical calculation of a_e in the purview of quantum electrodynamics was due to Schwinger [24] and it was estimated to be $a_e = \alpha/2\pi$. The quantum electrodynamics theoretical calculations of a_e almost over fifty years by several authors showed an excellent agreement between theory and experiment and an extensive review of a_e was given by Kinoshita [25]. High precession penning trap measurements of a_e were done by several authors and a recent measurement of a_e was given by Henneke *et al.* [26], $a_e(exp) = 1.15965218073(28)\times 10^{-3}$. In this section we shall explore an entirely different classical approach for the calculation of a_e.

Any change in the mass of the particle due to particle motion in the fluctuating zero-point field brings a change in the spin angular frequency in (12).

$$(m+\Delta m)c^2 = \Omega\cdot S\,. \tag{20}$$

Combining (12) and (20) gives the ratio

$$\frac{\Delta m}{m} = \left|\frac{\Omega - \Omega_s}{\Omega_s}\right| . \tag{21}$$

The ratio of change in spin frequency to the spin frequency represents the anomalous magnetic moment. In an alternative way, this can be arrived by considering the energy term $(ge\mathbf{B}/2mc)\cdot S$ and identifying m as the theoretical mass and replacing $m_{th} = m_{obs} - \Delta m$. To a first approximation we get $g/2\,(1+\Delta m/m)$ in place of $g/2$. Now, from (4) the anomalous magnetic moment of the electron can be expressed in the form

$$a_e = \frac{\Delta m}{m} = \frac{\alpha}{2\pi} + \frac{\alpha}{2\pi}\beta^2\,. \tag{22}$$

The first term on right of the above equation gives the well known Schwinger's result and to obtain this result we have chosen $\eta(\omega_c) \sim 3/4$ in (18). The velocity of an orbital electron in an atom is proportional to α. For a linear motion of the electron we approximate $\beta^2 = \alpha^2/3$ and to account for two modes of polarization of zero-point field, it is multiplied by 2. The reduced velocity is now written in the form $\beta^2 = 2\alpha^2/3$. Substituting this result in (22) and using charge correction relation $\alpha \to \alpha\,(1 - 2\alpha/3\pi)$ gives finally the anomalous magnetic moment of the electron as a function of fine-structure constant:

$$\begin{aligned}a_e = \frac{1}{2}\left(\frac{\alpha}{\pi}\right) - \frac{1}{3}\left(\frac{\alpha}{\pi}\right)^2 + \frac{\pi^2}{3}\left(\frac{\alpha}{\pi}\right)^3 - \frac{2\pi^2}{3}\left(\frac{\alpha}{\pi}\right)^4 + \\ + \frac{4\pi^2}{9}\left(\frac{\alpha}{\pi}\right)^5 - \frac{8\pi^2}{81}\left(\frac{\alpha}{\pi}\right)^6 .\end{aligned} \tag{23}$$

The calculation of a_e is performed using the CODATA recommended fine-structure constant $\alpha = 7.2973525376(50)\times 10^{-3}$ [27] and from (23) the value is estimated to be $a_e(th) = 1.15965227095\times 10^{-3}$. Though this classical estimate is not at par with the quantum electrodynamics calculations, the difference $a_e(th) - a_e(exp) = 90.22\times 10^{-12}$ shows the result is at least accurate up to ninth decimal place. With proper approximation to the reduced velocity, equation (22) may be used for finding the anomalous magnetic moment of any other lepton.

4 Lamb shift

Relativistic theory of a bound electron predicts that the energy levels $2S_{1/2}$ and $2P_{1/2}$ are degenerate. However, the energy level shift $2S_{1/2} - 2P_{1/2}$ was experimentally found to be 1058.27 + 1.0 MHz in 1947 by Lamb and Rutherford [28]. For the Lamb shift calculation, we consider the average deviation in the path of orbital electron is equal to twice the radius of rotation (diameter) of the extended electron. Thus the orbital radius spreads out over a distance 2ξ and the corresponding change in the Coulomb potential is expressed in the form $V(\mathbf{r} + 2\mathbf{i}\xi)$. Expanding this function in terms of Taylor series gives

$$V(\mathbf{r} + 2\mathbf{i}\xi) - V(\mathbf{r}) = 2\mathbf{i}\xi \,\frac{\partial V(\mathbf{r})}{\partial \mathbf{r}} - 2\xi^2 \left(\frac{\partial^2 V(\mathbf{r})}{\partial r^2}\right) + \ldots \quad (24)$$

In the Welton's approach of Lamb shift calculation [29], considering the symmetric potential, an additional multiplying factor 1/3 was introduced in the second term on right of (24). Since the deviation is considered as a bivector which represents rotation in local space, any such factor is not required in the present calculation. The radius of rotation is a vector in the spin plane and therefore, it can be expressed in the form $\xi = |\xi| \exp(-\mathbf{i}\sigma_s \omega_0 t)$, where $\mathbf{i}\sigma_s$ is a unit bivector in the spin plane [14]. Then, the stochastic average $\langle\xi\rangle = 0$ and the average of square of radius of rotation $\langle\xi^2\rangle = \langle|\xi|^2\rangle/2$. Using the relation $\dot{\xi} = -\mathbf{i}\sigma_s \omega_0 \xi$, we find $\langle|\xi^2|\rangle = \langle|\dot{\xi}|^2\rangle/\omega_0^2$. Now, taking the stochastic average on both sides of (24), we obtain the stochastic average of change in the potential energy:

$$\Delta E_L = \langle V(\mathbf{r} + 2\mathbf{i}\xi) - V(\mathbf{r})\rangle = \frac{\langle|\dot{\xi}^2|\rangle}{\omega_0^2} \left|\frac{\partial^2 V(\mathbf{r})}{\partial r^2}\right| \quad (25)$$

where the higher order terms are neglected. The energy in (25) corresponds to the Lamb shift in the energy levels due to the interaction of the electron with the zero-point field. We consider that the zero-point field around the atom is modified due to the extended electron in the orbit and as a consequence the electron orbit spreads out around the Coulomb source. Since the modifications in the zero-point field takes place at the atomic size, we choose the cut-off frequency equal to the de Broglie frequency ω_B. Such low frequency cut-off was not considered previously and this may be one of the reasons for not finding the exact estimate of the Lamb shift in stochastic electrodynamics. Considering the equation of motion of center of charge $\ddot{\xi} = eE_{zp}(\xi, t)/m$ and using the same method of derivation given in Section 3, and imposing the upper cut-off frequency ω_B, we obtain the zero-point energy associated with the orbital electron shift in the form

$$\begin{aligned} m\langle|\dot{\xi}|^2\rangle = {} & \frac{2\alpha}{3\pi} \frac{\hbar^2 \omega_B^2}{mc^2}\, \eta(\omega_B) \\ & \times \left[1 + \left\{\frac{2}{\omega_B^2 \tau^2} (1 - \cos\omega_B\tau + \omega_B\tau \sin\omega_B\tau)\right\}\right]. \end{aligned} \quad (26)$$

Since $\omega_B\tau \ll 1$,we neglect the terms in curly brackets and the converging form factor $\eta(\omega_B) = 1$. Now, (26) can be expressed in the form

$$\langle|\dot{\xi}|^2\rangle = \frac{2\alpha}{3\pi} \frac{\hbar^2 \omega_B^2}{m^2 c^2}\,. \quad (27)$$

Substituting this result in (25) and using the relation $\hbar\omega_0 = mc^2$ gives

$$\Delta E_L = \frac{2\alpha}{3\pi} \frac{\omega_B^2 c^2}{\omega_0^4} \left|\frac{\partial^2 V(\mathbf{r})}{\partial r^2}\right|. \quad (28)$$

For an orbital electron in a circular orbit, the magnitude of Coulomb potential is equal to twice the kinetic energy of the electron:

$$V(r) = \frac{Ze^2}{r} = m_r v^2 = m_r \omega_B^2 r^2\,. \quad (29)$$

Differentiating (29) twice with respect to r yields

$$\left|\frac{\partial^2 V(\mathbf{r})}{\partial r^2}\right| = m_r \omega_B^2\,. \quad (30)$$

Substituting the above result in (28) gives

$$\Delta E_L = \frac{4\alpha}{3\pi} \beta^4 m_r c^2\,. \quad (31)$$

Considering $\beta^2 = \alpha^2$, we finally arrive at the required energy shift given in (5). The charge correction of a free electron is given in (2) and in the case of an atomic electron it may be expected that it is three times that of the free electron. Then the correction for the fine-structure constant is $2\alpha/\pi$. Further, one may consider the mass correction of the reduced mass, same as $\alpha/2\pi$. Using these corrections in (5) and substituting the CODATA values of the electron mass, proton mass and other fundamental constants [27], the calculated Lamb shift in hydrogen spectra is found to be 1058.3696 MHz. Thus the present calculation is considerably in agreement with the standard value of Lamb shift 1057.8439 MHz [27] and the difference 0.5257 MHz may be attributed to the finite size of the proton.

In the quantum electrodynamics treatment, normally the expectation value of $|\nabla^2 V(r)|$ is found to be $\langle|\nabla^2 V(r)|\rangle \propto \alpha^4$ [30], the upper bound of integration is chosen to be ω_0 and the integration yields a logarithmic term. Comparing (5) with the Welton's result given by [31]

$$\Delta E_n = \frac{4\alpha^5}{3\pi} \frac{Z^4}{n^3} \ln\left(\frac{2}{16.55\alpha^2}\right) m_r c^2\,, \quad (32)$$

we get the correct order of fine-structure constant. The logarithmic term $\ln\left(2/16.55\alpha^2\right) \sim 8$ and one can approximate $\beta^4 = 8(Z\alpha)^4/n^3$. Then, if one wishes to include the principal quantum number, (5) may be rewritten in the form

$$\Delta E_L = \frac{4\alpha}{3\pi} \frac{8(Z\alpha)^4}{n^3} m_r c^2\,. \quad (33)$$

It may be noted that a complete relativistic quantum electrodynamics evaluation is free from high energy cut-off. However, the above calculation of Lamb shift is entirely different from the quantum electrodynamics treatment, where we consider radiative corrections, and the present calculation is purely based on classical considerations along with the extended structure of the electron.

5 Conclusions

Consideration of extended structure of the electron in zero-point field yields a classical, straightforward and simple approach to find mass and charge corrections. We find the mass correction depends on the particle velocity. The orbital electron reduced velocity is assumed to be proportional to the fine-structure constant. The anomalous magnetic moment of the electron has been expressed as a function of fine-structure constant and the estimated $a_e(th)$ value is found to be correct up to ninth decimal place. Using a low frequency cut-off equal to the de Broglie frequency, the Lamb shift of an extended electron in stochastic electrodynamics is derived and the estimated result deviates from the experimental value by 0.5257 MHz. The theory presented elucidates a classical approach to both anomalous magnetic moment of the electron and Lamb shift and paves the way for further research.

Received on August 13, 2018

References

1. Gabrielse G., Hanneke D., Kinoshita T., Nio M., Odom B. New Determination of the Fine Structure Constant from the Electron *g* Value and QED. *Phys. Rev Lett.*, 2006, v. 97, 030802.
2. Mathisson M. Neuemekhanikmaterietter system. *Acta. Phys. Pol.*, 1937, v. 6, 163–200.
3. Weyssenhoff J., Raabbe A. Relativistic dynamics of spin fluids and spin particles. *Acta. Phys. Pol.*, 1947, v. 9, 7.
4. Barut O. A., and Zanghi A. J. Classical model of the Dirac electron. *Phys. Rev. Lett.*, 1984, v. 52, 2009–2012.
5. Barut O. A., Bracken A. J. Zitterbewegung and the internal geometry of electron. *Phys. Rev. D*, 1981, v. 23, 2454.
6. Corben H. C. Classical and Quantum Theories of Spinning Particles. Holden and Day, New York, 1968.
7. Horvathy P. A. Mathisson's spinning electron: Non commutative mechanics and exotic Galilean symmetry 66 years ago. *Acta. Phys. Pol. B*, 2003, v. 34, 2611–2622.
8. Recami E., Salesi G. Kinematics and hydrodynamics of spinning particles. *Phys. Rev. A*, 1998, v. 57, 98–105.
9. Pavšič M, Recami E., Rodrigues W. A., Maccarrone G. D., Raciti F., Salesi G. Spin and electron structure. *Phys. Lett. B*, 1993, v. 318, 481.
10. Maruani J. The Dirac electron as a massless charge spinning at light speed: Implications on some basic physical concepts. *Prog. Theor. Chem. and Phys. B*, 2013, v. 27, 53–74.
11. Gouanère M., Spighel M., Cue N., Gaillard M. J., Genre R., Kirsch R., Poizat J. C., Remillieux J., Catillon P., Roussel L. Experimental observation compatible with the particle internal clock. *Annales de la Fondation Louis de Broglie*, 2005, v. 30, 109.
12. Hofer W. A. An extended model of electrons: experimental evidence from high-resolution scanning tunneling microscopy. *J. Phys. Conference Series*, 2012, v. 361, 012023.
13. Muralidhar K. Complex vector formalism of harmonic oscillator in geometric algebra: Particle mass, spin and dynamics in complex vector space. *Found. Phys.*, 2014, v. 44, 266–295.
14. Muralidhar K. Algebra of complex vectors and applications in electromagnetic theory and quantum mechanics. *Mathematics*, 2015, v. 3, 781–842.
15. Muralidhar K. Mass of a charged particle with complex structure in zerpoint field. *Progress in Physics*, 2016, v. 12, 224–230.
16. Muralidhar K. Theory of stochastic Schrödinger equation in complex vector space. *Found. Phys.*, 2017, v. 47, 532.
17. Muralidhar K. Classical approach to the quantum condition and biaxial spin connection to Schrödinger equation. *Quantum Stud.: Math. Found.*, 2016, v. 3, 31–39.
18. Puthoff H. E. Casimir Vacuum Energy and the Semiclassical Electron. *Int. J. Theor. Phys.*, 2007, v. 46, 3005–3008.
19. Boyer T. H. Random electrodynamics: The theory of classical electrodynamics with classical electromagnetic zeropoint radiation. *Phys. Rev. D*, 1975, v. 11, 790–808.
20. Boyer T. H. A brief survey of stochastic electrodynamics. In: Barut O. A., ed. Foundations of Radiation Theory and Quantum Electrodynamics. Springer Science + Bissinessmedia, New York, 1980, pp. 49–63.
21. Cavalleri G., Barbero F., Bertazzi G., Casaroni E., Tonni E., Bosi L., Spavieri G., Gillies G. T. A quantitative assessment of stochastic electrodynamics with spin (SEDS): Physical principles and novel applications. *Front. Phys. China*, 2010, v. 5, 107–122.
22. Rueda A. Behavior of classical particles immersed in electromagnetic zero-point field. *Phys. Rev. A*, v. 23, 2020.
23. Kusch P., Foley H. M. The Magnetic Moment of the Electron. *Phys. Rev.*, 1948, v. 74, 250.
24. Schwinger J. Collected Papers on Quantum Electrodynamics. Dover Publications Inc, New York, 1958.
25. Kinoshita T. Theory of the Anomalous Magnetic Moment of Electron – Numerical Approach. World Scientific, Singapore, 1990.
26. Henneke D., Fogwell S., Gabrielse G. New measurement of electron magnetic moment and the fine structure constant. *Phys. Rev. Lett.*, 2008, v. 100, 120801.
27. Mohr P. J., Taylor B. N., Newell D. B. CODATA recommended values of the fundamental physical constants: 2006. *Rev. Mod. Phys.*, 2008, v. 80, 633.
28. Lamb W. E. Jr., and Rutherford R. C. Fine structure of hydrogen atom by a microwave method. *Phys. Rev.*, 1947, v. 72, 241–243.
29. Welton T. A. Some observable effects of quantum mechanical fluctuations of electromagnetic field. *Phys. Rev.*, 1948, v. 74, 1157.
30. Milonni P. W. The Quantum Vacuum: An Introduction to Quantum Electrodynamics. Academic Press, San Diego, 1994, p. 410.
31. Schwabl F. Advanced Quantum Mechanics, Springer, New Delhi, 2005, p. 189.

On the Speed of Light and the Continuity of Physical Vacuum

Anatoly V. Belyakov

E-mail: belyakov.lih@gmail.com

It is shown that the speed of light can be calculated on the basis of the velocity equation of the waves propagating along a liquid surface. This gives a reason to believe that the vacuum medium, being discrete, simultaneously possesses the property of continuity like the surface of an ideal fluid.

The speed of light is one of a few fundamental values, which are not deducible from theory. However, it turns out that the propagation of light is similar to wave motion on a liquid surface, and *has a maximum, which is equal to the speed of light*. This maximum is determined on the basis of the well-known equation

$$v^2 = \frac{g\lambda}{2\pi} + \frac{2\pi\sigma}{\rho\lambda}\,, \tag{1}$$

where g is the acceleration, λ is the wavelength, σ is the surface tension (force-to-perimeter ratio, [N/m]), while ρ is the specific density. The first term means the influence of gravity on the wave speed, the second — the influence of surface tension.

Of course, various physical phenomena described by the same equations are not reducible to each other. Nevertheless, there must be something common between them. In this case, the common feature should be the *continuity of the medium* (physical vacuum). Thus, the physical vacuum, being discrete and being a source of virtual particles, at the same time also possesses the property inherent in the inviscid continuous medium surface through which electromagnetic oscillations propagate in the form of surface transverse waves!

In order to apply formula (1) and determine the parameters entering into it, it is necessary to isolate some unit element of the medium (a radiating cell), which they would apply to. In [1], when determining the critical vacuum density, it was shown that such an element can be a hydrogen atom as the most common element in the Universe.

From the point of view of John Wheeler's geometrodynamic concept, charged microparticles are singular points on a the three-dimensional surface of our world, connected by a "wormhole", i.e. a vortex tube or power current line (of the input-output kind) located in an additional dimension. As a result, a closed contour is formed along which the physical vacuum or some other medium circulates. The presence of contours (vortex tubes) is also postulated, for example, in [2], where the vacuum structure is considered as a network of one-dimensional flow tubes (knotted/linked flux tubes) and it is claimed that it is such a network that provides the spatial three-dimensionality of the Universe. Such a tube or a vacuum unit can be regarded as a field unit, in contrast to an atom — a matter unit [3].

Geometrodynamics in the mechanistic interpretation does not introduce any additional entities. On the contrary, it reduces them. So, from the dimensions set, Coulomb is eliminated: it is replaced by the ultimate momentum of the electron $m_e c$ [4]. In this case, the vortex tube is characterized by the electric constant and magnetic constant ε_0 and μ_0, where the electric constant becomes linear density of the vortex tube, and the reciprocal of the magnetic constant is the centrifugal force produced by rotation of a vortex tube element with the light velocity c along the electron radius r_e. It is also the force acting between elementary charges at a distance r_e:

$$\varepsilon_0 = m_e/r_e\,, \tag{2}$$

$$\mu_0 = \frac{1}{c^2\varepsilon_0} = \frac{r_e}{m_e c^2}\,. \tag{3}$$

It is assumed that the medium circulating along a contour with a radius R in the same time rotates spirally inside it, so that the contour (toroid) contains z structurally ordered units (in this case — the waves or photons). The speed of circulation and rotation is:

$$v = \frac{c\,c_0^{1/3}}{a^2 n^2}\,, \tag{4}$$

where c_0 is the dimensionless speed of light c/[m/sec], a is the inverse fine structure constant, and n is the main quantum number. In this interpretation for the single element (hydrogen atom) accepted, there is only g — the centrifugal acceleration appearing when the medium moves along the contour, i.e. square of the velocity-to-the radius of the spiral rotation ratio:

$$g = \frac{v^2}{R/z} = \frac{z c^2 c_0^{2/3}}{a^4 n^4 R}\,, \tag{5}$$

where

$$R = n^2 R_B = n^2 a^2 r_e\,, \tag{6}$$

where R_B is the Bohr radius.

The surface tension of a unit cell [N/m], using the force $1/\mu_0$ (there is no other force there), is represented as:

$$\sigma = \frac{1/\mu_0}{R} = \frac{m_e c^2}{r_e R}\,, \tag{7}$$

and the hydrogen atom density for an arbitrary n is:

$$\rho_H = \frac{m_p m_e}{R^3}\,, \tag{8}$$

where m_p is the proton relative mass in units of m_e. The wavelength is defined for the case of ionization:

$$\lambda = \frac{n^2}{R_\infty}, \tag{9}$$

where R_∞ is the Rydberg constant. As a result, assuming the speed of light to be unknown, replacing c by v and bearing in mind the above formulas, (1) can be represented as:

$$v^2 = \frac{z\, v^2 v_0^{2/3}}{2\pi a^4 n^4 R_B R_\infty} + \frac{2\pi a^2 n^2 R_B R_\infty v^2}{m_p}. \tag{10}$$

Making the transformations and bearing in mind that $R_B R_\infty = 1/(4\pi a)$, we obtain from (10):

$$v_0^{2/3} = \left(1 - \frac{an^2}{2m_p}\right)\frac{a^3 n^4}{2z}, \tag{11}$$

when differentiating (11) with respect to n, the value of n for the maximum velocity is found:

$$n_m = \sqrt{\frac{4m_p}{3a}} = 4.23. \tag{12}$$

It is noteworthy that the radiation wavelength during ionization, i.e. at the transition $n_m \leftarrow \infty$, corresponds to the temperature of blackbody radiation 1840°K, which is close to the temperatures of the red and brown dwarfs — the most common bodies in the Universe.

Further, replacing n^2 in formula (11) with the value n_m^2, from (11) the maximum of the velocity is determined by:

$$v_m = \left(\frac{a^3 n^4}{6\,z}\right)^{3/2} \times [\text{m/sec}] = 2.81 \times 10^8 \left(\frac{n^4}{z}\right)^{3/2} \times [\text{m/sec}]. \tag{13}$$

In [4], we give additional relations connecting the parameters v_0, z, n, and also the sine of the projection angle (the cosine of the Weinberg angle), which follow from that n^4/z does not depend on n and this value is slightly more than one. As a result, we obtained the value of v, which is very close to the speed of light and is determined only by the fine structure constant and velocity dimensionality as well as the Weinberg angle cosine. The last calculations as not having fundamental importance are not given here.

The obtained solution can be considered as a special case of the wave velocity maximum. However, unlike a liquid where the surface wave velocity has a minimum and these capillary and gravitational waves velocity depends on the surface tension and the basin depth, there is a natural mechanism for electromagnetic waves ensuring the independence of their speed from the wavelength. This follows even from the above formulas, which have a model-simplified character.

Indeed for this, it is necessary that there in formula (11) the ratio n^2/m_p remains constant. Since the wavelength is proportional to n^2, then, with increasing the interval between waves, the mass of the medium in a given interval must grow proportionally, which means that the medium remains homogeneous in the direction of wave propagation. This is true, because equation (1) is based on the law of a simple one-dimensional oscillation of a pendulum. Perhaps, someday, a more accurate equation for the general case made in electrodynamics terms will be deduced.

It should be noted that the fundamental difference between long-wave radiations and particle-like X-rays (gamma radiations) is associated with their different nature: the first is due to the medium surface tension, while the second is due to the medium acceleration in the radiating cell of the contour.

Thus, the physical vacuum as a medium is discrete at a certain level, and its unit is a vortex tube (the field unit). At the same time, it is capable of being infinitely densely filled with such units forming a continuous surface (the possibility of this was proved in the 19th century by J. Peano [5]). This surface, in turn, as it becomes more complex, can form three-dimensional material objects. When driving in such a continuous medium body does not feel any resistance up to the speed of light, i.e., until a surface wave forms, and, for the observer, the vacuum medium remains undetectable. Recall that even when moving in a real liquid body, an observer does not feel a resistance up to the speed when a surface wave is formed (for water, the speed is 0.3 … 0.5 m/sec).

Conclusion

The fact that the vacuum manifests properties of a continuous surface while electromagnetic waves propagate in the form of surface waves gives grounds to combine the light speed constancy with its wave nature and with the physical vacuum as a transmitting medium (and, at the same time, we can remain within the framework of Newtonian space and time). For this it is sufficient to accept the postulate that *an observer is always at rest with respect to the vacuum medium, and a source always moves with respect to it and, accordingly, with respect to the observer*. Thus, the passive element (an observer) does not detect the vacuum medium, but at the same time he receives an evidence of its existence as a continuous medium, namely — a change in the radiation wavelength (the Doppler effect) due to the motion of the active element (source).

Received on August 28, 2018

References

1. Belyakov A.V. On the independent determination of the ultimate density of physical vacuum. *Progress in Physics*, 2011, v.7, issue 2, 27–29.
2. Berera A., Buniy R. V., Kephart T. W., Päs H., and Rosa J. G. Knotty inflation and the dimensionality of spacetime. arXiv: 1508.01458.
3. Belyakov A.V. On Materiality and Dimensionality of the Space. *Progress in Physics*, 2014, v.10, issue 4, 203–206.
4. Belyakov A.V. Charge of the electron, and the constants of radiation according to J. A. Wheeler's geometrodynamic model. *Progress in Physics*, 2010, v.6, issue 4, 90–94.
5. Peano G. Sur une courbe, qui remplit toute une aire plane. *Mathematische Annalen*, 1890, v.36, issue 1, 157–160.

Unfalsifiable Conjectures in Mathematics

Craig Alan Feinstein
2712 Willow Glen Drive, Baltimore, Maryland 21209, USA
E-mail: cafeinst@msn.com

It is generally accepted among scientists that an unfalsifiable theory, a theory which can never conceivably be proven false, can never have any use in science. In this paper, we shall address the question, "Can an unfalsifiable conjecture ever have any use in mathematics?"

1 Introduction

It is generally accepted among scientists that an unfalsifiable theory, a theory which can never conceivably be proven false, can never have any use in science. As the philosopher Karl Popper said, "the criterion of the scientific status of a theory is its falsifiability, or refutability, or testability" [4]. In this paper, we shall address the question, "Can an unfalsifiable conjecture ever have any use in mathematics?" First, we shall present a famous mathematical conjecture and prove that it is unfalsifiable. Next, we shall discuss the implications of proving that a mathematical conjecture is unfalsifiable. And finally, we shall present some open problems.

2 An unfalsifiable conjecture

Landau's fourth problem is to prove that there are an infinite number of prime numbers of the form n^2+1, where $n \in \mathbb{N}$ [6]. We shall call this conjecture the $n^2 + 1$-Conjecture. And we shall prove that the n^2+1-Conjecture is unfalsifiable, i.e., that its negation is unprovable in any reasonable axiom system:

Theorem: The $(n^2 + 1)$-Conjecture is unfalsifiable.

Proof: Suppose there exists a proof that there are only a finite number of primes of the form $n^2 + 1$. Then there would exist an $N \in \mathbb{N}$ such that for any $n \in \mathbb{N}$ in which $n > N$, $n^2 + 1$ would be composite; thus, one could deduce that $n^2 + 1$ is composite from only the assumption that $n - N \in \mathbb{N}$. But this is impossible, since the polynomial $n^2 + 1$ is irreducible over the integers. Hence, it is impossible to prove that there are only a finite number of primes of the form $n^2 + 1$. So the $n^2 + 1$-conjecture is unfalsifiable. □

3 Implications

Let us assume that the ZFC axioms are consistent [10]. Then what are the implications of proving that a mathematical conjecture is unfalsifiable? The answer is that even though an unfalsifiable conjecture might not be true, there is still no harm in assuming that it is true, since there is no chance that one could derive any provably false statements from it; if one could derive any provably false statements from an unfalsifiable conjecture, this would imply that the conjecture is falsifiable, which is a contradiction.

For example, there is a probabilistic heuristic argument that the $n^2 + 1$-Conjecture is true [3]. This implies that all statements which can be derived from the $n^2 + 1$-Conjecture are almost certainly true. Since our theorem above says that the $n^2 + 1$-Conjecture is unfalsifiable, there is no chance that any of these statements could be proven false.

As a different type of example, in 2006 the author showed that the Riemann Hypothesis is unprovable in any reasonable axiom system [1]. This implies that the negation of the Riemann Hypothesis is unfalsifiable, so one might conjecture that the Riemann Hypothesis is false. However, there is a probabilistic heuristic argument that the Riemann Hypothesis is true [2]; therefore, if one were to assume that the Riemann Hypothesis is false, one could derive statements which are almost certainly false from this assumption. However, these statements could never be proven false, since the negation of the Riemann Hypothesis is unfalsifiable.

4 Open problems

Can the following famous conjectures also be proven to be unfalsifiable?

1. There are an infinite number of pairs of primes which differ by two. These are called twin primes [9].
2. There are an infinite number of primes of the form $2^p - 1$, where p is also prime. These are called Mersenne primes [7].
3. There are an infinite number of primes p, where $2p + 1$ is also prime. These are called Sophie Germain primes [8].
4. There are an infinite number of primes of the form $2^{2^n} + 1$. These are called Fermat primes [5].

5 Conclusion

An unfalsifiable theory can never have any use in science; however, an unfalsifiable conjecture can be very useful in mathematics: When an unfalsifiable conjecture is difficult to prove, one can assume that the conjecture is true and not have to worry about deriving any provably false statements from it, assuming that the ZFC axioms are consistent.

Acknowledgements

The author would like to thank Florentin Smarandache for his very helpful comments.

Received on September 6, 2018

References

1. Feinstein C.A. Complexity science for simpletons. *Progress in Physics*, 2006, issue 3, 35–42.
2. Good I.J. and Churchhouse R.F. The Riemann hypothesis and pseudorandom features of the Möbius Sequence". *Math. Comp.*, 1968, v.22, 857–861.
3. Hardy G.H. and Littlewood J.E. Some problems of "Partitio Numerorum". III. On the expression of a number as a sum of primes. *Acta Math.*, 1923, v.44, 1–70.
4. Popper K. Conjectures and Refutations: The Growth of Scientific Knowledge. London, Routledge, 1963.
5. Fermat Prime. From *MathWorld — A Wolfram Web Resource*. http://mathworld.wolfram.com/FermatPrime.html
6. Landau's Problems. From *MathWorld — A Wolfram Web Resource*. http://mathworld.wolfram.com/LandausProblems.html
7. Mersenne Prime. From *MathWorld — A Wolfram Web Resource*. http://mathworld.wolfram.com/MersennePrime.html
8. Sophie Germain Prime. From *MathWorld — A Wolfram Web Resource*. http://mathworld.wolfram.com/SophieGermainPrime.html
9. Twin Prime Conjecture. From *MathWorld — A Wolfram Web Resource*. http://mathworld.wolfram.com/TwinPrimeConjecture.html
10. Zermelo-Fraenkel Axioms. From *MathWorld — A Wolfram Web Resource*. http://mathworld.wolfram.com/Zermelo-FraenkelAxioms.html

The Helicon: A New Preon Model

Oliver Consa
Department of Physics and Nuclear Engineering, Universitat Politècnica de Catalunya
Campus Nord, C. Jordi Girona, 1-3, 08034 Barcelona, Spain
E-mail: oliver.consa@gmail.com

A new preon model is presented as an extension of the semiclassical Helical Solenoid Electron Model that was previously proposed by the author. This helicon model assumes as postulates both the Atomic Principle and the equality between matter and electric charge. These postulates lead us to a radical reinterpretation of the concepts of antimatter and dark matter and form a new framework for future preon theories.

1 Introduction

According to the Atomic Principle, "matter is composed of indivisible, indestructible and immutable elementary particles." This principle has guided the greatest successes in the history of science [2]. However, the currently-accepted Standard Model of Particle Physics (SM) does not comply with this principle since most of this model's elementary particles are unstable, and all of them can be created or destroyed by matter-antimatter interactions. In concurrence with Kalman [3], we consider the current state of particle physics to be anomalous. We propose that the Atomic Principle is an unrenounceable postulate. Any fundamental theory of elementary particles should strictly respect this principle. If necessary, we should reinterpret the experimental results and discard any theory that does not strictly comply with the Atomic Principle.

The large number of elementary particles described by the SM and the regularities of their properties suggest that there is a lower level of matter organization. In 1974, Pati and Salam [11] proposed that both leptons and quarks were composite particles formed by fundamental particles called preons. To date, no preon model has attracted the general interest of the particle physics community. However, preon models have continued to evolve with new proposals, including those by Terazawa (1977) [12], Harari (the Rishon Model, 1979) [13], Mandelbaum (the Haplon Model, 1981) [14], Dehmelt (the Cosmon Model, 1989) [15], Kalman and d'Souza (the Primon Model, 1992) [17], Dunge and Fredriksson (1997) [16], Bilson-Thompson (the Helon Model, 2005) [18], Yershov (the Y-particle Model, 2006) [19] and Lucas (the Intertwining Charged Fibers Model, 2006) [20].

The objective of this paper is to propose a new preon model as an extension of the Helical Solenoid Model of the electron [1] that is applicable to any subatomic particle and that strictly complies with the Atomic Principle. The Helicoidal Solenoid Model is a semiclassical model that proposes that the electron is a point-like electric charge that moves at the speed of light following a helical solenoid trajectory with an angular momentum equal to the reduced Planck constant. This model assumes that the Zitterbewegung is the mechanism that causes the helical movement of the electron (spin) and its corresponding magnetic moment.

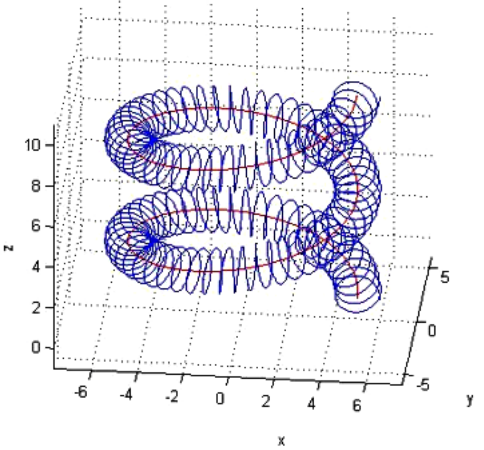

Fig. 1: Trajectory of the electron in the Helical Solenoid Model.

2 Nuclear Forces

The main challenge for preon theories is to explain the force that holds the preons together. Quantum Chromodynamics (QCD) defines a strong nuclear force based on the existence of gluons, but this theory is incompatible with the preon hypothesis. To date, it has not been possible to identify an extension of the QCD theoretical basis that would allow for the incorporation of a substructure common to both leptons and quarks. In addition, all attempts to expand the QCD theory involve an exponential increase in mathematical complexity, the opposite of what is intended with preon theories. Therefore, a preon theory that is compatible with the Atomic Principle will be, predictably, incompatible with QCD.

We are not bothered by this incompatibility because we start from a semiclassical Helical Solenoid Model that is incompatible in fundamental aspects with many of the modern dominant theories (Quantum Mechanics (QM), Quantum Electrodynamics (QED) and Quantum Chromodynamics (QCD)). This is not an insurmountable problem since it is well known that mutually incompatible theories can explain the same experimental results and, in certain cases, may even be useful. For example, the Bohr-Sommerfeld model was surpassed by QM but, nevertheless, produces the same results for the fine structure of the hydrogen atom.

In 1986, Barut [4] proposed that nuclear forces are manifestations of electromagnetic forces at very short distances. While electric fields decrease with the square of the distance, magnetic fields decrease with the cube of the distance. Magnetic forces are dominant over very small distances, but their influence decreases rapidly with respect to electrical forces as distances expand

$$F_{mag} \propto \frac{1}{R^3} \,, \tag{1}$$

$$F_{elec} \propto \frac{1}{R^2} \,. \tag{2}$$

This hypothesis is shared by Pati [5], the creator of the first preon theory, and by other lesser-known researchers such as Schaeffer [6], Dallacasa [7], Cook [8], Kaliambos [9], Kanarev [10] and Lucas [20].

Historically, it has been assumed that magnetic forces at the subatomic level are negligible, but in our Helical Solenoid Model, the magnetic field density at the center of the nucleon is enormous, about 100 trillion tesla. This magnetic field density is thousands of times greater than that of a neutron star. A magnetic field of these proportions must necessarily produce significant effects

$$R = \lambda\!\!\!^{-}_N = \frac{\hbar}{m_N c} = 2.103 \times 10^{-16} \text{ m}, \tag{3}$$

$$f = \frac{v_r}{2\pi R} = \frac{c}{2\pi \lambda\!\!\!^{-}_N} = 2.268 \times 10^{23} \text{ Hz}, \tag{4}$$

$$B = \frac{\mu_0 I}{2R} = \frac{\mu_0 e f}{2\lambda\!\!\!^{-}_N} = 1.088 \times 10^{14} \text{ T}. \tag{5}$$

In our preon model, we do not contemplate the existence of particles that mediate nuclear forces, such as gluons. Instead, we assume that elementary particles interact with each other through their respective electromagnetic fields. While it is outside the present work to explain the physical nature of photons, we conclude that photons (i) are not particles of matter, (ii) are not composed of preons and (iii) do not have to comply with the Atomic Principle. Therefore, photons can be created (by emission) and destroyed (by absorption) without any limitations. Many theories have tried to explain the photon as the union of an electron and a positron, however, all the experiments conducted to date are consistent with the idea that a photon transports electromagnetic energy but does not carry any type of electrical or magnetic charge.

3 Topology

The SM assumes that fermions are point particles and that it is impossible for a point particle to be formed by other point subparticles. For this reason, the more advanced preon models, such as those proposed by Bilson-Thompson [18], Yershov [19] and Lucas [20], describe preons and fermions as structures with a determined topology. In most cases, the proposed topology is toroidal or helical. This topology is suggested by the helical and chiral properties of the subatomic particles. The helical topology allows the composite particles to establish different structures that can be analyzed using knot theory (e.g., Rañada [21]) or braid theory (e.g., Bilson-Thompson [18]). The different combinations would give rise to the various symmetries of the subatomic particles, such as the conservation of the color charge.

The experimental data obtained in particle colliders suggest that fermions are point particles, so we need a model that can combine both point and helical topologies. Our Helical Solenoid Model [1] proposes a dynamic point-particle model, in which a point particle always moves at the speed of light in a closed path. This allows the advantages of the point particle to be combined with helical topology (which corresponds to the particle's trajectory).

In the Helical Solenoid Model, several point particles can form a single helical structure. For example, several particles could share the same closed trajectory in an equidistant fashion or they could share the trajectory in the same plane but with different radii. Finally, Lucas's Intertwining Charged Fibers Model [20] illustrates graphically how several helical paths could interlink with each other, giving rise to different subatomic particles.

4 Matter

In classical physics, matter is any substance that has mass and volume (i.e., that occupies space). This definition is valid for all matter composed of atoms, but when we analyze the subatomic particles that make up the atoms, this definition loses its meaning. In the SM, mass is considered only one form of energy, and the subatomic particles are considered quantum entities that do not have a definite volume or size. In this framework, matter no longer has a precise definition nor is it considered a fundamental concept.

But, to apply the Atomic Principle, matter must have a precise definition and be considered a fundamental concept. To define the concept of matter, we need to identify a fundamental property that strictly complies with three requirements: it must be absolute (the amount of matter cannot depend on the observer or the reference system), conserved (the amount of matter must be retained in any iteration) and quantified (the amount of matter must be composed of whole units).

Mass is an indicator of the kinetic energy and electromagnetic potential associated with the internal structure of each subatomic particle. But, as a property of matter, mass does not meet any of the three requirements. Only one property of matter satisfies the test, the electric charge. Therefore, we propose a new postulate: Electric charge is the fundamental property of matter.

All matter is composed of unitary electric charges. Phrased in a different manner, matter is everything that is composed of electric charges. Consequently, our second postulate is that matter and electric charge represent exactly the same thing. This postulate has important implications. It implies that all neutral particles must necessarily be composite particles of an equal number of negative and positive electric charge particles. Combining this postulate with the Atomic Principle, we conclude that all subatomic particles must be composed of a whole number of fundamental electric charges.

We also assume the validity of the minimalist hypothesis that postulates that all matter is composed of only two fundamental particles, the positive fundamental electric charge and the negative fundamental electric charge. In our model, we call these elementary particles helicons (H^+ and H^-), to differentiate them from those discussed in other preon models and to emphasize the relationship of this elementary particle with the Helical Solenoid Model. The three preon models that we consider the most advanced (Bilson-Thompson, Yershov and Lucas) concur with this minimalist hypothesis of only two fundamental particles.

All the preon models we have analyzed treat the mass of subatomic particles as an additive property. The greater the number of components in each subatomic particle and the more complex its internal structure, the greater the particle's mass. These models all group elementary particles into several sublevels of organization, forming increasingly complex structures. These models also assume that hadrons have a much more complex structure than leptons. The exact composition of each subatomic particle depends on the proposed preon model. We do not propose any particular organization scheme for subatomic particles; their composition should explain the value of the masses of each subatomic particle and explain all known modes of decay.

5 Antimatter

The concept of antimatter originated in 1898 when Schuster [22] speculated that there were particles with negative gravitational mass. Since antimatter would have negative gravity, antimatter would have a propensity to join together and separate from the matter of positive masses. Over time, antimatter would separate from matter, forming atoms, molecules or even stars and entire galaxies of antimatter. The difficulty occurs in the analysis of negative inertial mass. Negative inertial mass is a strange concept in physics; it causes serious problems and contradictions with the principles of conservation of energy and movement. For example, according to these theories, the more a particle of negative inertial mass accelerates, the more energy is created. In 1905, Einstein demonstrated that mass is only an expression of a particle's energy, implying that negative mass would be equivalent to negative energy.

In 1928, Dirac presented his electron equation, a relativistic half-integer spin version of the Schrodinger Equation, that correctly predicted the value of the electron's magnetic moment and the fine structure of the hydrogen atom. The Dirac Equation elegantly solved the main problems plaguing QM at that time. However, the Dirac Equation created new problems, since it predicted quantum electron states with negative energy. To resolve these issues, Dirac proposed the extravagant "sea of Dirac," where empty space would be formed by an infinite sea of negative energy particles that would occupy all the negative energy quantum states. In 1930, Dirac [23] proposed that there could be "gaps" in this "sea" of negative energy states. These "gaps" would be observed as a particle of positive energy with a positive charge, otherwise known as protons.

Oppenheimer [24] criticized Dirac's proton hypothesis. The positively charged particle predicted by Dirac could not be the proton since it would have the same mass as the electron; they would then annihilate each other upon contact, making the hydrogen atom unstable. Coincidentally, in 1932, while analyzing traces of cosmic rays in a cloud chamber, Anderson identified a particle with a positive electric charge and a mass identical to the mass of the electron that he called a positron. The positron corresponded with the particle predicted by Dirac, confirming the validity of his equation. In 1933, he was awarded the Nobel Prize for the discovery of antimatter.

However, there are many inconsistencies in antimatter theory that have been overlooked. According to Schuster, by definition, antimatter would have a negative mass, which does not happen with the positron. In addition, Dirac's antimatter is a consequence of his "sea of Dirac" theory, an implausible hypothesis that has been ruled out by modern physics. In reality, the current concept of antimatter is the result of a temporal coincidence between Dirac's hypothesis and Anderson's experiments, combined with a factual misinterpretation.

If we set aside the Dirac hypothesis and analyze the positron identified in Anderson's experiments, we find an unstable particle that is identical to the electron but with a positive charge. When a positron comes into contact with an electron, a large amount of energy is emitted, and neither the electron nor the positron presence is longer detected. The currently accepted explanation for this phenomenon is that there is a mutual annihilation of the positron with the electron, but this explanation is not supported by theory or experience. The annihilation theory is only applicable to particles with negative mass, but both the electron and the positron have positive masses. However, if we rely on experience, when a positive electric particle joins a negative electric particle, the result is a neutral electric particle (and radiation emission). There is a similar occurrence when an anion is attached to a cation, forming a neutral molecule, or when an electron is attached to a proton, forming a hydrogen atom.

Instead of mutual annihilation, a more logical explanation of the matter-antimatter interaction is the creation of neutral matter. This alternative explanation complies with the principles of conservation of electric charge and conservation of matter. According to our postulates, the electric charge is neither created nor destroyed, so the result of the electron-positron interaction must be the creation of one or several neutral particles that are currently unknown. Symmetrically, the creation of an electron-positron pair from energy would also not be possible. Instead, one or more of these unknown neutral particles would need to intervene, in addition to the necessary energy. Therefore, we should not call these processes of creation or annihilation of matter but of decomposition and aggregation of matter.

According to our interpretation, antimatter is characterized by having a topology that is symmetric to the topology of matter. Due to this symmetry, when particles of matter and antimatter come into contact, they have a strong tendency to decompose and reorder, producing simpler neutral particles. However, there is an asymmetry in the universe by which negative helicons tend to organize into simple subatomic structures (electrons), while positive helicons tend to organize into complex subatomic structures (protons and neutrons). This asymmetry in helicon grouping tendencies means that some structures are more common (electrons, protons and neutrons), while other structures form less frequently and decompose rapidly (antimatter). This asymmetry can be explained by assuming that the positive helicon is not exactly symmetric to the negative helicon, but that there is a slight asymmetry in some property of the helicon that causes this predisposition for different grouping tendencies.

The three preon models that we consider the most advanced (Bilson-Thompson, Yershov and Lucas) agree that antimatter is formed by positive and negative preons, in the same fashion as matter, and they reject the possibility of antipreons. Our interpretation of the matter-antimatter interaction is also consistent with Lucas's Intertwining Charged Fibers Model.

6 Dark Matter

Continuing with our minimalist hypothesis, a positive helicon bound to a negative helicon would result in a neutral particle ($H^o = H^+ + H^-$). This neutral particle would be the simplest possible composite particle; therefore, it should be the most abundant stable particle in the universe. The rest of the particles should be produced with a much lower probability. What we currently consider to be empty space would actually be space that is full of neutral particles. The hypothesis of an empty space full of neutral particles is not unusual for physics. Most of the matter in the universe is currently considered to be dark matter that does not correspond to known matter. The electromagnetic properties of this quantum vacuum could also be caused by a sea of neutral particles. We propose the term etheron for the neutral particle that is formed by the binding of a positive helicon to a negative helicon, to emphasize that the etherons form a sea that covers the entire universe, like the old concept of ether. In this case, the sea of etherons is not a fluid of a substance that is different from matter but a sea of neutral particles of ordinary matter.

An indirect consequence of the Sea of Etherons Hypothesis is the recovery of the Principle of Causality or Laplace's Principle of Causal Determinism, according to which every effect has a cause. According to this theory, apparently random processes, such as the disintegration of atomic nuclei or the decay of subatomic particles, are not in reality random processes but are instead determined by collisions with particles from the sea of etherons. Etherons have mass, so their spatial distribution should not be homogeneous. This allows us to establish the first experimentally testable hypothesis of this model: the average lifetime of atoms and subatomic particles must be different in different parts of the universe.

And there is experimental evidence: unexpected and unexplained fluctuations in the decay rates of ^{32}Si and ^{226}Ra have been reported and evidence of correlations between nuclear decay rates and Earth-Sun distance has been found (Jenkins-Fishbach effect [25]).

7 Conclusions

We are convinced of the validity of the Helical Solenoid Model's applicability to the electron, and we believe that this model can be extended to all subatomic particles. We must dispense with the mathematical and conceptual complexities of the SM and the theories that support it (QM, QED and QCD).

As a basis for our preon model, we postulate that the Atomic Principle should be strictly followed and that the fundamental property of matter is the electric charge. From there, we assume the minimalist hypothesis of only two fundamental particles, the negative helicon (H^-) and the positive helicon (H^+). These two point-like particles always move at the speed of light following a helical movement. When several helicons are combined, they form a subatomic particle. There is an asymmetry between the negative helicon and the positive helicon that leads to a propensity of the negative helicons to organize into simple structures (electrons), while the positive helicons tend to organize into complex structures (protons and neutrons). This asymmetry causes opposing structures to be generated with much less probability, as these structures are easily disorganized upon contact with a symmetric structure (matter-antimatter iteration). The union of a negative helicon and a positive helicon forms an etheron, the simplest and most abundant stable particle in the universe. What we know as empty space is actually replete with these neutral particles, forming a sea of etherons. Collisions of particles of matter with particles from the sea of etherons are the cause of many phenomena that are considered random, including:

- Spontaneous disintegration of atomic nuclei;

- Spontaneous disintegration of subatomic particles;
- Antimatter interactions;
- Gravitational dark matter; and
- Quantum effects of vacuum, as the Casimir effect.

Since etherons have mass, their distribution in the universe is not perfectly homogeneous. This allows us to make an experimentally verifiable prediction: the average lifetimes of atomic particles and atomic nuclei must be different in different parts of the universe. Experimental evidence has been reported in this matter [25].

This proposed preon model based on the helicon is not complete since the composition of each subatomic particle is not indicated, nor is the calculation of its masses or its modes of decay. Our main objective was to provide a framework based on new principles and a radical reinterpretation of the facts. We leave for other researchers the job of proposing a complete preon theory based on this framework, highlighting three preon models (Bilson-Thompson, Yershov and Lucas) that we believe are close enough to achieve this target and that can serve as inspiration for others.

Submitted on September 21, 2018

References

1. Consa O. Helical solenoid model of the electron. *Progress in Physics*, 2018. v. 14(2), 80–89.
2. Feynman R. The Feynman Lectures on Physics. 1964 volume I; lecture 1, “Atoms in Motion"; section 1–2, “Matter is made of atoms"; p. 1–2. *If, in some cataclysm, all of scientific knowledge were to be destroyed, and only one sentence passed on to the next generations of creatures, what statement would contain the most information in the fewest words? I believe it is the atomic hypothesis.*
3. Kalman C.S. Why quarks cannot be fundamental particles. *Nuclear Physics B: Proceedings Supplements*, 2005, v. 142, 235–237.
4. Barut A.O. Unification based on electromagnetism. A simple composite model of particles. *Annalen der Physik*, 1986, v. 498(1–2), 83–92.
5. Pati J.C. Magnetism as the origin of preon binding. *Physics Letters B*, 1981 ,v. 98(1-2), 40–44.
6. Schaeffer B. Electromagnetic theory of the nuclear interaction. *World Journal of Nuclear Science and Technology*, 2016, v. 6, 199–205
7. Cook N.D., Dallacasa V. Models of the Atomic Nucleus. 2nd Edition, Springer, Berlin, 2010.
8. Cook N.D., Dallacasa V. LENR and nuclear structure theory. *J. Condensed Matter Nucl. Sci.*, 2014, v,13, 68–79.
9. Kaliambos, L.A. Nuclear structure is governed by the fundamental laws of electromagnetism. *Indian Journal of Theoretical Physics*, 2003, v. 51(1), 1–37.
10. Kanarev M., Models of the atomic nuclei. *Journal of Theoretics*, 2002, v. 4, 1–7.
11. Pati J.C., Salam A. Lepton number as the fourth “color". *Physical Review D*, 1974, v. 10, 275–289.
12. Terazawa H. Unified model of the Nambu-Jona-Lasinio type for all elementary particles. *Physical Review D*, 1977, v. 15(2), 480–487.
13. Harari H. A schematic model of quarks and leptons. *Physics Letters B*, 1979, v. 86(1), 83–86.
14. Fritzsch H., Mandelbaum G. Weak interactions as manifestations of the substructure of leptons and quarks. *Physics Letters B*, 1981, v. 102(5), 319–322.
15. Dehmelt H.G. Experiments with an Isolated Subatomic Particle at Rest. *Nobel Lecture*, 1989.
16. Dugne J.J. Higgs pain? Take a preon! arXiv: hep-ph/9709227.
17. D’Souza I.A.; Kalman C.S. Preons: Models of Leptons, Quarks and Gauge Bosons as Composite Objects. *World Scientific*, 1992.
18. Bilson-Thompson S. A topological model of composite preons. arXiv: hep-ph/0503213.
19. Yershov V.N. Fermions as topological objects. *Progress in Physics*, 2006. v. 2 (4), 19–26.
20. Lucas C.W. A Classical theory of elementary particles. Part 2. Intertwining charge-fibers. *The Journal of Common Sense Science*, 2005, v. 8(2), 1–7.
21. Rañada A. Topological electromagnetism. *J. Phys A: Math. Gen.*, 1992 vol. 25, 1621–1641.
22. Schuster A. Potential matter. A holiday dream. *Nature*, 1898, v. 58, 367.
23. Dirac P.A.M. A Theory of electrons and protons. *Proc. R. Soc. Lond. A*, 1930, v. 126, 360–365.
24. Oppenheimer J.R. On the theory of electrons and protons. *Physical Review*, 1930, v. 35, 562–563.
25. Jenkins J.H. Evidence for correlations between nuclear decay rates and Earth-Sun distance, arXiv:0808.3283.

On the Acceleration of Free Fall inside Polyhedral Structures

Hartmut Müller, Renata Angeli, Roberta Baccara, Flavia Contenti, Rose Line Hofmann,
Simona Muratori, Giuliana Papa, Francesca Santoni, Alessandro Turiano, Simona
Turiano, Claudio Venegoni, Leili Khosravi

E-mail: hm@interscalar.com

In this paper we develop a fractal model of matter as stable eigenstates in chain systems of harmonic quantum oscillators and derive a fractal scalar field that should affect any type of physical interaction, regardless of its complexity. Based on this assumption, we discuss series of experiments on the timing of free falling solid particles inside polyhedral structures whose boundaries coincide with equipotential surfaces of the field.

Introduction

An essential aspect of scientific research is the distinction between empirical facts and theoretical models. This is not only about honesty and ethics in science, but a crucial condition of its evolution. The scientist should always be aware of this.

The nature and origin of gravitation is a key topic in modern physics. Gravitation manifests itself as universal force of attraction. It decreases with increasing distance, but it is thought as having unlimited range. Unlike electrical or magnetic forces, gravitation is considered as to be not shieldable.

The term 'gravitational shielding' is usually imagined as effect of reducing the weight of an object located in a constant gravitational field, neither changing the mass of the object nor its location in that field. Gravitational shielding is considered to be a violation of the equivalence principle and therefore inconsistent with both Newtonian theory and general relativity.

Nevertheless, some experimental evidence [1] indicates that such effect might exist under quite exotic conditions in which a superconductor is subjected to peak currents in excess of 10^4 A, surface potentials of 10^6 V, magnetic fields up to 1 T, and temperature down to 40 K.

In the context of classical physics, mass is considered as source of gravitation described by the Newtonian 'law of universal gravitation' as an instantaneous force acting through empty space. A fundamentally different understanding of gravitation arises from Einstein's general theory of relativity. In this case, gravity acts through a hypothetical 'curvature of space-time', while any kind of energy can cause it.

Gravitation is treated as dominant force at macroscopic scales that forms the shape and trajectory (orbit) of astronomical bodies including stars and galaxies. Advanced models were developed [2–4] in the last century which explain essential features of the formation of the solar system. Though, if numerous bodies are gravitationally bound to one another, classic models predict long-term highly unstable states that contradict with the astrophysical reality in the solar system.

Furthermore, many metric characteristics of the solar system are not predicted in standard models. A remarkably large number of coincidences are considered to be accidental and are not even topics of theoretical research. Until today none of the standard models of gravitation could explain why the solar system has established Jupiter's orbital period at 11.86 years and not 10.27 or 14.69 years; why the Sun and the Moon, the gas giant Jupiter and the planetoid Ceres, but also Earth and Mars have similar rotation periods; why Venus and Uranus, as well as Mars and Mercury have similar surface gravity accelerations; why several exoplanets in the Trappist 1 system have the same orbital periods as the moons of Jupiter, Saturn and Uranus etc. etc.

The standard theory of gravitation experiences also exceptional difficulties to explain the dynamics in star systems. The orbital velocities of stars should decrease in an inverse square root relationship with the distance from the Galactic Center, similar to the orbital velocities of planets in the solar system. But this is not observed. Outside of the central galactic bulge the orbital velocities are nearly constant.

Already in 1933, Fritz Zwicky [5] discovered that the fast movement of the galaxies in the Coma Cluster cannot be explained by the gravity effect of the visible galaxies only and hypothesized the existence of unseen mass that he called 'dark matter'. In 1957, Henk van de Hulst and then in 1959, Louise Volders demonstrated that the galaxies M31 and M33 do not spin as expected in accordance with Kepler's laws.

According to the hypothesis of mass as source of gravity, this deviation might be explained by the existence of a substantial amount of matter flooding the galaxy that is not emitting light and interacts barely with ordinary matter and therefore it is not observed. To explain the dynamics in galaxies and clusters, standard theories of gravitation need a lot of dark matter - 85% of the matter in the universe. Even particle physics has no idea what dark matter could be.

Nevertheless, it is still believed that gravitation of mass determines the orbits of planets and moons, planetoids and asteroids, comets and artificial satellites, and in the cosmos, the formation of stars and galaxies and their evolution. It is also thought that it is the mass of the Earth that causes all bodies to fall 'down'.

The universality of free fall means that the gravity acceleration of a test body at a given location does not depend on its mass, form, physical state or chemical composition. This discovery, made four centuries ago by Galilei, is confirmed by modern empirical research with an accuracy of $10^{-11} - 10^{-12}$. A century ago Einstein supposed that gravity is indistinguishable from, and in fact the same thing as, acceleration. Indeed, Earth's surface gravity acceleration can be derived from the orbital elements of any satellite, also from Moon's orbit:

$$g = \frac{\mu}{r^2} = \frac{\mu}{(6372000\ \text{m})^2} = 9.82\ \text{m/s}^2$$

$$\mu = 4\pi \frac{R^3}{T^2} = 3.9860044 \cdot 10^{14}\ \text{m}^3/\text{s}^2$$

where R is the semi-major axis of Moon's orbit, T is the orbital period of the Moon and r is the average radius of the Earth. No data about the mass or chemical composition of the Earth or the Moon is needed.

The 3^{rd} law of Johannes Kepler describes the ratio R^3/T^2 as constant for a given orbital system. Kepler's discovery is confirmed by high accuracy radar and laser ranging of the movement of artificial satellites.

Actually, Kepler's 3^{rd} law is of geometric origin and can be derived from Gauss's flux theorem in 3D-space within basic scale considerations. It applies to all conservative fields which decrease with the square of the distance and does not require the presence of mass.

It is important to underline that the orbital elements R and T are measured, but $\mu = GM$ is a theoretical presumption that provides mass as a source of gravity and the universality of the coefficient G, the 'gravitational constant'.

One of the basic principles of scientific research is the falsifiability of a theory. Occam's Razor that expresses the preference for simplicity in the scientific method is mainly based on the falsifiability criterion: simpler theories are more testable.

Obviously, any theory that postulates gravitation of mass as dominant forming factor of the solar system and the galaxy is not falsifiable, because there is no independent method to measure the mass of a celestial body. Actually, no mass of any celestial body is measured, but only calculated based on the theoretical presumption $\mu = GM$, and G is estimated in laboratory scale only.

This does not mean that those theories are compellingly wrong, but it should not surprise anyone if the assumption G = constant leads to problems in describing processes that differ by 40 orders of magnitude.

The big G is known only to three decimals, because gravity appears too weak on the scale of laboratory-sized masses for to be measurable with higher precision. As mentioned Quinn and Speake [6], the discrepant results may demonstrate that we do not understand the metrology of measuring weak forces or they may signify some new physics.

In the case of mass as source of gravity, in accordance with Newton's shell theorem, a solid body with a spherically symmetric mass distribution should attract particles outside it as if its total mass were concentrated at its center. In contrast, the attraction exerted on a particle should decrease as the particle goes deeper into the body and it should become zero at the body's center.

The Preliminary Reference Earth Model [7] affirms the decrease of the gravity acceleration with the depth. However, this hypothesis is still under discussion. In 1981, Stacey, Tuck, Holding, Maher and Morris [8, 9] reported anomalous measures (larger values than expected) of the gravity acceleration in deep mines and boreholes. In [10] Frank Stacey writes: "Modern geophysical measurements indicate a 1% difference between values at 10 cm and 1 km (depth). If confirmed, this observation will open up a new range of physics".

Anomalies have been discovered also under conditions of microgravity – in drop towers, abroad the NASA Space Shuttle and the ISS. Whenever an object is in free fall the condition of microgravity comes about. Microgravity significantly alters many processes – the behavior of liquids [11], plasma and granular materials [12, 13] as well, and there is no complete explanation for all the discovered phenomena yet.

Studies [14] of plant growth under different gravity conditions show that elongation growth is stimulated under microgravity conditions. Elongation growth is suppressed with increasing gravitational acceleration and varies in proportion to the logarithm of the magnitude of gravitational acceleration in the range from microgravity to hypergravity.

Already in 2010, Erik Verlinde [15] proposed an alternative explanation of gravitation as an entropic force caused by changes in the information associated with the positions of material bodies. An entropic force is thought as an effective macroscopic force that originates in a system with many degrees of freedom by the statistical tendency to increase its entropy. The term 'entropic force' was introduced by Bechinger and Grünberg [16] when they did demonstrate that in systems of particles of different sizes, entropy differences can cause forces of attraction between the largest particles. However, entropic models of gravitation [17] are still in development and under discussion [18].

It is remarkable that similar dynamics of plant growth observed in laboratory [19] and field experiments [20] are also known as the 'pyramid effect': Inside pyramidal constructions made of various materials, germination and elongation growth of plants are accelerated.

The diversity of sizes and materials (glass, plastic, wood, stone, metal) applied in the pyramidal constructions makes difficult to define the cause of the observed growth stimulation. At the same time, even this diversity supports the suspicion that the 'pyramid effect' could be caused by reduction of gravitation – as it is the most universal physical interaction.

To verify this hypothesis, we have designed an experimental setup that models the free fall of solid particles inside containers of various sizes, shapes and materials. The experimental design is based on global scaling [21] and considers Kosyrev's [22] temporal studies.

Methods

In [23] we have introduced a fractal model of matter as stable eigenstates in chain systems of harmonic quantum oscillators and could show the evidence of this model for all known hadrons, mesons, leptons and bosons as well. On this background, atoms and molecules emerge as eigenstates of stability in fractal chain systems of harmonically oscillating protons and electrons. Andreas Ries [24] demonstrated that this model allows for the prediction of the most abundant isotope of a given chemical element.

In [25] we have shown that the set of stable eigenstates in chain systems of harmonic quantum oscillators is fractal and can be described by finite continued fractions:

$$\mathcal{F}_{jk} = \ln\left(\omega_{jk}/\omega_{00}\right) = [n_{j0}; n_{j1}, n_{j2}, \ldots, n_{jk}]$$

where ω_{jk} is the set of angular eigenfrequencies and ω_{00} is the fundamental frequency of the set. The denominators are integer: $n_{j0}, n_{j1}, n_{j2}, \ldots, n_{jk} \in \mathbb{Z}$, the cardinality $j \in \mathbb{N}$ of the set and the number $k \in \mathbb{N}$ of layers are finite. In the canonical form, all numerators equal 1.

Any finite continued fraction represents a rational number [26]. Therefore, the ratios ω_{jk}/ω_{00} of eigenfrequencies are always irrational, because for rational exponents the natural exponential function is transcendental [27].

This circumstance provides for lasting stability of those eigenstates of a chain system of harmonic oscillators because it prevents resonance interaction [28, 29] between the elements of the system. In [30, 31] we have applied our model as criterion of stability in engineering.

The distribution density of stable eigenstates reaches local maxima near reciprocal integers $\pm 1/2, \pm 1/3, \pm 1/4, \ldots$ that are the subattractor points in the fractal set $\mathcal{F}_{jk}$ of natural logarithms (fig. 1). Integer logarithms $0, \pm 1, \pm 2, \ldots$ represent the most stable eigenstates (main attractors).

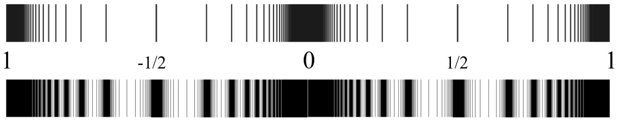

Fig. 1: The distribution of stable eigenvalues of $\mathcal{F}_{jk}$ for $k = 1$ (above) and for $k = 2$ (below) in the range $-1 \leqslant \mathcal{F}_{jk} \leqslant 1$.

In the case of harmonic quantum oscillators, the continued fractions $\mathcal{F}_{jk}$ define not only fractal sets of natural angular frequencies ω_{jk}, angular accelerations $a_{jk} = c \cdot \omega_{jk}$, oscillation periods $\tau_{jk} = 1/\omega_{jk}$ and wavelengths $\lambda_{jk} = c/\omega_{jk}$ of the chain system, but also fractal sets of energies $\mathrm{E}_{jk} = \hbar \cdot \omega_{jk}$ and masses $\mathrm{m}_{jk} = \mathrm{E}_{jk}/c^2$ which correspond with the eigenstates of the system. For this reason, we call the continued fraction $\mathcal{F}_{jk}$ the 'Fundamental Fractal' of stable eigenstates in chain systems of harmonic quantum oscillators.

The spatio-temporal projection of the Fundamental Fractal $\mathcal{F}_{jk}$ of stable eigenstates is a fractal scalar field of transcendental attractors, the Fundamental Field.

The connection between the spatial and temporal projections of the Fundamental Fractal is given by the speed of light $c = 299792458$ m/s. The constancy of c makes both projections isomorphic, so that there is no arithmetic or geometric difference. Only the units of measurement are different.

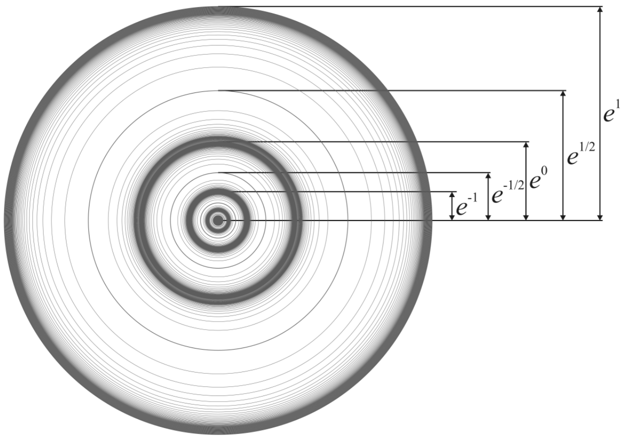

Fig. 2: The equipotential surfaces of the Fundamental Field in the linear 2D-projection for $k = 1$.

Figure 2 shows the linear 2D-projection $\exp(\mathcal{F}_{jk})$ of the first layer of the Fundamental Field for $\mathcal{F}_{j1} = n_{j0} + 1/n_{j1}$ in the interval $-1 < \mathcal{F}_{j1} < 1$. Figure 1 shows the same interval in the logarithmic representation.

At each layer k, the potential energy of the Fundamental Field is constant, therefore the layers are equipotential surfaces. The potential difference defines a gradient, a vector directed to the center of the field that causes a central force of attraction. However, the gradient exposes the logarithmically hyperbolic fractal metric of the Fundamental Field.

The Fundamental Field does not propagate, it is omnipresent. As spatio-temporal projection of the Fundamental Fractal, it is an inherent feature of the number continuum and it causes the fractality of the model space-time.

In physics, only field distortions (waves or currents), not the fields themselves have propagation speeds. In astronomic calculations, gravitation is traditionally considered as being instantaneous. First Laplace [32] demonstrated that gravitation as field does not propagate with the speed of light c. Modern estimations [33] confirm a lower limit of $2 \cdot 10^{10}\, c$.

The Fundamental Field is of pure mathematical origin, and there is no particular physical mechanism required as field source. It is all about numbers as ratios of physical quantities which inhibit destabilizing resonance. In this way, the Fundamental Field concerns all repetitive processes which share at least one characteristic — the frequency.

Therefore, we assume the universality and unity of the Fundamental Field. It might signify that everything in the universe is part of one giant oscillating chain system. This hypothesis we have called 'global scaling' and it is the basis of interscalar cosmology [34].

In fact, scale relations in particle physics [23, 35, 36] and nuclear physics [24, 37, 38], astrophysics [39, 40] and biophysics [41, 42] follow always the same Fundamental Fractal calibrated on the proton and electron, without any additional or particular settings. The proton-to-electron mass ratio itself is caused by the Fundamental Fractal [34].

Planetary and lunar orbits [43] correspond with equipotential surfaces of the Fundamental Field, as well as the metric characteristics of stratification layers in planetary atmospheres [44] and lithospheres [21]. Surface gravity accelerations [45] of the planets in the solar system correspond with attractors of stability in chain systems of oscillating protons and electrons. From this point of view, the metric characteristics of stable structures origin always from the same Fundamental Fractal and different only in scale. Because of its numerical origin, we assume that the Fundamental Field affects any type of physical interaction, regardless of its complexity.

Based on this assumption, we have designed an experimental setup that models the free fall of solid particles inside a container whose boundaries coincide with equipotential surfaces of the Fundamental Field $\exp(\mathcal{F}_{jk})$. The experimental setup consists of a vacuum hourglass (sand clock) and a closed container. The duration of the hourglass was measured inside and outside the container in alternating sequence.

Three different in size, material and duration (40 s, 8 min, 60 min) hourglasses and 18 different in shape (cubic, tetrahedral, octahedral), size (0.3 – 0.6 m diameter) and material (carton, acrylic glass, metal) containers were used.

Based on relevant studies [46], we conducted mechanical tests of the utilized hourglasses and could make sure that inclination below 5 degrees, rotation below 5 Hz and micro-vibration (vertical and horizontal) below 10 Hz do not increase the average fluctuation level (0.2 %) of the duration of the hourglasses.

The accuracy of the vertical was controlled by two orthogonal spirit levels. The complete setup was placed in an electromagnetic shielding chamber. During the measurement, the hourglass had direct contact to an aluminum plate for conduction of eventual electrostatic charge.

The environment control included electromagnetic fields in the frequency range of 1 Hz to 5 GHz, air temperature, pressure and humidity, micro-seismic activity. The experiments were conducted in different places, but always far from the city electrification net.

Results

In general, the measured deviations of the hourglass durations inside containers of different material, shape and size in comparison with the durations outside them did not exceed the average fluctuation level of the duration of the used hourglass. However, a stable significant deviation in the hourglass duration was measured with the 8-minute vacuum hourglass inside a closed truncated octahedron (fig. 3) made of 1/16 aluminum sheet. The 'sand' of this hourglass consists of glass beads of ca. 50 μm diameter.

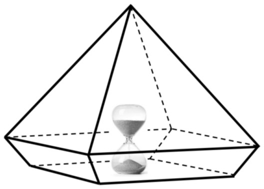

Fig. 3: The duration of the 8-minute hourglass was measured inside and outside the truncated octahedron in alternating sequence.

The truncated octahedron one can imagine as a square pyramid plus an inversed square frustum (fig. 3). The length of the edges of the pyramid coincides with the radius of the main equipotential surface $\mathcal{F}(35)$ of proton stability:

$$\mathcal{F}(35) = \lambda_{\text{proton}} \cdot \exp(35) = 33 \text{ cm}$$

Considering the height $r = 33 \text{ cm} \cdot \sqrt{2}/2 = 23$ cm of the pyramid, the orifice of the hourglass was placed in a distance from the vertices of the pyramid that equals to the radius of the main equipotential surface $\mathcal{F}(27)$ of electron stability:

$$\mathcal{F}(27) = \lambda_{\text{electron}} \cdot \exp(27) = 21 \text{ cm}$$

The height 7.5 cm of the frustum coincides with the radius of the main equipotential surface $\mathcal{F}(26)$ of electron stability:

$$\mathcal{F}(26) = \lambda_{\text{electron}} \cdot \exp(26) = 7.5 \text{ cm}$$

Furthermore, at 6 minutes after start, the continuing process of free fall passes the main temporal attractor $\mathcal{F}(54)$ of electron stability:

$$\mathcal{F}(54) = \tau_{\text{electron}} \cdot \exp(54) = 6 \text{ min}$$

The Compton angular wavelength of the electron is $\lambda_{\text{electron}} = 3.861593\dot{1}0^{-13}$ m, of the proton $\lambda_{\text{proton}} = 2,103089\dot{1}0^{-16}$ m, and the angular oscillation period of the electron is $\tau_{\text{electron}} = \lambda_{\text{electron}}/c = 1.288089\dot{1}0^{-21}$ s [47].

Probably, all these coincidences together caused an accumulated effect of damping the acceleration of free fall. Furthermore, we suppose that potential differences between equipotential surfaces of the Fundamental Field can change the entropy of the involved processes.

In series of crystallization experiments, we observed that inside the same truncated octahedron, sodium chloride crystals grow in salt solutions with concentrations far below the saturated concentration and develop octahedral shapes like diamonds instead of cubic.

The most widely accepted law that predicts the flowrate of mono-sized grains through an orifice and its dependence on different parameters was proposed by Beverloo, Leniger and van de Velde [48, 49]. They have shown that under otherwise

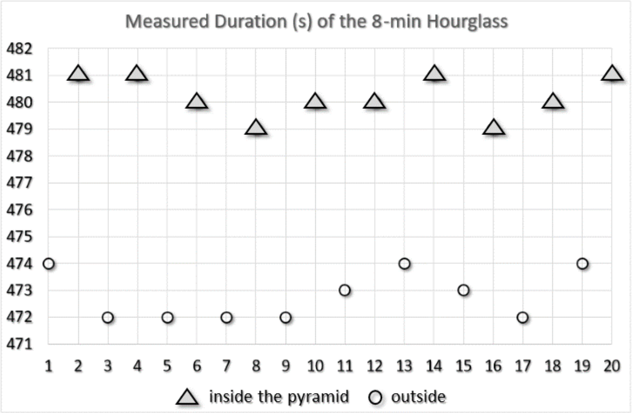

Fig. 4: Time series of the alternating measurements of the hourglass duration (s) inside the truncated octahedron (pyramid) and outside.

constant conditions k, the mass flowrate W is proportional to the square root of the gravity acceleration g:

$$W = k\sqrt{g}$$

This equation coincides with Torricelli's law for the speed of fluid flowing out of an orifice and allows for estimation of the equivalent gravity reduction Δg that corresponds to the ratio of the measured durations inside and outside the octahedron:

$$\Delta g = g\left(\frac{t_{\text{outside}}}{t_{\text{inside}}}\right)^2 - g$$

Table 1 contains representative samples of the durations measured inside and outside the truncated octahedron and the calculated corresponding equivalent gravity reduction in units of g. Fig. 1 shows time series of the alternating measurements.

series	out, s	inside, s	inside/out-1, %	Δg
1	474	481	1.48	-0.283
2	472	481	1.91	-0.364
3	472	480	1.69	-0.324
4	472	479	1.48	-0.285
5	472	480	1.69	-0.324
6	473	480	1.48	-0.284
7	474	481	1.48	-0.283
8	473	479	1.27	-0.244
9	472	480	1.69	-0.324
10	474	481	1.48	-0.283
average	473 ± 1	480 ± 1	1.57	-0.300

Table 1: The measured duration (s) of the 8-minute hourglass inside the truncated octahedron and outside, the relative deviation and the equivalent gravity reduction in units of g.

Over all series of the total 255 hours of measurements, the fluctuation level of the hourglass durations inside and outside the truncated octahedron did not exceed 0.2 %. The relative difference of the durations inside and outside the octahedron did not fall below 1.2%. The average relative difference was 1.67% that corresponds to an equivalent gravity reduction of -0.324 g inside the octahedron. Outside the octahedron, this amount of gravity reduction would correspond to an altitude of 100 km over sea level.

Only inside the described truncated octahedral container we observed a stable significant deviation in the duration of the hourglass, regardless of the location and time. In containers of different shape and size, even made of the same 1/16 aluminum sheet, the measured deviations did not exceed the average fluctuation level of the hourglass duration.

Currently we have no explanation for the extraordinariness of the octahedral (pyramidal) shape. However, in Finslerian multi-dimensional time models, the pseudo-Euclidean light cone becomes a light pyramid [50].

Conclusion

We are aware that our experiments cannot claim to be conclusive. However, they could point out that gravity is not just about the amount of the involved masses and energies. It may well be that 'subtle' factors like the spatial configuration of the system and its scale have higher influence than expected.

Acknowledgements

The authors are grateful to the Community of Living Ethics for permanent support on all stages of the study.

Submitted on September 20, 2018

References

1. Podkletnov E., Modanese G. Impulse Gravity Generator Based on Charged $YBa_2Cu_3O_{7-y}$ Superconductor with Composite Crystal Structure. arXiv:physics/0108005v2 [physics.gen-ph], (2001).
2. Williams I.O., Cremin A.W. A survey of theories relating to the origin of the solar system. *Qtly. Rev. RAS*, 1968, v. 9, 40–62.
3. Van Flandern T. Our Original Solar System – a 21st Century Perspective. *MetaRes. Bull.*, 2008, v. 17, 2–26.
4. Woolfson M.M. Planet formation and the evolution of the Solar System. arXiv:1709.07294, (2017).
5. Zwicky F. On the Masses of Nebulae and of Clusters of Nebulae. *The Astrophysical Journal*, 1937, v. 86, 217.
6. Quinn T., Speake C. The Newtonian constant of gravitation – a constant too difficult to measure? An introduction. *Phil. Trans. Royal Society A*, 2014, v. 372, 20140253.
7. Dziewonski A.M., Anderson D.L. Preliminary reference Earth model. *Physics of the Earth and Planetary Interiors*, 1981, v. 25, 297–356.
8. Stacey F.D. et al. Constraint on the planetary scale value of the Newtonian gravitational constant from the gravity profile within a mine. *Phys. Rev. D*, 1981, v. 23, 1683.
9. Holding S.C., Stacey F.D., Tuck G.J. Gravity in mines. An investigation of Newton's law. *Phys. Rev. D*, 1986, v. 33, 3487.
10. Stacey F.D. Gravity. *Science Progress*, 1984, v. 69, no. 273, 1–17.
11. Kundan A. et al. Condensation on Highly Superheated Surfaces: Unstable Thin Films in a Wickless Heat Pipe. *Phys. Rev. Lett.*, 2017, v. 118, 094501.
12. Alshibli Kh. et al. Strain Localization in Sand: Plane Strain versus Triaxial Compression. *Journal of Geotechnical and Geoenvironmental Engineering*, 2003, v. 129, no. 6.

13. Alshibli Kh. Behavior of granular materials in microgravity environment: implication for future exploration missions. *Infrastruct. Solut.*, 2017, v. 2, 22.
14. Hoson T. Plant Growth and Morphogenesis under Different Gravity Conditions: Relevance to Plant Life in Space. *Life*, 2014, v. 4, 205–216.
15. Verlinde E. On the Origin of Gravity and the Laws of Newton. arXiv:1001.0785v1 [hep-th], (2010).
16. Bechinger C., Grünberg H., Leiderer P. Entropische Kräfte. *Physikalische Blätter*, 1999, v. 55, no. 12.
17. Nicolini P. Entropic force, noncommutative gravity and ungravity. arXiv:1005.2996v3 [gr-qc], (2010).
18. Kobakhidze A. Gravity is not an entropic force. arXiv:1009.5414v2 [hep-th], (2010).
19. Motloch L.N. Effects of Pre-Sowing Incubation within a Pyramid on Germination and Seedling Growth of Phaseolus Vulgaris L. // Master of Science Thesis, Tarleton State University, (2017).
20. Skliarov A. Biological Experiments in the Egyptian Pyramids. LAH, www.lah.ru, (2009).
21. Müller H. Quantum Gravity Aspects of Global Scaling and the Seismic Profile of the Earth. *Progress in Physics*, 2018, v. 14, 41–45.
22. Kosyrev N.A. Astronomical observations through the physical properties of time. // Kosyrev N. A. Selected Works. Leningrad, 363–383, (1991).
23. Müller H. Fractal Scaling Models of Natural Oscillations in Chain Systems and the Mass Distribution of Particles. *Progress in Physics*, 2010, v. 6, no. 3, 61–66.
24. Ries A. Qualitative Prediction of Isotope Abundances with the Bipolar Model of Oscillations in a Chain System. *Progress in Physics*, 2015, v. 11, 183–186.
25. Müller H. Scale-Invariant Models of Natural Oscillations in Chain Systems and their Cosmological Significance. *Progress in Physics*, 2017, vol. 13, 187–197.
26. Khintchine A.Ya. Continued fractions. University of Chicago Press, Chicago, (1964).
27. Hilbert D. Über die Transcendenz der Zahlen e und π. *Mathematische Annalen*, 1983, v. 43, 216–219.
28. Dombrowski K. Rational Numbers Distribution and Resonance. *Progress in Physics*, 2005, v. 1, no. 1, 65–67.
29. Panchelyuga V.A., Panchelyuga M. S. Resonance and Fractals on the Real Numbers Set. *Progress in Physics*, 2012, v. 8, no. 4, 48–53.
30. Müller H. The general theory of stability and objective evolutionary trends of technology. Applications of developmental and construction laws of technology in CAD. Volgograd, VPI, (1987).
31. Müller H. Superstability as a developmental law of technology. Technology laws and their Applications. Volgograd-Sofia, (1989).
32. Laplace P. Mechanique Celeste. pp. 642–645, (1825).
33. Van Flandern T. The Speed of Gravity — What the Experiments Say. *Physics Letters A*, 1998, v. 250, 1–11.
34. Müller H. Global Scaling. The Fundamentals of Interscalar Cosmology. *New Heritage Publishers*, Brooklyn, New York, USA, (2018).
35. Müller H. Emergence of Particle Masses in Fractal Scaling Models of Matter. *Progress in Physics*, 2012, v. 8, no. 4, 44–47.
36. Ries A. A Bipolar Model of Oscillations in a Chain System for Elementary Particle Masses. *Progress in Physics*, 2012, v. 8, no. 4, 20–28.
37. Ries A., Fook M. Fractal Structure of Nature's Preferred Masses: Application of the Model of Oscillations in a Chain System. *Progress in Physics*, 2010, v. 6, no. 4, 82–89.
38. Ries A. The Radial Electron Density in the Hydrogen Atom and the Model of Oscillations in a Chain System. *Progress in Physics*, 2012, v. 8, no. 3, 29–34.
39. Müller H. Fractal scaling models of natural oscillations in chain systems and the mass distribution of the celestial bodies in the Solar System. *Progress in Physics*, 2010, v. 6, no. 4, 44–47.
40. Müller H. Global Scaling as Heuristic Model for Search of Additional Planets in the Solar System. *Progress in Physics*, 2017, v. 13, 204–206.
41. Müller H. Chain Systems of Harmonic Quantum Oscillators as a Fractal Model of Matter and Global Scaling in Biophysics. *Progress in Physics*, 2017, v. 13, 231–233.
42. Müller H. Astrobiological Aspects of Global Scaling. *Progress in Physics*, 2018, v. 14, 3–6.
43. Müller H. Global Scaling of Planetary Systems. *Progress in Physics*, 2018, v. 14, 99–105.
44. Müller H. Global Scaling of Planetary Atmospheres. *Progress in Physics*, 2018, v. 14, 66–70.
45. Müller H. Gravity as Attractor Effect of Stability Nodes in Chain Systems of Harmonic Quantum Oscillators. *Progress in Physics*, 2018, v. 14, 19–23.
46. Staude J. Untersuchung granularer Materie am Beispiel des Laufzeitverhaltes einer Sanduhr unter Einwirkung äußerer Kräfte. Bachelor Thesis Physics, Freie Universität Berlin, (2013).
47. Olive K.A. et al. (Particle Data Group), Physical Constants. *Chin. Phys. C*, 2016, v. 38, 090001.
48. Beverloo W.A., Leniger H.A., van de Velde J. The flow of granular solids through orifices. *Chem. Eng. Sci.*, 1961, v. 15, 260–269.
49. Mankoc C. et al. The flow rate of granular materials through an orifice. arXiv:0707.4550v1 [cond-mat.soft], (2007).
50. Pavlov D.G. Chronometry of the Three-Dimensional Time. // Space-Time Structure. Algebra and Geometry. Russian Hypercomplex Society, Moscow, (2007).

Janus Cosmological Model and the Fluctuations of the CMB

Jean-Pierre Petit
E-mail: jp.petit@mailaps.org

It is shown than, in the framework of the Janus Cosmological Model the gravitational instability which occurs in the negative sector makes an imprint in the positive one, which corresponds to the CMB inhomogeneities. So that their characteristic wavelength gives the ratio of the space scale factors of the two sectors, which differ from two orders of magnitude. Subsequently the speed of light in the negative sector is ten times highers than ours. So that, given to distant points, if the travel between them is managed along the negative geodesics paths, the corresponding travel time is reduced by a factor one thousand.

1 Introduction

A cosmological model must take account of the observations. From this point of view a recent paper [1] showed that the the Janus Cosmological Model (JCM) fits many.

- JCM explains the absence of observation of the so called primeval antimatter, opposite to the mainstream ΛCDM model.
- JCM describes precisely the nature of the invisible components of the universe, opposite to the mainstream ΛCDM model.
- JCM predicts that the antimatter produced in laboratory will react as the matter with respect to the gravitational field of the Earth (it will fall).
- Because positive and negative matter are repelling each other, the negative matter in the solar system is almost zero. So, JCM fits the classical relativistic observation, as presented in former papers [2, 3].
- JCM suggests a clear schema for VLS formation [4] when the mainstream model ΛCDM seems to struggle to give one.
- JCM explains the observed strange effect due to the Great Repeller [5]. The measured escape velocities of galaxies are due to the presence of an invisible repellent cluster made of negative mass, located in the centre of the big void. The mainstream model supporters suggest that such a repellent effect could be due to some kind of a hole in the dark matter field of the universe (positive masses). But, if the gravitational instability leads to the setting up of massive clusters, it does not provide ant scheme for such void formations. So that the mainstream model ΛCDM does not provide any explanation of the observation.
- JCM explains the confinement of galaxies and their flat rotation curves [1, 6]. Mysterious dark matter is no longer required, while the mainstream model ΛCDM does.
- After JCM the intensity of the observed gravitational lensing effect is mainly due to the negative matter that surrounds galaxies and clusters of galaxies. Mysterious dark matter is no longer required, while the mainstream model ΛCDM does.
- JCM suggests an explanation of the low magnitude of very young galaxies: this would be due to the negative lensing weakening, when their light are crossing the negative mass clusters located at the center of the big voids.
- JCM explains the spiral structure of galaxies, due to dynamical friction with the surrounding mass [1, 6]. The model ΛCDM don't give any model explaining the spiral structure.
- JCM explains the acceleration of the universe [1]. The so-called dark energy is the one associated to the negative mass content through $E = \rho c^2$, with $\rho < 0$.
- JCM explains the homogeneity of the primeval universe [2, 16].

JCM is definitively not a simple or pure product of mathematical physics. But it represents a deep paradigmatic change, on geometrical grounds. In the Einstein's model the universe is considered as a manifold, whose geometry corresponds to a single metric field , solution of a single field equation, without cosmological constant:

$$R_{\mu\nu} - \frac{1}{2}\, R\, g_{\mu\nu} = \chi T_{\mu\nu}\ . \tag{1}$$

Such model automatically generates the unmanageable runaway effect [7, 8], just because, if imbedded in a given gravitation field (the term $T_{\mu\nu}$), positive and negative masses react the same way (a single metric solution $g_{\mu\nu}$). If we give up such restrictive and non-logical hypothesis it means that, imbedded in a given gravitation field the geodesics of the two species derive from two metrics fields $g^{(+)}_{\mu\nu}$ and $g^{(-)}_{\mu\nu}$, solutions of two coupled field equations, as derived from Lagrangian method [9, 10].

$$\begin{aligned} R^{(+)}_{\mu\nu} - \frac{1}{2}\, R^{(+)}\, g^{(+)}_{\mu\nu} &= +\chi \left(T^{(+)}_{\mu\nu} + \sqrt{\frac{g^{(-)}}{g^{(+)}}}\, T^{(-)}_{\mu\nu} \right), \\ R^{(-)}_{\mu\nu} - \frac{1}{2}\, R^{(-)}\, g^{(-)}_{\mu\nu} &= -\chi \left(T^{(-)}_{\mu\nu} + \sqrt{\frac{g^{(+)}}{g^{(-)}}}\, T^{(+)}_{\mu\nu} \right). \end{aligned} \tag{2}$$

The physical meaning of the presence of the two square roots in the second members is the energy conservation requirement. We have a single manifold M_4, with two tensor fields $T^{(+)}_{\mu\nu}$ and $T^{(-)}_{\mu\nu}$, which refer to positive and negative mass contents. In some regions $T^{(+)}_{\mu\nu}$ dominates, in other $T^{(-)}_{\mu\nu}$ dominate. In others the two are zero. In any case we find everywhere two families of geodesics, as derived from the metric $g^{(+)}_{\mu\nu}$ and $g^{(-)}_{\mu\nu}$. The first refers to the paths of positive mass particles, and positive energy photons (null positive geodesics). The second refers to the paths of negative mass particles, and negative energy photons (null negative geodesics).

On pure geometric grounds the negative mass objects are invisible to us, because they emit negative energy photons that positive mass devices cannot capture. And vice versa. The positive and negative masses interact only trough (anti) gravitation.

The classical Newton's law comes from the Einstein's equation (1) through Newtonian approximation (small curvature, velocities small with respect to the speed of light, quasi Lorentzian metric).

Similarly from the system (2) we get [3, 11] the following Newtonian, and antinewtonian interaction laws:

- Positive masses do attract together, through Newton' law;
- Negative masses do attract together, through Newton's law;
- Opposed masses do repel each other, through anti Newton's law.

This interaction scheme fits the action-reaction principle.

The nature of the invisible components of the universe are determined from dynamic group theory [6, 12]. They are a copy of the ordinary antiparticles, with negative energy. This schema fits initial Sakharov's idea [13–15].

As evoked in [17], JCM may produce an original scheme for galaxies' formation. The structures of the positive and negative sectors are fairly different. After discoupling, with $\rho^- \gg \rho^+$, spheroidal globular clusters form first, the matter being confined in the remnant place, getting an alveolar structure. The compression of positive matter along flat structure is optimum for radiative cooling and Jeans' instability triggering, giving galaxies, stars and heavy atoms. At the contrary the negative mass antimatter is confined in spheroidal objects, that can be compared to huge proto-stars that will never ignite because their cooling time is longer that the age of the universe. As a consequence no galaxies, no stars, no heavy atomes and planets can form. Life is absent from such negative world.

2 A short remark about another model with negative mass

The model of L. Blanchet and G. Chardin is based on the Einstein's equation, so that the runaway effect belongs to it, which does not worry the authors.

Their scheme suggests, without theoretical grounds, that the primeval antimatter could have a negative mass.

From the Einstein's equation the interaction laws between positive and negative masses is the following (which contains the runaway effect):

- Positive masses mutually attract through the Newton's law;
- Negative masses mutually repel through "anti-Newton's law";
- Positive masses are repelled by negative masses;
- Negative masses are attracted by positive masses;

which contradicts the action-reaction principle. Howevever L.Blanchet and G.Chardin think that, thanks to such interaction scheme the primeval (negative mass) antimatter could have survived somewhere.

About cosmological evolution the authors opt for the Dirac-Milne model [17], which corresponds to a constant null gravitational field, with a constantly global zero mass. Then the expansion is linear in time, which contradicts the recent observation of the acceleration of the expansion.

JCM shows that there are two forms of antimatter. The positive mass, we can call it "Dirac antimatter" (C-symmetrical of our matter) reacts as the ordinary matter, if imbedded in a gravitational field This is the antimatter we produce in laboratory, so that we predict that the antimatter weighted if the alpha experiment will fall down.

The negative mass antimatter corresponds to the primeval antimatter and is located between galaxies. We may call it "Feynmann antimatter" (PT-symmetrical from our ordinary matter).

3 How to determine the parameters in the negative sector

According to the "variable constants" evolution schema [2, 16] the two sectors correspond to two different sets of so-called constants, time plus scale parameters:

$$\begin{gathered}\left\{c^{(+)};\ G^{(+)};\ h^{(+)};\ e^{(+)};\ m^{(+)};\ \mu_0^{(+)};\ a^{(+)};\ t^{(+)}\right\},\\ \left\{c^{(-)};\ G^{(-)};\ h^{(-)};\ e^{(-)};\ m^{(-)};\ \mu_0^{(-)};\ a^{(-)};\ t^{(-)}\right\}.\end{gathered} \tag{3}$$

Where are space and time factors. In both sectors the so-called constants and space and time factors experience "joint gauge variations" which keep the equations of physics invariant. It means that if one chooses one of the eight parameters the other seven can be expressed using that one. For example:

$$\begin{gathered}c^{(+)} \propto \frac{1}{\sqrt{a^{(+)}}}\,, \quad G^{(+)} \propto \frac{1}{a^{(+)}}\,, \quad h^{(+)} \propto (a^{(+)})^{3/2}\,,\\ e^{(+)} \propto \sqrt{a^{(+)}}\,, \quad m^{(+)} \propto a^{(+)}\,, \quad t^{(+)} \propto (a^{(+)})^{3/2}\,;\\ c^{(-)} \propto \frac{1}{\sqrt{a^{(-)}}}\,, \quad G^{(-)} \propto \frac{1}{a^{(-)}}\,, \quad h^{(-)} \propto (a^{(-)})^{3/2}\,,\\ e^{(-)} \propto \sqrt{a^{(-)}}\ ; \quad m^{(-)} \propto a^{(-)}\,, \quad t^{(-)} \propto (a^{(-)})^{3/2}\,.\end{gathered} \tag{4}$$

What is the ontological justification of such process? It makes no necessary to invoke inflation to justify the observed homogeneity of the primeval universe. In effect, the cosmological horizon becomes an integral [2, 16]:

$$horizon^{(+)} = \int c^{(+)}\, dt^{(+)} \propto a^{(+)}. \tag{5}$$

Same thing in the "negative sector".

A question arises immediately: when does this generalized gauge process era ends? This will be examined in a next paper.

Have a look on the Jeans' lengths $L_J^{(+)}$ and $L_J^{(-)}$ and times Jeans $t_J^{(+)}$ and $t_J^{(-)}$. In this gauge process all the velocities, including thermal velocities, vary like the speed of light of their corresponding sector:

$$\langle V^{(+)} \rangle \propto c^{(+)}\,, \qquad \langle V^{(-)} \rangle \propto c^{(-)} \tag{6}$$

so that

$$\begin{aligned} L_J^{(+)}\,, &\simeq a^{(+)}\,, & t_J^{(+)} &\simeq t^{(+)}\,, \\ L_J^{(-)}\,, &\simeq a^{(-)} & t_J^{(-)} &\simeq t^{(-)}\,. \end{aligned} \tag{7}$$

The fluctuations, due to gravitational instability are not observable in a given sector, by observers who live in.

Anyway, in a fully ionized plasma the strong link to the radiation backgrounds prevents clustering of matter in both sectors. What about the "gas of photons"?

4 Photons react to gravitational field

This gives the gravitational lensing effect. On another hand the photons contribute to the curvature. If the inertial mass of the photon is zero, we can introduce an individual equivalent gravitational mass of the photon:

$$\begin{aligned} m_\varphi^{(+)} &= \frac{h^{(+)}\, \upsilon^{(+)}}{c^{(+)2}} \propto a^{(+)} \propto m^{(+)}\,, \\ m_\varphi^{(-)} &= \frac{h^{(-)}\, \upsilon^{(-)}}{c^{(-)2}} \propto a^{(-)} \propto m^{(-)}\,. \end{aligned} \tag{8}$$

We may consider than the gravitational instability occurs in the "gaz of photons" but the corresponding Jeans' length becomes:

$$\begin{aligned} L_J^{(+)} &= \frac{c^{(+)}}{\sqrt{4\,\pi\, G^{(+)}\, \rho^{(+)}}} \simeq a^{(+)}\,, \\ L_J^{(-)} &= \frac{c^{(-)}}{\sqrt{4\,\pi\, G^{(-)}\, \rho^{(-)}}} \simeq a^{(-)}\,, \end{aligned} \tag{9}$$

again, such fluctuations in one sector cannot be observed by an observer that belongs to, because it extends beyond the corresponding cosmological horizon. But, from a conceptual point of view, this links to the idea of so-called "multivers". Beyond our cosmological universe we may consider that other "universes" extend, with different sets of physical constants and scale factors. But, as such they should obey the same equations, their histories would not be different from ours, giving, in the corresponding positive sectors, atoms, stars, galaxies, planets and life.

We get an infinite set of coupled (positive/negative mass) portions of the universe.

If the gravitational instability cannot occur in our sector of the universe, before decoupling, we have the imprint of such primeval instability, which occurs in the negative sector. We think that this produces the light inhomogeneities in the CMB.

The basic fluctuation extent is two order of magnitude smaller than the whole angular extent. It gives directly the order of magnitude of the ratio of the space scale factoirs. In the negative sector the fluctuations have a characteristic wavelength, so that the measure of the imprints in our sector gives the order of magnitude according to:

$$\frac{a^{(-)}}{a^{(+)}} \approx \frac{1}{100}\,. \tag{10}$$

As a conclusion, if we consider two points A and B of the manifold, we have two different lengths, which differ from the same ratio.

5 Link to the interstellar travel problem

During the gauge process era the two sectors experience evolution of their constants according to:

$$a^{(+)}\, c^{(+)2} = a^{(')}\, c^{(')2} = constant. \tag{11}$$

Combining with (10) we get:

$$\frac{c^{(-)}}{c^{(+)}} \approx 10. \tag{12}$$

According to the Einstein's model (1), interstellar travels at sub-relativistic velocity implies durations fairly incompatible with human lifetime. But if some distant civilizations could invert the mass of a vehicle (plus passengers) and travel along geodesics of the negative sector at $V^{(-)} < c^{(-)}$ the gain in time travel would correspond to three order of magnitude. So that a travel to, or from the nearest systems could be possible.

6 Conclusion

We review the many observational confirmations of the Janus Cosmological Model. We deal with the origin of the fluctuations in the CMB. Based on our primeval gauge process era, which explains the homogeneity of the primeval universe, without need to the inflation schema, we look at the gravitational instability during that era and show that the corresponding Jeans's length follows the extension of the cosmological horizon in both sectors. We notice that, even if we cannot make observation beyond the horizon, other portions of the universe could be ruled by different sets of so-called constants and scale factors. This links to the idea of "Multiverse". But, according to ou scheme such sets should derive from the same set of equations, so that the physical, an biological evolution in such sectors should give the same patter (atoms, stars, planets, life).

We point out that such primeval gravitational instability, occurring in the negative sector, make an imprint in ours, and that corresponds to the observed fluctuations in the CMB.

Then it gives the measure of the ration of the two scale factors $\frac{a^{(+)}}{a^{(-)}} \approx 100$.

According to our gauge process scheme it corresponds to $\frac{c^{(-)}}{c^{(+)}} \approx 10$.

As a conclusion it shortens the travel time, for sub-relativist journeys, by a factor 1000, which makes the impossibility of travels to nearest stars questionable, if mass inversion technique would be someday possible.

Submitted on September 26, 2018

References

1. D'Agostini G. and Petit J.P. Constraints on Janus Cosmological Model from recent observations of supernovae type Ia. *Astrophysics and Space Science*, 2018.
2. Petit J.P. Twin universe cosmology. *Astrophysics and Space Science*, 1995, v.222, 273.
3. Petit J.P. and D'Agostini G. Negative mass hypothesis and the nature of dark energy. *Astrophysics And Space Science*, 2014, v.353, issue 2.
4. De Lapparent V., Geller M.H. and Huchara J.P. A slice of the Universe. *Astrophysical Journal*, 1986, v. 102, L1–L2.
5. Hoffman Y., Pomarede D., Tully R.B. and Courtois H.M. The Dipole Repeller. *Nature Astronomy*, 2017, 0036.
6. Petit J.P., Midy P. and Landsheat F. Twin matter against dark matter. International meeting on astrophysics and Cosmology "Where is the matter"?, Marseille, June 2001, 25–29.
7. Bondi H. Negative mass in General Relativity. *Review of Modern Physics*, 1957, v. 29, no. 3.
8. Bonnor W.B. Negative mass in General Relativity. *General relativity and Gravitation*, 1989, v. 21, no. 11, 1143–1157.
9. Hossenfelder S. Antigravitation. *Physics Letters B*, 2006, v. 636, 119–125.
10. Hossenfelder S. A bimetric theory with exchange symmetry. *Physical Review D*, 2008, v. 78, 044015.
11. Petit J.P. and D'Agostini G. Cosmological model with interaction positive and negative masses and two different speeds of light, in agreement with the observed acceleration of the universe. *Modern Physics Letters A*, 2014, v. 29, no. 34.
12. Souriau J.-M. Structure des Systèmes Dynamiques. Dunod, Paris, 1970. (English translation: Souriau J.-M. Structure of Dynamical Systems. Birkhäuser, Boston, 1997).
13. Sakharov A.D. *ZhETF Pis'ma*, 1967, v. 5, 32; *JETP Lett.*, 1967, v. 5, 24.
14. Sakharov A.D. *ZhETF*, 1979, v. 76, 1172; *ZhETF*, 1979, v. 49, 594).
15. Sakharov A.D. (1980). Cosmological model of the Universe with a time vector inversion. *ZhETF*, 1980, v. 52, 349–351; *ZhETF*, 1980, v. 79, 689–693.
16. Petit J.P. Cosmological model with variable velocity of light. *Modern Phys. Letters A*, 1988, v. 3, 1988, 1527.
17. Petit J.P. The missing mass problem. *Il Nuovo Cimento*, 1994, v. 109, 697–710.
18. Benoit-Levy A. and Chardin G. Introducing the Dirac-Milne universe. arXiv:1110.3954v2 (astro-ph).

On the Supersymmetry Realization of Involving β^+-Orthopositronium. Phenomenology

Boris M. Levin
N. N. Semenov Inst. Chem. Phys. Russian Acad. of Sci., Moscow (1964–1987),
The creative cooperation with B. P. Konstantinov Leningrad Inst. Nucl. Phys. Russian Acad. of Sci., Gatchina (1984–1987),
A. F. Ioffe Phys. Tech. Inst. Russian Acad. of Sci., St. Petersburg (2005–2007)
E-mail: bormikhlev@yandex.ru

The absence of a Coulomb barrier in the interaction of the Vacuum-Like State of Matter with normal matter is the basis of the phenomenology of the Project of the New (Additional) $G\hbar/ck$-Physics "Outside" the Light Cone.

"*Of course, the most intriguing question is whether NEC-violation fields exist in Nature. Needless to say, no such fields have been discovered. The situation is not entirely hopeless, however: we may learn at some point in future that Universe went through the bounce or Genesis epoch, and that will be an indication that NEC-violation indeed took place in the past*" [1].

Closely adjoins this problem the phenomenology of the extension of the Standard Model/SM (as the possibility of two-valued/± vacuum states), the formulation of which is stimulated by observations (1956/USA, 1965/USA, 1967/Russia, 1975/USA, 1975/England, 1975/Canada, 1987/Russia, 1982–1990/USA, 2003/USA) anomalies of annihilation of β^+-decay positrons (β^+-orthopositronium) in the system

$$^{22}\text{Na}\,(3^+) \xrightarrow{e^+_\beta+\nu} {}^{22*}\text{Ne}\,(2^+) \xrightarrow{\gamma_n\simeq 1.274\ \text{MeV}}$$
$$^{22}\text{Ne}\,(0^+) \text{ – gaseous neon } (8.86\%\ ^{22}\text{Ne}).$$

The necessary definiteness in the construction of the model to explain the anomalies in neon is the result of our critical experiment [2] (the hypothesis about paradoxical realization of the Mossbauer effect/EM): at the indicated "*resonance conditions*" there is doubling 1.85 ± 0.1 of the contribution of the orthopositronium component $\boldsymbol{I}_2$ of the lifetime spectra of the β^+-positrons e^+_β at decrease in the fraction of the isotope ^{22}Ne in the natural isotope composition — from 8.86% to 4.91% — in the sample for comparison. From the SM position, the possible change in $\boldsymbol{I}_2$ is vanishingly small: $10^{-7} - 10^{-6}$.

Self consistent phenomenology in the proposed model is formulated with reference to the results and conclusions of a number of creative searches for theorists (1962–2012) — by including in the final state of the β^+-decay of nuclei ^{22}Na, ^{64}Cu, ^{68}Ga and the like ($\Delta J^\pi = 1^\pi$) of the bounded 4-volume of space-time "outside" the Light Cone, instead of counterproductive phenomenology "*tachyon*, as a particle" [3].

Otherwise, it is impossible to explain the "isotope anomaly".

It is necessary to return to this fact ignored by the scientific community: among the known and presumed vacuum effects — from the Lamb shift of atomic levels and Casimir effect to the birth of the universe "in the Laboratory" [1, 4] — there is no discussion of a paradoxical realization of EM in the "resonance conditions".

The effect can be represented as the result of a *Topological Quantum Transition/TQT* of a bounded 4-volume of space-time in the final state of β^+-decay into a two-valued/± *Vacuum-Like State of Matter/VSM*$^{\text{“}+\text{”}}$ "*Through the Looking Glass*"/*TLG*$^{\text{“}-\text{”}}$ — *Long-Range Atom/LRA* with a *LRA Core*. In phenomenology, this is a kind of realization of a string (the Hamiltonian chain), at the nodes of which there are quasiparticles of all the ingredients of stable matter – quasiprotons ($\bar{p}$), quasielectron ($\bar{e}$), quasineutrino ($\bar{\nu}$) [2, 3].

According to the SM, negative masses are not physically realized, since otherwise such physical states would be unstable with respect to the catastrophic generation of an unlimited number "particle-antiparticle" pairs (disintegration of the vacuum). The prohibition of such "pathological states" underlies the Weak Energy Condition/WEC (NEC) of the General Relativity.

The model proposed in [3] of the LRA of the two-valued/± Planck mass

$$\pm M_{\text{Pl}} = \pm\sqrt{\frac{(\pm\hbar)\cdot(\pm c)}{G}}\,, \quad G > 0,$$

with the total number of cells/nodes

$$\pm N^{(3)} = \frac{\pm M_{\text{Pl}}}{\pm m_{\bar{p}} \pm m_{\bar{e}} \pm m_{\bar{\nu}}} \simeq 1.3\cdot 10^{19}$$

and a LRA Core [5]

$$\pm n \simeq 5.3\cdot 10^4,$$

in the final state of the β^+-decay type $\Delta J^\pi = 1^\pi$ stops the disintegration of the vacuum and substantiated the EM in "resonance conditions".

The main thing is that presented model is based on the assumption of a fundamental difference between the QED-orthopositronium formed in the substance as result of the production of the $e^+ - e^-$ pair from the β^+-orthopositronium/β^+-o-Ps, since it is possible to justify [3] that in the process of formation and lifetime β^+-o-Ps in the substance a supersymmetry is realized [6]. The process is limited by the lifetime of β^+-o-Ps, which, being formed "inside" the Light Cone — oscillates due to single-quantum (virtual) annihilation.

So β^+-o-Ps objectively formalized the status of the physical observer.

In this case, the causality principle (global) is realized as a local causality principle due to the presence of β^+-o-Ps.

Because of the fundamental difference in the radii of interactions — infinite radius for electromagnetic and gravitational interactions and submicroscopic radii of "nuclear" interactions (weak ones, $r_w \sim 10^{-16}$ cm and $r_{str} \sim 10^{-13}$ cm) — there is no Coulomb barrier at interaction the LRA Core with ordinary substance.

In the gravitational field of the ground laboratory, the two-valued/± components of the LRA Core (VSM$^{\text{“}+\text{''}}$/TLG$^{\text{“}-\text{''}}$) diverge vertically by a distance h_G in the vertical during the lifetime of β^+-o-Ps ($\tau_{\text{o–Ps}} \leqslant 1.42 \cdot 10^{-7}$ s)

$$h_G = 2 \cdot \frac{g\,\tau^2_{\text{o–Ps}}}{2} \leqslant 10^{-11} \text{ cm.}$$

Since $h_G \gg r_w$ and r_{str}, in the final start of the β^+-decay of ^{22}Na, ^{64}Cu, ^{68}Ga nuclei (TQT in the presence of β^+-o-Ps) at the nodes of the LRA Core, the quasiprotons of the VSM$^{\text{“}+\text{''}}$ ($\bar{p}$) are released (decompensation of the baryon charge) but the electric charges of the quasiprotons and the charges of the quasi-electrons of the VSM$^{\text{“}+\text{''}}$ ($\bar{p}^+$, $\bar{e}^-$) are compensated by the TLG$^{\text{“}-\text{''}}$ ($\bar{p}^-$, $\bar{e}^+$).

This means that there is no Coulomb barrier in the interaction of the LRA Core with the nuclei of the substance atoms. As a result, a Rigid Body/RB is formed (^{22}Ne) in the system

$$^{22}\text{Na}\,(3^+) \longrightarrow {}^{22*}\text{Ne}\,(2^+) \longrightarrow$$
$$^{22}\text{Ne}\,(0^+) - \text{gaseous neon } (8.86\%\ {}^{22}\text{Ne}).$$

by way exchange interaction of the quasiprotons of the ^{22}Na nuclei from gas with the quasiprotons of the LRA Core at nodes ($\bar{n}$) during the lifetime of the β^+-o-Ps ($\tau_{\beta^+-o-Ps} \leqslant 1.42 \cdot 10^{-7}$)-collectivization of the γ_n-quantum ("resonance conditions" — the Mössbauer effect)

$$^{*22}\text{Ne}\,(2^+) \xrightarrow{\gamma_n \simeq 1.274\text{ MeV}} {}^{22}\text{Ne}\,(0^+).$$

It is interesting that the ratio of the macroscopic dimensions of the LRA to the size of the LRA Core on the order of magnitude is equal to this ratio for atoms of the ordinary substance

$$\sqrt[3]{\frac{N^{(3)}}{\bar{n}}} \simeq \frac{r_H}{r_p} \simeq 10^5,$$

where r_H and r_p, respectively, are the radii of the hydrogen atom and the proton.

Conceptually, the stated phenomenology seems to have for a long time been foreseen:

"*A week energy conditions is not satisfied for the 'C-field' proposed by Hoyle and Narlikar* ⟨[7]⟩, *which is also a scalar field $m = 0$; only this time the energy-momentum tensor has the opposite sign and, consequently, the energy density is negative. In view of this, simultaneous production of quanta of fields with positive energy and C-field with negative energy is possible. This process take place in a stationary universe proposed by Hoyle and Narlikar, in which, as the particles increase, a new substance is continuously created as a result of the general expansion of the universe, so that a constant average density is maintained. However, such a process causes difficulties in terms of quantum mechanics. Even if the cross section of such process is very small, the presence of an infinite phase volume for quanta of positive and negative energy would lead to the production of an infinite number of pairs in a finite region of space-time*" [8].

With the adoption of the considered model, the process of real one-quantum annihilation of the β^+-o-Ps is

$$\beta^+\text{–o–Ps/p-Ps}' \longrightarrow \gamma\, U^{\pm}(\gamma^{\circ}/2\gamma'),$$

where γ° is a notoph [9], p-Ps′ is a parapositronium in the TLG, γ' is a photon/notoph in TLG and β^+-decay of nuclei of the type $\Delta J^{\pi} = 1^{\pi}$ with "resonance conditions" (EM) in the final state of the TQT [2, 3]

$$^{22}\text{Na}\,(3^+) \xrightarrow{e^+_{\beta}\,+\,\nu\,+\,U^{\pm}} {}^{22*}\text{Ne}\,(2^+) \xrightarrow{\gamma_n \simeq 1.274\text{ MeV}}$$
$$^{22}\text{Ne}\,(0^+) - \text{gaseous neon } (8.86\%\ {}^{22}\text{Ne}).$$

At the same due to the interaction of the neon atoms from the gas (90.88% ^{20}Ne, 0.26% ^{21}Ne) with the lattice nodes of the LRA Core, a quasi-nucleus [^{22}Ne–$\bar{p}$] ⇔ ^{22}Na is formed, since the nuclear-mass defect ^{23}Na (−9.5296) is maximal in comparison with ^{22}Na (−5.1840) and ^{21}Na (−2.1858).

The model realizes the thought first expressed in the report of M. Faraday to the Royal Society "*On the possible connection of gravity to electricity*" (November 28, 1850) — "*A long and unchanging conviction that all the forces of Nature are in mutual communication, having a common or rather, representing different manifestations of the single basic force…*" — the connection of physical interactions, including strong and weak (electroweak) interaction [10], open in the twentieth century.

Submitted on September 27, 2018

References

1. Rubakov V.A. The Null Energy Condition and its violation. arXiv: 1401.4024v2 [hep-th]; *Phys. Usp.*, 2014, v. 57(2), 128.
2. Levin B.M., Kochenda L.M., Markov A.A., Shantarovich V.P. Time spectra of annihilation of positrons (^{22}Na) in gaseous neon of various isotopic compositions. *Sov. J. Nucl. Phys.*, 1987, v. 45(6), 1119.
3. Levin B.M. Atom of Long-Range Action Instead of Counter-Productive Tachyon Phenomenology. Decisive Experiment of the New (Additional) Phenomenology Outside of the Light Cone. *Progress in Physics*, 2017, v.13(1), 11; Levin B.M. Half-Century History of the Project of New (Additional) Physics. *Progress in Physics*, 2017, v. 13(1), 18.

4. Rubakov V.A. Consistent NEC-violation: towards creating a universe in the laboratory. arXiv:1305.2614v2 [hep-th]; *Phys. Rev. D*, 2013, v. 88, 044015.
5. Levin B.M. On the kinematics of one-photon annihilation of orthopositronium. *Phys. Atom. Nucl.*, 1995, v. 58(2), 332.
6. Di Vecchia P., and Schuchhardt V. $N = 1$ and $N = 2$ supersymmetric positronium. *Phys. Lett. B*, 1985, v. 155(5/6), 427.
7. Hoyle F., Narlikar J.V. C-field as direct field of particles. *Proc. Roy. Soc. A*, 1964, v. 282, issue 1382, 178.
8. Hawking S.W., Ellis J.F.R. Large-Scale Structure of Space-Time. Camb. Univ. Press, 1973.
9. Ogievetsky V.I. and Polubarinov I.V. The notoph and its possible interactions. *Sov. J. Nucl. Phys.*, 1967, v. 4(1), 156.
10. Kotov B.A., Levin B.M., Sokolov V.I. Orthopositronium: "On the possible relation of gravity to electricity". Preprint No. 1784, A. F. Ioffe Physical Technical Institute Russian Academy of Sciences, Saint-Petersburg, 2005; arXiv: quant-ph/0604171.

On the Nature and Values of the Gravitational and Cosmological Constants

Anatoly V. Belyakov
E-mail: belyakov.lih@gmail.com

Stable particles of the Universe — protons and electrons — are in constant motion (there is a background component of their velocity), which is the source of the vacuum energy, explains the non-Newtonian vacuum potential and the curvature of space and determines the values of the gravitational and cosmological constants. This follows from the balance of interactions between a free electron and a proton, provided that there are no electrical forces and external influences.

1 Introduction

The origin and nature of the gravitational constant γ and, in particular, the cosmological constant Λ, introduced by Einstein into the equations of the general theory of relativity, are still the subject of discussion [1–3]. The cosmological constant determines the non-Newtonian gravitational forces and characterizes the curvature of empty space, as if additional mass or energy was introduced into it, and has a dimension of m^{-2}.

One of the points of view is that the vacuum itself is material, and the space containing it rotates. That is, for the Universe being in the stationary state, it is necessary that the inertial forces field generated by rotation compensate for the vacuum gravitational attraction [3]. However, the question arises, is it really necessary to endow vacuum with a mass and space with rotation to maintain such a balance?

Indeed, there is a geometrodynamic concept (J. Wheeler et al. [4, 5]), in which, in fact, the materiality of space itself is postulated, and in this space the initial one-dimensional spatial elements can be organized into the three-dimensional objects that one can observe. Then the original primary elements, if they are real entities, not mathematical abstractions, should in its physical incarnation be vortex structures being based on the phase boundary (surface).

So, according to Wheeler, charged microparticles are singular points on the three-dimensional surface of our world, connected by a "wormhole", i.e. a vortex tube or a power current line (of the input-output kind) located in an additional dimension. As a result, a *closed* contour is formed which a physical vacuum or some medium circulates along. Wheeler's idea, even in a simple mechanistic interpretation, allows to use macroanalogies successfully for objects of any matter organization levels: see [6, 7] etc. In particular, in determining the speed of light, it was sufficient to apply Wheeler's scheme for a single closed proton-electron contour [8].

2 The gravitational constant in geometrodynamics

Let us consider, as in the case of determining of the light speed, a single spatial-material cell, where there is a balance of forces acting between a proton and an electron. Assume that in this case the particles are in a free state, not bound to an atom, and there are no electrical forces and external influences. That is, it is assumed that a hydrogen atom is formed only when the particles approach the distance of the Bohr radius, and as for the atom larger size (the excited state), it arises only when the atom receives additional energy.

Indeed, if the contour *is not closed*, then the "photon exchange" does not occur, and there are no electric forces between the proton and the electron, and the electron can not "rotate" around the proton if the distance between them exceeds the Bohr radius. Then, in the state of equilibrium particles must move rectilinearly, changing only their mutual position. The particles themselves, according to Wheeler, if the contour is open, can be considered as single-pole vortex formations. They interact with each other through gravity and also retain the magnetic interactions between their vortex tubes (force lines) extending into "extra" dimension. These forces between the particles must be compensated by the inertial quasi-centrifugal forces, determined in the case of rectilinear motion of particles with respect to the instantaneous radius equal to the distance between the particles.

We recall that in [6, 7] the formula for electric and magnetic forces are written in the "Coulombless" form, where the charge is replaced by the electron ultimate momentum. It is assumed that the unit element of such a tube is an element having the size of the classical electron radius r_e and its mass m_e. In this case, the electric and magnetic constants have the form:

$$\varepsilon_0 = \frac{m_e}{r_e} = 3.23 \times 10^{-16}\ \text{kg/m}, \tag{1}$$

$$\mu_0 = \frac{1}{\varepsilon_0 c^2} = 0.0344\ \text{N}^{-1}, \tag{2}$$

where m_e, r_e, c are the electron mass, the electron radius, and the light speed. The balance between magnetic, inertial and gravitational forces has the form:

$$z_{e_1}\, z_{e_2}\, \mu_0^{-1}\, \frac{l}{2\pi r}\left(\frac{r_e}{c \times [\text{sec}]}\right)^2 + z_{g_1}\, z_{g_2}\, \mu_0^{-1}\, \frac{\varepsilon_0 \gamma / c^2}{r^2} = z_g\, \mu_0^{-1}\, \frac{(v_0/c)^2}{r}\,, \tag{3}$$

where l, r, v_0, z_e, z_g are the relative length of the vortex tube in units of r_e, the relative distance between the particles in units of r_e, the relative to each other velocity of the particles, the relative charge and mass in electron charges and masses. Making transformations and neglecting the electron mass, we represent (3) in the form:

$$r\,\frac{l}{m_p}\,\frac{r_e^2}{2\pi\times[\mathrm{sec}^2]} - r v_0^2 = \varepsilon_0\gamma\,, \tag{4}$$

where m_p is the relative proton mass in units of m_e. Thus, an equation has been obtained having the velocity squares dimension, and these terms of the equation are proportional to the energies of the corresponding interactions.

As for the vortex tube length, then $a < l < m_p$ (a is the fine structure inverse constant), since the electron spin ($a r_e m_e c/2$) means the presence of either a "hidden" mass or a linear parameter in its structure which is increased not less than 137 times with respect to the electron standard parameters, even if the spin speed of rotation is equal to the light speed. On the other hand, l can not exceed of the proton vortex tube length (with correction for the projection angle) [7].

To maintain the equilibrium state, the velocity v_0 must be constant for any distance between particles, including for limiting cases. Neglecting the gravitational component at $r \to \infty$ and $l = m_p$, we obtain from (4):

$$v_0 = \frac{r_e}{(2\pi)^{1/2}\times[\mathrm{sec}]} = 1.12\times10^{-15}\ \mathrm{m/sec}. \tag{5}$$

Neglecting the magnetic component, when the distance between the particles is equal to the Bohr radius R_B, i.e. for $r = a^2$, we obtain:

$$v_0 = \frac{(\varepsilon_0\gamma)^{1/2}}{a} = 1.07\times10^{-15}\ \mathrm{m/sec}, \tag{6}$$

which actually coincides with the previous value. It can be reasonably assumed that this velocity is constant throughout the entire range of distances between particles — from the Bohr radius size to infinity — and it is a fundamental value, so that one can derive a formula for the gravitational constant. Bearing in mind (4) and (5), we obtain:

$$\gamma = r\left(1-\frac{l}{m_p}\right)\frac{v_0^2}{\varepsilon_0}\,. \tag{7}$$

At the Bohr radius distance, substituting $r = a^2$, $l = 137$ and the v_0 value, we find $\gamma = 6.79\times10^{-11}\ \mathrm{m^3kg^{-1}sec^{-2}}$, which is close to the actual value. Since $\gamma = const$, an increase in the distance between particles must be accompanied by in the vortex tubes length increase (the "hidden" mass) up to the value m_p.

We note that homogeneous particles behave otherwise. From the balance of interactions it follows that the free electrons must come together, and the free protons, on the contrary, move away from each other, starting from some distance between them. This difference, perhaps, contributes to the separation of particles in outer space.

The correct value of the gravitational constant for a single proton-electron unit cell has been obtained, and its value does not change when passing to cosmological scales. This gives grounds to believe that this scheme can be extended to the Universe level as a whole.

3 The cosmological constant

The equation (4) can be interpreted in the sense that the gravitational energy proportional to $\varepsilon_0\gamma$ is, as it were, a background or additional constant that ensures the equilibrium state of an elementary space-material cell regardless of its size, and the motion of free particles with velocity v_0 is something similar to cosmic "Brownian motion". Within the framework of this model, it is this motion of free particles that, when passing to cosmological scales, creates its own vacuum potential (which is perceived by an external observer as a manifestation of non-Newtonian forces) and determines the cosmological constant magnitude.

The inverse quantity Λ^{-1} can be regarded as the surface area on which the inertial forces, arising during rotation of the Universe as a whole with a background velocity v_0 over some radius L, act.

These forces counteract gravitational forces. In this case, the magnetic forces can be neglected, since in space macrobodies are in general electrically neutral. For the Universe being in equilibrium state, taking into account only the forces associated with masses, bearing in mind (4), one can write down the balance of pressures produced by these forces:

$$\frac{M\varepsilon_0\gamma}{L^3} = \frac{M r v_0^2}{L\,\Lambda^{-1}}\,, \tag{8}$$

where M is an arbitrary mass, L is a linear parameter (radius).

The balance does not depend on the mass of the Universe, but depends on its parameter L. Both the shape of the Universe and the position of its center are undefined, and any of its points can be taken as the center of rotation, so its volume can be taken equal to L^3, and the radius of rotation is equal to the parameter L. In [9] the basic parameter of the Universe L_v is uniquely defined as the length of a vacuum structural unit (vortex tube):

$$L_v = \frac{R_c^2}{R_B}\,, \tag{9}$$

where R_c is a mean geometric, the linear parameter obtained from the balance of electric and magnetic forces and equal to $(2\pi)^{1/2}c\times[\mathrm{sec}] = 7.51\times10^8$ m. The parameter L_v is the *greatest* length to which the *lowest* peripheral speed v_0 corresponds.

The formal increase in the kinetic energy component in formula (8) a multiple of r, while maintaining the balance of pressures, requires that in this case there should be $L = L_v r^{-1/2}$, so the parameter r in (8) is reduced. As a result, referring to (5), (9) and revealing R_c and R_B, (8) we obtain:

$$\Lambda = \frac{\varepsilon_0 \gamma}{(L_v\, v_0)^2} = \frac{1}{2\pi}\left(\frac{a}{c}\right)^4 \varepsilon_0 \gamma \times [\text{sec}^{-2}] = \\ = 1.49 \times 10^{-52}\ \text{m}^{-2}, \quad (10)$$

and such a value must correspond to the equilibrium state of the Universe. At present, based on the assumed age of the Universe, the value of Λ is estimated at 10^{-52} m^{-2} [10].

Perhaps there are regions of space filled with free elementary particles that are not bound to atoms (voids). Then it is necessary to consider the sum of set of unit elementary cells, taking into account the magnetic forces, and then the sum in brackets in an analogous formula is close to one:

$$\Lambda = \left(\frac{l}{m_p} + \frac{\varepsilon_0 \gamma}{r v_0^2}\right)\frac{1}{L^2} \approx L^{-2}. \quad (11)$$

In this case, there is a trivial uncertain result, depending only on the region size $\Lambda^{-1/2}$.

As for the hypothetical form of the Universe, the ratio $L_v/\Lambda^{-1/2} = 130.6$ is a very characteristic value close to a. Let us assume that the properties of vorticity and helicity are inherent in the structure of the Universe as a whole, as well as of its constituent units. Then the size $\Lambda^{-1/2} = 8.2 \times 10^{25}$ m can be associated with the diameter of its vortex tube, and the size $L_v = 1.06 \times 10^{28}$ m with the size of a spiral turn, the number of turns is indeterminate and they are directed along the time axis to infinity. Note that this size has the same order of magnitude as the ultimate radius of the event horizon (0.59×10^{28} m), calculated by di Bartini [11]. Some hints on the unusual form of the Universe are found in [12], where cosmological effects are given, which the authors explain by the shape of the Universe resembling a horn or a saddle.

4 Conclusions

The stable particles of matter — protons and electrons are in continuous motion (the background component of its velocity). This follows from the balance of magnetic, gravitational and inertial interactions under the condition that there are no electrical forces and external influences. At cosmological scales, the field of inertial forces generated by their motion compensates for the gravitational attraction of the Universe matter as a whole. It is this balance applied to a unit cell containing a proton and an electron that determines the gravitational constant value, and, as applied to the Universe as a whole, determines the cosmological constant value. From the observer's point of view, Λ-field manifests itself as a result of the action of non-Newtonian gravitational forces, and therefore there is no need to involve dark energy and dark matter to substantiate this field.

Submitted on September 18, 2018

References

1. Weinberg C. S. The cosmological constant problem. *Reviews of Modern Physics*, 1989, v.61, 1–23.
2. Carroll S.M. The Cosmological Constant. *The Living Reviews in Relativity*, 2001, v.4, 1–56.
3. Yermolenko Yu. The cosmological constant problem. http://cdn.scipeople.ru/materials/55751/The_cosmological_constant_problem.pdf
4. Dewitt B.S. Quantum gravity. *Scientific American*, December 1983, v.249, 112–129.
5. Berera A., Buniy R.V., Kephart T.W., Päs H., and Rosa J.G. Knotty inflation and the dimensionality of spacetime. arXiv: 1508.01458.
6. Belyakov A.V. Charge of the electron, and the constants of radiation according to J.A.Wheeler's geometrodynamic model. *Progress in Physics*, 2010, v.6, issue 4, 90–94.
7. Belyakov A.V. Macro-analogies and gravitation in the micro-world: further elaboration ofWheeler's model of geometrodynamics. *Progress in Physics*, 2012, v.8, issue 2, 47–57.
8. Belyakov A.V. On the Speed of Light and the Continuity of Physical Vacuum. *Progress in Physics*, 2018, v. 14, issue 4, 211–212.
9. Belyakov A.V. On the independent determination of the ultimate density of physical vacuum. *Progress in Physics*, 2011, v. 7, issue 2, 27–29.
10. Borissova L., Rabounski D. Fields, Vacuum and the Mirror Universe. Swedish Physical Archive, Stockholm, 2009, Ch. 5, §5.4.
11. Oros di Bartini R. Relations Between Physical Constants. *Progress in Physics*, 2005, v.1, issue 3, 34–40 (English translation from the 1966 original manuscript).
12. Aurich R., Lustig S., Steiner F., and Then H. Hyperbolic Universes with a Horned Topology and the CMB Anisotropy. arXiv: astro-ph/0403597.

Progress in Physics is an American scientific journal on advanced studies in physics, registered with the Library of Congress (DC, USA): ISSN 1555-5534 (print version) and ISSN 1555-5615 (online version). The journal is peer reviewed and listed in the abstracting and indexing coverage of: Mathematical Reviews of the AMS (USA), DOAJ of Lund University (Sweden), Scientific Commons of the University of St.Gallen (Switzerland), Open-J-Gate (India), Referential Journal of VINITI (Russia), etc. Progress in Physics is an open-access journal published and distributed in accordance with the Budapest Open Initiative: this means that the electronic copies of both full-size version of the journal and the individual papers published therein will always be accessed for reading, download, and copying for any user free of charge. The journal is issued quarterly (four volumes per year).

Electronic version of this journal: http://www.ptep-online.com

Postal address:
Department of Mathematics and Science, University of New Mexico,
705 Gurley Avenue, Gallup, NM 87301, USA